JOURNAL OF BIOLOGICAL REGULATORS & HOMEOSTATIC AGENTS
Volume 33, No. 2, March - April, 2020

CONTENTS

Editorials

L. Della Valle, A. Gatta, A. Farinelli, G. Scarano, A. Lumaca, N. Tinari, F. Cipollone, R. Paganelli and M. Di Gioacchino. Allergooncology: an expanding research area 319

P. Conti, G. Ronconi, Al. Caraffa, C.E. Gallenga, R. Ross, I. Frydas and S.K. Kritas. Induction of pro-inflammatory cytokines (IL-1 and IL-6) and lung inflammation by coronavirus-19 (COVI-19 or SARS-CoV-2): Anti-inflammatory strategies 327

P. Conti, C.E. Gallenga, G. Tetè, Al. Caraffa, G. Ronconi, A. Younes, E. Toniato, R. Ross and S.K. Kritas. How to reduce the likelihood of coronavirus-19 (CoV-19 or SARS-CoV-2) infection and lung inflammation mediated by IL-1 333

P. Conti and A. Younes. Coronavirus COV-19/SARS-CoV-2 affects women less than men: clinical response to viral infection 339

Original articles

Y. Xu, S. Zhang, D. Fu and D. Lu. Circulating miR-374b-5p negatively regulates osteoblast differentiation in the progression of osteoporosis via targeting Wnt3 and Runx2 345

Z.-Z. Yao, H.-C. Tan, J.-F. Chen, T. Jin, C.-S. Zhou, J. Liang and A.-X. Hu. Suppression of P38/HBP1 pathway alleviates hyperosmotic stress-induced senescent progression of chondrocyte senescence 357

SJ. Li, QH. Mei, SY. Zeng, LL. Lai, J. Quan and X. Zhang. Protective effect of sonic hedgehog signaling pathway activation on acute myocardial infarction 367

L-P. Lian and X-Y. Xi. Long non-coding RNA XIST protects chondrocytes ATDC5 and CHON-001 from IL-1β-induced injury via regulating miR-653-5p/SIRT1 axis 379

XQ. Kan, YB. Li, B. He, SF. Cheng, YJ. Wei and JL. Sun. MiR-1294 acts as a tumor inhibitor in cervical cancer by regulating FLOT1 expression 393

B. Liu, T. Xu and Y. Meng. lncRNA NEAT1 aggravates cerebral ischemia/reperfusion injury by sponging miR-874-3p 403

S. Wang, X. Wang and SL. Xu. LINC00473 promotes lung adenocarcinoma progression by regulating miR-1294/ROBO1 axis 411

H. Li, MW. Liu, W. Yang, LJ. Wan, HL. Yan, J-C. Li, SY. Tang and YQ. Wang. Naringenin induces neuroprotection against homocysteine-induced PC12 cells via the upregulation of superoxide dismutase 1 expression by decreasing miR-224-3p expression 421

X.-B. Liu, H. Xia, G. Wang, W. Zhang, Y. Hu and J. Zhang. Propofol relieves oxidative stress response of cerebral ischemia-reperfusion injury through SIRT1 signaling pathway 435

H.-L. Lv, J. Yu, J.-F. Pei, H.-Y. Wang and Z.-L. Guo. TIR-domain-containing adapter-inducing interferon-β contributes to TLR3/TLR4 triggered apoptosis and inflammation in nucleus pulposus cells 445

P. Guan, W.-T. Cai, F. Jiang, W. Li, M. Zeng and J. Wu. Caveolin-1 improves lung injury in rats with chronic obstructive pulmonary disease partially through Wnt/β-catenin signaling pathway 457

L-M. Tao, Y-F. Gong, H-M. Yang, J-H. Pei, X-J. Zhao and S-S. Liu. LINC00662 promotes glycolysis and cell survival by regulating miR-375/HIF-1α axis in ovarian cancer 467

Q. Guo, X-H. Ren, C-P. Zhao and B-H. Zhang. MicroRNA-206 inhibits tumor metastasis of nasopharyngeal carcinoma through targeting G6PD 479

X. Qin, XY. Wang, JW. Fei, FH. Li, J. Han and HX. Wang. MiR-20a promotes lung tumorigenesis by targeting RUNX3 via TGF-β signaling pathway 487

F. Yan, S-W. Liu, X-Y. Li, C-C. Li and Y. Wu. Silencing LncRNA LINC01305 inhibits epithelial mesenchymal transition in lung cancer cells by regulating TNXB-mediated PI3K/Akt signaling pathway 499

X.-L. Zhang and Z. Liu. MiR-19a inhibitor improves diabetic retinopathy in rats through PTEN/Akt/P-Akt signaling pathway 509

G-B. Zhong, C-Q. Jiang, X-S. Yu, Z-D. Liu, W-L. Wang and R-D. Xu. Long noncoding RNA SNHG8 promotes the proliferation of osteosarcoma cells by downregulating miR-542-3p 517

LJ. Cai, MF. Wang, XL.Wang, HF. Zhu and XZ. Chen. Effects of sDR5-Fc fusion protein on infant mice with ulcerative colitis via the TRAIL-DR5 pathway 525

Letters to the Editor

KL. Liu, HX. Chen, Y. Liu and QM. Fu. Correlation of maternal components and blood lipids during pregnancy with the onset of preeclampsia 535

LF. Xiong, YM. Lou and L. Wang. Expressions of Kif2c and Ki-67 in non-small cell lung cancer and their relationship with invasion and metastasis 541

H. Jiang, XF. Yin, JY. Yu and CY. Su. The implication of interleukin-1β in the development and progression of multiple myeloma 547

Y. Xu, L. Wang and J. Liu. miR-130a inhibits cell viability and migration through FOSL1 in lung cancer 553

YL. Huang, F. Ju, SC. Lai, ZC. Chen, XY. Chen, LH. Zhou and MX. Fu. Effects of negative pressure wound therapy associated with local insulin injection on TGF-β1 expression in diabetic foot wounds 559

A. Almousa, M.A. Kamran, A. Alshahrani and I. Alshahrani. Influence of diabetes mellitus on tooth eruption and occurrence of malocclusion 565

ZQ. Zhou, HH. Yang, GZ. Cui, CF. Wang, XF. Zheng, XF. Wang, J. Liu and HL. Li. Expression levels of alpha-smooth muscle actin in intrarenal arterioles of patients with different stages of chronic kidney disease 571

YJ. Yang, Z. Wang, RX. Zheng, Y. Li, L. Wang, YM. Liu, X. Wang, R. Su, QH. Dai and C. Liu. DNA microarray analysis of dendritic cells infected by *Enterovirus 71* 577

Y. Liu, Z. Wang, R. Wang, Y. Liu, X. Yu, Y. Zhang, Y. Li. and Q. Xu. A rat model of buccal orthodontic force on periodontal tissues 585

M. Li, CY. Zhang, WJ. Li, CF. Zhu and WH. Zhang. Improving model of corneal fungal-induced ulcer in rabbit 593

LL. Zheng, XY. Zhang, H. Zhang, Y. Wang and Y. Zhou. Expression levels of filamin A in preeclampsia placenta 599

C. Deng, BY. Ren, XP. Huang, JJ. Tan, JJ. Wu, W. Wang and C. Zhu. Role of lymphocyte subsets and IL-17 in non-small cell lung cancer 605

E. Anitua and M.H. Alkhraisat. Plasma rich in growth factors in the management of medically compromised patients in oral surgery 611

YD. Kim, YS. Choi, HG. Na, SY. Song and CH. Bae. Ginsenoside Rb1 attenuates LPS-induced MUC5AC expression via the TLR4-mediated ERK1/2 and NF-κB pathway in human airway epithelial NCI-H292 cells 613

WJ. Lian, P. Duan, XP. Lu, TT. Lu and H. Zheng. Chromosome 14-linked disease misdiagnosed as Prader-Willi syndrome 619

F. Gao, J-Y. Ren, B-J. Bi, L-J. Lu, Z. Han and Y-H. Pan. Double Kirschner-wires percutaneous antegrade intramedullary fixation for treatment of unstable phalangeal neck fractures in adults 623

JW. Dai, LQ. Hong, MF. Han, L. Lin and ZW. Duan. Effects of propofol and gas anesthesia on cognitive impairment in elderly patients after surgery 629

S.K. Bhavikatti and N.A. Alqahtani. Antimicrobial efficacy of a new *Mimusops elengi (Linn*) incorporated herbal product on selected oral and periodontal pathogens: an *in-vitro* microbiological study 635

H. Meng, Y. Mo, T. Cheng, H. Zhang, L. Wu, N.K. Shah, C. Shu and J. He. Spontaneous rupture of kidney during pregnancy 643

T. Fei, CX. Guo, J. Zhang, LN. Wang and WW. Fan. The role of p38MAPK signaling pathway in hepatocellular carcinoma recurrence 647

S-Z. Wang, L-R. Guo, X. Duan, Y. Yao, D. Wang, X-J. Zhang and Y-S. Tian. Application of endoscopic sinus surgery in hemostasis for epistaxis 655

A. Sharma, R. Surve, R. Dhurat, R. Sinclair, Y. Tan, Y. Zou, P. Müller Ramos, C. Wambier, I. Verner, M. Kovacevic and A. Goren. Microneedling improves minoxidil response in androgenetic alopecia patients by upregulating follicular sulfotransferase enzymes 659

YH. Gao, GN. Li, J. Jia, WC. Wang, Y. Duan, H. Wei, T. Li, MY. Li, X. Zhong and XQ. Li. Significance of tissue transglutaminase in myocardial fibrosis after myocardial infarction in rats 663

DQ. Deng, ZF. Lang, CX. Xing and S. Li. Mechanism of genistein combined with changes in CaSR activity on gastric cancer cells 669

S.P. Cannavò, G. Riso, E. Di Salvo, M. Casciaro, R. Giuffrida, P.L. Minciullo, F. Guarneri, E. Nettis and S. Gangemi. Oxidative stress involvement in urticaria 675

P.C. Passarelli, V. Desantis, P. De Angelis, G.B. Piccirillo, V. Giovannini, P. Papi, G. Pompa and A. D'Addona. Prophylaxis with rFVIIa before third molar extraction in a patient with Factor VII deficiency 679

D. Melchionda, G. Varvara, D. Perfetto, B. Mascolo and C. Avolio. Perceptive and subjective evaluation of speech disorders in Parkinson's disease 683

G. Ferrone, E. Tamburello, R. Nestorini, G. Concina, A. Chierichini, M. Rossi and A. Vergari. Dexmedetomidine sedation associated with suprainguinal fascia iliaca block for hip fracture surgery in high risk elderly patients 687

G.A. Pacino, L.M. Redondo, S. Cocuzza, A. Maniaci, M.C. Da Mosto, P. Boscolo-Rizzo, G. Tonoli, G. Mannelli and G. Spinato. Primary hemangiopericytoma of the infratemporal fossa 691

A. Notarnicola, G. Maccagnano, L. Moretti, M. Salvemini, F.P. Bianchi, I. Covelli, S. Tafuri and B. Moretti. Conservative treatment of sacroiliac joint pain with extracorporeal shockwave therapy 697

G. Ronconi, S. Salini, G. Maccauro, M. Mammucari and P.E. Ferrara. Adverse events in dry needling and mesotherapy treatment for localized myofascial and muscoloskeletal pain 705

A. Notarnicola, G. Maccagnano, L. Maresca, M.C. Oliva, G. Farì, G. Papagni, G. Pignatelli, I. Covelli, G. Gioia, F.P. Bianchi, S. Tafuri and B. Moretti. Is extracorporeal shockwave therapy effective even in the treatment of partial rotator cuff tear? 709

G. Magliulo, A. Pace, R. Plateroti, A.M. Plateroti, R. Cascella, C. Solito, V. Rossetti and G. Iannella. Laryngopharyngeal reflux disease in adult patients: tears and pepsin 715

M. Rondanelli, D. Guido, M.A. Faliva, C. Gasparri, G. Peroni, G. Iannello, M. Nichetti, M. Naso, V. Infantino, D. Spadaccini, S. Perna and R. Aquilani. Effects of essential amino acid supplementation on pain in the elderly with hip fractures: a pilot, double-blind, placebo-controlled, randomised clinical trial 721

L. Santacroce, N. Sardaro, S. Topi, F. Pettini, L. Bottalico, S. Cantore, G. Cascella, R. Del Prete, G. Dipalma and F. Inchingolo. The pivotal role of oral microbiota in health and disease 733

A. Giudice, F. Bennardo, A. Antonelli, S. Barone, F. Wagner, L. Fortunato and H. Traxler. Influence of clinician's skill on primary implant stability with conventional and piezoelectric preparation techniques: an *ex-vivo* study 739

JOURNAL OF BIOLOGICAL REGULATORS & HOMEOSTATIC AGENTS Vol. 34, no. 2, 319-326 (2020)

EDITORIAL

ALLERGOONCOLOGY: AN EXPANDING RESEARCH AREA

L. DELLA VALLE[1], A. GATTA[1], A. FARINELLI[1], G. SCARANO[1], A. LUMACA[1], N. TINARI[2], F. CIPOLLONE[3], R. PAGANELLI[1] and M. DI GIOACCHINO[1]

[1]Specialization School of Allergy and Clinical Immunology, G. d'Annunzio University, Chieti-Pescara, Italy; [2]Specialization School of Oncology Department of Medicine and Science of Ageing, G. d'Annunzio University, Chieti-Pescara, Italy; [3]Internal Medicine of the Department of Medicine and Science of Ageing, G. d'Annunzio University, Chieti-Pescara, Italy

Received September 30, 2019 – Accepted March 10, 2020

The relationship between allergic diseases and cancer is a very controversial topic, widely discussed in the last decades. Many studies have demonstrated inverse association between allergy and cancer, but others have reached neutral conclusions or have indicated a positive role of allergy in the development of cancer. However, either inhibiting or favoring, many cells and molecules relevant in the allergic process play a role in tumorigenesis. On the one hand, activated immune cells, like classically activated macrophages "M1", activated dendritic cells, IL-33 and amphiregulin stimulated Innate Lymphoid Cells (ILC2), Th1, IFN-γ producing T CD8+ and B lymphocytes have inhibitory effects on tumorigenesis and tumor progression. On the other hand, tolerogenic immune cells, like alternatively activated macrophages "M2" (M2a, M2b and M2c), tolerogenic dendritic cells, ILC3, T regulatory and B regulatory lymphocytes, while inhibiting allergic sensitization and response, appear to favour carcinogenesis. Furthermore, M2 subtypes macrophages (M2a, M2b), IL-25 stimulated ILC2 and Th2 lymphocytes have a role both in inducing allergic reactions and in favouring cancer progression. In addition, mast cells, pivotal cells in allergy, have a different effect of tumorigenesis based on their location - they can promote cancer progression or inhibit it. Finally, eosinophils have shown a prevalent tumoricidal function mediated by α-defensins, TNF-α, granzymes A and IL-18. Better understanding the role of various cells on carcinogenesis can help in developing new strategies (diagnostic, therapeutic and of follow up) against tumor.

The relationship between allergic diseases and cancer is a very controversial topic, widely discussed in the last decades. Allergy published two well-documented studies on this topic in 2005. The first, carried out at the Stockholm Karolinska Institute, analyzed the possible presence of neoplasia in various organs and the allergic condition of 70,000 patients, reaching a neutral conclusion that allergy does not protect or promote the onset of tumors. The second, performed at the University of Heidelberg in Germany, was a review based on 80 previous epidemiological studies. In total, the clinical condition of 52,000 patients was analyzed, reaching a conclusion that allergy has a certain protective activity (currently, with some discrepancies) for tumors of colorectal cancer, breast, pancreas, brain (glioma, but not for meningioma) and leukemia. On the contrary, allergy could be a risk factor for lung

Key words: allergy; cancer; eosinophils; macrophages; mast cells; lymphocytes; innate lymphoid cells; dendritic cells

Corresponding Author:
Prof. Mario Di Gioacchino MD,
Department of Medicine and Science of Ageing,
G. d'Annunzio University, Chieti-Pescara,
Via dei Vestini, 66100, Chieti, Italy
Tel./fax: +39 0871357451
e-mail: mario.digioacchino@unich.it

0393-974X (2020)
Copyright © by BIOLIFE, s.a.s.
This publication and/or article is for individual use only and may not be further reproduced without written permission from the copyright holder.
Unauthorized reproduction may result in financial and other penalties
DISCLOSURE: ALL AUTHORS REPORT NO CONFLICTS OF INTEREST RELEVANT TO THIS ARTICLE.

cancer. The authors concluded that "Further research should focus on a more carefully defined 'atopy' status and manifestation of different atopic diseases, to advance our understanding of the role that allergies might play in the risk of developing cancer" (1).

Other epidemiologic studies have explored the potential association between allergy history and cancer (first of all brain, lymphatic and hematopoietic cancers). However, the majority of studies has relied on self-reported allergic history, being typically limited, retrospective and associated with potential biases. Successive observations have reported an inverse association between allergy and colorectal carcinoma, but not with hematopoietic or prostate cancer. Other studies evaluated also biological indicators of allergy history and immune function. In particular, recent evidence suggests a role for IgE

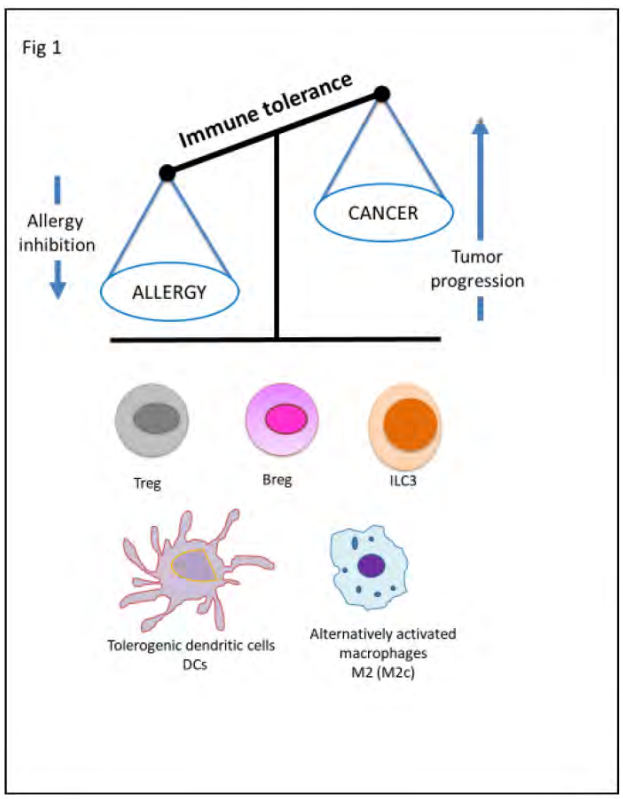


Fig. 1. *When the "immunebalance" hangs towards immune tolerance, the allergy response is inhibited and tumor progression is favored. Alternatively activated macrophages M2 (M2c), tolerogenic dendritic cells (DCs), Treg, Breg and ILC3s (Innate Lymphoid Cells type 3) appear to promote tumor progression, while inhibiting allergy sensitization and response.*

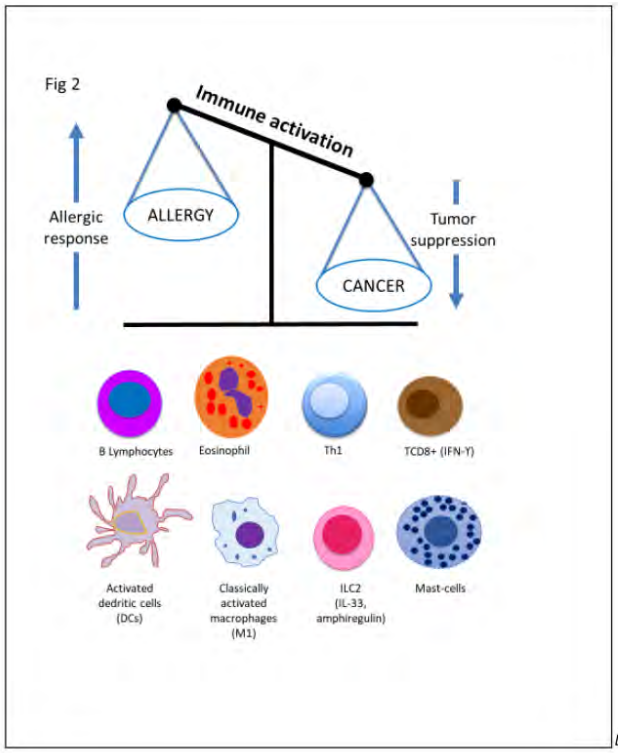


Fig. 2. *When the "immunebalance" hangs towards immune activation, the allergic response is favored and tumor progression is inhibited. Classically activated macrophages M1, activated dendritic cells (DCs), Il-33 and amphiregulin stimulated ILC2 (Innate Lymphoid Cells type2), eosinophils, mast-cells, Th2, Th1, TCD8+ (IFN-γ delivery) and B lymphocytes seem to have inhibitory effects on tumorigenesis and tumor progression. Activated dendritic cells, Th2 and eosinophils are also involved in the enhancement of allergic response.*

antibodies in natural tumor surveillance as well as in active and passive cancer immunotherapy (1). The level of total and specific IgE seems to have an inverse relationship with the development of neoplasia such as melanoma, glioma, gynecological tumors and female breast cancer (2). Further research in large-scale prospective studies using validated measures of self-reported allergy history and/or biomarkers of allergy is needed.

At present, no conclusive results have been achieved and the literature data are inconsistent and contradictory, suggesting the importance of immuno-epidemiology studies on cancer (1) that take into account other interfering factors, such as environment, lifestyle, age, sex, job, alcohol, smoking

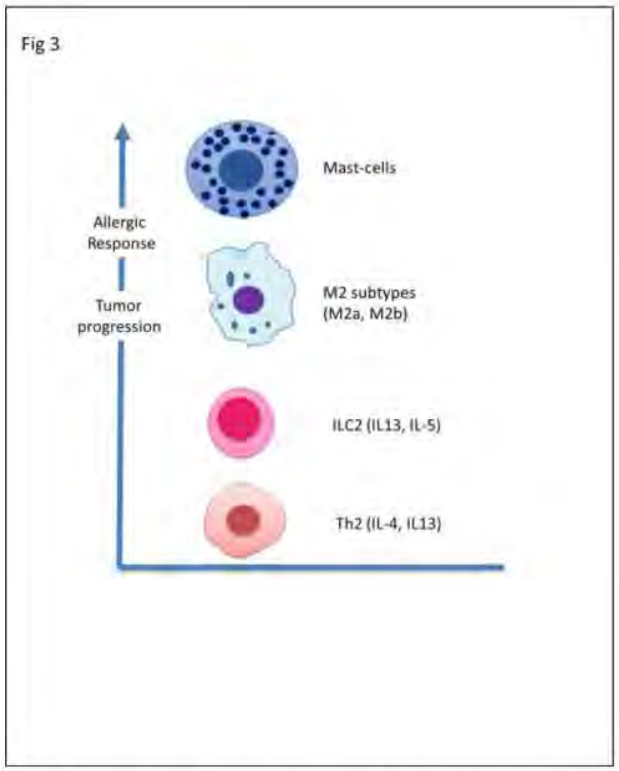


Fig. 3. *M2 subtypes (M2a, M2b), mast-cells, IL-25 stimulated ILC2 (Innate Lymphoid Cells type2) (IL-13, IL- 5,TSLP), Th2 (IL-4, IL-13) promote sensitization and allergic reactions and are associated with tumor progression.*

use, type and duration of allergic disease, other than the simple allergic status. The European Academy of Allergy and Clinical Immunology established a Task Force on AllergoOncology to evaluate the relationships between cancer and allergy with the goal of studying both allergic problems in clinical oncology and the immunomodulatory mechanisms eventually protecting cancer in order to develop new oncological immunotherapy (cellular vaccines expressing IgE-binding tumor antigens; recombinant antitumor IgE) (1).

Some speculative observations support the hypothesis of an inverse relationship between tumor growth and allergy. For example, the fact that in allergic patients the immunotolerance is desirable and is the goal of specific immunotherapy, while it is a negative mechanism in tumor microenvironment, inducing an evasion from the immune-surveillance with a promotion of tumor progression. Effectors of immunotolerance are regulatory cells and therapies blocking these cells, such as monoclonal antibodies (mAbs) against immune checkpoints, have a profound role in inhibiting tumor growth (e.g., mAbs anti-CTLA-4 and PD-1/PD-L1) (3).

Immune cells of relevance in allergy development include dendritic cells (DC), macrophages, innate lymphoid cells (ILC), lymphocytes, mast cells and eosinophils (Figs. 1, 2, 3); the comprehension of their activity on carcinogenesis and tumor restriction can explain the different results observed in epidemiological studies. Hereafter, the present knowledge on the matter is discussed (Table I).

Role of immune cells in allergy and cancer

Macrophages - Macrophages are involved in innate as well as in acquired immunity. They play an important role in the defense against pathogens through phagocytosis and the ability to generate reactive oxygen species (ROS), nitrogen intermediates and other cytotoxic factors. ROS and nitrogen intermediates are also responsible for the exacerbation of allergy and asthma severity (4). They are professional antigen-presenting cells (APC) involved in various mechanisms of allergic and autoimmune response, especially in delayed-type hypersensitivity.

Due to their microenvironmental condition, macrophages could be polarized into two phenotypes: classically activated or "M1", induced by IFN-γ and lipopolysaccharide (LPS), predominant in the first phase of inflammatory response, and alternatively activated or "M2", induced by IL-4 and IL-13, predominant in the delayed-response (wound healing, tissue repairing, carcinogenesis).

M1 were observed in exacerbation of lung injury and airway remodeling in allergic asthma via nitric oxide production. The presence of M1 macrophages in tumor microenvironment has been associated with extended survival of certain cancers (5) also through the production of several angiogenic and lymphangiogenic factors (6).

M2-polarized macrophages can be further divided into three subpopulations: M2a, M2b and M2c, according to specific stimulators (cytokines, chemokines). M2a are triggered by IL4 and IL-13

and positively correlate with the severity of airway inflammation in allergic asthma (7). In cancer, a low M1/M2a ratio was associated with poor prognosis in a variety of murine and human malignancies. M2b and M2c are involved in immune regulation, tissue remodeling, angiogenesis and tumor progression. M2b are induced by IgG immunoglobulin complex and lipopolysaccharide (LPS) and are reported in the context of allergy as well as cancer (8). M2c induced by glucocorticoids, TGF-β and IL-10 and support induction of Tregs, correlate with tumor progression and poor prognosis (1, 9).

Tumor-associated macrophages (TAMs) differentiate from circulating monocytes, recruited to tumor sites by pro-inflammatory chemokines (CCL2, CCL3, CCL5, VEGF, colony-stimulating factors GM-CSF and M-CSF). The prevalence of macrophage phenotype in tumor environment depends on the type, the stage and the place of the tumor. M1/M2 ratio determines the negative prognosis in glioma and breast cancer and the best prognosis in carcinoma of the stomach, colon, prostate and non-small cell lung (10).

The M2 phenotype predominates in hypoxic areas and seems to have unfavorable effects in tumor growth. New therapeutic strategies will be available in order to re-educate these macrophages promoting the positive effect of M1 phenotype (11).

Dendritic cells – DCs are "skilled" cells responsible for uptake, proteolytic processing and presentation of antigens to T cells. In an allergic condition, they activate naïve CD4+ T cells to differentiate into Type 2 helper T cell through the production of specific cytokines. Th2 cells and their cytokine production driven by IL-4 and IL-13 promote/facilitate the production of allergen-specific immunoglobulin E (IgE) antibodies from B cells**.** Therefore, IgE-mediated antigen presentation supports DC-based immunity rather than leading to DC-mediated tolerance. On the contrary, activated DCs are converted into tolerogenic phenotypes in the tumor microenvironment, where they promote Tregs (and not T-effector cells), with the production of TGFβ and IL-10 as an escape mechanism from immune clearance (5). Therefore, allergy and cancer have different dendritic cell phenotypes, prevailing the activated DC in atopic subjects, while the antigen presentation by tolerizing DCs is induced in cancer

Table I. *Different roles of immune cells in tumor environment*

CELLS	Tumor-promoting effect	Tumor-inhibiting effect
Macrophages	M2 phenotype (M2a, M2b, M2c)	M1 phenotype
Dendritic cells (DC)	DCs tolerogenic phenotype	DCs activated phenotype
Innate Lymphoid Cells	IL-25 stimulated (IL-13, IL-5) ILC2 ILC3	IL-33 and amphiregulin stimulated ILC2
Lymphocytes	Th2 (IL-4, IL-13, TSLP) Treg lymphocytes Breg lymphocytes	Th2 (Hodgkin's lymphoma, colon cancer cells) Th1 TCD8+ (IFN-Y) B lymphocytes
Mast cells	Mast cells	Mast cells
Eosinophils		Eosinophils

environment, preventing anti-tumor T cell responses. The possibility to drive the activation of effector DCs can be a key to stimulate anti-tumor immunity by the activation of cytotoxic CD8+ lymphocytes against tumor antigens (12).

Innate lymphoid cells– Innate lymphoid cells (ILCs) broadly reflect helper T-cell subsets. Based on their cytokine production, they are classified into 3 groups (13). ILC1s phenotypically like Th1, respond to IL-12, IL-15 and IL-18 and are defined by the production of IFN-γ. ILC2s, similar to Th2 cells, respond to epithelium-derived cytokines, such as IL-33, IL-25, TSLP, eicosanoids and IL1-β. The cells are defined by production of IL-4, IL-5, IL-9 and IL-13. Activated ILC2s participate in both initiation and enhancement of allergy, interacting with other immune cells, such as macrophages and DCs. In cancer, the stimulation of ILC2s activated by macrophages through IL-33 induces the secretion of IL-13 and IL-5, which favor tumor progression. On the other hand, amphiregulin-stimulated ILC2s can establish an immunosuppressive tumor microenvironment (13). ILC3s resemble Th17 and Th22 cells. They respond to IL-1β and IL-23 and are defined by the production of IL-17 A ed IL-22. Cells of the ILC3 subtype secrete IL-22 upon IL-23-stimulation by macrophages and have tumorigenic effects. Furthermore, ILC3 could induce tolerance by increasing IL-10 and retinoic acid secretion by DCs upon stimulation by microbiota and macrophages or by enabling T-cell tolerance through the expression of MHC Class II in the absence of costimulatory molecules. Among the ILC type, ILC3s seem to favor tumor growth and tolerance.

T and B Lymphocytes - Th2 cells play an important role in the induction and maintenance of the allergic inflammatory modulation by the production of IL-4, IL-5, IL-6, IL-9, IL-10, and IL-13. They induce differentiation, activation and in situ survival of eosinophils (through IL-5), stimulate B-lymphocytes to produce IgE (through IL-4 or IL-13), and favor mast cell and basophil growth (through IL-4, IL-9, and IL-10). Their role in cancer is controversial. It has been observed that the shift in immune response from Th1 to Th2 is characteristic of patients with more aggressive tumors (14). In some cancers, including breast, gastric and pancreas, Th2 cells and associated cytokines (IL-4 and IL-13 and TSLP) contribute to tumor progression (1). Thus, IL-4 and IL-13 receptors are promising anticancer targets. However, in some types of cancer, the Th2 have a protective role (Hodgkin's lymphoma, and colon cancer cells). Th1 and T CD8+ lymphocytes play a central role in the suppression of cancer cells both directly and through the production of IFN-γ, which mediates the activation of macrophages, as well as the presentation and processing of antigens (15).

B lymphocytes, stimulated by Th2 cytokines, produce IgE which are essential in the development of allergy. On the contrary, B regulatory cells, parallel to Treg cells, inhibit allergic sensitization.

B cells are present in many solid tumors (melanoma, colorectal, non-small cell lung) and are associated with an improved prognosis. In particular, B cells associated with T CD8+ cells suggest a cooperation between T and B lymphocytes in inducing an effective immune reaction (5). Breg cells, parallel to Treg cells, favor tumor progression, by promoting immune tolerance.

Mast cells – Mast cells are the main effector cells of allergy. They produce a large number of cytokines, chemokines, growth factors (IL-1, IL-3, IL-4, IL-5, IL-6, IL-8, IL-10, IL-13, IL-16, TNF-α, MCP-1, VEGF, NGF) and eicosanoids (prostaglandin D_2 and cysteinyl leukotrienes). These cells also release preformed mediators, such as histamine, heparin and neutral proteases (chymase and tryptase) when activated by both FcεRI-dependent and FcεRI-independent stimuli. Mast cells can also be activated by other stimuli (CD30 ligand, IL1, TLR-2), to release selected cytokines and chemokines without degranulation. They have a central role not only as effector cells of an IgE-dependent reaction, but through released proteins, participate in the initiation of the allergic immune response, providing signals inducing IgE synthesis by B-lymphocytes and Th2 lymphocyte differentiation. Beyond allergy, mast cells have critical proinflammatory activity, as well as potential immunoregulatory roles, in various immune and inflammatory disorders. They are also involved in host defense mechanisms against parasitic infestations, tissue repair and angiogenesis. Human mast cells produce VEGFs and have VEGF receptors

on their surface. They are both a source and a target of VEGF. Targeting mast cells and their angiogenic factors could be a strategy with which to block inflammatory and neoplastic angiogenesis (16).

In the context of the tumor microenvironment, multiple stimuli may serve to activate mast cells including anti-tumor antibodies, hypoxia, alarmins, cytokines and chemokines. Therefore, mast cells can have both profound tumor-promoting and tumor-inhibiting immunoregulatory effects. It seems that their role depends on microlocalization, stage of tumor and on mast cells density in intratumoral and/or peritumoral localization. In certain neoplasias (e.g, thyroid, gastric, bladder, pancreas, Hodgkin's and non-Hodgkin's lymphoma mast cells play a pro-tumorigenic role, in others (e.g., breast cancer) a protective role, whereas in yet others they are apparently innocent bystanders (17). In stage I non-small-cell lung cancer (NSCLC), but not in stage II, peritumoral but not intratumoral mast cell density was an independent favourable prognostic factor; mast cells were pro-tumorigenic in the initial stages of prostate cancer but not in the later ones; mast cells in perilesional stroma of melanoma play a protective role. In pancreatic ductal adenocarcinoma, mast cell density in the intratumoral border zone, but not the peritumoral or the intratumoral center zone, was associated with a worse prognosis. In prostate cancer, high intratumoral mast cell density was initially associated with good prognosis. Subsequently, it was reported that intratumoral mast cells inhibited tumor growth, whereas peritumoral mast cells stimulated human prostate cancer (17). These findings suggest that the microlocalization of mast cells should be investigated in different stages of clinical and experimental tumors.

Stem cell factor (SCF) seems to be one of the most important substances attracting mast cells into the tumor microenvironment where they secrete pro-angiogenic factors, which promote tumor vascularization and invasiveness. The list of tumor products attracting mast cells in TME includes angiopoietins and several chemokines (CXCL8, CXCL2, CXCL1, and CXCL10, PGE_2, TSLP, and osteopontin). Furthermore, SCF stimulates mast cells to produce matrix metalloprotease-9 (MMP-9) that facilitates the recruitment of other mast cells to the tumor and increases tumor-derived SCF production in an amplification feedback loop. Mast cells may also suppress the development of protective antitumor immune responses by promoting regulatory T cell (Treg) mediated suppression in the tumor microenvironment.

Last but not least, the protumorigenic activities of mast cells can be subverted by targeting cells to promote tumor destruction. In a murine allograft model, the activation of mast cell degranulation by IgE antibodies blocked Treg and allowed tumor destruction through a CD4 + CD8 + mediated response. Furthermore, mast cells cause tumor cell death, in an *in vitro* lymphoma model, when incubated with an anti-CD20 IgE antibody (18). These findings represent the potential to deviate the response of these cells against cancer through immunotherapies.

Eosinophils - Eosinophils are multifunctional cells with pleiotropic functions. They are not only implicated in protection against parasitic infections but play a major role in allergic reactions and chronic inflammatory diseases. Activated eosinophils release cytotoxic proteins (e.g., ECP, MBP, EPX, EDN), growth factors, cytokines, chemokines and lipid mediators contributing to inflammation. Eosinophils have also been reported to participate in the control of tumor growth and the formation of metastasis. Increasing evidence indicates that IL-33, released in the extracellular space, where it functions as an alarmin for the immune system, may have opposing functions, promoting, or dampening tumour immunity, depending on the tumor type, site of expression, and local concentration (19).

In most epidemiological and clinical studies, eosinophils demonstrate "tumoricidal" action mediated by α-defensins, TNF-α, granzymes A and IL-18 (19). Moreover, eosinophils might support antitumor immune responses indirectly (for example, by facilitating T cell migration into tumors). Tumor cells themselves can attract eosinophils by producing CCL1 and stimulating eosinophils to secrete IL-8 that facilitates eosinophil-cancer cell interaction leading to tumor cell death. In allergic patients, they show a greater cytotoxic action, and this suggests that the "allergy state" promotes anticancer processes. In

future, eosinophils can be activated by immunotherapy such as checkpoint inhibitors or GM-CSF-based vaccines, or by adoptive transfer of these cells in an appropriate setting.

In several neoplasias (e.g., melanoma, gastric, colorectal, oral and prostate cancer) eosinophils play an anti-tumorigenic role, in others (e.g., Hodgkin's lymphoma, cervical carcinoma) have been linked to poor prognosis, whereas in yet others they are apparently innocent bystanders. The role of eosinophils and their mediators appears to be cancer-dependent. The microlocalization (e.g., peritumoral *vs* intratumoral) of eosinophils could be another important aspect in the initiation/progression of solid and hematological tumors (20).

Recently, Holland et al. demonstrated that the increased expression of dipeptidyl peptidase 4 (also known as CD26) has been observed in mouse and human tumors and is associated with worse survival. On the contrary, the inhibition of CD26 can improve antitumor immune response by enhancing the effect of eosinophils through IL-33-dependent eosinophil-mediated control of tumor growth. IL-33, a tumor-derived alarmin, in solid tumor induces eosinophil migration and promotes CCL11–mediated eosinophil infiltration and degranulation, which in turn leads to tumor cell cytotoxicity and reduced tumor growth. In addition, it has been demonstrated that combined immunotherapy using checkpoint blockade in the presence of CD26i inhibits tumor growth (21).

In summary, it can be hypothesized that type 1 and type 2 immune responses are not entirely antagonistic pathways, and, in some instances, they may collaborate to control tumor growth.

CONCLUSION

There are unclear answers whether allergies in general can protect against cancer. Current evidence does not provide definitive results. Generally, the mechanisms of immunotolerance are known to be low in allergy and enhanced in cancer but recent evidence highlights more complex mechanisms. Much seems to depend on the type of cancer and the microenvironment, and every immune cell may have different actions based on this. However, there are no data associating cancer development in subjects treated by allergen immunotherapy, the efficacy of which is at least partially due to potentiated immune tolerance. Cells involved in allergy are associated with a variable cancer prognosis, depending on the phenotype, tolerogenic cells (such as M2 macrophages and tolerogenic DC) induce tumor growth and progression, whereas activated cells (such as M1 macrophages and effector DCs) have an unfavorable effect on tumor cell growth. Mast cells have been correlated with tumor progression, while mast cell degranulation, normally associated with IgE–immune complex formation, have been correlated with a more favorable prognosis. The stimulation of ILC2s activated by macrophages through IL-33 favor tumor progression while amphiregulin-stimulated ILC2s inhibit tumor progression. ILC3 have a preponderant role in promoting cancer. Eosinophils appear to have a prevalent tumoricidal effect.

Therapeutic strategies for anticancer treatment are directed to modify the tolerogenic environment protecting carcinogenesis into effector cells/proteins able to activate an effective antitumor immunity. A clinical trial evaluating an antitumor IgE antibody in patients with cancer is ongoing, based on the presupposition that IgE directed against tumor antigens engenders antibody-dependent cell-mediated cytotoxicity by human monocytes. IgE are cross-linked by densely packed tumor antigens forming tumor-associated molecular patterns on a cancer cell surface and therefore triggering effector cell activation at sites where antitumor immunity is needed. Although further research is needed, treatments based on the knowledge gained studying the relationships between allergy and oncology might provide strategies that complement existing and emerging immuno-oncology therapies.

REFERENCES

1. Jensen-Jarolim E, Bax HJ, Bianchini R, et al. AllergoOncology – the impact of allergy in oncology: EAACI position paper. Allergy 2017; 72:866-87.
2. Wulaningsih W, Holmberg L, Garmo H, et al.

Investigating the association between allergen-specific immunoglobulin E, cancer risk and survival. OncoImmunology 2016; 5:e1154250.7.
3. Hui E. Immune checkpoint inhibitors. J Cell Biol 2019; 218:740-41.
4. Sugiura H, Ichinose M. Oxidative and nitrative stress in bronchial asthma. Antioxid Redox Signal 2008; 10(4):785-97.
5. Jensen-Jarolim E, Bax HJ, Bianchini R et al. Allergooncology: Opposite outcomes of immune tolerance in allergy and cancer. Allergy 2018; 73:328-40.
6. Varricchi G, Loffredo S, Galdiero MS, et al. Innate effector cells in angiogenesis and lymphangiogenesis. Curr Opin Immunol 2018; 53:152-60.
7. Jiang Z, Zhu L. Update on the role of alternatively activated macrophages in asthma. J Asthma Allergy 2016; 9:101-7.
8. Martinez FO, Gordon S. The M1 and M2 paradigm of macrophage activation: time for reassessment. F1000Prime Rep 2014; 6:13.
9. Saradna A, Do DC, Kumar S, Fu QL, Gao P. Macrophage polarization and allergic asthma. Transl Res 2018; 191:1-14.
10. Beyer M, Mallmann MR, Xue J, et al. High-resolution transcriptome of human macrophages. PLoS One 2012; 7:e45466.
11. Mills CD, Lenz LL, Harris RA. A breakthrough: macrophage-directed cancer immunotherapy. Cancer Res 2016; 76:513-16.
12. Farhood B, Najafi M, Mortezaee K. CD8+ cytotoxic T lymphocytes in cancer immunotherapy: A review. J Cell Physiol 2019; 234:8509-21.
13. Chiossone L, Dumas PY, Vienne M, Vivier E. Natural killer cells and other innate lymphoid cells in cancer. Nat Rev Immunol 2018; 18:671-88.
14. Kumar S, Saini RV, Mahindroo N. Recent advances in cancer immunology and immunology-based anticancer therapies. Biomed Pharmacother 2017; 96:1491-500.
15. Yue W, Lin Y, Yang X, Li B, Liu J, He R. Thymic stromal lymphopoietin (TSLP) inhibits human colon tumor growth by promoting apoptosis of tumor cells. Oncotarget 2016; 7:16840-54.
16. Conti P, Caraffa Al, Kritas SK, Ronconi G, Lessiani G, Toniato E, Theoharides TC. Mast cell, pro-inflammatory and anti-inflammatory: Jekyll and Hyde, the story continues. J Biol Regul Homeost Agents 2017; 31(2):263-67.
17. Varricchi G, Galdiero MR, Loffredo S, et al. Are mast cells MASTers in cancer? Front Immunol 2017; 8:424
18. Teo PZ, Utz PJ, Mollick JA. Using the allergic immune system to target cancer: activity of IgE antibodies specific for human CD20 and MUC1. Cancer Immunol Immunother 2012; 61:2295-309.
19. Afferni C, Buccione C, Andreon S, et al. The pleiotropic immunomodulatory functions of IL-33 and its implications in tumor immunity. Front. Immunol 2018; 9:2601.
20. Varricchi G, Galdiero MR, Loffredo S, et al. Eosinophils: The unsung heroes in cancer? Oncoimmunology 2018; 7:e1393134.
21. Hollande C, Boussier J, Ziai J et al. Inhibition of the dipeptidyl peptidase DPP4 (CD26) reveals IL-33-dependent eosinophil-mediated control of tumor growth. Nature Immunol 2019; 20:257-67.

EDITORIAL

INDUCTION OF PRO-INFLAMMATORY CYTOKINES (IL-1 and IL-6) AND LUNG INFLAMMATION BY CORONAVIRUS-19 (COVI-19 or SARS-CoV-2): ANTI-INFLAMMATORY STRATEGIES

P. CONTI[1], G. RONCONI[2], Al. CARAFFA[3], C.E. GALLENGA[4], R. ROSS[5], I. FRYDAS[6] and S.K. KRITAS[7]

[1]Postgraduate Medical School, University of Chieti, Chieti, Italy; [2]Clinica dei Pazienti del Territorio, Fondazione Policlinico Gemelli, Rome, Italy; [3]School of Pharmacy, University of Camerino, Camerino, Italy; [4]Department of Biomedical Sciences and Specialist Surgery, Section of Ophthalmology, University of Ferrara, Ferrara, Italy: [5]University of Pennsylvania School of Veterinary Medicine, Philadelphia, PA, USA; [6]Aristotelian University, Thessaloniki, Greece; [7]Department of Microbiology and Infectious Diseases, School of Veterinary Medicine, Aristotle University of Thessaloniki, Macedonia, Greece

Received February 16, 2020 – Accepted March 26, 2020

Coronavirus-19 (COVI-19) involves humans as well as animals and may cause serious damage to the respiratory tract, including the lung: coronavirus disease (COVI-19). This pathogenic virus has been identified in swabs performed on the throat and nose of patients who suffer from or are suspected of the disease. When COVI-19 infect the upper and lower respiratory tract it can cause mild or highly acute respiratory syndrome with consequent release of pro-inflammatory cytokines, including interleukin (IL)-1β and IL-6. The binding of COVI-19 to the Toll Like Receptor (TLR) causes the release of pro-IL-1β which is cleaved by caspase-1, followed by inflammasome activation and production of active mature IL-1β which is a mediator of lung inflammation, fever and fibrosis. Suppression of pro-inflammatory IL-1 family members and IL-6 have been shown to have a therapeutic effect in many inflammatory diseases, including viral infections. Cytokine IL-37 has the ability to suppress innate and acquired immune response and also has the capacity to inhibit inflammation by acting on IL-18Rα receptor. IL-37 performs its immunosuppressive activity by acting on mTOR and increasing the adenosine monophosphate (AMP) kinase. This cytokine inhibits class II histocompatibility complex (MHC) molecules and inflammation in inflammatory diseases by suppressing MyD88 and subsequently IL-1β, IL-6, TNF and CCL2. The suppression of IL-1β by IL-37 in inflammatory state induced by coronavirus-19 can have a new therapeutic effect previously unknown. Another inhibitory cytokine is IL-38, the newest cytokine of the IL-1 family members, produced by several immune cells including B cells and macrophages. IL-38 is also a suppressor cytokine which inhibits IL-1β and other pro-inflammatory IL-family members. IL-38 is a potential therapeutic cytokine which inhibits inflammation in viral infections including that caused by coronavirus-19, providing a new relevant strategy.

The virus that causes severe acute respiratory syndrome, as many people now know, is called CoV-19 (coronavirus disease-19 or SARS-CoV-2), which compares with the flu (1). CoV-19 potentially has a pandemic power that involves humans as well as animals and causes serious damage to the respiratory

Key words: coronavirus; COV-19; SARS-CoV-2; IL-1; IL-6; lung; inflammation; anti-inflammatory

Corresponding Author:
Prof. Pio Conti,
Postgraduate Medical School,
University of Chieti-Pescara,
Chieti 66013, Chieti, Italy
Tel./Fax: +39 08711 574136
e-mail: pconti@unich.it

0393-974X (2020)
Copyright © by BIOLIFE, s.a.s.
This publication and/or article is for individual use only and may not be further reproduced without written permission from the copyright holder.
Unauthorized reproduction may result in financial and other penalties
DISCLOSURE: ALL AUTHORS REPORT NO CONFLICTS OF INTEREST RELEVANT TO THIS ARTICLE.

tract including the lung. The cases of infections that occurred a few months ago are all related to the Wuhan seafood wholesale market, which trades fish and a variety of live animals including poultry, bats and snakes, and not to the creation of CoV-19 in the laboratory, as someone imaginatively suggested. The pathogen has been identified in swabs performed on the throat and nose of patients who suffer from or are suspected of the disease (2). The factors that influence the survival of the virus on surfaces depend on various conditions such as the number of viruses deposited (viral load), the type of surface, suspension medium, temperature, relative humidity among others (3). Therefore, the exact survival time of CoV-19 on non-biological material is not known. The transmission by indirect contact, that is with the contamination of inanimate surfaces, is also uncertain, while direct contact transmission and air transport between persons close to each other is certain. Once CoV-19 contaminates the environment, it can penetrate the mucous membranes of the nose, eyes and/or mouth and then reach the vital organs including the lung (4). COV-19 in the open air does not survive more than approximately 9 days, although influenza viruses in general can remain active for months (5).

High temperature certainly reduces the replication of any species of virus. Currently, the inactivation temperature of CoV-19 is not entirely known, but some studies report that it can be inactivated at about 27° C, but resists the cold even below 0°C.

Human COV-19 are divided into low pathogenic and highly pathogenic; however, infection is not necessarily followed by the characteristic symptoms, but can be silent (6). Low pathogenic CoV-19 infect the upper respiratory tract and cause mild respiratory diseases, similar to colds; on the contrary, highly pathogenic ones. such as CoV-19. cause severe acute respiratory syndrome, mainly by infecting the lower airways with consequent pro-inflammatory cytokine release and pneumonia, which can be fatal, especially in debilitated subjects or those suffering from relevant pathologies (7). Furthermore, it is not excluded that several CoV-19 strains may exist, but this will be studied in the near future. The average age of the deceased patients is around 70, with greater morbidity and mortality among older subjects. CoV-19 affects more than 50% of male patients, while the female gender is less affected, perhaps because it is more immunologically covered since many immune cell genes reside on the X chromosome (8).

Severe pneumonia caused by coronavirus is often associated with rapid virus replication, infiltration of inflammatory cells and elevated responses to inflammatory proteins such as cytokines, resulting in damage of internal organs and acute respiratory stress syndrome. Children are less likely to become infected, however if they are, the effect is only slight. It is interesting that there have been very few cases of infection in children under the age of 15, probably because they are more protected from acquired maternal immunity and also because they have a larger and more efficient thymus than older people (9). The mortality rate due to CoV-19 is currently reported around 2-3%, slightly higher than a severe seasonal flu, while SARS had a mortality rate between 9% and 10%. On average, each virus carrier can potentially spread the infection to 2-3 or more other people; until this number drops below 1 it is likely that the epidemic will continue to spread. The prevention and control of infections include hand hygiene and protective devices of the mucous membranes and respiratory tract, as well as better cleansing and disinfection of environmental surfaces (10).

Therefore, in order to attack the efficiency of viral transmission, infected people must be placed in quarantine, implementing a containment strategy, which could include, where possible, isolation of the sick, including voluntary isolation at home, closing of schools, the use of collective means of transport and the frequency of crowded places. The new coronavirus is structurally related to the virus that causes severe acute respiratory syndrome (SARS) and currently there are no effective therapeutic elements that can block it, but only supportive drugs (11). Constant surveillance, timely diagnosis and intense research are important to understand the biology of the virus and its pathogenetic power as these elements allow to develop defense strategies. Many research studies are currently underway around the world to develop a CoV-19 vaccine that is expected in 3-9 months. Therapy today is carried

out with non-specific anti-viral drugs, including interferon and monoclonal antibodies (12). The antibodies taken from the serum of healed subjects have also proved to be helpful, although the efficacy was very mild.

Despite the rigorous global containment and the quarantine adopted in all the affected countries, the incidence of CoV-19 continues to increase all over the world, even if the percentage of deaths has been partially stemmed and is more related to individuals with previous diseases. To date, the countries affected are over 100 and the most affected are probably because the virus was prematurely imported from the infected countries. It is also probable that in some countries there were more carriers who transmitted the infection, and the percentage of deaths compared to the number of infected subjects was higher than in other countries, because the deaths that would have occurred in any case with normal seasonal flu were not separated in those percentages. The governments of the affected countries are preventing a possible pandemic by sensibly isolating the subjects positive to CoV-19. Certainly, in a few months the number of patients will decrease and with the passage of time the virulence will significantly diminish or die out, as happened with previous viral infections. In addition to the many negative effects related to this infection, a positive effect of the CoV-19 virus, as for other flu viruses, is to cause the increase of interferons (IFNs) in immune cells, which reinforces protection against cancer and autoimmune diseases (13).

CoV-19 induces pro-inflammatory cytokine generation and secretion: Proposed mechanisms

Pro-inflammatory cytokines, and in particular interleukin (IL)-1, are important mediators in local and systemic inflammation (14). Stimulated IL-1 in viral infections mediates lung and tissue inflammation, fever and fibrosis (15). Macrophages activated by CoV-19 are crucial for the pathogenesis of fibrosis, since macrophages perform phagocytic activity on debris of dead cells and tissues, releasing inflammatory substances. These reactions can be related to danger-associated molecular patterns (DAMPs) which have receptors called "pattern recognition receptors" (PRRs) which also include toll-like receptors (TLRs). Activation of TLR2, TLR3 or TLR4 by COV-19 leads to the release of inflammatory cytokines, including IL-1β. Suppression of IL-1 has been shown to be effective in many inflammatory diseases including rheumatoid arthritis (16-17).

CoV-19 infection is catered for by a large replication of the virus in respiratory epithelial cells provoking acute inflammation and violent respiratory disease. In the place of infection pro-inflammatory cytokines are produced which worsen the clinical picture of the disease. Among these cytokines interferon-alpha (IFNα), tumor necrosis factor (TNF) and IL-1 are of considerable importance (2, 18-19)

Inflammation is mediated by pro-inflammatory cytokines including IL-1, IL-6, TNF and IL-8. IL-1 is the most studied cytokine with properties that are relevant to several inflammatory diseases including viral infections (20-21). The complex synthesis and release of inflammatory IL-1 occurs after the binding of CoV-19 to the Toll Like Receptor (TLR). Activation of this receptor causes a biochemical cascade that begins with the formation of pro-IL-1 cleaved by caspase-1, and followed by activation of inflammasome (22). High levels of adenosine triphosphate (ATP) (over 100 μM) are correlated with the activation of the P2X7 receptor, which belongs to the P2 (purinergic 2) receptor family, with pharmacological activity, cellular toxicity, and autoinflammatory mediation. The P2X7 receptor causes the activation of the inflammasome with the production of mature interleukins. Through pro-caspase-1 and Ca^{++} flow, there is the synthesis of IL-1β in the lysosome (23). IL-1β is then secreted outside the macrophage, mediating lung inflammation, fever and fibrosis, and provoking severe respiratory problems. Immune cells are attracted to the place of infection by IL-8, a chemokine that is generated at the inflammatory site. Pro-inflammatory cytokine levels are correlated with CoV-19 replication and disease. It is intuitive to think that anti-inflammatory cytokines, such as IL-1Ra, IL-37 or IL-38, can provide relief in both systemic inflammation and fever that occur after infection (23).

Inflammation occurs to restore the homeostasis

after CoV-19 infection and can be very harmful if not controlled. IL-1 generated during inflammation by immune cells, fibroblasts and endothelial cells is a response to the pathogenic virus and plays an important role in the pathogenesis of both acute and chronic obstructive respiratory disease and in the progression of pulmonary fibrosis (24). In CoV-19 infection, IFN type I is essentially produced, which has various effects on both innate and acquired immunity, but above all against viral infections. The generation of IFN, however, can cause side effects. such as inflammation, and also in some cases suppression of the immune system (25).

Therefore, in addition to anti-viral functions, IFNs can have harmful effects, such as induction of apoptosis, suppression of cell proliferation, tissue damage and inflammation. CoV-19 infection can be followed by a bacterial infection to aggravate the state of the patient and, in particular, lung function (26).

IL-37

IL-37 is a member of the IL-1 family with the ability to suppress innate and acquired immune response (27). IL-37 carries out its suppressive inflammatory activity by acting on the IL-R5 or IL-18Rα receptor. IL-37 orchestrates several mechanisms that suppress inflammation and immunity and performs its immunosuppressive activity by acting on mTOR and increasing the AMP kinase of IL-37. This cytokine inhibits histocompatibility complex (MHC) molecules and inflammation in rheumatic diseases by suppressing IL-1β, IL-6, TNF and CCL2 (28).

Since IL-37 inhibits IL-1, which induces other pro-inflammatory cytokines and inflammatory response, it is reasonable to think that IL-37 could inhibit inflammation induced by CoV-19 which provokes pro-inflammatory IL-1 family member release. The suppression with IL-37 of CoV-19-induced inflammation opens a new interesting pathway for the use of this inhibitory cytokine in the treatment of viral and other inflammatory diseases.

IL-38

IL-38 is the newest member of the IL-1 family and is a cytokine of the IL-36 subfamily (29). IL-38 binds to the IL-1R6 receptor and causes suppression of inflammation. *In vitro* cultures of activated peripheral blood mononuclear cells (PBMCs) are inhibited by IL-38 in the production of several cytokines, including IL-1, IL-17 and IL-22. Circulating levels of IL-38 are elevated in many inflammatory diseases, as a natural response to inflammation, and mice that do not produce IL-38 are more sensitive to inflammation. IL-38 produced by various cells, including B cells and macrophages, is capable of reducing virus-induced inflammation and other inflammatory diseases. This reduction is due to its ability to inhibit pro-inflammatory cytokines such as IL-1, IL-6 and TNF. These cytokines are stimulated by CoV-19 and mediate lung inflammation, fever and fibrosis, therefore, the use of IL-38 as a potential therapeutic cytokine may be relevant and will provide a theoretical basis for developing of new strategies.

REFERENCES

1. Wang C, Horby PW, Hayden FG, Gao GF. A novel coronavirus outbreak of global health concern. Lancet 2020; 395(10223):470-73.
2. Kritas SK, Ronconi G, Caraffa A, Gallenga CE, Ross R, Conti P. Mast cells contribute to coronavirus-induced inflammation: new anti-inflammatory strategy. J Biol Regul Homeost Agents 2020; 34(1).
3. Carinci F. CoV-19: preparedness, decentralisation, and the hunt for patient zero. BMJ 2020; 368:bmj. m799.
4. Huh S. How to train the health personnel for protecting themselves from novel coronavirus (COV-19) infection during their patient or suspected case care. J Educ Eval Health Prof 2020; 17:10.
5. Lim J, Jeon S, Shin HY, et al. Case of the index patient who caused tertiary transmission of COV-19 infection in Korea: the application of lopinavir/ritonavir for the treatment of COV-19 infected pneumonia monitored by quantitative RT-PCR. J Korean Med Sci 2020; 35(6):e79.
6. Zhang MQ, Wang XH, Chen YL, et al. [Clinical features of 2019 novel coronavirus pneumonia in the early stage from a fever clinic in Beijing]. Zhonghua Jie He He Hu Xi Za Zhi 2020; 43(0):E013.

7. Rubin EJ, Baden LR, Morrissey S. Audio Interview: making decisions about CoV-19 testing and treatment for your patients. N Engl J Med 2020; 382(11):e25.
8. Ghosh S, Klein RS. Sex Drives dimorphic immune responses to viral infections. J Immunol. 2017; 198(5):1782-90.
9. Liu W, Zhang Q, Chen J, et al. Detection of CoV-19 in children in early January 2020 in Wuhan, China. N Engl J Med 2020; doi: 10.1056/NEJMc2003717.
10. Legido-Quigley H, Asgari N, Teo YY, et al. Are high-performing health systems resilient against the COV-19 epidemic? Lancet 2020; pii: S0140-6736(20)30551-1.
11. Deng SQ, Peng HJ. Characteristics of and public health responses to the coronavirus disease 2019 outbreak in China. J Clin Med 2020; 9(2). pii: E575. doi: 10.3390/jcm9020575.
12. Li G, Fan Y, Lai Y, et al. Coronavirus infections and immune responses. J Med Virol 2020; 92(4):424-32. doi: 10.1002/jmv.25685.
13. Guan WJ, Ni ZY, Hu Y, et al. Clinical characteristics of coronavirus disease 2019 in China. China Medical Treatment Expert Group for CoV-19. N Engl J Med 2020; doi: 10.1056/NEJMoa2002032.
14. Dinarello CA, Conti P, Mier JW. Effects of human interleukin-1 on natural killer cell activity: is fever a host defense mechanism for tumor killing? Yale J Biol Med 1986; 59(2):97-106.
15. Conti P, Gallenga CE, Tetè G, et al. How to reduce the likelihood of coronavirus-19 (CoV-19 or SARS-CoV-2) infection and lung inflammation mediated by IL-1. J Biol Regul Homeost Agents. 2020;34(2). doi: 10.23812/Editorial-Conti-2.
16. Conti P, Lauritano D, Caraffa Al, et al. Microglia and mast cells generate proinflammatory cytokines in the brain and worsen inflammatory state: Suppressor effect of IL-37. Eur J Pharmacol 2020; 875:173035.
17. Theoharides TC, Tsilioni I, Conti P. Mast cells may regulate the anti-inflammatory activity of IL-37. Int J Mol Sci 2019; 20(15).
18. Borthwick LA. The IL-1 cytokine family and its role in inflammation and fibrosis in the lung. Semin Immunopathol 2016; 38(4):517-34.
19. Lauritano D, Ronconi G, Caraffa A, et al. New aspect of allergic contact dermatitis, an inflammatory skin disorder mediated by mast cells: Can IL-38 help? Med Hypotheses 2020; 139:109687.
20. Van Reeth K. Cytokines in the pathogenesis of influenza. Vet Microbiol 2000; 74(1-2):109-16.
21. Caraffa A, Gallenga CE, Kritas SK, Ronconi G, Di Emidio P, Conti P. CAR-T cell therapy causes inflammation by IL-1 which activates inflammatory cytokine mast cells: anti-inflammatory role of IL-37. J Biol Regul Homeost Agents 2019; 33(6):1981-85.
22. Marchetti C, Swartzwelter B, Koenders MI, et al. NLRP3 inflammasome inhibitor OLT1177 suppresses joint inflammation in murine models of acute arthritis. Arthritis Res Ther 2018; 20(1):169.
23. Dinarello CA. The IL-1 family of cytokines and receptors in rheumatic diseases. Nat Rev Rheumatol 2019; 15(10):612-32.
24. dos Santos G, Kutuzov MA, Ridge KM.The inflammasome in lung diseases. Am J Physiol Lung Cell Mol Physiol 2012; 303(8):L627-33. doi: 10.1152/ajplung.00225.2012. Epub 2012.
25. McNab F, Mayer-Barber K, Sher A, Wack A, O'Garra A Type I interferons in infectious disease. Nat Rev Immunol 2015; 15(2):87-103.
26. Davidson S, Maini MK, Wack A.Disease-promoting effects of type I interferons in viral, bacterial, and coinfections. J Interferon Cytokine Res 2015; 35(4):252-64.
27. Cavalli G, Dinarello CA. Suppression of inflammation and acquired immunity by IL-37. Immunol Rev 2018; 281(1):179-90. doi: 10.1111/imr.12605
28. Conti P, Gallenga CE, Caraffa A, Ronconi G, Kritas SK. Impact of mast cells in fibromyalgia and low-grade chronic inflammation: Can IL-37 play a role? Dermatol Ther. 2020; 33(1):e13191.
29. van de Veerdonk FL, de Graaf DM, Joosten LA, Dinarello CA. Biology of IL-38 and its role in disease. Immunol Rev 2018; 281(1):191-96.

JOURNAL OF BIOLOGICAL REGULATORS & HOMEOSTATIC AGENTS Vol. 34, no. 2, 333-338 (2020)

EDITORIAL

HOW TO REDUCE THE LIKELIHOOD OF CORONAVIRUS-19 (CoV-19 or SARS-CoV-2) INFECTION AND LUNG INFLAMMATION MEDIATED BY IL-1

P. CONTI[1], C.E. GALLENGA[2], G. TETÈ[3], Al. CARAFFA[4], G. RONCONI[5], A. YOUNES[6], E. TONIATO[7], R. ROSS[8] and S.K. KRITAS[9]

[1]Postgraduate Medical School, University of Chieti, Chieti, Italy; [2]Department of Biomedical Sciences and Specialist Surgery, Section of Ophthalmology, University of Ferrara, Ferrara, Italy; [3]Specialization School in Oral Surgery, Vita-Salute San Raffaele University, Milan, Italy; [4]School of Pharmacy, University of Camerino, Camerino, Italy; [5]Clinica dei Pazienti del Territorio, Fondazione Policlinico Gemelli, Rome, Italy; [6]Medical Center "Mai più Dolore", Pescara, Italy; [7]Department of Medical, Oral and Biotechnological Sciences, University of Chieti, Chieti, Italy; [8]University of Pennsylvania School of Veterinary Medicine, Philadelphia, PA, USA; [9]Department of Microbiology and Infectious Diseases, School of Veterinary Medicine, Aristotle University of Thessaloniki, Macedonia, Greece

Received March 1, 2020 – Accepted March 30, 2020

SARS-CoV-2, also referred to as CoV-19, is an RNA virus which can cause severe acute respiratory diseases (COVID-19), with serious infection of the lower respiratory tract followed by bronchitis, pneumonia and fibrosis. The severity of the disease depends on the efficiency of the immune system which, if it is weak, cannot stem the infection and its symptoms. The new CoV-19 spreads in the population at a rate of 0.8-3% more than normal flu and mostly affects men, since immune genes are more expressed on the X chromosome. If CoV-19 would spread with a higher incidence rate (over 10%), and affect the people who live in closed communities such as islands, it would cause many more deaths. Moreover, people from the poorest classes are most at risk because of lack of health care and should be given more assistance by the competent authorities. To avoid the aggravation of CoV-19 infection, and the collapse of the health system, individuals should remain at home in quarantine for a period of approximately one month in order to limit viral transmission. In the case of a pandemic, the severe shortage of respirators and protective clothing, due to the enormous demand and insufficient production, could lead the CoV-19 to kill a large number of individuals. At present, there is no drug capable of treating CoV-19 flu, the only therapeutic remedies are those aimed at the side effects caused by the virus, such as inflammation and pulmonary fibrosis, recognized as the first causes of death. One of the COVID-19 treatments involves inhaling a mixture of gaseous hydrogen and oxygen, obtaining better results than with oxygen alone. It was also noted that individuals vaccinated for viral and/or bacterial infectious diseases were less likely to become infected. In addition, germicidal UV radiation "breaks down" the oxygen O_2 which then aggregates into O_3 (ozone) molecules creating the ozone layer, capable of inhibiting viral replication and improving lung respiration. All these precautions should be taken into consideration to lower the risk of infection by CoV-19. New anti-viral therapies with new drugs should also be taken into consideration. For example, microbes are known to bind TLR, inducing IL-1, a pleiotropic cytokine, highly inflammatory, mediator of fever and fibrosis. Therefore, drugs that suppress IL-1 or IL-1R, also used for the treatment of rheumatoid arthritis, are to be taken into consideration. to treat COVID-19. We strongly believe

Corresponding Author:
Prof. Pio Conti,
Postgraduate Medical School,
University of Chieti-Pescara,
Chieti 66013, Chieti, Italy
Tel./Fax: +39 08711 574136
e-mail: pconti@unich.it

0393-974X (2020)
Copyright © by BIOLIFE, s.a.s.
This publication and/or article is for individual use only and may not be further reproduced without written permission from the copyright holder.
Unauthorized reproduction may result in financial and other penalties
DISCLOSURE: ALL AUTHORS REPORT NO CONFLICTS OF INTEREST RELEVANT TO THIS ARTICLE.

that all these devices described above can lead to greater survival and. therefore, reduction in mortality in patients infected with CoV-19.

Key words: coronavirus; inflammation; CoV-19; COVID; SARS-CoV-2; lung; fibrosis; virus

Coronaviruses are a family of common RNA viruses that can cause seasonal colds and even serious infections of the lower respiratory tract followed by bronchitis and pneumonia (1). Acute respiratory viral diseases are caused by respiratory tract infections that afflict the world community globally and cause about 4 million deaths per year, of which about 40% are caused by coronavirus (2). Severe acute respiratory syndrome is given by coronavirus-19 (SARS-CoV-2 also referred to as CoV-19), a family of common RNA viruses that can provoke seasonal colds, and even serious infections, followed by bronchitis and pneumonia, particularly in vulnerable subjects (3). Many inflammatory phenomena of severe pneumonia can occur with the flu, and can be avoided through vaccination thus effectively reducing the number of deaths (4). The severity of the disease depends on the efficiency of the immune system, which in a healthy subject allows to respond better to antibiotics and anti-inflammatories in order to obtain a better prognosis (5). The new CoV-19 spreads in the population at a rate of 0.8-3% more than normal influenza. If CoV-19 would spread with a higher incidence rate (over 10%), and affect the people who live in closed communities such as islands, it would cause many more deaths. This is because the inhabitants of islands, often far from societies with greater communication, have less contact with the various strains of coronavirus. The immune system of the islanders who have never come into contact with coronaviruses does not have an effective immune response, therefore they would be more affected by the disease (COVID-19). When the Spanish pandemic occurred in 1918, the mortality rate of the people living on the islands was many times higher than that of the Americans. The new coronavirus is similar to, or perhaps more lethal than, the Spanish flu, and could cause genocide in closed communities (6). Therefore, various international health organizations and competent authorities should provide medical assistance to these communities in order to avoid a tragedy. In case of an irrepressible pandemic occurring, each community would benefit from a large and efficient hospital for infectious diseases or suitable environments for hospitalizations. In addition, in the case of a pandemic, the severe shortage of respirators and protective clothing, due to the enormous demand and insufficient production, could lead the CoV-19 to kill a large number of individuals (7). For example, people from the poorest classes are most at risk for lack of health care and should be given more assistance by the competent authorities. To avoid the aggravation of CoV-19 infection, individuals should remain at home for a period of approximately one month in order to limit viral transmission from man to man (8). At present, there is no drug capable of treating CoV-19 flu, the only therapeutic remedies are those aimed at the side effects of the virus, such as inflammation and pulmonary fibrosis, recognized as the first causes of death (9). Many therapeutic solutions have been proposed to date: transfusion of plasma containing antibodies from individuals with COVID-19; use of monoclonal antibodies against CoV-19; anti-SARS drugs used against malaria, and others, but they are all to be carefully checked.

Some hospitals have treated COVID-19 pneumonia with a mixture of gaseous hydrogen and oxygen. In 1875, it was discovered that the mixture of hydrogen and oxygen could be used for severe pneumonia, although the specific mechanism to date is still unclear. At present, patients with coronavirus-19 pneumonia are treated with high flow pure oxygen (without adding hydrogen), although the effect of O_2 when associated with hydrogen may give better results (10). The production of mucus in these patients reduces the absorption of oxygen, while with a mixture of oxygen and hydrogen the bronchioles and the alveoli of the lungs are further expanded, optimizing the absorption of oxygen

(11). Hydrogen is used as a catalyst to accelerate the binding of hemoglobin with oxygen and the release of hemoglobin with carbon dioxide (12). It has recently been noted that there is a low incidence rate of CoV-19 in individuals who have had recent bacterial or viral vaccinations (13).

Infectious viral diseases that affect animals, but can also be accidentally transmitted to humans through direct contact with the animal, can be characterized by fever, pneumonia, fibrosis and many other pathophysiological effects, which are much milder in cases in which the subjects have already had bacterial infections. In fact, it has been noted that individuals affected by bacterial infections with production of exotoxins seem to be able to create COV-19-inhibiting antibodies, hindering their harmful effects, but these results are still under study (14). If these biological effects are effective, the vaccine for these infections should be used to prevent COVID-19. What has just been described would represent an indirect therapeutic intervention capable of avoiding the onset of pneumonia and pulmonary fibrosis. In the battle against the new coronavirus, healthcare professionals wear protective clothing that must comply with some basic rules to avoid creating gaps in protection and serious inconvenience to healthcare professionals (15). For example, wearing protective masks may cause suffocation and anoxia and often the masks are not sufficiently protective; furthermore, they also cause anaerobic metabolism increase and oxygen free radical production. In addition, wearing protective clothing for a long time, without having the time to replace them, can lead to urinary retention, which causes excessive expansion of the bladder of medical personnel with serious inconvenience at work (16). Excessive sweating can also be a problem as it causes the loss of water and electrolytes. Lack of oxygen, urine retention, sweating, physical stress, pressure of work rhythms and fear of infectious diseases can cause alteration of the sympathetic nervous system, affecting the health of medical personnel. Therefore, to avoid the drawbacks described, it would be necessary to speed up the work shift program of the clinicians who are in the front line. In the pandemic phase, if individuals are not isolated for about one month in quarantine, the health system could collapse and the mortality rate would increase dramatically (17), and even a large number of medical personnel could become infected in hospital settings. Moreover, COV-19 can nest in the protective clothing of healthcare professionals, with infectious potential. In addition, UV ultraviolet rays, commonly used in medical research laboratories to avoid germ contamination of cell cultures, should be taken into consideration (18). In this regard, it has been thought that if UV sterilizing lamps are installed in infectious risk environments, CoV-19 infections may be less frequent. Furthermore, since the entire body of the healthcare professional is covered with protective clothing, there is no risk of harmful UV radiation for the operator. At the moment, many hospital environments are almost completely devoid of UV lamps that can counteract the spread of the virus (19). Germicidal UV radiation is absorbed by oxygen (O_2) with breakage of the covalent bond creating the ozone layer, i.e. air containing ozone (O3) capable of inhibiting viral replication and improving lung respiration (20). Ozone generators are also available on the general market and are not expensive, therefore infectious risk environments should make use of them. In irradiated environments for at least one day, a large amount of ozone is formed in the air which, if breathed into the lungs by health workers and held for about a minute, can represent an effective weapon to contrast COVID-19. If this practice is repeated several times, the new CoV-19 can be inactivated by ozone (21). It is reasonable to think that in rooms equipped with an air purifier, or well-ventilated, and equipped with UV, the internal infection rate is significantly lower than that found in rooms that do not have it. These are all precautions that should be taken into consideration to lower the risk of infection. All these measures, designed to counter the advance of the virus, could be decisive and helpful. Currently, many countries are devastated by CoV-19 infection and inflammation, and the population is exhausted and eagerly awaits the resolution of the COVID-19. Therefore, the discovery of new effective therapeutic weapons, including vaccine and pro-inflammatory cytokine inhibitors are strongly needed (22).

Interleukin-1

The interleukin (IL)-1 family has recently expanded and comprises 11 members including IL-1. There are two molecules of IL-1 divided into IL-1α (also referred to as IL-1F1) and IL-1β (also referred to as IL-1F2) associated mostly with innate immunity (23). This article only takes into account IL-1β which will simply be called IL-1. IL-1 is a pleiotropic cytokine, active in different biological processes, mainly in inflammation, immunity and hematopoiesis. IL-1 binds IL-1R receptor, and IL-1R2 in a similar manner - a reaction which allows it to recruit the co-receptor IL-1R3 (23). These processes lead to the recruitment of MyD88 and activation of phosphorylation with the production of the pro-inflammatory pathways and formation of cytokines that induce other cytokines, amplifying the inflammatory state in many diseases including COVID-19 (24). The activation of Toll Like Receptor (TLR) receptor by IL-1 can be inhibited by IL-1Ra (IL-1 receptor antagonist, also called IL-1F3). IL-1 is produced by many immune cells including lymphocytes, macrophages and mast cells (MCs), but is also generated by non-immune cells, such as fibroblasts and endothelial cells, that take part in infectious processes (25). IL-1RI, shares a 50% amino acid homologous domain and functional properties with the TLR protein which is made up of 11 members and all share TIR domain, as does the IL-1RI. Many mechanisms can activate TLR which triggers inflammation via microbial product activation including CoV-19 and damage-associated molecular patterns (DAMPs), similar to IL-1 which functions as DAMP. In addition IL-1 can also play a role in acquired immunity (23). Therefore, microbes including CoV-19 and microbial products induce IL-1 via TLR. Drugs that block the IL-1 receptor such as anakinra, approved by FDA for the treatment of rheumatoid arthritis in 2002, are used in therapy for a multitude of inflammatory diseases common to rheumatoid arthritis (23). Indeed, patients with microbial infections treated with anakinra have shown greater survival and therefore reduction in mortality. As IL-1 is an important mediator in CoV-19-induced lung inflammation and fibrosis, suppression of this highly pro-inflammatory cytokine could have an important therapeutic role (26). IL-37 protein is expressed by human blood monocytes from healthy subjects, but also by human macrophages, B cells, plasma cells, T cells, and neoplastic cells (23). The inhibition of IL-1 can also be achieved by using IL-37, a new member of the IL-1 family, and subjects deficient in IL-37 are more likely to encounter inflammatory diseases (27). IL-37 signaling suppresses mTOR with inhibition of phosphorylation and inflammation. IL-37 mRNA is increased in several inflammatory and infectious diseases in proportion to the severity of the disease. In viral infections IL-37 increases in relation to the inflammatory response, and inhibits pro-inflammatory IL-1 family members and IL-6 but, on the other hand, IL-37 leads to unwanted immunosuppression (23).

IL-38 is also a member of the IL-1 family with anti-inflammatory properties. IL-38 is an inhibitor of IL-1-related pro-inflammatory cytokines and is also capable of suppressing IL-6 induced in viral infections such as CoV-19 (23).

Tumor necrosis factor

Tumor necrosis factor (TNF) is a potent pro-inflammatory and pro-apoptotic protein which can be induced by IL-1 (28). Its inhibition alleviates the inflammation and suppresses the production of other pro-inflammatory cytokines induced by this cytokine. TNF is released by several immune and non-immune cells after stimulation with a number of activator compounds such as microbial products and inflammatory cytokines including IL-1 (29). MCs are immune cells and mediators of inflammation which contain TNF preformed in their granules released quickly after activation of IgεRI receptor with appropriate ligands, including IgE. Furthermore, in MCs, TNF can be synthesized *de novo* after several hours and appears to require mitochondrial translocation. TNF induces endothelial leukocyte adhesion in inflammation by recruiting neutrophils through stimulation of ELAM-1, ICAM-1, VCAM-1 on vascular endothelial cells, contributing to inflammation (30). Moreover, it is known that TNF, as well as IL-1 are capable of inducing the pro-inflammatory cytokine IL-6 (31) in virus-

induced diseases, such as COVID-19. In addition to performing the inflammatory function, TNF shares the signaling pathways with IL-1. TNF mediates inflammation in innate and adaptive immune responses by contributing to the recruitment of white blood cells to the sites of inflammation. This suggests that TNF can modulate immunity and inflammation in various pathological states including those caused by CoV-19. TNF and TGFβ1 derived from activated MCs via TLR4 can provoke an augmentation of type-I collagen with the increase of production of fibroblasts by means of the fibrotic phenomenon, as can occur in CoV-19 infection. TNF can increase mortality after microbial infection, improve microbial growth and after inhibition it can decrease inflammation. In this regard, the anti-TNF antibody which is effective in inflammatory monoarthritis by inhibiting this cytokine, may also be helpful in CoV-19-induced TNF-mediated inflammation (32). The administration of a TNF neutralizing antibody could contribute to an improvement of inflammation and greater survival. TNF inhibitors play a role in immunotherapy, alone or in combination with anti-inflammatory or anti-rheumatic drugs. However, since TNF is an immune response mediator of viral infections, the use of anti-TNF inhibitors in CoV-19-infected patients may promote viral reactivation. In conclusion, TNF can strongly contribute to the initiation and amplification of inflammation, and its neutralization can certainly give relief, also in CoV-19 infections. However, anti-TNF therapies are known to increase the risk of numerous infections due to suppression of the immune system involved in the battle against viral diseases including those induced by CoV-19.

REFERENCES

1. Jordan PC, Stevens SK, Deval J. Nucleosides for the treatment of respiratory RNA virus infections. Antivir Chem Chemother 2018; 26:2040206618764483. doi: 10.1177/2040206618764483.
2. Conti P, Ronconi G, Caraffa A, et al. Induction of pro-inflammatory cytokines (IL-1 and IL-6) and lung inflammation by Coronavirus-19 (COVI-19 or SARS-CoV-2): anti-inflammatory strategies. J Biol Regul Homeost Agents 2020; 34(2). pii: 1. doi: 10.23812/CONTI-E. [Epub ahead of print]
3. Beigel JH, Nam HH, Adams PL, et al. Advances in respiratory virus therapeutics - A meeting report from the 6th isirv Antiviral Group conference. Antiviral Res 2019; 167:45-67.
4. Johnston RE. A candidate vaccine for severe acute respiratory syndrome.. N Engl J Med 2004; 351(8):827-28.
5. Conti P, Lauritano D, Caraffa A, Gallenga CE, Kritas SK, Ronconi G, Martinotti S. Microglia and mast cells generate proinflammatory cytokines in the brain and worsen inflammatory state: Suppressor effect of IL-37. Eur J Pharmacol 2020; 875:173035. doi: 10.1016/j.ejphar.2020.173035. [Epub ahead of print] Review.
6. Lu R, Zhao X, Li J, Niu P, et al. Genomic characterisation and epidemiology of 2019 novel coronavirus: implications for virus origins and receptor binding. Lancet 2020; 395(10224):565-574. doi: 10.1016/S0140-6736(20)30251-8.
7. Wang X, Zhang X, He J. Challenges to the system of reserve medical supplies for public health emergencies: reflections on the outbreak of the severe acute respiratory syndrome coronavirus 2 (SARS-CoV-2) epidemic in China. Biosci Trends 2020; 14(1):3-8. doi: 10.5582/bst.2020.01043.
8. Leung C. The difference in the incubation period of 2019 novel coronavirus (SARS-CoV-2) infection between travelers to Hubei and non-travelers: The need of a longer quarantine period. Infect Control Hosp Epidemiol 2020; 1-8.
9. Li H, Du S, Yang L, et al. Rapid pulmonary fibrosis induced by acute lung injury via a lipopolysaccharide three-hit regimen. Innate Immun 2009; 15(3):143-54.
10. Zhao Q, Li S, Xue F, Zou Y, Chen C, Bartlam M, Rao Z. Structure of the main protease from a global infectious human coronavirus, HCoV-HKU1 J Virol.; 82(17):8647-55.
11. Wang R, Xiao H, Guo R, Li Y, Shen B. The role of C5a in acute lung injury induced by highly pathogenic viral infections. Emerg Microbes Infect 2015; 4(5):e28.
12. Woo PC, Lau SK, Tsoi HW, et al. Clinical and molecular epidemiological features of coronavirus HKU1-associated community-acquired pneumonia. J Infect Dis 2005; 192(11):1898-907.

13. Ison MG, Hirsch HH. Community-acquired respiratory viruses in transplant patients: diversity, impact, unmet clinical needs. Clin Microbiol Rev 2019; 32(4).
14. Schindewolf C, Menachery VD. middle east respiratory syndrome vaccine candidates: cautious optimism. Viruses 2019; 11(1). pii: E74.
15. Lie SA, Wong SW, Wong LT, Wong TGL, Chong SY. Practical considerations for performing regional anesthesia: lessons learned from the COVID-19 pandemic. Hosp Pract (1995) 2015; 43(3):158-63.
16. Ng PC, So KW, Leung TF,et al. Infection control for SARS in a tertiary neonatal centre. Arch Dis Child Fetal Neonatal Ed 2003; 88(5):F405-9.
17. Kruse RL. Therapeutic strategies in an outbreak scenario to treat the novel coronavirus originating in Wuhan, China. F1000Res 2020; 9:72. doi: 10.12688/f1000research.22211.2.
18. Eickmann M, Gravemann U, Handke W, Tolksdorf F, Reichenberg S, Müller TH, Seltsam A. Inactivation of Ebola virus and Middle East respiratory syndrome coronavirusin platelet concentrates and plasma by ultraviolet C light and methylene blue plus visible light, respectively. Transfusion 2018; 58(9):2202-07.
19. Walker CM, Ko G. Effect of ultraviolet germicidal irradiation on viral aerosols. Environ Sci Technol 2007; 41(15):5460-5.
20. Ohnaka T. [Health effects of ultraviolet radiation]. Ann Physiol Anthropol. 1993;12(1):1-10.
21. Rowen RJ. Ozone and oxidation therapies as a solution to the emerging crisis in infectious disease management: a review of current knowledge and experience. Med Gas Res 2019; 9(4):232-237.
22. Conti P, Lauritano D, Caraffa A, Gallenga CE, Kritas SK, Ronconi G, Pandolfi F. New insight into systemic mastocytosis mediated by cytokines IL-1β and IL-33: Potential inhibitory effect of IL-37. Eur J Pharmacol 2019; 858:172473.
23. Dinarello CA. The IL-1 family of cytokines and receptors in rheumatic diseases. Nat Rev Rheumatol 2019; 15(10):612-32.
24. Hara N, Alkanani AK, Dinarello CA, Zipris D. Modulation of virus-induced innate immunity and type 1 diabetes by IL-1 blockade. Innate Immun 2014; 20(6):574-84.
25. Conti P, Gallenga CE, Ronconi G, Caraffa A, Kritas SK. Activation of mast cells mediates inflammatory response in psoriasis: Potential new therapeutic approach with IL-37. Dermatol Ther 2019; 32(4):e12943.
26. Kritas SK, Ronconi G, Caraffa A, Gallenga CE, Ross R, Conti P. Mast cells contribute to coronavirus-induced inflammation: new anti-inflammatory strategy. J Biol Regul Homeost Agents 2020;34(1).
27. Tsilioni I, Patel AB, Pantazopoulos H, Berretta S, Conti P, Leeman SE, Theoharides TC. IL-37 is increased in brains of children with autism spectrum disorder and inhibits human microglia stimulated by neurotensin. Proc Natl Acad Sci U S A. 2019;116(43):21659-21665.
28. Conti P, Caraffa A, Ronconi G, Frydas I, Theoharides TC. Recent progress on pathophysiology, inflammation and defense mechanism of mast cells against invading microbes: inhibitory effect of IL-37. Cent Eur J Immunol 2019; 44(4):447-454. doi: 10.5114/ceji.2019.92807.
29. Dinarello CA. The IL-1 family and inflammatory diseases. Clin Exp Rheumatol 2002; 20(5 Suppl 27):S1-13.
30. Taracanova A, Alevizos M, Karagkouni A, et al. SP and IL-33 together markedly enhance TNF synthesis and secretion from human mast cells mediated by the interaction of their receptors. Proc Natl Acad Sci U S A 2017; 114(20):E4002-E4009.
31. Dinarello CA. Interleukin-1 and tumor necrosis factor: effector cytokines in autoimmune diseases. Semin Immunol 1992; 4(3):133-45.
32. Buskila D. Hepatitis C-associated rheumatic disorders. Rheum Dis Clin North Am 2009; 35(1):111-23.

JOURNAL OF BIOLOGICAL REGULATORS & HOMEOSTATIC AGENTS Vol. 34, no. 2, 339-343 (2020)

EDITORIAL

CORONAVIRUS COV-19/SARS-CoV-2 AFFECTS WOMEN LESS THAN MEN: CLINICAL RESPONSE TO VIRAL INFECTION

P. CONTI[1] and A. YOUNES[2]

[1]Postgraduate Medical School, University of Chieti, Chieti, Italy;
[2]Medical Center "Mai più Dolore", Pescara, Italy

Received March 31, 2020 – Accepted April 6, 2020

CoV-19/SARS-CoV-2 is a highly pathogenic virus that causes coronavirus-19 disease (COVID-19) an acute respiratory distress syndrome which provokes serious problems for global health. Studies suggest that there are many differences between men and women in the immune response to CoV-19 infection and inflammatory diseases. Women, compared to men, are less susceptible to viral infections based on a different innate immunity, steroid hormones and factors related to sex chromosomes. The presence of two X chromosomes in women emphasize the immune system even if one is inactive. The immune regulatory genes encoded by X chromosome in female gender causes lower viral load levels, and less inflammation than in man, while $CD4^+$ T cells are higher with better immune response. In addition, women generally produce higher levels of antibodies which remain in the circulation longer. The levels of activation of the immune cells are higher in women than in men, and it is correlated with the trigger of TLR7 and the production of IFN. TLR7 is higher in women than in men and its biallelic expression leads to higher immune responses and increases the resistance to viral infections. TLR7 is expressed in innate immune cells which recognizes single strand RNA virus by promoting the production of antibodies against the virus and the generation of pro-inflammatory cytokines including IL-6 and IL-1 family members. Moreover, in women the production of inflammatory IL-6 after viral infection is lower than in males and is often correlated with a better longevity. In addition, on the X chromosome there are loci that code for the genes involved in the regulation of immune cells such as FOXP3, and transcription factor for Treg involved in virus pathogenesis. The X chromosome influences the immune system by acting on many other proteins, including TLR8, CD40L and CXCR3 which can be over-expressed in women, and influence the response to viral infections and vaccinations. However, the biallelic expression of the X-linked genes can promote harmful autoimmune and inflammatory responses. Cardiovascular diseases are more frequent in males and subjects without cardiovascular dysfunctions infected by CoV-19 have a better prognosis, but these effects are still under study. It is hoped that certain drugs, such as CoV-19 receptor blockers, anti-inflammatories (against rheumatic diseases), monoclonal antibodies, anti-IL-1 and anti-IL-6, the remdesevir drug (analogue adenosine, effective against ebola), hydroxychloroquine (for the treatment of malaria) and vaccines, will open up new strategies and new therapeutic ways to combat this terrible virus.

The living beings around us, including the plant world, all coexist with microorganisms, including viruses, which normally host their species and do not attack man. This also happens with fertilization, the human species can reproduce only with individuals of the same species, but when a

Key words: coronavirus 19; CoV-19, gender; virus; immunity; cytokine

Corresponding Author:
Prof. Pio Conti,
Postgraduate Medical School,
University of Chieti-Pescara,
Chieti 66013, Chieti, Italy
Tel./Fax: +39 08711 574136
e-mail: pconti@unich.it

0393-974X (2020)
Copyright © by BIOLIFE, s.a.s.
This publication and/or article is for individual use only and may not be further reproduced without written permission from the copyright holder.
Unauthorized reproduction may result in financial and other penalties
DISCLOSURE: ALL AUTHORS REPORT NO CONFLICTS OF INTEREST RELEVANT TO THIS ARTICLE.

species jumps (for example from animal to man, zoonotic disease, a fortunately infrequent event), a biological revolution takes place which leads to the formation of "monsters" or lethal pathologies. This is what happened with SARS-CoV-2 (CoV-19). Wild animals, such as snakes and pangolis, slaughtered by humans, can transmit CoV-19 to humans, who do not have an efficient immune system for this unknown microorganism which can cause COVID-19.

A number of studies suggest that there are many differences between men and women in the immune response to infectious and inflammatory diseases such as tuberculosis, malaria, hepatitis, HIV-1, mumps, measles, adenovirus, flu, etc. (1). Data from hospitals around the world tell us that males suffer more than women (25%) from respiratory system diseases, including those caused by acute viral infections. Women, compared to men, are less susceptible to viral infections based on a different innate and adaptive immunity, steroid hormone production by the gonads and factors related to sex chromosomes. Sex hormones are known to modulate innate immune responses in various infectious diseases including viral infections (2). In CoV-19 infections, sexual differences can affect several aspects, such as anti-viral immune response, morbidity, transmission and pathogenesis. Estrogen treatment prevents osteoporosis by inhibiting the cytokine pathway necessary for the differentiation and activation of osteoclasts. Estrogens modulate receptor response and pro-inflammatory cytokine production which, when released in excess can be very harmful and may lead to death (3). Therefore, the immune system can be modulated by estrogens that bind to the ER (estrogen receptor) alpha or beta receptor. ER-alpha is expressed by all immune cells and is involved in their maturation and regulation, and also is immune protective, since it is responsible for the production of IFN type I and the activation of NK cells. ERβ has opposite effects to ERα and is involved in pro-inflammatory phenomena (4). ERα loss in older women is correlated with immunosuppression, demonstrating that estrogen can protect against COVID-19.

Peripheral blood mononuclear cells (PBMCs) treated with estrogen respond better to the antigen and express Toll-like 7 (TLR7) with greater efficiency. CoV-19 binds to TLRs (key molecules in triggering innate immunity) of macrophages, dendritic cells and mast cells, causing an inflammatory cytokine storm with respiratory distress syndrome. Activation of TLR in the lung due to CoV-19 can promote vascularization and hyperemia with the production of inflammatory cytokines and chemokines that aggravate the state of the patient with COVID-19 (5). The presence of two X chromosomes in women affects the immune system even if one is inactive. The X chromosome acts on various elements of the immune system such as FOXP3, TLR7, TLR8, CD40L and CXCR3 which can be over-expressed in women and influence the response to viral infections and vaccinations (6). In CoV-19 infection, plasma viral load levels are lower in women than in men, while $CD4^+$ T cells are higher, demonstrating higher response of the immune system in women. In addition, after vaccination, women generally produce in the circulation higher levels of antibodies, which have longer life than in men. The immune regulatory genes encoded by the X chromosome in the female gender cause lower viral load levels, inflammation and death after CoV-19 infection (7). Furthermore, the levels of activation of the immune cells influenced by sex hormone are higher in women than in males, and this is correlated with the activation of TLR7 and the production of IFN. Immune cells respond to CoV-19 infection with the production of IFNs which are cytokines that modulate the immune response, activate the host's cytotoxic cells and have anti-viral activity, even if it is highly pro-inflammatory (8). Low levels of IFNs control CoV-19 replication in absence of inflammation. In the immune cells of female individuals, the biallelic expression of the X-linked genes can promote harmful autoimmune and inflammatory responses; on the other hand it can be useful in the case of immune depression, as occurs in COVID-19. Hence, related to the X chromosomes, TLR7 is higher in women than in men and its expression leads to higher immune responses, although these reactions can cause autoimmune phenomena (9). Therefore, the female has a greater predisposition to autoimmunity, due to the overexpression of the endosomal TLR7 receptor

gene located on the X chromosome and the amount of TLR7 is crucial. It has been noted that TLR7 over-expression in women increases resistance to viral infections, as happens in Cov-19 infection. TLRs are important in controlling virus replication which can be inhibited by specific ligands for TLRs. Furthermore, TLR7 is expressed in dendritic cells, circulating monocyte, macrophages, and B cells which recognize single strand RNA CoV-19 by promoting the production of anti-CoV-19 antibodies and the generation of pro-inflammatory cytokines including IL- 6 and IL-1 family members. On the X chromosome there are loci that code for the genes involved in the regulation of immune cells such as FOXP3, transcription factor of Treg (T regulatory) cells, TLR7 and TLR8 that bind the virus. TLR7 allows women to have a lower mortality rate, in most acute viral diseases with severe inflammation. In fact, in women, the production of inflammatory IL-6 in viral infections is lower than in males, and is often correlated with better health, even if sometimes the data are contradictory.

CoV-19 binds to immune cells, causing the antibody response in both COVID-19 and healthy non-symptomatic carrier patients (10). Early viral detection occurs through pattern recognition receptors (PRRs) expressed by APC cells and lung fibroblasts. These receptors activated by CoV-19 trigger NF-kB which overproduce pro-inflammatory cytokines and chemokines, which aggravate the pathological state and lung funtions. The PRRs are TLRs such as TLR-4, TLR3, TLR2/6, TLR7/8, which activate IL-4 as a protector cytokine and can trigger pro-inflammatory IL-6 production, which increases inflammation.

Damage-associated molecular pattern (DAMP)] as high-mobility group box (HMGB) -1 (that activates the NF-kB), and adenosine triphosphate (ATP) proteins are mainly associated with virus inflammation and other pathologies. CoV-19 infection induces stress and cellular inflammation and also the production of DAMP which in physiological conditions is not detected by the immune system. DAMP is involved in inflammation of the upper airways infected with CoV-19, mediates muscle weakness in several diseases and plays a crucial role in the pathogenesis of fever. NLRP inflammasome protein is associated with DAMP secretion and is passively secreted in non-apoptotic cell death or actively in CoV-19-induced lung damage (11). The TLR2 receptor is involved in the secretion of DAMP, while the TLR4 acts as an inflammatory signal and can be activated by DAMP molecules. DAMPs have also been associated with nociceptive signaling and with increased virus spread and replication. After CoV-19 infection, DAMP molecules, such as ATP protein, can be released in stress and bind to P2X receptors (P2XRs) or P2Y receptors (P2YRs) which are involved in inflammation. ATP also plays a role in the activation of NLRP3 inflammasome linked with the generation of caspase-1, resulting in the formation of IL-1 which produces fever, inflammation and pain, and induces other pro-inflammatory cytokines. Antibodies against DAMP molecules confer significant protection and therapeutic target against damage inflammation and infection by CoV-19.

In innate immunity, CoV-19 stimulates immune cells, such as lymphocytes and monocytes, to produce IFN, important cytokines of the immune system; on the other hand the virus binds to the target cells, such as lung macrophages, pneumocytes and endothelial cells, and infects them (12). Activated natural killer (NK) cells recognize the infected CoV-19 cells as not-self and they kill them by fueling inflammation. In specific immunity, CoV-19 stimulates B lymphocytes and plasma cells to produce CoV-19 neutralizing IgG antibodies. IgG located on the infected cell are recognized by the FcgRIII receptor (CD16) of killer cells that enhance phagocytes, lysis and cell killing (antibody-dependent cell-mediated cytotoxicity) with consequent production of pro-inflammatory cytokines. CoV-19 infection can cause interstitial pneumonia with the formation of alveolar exudates, fibrosis and respiratory failure. In addition to this clinical picture, patients can develop *Stophylococcus* bacteria super-infection, a necrosis of the alveolar coatings and hemorrhagic exudation, severe respiratory syndrome, with a very high mortality rate (13). In CoV-19-infected lung, hyperemic and emphysematous areas are found with highly dilated vessels, micro-thrombus, diffuse alveolar damage, jalinous tissue formation and fibrosis. The other

organs of affected patients by the virus are also altered, such as heart, which is hypertrophic (with ventricular hypertrophy in hypertensive patients), and liver, which appears enlarged (hepatomegaly). The peripheral blood presents a marked neutrophilia with thrombocytopenia and lymphopenia. If the alveolar bronchial lavage fluid is analyzed, an overproduction of some major pro-inflammatory cytokines, such as IL-6, IL-1, and TNF, can be found, as well as a high concentration of chemokines including CXCL10 (IP- 10), CXCL8 (IL-8), CCL2 (MCP1), CCL3 (MIP-1α), and CCL5 (RANTES). Cytokines IL-1 and TNF are produced to limit the pathogenic action of CoV-19, but when they are released in excess in the surrounding tissues produce acute inflammation and may lead to death (14).

In clinical tests where testosterone levels were high, increased predisposition and susceptibility have been noted to cardiovascular inflammation, that is more frequent in males who are more vulnerable to CoV-19. Patients without cardiovascular disease infected by CoV-19 have a better prognosis compared to those with cardiac dysfunction and hypertension.

The angiotensin converting enzyme divides angiotensin I to generate angiotensin II and is a peptide that has various biological functions. A homologue of angiotensin-converting enzyme, termed angiotensin-converting enzyme 2 (ACE2), which protects murine lungs from acute respiratory distress syndrome (ARDS), has been recently identified as a receptor for CoV-19. CoV-19 binds to the ACE2 receptor, which is in various animal species, such as cats, pigs, but probably also in dogs and mice, which can develop COVID-19. CoV-19 and its Spike protein binds to ACE2 by weakening lung protection against the 'flu. Men compared to women expose more ACE2 receptor, located on the endothelium of the pulmonary vessels, that binds the virus and allows it to enter the cell. Several organs express ACE2 including heart, lung and kidney, therefore, the blockade or preventing the expression of this receptor could open new therapeutic ways to combat COVID-19. Inhibitors of the angiotensin converting enzyme (ACEI) and/or angiotensin II receptor type 1 are used in some clinical cases to stem the devastating effects of CoV-19 (15). These inhibitors alleviate COVID-19 disease by reducing the viral load and also IL-6 levels that control viral replication via NF-kB. They also have an effect on the immune system by increasing the number of $CD3^+$ and $CD8^+$ T cells in the peripheral blood of patients affected by CoV-19.

Many studies describe the influence of sex hormones on autoimmunity. and there are several autoimmune diseases more common to women than men, such as systemic lupus erythematosus, rheumatoid arthritis, psoriasis, dermatomyositis, Sjogren syndrome, Hashimoto's thyroiditis, scleroderma, etc. For example, one of the most common autoimmune diseases in the female gender compared to the male is chronic autoimmune thyroiditis (or Hashimoto's thyroiditis) which in Western population affects 5-15% of women, while in men it is present in 1-5%. In this disease, the immune system produces anti-thyroglobulin antibodies by preventing the binding to iodine. An anti-thyroid stimulating hormone antibody . is also generated which inhibits the pathway that leads to the production of T3 and T4. In both cases, follicular cells undergo apoptosis by reducing hormone production (16).

It is hoped that certain drugs, such as CoV-19 receptor blockers, anti-inflammatories (against rheumatic diseases), monoclonal antibodies, anti-IL-1 and anti-IL-6, the remdesevir drug (analogue adenosine, effective against ebola), hydroxychloroquine (for the treatment of malaria), and vaccines, will open up new strategies and new therapeutic ways to combat this terrible virus.

REFERENCES

1. Fung TS, Huang M, Liu DX. Coronavirus-induced ER stress response and its involvement in regulation of coronavirus-host interactions. Virus Res 2014; 194:110-23.
2. Kadel S, Kovats S. Sex hormones regulate innate immune cells and promote sex differences in respiratory virus infection. Front Immunol 2018; 9:1653.
3. Angele MK, Pratschke S, Hubbard WJ, Chaudry IH. Gender differences in sepsis: cardiovascular and immunological aspects. Virulence 2014;5(1):12-19.

4. Huang Z, Fang F, Wang J, Wong CW. Structural activity relationship of flavonoids with estrogen-related receptor gamma. FEBS Lett 2010; 584(1):22-26.
5. Hayashi K, Hooper LC, Detrick B, Hooks JJ. HSV immune complex (HSV-IgG: IC) and HSV-DNA elicit the production of angiogenic factor VEGF and MMP-9. Arch Virol 2009; 154(2):219-26.
6. Quakkelaar ED, Melief CJ. Experience with synthetic vaccines for cancer and persistent virus infections in nonhuman primates and patients. Adv Immunol 2012; 114:77-106.
7. Haque A, Akçeşme FB, Pant AB. A review of Zika virus: hurdles toward vaccine development and the way forward. Antivir Ther 2018; 23(4):285-93.
8. Qureshi S, Medzhitov R. Toll-like receptors and their role in experimental models of microbial infection. Genes Immun 2003; 4(2):87-94.
9. Souyris M, Mejía JE, Chaumeil J, Guéry JC. Female predisposition to TLR7-driven autoimmunity: gene dosage and the escape from X chromosome inactivation. Semin Immunopathol 2019; 41(2):153-164.
10. Conti P, Gallenga CE, Tetè G, et al. How to reduce the likelihood of coronavirus-19 (CoV-19 or SARS-CoV-2) infection and lung inflammation mediated by IL-1. J Biol Regul Homeost Agents 2020; 34(2). doi: 10.23812/Editorial-Conti-2. [Epub ahead of print].
11. Pandolfi F, Altamura S, Frosali S, Conti P. Key Role of DAMP in inflammation, cancer, and tissue repair. Clin Ther 2016; 38(5):1017-28.
12. Conti P, Ronconi G, Caraffa A, et al. Induction of pro-inflammatory cytokines (IL-1 and IL-6) and lung inflammation by Coronavirus-19 (COVI-19 or SARS-CoV-2): anti-inflammatory strategies. J Biol Regul Homeost Agents 2020; 34(2). pii: 1. doi: 10.23812/CONTI-E. [Epub ahead of print].
13. Shifrin N, Raulet DH, Ardolino M. NK cell self tolerance, responsiveness and missing self recognition. Semin Immunol 2014;26(2):138-44.
14. Seki M, Kohno S, Newstead MW, et al. Critical role of IL-1 receptor-associated kinase-M in regulating chemokine-dependent deleterious inflammation in murine influenza pneumonia. J Immunol 2010; 184(3):1410-18.
15. Hamming I, Timens W, Bulthuis ML, Lely AT, Navis G, van Goor H. Tissue distribution of ACE2 protein, the functional receptor for SARS coronavirus. A first step in understanding SARS pathogenesis. J Pathol 2004; 203(2):631-37.

CIRCULATING miR-374b-5p NEGATIVELY REGULATES OSTEOBLAST DIFFERENTIATION IN THE PROGRESSION OF OSTEOPOROSIS VIA TARGETING Wnt3 AND Runx2

Y. XU, S. ZHANG, D. FU and D. LU

Department of Gynaecology and Obstetrics, Northern Jiangsu People's Hospital, Yangzhou, P.R. China

Received November 20, 2019 – Accepted February, 2020

Osteoporosis is defined as an aging-related skeletal disorder involving deterioration of bone mass and bone structure, and consequently, increased risk of fractures. Emerging evidence indicates the dysregulation of microRNAs (miRNAs) in the progression of osteoporosis. However, whether such associated miRNAs control osteoblast differentiation or constitute therapeutic targets remains elusive. In the present study, we found elevated circulating miR-374b-5p level associated with postmenopausal osteoporosis. miR-374b-5p served as a critical suppressor of osteoblast differentiation. We further identified that miR-374b-5p directly targeted Wnt family member 3 (Wnt3) and Runt-related transcription factor 2 (Runx2) through its 3'-untranslated regions (3′UTRs). Moreover, the antagonist of miR-374b-5p could promote bone formation in ovariectomy (OVX)-induced mice. Together, our results revealed that miR-374b-5p directly targeted Wnt3 and Runx2, negatively regulating osteoblast differentiation and bone formation. Collectively, circulating miR-374b-5p in the serum might serve as a potential diagnostic and therapeutic strategy for osteoporosis.

Clinical characteristics of osteoporosis are a decrease in bone mass, an increase in bone fragility and fracture susceptibility (1-2). In this prevalent and systematic disease, maintenance of bone remodeling is disrupted with bone resorption exceeding bone formation (3-4). The mainstay of treatment for osteoporosis is limited to anti-resorptive therapies, but these drugs have adverse effects and non-specificity to organs (5). Therefore, novel drugs of high bone-targeting ability and low toxicity hold great promise (6).

As the most extensively studied class of ncRNAs, miRNAs act as a 'hub' in gene regulatory networks that govern numerous targets, typically by binding to specific sites in the 3′UTRs of mRNAs (7-8). Aside from the well-documented regulatory mechanism in bone-forming osteoblasts and bone-resorbing osteoclasts, accumulating evidence presents a series of miRNAs associated with the skeletal disorders (9-11). In addition to tissues, emerging miRNAs exist in serum and plasma as circulating ncRNAs, releasing extracellular signals between cells and their extracellular matrix (12-13). With the advancement of high-throughput sequencing, novel circulating miRNAs existing in the peripheral blood of patients result as being associated with osteoporosis (14-16). Owing to their high abundance and stability, circulating miRNAs are promising biomarkers in many fields (7-8). However, the role of circulating miRNAs in the etiology of osteoporosis remains largely unclear.

Key words: miR-374b-5p; osteoblast differentiation; bone formation; osteoporosis

Corresponding Author:
Dr Yuexin Xu,
Department of Gynaecology and Obstetrics,
Northern Jiangsu People's Hospital,
Yangzhou 225001, P.R. China
e-mail: xuyuexinxin@126.com

0393-974X (2020)
Copyright © by BIOLIFE, s.a.s.
This publication and/or article is for individual use only and may not be further reproduced without written permission from the copyright holder.
Unauthorized reproduction may result in financial and other penalties
DISCLOSURE: ALL AUTHORS REPORT NO CONFLICTS OF INTEREST RELEVANT TO THIS ARTICLE.

Here, we identified that miR-374b-5p level was significantly elevated in patients with osteoporosis. *In vitro* evidence demonstrated that miR-374b-5p inhibited osteoblast differentiation of amniotic fluid-derived cells (hAFDCs) and human umbilical cord-derived cells (hUCDCs). Furthermore, we determined that Wnt3 and Runx2 were direct targets of miR-374b-5p. Moreover, we verified that antagomir-miR-374b-5p treatment could promote bone formation in ovariectomized mice. Hence, our results suggest that circulating miR-374b-5p could be used as a potential diagnostic tool for osteoporosis, or serve as a novel therapeutic target.

MATERIALS AND METHODS

The Ethics Committee of Northern Jiangsu People's Hospital approved the study (Approval number: 2016KY-139) in accordance with the principles of the Helsinki Declaration. Female patients with osteoporosis (n=90) and age-matched patients without osteoporosis (n=58) aged between 50 and 90 years were enrolled between October 2018 and April 2019 (Table I). For measuring total bone mineral density (BMD), assessment of the most susceptible sites of osteoporotic fractures (the lumbar spine and the head of the femur) by dual X-ray absorptiometry was used as the reference method. According to the diagnostic criteria by WHO, osteoporosis is defined as a bone mineral density (BMD) T score ≤-2.5. Informed consent was obtained from all participants prior to sample collection. Patients with systemic and metabolic bone diseases (diabetes, malignancy, coronary heart disease or other severe diseases) other than osteoporosis in the previous 5 years were excluded from the study. Serum was prepared by centrifugation at 2,500×g for 30 min at room temperature and was stored frozen at −80°C for later RNA extraction.

For cell culture and osteoblast differentiation, human amniotic fluid-derived cells (hAFDCs) and human umbilical cord-derived cells (hUCDCs) (procured from Northern Jiangsu People's Hospital, China) were maintained in AmnioGrow Plus Medium (Cytogen, Germany). HEK-293 T cells were maintained in DMEM supplemented with 10% fetal bovine serum (FBS) and 1% penicillin/streptomycin (PS). Cultured cells were incubated at 37°C in a humidified chamber containing 5% CO_2. To induce osteogenesis, cells were cultured with additional ascorbic acid (50 mg/l) and β-glycerophosphate (10 mM) in the indicated time with regular medium changes.

RNA oligonucleotides and transfection assay

Transfection of mimics, inhibitors and non-specific control oligonucleotides of miR-374b-5p (RiboBio Co, Guangzhou, China) into cultured cells were carried out with a delivery agent, Lipofectamine 2000 (Invitrogen, Carlsbad, CA, USA). At 48 h post-transfection, the cells were harvested for mRNA analysis.

RNA isolation and real-time PCR

Total RNA was isolated from cultured cells using the RNAiso Plus according to the manufacturer's protocol (TaKaRa Biotechnology, Dalian, China). cDNA was synthesized from 1 μg total RNA in reverse transcription reactions with the PrimeScript RT reagent kit (TaKaRa Biotechnology, Dalian, China), and real-time PCR was conducted with SYBR Green Master (Roche Diagnostics, Indianapolis, IN, USA) on a Roche LightCycler 96 real-time PCR system. The PCR amplification conditions for real-time PCR were 95°C for 5 min, followed by 40 amplification cycles of 95°C for 15 s and 60°C for 1 min. The expression level of mature miR-374b-5p was determined by stem-loop reverse transcription-quantitative PCR. U6 was used for normalization. The following primer sequences were used: miR-374b-5p, RT 5'-GTCGTATCCAGTGCAGGGTCCGAGGTATTCGCACTGGATACGACCACTTA-3', forward 5'-AGCCCGGATATAATACAACCTGC-3', reverse 5'-CAGTGCAGGGTCCGAGGT-3'; U6, forward 5'-CTCGCTTCGGCAGCACA-3', reverse 5'-AACGCTTCACGAATTTGCGT-3'; mRNA levels were normalized to β-actin, and the primers used for amplification were: Runx2, forward 5'-ATGATGACACTGCCACCTCTGAC-3', reverse 5'-AACTGCCTGGGGTCTGAAAAAGG-3'; Wnt3, forward 5'-CTCGCTGGCTACCCAATTTG-3', reverse 5'-AGGCTGTCATCTATGGTGGTG-3'; alkaline phosphatase (ALP), forward 5'-ACCACCACGAGAGTGAACCA-3', reverse 5'-CGTTGTCTGAGTACCAGTCCC-3'; osteocalcin (OC), forward 5'-CAGCGAGGTAGTGAAGAGAC-3', reverse 5'-GCCGATGTGGTCAGCCAACT-3'; bone sialoprotein

(BSP), forward 5'-TACACGGGCGCCAATGAATA-3', reverse 5'-AGGTTCCCCGTTCTCACTTT-3'; type I collagen (Col1α1), forward 5'-GAGGGCCAAGACGAAGACATC-3', reverse 5'-CAGATCACGTCATCGCACAAC-3'; β-actin, forward 5'-AGATGTGGATCAGCAAGCAG-3', reverse 5'-GCGCAAGTTAGGTTTTGTCA-3'.

Plasmid construction and luciferase reporter assay

Potential target binding sites for miR-374b-5p were obtained from TargetScan Human (http://www.targetscan.org). Fragments of the Wnt3 and Runx2 3′UTR containing the predicted miR-374b-5p-binding sites were cloned behind the luciferase coding sequence at the X baI site in the pGL3-promoter vector (Promega, Mannheim, Germany). For the luciferase assay, HEK-293 T cells were co-transfected with the above reporter constructs along with phRL-null (Renilla plasmid for normalization) and 100 nM control or miR-374b-5p mimic. After 48 h transfection, the cells were collected and the luciferase activities were measured with a Dual-luciferase Reporter Assay System and a GloMax™ Base Instrument (Promega, Mannheim, Germany).

For alkaline phosphatase (ALP) staining, after osteogenic induction for 5-7 days, cells were fixed with 95% ethanol and stained with a BCIP/NBT solution staining kit according to the manufacturer's protocol (Beyotime, Shanghai, China). The ALP-positive cells were stained blue/purple.

Therapeutic inhibition of miR-374b-5p in ovariectomy (OVX)-induced osteoporotic mouse model

All the female C57BL/6J mice aged 8–12 weeks used were maintained under standard animal housing conditions (12-h light/dark cycles and free access to food and water) in a temperature-controlled room (24±1°C) with relative humidity (50±10%). The mice were randomly divided into two groups to receive either sham (n=5) or bilateral OVX surgery (n=7). At 8 weeks post-surgery, OVX-induced osteoporotic mouse model had been constructed; these mice received every three days for 4 times either agomir-374b-5p or negative control agomir (agomir-NC) (RiboBio Co, Guangzhou, China) at a dose of 1 nmol via periosteal injection at the distal femurs, while sham-operated mice were given a comparable volume of physiological saline (40 μl). Five days after the last injection, the mice were sacrificed. Bone and serum samples were harvested for further analysis.

Table I. *Age distribution of the patients and controls*

Age	Non-osteoporosis	Osteoporosis
50-59	19	15
60-69	32	31
70-79	5	32
80-90	2	12

Micro-computed tomography (Micro-CT) analysis

For the analysis of distal femurs, specimens excised from the indicated mice were fixed in PBS and scanned *ex-vivo* with a resolution of 9.8 μm using a Skyscan1174 X-ray Microtomography (Bruker microCT, Kontich, Belgium) for evaluating bone volume and architecture. Briefly, the image was acquired at 50 kV and 800 μA with a 0.98-degree rotation between frames. For visualization, the 3D Creator software supplied with the instrument implemented a three-dimensional reconstruction from the imported segmented data. The following parameters were measured: BMD, bone volume/total volume (BV/TV), and trabecular number (Tb.N).

Serum Trap5b ELISA analysis

As trap5b was a sensitive marker of bone resorption and osteoclast function, serum was collected for an ELISA analysis. The amount of serum TRAP5b was measured with an ELISA Kit for acid phosphatase 5, tartrate resistant (ACP5) according to the manufacturer's instructions (UScnlife, Wuhan, China).

Statistical analyses

Experimental data were analyzed by Student's *t*-test or one-way analysis of variance (ANOVA) using GraphPad Prism 6.0 (GraphPad Software Inc., USA). All pairs of columns were compared, and the bars denote the mean ± standard deviation (SD). P values less than 0.05 were considered statistically significant. * = $P<0.05$, ** = $P<0.01$, *** = $P<0.005$. n.s.: non-significant ($P>0.05$).

RESULTS

Circulating miR-374b-5p level in serum is associated with osteoporosis.

To search for candidate miRNAs potentially

involved in the progression of osteoporosis, the expression was examined of miR-374b-5p in serum collected from 90 female patients with osteoporosis and 58 non-osteoporosis controls (age range from 50 to 90 years) by real-time PCR. Using stem-loop reverse transcription quantitative PCR, circulating miRNAs from serum samples were identified. The results manifested that the level of miR-374b-5p was remarkably higher in patients with osteoporosis than in non-osteoporosis controls (Fig. 1). These data suggest that the elevated level of miR-374b-5p in clinical samples might be associated with the development of osteoporosis in these patients.

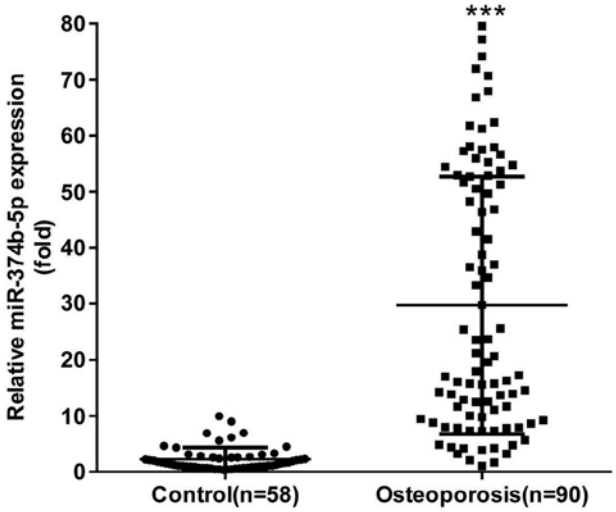


Fig. 1. *Circulating miR-374b-5p level in serum is associated with osteoporosis. Real-time PCR analysis of circulating miR-374b-5p levels in serum from female patients with osteoporosis (n=90) or female non-osteoporosis controls (n=58). U6 was used as the internal control.*

miR-374b-5p blocks osteoblast differentiation of hAFDCs and hUCDCs in vitro

To calculate the cellular basis of osteoporosis, the role of miR-374b-5p in osteoblast differentiation was explored. We first examined the level of miR-374b-5p by culturing amniotic fluid-derived cells (hAFDCs) and human umbilical cord-derived cells (hUCDCs) in osteogenic medium for different times periods. The results presented that the level of miR-374b-5p and Runx2 in hAFDCs began to ascend gradually through the course of osteoblast differentiation from day 3 and reached their highest levels on day 7; then, both of them decreased on day 12 (Fig. 2A). Consistently, the level of miR-374b-5p peaked on day 7 in hUCDCs. While the level of Runx2 rose steadily through the course of osteoblast differentiation in hUCDCs (Fig. 2B). These findings suggest that miR-374b-5p may function as a potential miRNA that modulates osteoblast differentiation.

To evaluate the physiological role of miR-374b-5p in osteoblast differentiation *in vitro*, miR-374b-5p mimic was used to enhance the level of miR-374b-5p (Fig. 3A). Conversely, the mRNA levels of osteoblast markers genes, including alkaline phosphatase

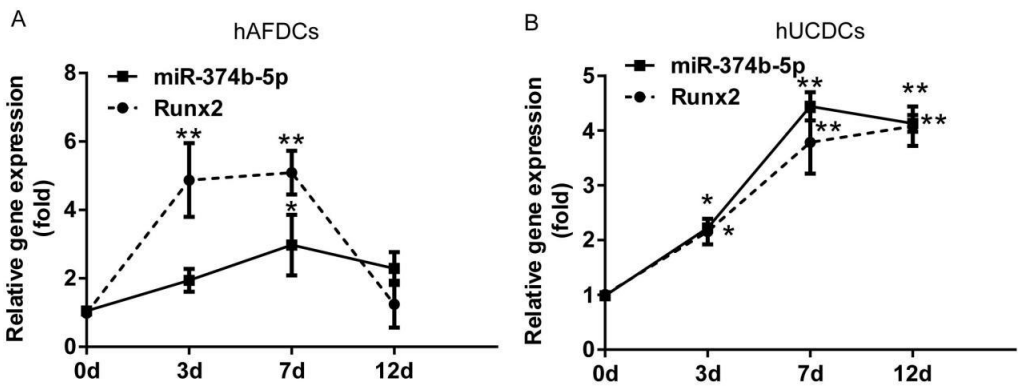


Fig. 2. *miR-374b-5p expression is up-regulated during osteoblast differentiation. **A)** Real-time PCR analysis of the time course changes of miR-374b-5p and Runx2 levels in hAFDCs cultured in osteogenic medium for 12 days. β-actin was used as the internal control. **B)**Real-time PCR analysis of the time course changes of miR-374b-5p and Runx2 levels in hUCDCs cultured in osteogenic medium for 12 days. β-actin was used as the internal control.*

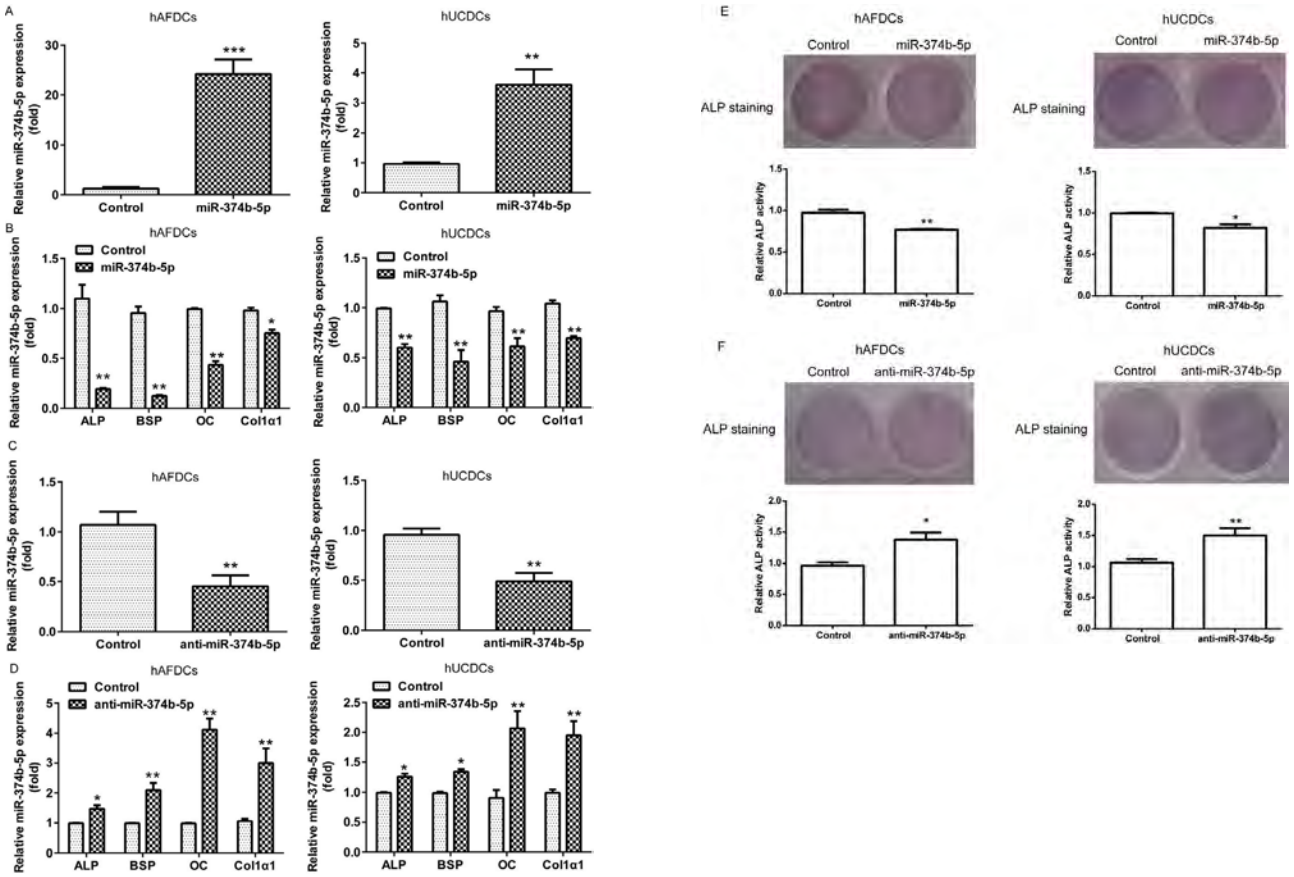


Fig. 3. *miR-374b-5p blocks osteoblast differentiation of hAFDCs and hUCDCs in vitro. **A**) Expression of miR-374b-5p in hAFDCs and hUCDCs after transfection with miR-374b-5p mimic or control for 48 h, as determined by real-time PCR. U6 was used as the internal control. **B**) Real-time PCR detection of the levels of osteoblast markers genes in hAFDCs and hUCDCs after transfection with miR-374b-5p mimic or control for 48 h. β-actin was used as the internal control. **C**) Expression of miR-374b-5p in hAFDCs and hUCDCs after transfection with miR-374b-5p inhibitor or control for 48 h, as determined by real-time PCR. U6 was used as the internal control. **D**) Real-time PCR detection of the levels of osteoblast markers genes in hAFDCs and hUCDCs after transfection with miR-374b-5p inhibitor or control for 48 h. β-actin was used as the internal control. **E**) Representative images of ALP staining after treatment with miR-374b-5p mimic or control in hAFDCs and hUCDCs in osteogenic medium for 7 days. Quantification of ALP activity is shown. **F**) Representative images of ALP staining after treatment with miR-374b-5p inhibitor or control in hAFDCs and hUCDCs in osteogenic medium for 7 days. Quantification of ALP activity is shown.*

(ALP), osteocalcin (OC), bone sialoprotein (BSP) and type I collagen (Col1α1), were significantly decreased in hAFDCs transfected with miR-374b-5p mimic compared with cells transfected with negative control (Fig. 3B). Furthermore, the alkaline phosphatase staining represented impaired ALP activity in hAFDCs transfected with miR-374b-5p mimic (Fig. 3E).

To further describe the role of miR-374b-5p in osteoblast differentiation, we then carried out the converse experiment, where a miR-374b-5p inhibitor was introduced into hAFDCs. As shown in Fig. 3C, miR-374b-5p expression was drastically decreased by 50%, whereas the mRNA levels of osteoblast markers genes were up-regulated in hAFDCs transfected with miR-374b-5p inhibitor (Fig. 3D).

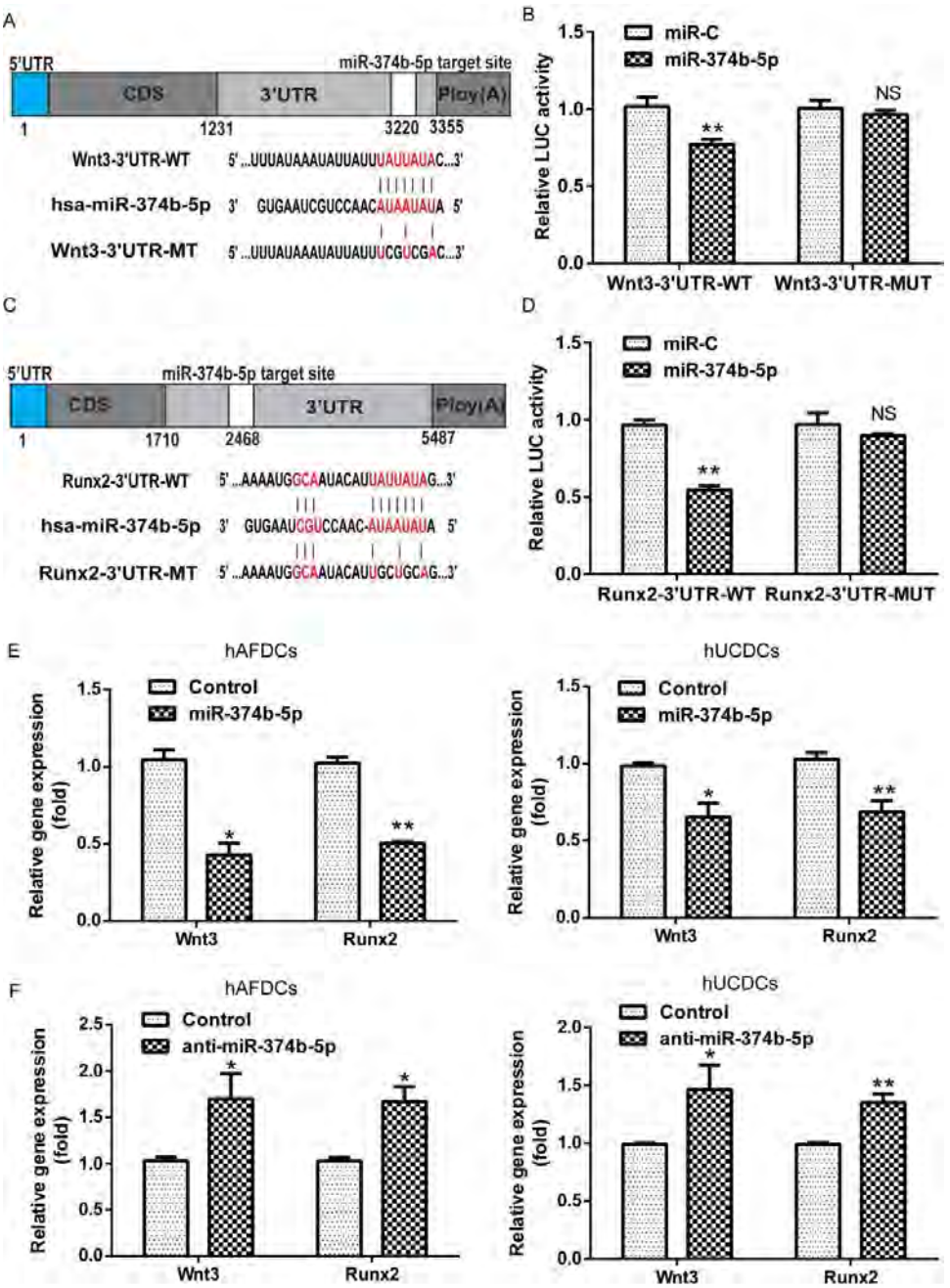


Fig. 4. *Wnt3 and Runx2 directly target miR-374b-5p.* ***A****) Schematic diagram illustrating the design of luciferase reporters construct with WT Wnt3 3'UTR or site-directed mutant Wnt3 3'UTR.* ***B****) Luciferase readout from WT or mutant Wnt3 3'UTR reporter co-transfected in HEK-293 T cells with miR-374b-5p mimic. The relative luciferase activity, defined as the ratio of 3'UTR reporter activity to that of the internal control (Renilla), was determined 48 h after transfection.* ***C****) Schematic diagram illustrating the design of luciferase reporters construct with WT Runx2 3'UTR or site-directed mutant Runx2 3'UTR.* ***D****) Luciferase readout from WT or mutant Runx2 3'UTR reporter co-transfected in HEK-293 T cells with miR-374b-5p mimic. The relative luciferase activity, defined as the ratio of 3'UTR reporter activity to that of the internal control (Renilla), was determined 48 h after transfection.* ***E****) Real-time PCR analysis of Wnt3 and Runx2 mRNA levels after transfection with miR-374b-5p mimic or control in hAFDCs and hUCDCs. β-actin was used as the internal control.* ***F****) Real-time PCR analysis of Wnt3 and Runx2 mRNA levels after transfection with miR-374b-5p inhibitor or control in hAFDCs and hUCDCs. β-actin was used as the internal control.*

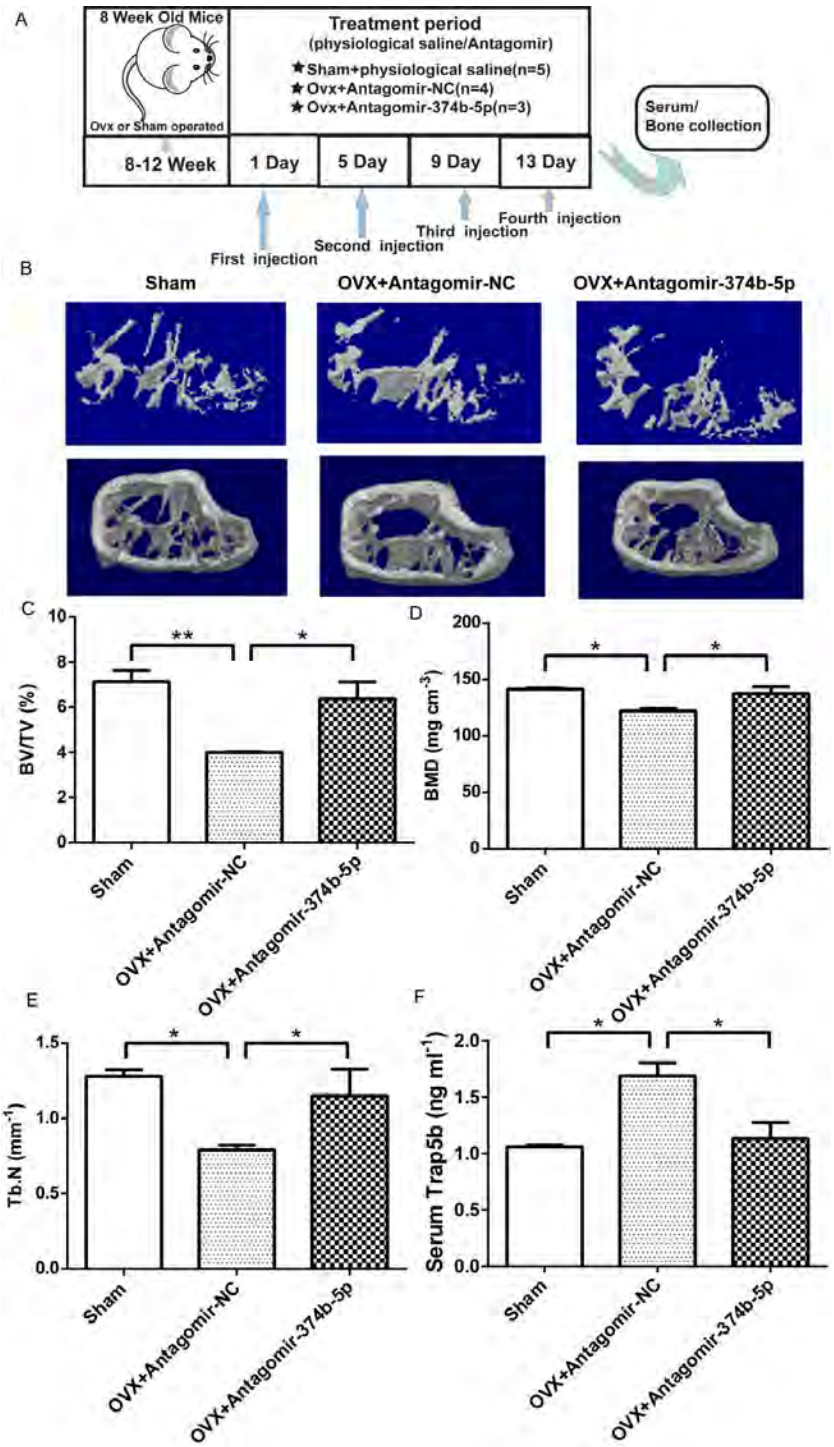


Fig. 5. *Therapeutic inhibiton of miR-374b-5p improves ovariectomy-induced bone loss.* ***A****) Schematic diagram illustrating the experimental design.* ***B****) Representative micro-CT reconstructive images of trabecular bone of femurs from Sham, OVX+Antagomir-NC and OVX+Antagomir-374b-5p mice.* ***C****) The values of the microstructural parameter-bone mineral density (BMD) of femurs in the groups of mice indicated.* ***D****) The values of bone volume/tissue volume (BV/TV) of femurs in the groups of mice indicated.* ***E****) The values of trabecular number (Tb.N) of femurs in the groups of mice indicated.* ***F****) ELISA analysis of Serum Trap5b concentrations in the groups of mice indicated.*

In agreement with the changes in the osteoblast marker genes, the alkaline phosphatase staining in these conditions confirmed these observations (Fig. 3F). Additionally, a similar role of miR-374b-5p was observed in hUCDCs. Taken together, these results demonstrate that miR-374b-5p could block the osteoblast differentiation of hAFDCs and hUCDCs.

Wnt3 and Runx2 directly target miR-374b-5p

To investigate the molecular mechanisms through which miR-374b-5p modulate osteoblast differentiation, we screened putative targets involved in osteoblast differentiation to establish a link between them. Single putative miR-374b-5p recognition sites were identified within gene 3′UTR sequences by TargetScan.

Interestingly, Wnt3 was selected as a target for validation. According to the sequence analysis, Wnt3 contains a 7-nucleotide site within its 3′UTR that matched the seed region of miR-374b-5p. To gain insight into the mechanism by which regulation of Wnt3 by miR-374b-5p is specifically mediated, a luciferase reporter assay was performed by fusing the 3′UTR of Wnt3 containing one miR-374b-5p-binding site downstream of the reporter. Meanwhile, another luciferase reporter with the Wnt3 3′UTR containing mutant sequences of the miR-374b-5p was constructed (Fig. 4A). In the presence of miR-374b-5p overexpression, luciferase activity decreaed, and this suppression was relieved by mutating the miR-374b-5p-binding site (Fig. 4B).

More interestingly, Runx2, a transcription factor essential for skeletal morphogenesis, was also selected as a target for validation due to a miR-374b-5p-binding site within its 3′UTR. Similarly, we cloned the 3′UTR of the Runx2 containing the binding site and constructed another luciferase reporter with mutant sequences of the binding site (Fig. 4C). As shown in Fig. 4D, luciferase activity exhibited a similar pattern of decline in the presence of miR-374b-5p overexpression and the impaired binding site removed this suppression. Together, introduction of mutations in these sequences abolished the ability of miR-374b-5p to inhibit luciferase activity, further supporting selective miR-374b-5p interactions with Wnt3 and Runx2. Accordingly, transfection with miR-374b-5p mimic could reduce Wnt3 and Runx2 mRNA levels in cultured cells (Fig. 4E). Furthermore, the suppression of miR-374b-5p enhanced Wnt3 and Runx2 mRNA levels in cultured cells (Fig. 4F). These data suggest that Wnt3 and Runx2 are direct targets of miR-374b-5p.

Therapeutic inhibition of miR-374b-5p improves ovariectomy-induced bone loss

After confirming the role of miR-374b-5p in osteogenesis *in vitro*, underlying mechanisms were investigated *in vivo*. To mimic estrogen deficiency-induced bone loss, an OVX-induced osteoporotic mouse model was established. At 8 weeks post-surgery, to examine the therapeutic effects, these mice received every 3 days for 4 times either agomir-374b-5p or agomir-NC at a dose of 1 nmol via periosteal injection at the distal femurs (Fig. 5A). micro-CT analysis of distal femur illustrated a striking loss in trabecular bone mass (lower in both BMD and BV/TV) in OVX+Antagomir-NC mice compared with sham-operated mice, whereas the trabecular bone mass was remarkably higher in OVX+Antagomir-374b-5p mice when compared with OVX+Antagomir-NC mice (Fig. 5B, C, D). Moreover, as revealed by bone parameter quantitative analysis, the trabecular architecture was remarkably impaired (lower in Tb.N) in OVX+Antagomir-NC mice compared with sham-operated mice, whereas the trabecular architecture was dramatically improved in OVX+Antagomir-374b-5p mice when compared with OVX+Antagomir-NC mice (Fig. 5E). Accordingly, to further verify the role of miR-374b-5p *in vivo*, serum trap5b, which is the bone resorption-related marker, was detected by ELISA. As shown by the results of ELISA, serum trap5b was slightly elevated in OVX+Antagomir-NC mice compared with sham-operated mice, while serum trap5b was notably reduced in OVX+Antagomir-374b-5p mice when compared with OVX+Antagomir-NC mice. Collectively, these results imply that therapeutic inhibition of miR-374b-5p might improve ovariectomy-induced bone loss and promote bone formation in OVX mice.

DISCUSSION

Osteoporosis, one of the most challenging age-related disorders, results from bone resorption exceeding bone formation (17). The imbalance of bone homeostasis is mediated by differentiation, activity, and apoptosis of bone-forming osteoblasts and bone-resorbing osteoclasts (18). Amniotic fluid-derived cells (hAFDCs) and human umbilical cord-derived cells (hUCDCs), with the capacity for proliferation and multilineage differentiation, have been promising agents for regenerative medicine applicable in therapy (19-21). In this study, hAFDCs and hUCDCs from pregnant women and lying-in women were isolated for further research.

Currently, as minimally invasive markers, an increasing number of studies have elaborated on the use of circulating miRNAs in patients with osteopenia, osteoporosis, and fragility fractures (14). Subsequently, circulating miR-133a, miR-503, miR-148a, and miR-21 were demonstrated to act as sensitive biomarkers for osteoporosis (22-25). Consistently, in these patients with osteoporosis, we detected the level of serum circulating miRNAs and established a close association between the elevated circulating miR-374b-5p and osteoporosis. However, the association between the circulating miR-374b-5p and male patients with osteoporosis remains to be explored. During osteoblast differentiation of MC3T3-E1 cells, bone marker genes such as Runx2, ALP, and OC, were significantly up-regulated. As potent inhibitors of Runx2 protein accumulation, 11 predicted Runx2-targeting miRNAs (miR-23a, miR-30c, miR-34c, miR-133a, miR-135a, miR-137, miR-204, miR-205, miR-217, miR-218, and miR-338) were up-regulated by day 28, compared with day 0. Especially, miR-34c and miR-218 were up-regulated at early stages of differentiation (days 0-7) with an increase of 10-fold (26). Consistent with these changes in osteoblast differentiation of MC3T3-E1 cells, our *in vitro* data found that miR-374b-5p, the Runx2-targeting miRNA, was up-regulated at early stages of osteoblast differentiation (days 0-7) of hAFDCs and hUCDCs. These findings imply that miR-374b-5p may serve as a promising marker for the detection of osteoporosis.

Several studies have established the vital role of miR-374 in bone biology (27). Compared to the hypertrophic zone, the higher expression levels of miR-374-5p in the proliferative zone promoted chondrocyte proliferation and inhibited chondrocyte hypertrophic differentiation (28). Furthermore, in fractured mice, the expression of miR-374b was significantly increased in mouse bone marrow mesenchymal stem cells. However, the stimulative effects of miR-374b on the expression of osteoblast-associated genes (ALP, OC, and Runx2) in bone marrow stromal cells have been demonstrated (29). Consistent with the vital role of miR-374 in bone biology described by these studies, our *in vitro* data reflected that overexpression of miR-374b-5p could suppress osteoblast differentiation, as evidenced by the markedly down-regulated mRNA levels of osteoblast markers genes in the hAFDCs and hUCDCs. These effects could be reversed by suppression of miR-374b-5p. Consequently, all these data manifest that miR-374b-5p is a negative regulator of osteoblast differentiation.

To investigate how miR-374b-5p modulated osteoblast differentiation, we predicted the potential targets of miR-374b-5p. In this study, we identified that Wnt3 and Runx2 were direct targets of miR-374b-5p by binding to its 3′ UTR. Wnt3, a ligand for the canonical Wnt signaling pathway, has been confirmed as a target of miR-376c, which inhibits osteoblastogenesis (30). As the master transcription factor in osteoblast differentiation, Runx2 has been determined to be governed by miRNAs (31). Here, we report that Wnt3 and Runx2 are direct targets of miR-374b-5p and are involved in osteogenic differentiation. Moreover, we found that miR-374b-5p transfection reduced Wnt3 and Runx2 mRNA levels in cultured cells, suggesting that miR-374b-5p might negatively regulate Wnt3 and Runx2. Generally, to suppress the expression of target proteins, miRNA could directly block the translation process or enhance the degradation of mRNAs (31). Thus, the interaction between miR-374b-5p and Wnt3 and Runx2 expression reported

in this study, remains to be fully elucidated.

To delineate the role of miR-374b-5p in regulating bone formation, we generated an OVX-induced osteoporotic mouse model to mimic estrogen deficiency-induced bone loss. A growing body of evidence has demonstrated the significant effects of miRNAs on bone formation. In the OVX mouse model, miR-185 deficiency attenuated bone mass loss (32). Furthermore, administering miR-672-5p mimic through tail vein could restore OVX-induced bone loss (33). Considering the role of miR-374b-5p in regulating osteoblast differentiation, inhibition of this miRNA may exert a beneficial effect on bone formation. In this study, we assessed the therapeutic effect by the administration of agomir-374b-5p in OVX mice. More importantly, we observed that agomir-374b-5p could enhance bone mass and improve the trabecular architecture. All these data suggest that inhibition of miR-374b-5p could improve bone mass in OVX mice. For future study, the construction of miR-374b-knockout mice might be a better strategy to reveal the role of miR-374b-5p on bone formation and osteoporosis.

Taken together, we demonstrated that miR-374b-5p acted as a suppressor in regulating osteoblast differentiation via targeting Wnt3 and Runx2. Our findings reveal the regulatory role of miR-374b-5p in osteoblast differentiation and bone formation and suggest that therapeutic inhibition of miR-374b-5p might serve as a promising diagnostic and therapeutic strategy for osteoporosis.

ACKNOWLEDGEMENTS

This work was supported by grants from the Natural Science Foundation of Jiangsu Province (No. BK20161323).

REFERENCES

1. Compston JE, McClung MR, Leslie WD. Osteoporosis. Lancet 2019; 393:364-76.
2. Seeliger C, Balmayor ER, van Griensven M. miRNAs related to skeletal diseases. Stem Cells Dev 2016; 25:1261-81.
3. Saito H, Gasser A, Bolamperti S, et al. TG-interacting factor 1 (Tgif1)-deficiency attenuates bone remodeling and blunts the anabolic response to parathyroid hormone. Nat Commun 2019; 10:1354.
4. Yadav VK, Ryu JH, Suda N, et al. Lrp5 controls bone formation by inhibiting serotonin synthesis in the duodenum. Cell 2008; 135:825-37.
5. Ng KW. Future developments in osteoporosis therapy. Endocr Metab Immune Disord Drug Targets 2009; 9:371-84.
6. Song H, Li X, Zhao Z, et al. Reversal of Osteoporotic Activity by Endothelial Cell-Secreted Bone Targeting and Biocompatible Exosomes. Nano Lett 2019; 19:3040-48.
7. Anfossi S, Babayan A, Pantel K, Calin GA. Clinical utility of circulating non-coding RNAs - an update. Nat Rev Clin Oncol 2018; 15:541-63.
8. Schwarzenbach H, Nishida N, Calin GA, Pantel K. Clinical relevance of circulating cell-free microRNAs in cancer. Nat Rev Clin Oncol 2014; 11:145-56.
9. Makitie RE, Hackl M, Niinimaki R, Kakko S, Grillari J, Makitie O. Altered MicroRNA profile in osteoporosis caused by impaired WNT signaling. J Clin Endocrinol Metab 2018; 103:1985-96.
10. Seeliger C, Karpinski K, Haug AT, Vester H, Schmitt A, Bauer JS, van Griensven M. Five freely circulating miRNAs and bone tissue miRNAs are associated with osteoporotic fractures. J Bone Miner Res 2014; 29:1718-28.
11. Lian JB, Stein GS, van Wijnen AJ, et al. MicroRNA control of bone formation and homeostasis. Nat Rev Endocrinol 2012; 8:212-27.
12. Thomou T, Mori MA, Dreyfuss JM, et al. Adipose-derived circulating miRNAs regulate gene expression in other tissues. Nature 2017; 542:450-55.
13. Li D, Liu J, Guo B, et al. Osteoclast-derived exosomal miR-214-3p inhibits osteoblastic bone formation. Nat Commun 2016; 7:10872.
14. Hackl M, Heilmeier U, Weilner S, et al. Circulating microRNAs as novel biomarkers for bone diseases - Complex signatures for multifactorial diseases? Mol Cell Endocrinol 2016; 432:83-95.
15. Kocijan R, Muschitz C, Geiger E, Grillari J. Circulating microRNA signatures in patients with idiopathic and postmenopausal osteoporosis and fragility fractures. J Clin Endocrinol Metab 2016; 101:4125-34.

16. Mandourah AY, Ranganath L, Barraclough R, et al. Circulating microRNAs as potential diagnostic biomarkers for osteoporosis. Sci Rep 2018; 8:8421.
17. Yang M, Guo Q, Peng H, et al. Kruppel-like factor 3 inhibition by mutated lncRNA Reg1cp results in human high bone mass syndrome. J Exp Med 2019; 216:1944-64.
18. Mora-Raimundo P, Lozano D, Manzano M, Vallet-Regi M. Nanoparticles to knockdown osteoporosis-related gene and promote osteogenic marker expression for osteoporosis treatment. ACS Nano 2019; 13:5451-64.
19. Borlongan CV. Amniotic fluid as a source of engraftable stem cells. Brain Circ 2017; 3:175-79.
20. Ding DC, Chang YH, Shyu WC, Lin SZ. Human umbilical cord mesenchymal stem cells: a new era for stem cell therapy. Cell Transplant 2015; 24:339-47.
21. Zhou J, Wang D, Liang T, Guo Q, Zhang G. Amniotic fluid-derived mesenchymal stem cells: characteristics and therapeutic applications. Arch Gynecol Obstet 2014; 290:223-31.
22. Wang Y, Li L, Moore BT, et al. MiR-133a in human circulating monocytes: a potential biomarker associated with postmenopausal osteoporosis. PLoS One 2012; 7:e34641.
23. Cheng P, Chen C, He HB, et al. miR-148a regulates osteoclastogenesis by targeting V-maf musculoaponeurotic fibrosarcoma oncogene homolog B. J Bone Miner Res 2013; 28:1180-90.
24. Chen C, Cheng P, Xie H, Zhou HD, Wu XP, Liao EY, Luo XH. MiR-503 regulates osteoclastogenesis via targeting RANK. J Bone Miner Res 2014; 29:338-47.
25. Li H, Wang Z, Fu Q, Zhang J. Plasma miRNA levels correlate with sensitivity to bone mineral density in postmenopausal osteoporosis patients. Biomarkers 2014; 19:553-56.
26. Zhang Y, Xie RL, Croce CM, et al. A program of microRNAs controls osteogenic lineage progression by targeting transcription factor Runx2. Proc Natl Acad Sci U S A 2011; 108:9863-68.
27. Bian H, Zhou Y, Zhou D, Zhang Y, Shang D, Qi J. The latest progress on miR-374 and its functional implications in physiological and pathological processes. J Cell Mol Med 2019; 23:3063-76.
28. Jee YH, Wang J, Yue S, et al. mir-374-5p, mir-379-5p, and mir-503-5p regulate proliferation and hypertrophic differentiation of growth plate chondrocytes in male rats. Endocrinology 2018; 159:1469-78.
29. Ge JB, Lin JT, Hong HY, Sun YJ, Li Y, Zhang CM. MiR-374b promotes osteogenic differentiation of MSCs by degrading PTEN and promoting fracture healing. Eur Rev Med Pharmacol Sci 2018; 22:3303-10.
30. Kureel J, John AA, Prakash R, Singh D. MiR 376c inhibits osteoblastogenesis by targeting Wnt3 and ARF-GEF-1 -facilitated augmentation of beta-catenin transactivation. J Cell Biochem 2018; 119:3293-303.
31. Marini F, Cianferotti L, Brandi ML. Epigenetic mechanisms in bone biology and osteoporosis: can they drive therapeutic choices? Int J Mol Sci 2016; 17.
32. Cui Q, Xing J, Yu M, et al. Mmu-miR-185 depletion promotes osteogenic differentiation and suppresses bone loss in osteoporosis through the Bgn-mediated BMP/Smad pathway. Cell Death Dis 2019; 10:172.
33. Ahmad N, Kushwaha P, Karvande A, et al. MicroRNA-672-5p Identified during weaning reverses osteopenia and sarcopenia in ovariectomized mice. Mol Ther Nucleic Acids 2019; 14:536-49.

SUPPRESSION OF P38/HBP1 PATHWAY ALLEVIATES HYPEROSMOTIC STRESS-INDUCED SENESCENT PROGRESSION OF CHONDROCYTE SENESCENCE

Z.-Z. YAO, H.-C. TAN, J.-F. CHEN, T. JIN, C.-S. ZHOU, J. LIANG and A.-X. HU

Department of Orthopedic Surgery, The People's Hospital of China Three Gorges University/The First People's Hospital of Yichang, Yichang, China

Received February 3, 2020 – Accepted February 28, 2020

The first two Authors contributed equally to this paper

This study aims to explore the effect of p38 mitogen-activated protein kinase and its downstream target HMG-box transcription factor 1 (HBP1) in the chondrocyte (CH) senescence caused by hyperosmotic stress. Human cartilage tissue with or without osteoarthritis (OA) were collected to detect the differential expression of p38 and HBP1 by Western blot. CHs were isolated from cartilage without OA and used the hyperosmotic medium to accelerate CH senescence *in vitro*. A p38 inhibitor and siRNA were used to mediate the expression of p38 and HBP1. The viability of CHs was determined by cell counting kit 8 (CCK8) assay. CH-related mRNA expression was analyzed by quantitative real-time polymerase chain reaction (RT-PCR). Immunofluorescence was also used to detect collagen II and beta-galactosidase expression. Senescent cells were increased in both OA cartilage and hyperosmotic stress treatment with a marked upregulation of p38 and HBP1. Suppression of p38 activation reversed the hyperosmotic stress-induced CH senescence and led to an inhibition of HBP1, p16, Runx-2, MMP-13, collagen X expression, and an upregulation of collagen II and SOX-9 expression. Moreover, the silencing of HBP1 also played a protective effect on CH senescence. The suppression of the p38/HBP1 pathway alleviates the hyperosmotic stress-induced senescent progression of CHs.

Osteoarthritis (OA) is the most common form of degenerative joint disease worldwide, mainly causing pain and disability in patients, mostly in the elderly population. OA affects various tissues around the joint, such as articular cartilage, subchondral bone, synovium, and ligaments with chronic progressive deterioration of the articular cartilage (AC) and abnormal bone remodeling (1). Gender, genetic predisposition, and obesity all contribute to the pathogenesis of OA. However, aging has always been considered a crucial etiological factor for OA (2). The onset of OA and the accumulation of aging chondrocytes (CHs) lead to an imbalance of the synthesis, degradation of extracellular matrix (ECM), decomposition and degeneration of AC tissue, and sustained pathological inflammation in the joint (3). CH senescence plays a vital role in the development of OA, therefore, delaying or eradicating aging CHs may inhibit the inflammatory response of OA, protect the integrity of AC tissue, alleviate the pain of OA patients, and improve the pathological changes of OA (4).

Cellular aging is characterized by growth arrest, metabolic changes, and loss of proliferative capacity (5). Aging can be a normal physiological process,

Key words: p38, HBP1, chondrocyte, senescence, osmolality stress

Corresponding Author:
Aixin Hu, MM
Department of Orthopedic Surgery,
The People's Hospital of China Three Gorges University,
The First People's Hospital of Yichang, Jiefang Road,
XiLing District, Yichang City, Hubei Province, 443000China
Tel.: +86013997689430
e-mail: baixin19640414@163.com

0393-974X (2020)
Copyright © by BIOLIFE, s.a.s.
This publication and/or article is for individual use only and may not be further reproduced without written permission from the copyright holder.
Unauthorized reproduction may result in financial and other penalties
DISCLOSURE: ALL AUTHORS REPORT NO CONFLICTS OF INTEREST RELEVANT TO THIS ARTICLE.

or it can be used as a cause to promote tissue aging and induce lesions. Repeated mechanical trauma, and oxidative stress can boost the senescence of CHs, causing chronic inflammation and leading to the aging phenotype of CHs. Aging CHs acquire a new secretory phenotype, releasing pro-inflammatory cytokines, angiogenic factors, and catabolic enzymes, causing the phenotype to be disordered toward hypertrophic CHs and impairing the stability of ECM, aggravating the OA process. Aging CH can affect the ability of AC to regenerate (6). Persistent mechanical pressure, intrinsic hypoxia, low pH, and high osmotic pressure in the joint cavity microenvironment make CHs more susceptible to aging (7). Injection of senescent CHs into joints sufficiently promotes cartilage damage similar to OA in mice (8). However, the removal of senescent CHs reduces AC damage and pain in the post-traumatic mice model (9).

The regulatory mechanism of cellular senescence is complex, involving DNA damage response, p38 mitogen-activated protein kinase (MAPK) signaling pathway, nuclear factor κB (NF-κB) and CCAAT/enhancer-binding protein β (C/EBPβ) activation (10). p38 activates downstream aging-associated p53, p16, and p53/p16-independent signaling pathways and regulates standard cell-associated secretory phenotypic transformation until arrested in irreversible senescence (11). Studies have shown that inhibition of p38 can attenuate the cell aging phenotype, and activation of the p38 signaling pathway induces cell senescence-associated phenotypes (SASP) (12, 13). HMG-box transcription factor 1 (HBP1) is a broad-spectrum cellular transcription factor that functions to regulate cell proliferation as a transcriptional repressor (14). HBP1 itself can induce premature cell senescence and is also involved in the blockade of p38 MAPK-induced G1 phase, which arrests cell growth, a process associated with increased p16 expression (15, 16). Nevertheless, whether p38 mediates CHs senescence through HBP1 is still not clear.

Articular CHs always exist in the unstable osmotic environment, and exceeding osmotic loading severely compromises CH function resulting in degenerative changes (17, 18). In this study, hyperosmotic conditions were used to make a senescent CH model and elucidate the potential effect of the p38/HBP1 pathway in the aging progression of CHs. Our results can serve as a new strategy for inhibiting or eliminating aging CHs and provide a theoretical basis for the prevention and treatment of OA.

MATERIALS AND METHODS

AC tissue samples

AC tissues were collected from ten patients (patient information is listed in Table I) undergoing two different operations. Tissues from amputees with distal chondrosarcoma without any OA history were used as a control group. Tissues from joint replacement patients with advanced OA were used as the OA group. This research was approved by the Ethics Committee of The People's Hospital of China Three Gorges University/The First People's Hospital of Yichang. Signed written informed consent were obtained from all participants before the study. The samples were conserved in a cold cell culture medium immediately after excising from the patients.

CHs isolation and treatment

AC tissues from amputees with distal chondrosarcoma without OA were washed with a phosphate-buffered saline solution (PBS) and cut as small as possible. The fragmented AC was digested with 0.25% type XI collagenase solution in an incubator overnight. Then, the solution was filtrated using a cell strainer, centrifuged to get CHs and resuspend with culture medium (DMEM/F12 containing 10% fetal bovine serum (FBS), Gibco, Rockville, MD, USA). CHs were seeded in 6-well plates at 1×10^5 density and passaged to generation 1 or 2 for the following experiments. In addition to the regular culture medium used as a control, hyperosmotic stress medium of 400 mOsm and 600 mOsm were prepared by extra supplements of NaCl, as previously described. CHs were treated with hyperosmotic stress medium for 6 h, and then with or without SB203580 (5 μM, Selleck, Houston, TX, USA), an inhibitor of p38, for another 6 h. Moreover, to block the HBP1 expression, siRNA targeting HBP1 or Null was used to transfect CHs.

Western blot analysis

Western blot (WB) was used to determine the protein expression both in AC tissues and CHs. AC fragments and harvested CHs were lysed by lysis buffer (Beyotime,

Shanghai, China) according to the manufacturer's instructions. Protein concentration was analyzed by bicinchoninic acid (BCA) Kit (Beyotime, Shanghai, China). Equal amounts of protein samples were separated by sodium dodecyl sulfate-polyacrylamide gel electrophoresis (SDS-PAGE) onto polyvinylidene fluoride (PVDF) membranes (Millipore, Billerica, MA, USA). Then, PVDF membranes were blocked by 5% milk and incubated with anti-collagen-II (MAB8887, Sigma-Aldrich, St. Louis, MO, USA), anti-p38 (MABS1754, Sigma-Aldrich, St. Louis, MO, USA), anti-phosphorylated p38 (p-p38, 09-272, Sigma-Aldrich, St. Louis, MO, USA), anti-HBP1 (ab216844, Abcam, Cambridge, MA, USA), anti-p16 (ab51243, Abcam, Cambridge, MA, USA), and anti-β-actin (ab179467, Abcam, Cambridge, MA, USA) overnight at 4°C. After washing, the membranes were coated with a secondary antibody for 1 h. Bands of protein were detected using enhanced chemiluminescence reagent (Beyotime, Shanghai, China).

Immunofluorescent staining

CHs were successively washed with cold PBS, fixed with 4% formaldehyde, 0.05% TritonX-100, and blocked with 5% bovine serum albumin (BSA). Then incubated with anti-collagen-II (MAB8887, Sigma-Aldrich, St. Louis, MO, USA), or anti-beta galactosidase antibody (β-gal, ab9361, Abcam, Cambridge, MA, USA) overnight at 4°C, followed by a secondary antibody for 1 h in the dark. Nuclei were stained by 4',6-diamidino-2-phenylindole (DAPI) (Beyotime, Shanghai, China), and the fluorescent intensity was visualized using a fluorescence microscope.

Quantitative real-time polymerase chain reaction (RT-PCR)

Total RNA was isolated from CHs with TRIzol reagent (Invitrogen, Carlsbad, CA, USA) according to the manufacturer's instructions. RNA was then reverse-transcribed into cDNA by PrimeScript Mix (Invitrogen, Carlsbad, CA, USA). RT-PCR was conducted using SYBR Green Master Mix (Invitrogen, Carlsbad, CA, USA) to quantify SOX-9, Runx-2, MMP-13, and collagen-X and glyceraldehyde 3-phosphate dehydrogenase (GAPDH) (used as normalization) mRNA levels. Primers used for RT-PCR are listed in Table II. Relative mRNA levels were calculated by the $2^{-\Delta\Delta Ct}$ method.

siRNA transfection

CHs were transfected by siRNA targeting HBP1 or Null (NM_012257, Sigma-Aldrich, St. Louis, MO, USA). Lipofectamine 2000 (Invitrogen, Carlsbad, CA, USA) was used for the transfection of siRNA into CHs according to the manufacturer's protocol. The cells were incubated for a further 24 h after transfection. Transfection efficacies were measured *via* WB.

Cell viability assay

The viability of CHs was determined using the cell counting kit 8 (CCK8) assay. CHs were seeded in a 96-well plate at 1×10^4 cells/well and cultured with a CCK8 assay kit (Beyotime, Shanghai, China) according to the manufacturer's instructions. Absorbance was analyzed with a microtiter plate reader at 450 nm.

Table I. *Patient information*

NO.	Gender	Age	Diagnosis	NO.	Gender	Age	Diagnosis
1	F	19	chondrosarcoma	6	M	52	OA
2	F	23	chondrosarcoma	7	M	69	OA
3	M	36	chondrosarcoma	8	M	57	OA
4	F	43	chondrosarcoma	9	F	46	OA
5	M	32	chondrosarcoma	10	F	49	OA

NO: Number; M: male; F: female; OA: osteoarthritis

Statistical analysis

Data were all displayed by the means ± standard deviations. Differences between two groups were analyzed by using the Student's *t*-test. A comparison between multiple groups was made using one-way ANOVA test followed by Post Hoc Test (Least Significant Difference). P-value <0.05 was considered statistically significant.

RESULTS

p38 and HBP1 were upregulated in human OA cartilage

To make a clear recognition of the p38 and HBP1 expression in cartilage with or without OA, AC was collected from OA patients, and distal chondrosarcoma patients without OA as control. The results of WB indicated that OA cartilage expressed a lower amount of collagen II, but a higher p16 level compared to the control, meaning the ECM of AC was destroyed and the senescent cells accumulated in the cartilage (Fig. 1 A, B). Furthermore, the total of p38 expression was increased in OA, especially the phosphorylated p38. Healthy cartilage expressed little HBP1, but it raised substantially in OA condition. The data suggest that HBP1 was upregulated in OA therefore the activation of p38 by phosphorylation, and the p38/HBP1 axis might play roles in the aging progression of AC.

Table II. *Primer sequences used in RT-PCR*

Gene name	Forward (5'>3')	Reverse (5'>3')
Collagen X	ATGCTGCCACAAATACCCTTT	GGTAGTGGGCCTTTTATGCCT
SOX-9	AGCGAACGCACATCAAGAC	CTGTAGGCGATCTGTTGGGG
Runx-2	TGGTTACTGTCATGGCGGGTA	TCTCAGATCGTTGAACCTTGCTA
MMP-13	ACTGAGAGGCTCCGAGAAATG	GAACCCCGCATCTTGGCTT
GAPDH	ACAACTTTGGTATCGTGGAAGG	GCCATCACGCCACAGTTTC

RT-PCR: quantitative reverse-transcription polymerase chain reaction

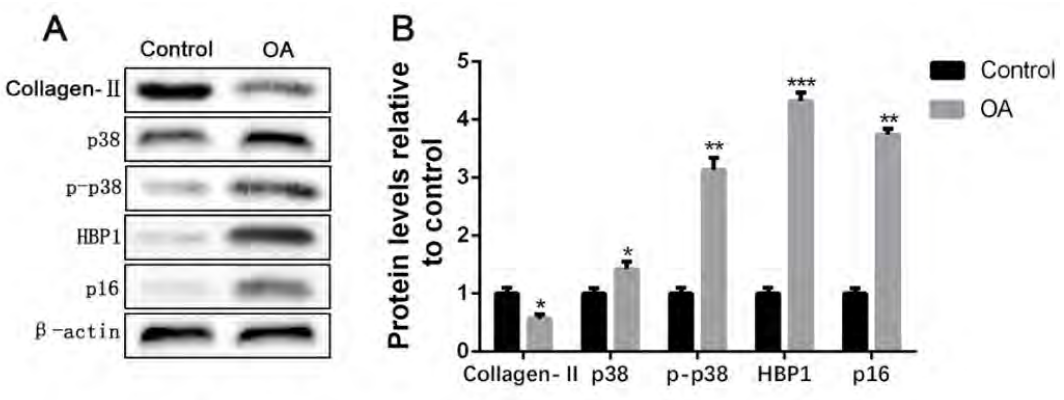


Fig. 1. *Total protein analysis of AC with or without OA. A, B. The protein expression levels were determined by (**A**) WB and (**B**) quantification analysis. Data are presented as mean ± SD of three independent experiments. (*P<0.05, **P<0.01, ***P<0.001 compared to control).*

p38 and HBP1 were upregulated in hyperosmotic stress-induced CHs senescence

To determine the phosphorylated p38 and HBP1 expression in senescent CHs *in vitro*, hyperosmotic medium was used to accelerate the senescent progress of CHs. As shown in Fig. 2 A, B, collagen II levels in CHs were significantly decreased due to the hyperosmotic stress in a concentration-dependent way. However, the senescent marker β-gal was upregulated as the osmotic pressure increased. Hyperosmotic stress also affected the cell viability of CHs (Fig. 2C). The protein expression of p16 was markedly upregulated in hyperosmotic conditions compared to the control, which also showed signs of senescence in CHs (Fig. 2 D, E). Apart from this, p-p38 and HBP1 were increased, resulting from the hyperosmotic stress also in a concentration-dependent manner. With the development of CHs senescence, the chondrogenic mRNA expression of SOX-9 was reduced. On the contrary, the hypertrophic mRNA expression of MMP-13, Runx-2, and collagen X significantly overexpressed compared to the control (Fig. 2F). Taken together, the hyperosmotic medium induced a typical senescence in CHs containing a hyposecretion of collagen II, low viability, senescent cell accumulation, and hypertrophic progression, which also accompanied the upregulation of p-p38 and HBP1 expression.

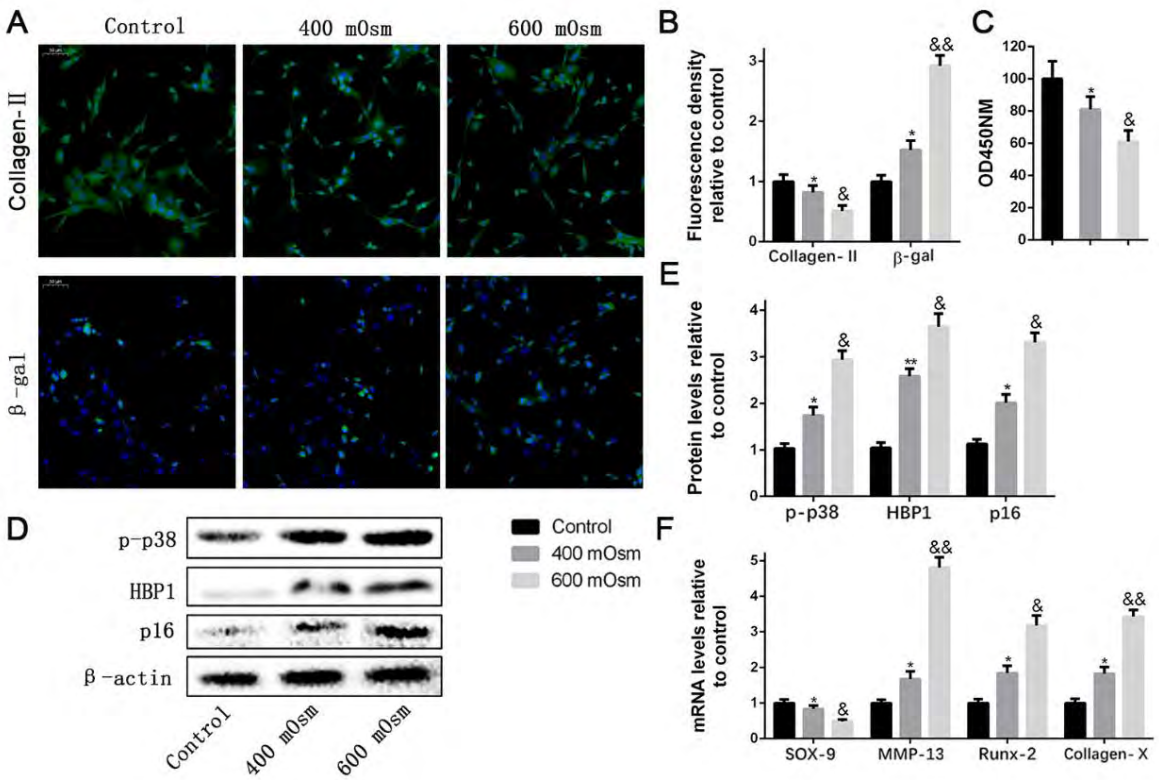


Fig. 2. *p38/HBP1 was activated in hyperosmotic stress-treated CHs senescence. CHs were pre-treated with 400 mOsm or 600 mOsm medium for 6 hours and changed to isotonic medium.* ***A)*** *IF staining (magnification: 400×).* ***B)*** *Quantification analysis. C) CHs viability was determined by CCK8 assay. The protein expression levels were determined by (**D**) WB and (**E**) quantification analysis.* ***F)*** *The mRNA expression levels were assayed by RT-PCR. Data are presented as mean ± SD of three independent experiments. (*P<0.05, **P<0.01 compared to the control; $^{\&}$P<0.05, $^{\&\&}$P<0.01 compared to the 400 mOsm group)*

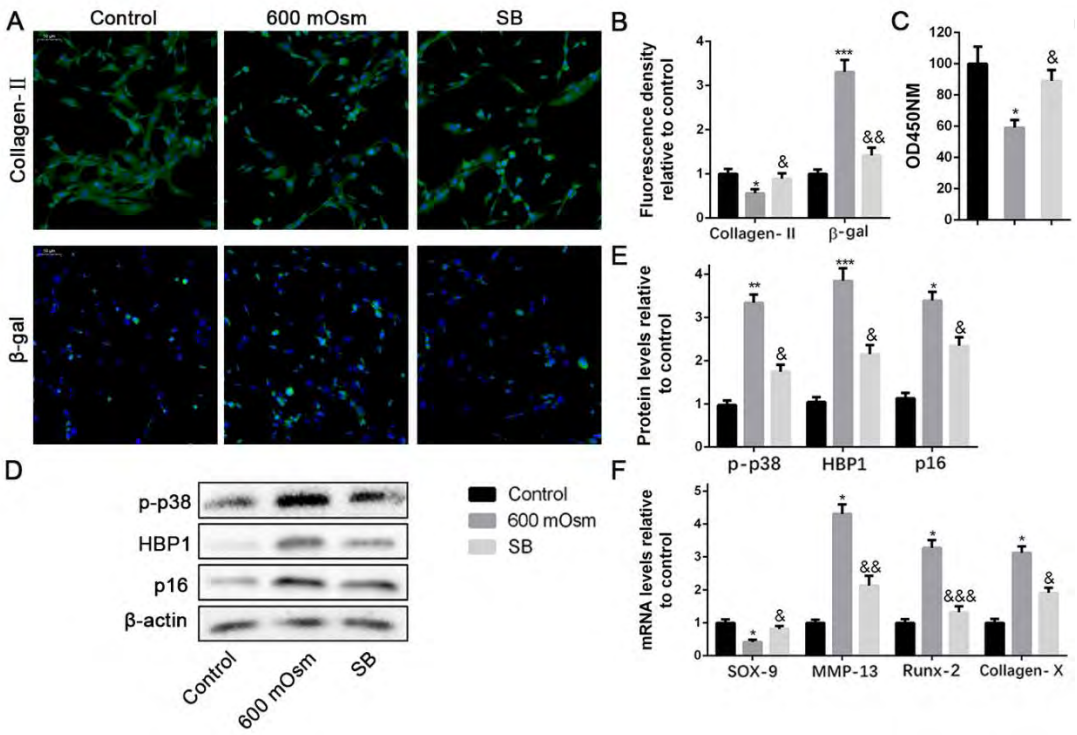


Fig. 3. *Suppression of p38 alleviated CHs senescence caused by hyperosmotic stress. CHs were pre-treated with 600 mOsm medium for 6 hours and changed to isotonic medium, and then treated with (5 μM) for another 6 hours.* ***A)*** *IF staining (magnification: 400×).* ***B)*** *quantification analysis.* ***C)*** *CCK8 assay. The protein expression levels were determined by (****D****) WB and (****E****) quantification analysis.* ***F)*** *The mRNA expression levels were assayed by RT-PCR. Data are presented as mean ± SD of three independent experiments. (*P<0.05, **P<0.01, ***P<0.001 compared to the control; $^{\&}$P<0.05, $^{\&\&}$P<0.01, $^{\&\&\&}$P<0.001 compared to the 600 mOsm group)*

The suppression of p38 alleviated CHs senescence in hyperosmotic stress

Since p38 was activated in the CH senescence, we wondered whether the suppression of p38 would alleviate the degree of senescence and affect the HBP1 expression. Compared to the hyperosmotic condition of 600 mOsm, the supplement of SB recalled the secretion of collagen II and reduced the β-gal positive cells (Fig. 3 A, B). SB also protected the CH viability after hyperosmotic stress treatment (Fig. 3C). As the inhibitory function of p38, SB suppressed the p38 phosphorylation, which was activated by 600 mOsm hyperosmotic medium, resulting in the reduction of HBP1 and p16 expression compared to the hyperosmotic group (Fig. 3 D, E). Furthermore, the suppression of p-p38 led to the upregulation of SOX-9, and the downregulation of MMP-13, Runx-2, and collagen X mRNA expression compared to the 600 mOsm groups (Fig. 3F). In this part, the suppression was found of p38 activation alleviated the senescent degree caused by hyperosmotic stress, with the downregulation of HBP1. Therefore, the p-p38 activation caused by hyperosmotic stress induced the upregulation of HBP1, and the suppression of p38 also affected the HBP1 expression.

Silencing of HBP1 alleviated CHs senescence in hyperosmotic stress

To determine the effect of HBP1 in the senescent progression of CHs, we used siRNA to silence HBP1 gene expression. As shown in Fig. 4 A, B, HBP1 was originally low expressed in the AC with no degradation, the siRNA with null sequence did not affect HBP1 expression statistically, but

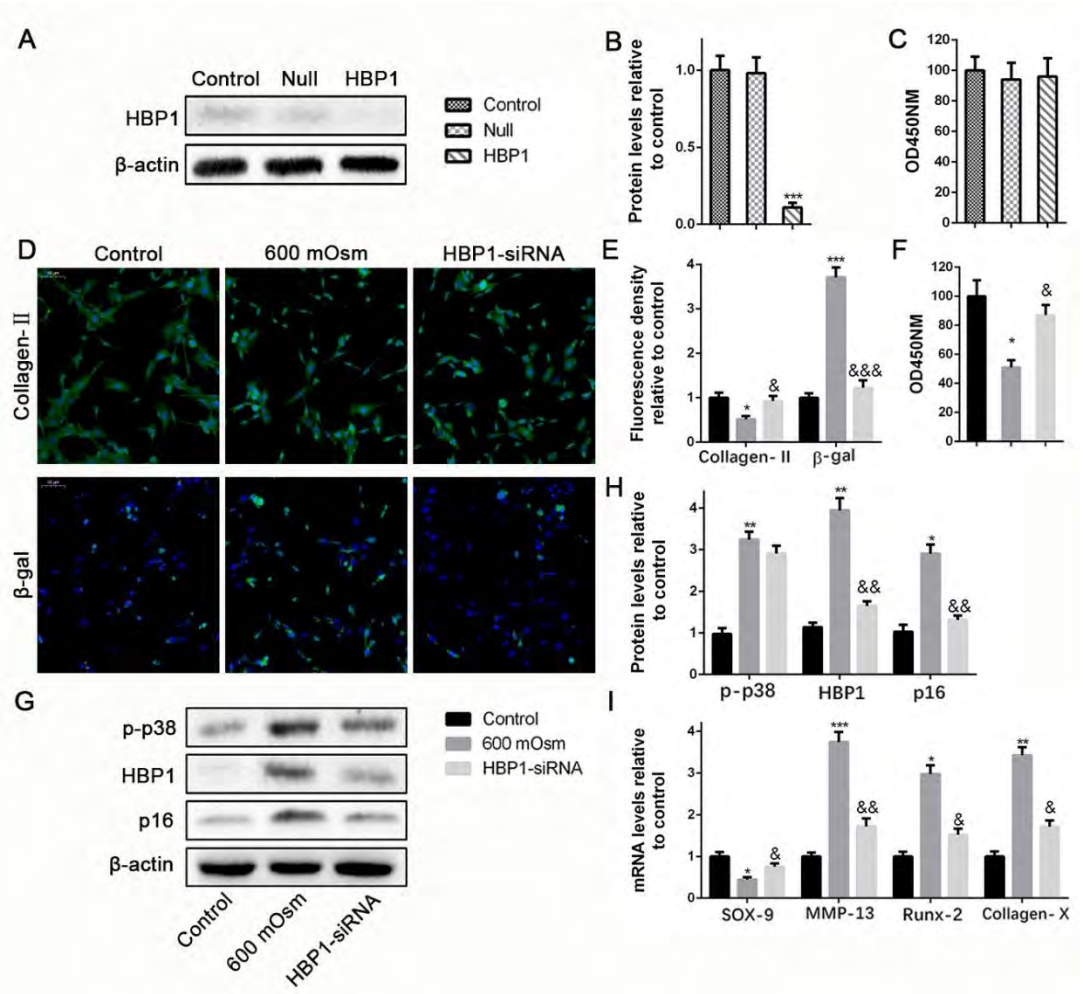


Fig. 4. *The silencing of HBP1 alleviated CHs senescence caused by hyperosmotic stress. CHs were transfected with siRNA target HBP1 or null, and WB and CCK8 assay were used to detect the safety and silencing efficiency of siRNA. CHs with or without HBP1-siRNA transfection were treated with 600 mOsm medium for 6 hours. A, B. The HBP1 protein expression of CHs without transfection, with null-siRNA or HBP1-siRNA transfection, was determined by (**A**) WB and (**B**) quantification analysis. **C**) CCK8 assay. **D**) IF staining of collagen II and β-gal in CHs with or without HBP1-siRNA transfection in hyperosmotic treatment (magnification: 400×) **E**) quantification analysis of collagen II and β-gal in CHs with or without HBP1-siRNA transfection in hyperosmotic treatment. **F**) CCK8 assay. The protein expression levels were determined by (**G**) WB and (**H**) quantification analysis. **I**) The mRNA expression levels were assayed by RT-PCR. Data are presented as mean ± SD of three independent experiments. (*P<0.05, **P<0.01, ***P<0.001 compared to the control; $^{\&}$P<0.05, $^{\&\&}$P<0.01, $^{\&\&\&}$P<0.001 compared to the none transfected 600 mOsm group).*

siRNA targeting HBP1 blocked the most HBP1 protein expression. The siRNA transfection also did not affect CH viability, indicating a barely negative effect on CHs (Fig. 4C). We used CHs with or without HBP1-siRNA transfection suffering hyperosmotic medium. The result of IF indicated that HBP1 deficiency played a protective role in the maintaining of collagen II expression and decreased the β-gal positive population compared to the non-transfected 600 mOsm group (Fig. 4 D, E). The silencing of HBP1 also protected the CH viability in 600 mOsm hyperosmotic medium (Fig. 4F). In addition, the silencing of HBP1 obviously decreased the p16 expression but did not affect the p-p38 level statistically compared to non-transfected CHs (Fig. 4 G, H). Finally, mRNA expression of SOX-9, MMP-

13, Runx-2, and collagen X were also measured, which indicted a chondrogenic friendly effect of HBP1 gene deficiency (Fig. 4I). The results suggested that HBP1 contributed to the senescent development of CHs, and the blocking of its expression played a protective role in CH aging progression.

DISCUSSION

There is no blood vessel, lymph, or nerve in the AC, making it difficult to repair after damage. OA is mainly concentrated in ACs where it is not easy to repair. In the whole pathological progress of OA, even if there is a repair of AC morphology and function, the degeneration is still dominant. The senescence of CHs is therefore closely related to the degeneration process of OA (19, 20). The present study shows that OA tissue expressed a higher level of p16, the indicator of cell senescence compared to the control. p16 is a tumor suppressor gene, and the p16 protein is affected by preventing the cell from the G1 phase into the S phase and inhibiting cell proliferation through inactivating the CDK4 enzyme (21). In addition to the accumulation of senescent cells, we also found an upregulation of p-p38 and HBP1 protein expression. The p38 mitogen-activated protein kinase pathway belongs to the stress-activated protein kinase in the mitogen-activated protein kinase family and is one of the channels for extracellular signal-induced nuclear responses, playing an essential role in the pathogenesis of OA (22). In the AC of OA patients, activation of p38 is involved in the imbalance of cartilage matrix synthesis and metabolism, promoteing hypertrophy, calcification, senescence, and apoptosis of CHs (23).

The p38 signaling pathway in mammals is activated by extracellular stimuli such as ultraviolet radiation, heat shock, high osmotic pressure, inflammatory factors, and growth factors (24, 25). Under different stimuli, phosphorylated p38 activates various transcription factors, such as ATF, Sap1, CHOP, MEF2C, and HBP1 (26). Chung et al. (27) found that arsenic causes AC senescence through the phosphorylation of p38 and c-Jun N-terminal kinase (JNK) pathway and the suppression of p38 and JNK could reverse the senescence of CH caused by arsenic. Hong et al. (28) reported ionizing radiation induces CH senescence through p38 activation based on reactive oxygen species. In yeast, osmotic challenge induces p38 phosphorylation and triggers the activation of a subset of kinases to controll cellular metabolism (29). Tew et al. found osmotic pressure regulates CHs SOX9 and collagen II mRNA expression by p38 (30). However, whether HBP1 is related to the p38 mediated CH senescence is still unknown. HBP1 is a target of p38 and acts to inhibit cell cycle protein D1, which affects the cell cycle and blocks cell growth arrest, contributing to cell senescence (31). In our study, the activation of p38 by hyperosmotic conditions significantly increased the expression of HBP1, and the suppression of p38 also led to a reduction in HBP1 expression.

In healthy individuals, the osmotic pressure in the synovial fluid ranges from 295 to 340 mOsm (32). The osmotic pressure constantly changes between hyposmotic and hyperosmotic conditions due to different physiological processes, and CHs adapt to these changes within the ability of adjustment (33). It has been demonstrated that hyperosmotic pressure induces irreversible changes in the protein synthesis, amino acid transport, morphology and proliferating capacity of CHs (15). However, when osmotic stress is beyond the physiological compensation of CHs, apoptotic cell death and degenerative changes occur (18, 34). The hyperosmotic medium made a senescent phenotype in our CHs with a marked decreased chondrogenic gene level and a significant p16 protein expression. p16 is accumulated in the aging tissues and the senescence cell, and the clearance of p16 contributes to the relief of aging in cells (35, 36). p16 is an essential downstream target gene for HBP1, and it can be upregulated by HBP1 *via* the promoter activation, leading to irreversible premature aging of cells (16, 37). In accordance with previous reports, p16 protein was obviously decreased, resulting form the silencing of HBP1 in CHs *in vitro*.

In summary, the present observation elucidated the effect of p38 and HBP1 in the senescent progression in CHs caused by hyperosmotic stress. p38/HBP1 pathway is activated in hyperosmotic stress-induced CHs by upregulation of the p16 expression,

resulting in a senescent phenotype with lower viability, weak chondrogenic gene expressions, and strong hypertrophic gene expression. However, the suppression of p38 activation leads to the inhibition of HBP1 and reverses the hyperosmotic stress-induced senescence. Moreover, HBP1 deficiency also contributes to the alleviation of CHs senescence. Therefore, the p38/HBP1 pathway seems to be associated with the hyperosmotic stress-induced CH senescence, which might be an active target for the treatment of OA in the future.

ACKNOWLEDGEMENTS

This study was supported by the Scientific Programs of Yichang Municipal Commission of Technology Bureau Planning (A16-301-21).

REFERENCES

1. Hunter DJ, Bierma-Zeinstra S. Osteoarthritis. Lancet 2019; 393:1745-59.
2. Sandell LJ, Aigner T. Articular cartilage and changes in arthritis. An introduction: cell biology of osteoarthritis. Arthritis Res 2001; 3:107-13.
3. Lotz M, Loeser RF. Effects of aging on articular cartilage homeostasis. Bone 2012; 51:241-48.
4. Atesok K, Fu FH, Sekiya I, Stolzing A, Ochi M, Rodeo SA. Stem cells in degenerative orthopaedic pathologies: effects of aging on therapeutic potential. Knee Surg Sports Traumatol Arthrosc 2017; 25:626-36.
5. Musumeci G, Szychlinska MA, Mobasheri A. Age-related degeneration of articular cartilage in the pathogenesis of osteoarthritis: molecular markers of senescent chondrocytes. Histol Histopathol 2015; 30:1-12.
6. Loeser RF. Aging and osteoarthritis. Curr Opin Rheumatol 2011; 23:492-96.
7. Blanco FJ, Rego I, Ruiz-Romero C. The role of mitochondria in osteoarthritis. Nat Rev Rheumatol 2011; 7:161-69.
8. Xu M, Bradley EW, Weivoda MM, et al. Transplanted Senescent Cells Induce an Osteoarthritis-Like Condition in Mice. J Gerontol A Biol Sci Med Sci 2017; 72:780-85.
9. Jeon OH, Kim C, Laberge RM, et al. Local clearance of senescent cells attenuates the development of post-traumatic osteoarthritis and creates a pro-regenerative environment. Nat Med 2017; 23:775-81.
10. Sikora E, Arendt T, Bennett M, Narita M. Impact of cellular senescence signature on ageing research. Ageing Res Rev 2011; 10:146-52.
11. Rodier F, Campisi J. Four faces of cellular senescence. J Cell Biol 2011; 192:547-56.
12. Alspach E, Flanagan KC, Luo X, et al. p38MAPK plays a crucial role in stromal-mediated tumorigenesis. Cancer Discov 2014; 4:716-29.
13. Freund A, Patil CK, Campisi J. p38MAPK is a novel DNA damage response-independent regulator of the senescence-associated secretory phenotype. Embo J 2011; 30:1536-48.
14. Shih HH, Tevosian SG, Yee AS. Regulation of differentiation by HBP1, a target of the retinoblastoma protein. Mol Cell Biol 1998; 18:4732-43.
15. Lavender P, Vandel L, Bannister AJ, Kouzarides T. The HMG-box transcription factor HBP1 is targeted by the pocket proteins and E1A. Oncogene 1997; 14:2721-28.
16. Li H, Wang W, Liu X, Paulson KE, Yee AS, Zhang X. Transcriptional factor HBP1 targets P16(INK4A), upregulating its expression and consequently is involved in Ras-induced premature senescence. Oncogene 2010; 29:5083-94.
17. Borghetti P, Della SL, De Angelis E, et al. Adaptive cellular response to osmotic stress in pig articular chondrocytes. Tissue Cell 1995; 27:173-83.
18. Guilak F, Erickson GR, Ting-Beall HP. The effects of osmotic stress on the viscoelastic and physical properties of articular chondrocytes. Biophys J 2002; 82:720-27.
19. Shen T, Alvarez-Garcia O, Li Y, Olmer M, Lotz MK. Suppression of Sestrins in aging and osteoarthritic cartilage: dysfunction of an important stress defense mechanism. Osteoarthritis Cartilage 2017; 25:287-96.
20. Toh WS, Brittberg M, Farr J, et al. Cellular senescence in aging and osteoarthritis. Acta Orthop 2016; 87:6-14.
21. Bennett DC. Genetics of melanoma progression: the rise and fall of cell senescence. Pigment Cell Melanoma Res 2016; 29:122-40.
22. Kim SJ, Ju JW, Oh CD, et al. ERK-1/2 and p38 kinase oppositely regulate nitric oxide-induced

apoptosis of chondrocytes in association with p53, caspase-3, and differentiation status. J Biol Chem 2002; 277:1332-39.

23. Rasheed Z, Akhtar N, Haqqi TM. Pomegranate extract inhibits the interleukin-1beta-induced activation of MKK-3, p38alpha-MAPK and transcription factor RUNX-2 in human osteoarthritis chondrocytes. Arthritis Res Ther 2010; 12:R195.
24. Raingeaud J, Gupta S, Rogers JS, Dickens M, Han J, Ulevitch RJ, Davis RJ. Pro-inflammatory cytokines and environmental stress cause p38 mitogen-activated protein kinase activation by dual phosphorylation on tyrosine and threonine. J Biol Chem 1995; 270:7420-26.
25. Ono K, Han J. The p38 signal transduction pathway: activation and function. Cell Signal 2000; 12:1-13.
26. Zarubin T, Han J. Activation and signaling of the p38 MAP kinase pathway. Cell Res 2005; 15:11-18.
27. Chung YP, Chen YW, Weng TI, Yang RS, Liu SH. Arsenic induces human chondrocyte senescence and accelerates rat articular cartilage aging. Arch Toxicol 2019; 94(1):89-101.
28. Hong EH, Lee SJ, Kim JS, et al. Ionizing radiation induces cellular senescence of articular chondrocytes via negative regulation of SIRT1 by p38 kinase. J Biol Chem 2010; 285:1283-95.
29. Tew SR, Peffers MJ, Mckay TR, Lowe ET, Khan WS, Hardingham TE, Clegg PD. Hyperosmolarity regulates SOX9 mRNA posttranscriptionally in human articular chondrocytes. Am J Physiol Cell Physiol 2009; 297:C898-906
30. Sheikh-Hamad D, Gustin MC. MAP kinases and the adaptive response to hypertonicity: functional preservation from yeast to mammals. Am J Physiol Renal Physiol 2004; 287: F1102-10.
31. Xiu M, Kim J, Sampson E, Huang CY, Davis RJ, Paulson KE, Yee AS. The transcriptional repressor HBP1 is a target of the p38 mitogen-activated protein kinase pathway in cell cycle regulation. Mol Cell Biol 2003; 23:8890-901.
32. Bertram KL, Krawetz RJ. Osmolarity regulates chondrogenic differentiation potential of synovial fluid derived mesenchymal progenitor cells. Biochem Biophys Res Commun 2012; 422:455-61.
33. Le D, Hofbauer MA, Towle CA. Differential effects of hyperosmotic challenge on interleukin-1-activated pathways in bovine articular cartilage. Arch Biochem Biophys 2006; 445:1-8.
34. Racz B, Reglodi D, Fodor B, Gasz B, Lubics A, Gallyas F, Jr., Roth E, Borsiczky B. Hyperosmotic stress-induced apoptotic signaling pathways in chondrocytes. Bone 2007; 40: 1536-43.
35. Baker DJ, Childs BG, Durik M, et al. Naturally occurring p16(Ink4a)-positive cells shorten healthy lifespan. Nature 2016; 530:184-89.
36. Baker DJ, Wijshake T, Tchkonia T, et al. Clearance of p16Ink4a-positive senescent cells delays ageing-associated disorders. Nature 2011; 479:232-36.
37. Wang W, Pan K, Chen Y, Huang C, Zhang X. The acetylation of transcription factor HBP1 by p300/CBP enhances p16INK4A expression. Nucleic Acids Res 2012; 40:981-95.

PROTECTIVE EFFECT OF SONIC HEDGEHOG SIGNALING PATHWAY ACTIVATION ON ACUTE MYOCARDIAL INFARCTION

SJ. LI[1*], QH. MEI[1], SY. ZENG[1], LL. LAI[2], J. QUAN[1] and X. ZHANG[1]

[1]Department of Pharmacy, Guangdong Second Provincial General Hospital, Guangzhou, China;
[2]Department of Drug Clinical Trials, Guangdong Second Provincial General Hospital, Guangzhou, China

Received October 10, 2019 – Accepted March 3, 2020

To study changes in the sonic hedgehog (Shh) signaling pathway in acute myocardial infarction (AMI) and the protective effect of changes in Shh signaling pathway activity on AMI, specific pathogen-free (SPF) C57BL/6 mice were treated with left anterior descending (LAD) ligation to establish an AMI model. The samples were collected on the 1st, 3rd, 14th, and 21st days after AMI induction. After the operations, the mice were administered the Shh signaling pathway receptor agonist SAG1.3 (5 mg/kg/d) and antagonist SANT-1 (3.3 mg/kg/d) by intraperitoneal injection. The myocardial ischemia model was established by oxygen glucose deprivation (OGD) *in vitro*. The AMI mouse model and the *in vitro* OGD-induced myocardial ischemia model were established. The Smo agonist SAG1.3 was used to activate the Shh signaling pathway, thereby reducing the expression of Bcl-2 and Bax. The number of apoptotic cells was reduced. Administration of the antagonist SANT-1 inhibited Shh signaling pathway activity by increasing the expression of Bcl-2 and Bax, and the number of apoptotic cells increased. In conclusion, activation of the Shh signaling pathway improved cardiac functions and myocardial remodeling and reduced the apoptosis of myocardial cells.

Acute myocardial infarction (AMI) has become one of the major cardiovascular diseases that threatens human life and health (1). Once AMI occurs, opening the infarct-related artery (IRA) as soon as possible is particularly urgent to reduce the area of myocardial infarction and improve left ventricular function. Promoting angiogenesis provides a new treatment for improving blood supply in patients with AMI. The vascular system establishes effective collateral circulation through regeneration and remodeling, thereby improving tissue and organ damage caused by ischemia and hypoxia (2). During embryonic development and adulthood, the Sonic Hedgehog (Shh) signaling pathway is involved in the growth of various organs and tissues and in the repair of damaged adult tissue (3, 4). Pola et al. (5) explained that in adulthood, the Hedgehog signaling pathway plays an essential role in the pathophysiology of vascular injury and upregulates the expression of target genes that are related to angiogenesis. Paulis et al. suggested that Shh activates the intracellular pathway, which is related to protection against ischemia/reperfusion (IR) (6). However, the relationship between Shh and myocardial infarction is unclear. Xiao et al. (7-9) suggested that the Shh signaling pathway

Key words: Shh signaling pathway; acute myocardial infarction; agonist SAG1.3; antagonist SANT; cell apoptosis

Corresponding Author:
Dr Sujuan Li,
Department of Pharmacy,
Guangdong Second Provincial General Hospital,
Xingangzhong Road No 466,
Zhuhai District, Guangzhou 510317, Guangdong Province, China
e-mail: lsj_purejanet@163.com

0393-974X (2020)
Copyright © by BIOLIFE, s.a.s.
This publication and/or article is for individual use only and may not be further reproduced without written permission from the copyright holder.
Unauthorized reproduction may result in financial and other penalties
DISCLOSURE: ALL AUTHORS REPORT NO CONFLICTS OF INTEREST RELEVANT TO THIS ARTICLE.

is activated in acute and chronic myocardial infarction models, and Shh gene therapy improves myocardial dysfunction and promotes myocardial repair. However, the specific protection mechanism is still unclear. Therefore, in this study, ligation of the coronary artery left anterior descending branch (LAD) and oxygen-glucose deprivation (OGD) were used to establish animal and cell models, respectively, of AMI to investigate the protective effect of the Shh signaling pathway in AMI.

MATERIALS AND METHODS

Specific pathogen-free (SPF) inbred male C57BL/6 mice weighing 20±2 g and aged 6-7 weeks and male or female SPF Sprague-Dawley (SD) neonatal rats (aged 1-3 days) were used in this study. All animals were provided by Guangdong Medical Laboratory Animal Center (Certificate number: SCXK (Guangdong) 2008-0002). The protocol was approved by the Ethics Committee of Guangdong Second Provincial General Hospital, and the study also followed the regulations of the State Science and Technology Commission on the management of experimental animals.

In-vivo experiments

Groupings

C57BL/6 mice (aged 6-7 weeks and weighing 18-22 g) were divided into 4 groups: a Sham group (sham operation group), an AMI group (acute myocardial infarction model group), an AMI+SAG group (AMI model and SAG1.3 group), and an AMI+SANT group (AMI model and SANT-1 group).

The mice were intraperitoneally injected with the Shh signaling pathway Smo agonist SAG1.3 (5 mg/kg/d) and antagonist SANT-1 (3.3 mg/kg/d) for 7 consecutive days, and the other groups were administered the same dose of 5% DMSO saline solution. The dosages of SAG1.3 and SANT-1 were administered through intraperitoneal injection as previously described (10-12).

Establishment of the mouse AMI model

The mice were intraperitoneally injected with 1% sodium pentobarbital solution and 0.002% buprenorphine hydrochloride solution simultaneously for pain relief (0.1 mg/kg). After anesthesia, the mice were fixed on the operating table for LAD ligation. After successful tracheal intubation, a ventilator was used to control the respiratory frequency. The hair on the left chest of each mouse was shaved. The thoracic cavity was cut in the third intercostal space to expose the left side of the heart. The coronary artery was sutured approximately 2 mm from the lower edge of the left atrial appendage using an 8-0 needle with nylon threads. After the ligation was completed, the thoracic cavity was closed. Then, when the mice woke up, they were fed in cages. After the feeding and treatment administration met the experimental requirements, the relevant specimens were collected.

Detection methods

At the 7th week, 6 C57BL/6 mice were treated with LAD ligation to establish the AMI model. The samples were collected on the 1st, 3rd, 14th, and 21st days after AMI induction. Western blot analysis was used to detect the protein expression of Ptc, Gli1, Gli2, and Shh in the myocardial tissue of the peri-infarcted areas of AMI mice. On the 7th day of the acute stage, the expression levels of signaling molecules Ptc1 and Gli1/2 stabilized. Therefore, beginning 10 min after LAD ligation, 10 AMI mice were intraperitoneally injected with the Shh signaling pathway Smo agonist SAG1.3 (5 mg/kg/d) and antagonist SANT-1 (3.3 mg/kg/d) once a day for 7 consecutive days. The daily weight changes of the mice in each group were recorded. The expression levels of Bcl-2 and Bax were also determined by Western blotting. TTC staining was utilized to determine the area of myocardial infarction. Myocardial fibrosis was stained with Masson's trichrome. The changes in cardiac systolic function were observed by a high-definition (HD) small animal ultrasound imaging system. The TUNEL method was used to detect cardiomyocyte apoptosis.

In vitro experiments

Groupings

The cells were divided into the following 4 groups: Con group (blank control group), OGD group (OGD treatment group cells were treated with sugar-free EBSS medium and cultured to predetermined times under hypoxic conditions), OGD+SAG group (OGD + SAG1.3 treatment group cells were treated with sugar-free EBSS medium and different concentrations of SAG1.3 (1 μM and 2 μM)), OGD+SANT group (OGD + SANT-1

treatment group cells were treated with sugar-free EBSS medium and different concentrations of SANT-1 (10 μM and 20 μM)).

The doses of the Shh signaling pathway Smo agonist SAG1.3 and antagonist SANT-1 are described in the literature (13-15).

Establishment of the cellular OGD model

Primary cultured myocardial cells from SPF neonatal SD rats were utilized. The neonatal rat myocardial cells were inoculated in a 60-mm culture dish containing 3 mL of 15% FBS-DMEM at a density of 1×10^6 cells/mL. After 24 h of culture at 37°C in a 5% CO_2 cell incubator, the cells were washed twice with PBS, and the 10% FBS-DMEM was renewed. After culturing in a 5% CO_2 cell incubator at 37°C for 12 h, the medium was discarded, the cells were washed three times with PBS, and sugar-free EBSS was added. The culture dish was placed in an anaerobic (94% N_2, 5% CO_2, and 1% O_2) incubator at 37°C for hypoxia and incubated for predetermined times (3 h, 6 h, 12 h, 24 h, and 48 h).

Detection methods

OGD treatment was performed on neonatal rat myocardial cells for different times (3 h, 6 h, 12 h, 24 h, and 48 h). The cell viability was determined by measuring the absorbance at 570 nm according to the MTT method. The expression levels of Shh pathway proteins (Ptc1, Gli1, Gli2, and Shh) were detected by Western blotting.

To observe the effects of the Shh pathway agonist SAG and antagonist SANT on OGD-induced neonatal rat myocardial cells, the OGD-induced cells were treated with SAG (1, 2 μM) and SANT (10, 20 μM) for 12 h. The proteins expression levels (Ptc1, Gli1, and Gli2) were determined by Western blotting. The cell viability was determined by measuring the absorbance of the cells in each group at a wavelength of 570 nm according to the MTT method. The TUNEL method was used to detect cardiomyocyte apoptosis. Western blotting was used to detect the protein expression of Bcl-2 and Bax, and the gray value was used to calculate the ratio of Bcl-2 to Bax.

Statistical analysis

The experimental data are expressed as the mean ± standard deviation ($\bar{x}\pm s$) and were analyzed with GraphPad Prism 5.0 statistical software. Two groups were compared using *t*-tests, and multiple groups were compared using single factor analysis of variance. A value of $P<0.05$ was considered statistically significant.

RESULTS

In vivo experiments

Expression of the Shh signaling pathway in myocardial tissues of AMI mice

Western blot results showed that the expression of Ptc, Gli1, Gli2, and Shh in myocardial tissues of the AMI group increased significantly on days 7, 14, and 21 compared with those in the Sham group ($P<0.05$), as shown in Fig. 1. On the 7th day of the acute stage of AMI, the expression of Ptc1 and Gli1/2 of the Shh signaling pathway reached a plateau. Therefore, the acute phase at the 7th day of the acute myocardial infarction group was selected as the subsequent experiment.

Effects of variations in Shh signaling pathway activity on cardiac damage in AMI mice

The weights of the mice increased slowly beginning 7 days after AMI induction compared with those in the Sham group, and the weights of mice in the AMI+SANT group showed a significant decrease from the 5th day, as shown in Fig. 2A. Compared with the ratio in the Sham group (0.74±0.06), the heart-to-weight ratio of the AMI group (19.27±1.83) was significantly higher ($P<0.05$) than that of the AMI group. The heart-to-weight ratio of the AMI+SAG group (12.27±2.07) was significantly reduced ($P<0.05$), while that of the AMI+SANT group (33.28±1.97) was significantly increased ($P<0.05$) (infarct area was expressed as the ratio of infarct weight to left ventricular weight).

To observe the effect of intraperitoneal injection of SAG and SANT on the area of myocardial infarction in AMI mice, TTC staining was used (Fig. 3A). The infarction level of the AMI group was significantly increased compared with that in the Sham group; the ratio of the infarcted area of the AMI+SAG group was significantly decreased compared with that in the AMI group, while the infarction level of the AMI+SANT group was significantly increased, as shown in Fig. 3B.

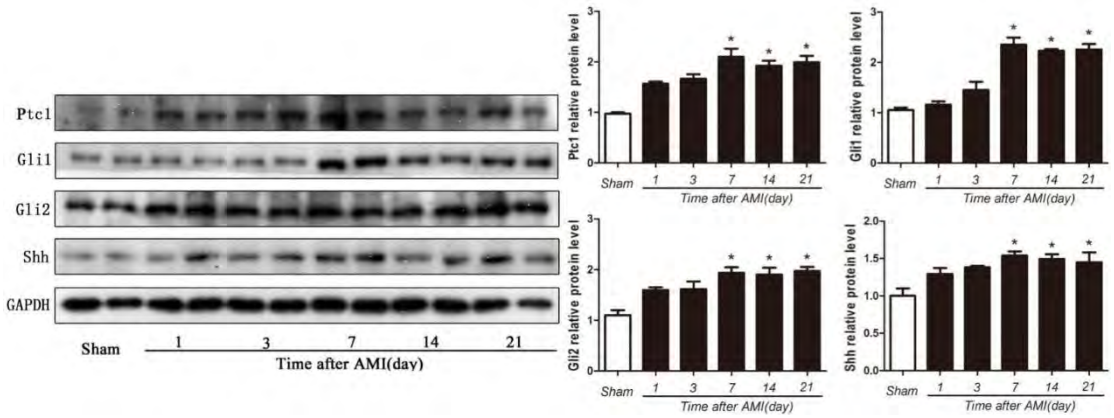


Fig. 1. *Expression of the Shh signaling pathway in myocardial tissues of AMI mice.* ***A****) Results of Western blotting.* ***B****) Statistical results of Ptc gray values.* ***C****) Statistical results of Gli1 gray values.* ***D****) Statistical results of Gli2 gray values.* ***E****) Statistical results of Shh gray values. *P<0.05, compared to the Sham group, n=6.*

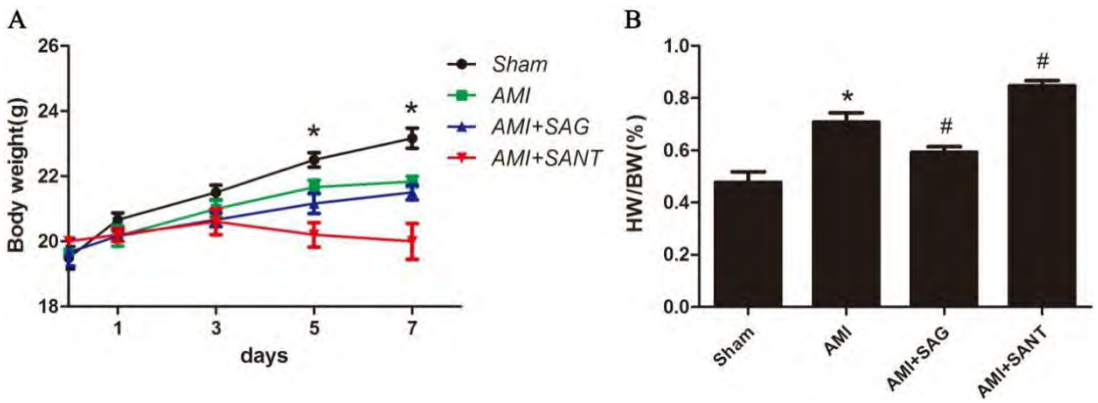


Fig. 2. *Statistical charts of body weights and the heart-to-weight ratios of mice in the groups.* ***A****) Body weight changes of mice.* ***B****) Statistical chart of heart-to-weight ratios of mice. *P<0.05, compared to the Sham group, #P<0.05, compared to the AMI group, n=1.*

On the 7th day after surgery, the degree of myocardial fibrosis in the AMI group was significantly increased compared with that in the Sham group, as shown in Fig. 3A. SAG significantly reduced the degree of myocardial fibrosis in myocardial infarcted mice compared with that in the AMI group, and the use of SANT significantly increased myocardial fibrosis in infarcted mice (Fig. 3B).

As shown in Fig. 4, the diameters of end-systole and end-diastole of the left ventricle in the AMI group increased significantly compared with those in the Sham group, while the short-axis shortening rate and ejection fraction were significantly reduced. The left ventricular systolic and end-diastolic diameters in the AMI+SAG group were significantly reduced compared with those in the AMI group, and the short-axis shortening rate and ejection fraction were significantly increased. The left ventricular systolic and end-diastolic diameters of the AMI+SANT group decreased significantly, while the short-axis shortening rate and ejection fraction increased significantly.

Effects of variations in Shh signaling pathway activity on the degree of myocardial apoptosis in AMI mice

As shown in Fig. 5, dUTP labeling showed that the number of apoptotic cells in the peripheral area

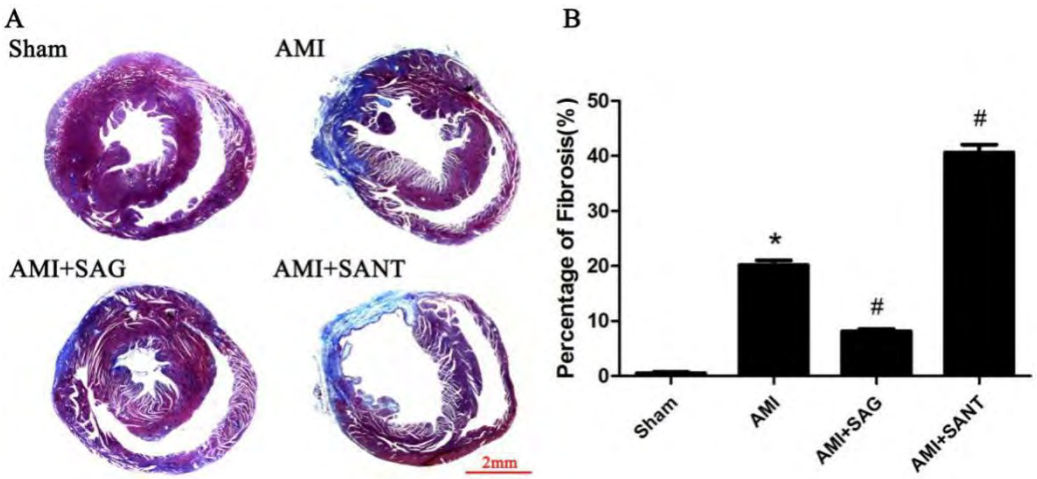


Fig. 3. *Effects of variations in Shh signaling pathway activity on heart muscle fibrosis in AMI mice.* ***A)*** *Representative diagram of Masson's trichome staining.* ***B)*** *Statistical chart of the fibrosis percentage.* $^{*}P<0.05$*, compared to the Sham group,* $^{\#}P<0.05$*, compared to the AMI group, n=6.*

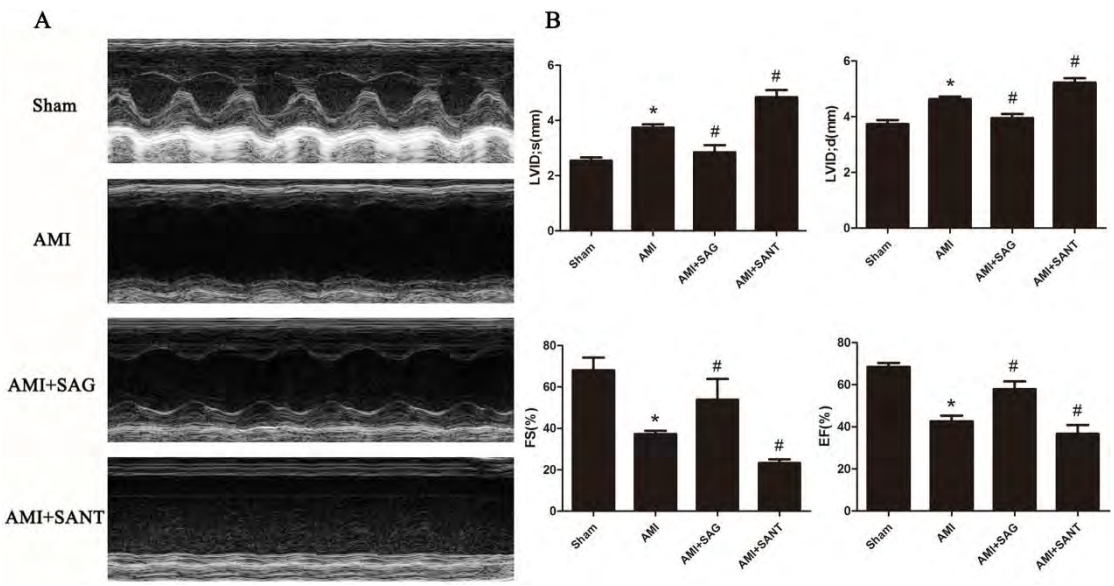


Fig. 4. *Examination of cardiac function.* ***A)*** *M-mode representative diagram.* ***B)*** *Statistical chart of data; LVID; s: left ventricular end-systolic diameter; LVID; d: left ventricular end-diastolic diameter; FS: short-axis shortening rate; EF: ejection fraction.* $^{*}P<0.05$*, compared to the Sham group,* $^{\#}P<0.05$*, compared to the AMI group, n=6.*

of the infarcted hearts of AMI mice was significantly increased compared with that in the Sham group. The number of apoptotic cells in the SAG group was significantly reduced compared with that of the AMI group, and the number of apoptotic cells in the SANT group was significantly increased.

As shown in Fig. 6, the expression of Bcl-2 in the AMI group was significantly reduced compared with that in the Sham group, and the expression of Bax was significantly increased. The expression of Bcl-2 increased compared with that in the AMI group, and the expression of Bax was significantly

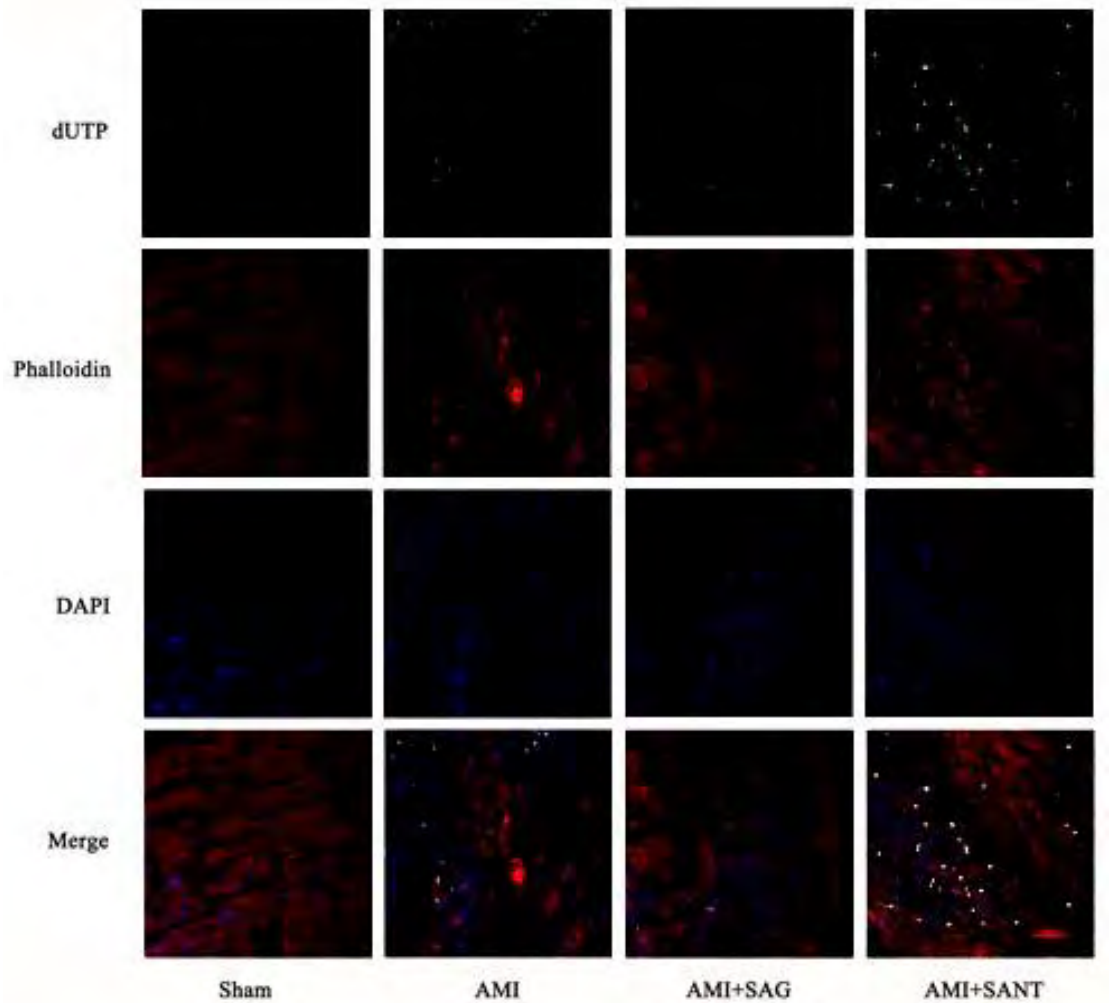


Fig. 5. *Detection of apoptotic myocardial cells by TUNEL assay (200×).*

decreased after SAG administration. After SANT administration, Bcl-2 expression decreased significantly, and Bax expression increased significantly. Moreover, the Bcl-2/Bax ratio in the AMI group was significantly lower than that in the Sham group. The Bcl-2/Bax ratio after SAG administration was significantly increased after the administration of SANT compared with that of the AMI group. After SANT administration, the Bcl-2/Bax ratio increased significantly.

In vitro experiments

Time-dependent reduction in the activity of OGD-induced myocardial cells from suckling rats

MTT results showed that the living cell ratios in the OGD group (OGD 3 h: 89.82±3.18%; OGD 6 h: 78.93±2.77%; OGD 12 h: 70.66±2.81%; OGD 24 h: 53.17±2.18%; and OGD 48 h: 19.96±1.38%) began to decrease in comparison with those in the Con group (100±2.12%), indicating that the effect of OGD on myocardial cell activity was time-dependent. Among them, the cell survival rate of the OGD 12-h group was 70.66±2.81%. Therefore, 12-h OGD treatment was selected to establish an *in vitro* myocardial infarction model.

Activated Shh signaling pathway in OGD-induced myocardial cells from neonatal rats

The expression levels of the Shh signaling pathway proteins (Ptc1, Gli1, Gli2, and Shh) in

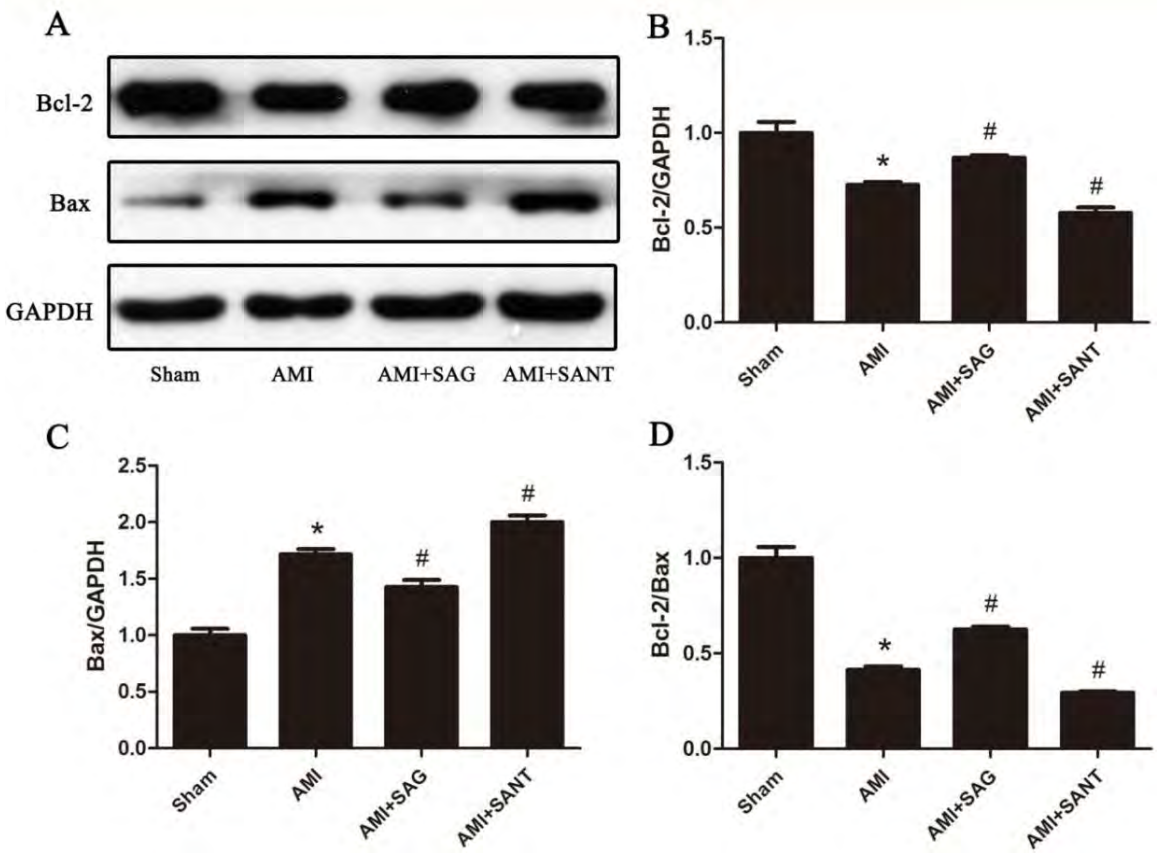


Fig. 6. *The expression of Bcl-2 and Bax.* ***A****) Results of Western blotting.* ***B****,* ***C****, and* ***D****) The statistical charts of the gray values.* $^{*}P<0.05$*, compared to the Sham group,* $^{\#}P<0.05$*, compared to the AMI group, n=6.*

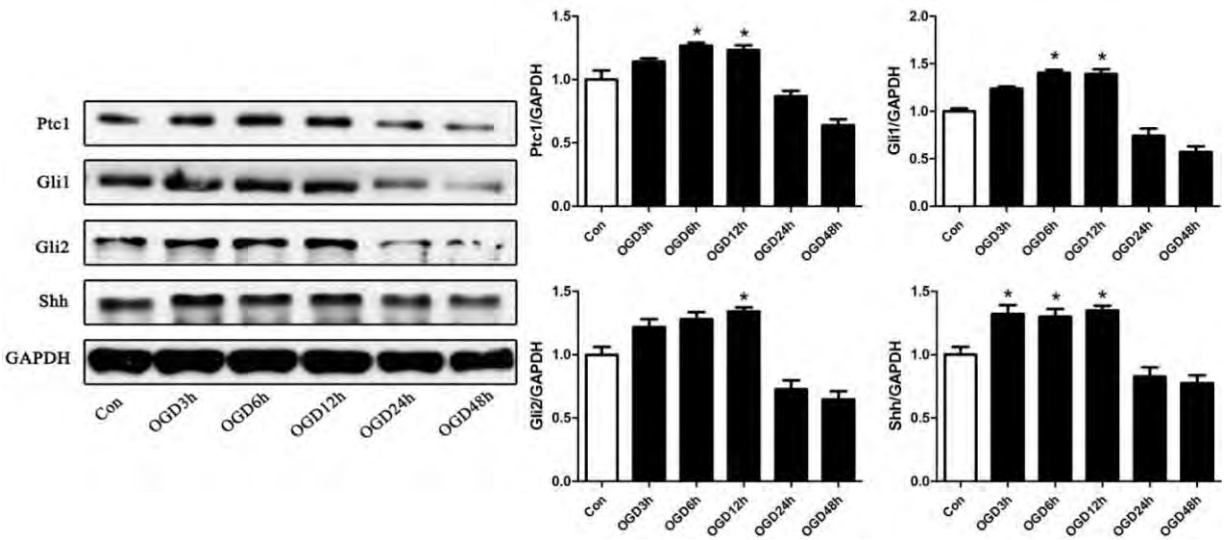


Fig. 7. *Activation of the Shh signaling pathway in myocardial cells by OGD at different time points.* $^{*}P<0.05$*, compared to the Con group, n=6.*

the OGD 12-h group were significantly increased compared with those in the Con group. The results showed that 12 h of OGD treatment significantly activated the Shh signaling pathway (Fig. 7).

Expression of Ptc1 and Gli1/2 in OGD-induced myocardial cells and the survival rate of myocardial cells

Different concentrations of SAG (1 and 2 μM) and SANT (10 and 20 μM) were administered to neonatal rat myocardial cells that received OGD treatment for 12 h. The results showed that the expression levels of Ptc1, Gli1, and Gli2 in the OGD 12-h group were significantly higher than those in the Con group. Compared with the effects in the OGD 12-h group, there was no significant change after administration of SAG 1 μM or SANT 10 μM. However, SAG 2 μM administration significantly increased the expression levels of Ptc1, Gli1, and Gli2 in the OGD 12-h group, while the expression levels of Ptc1, Gli1, and Gli2 were significantly decreased after SANT 20 μM administration. Therefore, the Shh pathway agonist SAG (2 μm) and antagonist SANT (20 μm) effectively modulated the activity of the Shh signaling pathway in OGD-induced neonatal rat cardiomyocytes (Fig. 8).

Different concentrations of SAG1.3 (1 and 2 μM) and SANT-1 (10 and 20 μM) were administered to neonatal rat myocardial cells that received 12 h of OGD treatment. The MTT results showed that the survival rate of the OGD 12-h group (65.18±1.18%) was significantly reduced compared with that of the control group (100±2.32%). There was no significant difference in the viability of cells that were administered 1 μM SAG and 12 h of OGD treatment (73.24±2.36%) compared with those of the OGD 12-h group (65.18±1.18%). After administration of SAG

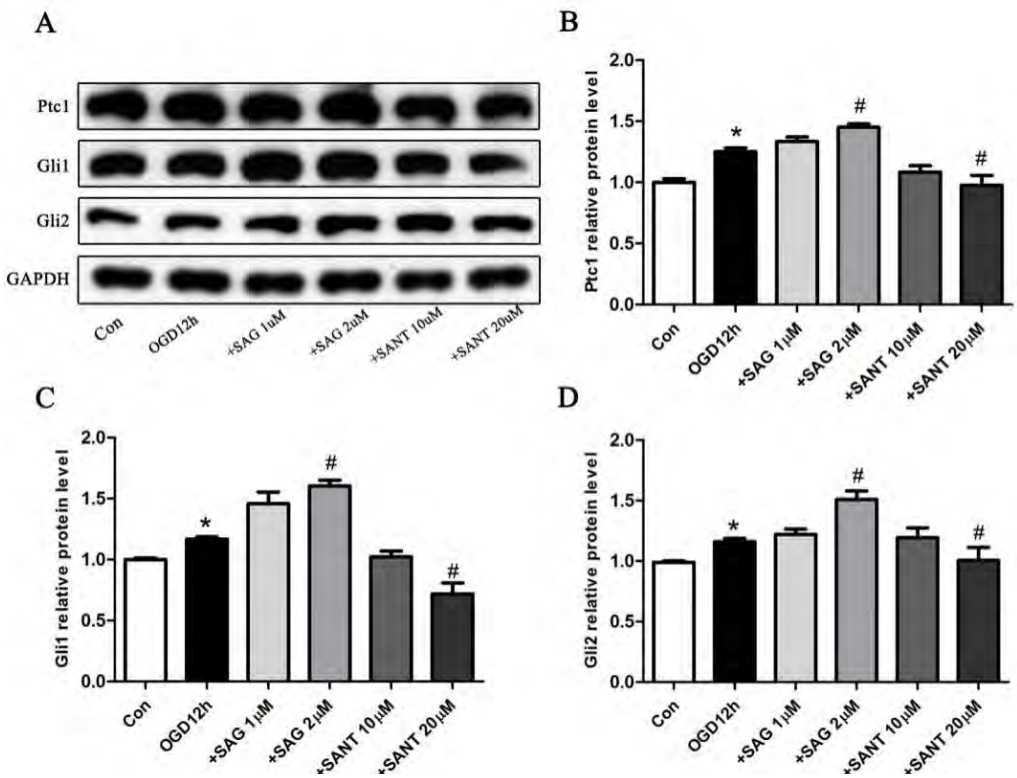


Fig. 8. *Protein expression of Ptc1 and Gli1/2 in OGD myocardial cells. **A)** Diagrams of protein bands. **B)** Statistical charts of the ratio of proteins to GAPDH gray values. *P<0.05, compared to the Con group, #P<0.05, compared to the OGD 12-h group, n=6.*

2 μM and 12-hour OGD treatment (78.94±1.52%), the proportion of living cells increased significantly. Furthermore, there was no significant difference between the SANT 10 μM (63.28±1.64%) and OGD 12-h treatment groups (65.18±1.18%). The cell survival rate in the SANT 20 μM treatment group (53.57±0.94%) was significantly improved compared with that in the OGD 12 h treatment group (65.18±1.18%), indicating that the Shh pathway agonist SAG effectively improved the survival rate OGD-induced neonatal rat myocardial cells, while the antagonist SANT antagonized the activity of the Shh pathway and reduced the survival rate of OGD-induced neonatal rat cardiomyocytes.

Effective improvement in OGD-induced myocardial cell apoptosis by activation of the Shh signaling pathway

As shown in Fig. 9, the number of apoptotic myocardial cells increased significantly after OGD treatment compared with that of the control group. SAG 1 μM and SANT 10 μm had no significant effects after administration compared with those of the OGD 12-h group. However, after SAG 2 μM administration and OGD treatment for 12 h, the number of apoptotic myocardial cells decreased significantly, and the number of apoptotic myocardial cells increased significantly in the group that was treated with OGD for 12 h after SANT 20 μM.

Different concentrations of SAG (1 and 2 μM) and SANT (10 and 20 μM) were administered to neonatal rat myocardial cells that received OGD treatment for 12 h. The expression of the apoptosis-associated proteins Bcl-2 and Bax was detected by Western blotting. As shown in Fig. 10, the Bcl-2/Bax in the OGD 12-h group was significantly reduced compared with that in the Con group. There was no significant change after administration of SAG 1 μM or SANT 10 μM compared with that of the OGD 12-h group. However, after SAG 2 μM administration, Bcl-2/Bax increased significantly after 12 h of OGD treatment, and Bcl-2/Bax increased significantly after 12 h of SANT 20 μm administration.

DISCUSSION

AMI is a common cardiovascular disease that threatens human health. The specific mechanism of improving cardiac function and myocardial repair after AMI has important practical significance for clinical treatment. The Shh signaling pathway is activated when the Shh protein binds to its receptor Ptc1, thereby eliminating the inhibitory effect of Ptc1 on the Smo receptor, allowing the downstream nuclear transcription factor Gli to enter the nucleus and activate expression of downstream genes, including Ptc1 and Gli1/2 (16, 17). In this study, the LAD permanent ligation mouse AMI model was constructed with reference to the study by Kolk MV

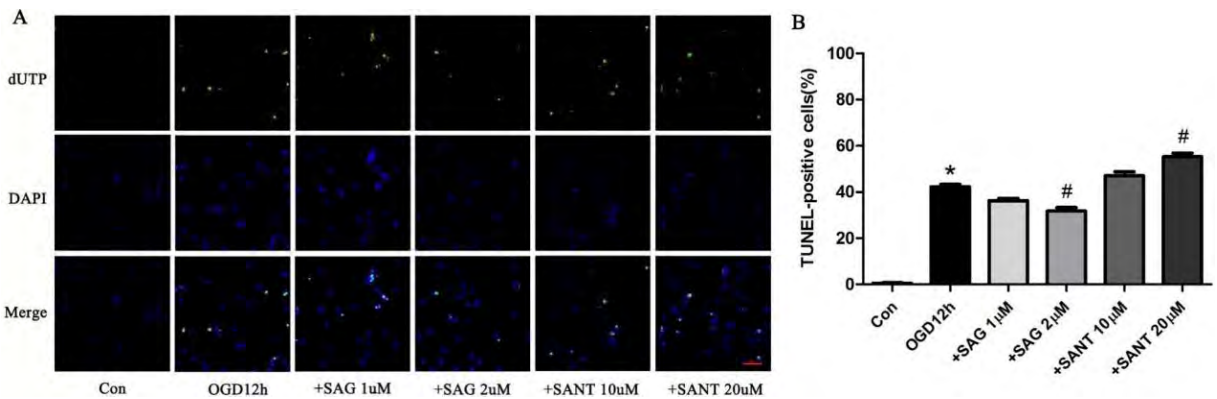


Fig. 9. *Detection of apoptotic myocardial cells by TUNEL assay (400×). **A)** Fluorescence diagrams of each group. **B)** Ratio of the number of green fluorescent cells to the number of blue fluorescent nuclei. $^{*}P<0.05$, compared to the Con group, $^{\#}P<0.05$, compared to the OGD 12-h group, n=10.*

et al. (18). The results showed that expression of the Shh signaling pathway continued to increase during the acute phase at 1, 3, and 7 days after AMI and peaked at 7 days. Then, the expression decreased slowly. At this point, the AMI repair phase occurred. Therefore, the seventh day of the acute phase was chosen to study the effect of Shh signaling pathway activation on myocardial repair in AMI. *In vitro* experiments were performed using neonatal rat cardiomyocytes for cell viability testing. Cells underwent OGD treatment for 3, 6, 12, 24, and 48 h, and after 12 h of OGD treatment, the cell survival rate reached 70.66%. After 24 h of OGD treatment, the cell survival rate reached 55.18%. After 48 h of OGD treatment, the cell survival rate was 22.56%. Therefore, an isolated myocardial ischemia model was constructed using this time point for subsequent experiments. The results showed that the expression of Ptc1, Gli1, and Gli2 in the Shh signaling pathway increased after 12 h of OGD treatment, indicating that the Shh signaling pathway was activated, which was consistent with the results of *in vivo* experiments.

In recent years, the Shh signaling pathway has attracted increasing attention in basic and clinical cardiovascular disease research. One study (19) found that when H_2O_2 was added to cells to simulate oxidative stress, the Shh signaling pathway was activated, indicating that the Shh signaling pathway is involved in oxidative stress. Mackie et al. (20) injected recombinant human Shh protein-modified human CD34 hematopoietic stem cells into the infarct margin area of AMI mice. SHH protein-modified CD34 cells reduced the infarct area, increased the capillary density of the infarct margin

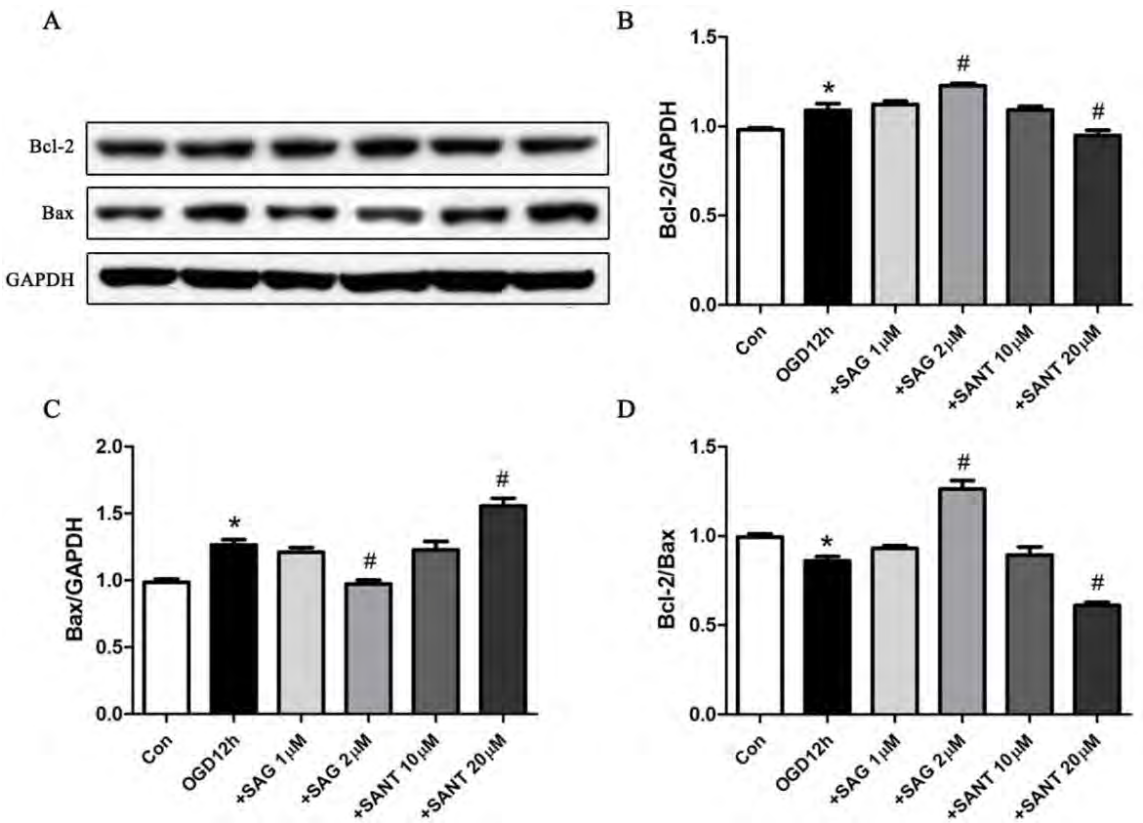


Fig. 10. *Increased ratios of the apoptosis-associated proteins Bcl-2 to Bax in OGD-induced neonatal rat myocardial cells by activation of the Shh signaling pathway. $^{*}P<0.05$, compared to the control group, $^{\#}P<0.05$, compared to the OGD 12-h group, n=6.*

area, and prevented ventricular dilatation and cardiac function decline compared with those of empty body-modified CD34 cells. In addition, the Shh signaling pathway is also involved in the repair of adult tissue ischemia injury and plays an important role in vascular regeneration in many tissues and organs, thus promoting tissue repair (21). The exogenous Shh gene not only directly regulates angiogenesis but also promotes angiogenesis by regulating VEGF and other angiogenesis factors secreted by stromal cells. Compared with VEGF, Shh activation has more advantages in inducing artery formation, forming new vessels with larger diameters, more branches and more maturity. Lavine et al. (22) found that activation of the Shh signaling pathway promoted angiogenesis in the rat myocardium. Tang et al. (23) found that transplantation of Shh gene-transfected bone marrow mesenchymal stem cells into the myocardial infarction area of rats promoted angiogenesis in the local infarcted area and improved cardiac dysfunction after chronic myocardial ischemia. To verify whether activation of the Shh signaling pathway promotes the apoptosis of AMI cells, we established a mouse AMI model and an in vitro OGD model of myocardial ischemia. Through SAG-induced activation of the Shh signaling pathway, the cardiac function of AMI mice was improved, the survival rate of myocardial cells was improved, the myocardial infarcted area was reduced, fibrosis of the myocardium was alleviated, and the expression of Bcl-2 and Bax were reduced. TUNEL assay results showed that both apoptotic cells and cardiomyocytes decreased. Moreover, SANT inhibited activity of the Shh signaling pathway, exacerbated the degree of cardiac dysfunction, and increased the apoptosis rate of cardiomyocytes, leading to an increase in Bcl-2 and Bax expression and TUNEL-labeled apoptotic cells. These findings suggest that activation of the Shh signaling pathway improves myocardial function and remodeling and reduces cardiomyocyte apoptosis.

In conclusion, the Shh signaling pathway is activated in AMI mice and OGD cardiomyocytes. Activation of the Shh signaling pathway by SAG enhanced myocardial function, reduced infarct area and myocardial fibrosis, and reduced cardiomyocyte apoptosis. Furthermore, activation of the Shh signaling pathway increased the viability of neonatal rat cardiomyocytes and reduced the apoptosis of cardiomyocytes.

ACKNOWLEDGEMENTS

This work was supported by the Science Foundation of Guangdong Second Provincial General Hospital (YQ2016059) and the Guangdong Medical Scientific Research Fund (B2019081).

REFERENCES

1. Abbate A, Salloum FN, Vecile E, et al. Anakinra, a recombinant human interleukin-1 receptor antagonist, inhibits apoptosis in experimental acute myocardial infarction. Circulation 2008; 117(20):2670-83.
2. Tritsaris K, Myren M, Ditlev SB, et al. IL20 is an arteriogenic cytokine that remodels collateral networks and improves functions of ischemic hind limbs. Proc Natl Acad Sci U S A 2007; 104(39):15364-69.
3. Kusano KF, Pola R, Murayama T, et al. Sonic hedgehog myocardial gene therapy: tissue repair through transient reconstitution of embryonic signaling. Nat Med 2005; 11(11):1197-204.
4. Roncalli J, Renault MA, Tongers J, et al. Sonic hedgehog-induced functional recovery after myocardial infarction is enhanced by AMD3100-mediated progenitor-cell mobilization. J Am Coll Cardiol 2011; 57(24):2444-52.
5. Pola R, Ling LE, Silver M, et al. The morphogen Sonic hedgehog is an indirect angiogenic agent upregulating two families of angiogenic growth factors. Nat Med 2001; 7(6):706-11.
6. Paulis L, Fauconnier J, Cazorla O, et al. Activation of Sonic hedgehog signaling in ventricular cardiomyocytes exerts cardioprotection against ischemia reperfusion injuries. Sci Rep 2015; 5:7983.
7. Xiao Q, Hou N, Wang YP, et al. Impaired sonic hedgehog pathway contributes to cardiac dysfunction in type 1 diabetic mice with myocardial infarction. Cardiovasc Res 2012; 95(4):507-16.
8. Ueda K, Takano H, Niitsuma Y, et al. Sonic hedgehog is a critical mediator of erythropoietin-

induced cardiac protection in mice. J Clin Invest, 2010;120(6):2016-29.
9. Lavine KJ, Kovacs A, Ornitz DM. Hedgehog signaling is critical for maintenance of the adult coronary vasculature in mice. J Clin Invest 2008; 118(7):2404-14.
10. Wentzel P, Eriksson UJ. Altered gene expression in neural crest cells exposed to ethanol in vitro. Brain Res, 2009; 1305 Suppl:S50-60.
11. Roper RJ, Baxter LL, Saran NG, Klinedinst DK, Beachy PA, Reeves RH. Defective cerebellar response to mitogenic Hedgehog signaling in Down [corrected] syndrome mice. Proc Natl Acad Sci U S A 2006; 103(5):1452-6.
12. El-Zaatari M, Grabowska AM, McKenzie AJ, Powe DG, Scotting PJ, Watson SA. Cyclopamine inhibition of the sonic hedgehog pathway in the stomach requires concomitant acid inhibition. Regul Pept, 2008; 146(1-3):131-39.
13. Frank-Kamenetsky M, Zhang XM, Bottega S, et al. Small-molecule modulators of Hedgehog signaling: identification and characterization of Smoothened agonists and antagonists. J Biol 2002; 1(2):10.
14. Xiao Q, Yang Y, Qin Y, et al. AMP-activated protein kinase-dependent autophagy mediated the protective effect of sonic hedgehog pathway on oxygen glucose deprivation-induced injury of cardiomyocytes. Biochem Biophys Res Commun, 2015; 457(3):419-25.
15. Protti A, Mongue-Din H, Mylonas KJ, et al. Bone marrow transplantation modulates tissue macrophage phenotype and enhances cardiac recovery after subsequent acute myocardial infarction. J Mol Cell Cardiol 2016; 90:120-28.
16. Chari NS, McDonnell TJ. The sonic hedgehog signaling network in development and neoplasia. Adv Anat Pathol 2007; 14(5):344-52.
17. Lu FL, Yu CC, Chiu HH. Sonic hedgehog antagonists induce cell death in acute myeloid leukemia cells with the presence of lipopolysaccharides, tumor necrosis factor-alpha, or interferons. Invest New Drugs 2013; 31(4):823-32.
18. Kolk MV, Meyberg D, Deuse T, et al. LAD-ligation: a murine model of myocardial infarction. J Vis Exp 2009; 32.
19. Dai RL, Zhu SY, Xia YP, et al. Sonic hedgehog protects cortical neurons against oxidative stress. Neurochem Res 2011; 36(1):67-75.
20. Mackie AR, Klyachko E, Thorne T, et al. Sonic hedgehog-modified human CD34+ Cells preserve cardiac function after acute myocardial infarction. Circ Res 2012; 111(3):312-21.
21. Singh BN, Koyano-Nakagawa N, Donaldson A, Weaver CV, Garry MG, Garry DJ. Hedgehog signaling during appendage development, and regeneration. Genes (Basel) 2015; 6(2):417-35.
22. Lavine KJ, Kovacs A, Weinheimer C, Mann DL. Repetitive myocardial ischemia promotes coronary growth in the adult mammalian heart. J Am Heart Assoc 2013; 2(5):e000343.
23. Tang T, Wu M, Yang J. Transplantation of MSCs transfected with SHH gene ameliorates cardiac dysfunction after chronic myocardial infarction. Int J Cardiol 2013; 168(5):4997-99.

LONG NON-CODING RNA XIST PROTECTS CHONDROCYTES ATDC5 AND CHON-001 FROM IL-1β-INDUCED INJURY VIA REGULATING miR-653-5p/SIRT1 AXIS

L-P. LIAN[1] and X-Y. XI[2]

[1]Second Department of Orthopaedics, Weinan Central Hospital, Weinan, Shaanxi Province, China;
[2]Department of Oncology surgery, Weinan Central Hospital, Weinan, Shaanxi Province, China

Received December 18, 2019 – Accepted March 18, 2020

Chondrocyte apoptosis is linked to cartilage degeneration, and considered as a crucial event during the development of osteoarthritis (OA). X inactive specific transcript (XIST) is an oncogenic long non-coding RNA (lncRNA). However, its role in the pathophysiological process of OA remains largely unknown. In this work, quantitative real-time reverse transcriptase PCR (qRT-PCR) was employed to measure the expression of XIST, miR-653-5p and sirtuin1 (SIRT1) mRNA in OA and normal cartilage tissues. Chondrocyte cell lines, CHON-001 and ATDC5, were treated with different doses of interleukin-1β (IL-1β) to mimic the inflammatory environment of OA *in vitro*. Overexpression plasmids, microRNA (miRNA) mimics, miRNA inhibitors and small interfering RNAs (siRNAs) were constructed and transfected into CHON-001 and ATDC5 cells. 3-(4,5-dimethyl-2-thiazolyl)-2, 5-diphenyl-2H-tetrazolium bromide (MTT) assay was adopted to determine the cell viability. Western blot was used to detect the expression of apoptosis-related proteins. Enzyme-linked immunosorbent assay (ELISA) was employed to probe the expression levels of inflammatory factors. Flow cytometry was used to analyze the cell apoptosis. StarBase and TargetScan databases were used to predict the binding sites between XIST and miR-653-5p, miR-653-5p and 3'UTR of SIRT1, respectively, which were then verified by dual luciferase reporter assay. The data in the present study demonstrated that XIST and SIRT1 were down-regulated while miR-653-5p was up-regulated in OA tissues and cell models. The up-regulation of XIST increased the viability of CHON-001 and ATDC5 cells, while it impeded their apoptosis and inflammatory response induced by IL-1β. Conversely, miR-653-5p had opposite effects. It was proved that miR-653-5p could be sponged and suppressed by XIST. Additionally, SIRT1 was identified as a target of miR-653-5p, and SIRT1 could be suppressed by XIST indirectly. In conclusion, down-regulated XIST was involved in the injury of chondrocytes during the pathophysiological process of OA, and XIST up-regulation protected chondrocytes from inflammatory injury via regulating miR-653-5p/SIRT1 axis.

Osteoarthritis (OA) is a common joint disorder affecting human health, and is frequently diagnosed in middle-aged and elderly patients. The main clinical manifestations are pain, joint stiffness, joint swelling, and bone friction, accompanied with dyskinesia (1). The main pathological features of OA are degeneration of articular cartilage and secondary hyperosteogeny, resulting in destruction of articular cartilage, formation of osteophyte, hyperplasia of synovial cells, synovitis and narrowing of the joint space (2, 3). In recent years, accumulating studies on OA indicate that the occurrence of OA is related

Key words: miR-653-5p/SIRT1; XIST; OA; CHON-001 and ATDC5

Corresponding Author:
Dr Xi Xuyan,
Department of Oncology Surgery,
Weinan Central Hospital, Shengli Street, Weinan 714000,
Shaanxi Province, China
Tel.: +86 0931-2168372
e-mail: yanyuexin7337@163.com

0393-974X (2020)
Copyright © by BIOLIFE, s.a.s.
This publication and/or article is for individual use only and may not be further reproduced without written permission from the copyright holder.
Unauthorized reproduction may result in financial and other penalties
DISCLOSURE: ALL AUTHORS REPORT NO CONFLICTS OF INTEREST RELEVANT TO THIS ARTICLE.

to various factors such as age, trauma, genetic susceptibility, inflammation, metabolic disorder of cartilage tissue, and abnormal apoptosis and proliferation of chondrocytes (4). However, there are relatively few effective drugs for the treatment of OA, thefore it is necessary to further study the pathogenesis to explore novel drugs.

Long non-coding RNAs (lncRNAs) are non-coding transcripts of over 200 nucleotides in length. Although lncRNAs are deficient in protein-coding function, accumulating evidence indicates that abnormal expression and dysfunction of lncRNAs can lead to diseases (5). Recently, it was also proved that lncRNAs are enrolled in the development of bone and joint diseases including OA (6-10). For example, the expression of lncRNA growth arrest specific transcript 5 (GAS5) is increased in OA chondrocytes, and the high expression of GAS5 can not only promote the expression of matrix metalloproteinases (MMPs) such as MMP-2, MMP-3, MMP-9 and MMP-13, but also restrain the autophagy pathway and promote chondrocyte apoptosis, thereby causing destruction of articular cartilage (9). LncRNA HOX transcript antisense RNA (HOTAIR) is elevated in OA tissues and is involved in interleukin-1 beta (IL-1β)-induced MMP overexpression, thus promoting chondrocyte apoptosis (10). LncRNA X inactive-specific transcript (XIST) has been reported to be involved in various diseases (11, 12). A recent study implies that XIST could regulate the inflammatory microenvironment in OA via modulating M1 macrophages (13). Instead, the function of XIST in OA development is still largely unknown and awaits further study.

MicroRNAs (miRNAs) are single-stranded, non-coding RNAs that are 18 to 24 bases in length. They regulate gene expression via impeding mRNA translation or cleavage of mRNA at the post-transcriptional level. MiRNAs regulate proliferation, apoptosis, migration, and differentiation. There is growing evidence that miRNAs are linked to the development of OA. For example, the expression of miR-125b in OA chondrocytes is lower than that in normal chondrocytes, and participates in OA development via regulating aggrecanase-1 (14). It was reported that miR-558 expression in OA chondrocytes was also significantly reduced; it could directly inhibit the activity of cyclooxygenase-2 (COX-2), nuclear factor kappa B (NF-κB) and MMPs, playing a protective role (15). As a member of miRNA, miR-653-5p is reported to be related to the progression of neuroblastoma and non-small cell lung cancer (16, 17). However, it is unclear whether miR-653-5p regulates the development of OA.

In this work, it was demonstrated that in OA tissues XIST was lowly expressed while miR-653-5p was highly expressed. Interestingly, XIST expression was positively correlated with the expression of sirtuin1 (SIRT1), an anti-catabolic, anti-inflammatory, anti-oxidative stress and anti-apoptosis gene in OA (18). It was proved that XIST could negatively regulate miR-653-5p, and promote the viability of chondrocytes under inflammatory microenvironment induced by IL-1β. Additionally, it was also validated that SIRT1 was a target of miR-653-5p, which could be indirectly and positively regulated by XIST. Our work helps clarify the mechanism of OA development and provides potential therapeutic targets for this disease.

MATERIALS AND METHODS

Human samples

Articular cartilage samples from 30 patients with OA who received surgery between August 2015 and October 2018 were collected. As controls, 30 cases of normal cartilage specimens were taken from patients who had received traumatic amputation, with no record of OA or other joint diseases before surgery. The study was backed by the Research Ethics Committee of Weinan Central Hospital. Written informed consent was obtained from all of the participants prior to sample collection.

Cell lines and cell culture

The American Type Culture Collection (ATCC, Manassas, Virginia) was the provider of the human chondrocyte cell line CHON-001 and the mice chondrocyte cell line ATDC5. Cells were cultured in Dulbecco's Modified Eagle's Medium (DMEM)/Ham's F12 (HyClone, Logan, UT, USA) supplemented with 10% fetal bovine serum (FBS, HyClone, South Logan, UT, USA). 100 U/ml penicillin G and 100 μg/mL

streptomycin solution (Gibco, Carlsbad, CA, USA) were added into the medium for preventing contamination. Cells were cultured in a humidified incubator with 5% CO_2 at 37°C. The medium was changed every 3-4 days. Cells were subcultured with 0.25% trypsin (Americesco, Framingham, MA, USA). To mimic inflammatory microenvrionment, the cells were treated with different concentrations of IL-1β (Amyjet Scientific, Wuhan, China) (0, 2, 5 and 10 ng/mL) for 12 h.

Quantitative real-time polymerase chain reaction (qRT-PCR)

The total RNA from tissues and cells, was extracted by TRIzol reagent (Invitrogen, Carlsbad, CA, USA) and its purity was determined. Then RNA was reverse transcribed into cDNA in according to the instructions of SuperScript First Strand cDNA System (Invitrogen, Carlsbad, CA, USA). Fluorescence quantification was performed using the miRNA-specific primer for miR-653-5p (RiboBio, Guangzhou, China) with U6 as its internal reference. The primer sequences for U6 were: (forward): 5'-CTCGCTTCGGCAGCACA-3', (reverse): 5'-AACGCTTCACGAATTTGCGT-3'. Other primers were synthesized by Sangon Biotech Co., Ltd. (Shanghai, China). The primer sequences were as follows: XIST (forward): 5'-AGGGAGCAGTTTGCCCTACT-3', (reverse): 5'-CACATGCAGCGTGGTATCTT-3; SIRT1 (forward): 5'-CGTCTCAGCGTCACTCCCAAGC-3', (reverse): 5'-ACGCAATCCTGCTCCCTCCC-3'; glyceraldehyde-3-phosphate dehydrogenase (GAPDH) (forward): 5'-CTCTGCTCCTCCTGTTCGAC-3', (reverse): 5'-GCGCCCAATACGACCAAATC-3'. GAPDH was the internal reference. SYBR Green Premix Ex Taq II (TaKaRa, Dlian, China) and ABI 7500 real-time PCR system (Applied Biosystems, Foster City, CA, USA) was applied for qPCR, and the relative expression of the target gene was calculated by $2^{-\Delta\Delta CT}$ method.

Cell viability assay

Cell viability assay was performed with 3-(4,5-dimethyl-2-thiazolyl)-2, 5-diphenyl-2H-tetrazolium bromide (MTT) kit (Beyotime Biotechnology, Shanghai, China). CHON-001 and ATDC5 cells during the logarithmic phase of growth were harvested and inoculated in 96-well plates with a density of 4×10^3 cells/well. After treated with IL-1β for 12 h, cells were cultured in a 100% humidity incubator at 37 °C with 5% CO_2. Cell proliferation was detected according to instructions of MTT kit . In this experiment, the absorbance at 490 nm of each well was measured at 0, 24, 48 h, 72 h, and 96 h with a microplate reader (Perlang New Technology Co., Ltd., Beijing, China), and the values were used to compare the cell viability.

Western blot

Cells were collected and washed 3 times with pre-cool phosphate-buffered saline (PBS), and RIPA lysate (Beyotime Biotechnology, Shanghai, China) with protease inhibitors phenylmethylsulfonyl fluoride (PMSF; Roche, Basel, Switzerland) was used for total protein extraction. The protein concentration was examined by the bicinchoninic acid (BCA) assay. Same amount of protein sample was loaded into each well, and the total protein was separated by 10% sodium dodecyl sulphate-polyacrylamide gel electrophoresis (SDS-PAGE). Then the protein was transferred to polyvinylidene fluoride (PVDF) membrane (Millipore, Bedford, MA, USA). Then then PVDF membrane was blocked with 5% defatted milk for 2 h, and incubated with primary antibodies at 4°C overnight. Primary antibodies included anti-Cytochrome C (Cyto.C) (1:500, Rabbit, ab133504, Abcam, UK), anti-SIRT1 (1:500, Rabbit, ab189494, Abcam, UK) and anti-GAPDH (1:2000, Rabbit, ab181602, Abcam, UK). After that, the membrane was rinsed with Tris-buffered saline with 0.1% Tween 20 (TBST), and horseradish peroxidase (HRP)-labeled secondary antibody was added and incubated with the PVDF membrane at room temperature for 1.5 h, then the bands were developed by hypersensitive ECL (Thermo Scientific, Rockford, IL, USA) and scanned by Tanon-5200 imaging system (Shanghai, China).

ELISA

The levels of inflammatory factors IL-1β, interleukin-1 (IL-6), tumor necrosis factor-α (TNF-α) in cell culture supernatant were detected by ELISA kits (Boster Biotech, Wuhan, China) according to the manufacturer's instructions.

Cell transfection

CHON-001 and ATDC5 cells were inoculated in a 6-well plate at a density of 1×10^5 cells/mL, cultured at 37°C, in 5% CO_2 for 16 h, and then were transfected. XIST-overexpressing plasmid, XIST targeting small interfering RNA (siRNA), miR-653-5p mimics, miR-653-

5p inhibitors, SIRT1-overexpressing plasmid and negative controls (NC) were purchased from RiboBio Co., Ltd. (Guangzhou, China). The sequences of the siRNAs were: si-XIST, 5'-GACCUUGUCAUGUGGAUAUTT-3' (sense) and 5'-AUAUCCACAUGACAAGGUCTT-3'(antisense); si-NC, 5'-UUCUCCGAACGUGUCACGUTT-3' (sense) and 5'-ACGUGACACGUUCGGAGAATT-3' (antisense). The sequences of miR-653-5p mimics, miR-653-4p inhibitors and miR-NC were 5′-UUGAAACAAUCUCUACUGAACC-3′, 5′-UUCACUGGAGUUUGUUUCAGU-3′ and 5′-GCCAGCCCUGUAAGUCCCGCAU-3′ respectively. CHON-001 and ATDC5 cells were transfected with Lipofectamine® 3000 (Invitrogen; ThermoFisher Science, Inc.) in compliance with the supplier's protocols. Cells were then cultured for 24 h, and then the transfection efficiency was probed by qRT-PCR.

Luciferase reporter gene assay

Wild type and mutant type sequences of XIST and 3'UTR of SIRT1 with the binding site of miR-653-5p were constructed and integrated into the pmirGLO dual-luciferase vector (Promega, Madison, WI, USA). CHON-001 cells and ATDC5 cells were inoculated in 24-well plates at a density of 5×10^4 cells/well. XIST-wt, XIST-mut or SIRT1-3'UTR-wt, SIRT1-3'UTR-mut were transfected into CHON-001 cells and ATDC5 cells, respectively, and treated with miR-653-5p mimics or miR-NC. Plasmid transfection was mediated by Lipofectamine® 3000 (Invitrogen; Thermo Fisher Scientific, Inc.), and after 48 h of transfection, the luciferase activity was determined by dual-luciferase reporter assay system (Promega, Madison, WI, USA) in accordance with the protocols.

Apoptosis detection

Apoptosis was detected by Annexin V-FITC/PI Apoptosis Detection Kit (Shanghai Yeasen BioTechnologies co.,Ltd.). Cells were trypsinized, centrifuged and washed after transfection. The cells were resuspended, and FITC-Annexin V and PI solution were loaded and incubated in dark for 15 min. Afteerwards, apoptosis was detected through flow cytometry (BD Biosciences, New Jersey, USA).

Statistical analysis

Data were statistically analyzed using SPSS software (version 20.0, Chicago, IL, USA). Multivariate comparisons were analyzed by one-way analysis of variance, and independent sample *t*-test was adopted for comparison between the two groups. $P < 0.05$ was statistically meaningful.

RESULTS

XIST and SIRT1 expressions were down-regulated and miR-653-5p expressions were up-regulated in OA cartilage

Above all, qRT-PCR was adopted to detect XIST, miR-653-5p and SIRT1 expressions in 30 OA cartilage tissues and 30 normal cartilage tissues. The results depicted that the expression of XIST and SIRT1 were significantly down-regulated in OA cartilage as against the normal group, while the expression of miR-653-5p was significantly increased (Fig. 1 A-C). To further investigate the relationship among three molecules, a correlation analysis was performed. The results demonstrated that the expression of XIST was negatively interrelated with the expression of miR-653-5p (Fig. 1D), but positively associated with the expression of SIRT1 (Fig. 1E). Furthermore, miR-653-5p was significantly negatively correlated with the expression of SIRT1 (Fig. 1F). The above results implied that these three molecules were involved in the development of OA.

XIST directly targeted miR-653-5p

To further elucidate the relationship between XIST and miR-653-5p, StarBase (http://starbase.sysu.edu.cn/) was utilized to predict the potential binding sites between them. The results displayed that there were two potential targeting sites between XIST and miR-653-5p (Fig. 2A). Dual luciferase reporter assay indicated that, in both ATDC5 and CHON-001 cells, miR-653-5p mimics could only reduce the luciferase activity of the wild type sequence of site 1, suggesting only site 1 was a validated binding site (Fig. 2B). Additionally, it was explored whether XIST could regulate the expression of miR-653-5p. The XIST low expression model were successfully constructed by transfecting ATDC5 or CHON-001 cell lines with siRNA (Fig. 2C), and the results proved that

the expression of miR-653-5p in si-XIST group was remarkably higher than that in the si-NC group (Fig. 2D). In contrast, XIST overexpression inhibited the expression of miR-653-5p (Fig. 2 D, F). The above results indicated that XIST inhibited the expression of miR-653-5p by directly binding with it.

XIST affected the cell viability of chondrocytes induced by IL-1β and regulated the inflammatory injury of chondrocytes

To explore the role of XIST in OA, ATDC5 and CHON-001 cells were treated with different concentrations of IL-1β (0, 2, 5, and 10 ng/mL) to mimic the inflammatory microenvrionment of OA. Then XIST and miR-653-5p expression in the cells were examined. The results showed that IL-1β induced down-regulation of XIST and up-regulation of miR-653-5p in ATDC5 and CHON-001 cells in a dose-dependent manner (Fig. 3 A, B). Next, ATDC5 and CHON-001 cells were treated with 10 ng/ml IL-1β, and the effect of XIST on cell viability was determined by MTT assay. The results indicated that XIST overexpression enhanced the cell viability of IL-1β-induced chondrocytes ATDC5 and CHON-001; on the contrary, si-XIST impaired the viability of chondrocytes (Fig. 3C). Moreover, co-transfection of miR-653-5p mimics reversed the promoting effect of XIST overexpression on cellular viability (Fig. 3D). To calculate the effect of XIST on chondrocyte apoptosis and inflammatory reaction, the protein expression of apoptosis-related protein cyto.C was detected by Western blot. The results depicted that IL-1β-induced up-regulation of cyto.C expression in chondrocytes, while transfection of XIST

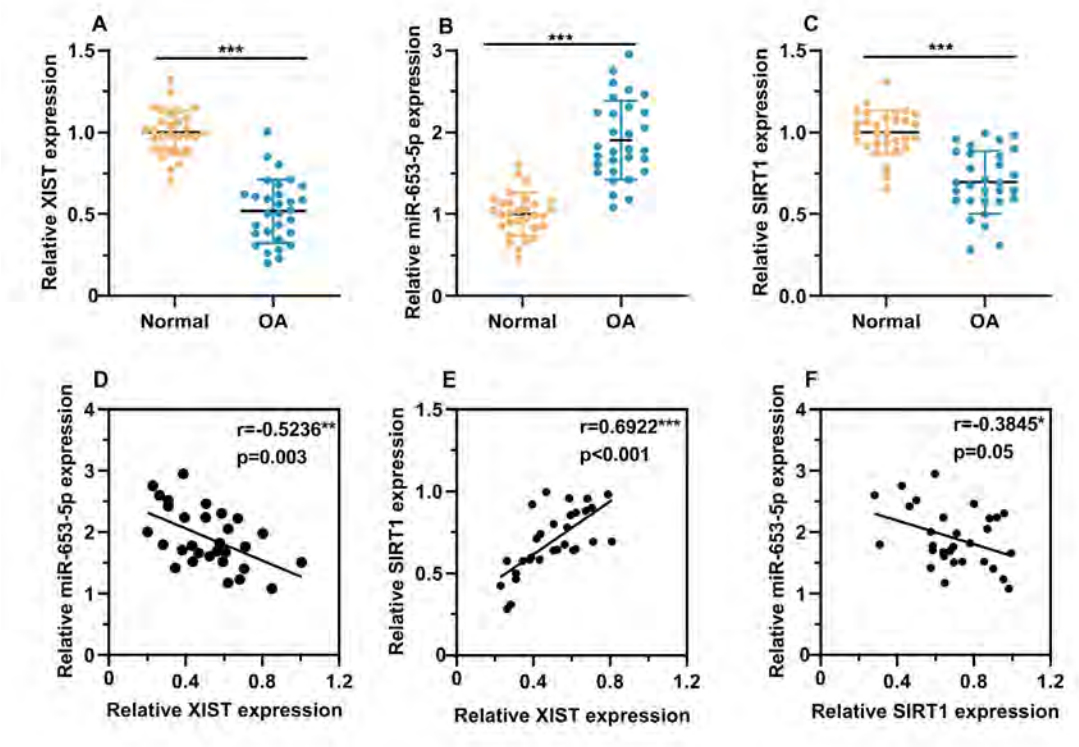


Fig. 1. *Down-regulation of XIST and SIRT1 expression and up-regulation of miR-653-5p expression in OA cartilage.* ***A-C****) qRT-PCR was used to measure the expression of XIST, miR-653-5p and SIRT1 in OA cartilage and normal groups (n=30).* ***D-E****) The correlation among XIST, miR-653-5p, SIRT1 were analyzed by Spearman's correlation analysis. All experiments were performed in triplicate.*

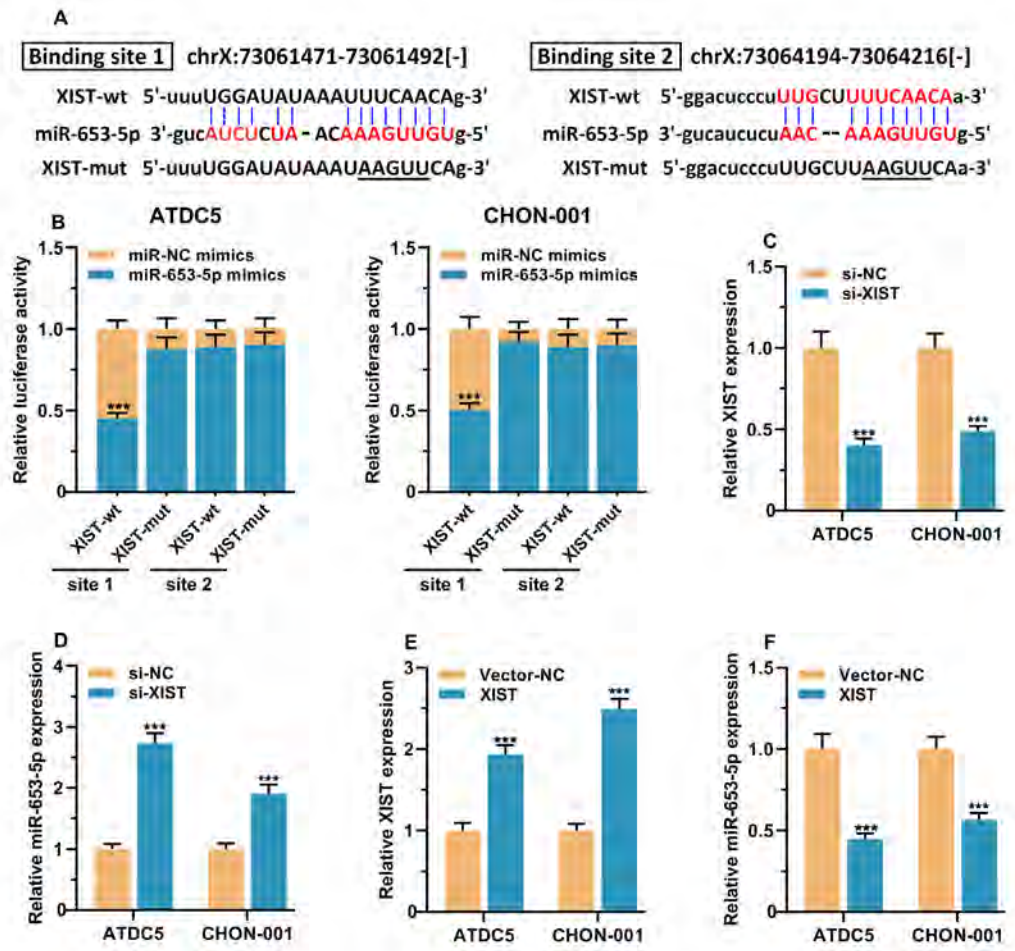


Fig. 2. *XIST repressed miR-653-5p expression by binding with it.* ***A****) StarBase was used to predict the conserved binding sites between XIST and miR-653-5p.* ***B****) Relative luciferase activity of site1 and site2 XIST-wt /mut in chondrocytes ATDC5 and CHON-001 were determined by luciferase reporter gene when XIST-wt or XIST-mut were co-transfected with miR-653-5p mimics.* ***C, D****) After siRNA was transfected into chondrocytes ATDC5 and CHON-001, the expression of XIST and miR-653-5p were detected by qRT-PCR.* ***E, F****) After pcDNA3.1-XIST (XIST) vector was transfected into chondrocytes ATDC5 and CHON-001, the expression of XIST and miR-653-5p were detected by qRT-PCR. All experiments were performed in triplicate.* *** $P < 0.001$.

significantly inhibited the expression of cyto.C, while si-XIST further promoted the expression of cyto.C (Fig. 3E). ELISA was employed to study inflammatory factors IL-6, IL-8 and TNF-α expressions in cell culture supernatant. As shown, in both cell lines, IL-1β treatment promoted the release of inflammatory factor IL-6, IL-8 and TNF-α, while transfection of XIST-overexpressing vector can effectively reduce the inflammation, and si-XIST further promoted the release of inflammatory factors (Fig. 3F). Furthermore, it was found that miR-653-5p can reverse the effects of XIST overexpression on the expression of cyto.C and inflammatory factors (Fig. 3 G, H). Additionally, IL-1β treatment promoted cell apoptosis, while transfection of XIST-overexpressing vector can significantly attenuate apoptosis and si-XIST had the opposite effect (Fig. 3I). Besides, miR-653-5p also significantly reversed the inhibitory effects on cell apoptosis induced by XIST overexpression (Fig. 3J). The above results indicated that XIST overexpression inhibited chondrocyte apoptosis and inflammatory reaction

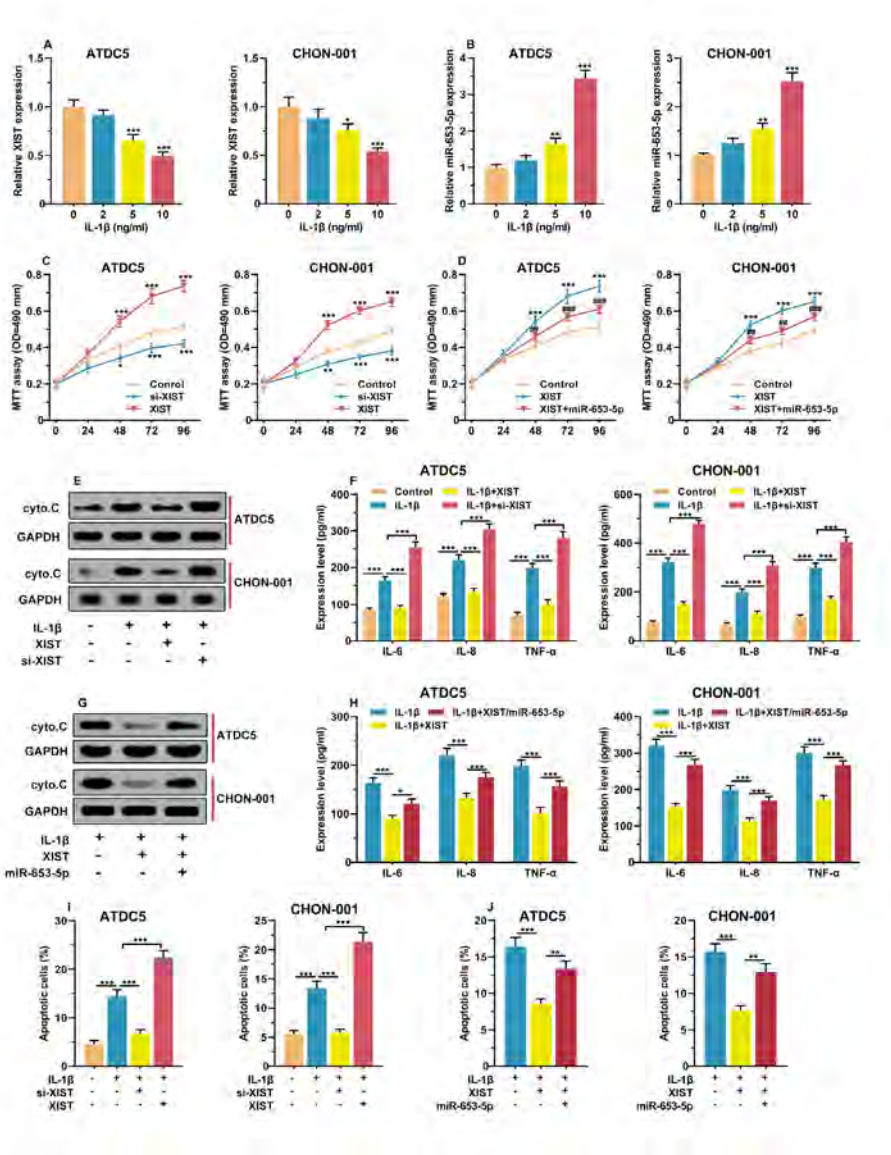


Fig. 3. *XIST affected the cell viability and regulated the inflammatory reaction of chondrocytes induced by IL-1β through miR-653-5p.* ***A, B****) Chondrocytes ATDC5 and CHON-001 were treated with different concentrations of IL-1β for 24 h, and the expression of XIST and miR-653-5p were detected by qRT-PCR.* ***C****) When chondrocytes ATDC5 and CHON-001 induced by 10ng/ml IL-1β were transfected with si-XIST or XIST vector, the cell viability of chondrocytes was detected by MTT assay.* ***D****) When chondrocytes ATDC5 and CHON-001 induced by 10ng/ml IL-1β were co-transfected with XIST vector and miR-653-5p mimics, the cell viability of chondrocytes was detected by MTT assay.* ***E****) Protein expression of the apoptotic factor cyto.C in chondrocytes transfected with si-XIST and XIST vectors was detected by Western blot.* ***F****) ELISA was used to detect the expression of inflammatory factors IL-6, IL-8 and TNF-α when ATDC5 and CHON-001 were transfected with si-XIST or XIST vector.* ***G****) After IL-1β-induced chondrocytes ATDC5 and CHON-001 were only transfected with XIST vector or co-transfected with miR-653-5p mimics, the expression of cyto.C protein was detected by Western blot (n=3).* ***H****) After IL-1β-induced chondrocytes ATDC5 and CHON-001 were only transfected with XIST vector or co-transfected with XIST and miR-653-5p mimics, the expression of inflammatory factors IL-6, IL-8 and TNF- α were detected by qPCR.* * *P < 0.05.* ***I****) Flow cytometry was used to analyze the apoptosis of ATDC5 and CHON-001 transfected with si-XIST or XIST vector.* ***P < 0.01; ****P < 0.001.* ***J****) Flow cytometry was used to analyze the apoptosis of ATDC5 and CHON-001 only transfected with XIST vector or co-transfected with XIST and miR-653-5p mimics. All experiments were performed in triplicate.* * *P < 0.05,* ** *P < 0.01,* *** *P < 0.001. In figure D,* *** *P < 0.001 vs control groups;* $^{\#\#}$ *P < 0.01,* $^{\#\#\#}$ *P < 0.001 vs XIST groups.*

induced by IL-1β, which was partially mediated by the suppression of miR-653-5p.

SIRT1 was the direct target of miR-653-5p

To further explore the role of miR-653-5p in OA, TargetScan database (http://www.targetscan.org/vert_72/) was used for bioinformatics analysis and it predicted that that there was a complementary binding region for the 3'UTR of SIRT1 and miR-653-5p (Fig. 4A). Dual luciferase reporter assay confirmed this targeting relationship in both ATDC5 and CHON-001 cell (Fig. 4B). The interaction between miR-653-5p and SIRT1 was further analyzed by qRT-PCR. The results demonstrated that miR-

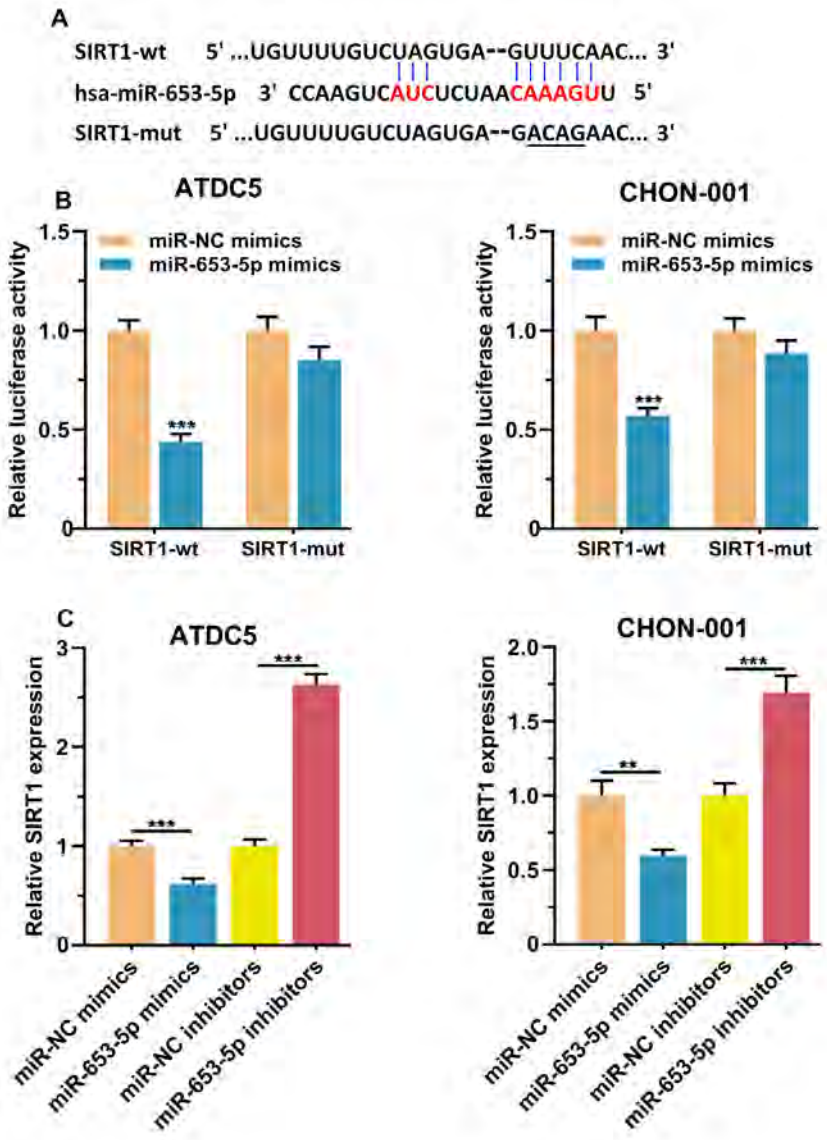


Fig. 4. *SIRT1 was the direct target of miR-653-5p.* ***A)*** *The binding site between SIRT1 and miR-653-5p were predicted by the database TargetScan (http://www.targetscan.org/).* ***B)*** *Relative luciferase activity of SIRT1-wt/mut in chondrocytes ATDC5 and CHON-001 were determined by luciferase reporter gene when SIRT1-wt or SIRT1-mut were co-transfected with miR-653-5p mimics.* ***C)*** *SIRT1 mRNA expressions were detected by qRT-PCR after transfection of chondrocytes with miR-653-5p mimics or inhibitors. All experiments were performed in triplicate.* $^{*}P < 0.05$, $^{**}P < 0.01$, $^{***}P < 0.001$.

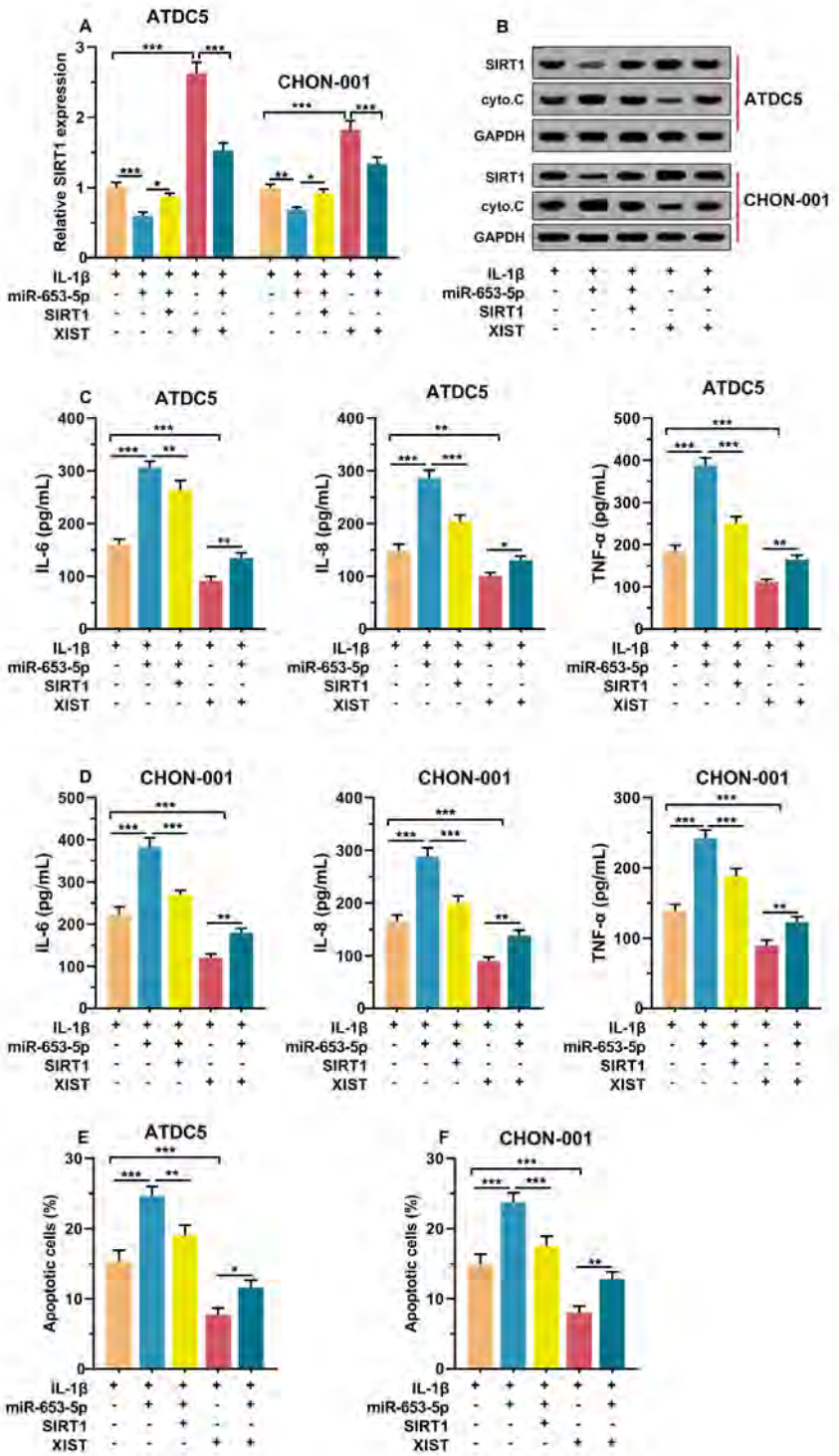


Fig. 5. *XIST/miR-653-5p axis modulated IL-1β-induced chondrocyte inflammatory reaction via regulating SIRT1. After ATDC5 and CHON-001 were treated with 10 ng/mL IL-1β, they were transfected with XIST alone, co-transfected with XIST and miR-653-5p mimics, transfected with miR-653-5p mimics alone, or co-transfected with miR-653-5p mimics and SIRT1-overexpressing plasmid.* ***A****) The expression of SIRT1 mRNA was detected by qPCR.* ***B****) The protein levels of SIRT1 and apoptosis factor cyto.C were detected by Western blot.* ***C, D****) ELISA was used to detect the expression of inflammatory factors IL-6, IL-8 and TNF-α in chondrocytes ATDC5 and CHON-001.* ***E, F****) Flow cytometry was used to analyze the apoptosis of ATDC5 and CHON-001. All experiments were performed in triplicate.* $^{*}P < 0.05$ $^{**}P < 0.01$, $^{***}P < 0.001$.

653-5p overexpression significantly reduced SIRT1 mRNA expressions in ATDC5 and CHON-001 cells, and SIRT1 mRNA expressions were dramatically increased after cells were transfected with miR-653-5p inhibitors (Fig. C). The above results validated that SIRT1 was a target of miR-653-5p.

XIST/miR-653-5p modulated IL-1β-induced chondrocyte inflammatory reaction via regulating SIRT1

Given that XIST can negatively regulated expressions of miR-653-5p, and SIRT1 was a direct target of miR-653-5p, SIRT1-overexpressing plasmid was further transfected into chondrocytes. The results displayed that XIST overexpression promoted the expression of SIRT1 mRNA and protein in IL-1β-induced chondrocytes ATDC5 and CHON-001, and this effect was significantly inhibited after co-transfection with miR-653-5p (Fig. 5 A, B). In addition, Western blot and ELISA results proved that SIRT1 inhibited the expression of Cyto.C and inflammatory factors IL-6, IL-8 and TNF-α in chondrocytes ATDC5 and CHON-001 (Fig. 5 B - D). Besides, flow cytometry analysis also showed that SIRT1 could reverse the up-regulation of cell apoptosis rate in both cell lines (Fig. 5 E - F). In summary, it was concluded that XIST inhibited the chondrocyte apoptosis and inflammatory reaction during OA by regulating the miR-653-5p/SIRT1 axis.

DISCUSSION

In recent years, the role of lncRNAs in OA has gained increasing attention. Through high-throughput technology, a recent study reported that the expression profile of lncRNAs in OA cartilage of knee joint has changed: 3007 lncRNAs were up-regulated and 1707 were down-regulated (19). In OA articular cartilage, lncRNA maternally expressed gene 3 (MEG3) can inhibit angiogenesis by negatively regulating vascular endothelial growth factor, thus participating in the OA development (20, 21). Under the stimulation of inflammatory factors IL-β and TNF-α, the expression of lncRNA H19 in chondrocytes is inhibited, while in hypoxia condition, H19 expression is increased (22, 23). As a member of lncRNAs, XIST has been proved to be involved in the regulation of the progression of various tumors including osteosarcoma and gastric cancer (24, 25). In this work, it was demonstrated that XIST was down-regulated in OA tissues and could promote the viability of chondrocytes induced by IL-1β, suggesting it is a protective lncRNA during the development of OA.

Accumulating studies have indicated that lncRNA can adsorb specific miRNAs, and indirectly regulate the downstream genes by inhibiting the binding between miRNA and the 3'UTR of downstream genes (26). Increasing reports have revealed that this lncRNA/miRNA interaction participates in the development of OA. For example, lncRNA plasmacytoma variant translocation 1 gene (PVT1) is highly expressed in OA cartilage and can promote chondrocyte apoptosis through negative regulation of miR-488-3p (27). The expression of lncRNA UFC1 was down-regulated in OA cartilage, and its inhibition facilitates apoptosis and reduces viability of chondrocytes by promoting the expression of miR-34a (28). In this study, it was proved that XIST was negatively correlated with miR-653-5p expression in OA cartilage samples, and it was also demonstrated that XIST negatively regulated the expression of miR-653-5p through gain-of-function and loss-of-function experiments. Importantly, miR-653-5p inhibited the viability of chondrocytes. Our data implied that the function of XIST was partly mediated by miR-653-5p during OA development.

Inflammation is crucial in the development of OA, and the proinflammatory cytokine IL-1β plays important roles in the whole process of inflammation and chondrocyte apoptosis (29). IL-1β can activate NF-κB, accompanied with the increased expression of extracellular matrix remodeling-related genes such as MMPs and a disintegrin and metalloproteinase with thrombospondin motifs (ADAMTSs), which in turn degrade cartilage matrix (30, 31). By multiple mechanisms, SIRT1 is a crucial protective factor during OA development (18). Specifically, as a NAD-dependent deacetylase, SIRT1 inhibits NF-κB pathway through the deacetylation of p56 (a subunit of NF-κB), thus impeding the expression of catabolic genes as well

as pro-inflammatory genes (32, 33). It is reported that SIRT1 is regulated by multiple miRNAs. For example, a recent study reports that in OA and IL-1β-induced chondrocyte inflammation models, SIRT1 expression is decreased, while its modulator miR-449a is highly expressed; after inhibition of miR-449a, the up-regulation of SIRT1 can inhibit the expression of MMP-13 and ADAMTSs, so as to exert the role of protective regulation (34). In this work, our data consistently indicated that SIRT1 expression was significantly down-regulated in OA tissues and IL-1β-induced chondrocytes. It was also proved that XIST/miR-653-5p could modulate SIRT1 expression, which helped clarify the mechanism of SIRT1 dysregulation in OA.

Interestingly, another study reports that XIST is up-regulated in OA tissues and its overexpression can induce the apoptosis of chondrocytes, which is contradictory to our demonstrations (35). It might due to the fact that samples were collected from different stages of disease and different cell lines. However, this work also demonstrates that XIST can up-regulate osteopontin (35). Osteopontin is considered as a promoter of chondrocyte viability and a protective of OA (36). From this point of view, it is reasonable to form a hypothesis that XIST can also promote the viability of chondrocytes via up-regulating osteopontin. Our data and the previous reports imply that the function of XIST in different stages of OA may be dynamically changing, and more detailed investigation on the role of XIST in OA is required in the future.

Recent studies have shown that chondrocyte apoptosis is crucial in the pathogenesis of osteoarthritis (37). In cell biology, the two main pathways that induce apoptosis are the receptor (extrinsic) pathway and the mitochondrial (intrinsic) pathway. In the extrinsic pathway, the stimulus of cell death receptors directly triggers caspase-8 and initiates the following cascade; in the intrinsic pathway, apoptosis is initiated by various stress signals (38-39). Signals of apoptosis through mitochondrial changes include reduced energy production, decreased mitochondrial transmembrane potential, increased mitochondrial membrane permeability, and release of pro-apoptotic factors such as cyto.C (40). Many studies have shown that cyto.C can trigger caspase-3 activation (41). The data in the present study showed that IL-1β induced up-regulation of cyto.C in chondrocytes, while XIST can effectively inhibit its expression. These results indicated that XIST/miR-653-5p/SIRT1 axis could regulate the apoptosis of chondrocytes via mitochondrial apoptotic pathway. However, the detailed mechanism by which XIST/miR-653-5p/SIRT1 regulates apoptosis of chondrocytes requires further investigations.

In summary, in the present work, a novel molecular mechanism contributing to OA development was discovered, namely XIST/miR-653-5p/SIRT1 axis. Our work provided potential targets for the diagnosis and treatments of OA. However, it is still necessary to collect more clinical samples and perform animal experiments to further verify our demonstrations in the future.

REFERENCES

1. Doherty M, Abhishek A, Hunter D. Clinical manifestations and diagnosis of osteoarthritis. UpToDate (last access 19 January 2016) 2017.
2. Bonnet C, Walsh D. Osteoarthritis, angiogenesis and inflammation. Rheumatology 2005; 44:7-16.
3. Fossey SL, Vahle JL, Leininger JR. Bones, joints, and synovia. In Boorman's Pathology of the Rat: Reference and Atlas. A.W. Suttie, J.R. Leininger, A.E. Bradley, eds. Elsevier. London, 2018; p. 299-319.
4. Jiménez G, Cobo-Molinos J, Antich C, López-Ruiz E. Osteoarthritis: Trauma vs Disease. In Osteochondral Tissue Engineering. J. Oliveira, S. Pina, R. Reis, R.J. San, eds. Springer. Cham, 2018; p. 63-83.
5. Bhan A, Mandal SS. Long noncoding RNAs: emerging stars in gene regulation, epigenetics and human disease. Chemmedchem 2014; 9: 1932-56.
6. Wu QY, Miao ZN, Ye JX, et al. Long non-coding RNAs: a new regulatory code for osteoporosis. Frontiers in Endocrinology 2018; 9:587.
7. Wang K, Jiang W, Cheng C, Li Y, Tu M. Pathological and therapeutic aspects of long noncoding RNAs in osteosarcoma. Anti-Cancer Agents Med Chem 2017; 17:1312-16.
8. Roberts S, Wootton E, De Ferrari L, Albagha O,

Salter D. Epigenetics of osteoarticular diseases: recent developments. Rheumatol Int 2015; 35:1293-305.
9. Song J, Ahn C, Chun CH, Jin EJ. A long non-coding RNA, GAS5, plays a critical role in the regulation of miR-21 during osteoarthritis. J Orthop Res 2014; 32:1628-35.
10. Zhang C, Wang P, Jiang P, et al. Upregulation of lncRNA HOTAIR contributes to IL-1β-induced MMP overexpression and chondrocytes apoptosis in temporomandibular joint osteoarthritis. Gene 2016; 586:248-53.
11. Li C, Wan L, Liu Z, et al. Long non-coding RNA XIST promotes TGF-β-induced epithelial-mesenchymal transition by regulating miR-367/141-ZEB2 axis in non-small-cell lung cancer. Cancer Lett 2018; 418:185-95.
12. Zheng R, Lin S, Guan L, et al. Long non-coding RNA XIST inhibited breast cancer cell growth, migration, and invasion via miR-155/CDX1 axis. Biochem Biophys Res Commun 2018; 498:1002-08.
13. Wang T, Liu Y, Wang Y, Huang X, Zhao W, Zhao Z. Long non-coding RNA XIST promotes extracellular matrix degradation by functioning as a competing endogenous RNA of miR-1277-5p in osteoarthritis. Int J Mol Med 2019; 44:630-42.
14. Matsukawa T, Sakai T, Yonezawa T, et al. MicroRNA-125b regulates the expression of aggrecanase-1 (ADAMTS-4) in human osteoarthritic chondrocytes. Arthritis Res Ther 2013; 15:R28.
15. Park S, Cheon E, Kim H. MicroRNA-558 regulates the expression of cyclooxygenase-2 and IL-1β-induced catabolic effects in human articular chondrocytes. Osteoarthritis Cartilage 2013; 21:981-89.
16. Fujimori K, Iguchi Y, Yamashita Y, Gohda K, Teno N. Synthesis of novel farnesoid x receptor agonists and validation of their efficacy in activating differentiation of mouse bone marrow-derived mesenchymal stem cells into osteoblasts. Molecules 2019; 24:E4155.
17. Zhang R, Liu J, Yu S, Sun D, Wang X, Fu J, Xie Z. LncRNA UCA1 affects osteoblast proliferation and differentiation by regulating BMP-2 expression. Eur Rev Med Pharmacol Sci 2019; 23:6774-82.
18. Deng Z, Li Y, Liu H, et al. The role of sirtuin 1 and its activator, resveratrol in osteoarthritis. Biosci Rep 2019; 39.
19. Fu M, Huang G, Zhang Z, et al. Expression profile of long noncoding RNAs in cartilage from knee osteoarthritis patients. Osteoarthritis Cartilage 2015; 23:423-32.
20. Henrotin Y, Pesesse L, Lambert C. Targeting the synovial angiogenesis as a novel treatment approach to osteoarthritis. Ther Adv Musculoskelet Dis disease 2014; 6:20-34.
21. Su W, Xie W, Shang Q, Su B. The long noncoding RNA MEG3 is downregulated and inversely associated with VEGF levels in osteoarthritis. BioMed Res Int 2015; 2015: 356893. doi: 10.1155/2015/356893
22. Xing D, Liang Jq, Li Y, Lu J, Jia Hb, Xu Ly, Ma Xl. Identification of long noncoding RNA associated with osteoarthritis in humans. Orthop Surg 2014; 6:288-93.
23. Steck E, Boeuf S, Gabler J, Werth N, Schnatzer P, Diederichs S, Richter W. Regulation of H19 and its encoded microRNA-675 in osteoarthritis and under anabolic and catabolic in vitro conditions. J Mol Med 2012; 90:1185-95.
24. Yang C, Wu K, Wang S, Wei G. Long non-coding RNA XIST promotes osteosarcoma progression by targeting YAP via miR-195-5p. J Cell Biochem 2018; 119:5646-56.
25. Chen D-l, Ju H-q, Lu Y-x, et al. Long non-coding RNA XIST regulates gastric cancer progression by acting as a molecular sponge of miR-101 to modulate EZH2 expression. J Exp Clin Cancer Res 2016; 35:142.
26. Tay Y, Rinn J, Pandolfi PP. The multilayered complexity of ceRNA crosstalk and competition. Nature 2014; 505:344-52.
27. Li Y, Li S, Luo Y, Liu Y, Yu N. LncRNA PVT1 regulates chondrocyte apoptosis in osteoarthritis by acting as a sponge for miR-488-3p. DNA Cell Biol 2017; 36:571-80.
28. Zhang G, Wu Y, Xu D, Yan X. Long noncoding RNA UFC1 promotes proliferation of chondrocyte in osteoarthritis by acting as a sponge for miR-34a. DNA Cell Biol 2016; 35:691-95.
29. Kapoor M, Martel-Pelletier J, Lajeunesse D, Pelletier J-P, Fahmi H. Role of proinflammatory cytokines in the pathophysiology of osteoarthritis. Nat Rev Rheumatol 2011; 7:33-42.
30. Wojdasiewicz P, Poniatowski ŁA, Szukiewicz D. The

role of inflammatory and anti-inflammatory cytokines in the pathogenesis of osteoarthritis. Mediat Inflamm 2014; 2014: 561459. doi: 10.1155/2014/561459
31. Roman-Blas J, Jimenez S. NF-κB as a potential therapeutic target in osteoarthritis and rheumatoid arthritis. Osteoarthritis Cartilage 2006; 14:839-48.
32. Liu-Bryan R, Terkeltaub R. Emerging regulators of the inflammatory process in osteoarthritis. Nat Rev Rheumatol 2015; 11:35.
33. Yeung F, Hoberg JE, Ramsey CS, Keller MD, Jones DR, Frye RA, Mayo MW. Modulation of NF-κB-dependent transcription and cell survival by the SIRT1 deacetylase. EMBO Jl 2004; 23:2369-80.
34. Park K, Lee K-M, Yoon D, et al. Inhibition of microRNA-449a prevents IL-1β-induced cartilage destruction via SIRT1. Osteoarthritis Cartilage 2016; 24:2153-61.
35. Li L, Lv G, Wang B, Kuang L. The role of lncRNA XIST/miR-211 axis in modulating the proliferation and apoptosis of osteoarthritis chondrocytes through CXCR4 and MAPK signaling. Biochem Biophys Res Commun 2018; 503:2555-62.
36. Shang H, Hao Y, Hu W, Hu X, Jin Q. OPN gene locus is associated with the risk of knee osteoarthritis: a case–control study. Biosci Rep 2019; 39.
37. Maldonado M, Nam J. The role of changes in extracellular matrix of cartilage in the presence of inflammation on the pathology of osteoarthritis. BioMed Res Int 2013; 2013.
38. Blanco FJ, López-Armada MJ, Maneiro E. Mitochondrial dysfunction in osteoarthritis. Mitochondrion 2004; 4:715-28.
39. Hengartner MO. The biochemistry of apoptosis. Nature 2000; 407:770-76.
40. Vander Heiden MG, Chandel NS, Li XX, Schumacker PT, Colombini M, Thompson CB. Outer mitochondrial membrane permeability can regulate coupled respiration and cell survival. Proceedings of the National Academy of Sciences 2000; 97:4666-71.
41. Joza N, Susin SA, Daugas E, et al. Essential role of the mitochondrial apoptosis-inducing factor in programmed cell death. Nature 2001; 410:549-54.

MiR-1294 ACTS AS A TUMOR INHIBITOR IN CERVICAL CANCER BY REGULATING FLOT1 EXPRESSION

XQ. KAN[1*], YB. LI[2*], B. HE[3], SF. CHENG[4], YJ. WEI[5] and JL. SUN[6]

[1]Department of Obstetrics, Zhangqiu Maternity and Child Care Hospital, Jinan, China; [2]Department of Blood Transfusion, Yantai Yuhuangding Hospital, Yantai, China; [3]Jinan Li Cheng District Maternal and Child Health and Family Planning Service Centre, Jinan, China; [4]Department of Nephrology, The People's Hospital of Zhangqiu Area, Jinan, China; [5]Clinical Medicine College, Jiamusi University, Heilongjiang, China; [6]Sterilization Supply Room, The People's Hospital of Zhangqiu Area, Jinan, China

Received January 10, 2020 – Accepted March 24, 2020

[*]These Authors contributed equally to this work.

Recently, important regulatory mechanisms of microRNAs (miRNAs) have been widely reported in human cancers including cervical cancer. The purpose of this study is to preliminarily clarify the function of miR-1294 in cervical cancer. The expression of miR-1294 or FLOT1 was detected using RT-qPCR or Western blot analysis. MTT, Transwell and luciferase reporter assays were used to explore the functional mechanism of miR-1294. The results showed that miR-1294 expression was decreased in cervical cancer. Functionally, overexpression of miR-1294 restrained the viability and metastasis of cervical cancer cells. MiR-1294 can also block EMT and suppress β-catenin expression in cervical cancer cells. Additionally, FLOT1 was confirmed to be a direct target of miR-1294. The knockdown of FLOT1 impeded the progression of cervical cancer. More importantly, miR-1294 inhibited the occurrence of cervical cancer by interacting with FLOT1. In conclusion, miR-1294 inhibits cell viability, migration and invasion by suppressing FLOT1 expression.

Cervical cancer is the most common gynecological malignancy, and its incidence is second only to breast cancer and ranks second in gynecological malignancies (1). Cervical cancer patients' age distribution is bimodal, 35-39 years old and 60-64 years old, respectively. However, the age of onset has increased significantly in recent years (2). Studies have found that many sexually transmitted diseases, such as human papillomavirus (HPV), can cause cervical cancer (3). Although cervical cancer is dangerous, it also has its own "ribs", which is the easiest way to detect and treat early. Previous studies have shown that the initial cure rate can reach 80-90%, while the cure rate for stage IV is only 10% (4). Therefore, regular inspection and timely treatment are very important for patients with cervical cancer.

It is well known that microRNAs (miRNAs) are involved in tumorigenesis by binding to target genes. Many studies have shown that miRNAs act as tumor suppressor or oncogene in cervical cancer. For example, miR-218 was downregulated and produced anti-tumor effect (5). In addition,

Key words: miR-1294; cervical cancer; viability; metastasis; FLOT1

Corresponding Author:
Jilan Sun, MM.
Sterilization Supply Room, The People's Hospital of Zhangqiu Area, Jinan, 250200, China
No.1920 Huiquan Road, Jinan, China
Tel/Fax: 860531-83251203
e-mail: xujfguangdong@163.com/jizxdnjf441@163.com

0393-974X (2020)
Copyright © by BIOLIFE, s.a.s.
This publication and/or article is for individual use only and may not be further reproduced without written permission from the copyright holder.
Unauthorized reproduction may result in financial and other penalties
DISCLOSURE: ALL AUTHORS REPORT NO CONFLICTS OF INTEREST RELEVANT TO THIS ARTICLE.

miR-378 was upregulated and functioned as an oncogene-miRNA (6). The regulatory mechanism of miR-1294 has been investigated in human cancers. Downregulation of miR-1294 has been found in many malignancies, such as oral squamous cell carcinoma and osteosarcoma (7, 8). Functionally, miR-1294 inhibited cell proliferation and enhanced the chemosensitivity of glioma to temozolomide (9). However, to date, the abnormal expression and role of miR-1294 in cervical cancer is unknown. Therefore, this study aims to elucidate the regulatory mechanism of miR-1294 in cervical cancer.

To further explain the regulatory mechanism of miR-1294 in cervical cancer, flotillin-1 (FLOT1) was predicted to be a target of miR-1294 in this study. FLOT1 has been reported to be upregulated in human cancers, including lung adenocarcinoma and esophageal squamous cell carcinoma (10, 11). Functionally, FLOT1 has been found to promote cell growth and metastasis in oral squamous cell carcinoma (12). In addition, the interaction between miRNAs and FLOT1 has been reported in previous studies. For example, miR-506 inhibited cell growth and metastasis in clear cell renal cell carcinoma by targeting FLOT1 (13). However, previous studies have not reported the relationship between miR-1294 and FLOT1 in cervical cancer.

Therefore, the regulatory mechanism of miR-1294/FLOT1 in cervical cancer was investigated. At the same time, specific roles of miR-1294 and FLOT1 were also confirmed. MiR-1294 may be developed as a new diagnostic biomarker and therapeutic target for cervical cancer treatment.

MATERIALS AND METHODS

Sixty-five patients with cervical cancer from the People's Hospital of Zhangqiu Area participated in the study. Experimental tissues were obtained from these patients who provided written informed consent. In addition, the patients had not received any treatment other than surgery. This study was approved by the Institutional Ethics Committee of The People's Hospital of Zhangqiu Area.

Cell culture and transfection

Normal human cervix epithelial cell line (Ect1) and cervical cancer cell lines (CaSki, Siha) were purchased from ATCC (Manassas, VA, USA). These cells were cultured in DMEM containing 10% FBS and incubated in an atmosphere with 5% CO_2 at 37°C.

MiR-1294 mimics or inhibitor and FLOT1 siRNA or overexpression plasmid (GenePharma, Shanghai, China) were transfected into Siha cells using Lipofectamine 2000 (Invitrogen, Carlsbad, USA), respectively.

RT-qPCR

TRIzol reagent (Invitrogen, USA) was used to extract total RNA. MicroRNA reverse transcription kit (Takara, Dalian, China) was used for reverse transcription of cDNA. Next, RT-qPCR analysis was performed using cDNA solution, primers and SYBR Green Master Mix II (Takara). The relative expressions of miR-1294 and FLOT1 were normalized to U6 and GAPDH. Their expressions were quantified by the $2^{-\square\square cq}$ method.

MTT assay

MTT assay was used to measure cell proliferation. Siha cells were seeded in 96-well plates. Transfected cells were incubated for 24, 48, 72 and 96 h, respectively. These cells were then incubated at 3°C for 4 h using MTT solution (Sigma, USA). The absorbance at 490 nm was detected with a spectrophotometer.

Transwell assay

The upper chamber with Matrigel is used for cell invasion. Siha cells (5×10^3 cells/well) were added to the upper chamber. DMEM medium (10% FBS) was added to the lower chamber. In addition, cell migration was detected in the absence of Matrigel, and other experimental steps are the same as cell invasion. After 24 h, the moving cells were stained with 0.1% crystal violet. The number of moving cells was counted using a light microscope.

Dual luciferase reporter assay

A pmirGLO luciferase reporter vector (Promega, USA) containing Wt-FLOT1 or Mut-FLOT1 and miR-1294 mimics were transfected into Siha cells. After 48 h, the luciferase activity was measured using dual luciferase assay system (Promega, USA).

Western blot analysis

Protein samples were lysed using RIPA buffer

(Beyotime, Shanghai, China). Next, proteins were separated using 10% SDS-PAGE. Protein samples were transferred into PVDF membranes and blocked with 5% non-fat milk. Protein samples were then incubatedwith Bax, Bcl-2, Vimentin, N-cadherin, E-cadherin, β-catenin, p-β-catenin and GAPDH primary antibodies (Abcam, Shanghai, China) overnight at 4°C. After washing, the protein samples were incubated with secondary antibodies (Abcam, USA) for 1 h. Finally, protein bands were evaluated using the ECL kit (Beyotime).

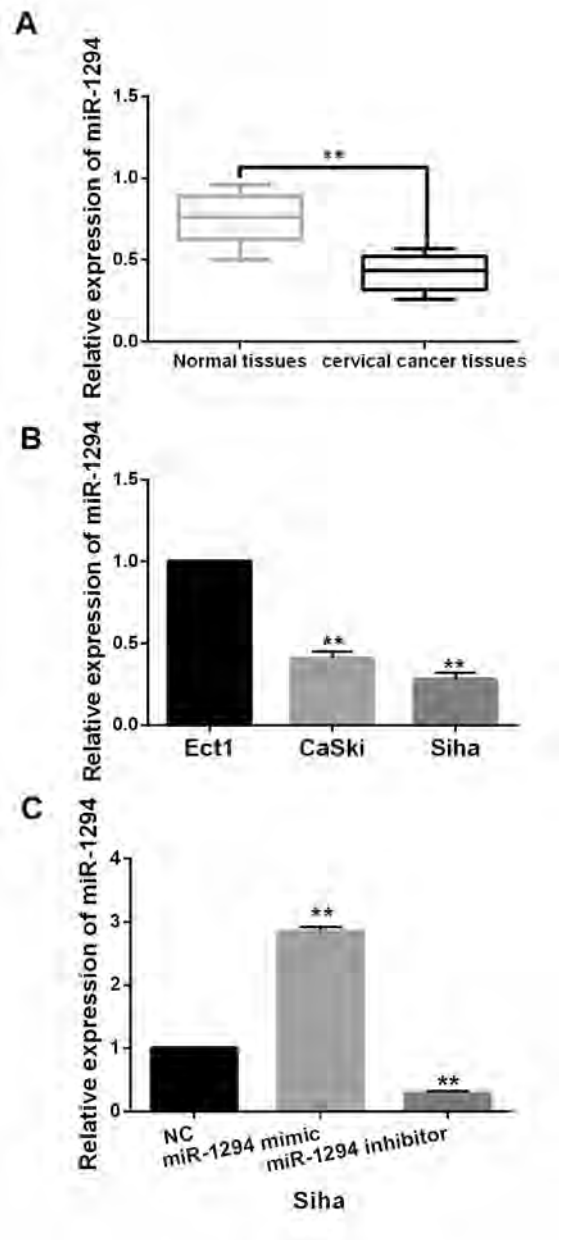


Fig. 1. *MiR-1294 expression is decreased in cervical cancer.* ***A)*** *MiR-1294 expression in cervical cancer tissues and normal tissues.* ***B)*** *MiR-1294 expression in CaSki, Siha and Ect1 cells.* ***C)*** *MiR-1294 expression in Siha cells with its mimics or inhibitor. **P < 0.01.*

Statistical analysis

Data are analyzed by SPSS 17.0 and graphed by Graphpad Prism 6. Data were shown as mean ± SD. Differences between groups were calculated using Student's *t*-test and ANOVA with Turkey's multiple comparison tests. $P < 0.05$ indicates that the difference is statistically significant.

RESULTS

MiR-1294 expression is decreased in cervical cancer

To explore whether miR-1294 is involved in the progression of cervical cancer, the abnormal expression of miR-1294 was detected in cervical cancer tissues and cells. Compared with normal tissues, downregulation of miR-1294 was found in cervical cancer tissues ($P<0.01$, Fig. 1A). Meanwhile, it was found that miR-1294 expression in CaSki and Siha cervical cancer cells was lower than that in cervix epithelial cells Ect1 ($P<0.01$, Fig. 1B). Next, because of the significant difference in miR-1294 expression, Siha cells were selected for functional experiments. MiR-1294 mimics or inhibitors were then transfected into Siha cells. We found that miR-1294 mimics increased its expression, while miR-1294 inhibitor reduced its expression in Siha cells ($P<0.01$, Fig. 1C).

MiR-1294 restrained cervical cancer cell viability and metastasis

Next, the effects of miR-1294 on cell viability and metastasis were evaluated by MTT and Transwell assays. MTT assay showed that miR-1294 mimics restrained cell proliferation, while miR-1294 inhibitor accelerated the proliferation of Siha cells ($P<0.01$, Fig. 2A). Western blot analysis showed that miR-1294 mimics promoted Bax expression and reduced the survival gene Bcl-2 expression. However, miR-1294 inhibitor showed opposite effects on Bax/Bcl-2 expression in Siha cells (Fig. 2B). In addition, it was found that the migration

and invasion of Siha cells were inhibited by miR-1294 overexpression and promoted by miR-1294 downregulation (P<0.01, Fig. 2C, 2D).

FLOT1 is a direct target of miR-1294

Further, FLOT1 was found to have a binding site to miR-1294 in TargetScan database (http://www.targetscan.org/, Fig. 3A). Luciferase reporter assay showed that miR-1294 mimics reduced the luciferase activity of Wt-FLOT1 (P<0.01, Fig. 3B), indicating that miR-1294 directly targets FLOT1. In addition, miR-1294 mimics reduced FLOT1 expression, while miR-1294 inhibitors increased FLOT1 expression in Siha cells (P<0.01, Fig. 3C). Then, upregulation of FLOT1 was detected in cervical cancer tissues compared to normal tissues (P<0.01, Fig. 3D). There was a negative correlation between miR-1249 and FLOT1 expression in cervical cancer tissues (P<0.01, R^2=0.5424; Fig. 3E).

Knockdown of FLOT1 impeded the progression of cervical cancer

The above results suggest that FLOT1 may be involved in the development of cervical cancer. We also found that FLOT1 was upregulated in cervical cancer cells CaSki and Siha compared to Ect1 cervix

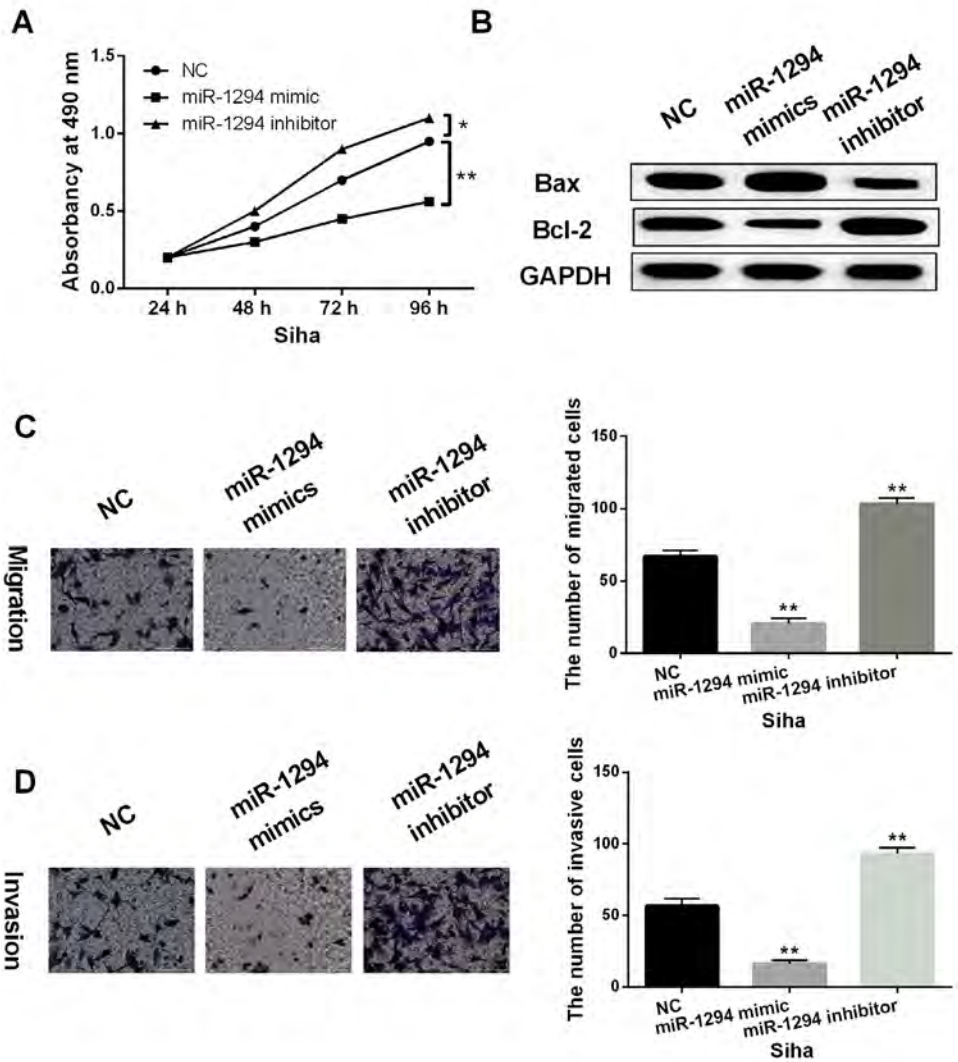


Fig. 2. *MiR-1294 restrained cervical cancer cell viability and metastasis. **A)** Cell proliferation was measured in Siha cells with miR-1294 mimics or inhibitor (**B**) MiR-1294 regulated protein expression of Bax and Bcl-2 in Siha cells. **C, D**) Cell migration and invasion were detected in Siha cells with miR-1294 mimics or inhibitor. *P < 0.05, ** P <0.01*

epithelial cells (P<0.01, Fig. 4A). FLOT1 siRNA was then transfected into Siha cells. RT-qPCR showed that FLOT1 siRNA significantly reduced its expression in Siha cells (P<0.01, Fig. 4B). Functionally, FLOT1 downregulation suppressed Siha cell proliferation (P<0.01, Fig. 4C). At the same time, FLOT1 siRNA was found to increase Bax expression and decrease Bcl-2 expression in Siha cells (P<0.01, Fig. 4D). Knockdown of FLOT1 also inhibited cell migration and invasion in Siha cells (P<0.01, Fig. 4E, 4F).

MiR-1294 regulates the occurrence of cervical cancer by interacting with FLOT1

The FLOT1 vector was then transfected into Siha cells with miR-1294 mimics to further confirm their interaction in cervical cancer. We found that the decreased expression of FLOT1 induced by miR-1294 mimics was restored by FLOT1 vector (Fig. 5A). More importantly, FLOT1 upregulation eliminated the inhibitory effect of miR-1294 on cell proliferation (Fig. 5B). In addition, the reversal effect of FLOT1 on Bcl-2/Bax expression was also detected in Siha cells with miR-1294 mimics (Fig. 5C). Besides, upregulation of FLOT1 restored the miR-1294-mediated inhibition of cell migration and invasion in Siha cells (Fig. 5 D, E).

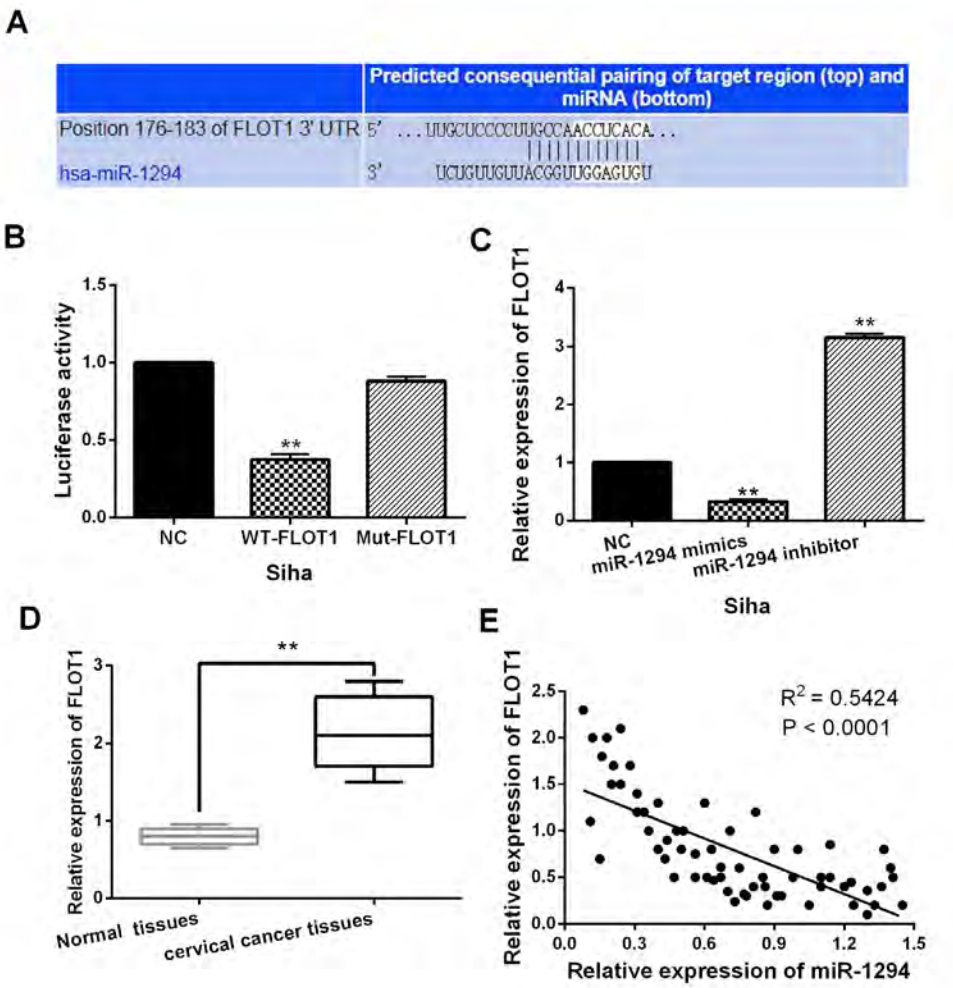


Fig. 3. *FLOT1 is a direct target of miR-1294. **A**) The binding sites between FLOT1 and miR-1294. **B**) Luciferase reporter assay (**C**) FLOT1 expression in Siha cells with miR-1294 mimics or inhibitor (**D**) FLOT1 expression in cervical cancer tissues and normal tissues. **E**) MiR-1294 was negatively correlated with FLOT1 expression in cervical cancer tissues. ** P <0.01.*

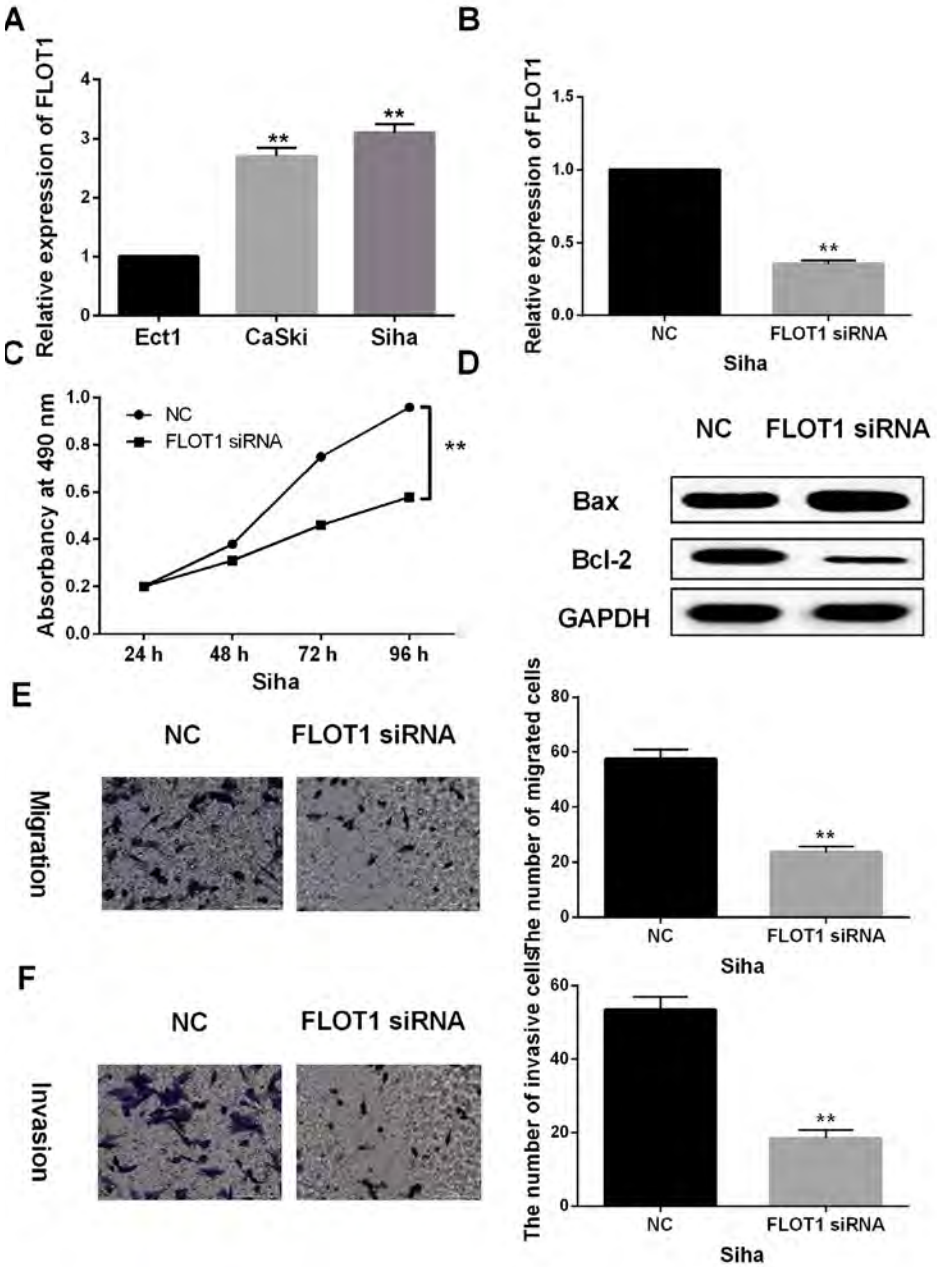


Fig. 4. *Knockdown of FLOT1 impeded the progression of cervical cancer.* ***A)*** *FLOT1 expression in CaSki, Siha and Ect1 cells* ***(B)*** *FLOT1 expression in Siha cells with FLOT1 siRNA.* ***C)*** *Cell proliferation in Siha cells with FLOT1 siRNA* ***(D)*** *FLOT1 regulated protein expressions of Bax and Bcl-2 in Siha cells.* ***E, F)*** *Cell migration and invasion in Siha cells with FLOT1 siRNA ** P < 0.01.*

MiR-1294 regulates EMT and β-catenin expression in cervical cancer cells

To further explain the effect of miR-1294 on the viability and metastasis of cervical cancer cells, how miR-1294 regulates EMT (N-cadherin, Vimentin, E-cadherin) and Wnt/β-catenin pathway (β-catenin, p-β-catenin) was investigated in Siha cells. MiR-1294 mimics were found to enhance E-cadherin expression and inhibit N-cadherin and vimentin expression (Fig. 6). MiR-1294 inhibitor had the opposite effect on these genes (Fig. 6). In addition, miR-1294 overexpression suppressed p-β-

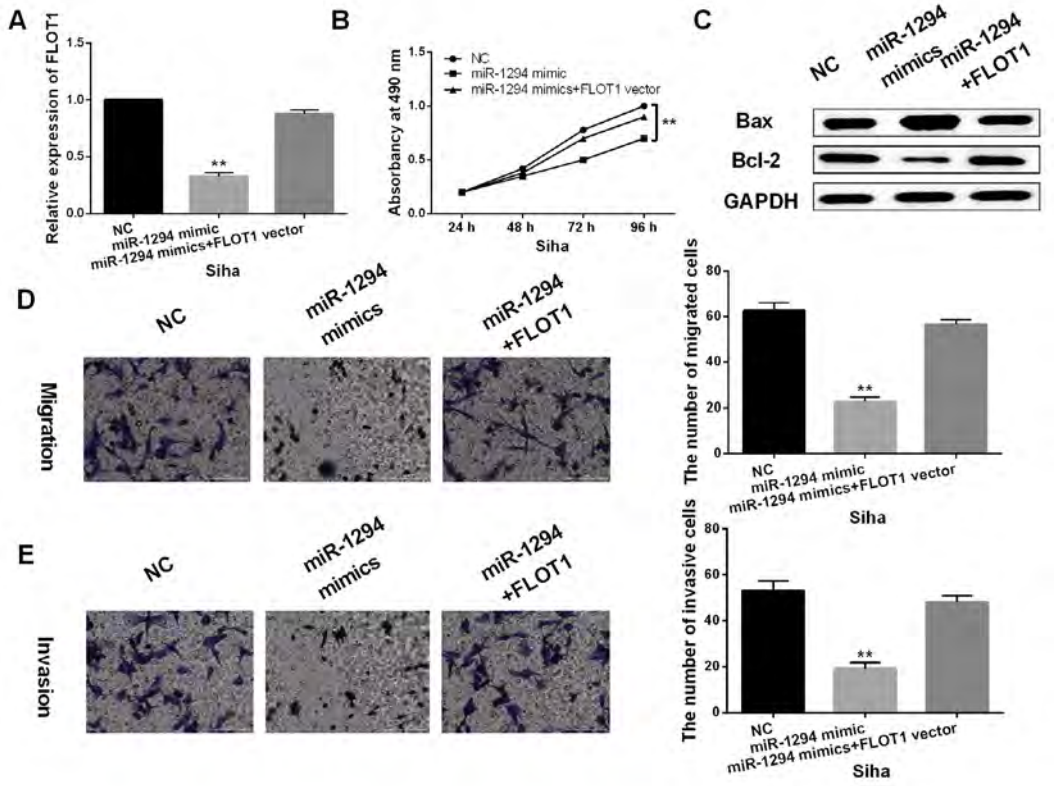


Fig. 5. *MiR-1294 regulates the occurrence of cervical cancer by interacting with FLOT1. **A**) FLOT1 expression in Siha cells containing miR-1294 mimics and FLOT1 vector. **B**) Cell proliferation in Siha cells containing miR-1294 mimics and FLOT1 vector (**C**) Bax and Bcl-2 in Siha cells containing miR-1294 mimics and FLOT1 vector (D, E) Cell migration and invasion in Siha cells containing miR-1294 mimics and FLOT1 vector ** P < 0.01.*

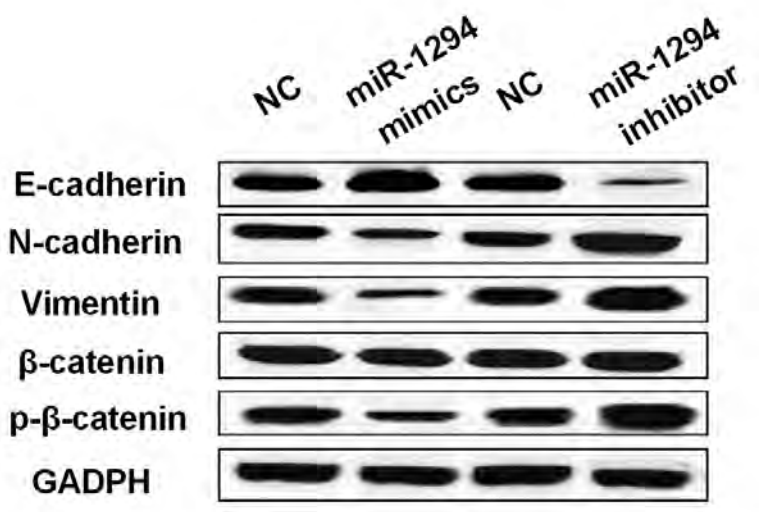


Fig. 6. *MiR-1294 regulates EMT and β-catenin expression in cervical cancer cells. MiR-1294 regulated expressions of E-cadherin, N-cadherin, Vimentin, β-catenin, p-β-catenin in Siha cells.*

catenin expression, while miR-1294 downregulation promoted p-β-catenin expression in Siha cells (Fig. 6). However, miR-1294 had little effect on β-catenin expression in Siha cells (Fig. 6).

DISCUSSION

Many studies have shown that dysregulation of miRNAs and mRNAs can regulate a variety of biological processes to participate in the carcinogenesis of cervical cancer. For example, miR-214 was found to down-regulate MKK3 and suppress the malignant phenotype of cervical cancer cells (14), and miR-449a was downregulated and inhibited cell proliferation, migration, and invasion (15). In this study, miR-1294 expression was also reduced. It was found that overexpression of miR-1294 restrained the viability, migration and invasion of cervical cancer cells. In addition, miR-1294 was also involved in the development of cervical cancer by blocking EMT and inhibiting β-catenin expression. β-catenin is an important regulator in the Wnt pathway. The Wnt/β-catenin pathway has been reported to be involved in cervical cancer (16). EMT is also an important biological process that regulates cervical cancer cell metastasis (17). To our knowledge, the inhibitory effect of miR-1294 on EMT and Wnt/β-catenin pathway is first reported in cervical cancer.

Consistent with our results, miR-1294 was also downregulated in gliomas and esophageal cancer (18, 19). Functionally, miR-1294 was found to act as a tumor suppressor in clear cell renal cell carcinoma by inhibiting cell proliferation and invasion (20). In this study, miR-1294 not only suppressed cell proliferation and invasion in cervical cancer, but also inhibited cell migration. Not only that, we also found that miR-1294 may regulate the cell cycle and apoptosis by regulating Bax/Bcl-2. It has been reported that overexpression of miR-1294 inhibited cell proliferation and cell cycle progression in epithelial ovarian cancer (21). These results indicate that miR-1294 acts as a tumor suppressor in the progression of cervical cancer.

In addition, miR-1294 has been reported to inhibit glioma progression by directly targeting TPX2 (9). Our findings are consistent with the above study, suggesting that the inhibitory effect of miR-1294 on cell growth and metastasis was achieved by regulating FLOT1 in cervical cancer. Additionally, upregulation of FLOT1 was foundKnockdown of FLOT1 suppressed cell proliferation, migration, and invasion in cervical cancer. Similar to our results, FLOT1 was also upregulated in bladder cancer and renal cell carcinoma (22, 23), and knockdown of FLOT1 has been reported to inhibit cell proliferation and tumorigenicity in breast cancer (24). These results demonstrate that FLOT1 functions as an oncogene in cervical cancer.

In summary, downregulation of miR-1294 and upregulation of FLOT1 were found in cervical cancer. Functionally, overexpression of miR-1294 or downregulation of FLOT1 inhibits the viability and metastasis of cervical cancer cells. Importantly, miR-1294 exerts a tumor suppressive effect on cervical cancer by downregulating FLOT1.

REFERENCES

1. Di J, Rutherford S, Chu C. Review of the Cervical Cancer Burden and Population-Based Cervical Cancer Screening in China. Asian Pac J Cancer Prev 2015; 16:7401-07.
2. Chen W, Zheng R, Baade PD, et al. Cancer statistics in China, 2015. CA Cancer J Clin 2016; 66:115-32.
3. Banister CE, Liu C, Pirisi L, Creek KE, Buckhaults PJ. Identification and characterization of HPV-independent cervical cancers. Oncotarget 2017; 8:13375-86.
4. Wright JD, Huang Y, Ananth CV, et al. Influence of treatment center and hospital volume on survival for locally advanced cervical cancer. Gynecol Oncol 2015; 139:506-12.
5. Zhu L, Tu H, Liang Y, Tang D. MiR-218 produces anti-tumor effects on cervical cancer cells in vitro. World J Surg Oncol 2018; 16:204.
6. Li S, Yang F, Wang M, Cao W, Yang Z. miR-378 functions as an onco-miRNA by targeting the ST7L/Wnt/beta-catenin pathway in cervical cancer. Int J Mol Med 2017; 40:1047-56.
7. Wang Z, Yan J, Zou T, Gao H. MicroRNA-1294

inhibited oral squamous cell carcinoma growth by targeting c-Myc. Oncol Lett 2018; 16:2243-50.
8. Zhang ZF, Li GR, Cao CN, et al. MicroRNA-1294 targets HOXA9 and has a tumor suppressive role in osteosarcoma. Eur Rev Med Pharmacol Sci 2018; 22:8582-88.
9. Chen H, Liu L, Li X, Shi Y, Liu N. MicroRNA-1294 inhibits the proliferation and enhances the chemosensitivity of glioma to temozolomide via the direct targeting of TPX2. Am J Cancer Res 2018; 8:291-301.
10. Zhang PF, Zeng GQ, Hu R, et al. Identification of flotillin-1 as a novel biomarker for lymph node metastasis and prognosis of lung adenocarcinoma by quantitative plasma membrane proteome analysis. J Proteomics 2012; 77:202-14.
11. Song L, Gong H, Lin C, et al. Flotillin-1 promotes tumor necrosis factor-alpha receptor signaling and activation of NF-kappaB in esophageal squamous cell carcinoma cells. Gastroenterology 2012; 143:995-1005 e1012.
12. Xiong P, Xiao LY, Yang R, et al. Flotillin-1 promotes cell growth and metastasis in oral squamous cell carcinoma. Neoplasma 2013; 60:395-405.
13. Yang FQ, Zhang HM, Chen SJ, Yan Y, Zheng JH. MiR-506 is down-regulated in clear cell renal cell carcinoma and inhibits cell growth and metastasis via targeting FLOT1. PLoS One 2015; 10:e0120258.
14. Peng R, Cheng X, Zhang Y, Lu X, Hu Z. miR-214 down-regulates MKK3 and suppresses malignant phenotypes of cervical cancer cells. Gene 2020; 724:144-46.
15. Wang L, Zhao Y, Xiong W, et al. MicroRNA-449a Is Downregulated in Cervical Cancer and Inhibits Proliferation, Migration, and Invasion. Oncol Res Treat 2019; 42:564-71.
16. Ji X, Guo H, Yin S, Du H. miR-139-5p functions as a tumor suppressor in cervical cancer by targeting TCF4 and inhibiting Wnt/beta-catenin signaling. Onco Targets Ther 2019; 12:7739-48.
17. Miao H, Wang N, Shi LX, Wang Z, Song WB. Overexpression of mircoRNA-137 inhibits cervical cancer cell invasion, migration and epithelial-mesenchymal transition by suppressing the TGF-beta/smad pathway via binding to GREM1. Cancer Cell Int 2019; 19:147.
18. Wang J, Li J, Wang H, Lv L, Sun J. Overexpression of circ_0005198 sponges miR-1294 to regulate cell proliferation, apoptosis, migration, and invasion in glioma. J Cell Biochem 2019; 120:15538-45.
19. Zhang Z, Lin W, Gao L, et al. Hsa_circ_0004370 promotes esophageal cancer progression through miR-1294/LASP1 pathway. Biosci Rep 2019; 39.
20. Pan W, Pang LJ, Cai HL, et al. MiR-1294 acts as a tumor suppressor in clear cell renal cell carcinoma through targeting HOXA6. Eur Rev Med Pharmacol Sci 2019; 23:3719-25.
21. Guo TY, Xu HY, Chen WJ, Wu MX, Dai X. Downregulation of miR-1294 associates with prognosis and tumor progression in epithelial ovarian cancer. Eur Rev Med Pharmacol Sci 2018; 22:7646-52.
22. Liang Z, Wang X, Xu X, et al. MicroRNA-608 inhibits proliferation of bladder cancer via AKT/FOXO3a signaling pathway. Mol Cancer 2017; 16:96.
23. Xu X, Wu J, Li S, et al. Downregulation of microRNA-182-5p contributes to renal cell carcinoma proliferation via activating the AKT/FOXO3a signaling pathway. Mol Cancer 2014; 13:109.
24. Lin C, Wu Z, Lin X, et al. Knockdown of FLOT1 impairs cell proliferation and tumorigenicity in breast cancer through upregulation of FOXO3a. Clin Cancer Res 2011; 17:3089-99.

lncRNA NEAT1 AGGRAVATES CEREBRAL ISCHEMIA/REPERFUSION INJURY BY SPONGING miR-874-3p

B. LIU[1*], T. XU[1*] and Y. MENG[2]

[1]First Department of Neurology, The First Hospital of Zibo, Zibo, Shandong Province, China;
[2]Hemodialyses Room, The First Hospital of Zibo, Zibo, Shandong Province, China

Received January 18, 2020 – Accepted March 25, 2020

[*]These Authors contributed equally to the work

Many lncRNAs have been reported to affect cerebral ischemia/reperfusion (I/R) injury. The purpose of this study is to elucidate the role of lncRNA NEAT1 as well as the regulatory mechanism of lncRNA NEAT1/miR-874-3p in cerebral I/R injury. A cellular model of cerebral I/R injury was built. RT-qPCR was used to detect NEAT1 and miR-874-3p expression. Cell viability was detected by MTT assay. The expression of apoptosis-related proteins (Bcl-2 and Bax) was measured by Western blot analysis. The relationship between NEAT1 and miR-874-3p was confirmed by dual luciferase reporter assay. We found that LncRNA NEAT1 was upregulated in the PC12 cells treated by I/R and upregulation of lncRNA NEAT1 can aggravate I/R injury of PC12 cells. Additionally, lncRNA NEAT1 overexpression decreased cell viability and induced apoptosis in PC12 cells treated by I/R. Furthermore, miR-874-3p was confirmed to be a target of lncRNA NEAT1. mR-874-3p and NEAT1 expression are found to be reciprocally inhibited in PC12 cells. In summary, LncRNA NEAT1 aggravates cerebral I/R injury by suppressing miR-874-3p expression.

Stroke is the rupture or blockage of cerebral blood vessels for various reasons, causing a series of corresponding brain neurological dysfunctions. The biggest features of stroke are rapid onset, severe symptoms, high mortality and disability (1). Ischemic stroke is a disorder of the blood supply to the brain caused by various causes, resulting in ischemia and hypoxic necrosis of local brain tissue and is the most common type of stroke, accounting for about 70-80% (2). Ischemia-reperfusion (I/R) injury refers to the main factor that causes damage to tissues, not the ischemia itself, but the damage caused by excessive free radicals attacking the cells in this part of the tissue that regains the blood supply after the blood supply is restored (3). The occurrence and development of various diseases such as delayed neuronal necrosis, irreversible shock, myocardial infarction, acute organ failure and organ transplant rejection are related to I/R (4). Therefore, better understanding of the delicate mechanisms involved in cerebral I/R injury may provide novel treatment for ischemia stroke.

Long-non-coding RNAs (lncRNAs) have been demonstrated to play regulatory roles in various biological processes, such as cell proliferation, apoptosis, autophagy and angiogenesis (5). It is reported that the involvement of lncRNAs in ischemic stroke

Key words: NEAT1; cerebral ischemia; reperfusion injury; miR-874-3p

Corresponding Author:
Dr Tao Xu,
First Department of Neurology, The First Hospital of Zibo,
No. 4 E'meishan East Road, Boshan District, Zibo,
255200, Shandong Province, China
Tel.: +86 13305332190
e-mail: duanittx1796@163.com.

0393-974X (2020)
Copyright © by BIOLIFE, s.a.s.
This publication and/or article is for individual use only and may not be further reproduced without written permission from the copyright holder.
Unauthorized reproduction may result in financial and other penalties
DISCLOSURE: ALL AUTHORS REPORT NO CONFLICTS OF INTEREST RELEVANT TO THIS ARTICLE.

is increasing and is expected to become an important regulator in the pathogenesis of stroke. For example, lncRNA SNHG12 as a potent autophagy inducer exerted neuroprotective effects against cerebral I/R injury (6). YY1/lncRNA GAS5 complex aggravated cerebral I/R injury through enhancing neuronal glycolysis (7). LncRNA NEAT1 has been reported to be correlated with higher disease risk, worse disease condition and predict poor recurrence-free survival of acute ischemic stroke (8). Dong et al found that YY1-induced upregulation of lncRNA NEAT1 contributed to OGD/R injury-induced inflammatory response in cerebral microglial cells (9). These results indicate that lncRNA NEAT1 is involved in ischemic stroke. However, the regulatory mechanism of lncRNA NEAT1 in cerebral I/R injury remains largely unknown. Therefore, this study was designed to preliminarily elucidate the function of lncRNA NEAT1 in cerebral I/R injury.

In this study, miR-874-3p was predicted to be downstream target of lncRNA NEAT1. Many studies have shown that microRNAs (miRNAs) are important regulators in the pathogenesis of ischemic stroke. MiRNAs are involved in cerebral I/R injury by mediating cell proliferation, apoptosis, and oxidative stress (10). For instance, miR-199a-5p protected against cerebral I/R Injury by down-regulating DDR1 in rats (11). In addition, miR-298 exacerbated I/R injury following ischemic stroke by targeting Act1 (12). It has been reported that miR-874 was down-regulated in ischemia-reperfusion model of rat (13). MiR-874 inhibition targeting STAT3 can protect the heart from I/R injury by attenuating cardiomyocyte apoptosis in a mouse model (14). In particularly, upregulation of miR-874-3p has been demonstrated to decrease cerebral I/R injury by directly targeting BMF and BCL2L13 (15). However, the interaction between lncRNA NEAT1 and miR-874-3p has not been investigated in previous studies. Therefore, the functional mechanism of lncRNA NEAT1/miR-874-3p as well as the role of lncRNA NEAT1 was investigated in cerebral I/R injury

MATERIALS AND METHODS

Cell culture and transfection

PC12 cells (ATCC, Manassas, VA, USA) were cultured in Dulbecco's Modified Eagle Medium (DMEM) with 10% fetal bovine serum (FBS) in a humid incubator with5% CO_2 at 37°C.

NEAT1 vector and siRNA or miR-874-3p mimics and inhibitor were purchased from GenePharma (Shanghai, China). They were transfected into PC12 cells based on experimental requirement. The I/R treated PC12 cells without transfection were used as the control group.

OGD/R model

PC12 cells were incubated in hypoxic conditions (3% O2/5% CO2/92% N2) at 37°C for 3 h. After that, the cells were transferred to normal culture medium and maintained under normoxic conditions (5% CO_2) at 37°C for 24 h.

RT-qPCR

TRIzol reagent (Invitrogen, USA) was used to extract total RNA in PC12 cells. First, cDNA was obtained using the microRNA reverse transcription kit (Takara, Dalian, China). Then, RT-qPCR was performed using SYBR Premix Ex TaqTM (Takara, Dalian, China). Data were normalized to GAPDH. The expression of NEAT1 and miR-874-3p was quantified by the $2^{-\square\square cq}$ method.

ROS, LDH, SOD and MDA levels

The commercial kits for determining lactate dehydrogenase (LDH), superoxide dismutase (SOD), malondialdelyde (MDA) and reactive oxygen species (ROS) were purchased from Jining Shiye (Shanghai, China). The ROS, LDH, SOD and MDA level were used to assess injury degree of PC12 cells.

Cell viability

Cell proliferation was evaluated using MTT assay. PC12 cells (2×10^3cells/well) were seeded in 96-well plates. Next, the cells were incubated with 15 μL/well MTT solution (5 mg/mL, Sigma) at 37°C for 4 h. The absorbance at 490 nm was detected by a BioRad microplate reader (Bio-Rad, Hercules, CA, United States).

Dual luciferase reporter assay

The pmirGLO luciferase reporter vectors (Promega, USA) containing Wt-NEAT1 or Mut-NEAT1 and miR-874-3p mimics were transfected into PC12 cells. After 48 h, dual luciferase assay system (Promega, USA) was used to detect luciferase activities.

Western blot analysis

Protein sample was lysed using RIPA buffer (Beyotime, Shanghai, China). BCA protein assay kit (Pierce, Rockford, IL, USA) was used to calculate the total protein concentrations. Next, protein samples were separated by 10% SDS-PAGE and transferred to PVDF membranes. After blocking with 5% non-fat milk for 2 h, membranes were incubated with Bax and Bcl-2 and GAPDH primary antibodies (Abcam, Shanghai, China) overnight at 4°C. After washing, protein samples were incubated with horseradish peroxidase-conjugated secondary antibodies (Abcam, USA) for 2 h. Finally, ECL kit (Beyotime) was used to assess protein bands.

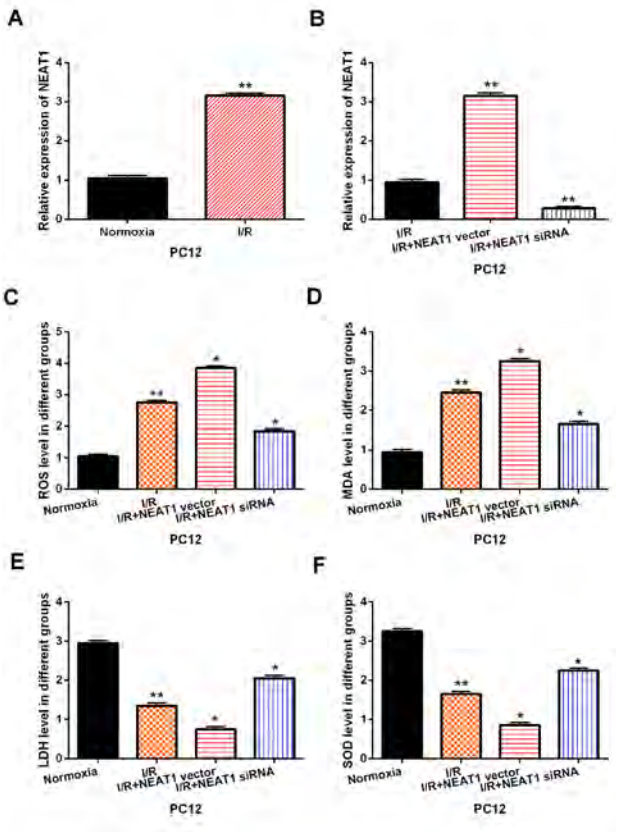


Fig. 1. *Upregulation of lncRNA NEAT1 exacerbates cerebral I/R injury in PC12 cells. **A)** LncRNA NEAT1 expression in I/R treated PC12 cells and Normoxia group **(B)** LncRNA NEAT1 expression in I/R treated PC12 cells with NEAT1 vector or siRNA (**C-F**). The levels of ROS, LDH, MDA and SOD in Normoxia group, I/R group, I/R+NEAT1 vector group and I/R+NEAT1 siRNA group *P < 0.05, **P < 0.01*

Statistical analysis

Data are shown as analyzed mean ± SD. Differences between multiple groups were analyzed using one-way analysis of variance with Tukey's post hoc test and Student's t-test in SPSS 19.0. Graphs are made by Graphpad Prism 6. $P < 0.05$ indicates a statistically significant difference.

RESULTS

Upregulation of lncRNA NEAT1 exacerbates cerebral I/R injury in PC12 cells

First, the expression of lncRNA NEAT1 was detected in PC12 cells treated with I/R. RT-qPCR showed that lncRNA NEAT1 expression in PC12 cells treated with I/R was higher than that in Normoxia group (Fig. 1A). To explore the effect of lncRNA NEAT1 on I/R injury, NEAT1 vector and siRNA were transfected into I/R treated PC12 cells. LncRNA NEAT1 vector significantly enhanced its expression, while NEAT1 siRNA decreased its expression in I/R treated PC12 cells (Fig. 1B). In addition, we found that ROS and MDA level was increased in I/R treated PC12 cells (I/R group) compared to Normoxia group. Meanwhile, upregulation of NEAT1 enhanced ROS and MDA level in I/R treated PC12 cells, while downregulation of NEAT1 reduced ROS and MDA level in I/R treated PC12 cells. But ROS and MDA level in I/R treated PC12 cells with NEAT1 siRNA is still higher than that in Normoxia group (Fig. 1 C, D). Compared with the Normoxia group, the levels of LDH and SOD were decreased in I/R group. LDH and SOD levels were lower in I/R + NEAT1 vector group than that in I/R group. And LDH and SOD levels were increased in I/R + NEAT1 siRNA group but could not return to the levels in Normoxia group (Fig. 1 E, .F). These results imply that lncRNA NEAT1 upregulation can exacerbate the oxidative damage of I/R treated PC12 cells.

LncRNA NEAT1 inhibits cell viability and induced apoptosis in I/R treated PC12 cells

Next, we investigated how lncRNA NEAT1 regulates cell viability in I/R treated PC12 cells. We found that cell proliferation was decreased in PC12 cells treated with I/R compared to Normoxia

group. And NEAT1 upregulation inhibited cell proliferation in I/R treated PC12 cells, while NEAT1 downregulation promote cell proliferation in I/R treated PC12 cells. However, the proliferation of PC12 cells in I/R + NEAT1 siRNA group is still lower than that in Normoxia group (Fig. 2A). Additionally, the expression of apoptosis-related protein (Bcl-2/Bax) was detected by Western blot analysis. Compared with the Normoxia group, increased expression of Bax and decreased expression of Bcl-2 were identified in I/R group. Compared with I/R group, NEAT1 upregulation enhanced the expression of Bax and suppressed Bcl-2 expression in I/R treated PC12 cells. In turn, knockdown of NEAT1 showed opposite effect on Bcl-2 and Bax expression. And the expression of Bax and Bcl-2 in I/R + NEAT1 siRNA group tended to the levels in Normoxia group but could not reach the levels in Normoxia group (Fig. 2B). Therefore, upregulation of lncRNA NEAT1 can restrain cell viability and induce apoptosis in I/R treated PC12 cells.

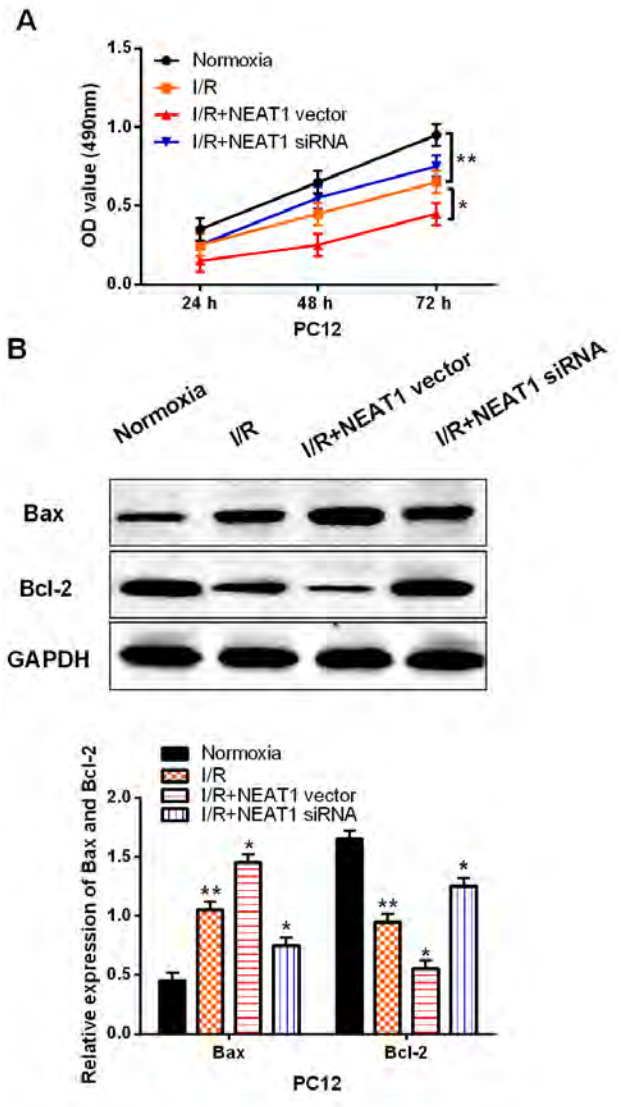


Fig. 2. *LncRNA NEAT1 inhibits cell viability and induced apoptosis in I/R treated PC12 cells.* ***A****) PC12 cell proliferation was measured in Normoxia group, I/R group, I/R+NEAT1 vector group and I/R+NEAT1 siRNA group.* ***B****) The apoptosis-related proteins (Bcl-2 and Bax) were detected in Normoxia group, I/R group, I/R+NEAT1 vector group and I/R+NEAT1 siRNA group *P < 0.05, ** P <0.01*

MiR-874-3p is a target of lncRNA NEAT1.

The starBase database (http://starbase.sysu.edu.cn) predicts that lncRNA NEAT1 has a binding site with miR-874-3p (Fig. 3A). Then, dual-luciferase reporter assay was performed to confirm their relationship. We found that miR-874-3p mimics reduced the luciferase activity of wt-NEAT1, but had little effect on mut-NEAT1 (Fig. 3B). Thus, miR-874-3p is a direct target of lncRNA NEAT1. In PC12 cells, miR-874-3p expression was found to be reduced by NEAT1 vector and promoted by NEAT1 siRNA (Fig. 3C). Furthermore, miR-874-3p mimics decreased NEAT1 expression, whereas miR-874-3p inhibitor increased NEAT1 expression in PC12 cells (Fig.3D). The results reveal that mR-874-3p and NEAT1 expression are reciprocally inhibited in PC12 cells.

Upregulation of lncRNA NEAT1 aggravates the damage of I/R treated PC12 cells by regulating miR-874-3p

The expression of miR-874-3p was measured in I/R treated PC12 cells. Compared with the Normoxia group, miR-874-3p was downregulated in I/R group. After transfection of NEAT1 vector, miR-874-3p expression was decreased compared to I/R group. And NEAT1 siRNA in I/R treated PC12 cells promotes miR-874-3p expression compared to I/R group, but miR-874-3p expression still lower than that in Normoxia group (Fig. 4A). Functionally, MTT assay showed that miR-874-3p overexpression

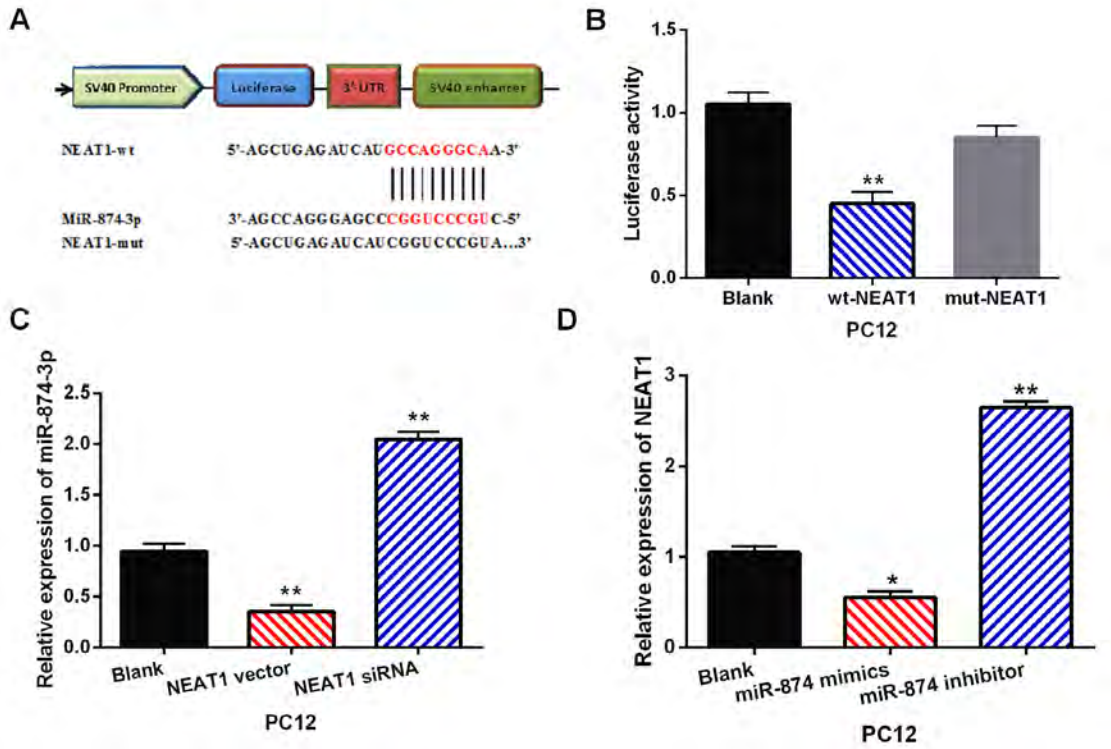


Fig. 3. *MiR-874-3p is a target of lncRNA NEAT1.* ***A****) The binding sites between NEAT1 and miR-874-3p.* ***B****) Luciferase reporter assay (****C****) MiR-874-3p expression regulated by NEAT1 vector or siRNA (****D****) NEAT1 expression in PC12 cells with miR-874-3p mimics or inhibitor *P < 0.05, ** P <0.01.*

in I/R treated PC12 cells facilitated cell viability compared with I/R group. And the increased cell proliferation induced by miR-874-3p mimics was weakened by NEAT1 vector in I/R treated PC12 cells (Fig. 4B). In addition, Western blot analysis suggested that miR-874-3p overexpression in I/R treated PC12 cells reduced Bax expression and promoted Bcl-2 expression compared to H/R group. But NEAT1 upregulation impaired the effect of miR-874-3p on Bcl-2 and Bax expression in I/R treated PC12 cells. NEAT1 upregulation increased Bax expression decreased Bcl-2 expression compared with I/R + miR-874-3p mimics group (Fig. 4C). Based on these results, we consider that miR-874-3p overexpression can decrease cerebral I/R injury. And lncRNA NEAT1 aggravates cerebral I/R injury by inhibiting miR-874-3p expression.

DISCUSSION

In recent years, more and more lncRNAs have been reported to patriciate in cerebral I/R injury. For example, knockdown of lncRNA Gm11974 alleviated cerebral I/R injury through mediating miR-766-3p/NR3C2 axis (16). Wei et al. proposed that lncRNA AK038897 aggravated cerebral I/R injury via acting as a ceRNA for miR-26a-5p (17). In this study, we also found that lncRNA NEAT1 promoted cerebral I/R injury by inhibiting miR-874-3p expression. Upregulation of lncRNA NEAT1 has been identified in acute myeloid leukemia and pancreatic ductal adenocarcinoma (18, 19). Functionally, lncRNA NEAT1 was found to promote hepatocellular carcinoma cell proliferation and reduced apoptosis through the regulation of Let-7b-

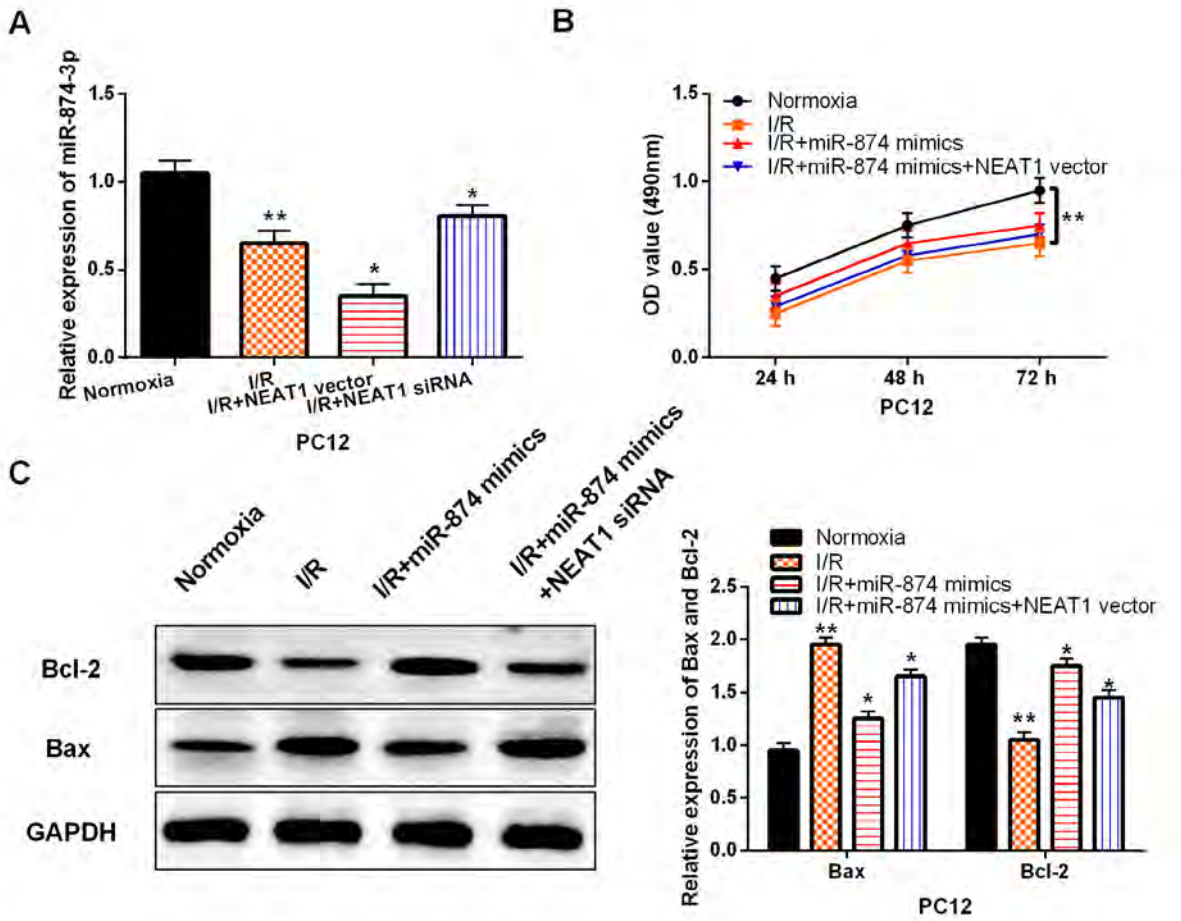


Fig. 4. *Upregulation of lncRNA NEAT1 aggravates the damage of I/R treated PC12 cells by regulating miR-874-3p.* ***A)*** *MiR-874-3p expression in Normoxia group, I/R group, I/R+NEAT1 vector group and I/R+NEAT1 siRNA group* ***(B)*** *PC12 cell proliferation was measured in Normoxia group, I/R group, I/R+miR-874-3p mimics group and I/R+miR-874-3p mimics+NEAT1 vector group* ***(C)****. The apoptosis-related proteins (Bcl-2 and Bax) were detected in Normoxia group, I/R group, I/R+miR-874-3p mimics group and I/R+miR-874-3p mimics+NEAT1 vector group *P < 0.05,** P < 0.01*

IGF-1R axis (20). Besides that, it has been reported that lncRNA NEAT1 sponging miR-495-3p enhanced myocardial I/R injury via MAPK6 activation (21). Downregulation of lncRNA NEAT1 promoted cell proliferation and inhibited apoptosis in myocardial I/R injury (22). These studies indicate that lncRNA NEAT1 is an important regulator in I/R injury.

Here, upregulation of lncRNA NEAT1 was found in PC12 cells treated by I/R. Similar to our results, lncRNA NEAT1 expression was found to be elevated in patients with acute ischemic stroke and it had a good predictive value for acute ischemic stroke risk (8). Functionally, we found that upregulation of lncRNA NEAT1 exacerbated the oxidative damage of I/R treated PC12 cells. And lncRNA NEAT1 overexpression decreased cell viability and induced apoptosis in I/R treated PC12 cells. The oxidative stress injury and apoptosis are important in the process of I/R injury (23). Han et al. reported that NEAT1 contributed to the OGD/R injury and neuroinflammation damage in microglial cells (9), which is consistent with our study. Further, miR-874-3p was confirmed to be a target of lncRNA NEAT1. And reciprocally inhibition between mR-874-3p and

NEAT1 expression were detected in PC12 cells.

More importantly, miR-874-3p was downregulated in I/R group. And miR-874-3p overexpression facilitated cell viability and reduced apoptosis in I/R treated PC12 cells. Also, many miRNAs have been demonstrated to regulate the development of cerebral I/R injury, which is similar to our results. For instance, miR-496 expression was significantly deceased in rats with cerebral I/R, and upregulation of miR-496 decreased cerebral I/R injury (24). In addition, abnormal expression of miR-874-3p has been found to participate in acute myocardial infarction, renal injury and intestinal ischemic injury (25-27). In particular, upregulation of miR-874-3p has been revealed to decrease cerebral I/R injury (15). These results imply that miR-874-3p plays a protective effect against cerebral I/R injury. Besides, lncRNA NEAT1 was found to weaken the protective effect of miR-874-3p on cerebral I/R injury, indicating that lncRNA NEAT1 can exacerbate cerebral I/R injury.

In summary, lncRNA NEAT1 aggravates the cerebral I/R injury by downregulating miR-874-3p. Furthermore, miR-874-3p overexpression can improve the cerebral I/R injury. Our study may provide a novel idea for the treatment of cerebral I/R injury. However, this study mainly depends on the cell experiment. Further *in vivo* studies are still needed to verify the present conclusion.

REFERENCES

1. Tobin MK, Bonds JA, Minshall RD, Pelligrino DA, Testai FD, Lazarov O. Neurogenesis and inflammation after ischemic stroke: what is known and where we go from here. J Cereb Blood Flow Metab 2014; 34:1573-84.
2. Benakis C, Garcia-Bonilla L, Iadecola C, Anrather J. The role of microglia and myeloid immune cells in acute cerebral ischemia. Front Cell Neurosci 2014; 8:461.
3. Miller JB, Merck LH, Wira CR, et al. The advanced reperfusion era: implications for emergency systems of ischemic stroke care. Ann Emerg Med. 2017; 69:192-201.
4. Matsuki T, Toyoda K. The future perspective of acute thrombolytic therapy for acute ischemic stroke. Nihon Rinsho 2016; 74:613-20.
5. Chen LL. Linking long noncoding RNA localization and function. Trends Biochem Sci 2016; 41:761-72.
6. Yao X, Yao R, Huang F, Yi J. LncRNA SNHG12 as a potent autophagy inducer exerts neuroprotective effects against cerebral ischemia/reperfusion injury. Biochem Biophys Res Commun 2019; 514:490-96.
7. Zhang XC, Gu AP, Zheng CY, et al. YY1/LncRNA GAS5 complex aggravates cerebral ischemia/reperfusion injury through enhancing neuronal glycolysis. Neuropharmacology 2019; 158:107682.
8. Li P, Duan S, Fu A. Long noncoding RNA NEAT1 correlates with higher disease risk, worse disease condition, decreased miR-124 and miR-125a and predicts poor recurrence-free survival of acute ischemic stroke. J Clin Lab Anal 2019; e23056.
9. Han D, Zhou Y. YY1-induced upregulation of lncRNA NEAT1 contributes to OGD/R injury-induced inflammatory response in cerebral microglial cells via Wnt/beta-catenin signaling pathway. In Vitro Cell Dev Biol Anim 2019; 55:501-11.
10. Volny O, Kasickova L, Coufalova D, Cimflova P, Novak J. microRNAs in Cerebrovascular Disease. Adv Exp Med Biol 2015; 888:155-95.
11. Li M, Luan L, Liu Q, Liu Y, Lan X, Li Z, Liu W. MiRNA-199a-5p Protects against cerebral ischemic injury by down-regulating DDR1 in rats. World Neurosurg 2019; 131:e486-e494.
12. Sun H, Zhong D, Wang C, Sun Y, Zhao J, Li G. MiR-298 Exacerbates ischemia/reperfusion injury following ischemic stroke by targeting Act1. Cell Physiol Biochem 2018; 48:528-39.
13. Wang C, Pan Y, Cheng B, Chen J, Bai B. Identification of conserved and novel microRNAs in cerebral ischemia-reperfusion injury of rat using deep sequencing. J Mol Neurosci 2014; 54:671-83.
14. Chen PJ, Shang AQ, Yang JP, Wang WW. microRNA-874 inhibition targeting STAT3 protects the heart from ischemia-reperfusion injury by attenuating cardiomyocyte apoptosis in a mouse model. J Cell Physiol 2019; 234:6182-93.
15. Jiang D, Sun X, Wang S, Man H. Upregulation of miR-874-3p decreases cerebral ischemia/reperfusion injury by directly targeting BMF and BCL2L13. Biomed Pharmacother 2019; 117:108941.
16. Cai J, Shangguan S, Li G, et al. Knockdown of

lncRNA Gm11974 protect against cerebral ischemic reperfusion through miR-766-3p/NR3C2 axis. Artif Cells Nanomed Biotechnol 2019; 47:3847-53.
17. Wei R, Zhang L, Hu W, Wu J, Zhang W. Long non-coding RNA AK038897 aggravates cerebral ischemia/reperfusion injury via acting as a ceRNA for miR-26a-5p to target DAPK1. Exp Neurol 2019; 314:100-110.
18. Zhao C, Wang S, Zhao Y, Du F, Wang W, Lv P, Qi L. Long noncoding RNA NEAT1 modulates cell proliferation and apoptosis by regulating miR-23a-3p/SMC1A in acute myeloid leukemia. J Cell Physiol 2019; 234:6161-72.
19. Luo Z, Yi ZJ, Ou ZL, et al. RELA/NEAT1/miR-302a-3p/RELA feedback loop modulates pancreatic ductal adenocarcinoma cell proliferation and migration. J Cell Physiol 2019; 234:3583-97.
20. Liu Q, Shi H, Yang J, Jiang N. Long non-coding RNA NEAT1 promoted hepatocellular carcinoma cell proliferation and reduced apoptosis through the regulation of Let-7b-IGF-1R Axis. Onco Targets Ther 2019; 12:10401-13.
21. Luo M, Sun Q, Zhao H, Tao J, Yan D. Long noncoding RNA NEAT1 sponges miR-495-3p to enhance myocardial ischemia-reperfusion injury via MAPK6 activation. J Cell Physiol 2020; 235:105-13.
22. Ren L, Chen S, Liu W, Hou P, Sun W, Yan H. Downregulation of long non-coding RNA nuclear enriched abundant transcript 1 promotes cell proliferation and inhibits cell apoptosis by targeting miR-193a in myocardial ischemia/reperfusion injury. BMC Cardiovasc Disord 2019; 19:192.
23. Shalavadi MH, Chandrashekhar VM, Muchchandi IS. Neuroprotective effect of Convolvulus pluricaulis Choisy in oxidative stress model of cerebral ischemia reperfusion injury and assessment of MAP2 in rats. J Ethnopharmacol 2020; 249:112393.
24. Yao X, Yao R, Yi J, Huang F. Upregulation of miR-496 decreases cerebral ischemia/reperfusion injury by negatively regulating BCL2L14. Neurosci Lett 2019; 696:197-205.
25. Yan Y, Song X, Li Z, et al. Elevated levels of granzyme B correlated with miR-874-3p downregulation in patients with acute myocardial infarction. Biomark Med 2017; 11:761-67.
26. Yao T, Zha D, Gao P, Shui H, Wu X. MiR-874 alleviates renal injury and inflammatory response in diabetic nephropathy through targeting toll-like receptor-4. J Cell Physiol 2018; 234:871-79.
27. Zhi X, Tao J, Li Z, et al. MiR-874 promotes intestinal barrier dysfunction through targeting AQP3 following intestinal ischemic injury. FEBS Lett 2014; 588:757-763.

LINC00473 PROMOTES LUNG ADENOCARCINOMA PROGRESSION BY REGULATING miR-1294/ROBO1 AXIS

S. WANG[1], X. WANG[2] and SL. XU[3]

[1]The Fifth Department of Oncology, The Fourth People's Hospital of Zibo, Zibo, Shandong Province, China; [2]Nursing Department, Zibo High tech Zone People's Hospital, Zibo, Shandong Province, China; [3]Department of Oncology, Zibo Central Hospital, Zibo, Shandong Province, China

Received February 6, 2020 – Accepted March 26, 2020

Long noncoding RNA (lncRNA) LINC00473 has been reported to be involved in the regulation of several human cancers. However, the regulatory mechanism of LINC00473 is still unknown in lung adenocarcinoma. In this study, RT-qPCR was used to measure the expression of LINC00473, miR-1294 and ROBO1. The functional mechanism of the LINC00473/miR-1294/ROBO1 pathway was investigated by CCK-8, Transwell and dual luciferase reporter assays. The results showed that LINC00473 was up-regulated and miR-1294 was down-regulated in lung adenocarcinoma tissues and cells. LINC00473 can bind to miR-1294, and reciprocal inhibition between LINC00473 and miR-1294 expression was identified in lung adenocarcinoma. Functionally, LINC00473 promoted cell proliferation and motility in lung adenocarcinoma by downregulating miR-1294. In addition, miR-1294 directly targets ROBO1. ROBO1 served as an oncogene in lung adenocarcinoma. In particular, LINC00473 promoted the progression of lung adenocarcinoma by upregulating ROBO1. In conclusion, LINC00473 acts as a tumor promoter in lung adenocarcinoma by regulating the miR-1294/ROBO1 axis.

Lung adenocarcinoma is a non-small cell lung cancer different from squamous cell carcinoma and small cell lung cancer. Compared with squamous cell carcinoma, lung adenocarcinoma is more prone to distant metastasis and lymphatic metastasis (1). The prognosis of lung adenocarcinoma patients is relatively poor, and the effect of treatment depends on its stage. Patients with early-stage can undergo surgical resection and have a good therapeutic effect (2). However, most patients have reached advanced stages after being diagnosed and have lost the opportunity for surgery. With the increase of treatment methods, the survival rate of advanced stage patients has improved (3). Recently, targeted therapy has become a hotspot in the treatment of lung adenocarcinoma (4). However, effective therapeutic targets are still lacking, and further exploration is needed.

Long noncoding RNAs (lncRNAs) are transcripts larger than 200 bp. An increasing number of studies have shown that lncRNAs act as competing endogenous RNAs (ceRNAs) and compete with downstream target genes of microRNAs (miRNAs) (5). The important roles of lncRNAs were also found in lung adenocarcinoma. For example, LINC00483 promoted the progression of lung adenocarcinoma by sponging miR-204-3p (6). In addition, LINC00472

Key words: LINC00473; lung adenocarcinoma; miR-1294; ROBO1

Corresponding Author:
Dr Shanlin Xu,
Department of Oncology,
Zibo Central Hospital, No.54 Gongqingtuan West Road,
Zhangdian District, Zibo, 255036, Shandong Province, China
Tel.: +86 13305332190.
e-mail: panzhiwen203989048@163.com

0393-974X (2020)
Copyright © by BIOLIFE, s.a.s.
This publication and/or article is for individual use only and may not be further reproduced without written permission from the copyright holder.
Unauthorized reproduction may result in financial and other penalties
DISCLOSURE: ALL AUTHORS REPORT NO CONFLICTS OF INTEREST RELEVANT TO THIS ARTICLE.

inhibited cell proliferation and promoted apoptosis of lung adenocarcinoma cells by regulating miR-24-3p/DEDD (7). However, the function of LINC00473 has not been investigated in lung adenocarcinoma. Moreover, different regulatory mechanisms of LINC00473 have been discovered in other cancers. In particular, LINC00473 promoted the proliferation and invasion of glioma cells by damaging the miR-637/CDK6 axis (8). The target of miR-34a, LINC00473 promoted the occurrence of cervical cancer by inhibiting ILF2 degradation (9). Because the role of LINC00473 in lung adenocarcinoma is elusive, this study aims to explain its functional mechanism.

Here, miR-1294 was found to have a binding site with LINC00473. The dysregulation of miR-1294 has been found in human cancers and its downregulation has been found in oral squamous cell carcinoma and gastric cancer (10, 11). miR-1294 alleviated epithelial-mesenchymal transition (EMT) by inhibiting FOXK1 in gastric cancer (12), and inhibited the proliferation of glioma cells by directly targeting TPX2 (13). In addition, downstream targets of miR-1294 were investigated in this study. TargetScan predicts that roundabout guidance receptor 1 (ROBO1) is a target of miR-1294. ROBO1 has been reported to be involved in tumorigenesis. and acted a tumor suppressor in prostate cancer and was a key molecular barrier for localized tumor cells to obtain an aggressive phenotype (14). ROBO1 was also found to have carcinogenic effects in hepatocellular carcinoma and gastric cancer (15, 16). The results suggest that the role of ROBO1 depends on the type of cancer. In addition, miR-218 suppresses EMT by targeting ROBO1 in lung adenocarcinoma cells (17). However, the interaction between miR-1294 and ROBO1 has not yet been demonstrated in lung adenocarcinoma. Therefore, the functional mechanism of miR-1294/ROBO1 in lung adenocarcinoma was investigated. This study also illustrated the relationship between LINC00473 and miR-1294/ROBO1 axis.

MATERIALS AND METHODS

Clinical tissues, cell culture and transfection

A total of 66 lung adenocarcinoma tissues and corresponding normal tissues were collected from patients with lung adenocarcinoma in the Zibo Central Hospital. Prior to the study, participants provided written informed consent. No patient with lung adenocarcinoma had been treated before diagnosis. The tissues were frozen in liquid nitrogen and stored at −80°C. This study was approved by the Institutional Ethics Committee of Zibo Central Hospital.

Normal lung epithelial cells BEAS-2B and A549, H1975 lung adenocarcinoma cell lines were purchased from the American type culture collection (ATCC, Manassas, VA, USA). These cells were cultured at 37°C in DMEM medium (HyClone), containing 10% FBS (Gibco) with 5% CO_2.

LINC00473 vector and siRNA, miR-1294 mimics and inhibitor or ROBO1 siRNA were purchased from GenePharma (Shanghai, China). Lipofectamine 2000 (Invitrogen) was used to transfect siRNAs or vectors into A549 cells. Transfected cells were cultured for 48 h.

RT-qPCR

Total RNA was obtained from tissues and cells using TRIzol reagent (Takara, Dalian, China). Total RNA (1 μg) was used to synthesize cDNA using a reverse transcription kit (Takara). The cDNA solution, primers and SYBR-Green Real-Time Master Mix (Takara) were used for RT-PCR reactions. U6 or GAPDH was used as an internal control. Data were analyzed by the $2^{-\triangle\triangle cq}$ method.

Cell Counting Kit-8 (CCK-8) assay

Transfected A549 cells (5×10^3 cells/well) were seeded in 96-well plates containing RPMI-1640 medium and incubated for 24, 48, 72 or 96 h, respectively. Next, the cells were incubated with 10 μL CCK-8 reagents for 4 h. The optical density (OD=450 nm) value of each well was read using a microplate reader (Olympus Corp., Tokyo, Japan).

Transwell assay

Transwell assay was used to assess cell migration and invasion. Matrigel was used for cell invasion but not for cell migration. Transfected A549 cells (5×10^3 cells/well) were placed in the upper chamber. RPMI-1640 medium containing 10% FBS was added to the chamber. After 24 h, the moving cells were stained with 0.1% crystal violet. Cells were counted and photographed under a light microscope.

Dual luciferase reporter assay

A pmiR-GLO vector with wt-LINC00473 and mut-LINC00473 or wt-ROBO1 and mut-ROBO1 was transfected into A549 cells with miR-1294 mimics. After 48 h, luciferase activity was measured using a dual-luciferase reporter assay system (Promega, USA).

Statistical analysis

Data are shown as mean ± SD. Statistical differences were detected using Student's *t*-test or one-way ANOVA in Graphpad Prism 6 software. P<0.05 was considered statistically significant.

RESULTS

Abnormal expression of LINC00473 and miR-1294 in lung adenocarcinoma tissues and cells

The expression level of LINC00473 in lung adenocarcinoma was determined, and T-qPCR suggested that the expression of LINC00473 in lung adenocarcinoma tissues was higher than that in normal tissues (Fig. 1A). Meanwhile, compared with normal lung epithelial cells BEAS-2B, upregulation of LINC00473 was identified in A549 and H1975 cells (Fig. 1B). In addition, miR-1294 was found to be downregulated in lung adenocarcinoma tissues compared to normal tissues (Fig. 1C). Compared to BEAS-2B cells, decreased expression of miR-1294 was detected in A549 and H1975 cells (Fig. 1D). We also found that abnormal expression of LINC00473 and miR-1294 was associated with TNM stage and lymph node metastasis in lung adenocarcinoma patients (Table I). Combining these results, we conclude that LINC00473 and miR-1294 may be involved in the development of lung adenocarcinoma.

Reciprocal inhibition between LINC00473 and miR-1294 expression

LINC00473 is predicted to have a binding site with miR-1294 in the starBase database (http://starbase.sysu.edu.cn, Fig. 2A). The dual luciferase reporter showed that miR-1294 mimics reduced

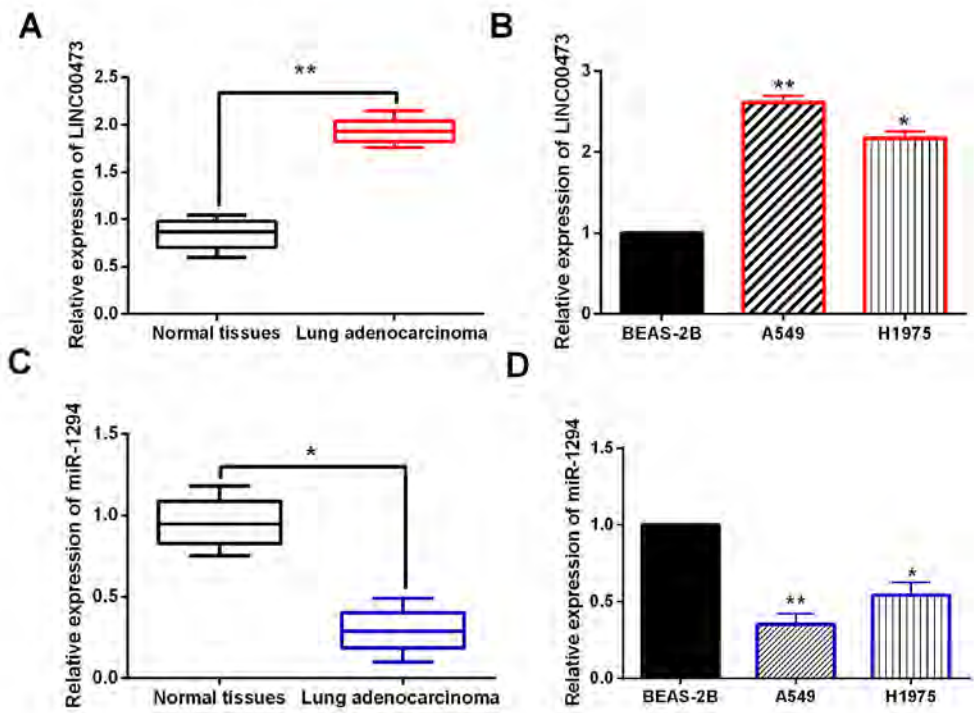


Fig. 1. *The abnormal expression of LINC00473 and miR-1294 in lung adenocarcinoma tissues and cells.* ***A)*** *LINC00473 expression in lung adenocarcinoma tissues and normal tissues.* ***B)*** *LINC00473 expression in A549, H1975 and BEAS-2B cells.* ***C)*** *MiR-1294 expression in lung adenocarcinoma tissues and normal tissues.* ***D)*** *MiR-1294 expression in A549, H1975 and BEAS-2B cells *P <0.05, *P < 0.01*

the luciferase activity of wt-LINC00473, but had little effect on mut-LINC00473 (Fig. 2B). This indicates that LINC00473 can directly target miR-1294. At the same time, we found that LINC00473 expression was negatively correlated with miR-1294 expression in lung adenocarcinoma tissues (Fig. 2C). In addition, miR-1294 expression was repressed by LINC00473 vector and promoted by LINC00473 siRNA in A549 cells (Fig. 2D). We also found that miR-1294 mimics reduced LINC00473 expression, while miR-1294 inhibitor enhanced LINC00473 expression in A549 cells

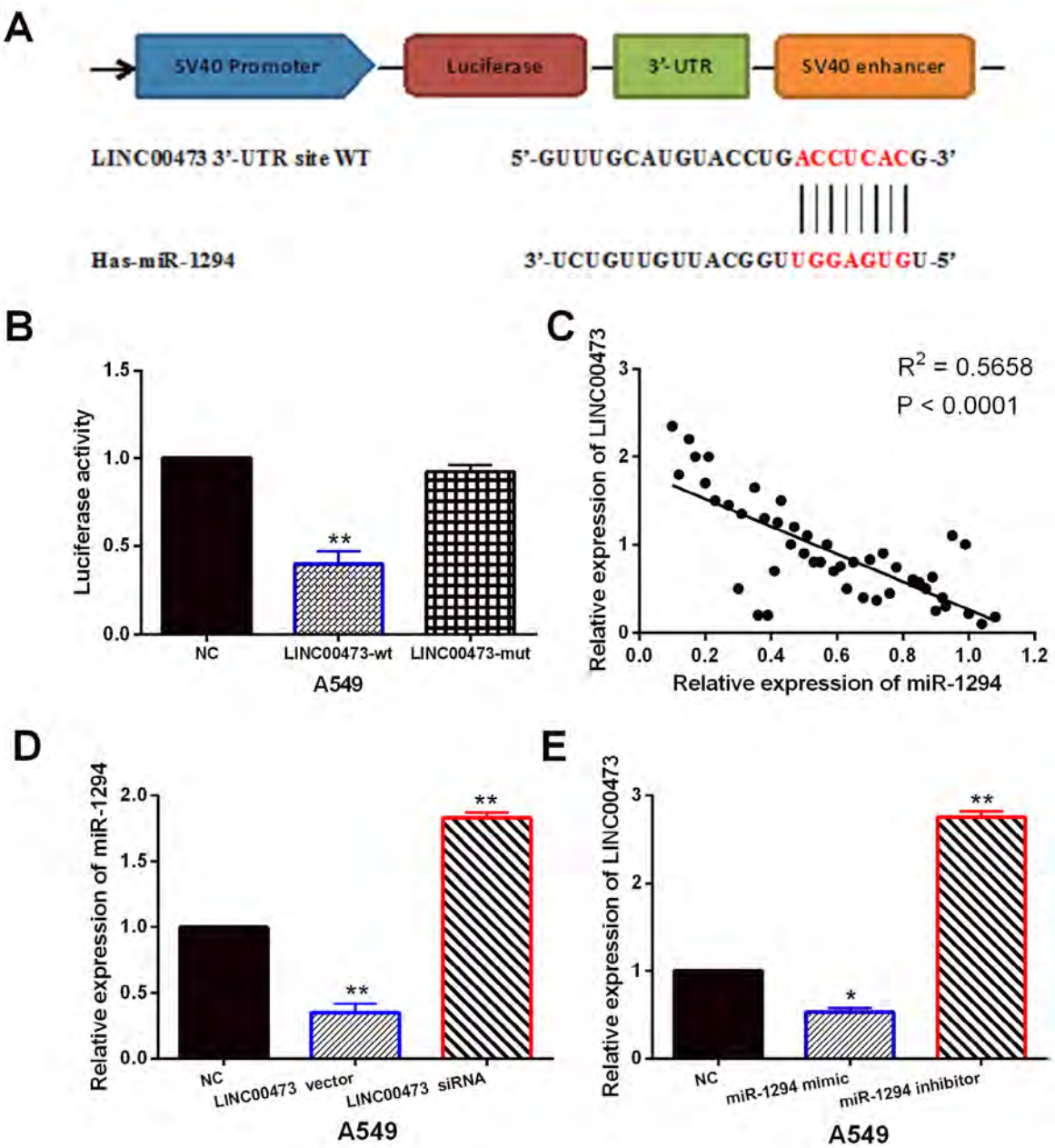


Fig. 2. *The reciprocal inhibition between LINC00473 and miR-1294 expression.* ***A****) The binding sites between LINC00473 and miR-1294.* ***B****) Luciferase reporter assay.* ***C****) MiR-1294 was negatively correlated with LINC00473 expression in lung adenocarcinoma tissues.* ***D****) MiR-1294 expression in A549 cells with LINC00473 vector and siRNA.* ***E****) LINC00473 expression in A549 cells containing miR-1294 mimics or inhibitor ** P <0.01.*

(Fig. 2E). These results imply that LINC00473 directly targets miR-1294. LINC00473 and miR-1294 expression is reciprocally inhibited in lung adenocarcinoma.

LINC00473 promotes cell proliferation and motility in lung adenocarcinoma by binding to miR-1294

Next, LINC00473 siRNA or LINC00473 siRNA + miR-1294 inhibitor was transfected into A549

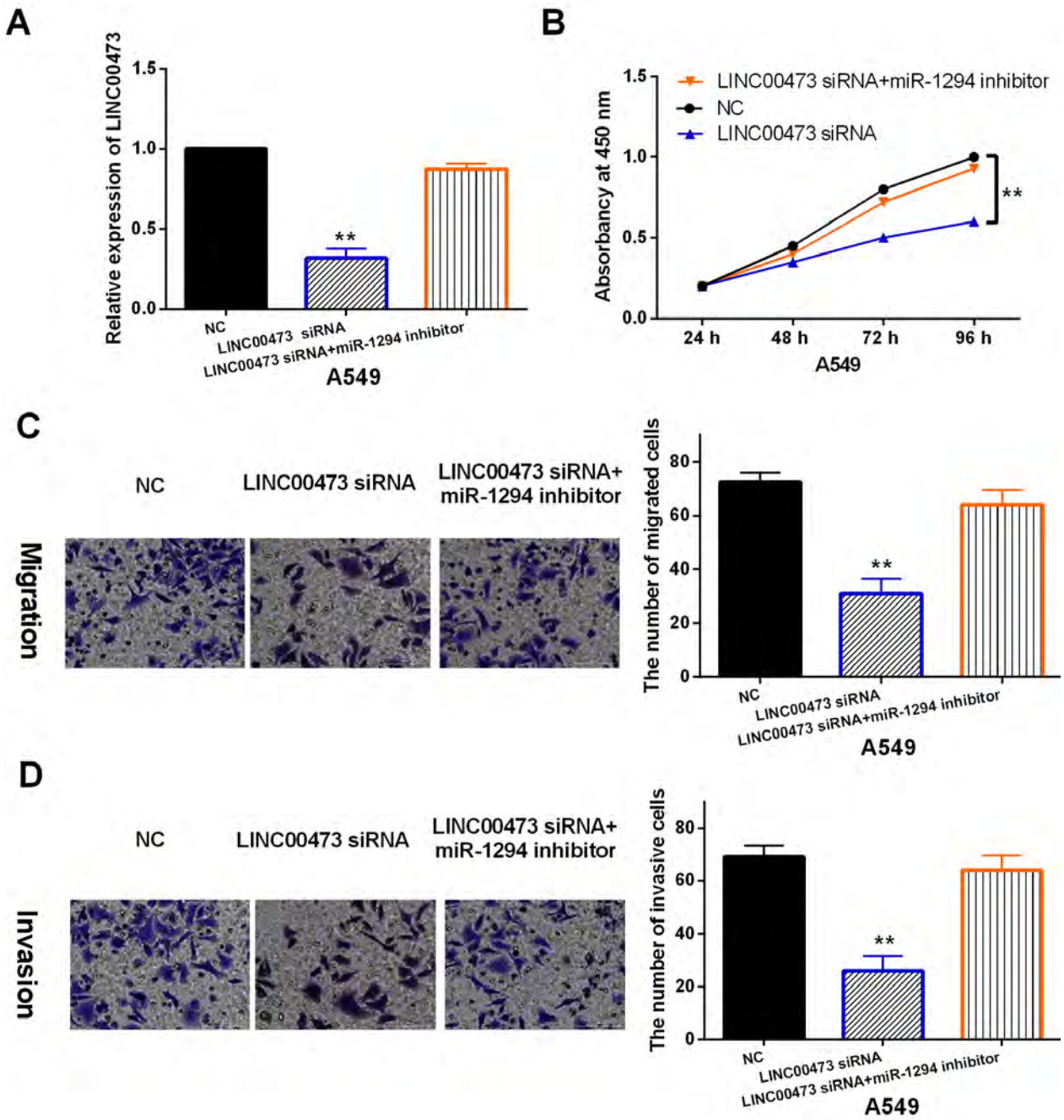


Fig. 3. *LINC00473 promotes cell proliferation and motility in lung adenocarcinoma by binding to miR-1294.* ***A)*** *LINC00473 expression in A549 cells with LINC00473 siRNA or LINC00473 siRNA+miR-1294 inhibitor.* ***B, C, D)*** *Cell proliferation, migration and invasion in A549 cells with LIN*C00473 siRNA or LINC00473 siRNA+miR-1294 inhibitor ** P <0.01

cells to explain its functional mechanism in lung adenocarcinoma. LINC00473 expression was inhibited by its siRNA in A549 cells. And miR-1294 inhibitor restored the decreased expression of LINC00473 (Fig. 3A). Functionally, knockdown of LINC00473 restrained A549 cell proliferation. And downregulation of miR-1294 recovered the inhibition of cell proliferation induced by LINC00473 siRNA (Fig. 3B). Transwell assay showed that LINC00473 downregulation inhibited cell migration and invasion in A549 cells. Similarly, miR-1294 inhibitor also abolished the inhibitory effect of LINC00473 siRNA on cell migration and invasion (Fig. 3 C, D). Therefore, LINC00473 promotes cell proliferation and motility in lung adenocarcinoma by downregulating miR-1294.

MiR-1294 directly targets ROBO1

TargetScan database (http://www.targetscan.org) shows that miR-1294 has a site that binds to the 3'-UTR of ROBO1 (Fig. 4A). Luciferase reporter assay was then performed to confirm their relationship. MiR-1294 mimics or LINC00473 siRNA was found to reduce the luciferase activity of wt-ROBO1. However, the luciferase activity of wt-ROBO1 had little change in A549 cells containing LINC00473 siRNA and miR-1294 inhibitor (Fig. 4B). These results indicate that miR-1294 directly targets ROBO1. And ROBO1 can be regulated by LINC00473. In addition, miR-1294 mimics reduced ROBO1 expression, while miR-1294 inhibitor increased ROBO1 expression in A549 cells (Fig. 4C). At the same time, LINC00473 siRNA reduced ROBO1 expression in A549 cells. However, miR-1294 inhibitor can restored the reduced ROBO1 expression induced by LINC00473 siRNA (Fig. 4D), which indicates that LINC00473 upregulates ROBO1 expression by downregulating miR-1294 in lung adenocarcinoma.

ROBO1 regulates lung adenocarcinoma progression by participating in LINC00473/miR-1294 axis

Finally, ROBO1 siRNA, ROBO1 siRNA+LINC00473 vector or ROBO1 siRNA+miR-1294 inhibitor were co-transfected into A549 cells to confirm their interaction in lung adenocarcinoma. RT-qPCR showed that ROBO1 expression was reduced by its siRNA in A549 cells. The LINC00473 vector and miR-1294 inhibitor can recover the reduction in ROBO1 expression induced by ROBO1 siRNA (Fig. 5A). In addition, CCK-8 suggested that knockdown of ROBO1 inhibited A549 cell proliferation. Up-regulation of LINC00473 or

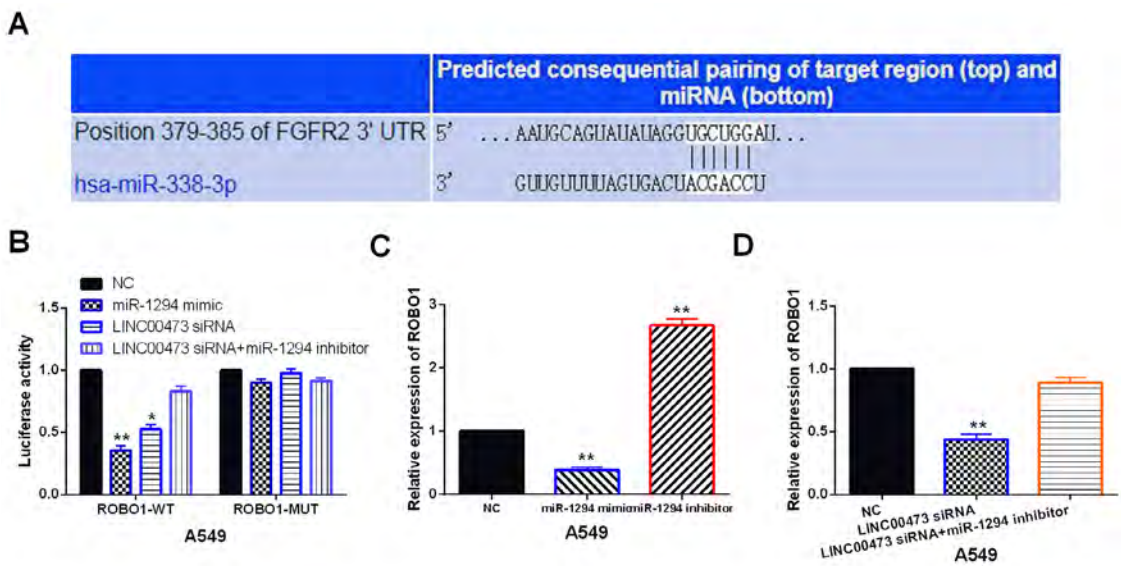


Fig. 4. *MiR-1294 directly targets ROBO1. **A)** The binding sites between ROBO1 and miR-1294. B) Luciferase activity assay (**C**) ROBO1 expression in A549 cells with miR-1294 mimic or inhibitor (**D**) ROBO1 expression in A549 cells with LINC00473 siRNA or LINC00473 siRNA+miR-1294 inhibitor. ** P <0.01*

down-regulation of miR-1294 attenuated the inhibitory effect of ROBO1 siRNA on cell proliferation (Fig. 5B). Transwell assay showed that ROBO1 downregulation suppressed cell migration and invasion in A549 cells. The LINC00473 vector and miR-1294 inhibitor also eliminated the inhibitory effect of ROBO1 siRNA on A549 cell migration and invasion (Fig. 5 C, D). Overall, ROBO1 serves as an oncogene in lung adenocarcinoma. LINC00473 promotes the development of lung adenocarcinoma by upregulating ROBO1.

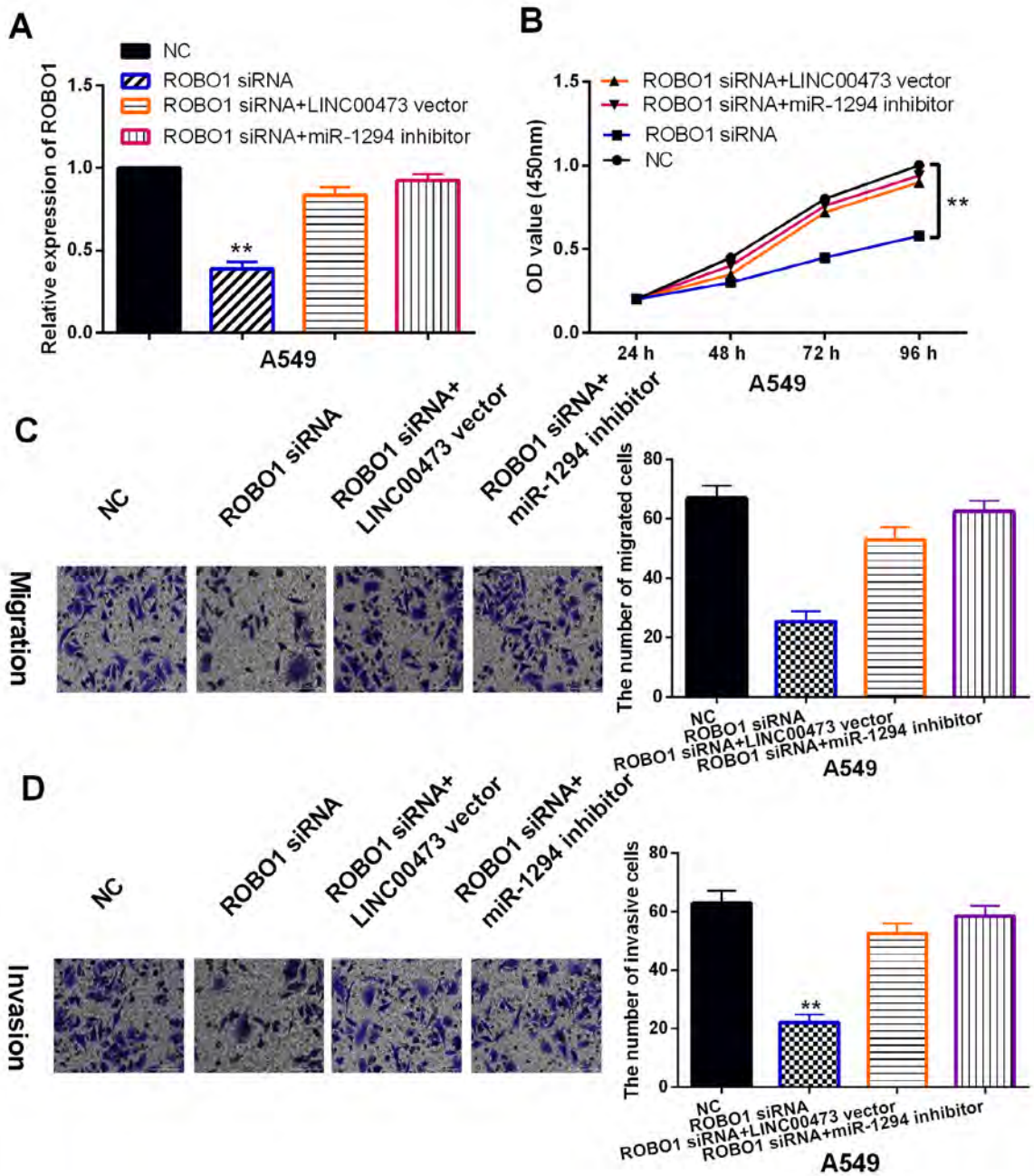


Fig. 5. *ROBO1 regulates lung adenocarcinoma progression by participating in LINC00473/miR-1294 axis.* ***A)*** *ROBO1 expression in A549 cells with ROBO1 siRNA, ROBO1 siRNA+ LINC00473 vector or ROBO1 siRNA +miR-1294 inhibitor* ***(B, C, D)*** *Cell proliferation, migration and invasion in A549 cells with ROBO1 siRNA, ROBO1 siRNA+ LINC00473 vector or ROBO1 siRNA +miR-1294 inhibitor. **P < 0.01*

DISCUSSION

In the past few years, many lncRNAs have been found to regulate the aggressive behavior of lung adenocarcinoma, such as GMDS-AS1 and SNHG14 (18, 19). In this study, upregulation of LINC00473 was found in lung adenocarcinoma and was associated with TNM stage and lymph node metastasis in lung adenocarcinoma patients. Functionally, the downregulation of LINC00473 suppressed cell proliferation and motility in lung adenocarcinoma. Similar to our results, high expression of LINC00473 was also detected in esophageal squamous cell carcinoma and breast cancer (20, 21). In addition, LINC00473 has been reported to enhance cell proliferation and invasion in hepatocellular carcinoma (22). And LINC00473 predicted a poor prognosis in gastric cancer and promoted cell migration and invasion (23). These studies are consistent with our results, suggesting that LINC00473 acts as an oncogene in lung adenocarcinoma.

In addition, LINC00473 promoted the progression of hepatocellular carcinoma by acting as ceRNA for miR-195 (24). Here, we also found that LINC00473 acts as a molecular sponge for miR-1294. Moreover, miR-1294 was downregulated in lung adenocarcinoma tissues and cells. The abnormal expression of miR-1294 was associated with TNM stage and lymph node metastasis in lung adenocarcinoma patients. Functionally, miR-1294 can impair the carcinogenesis of LINC00473 in lung adenocarcinoma, indicating that miR-1294 has a tumor suppressive effect in lung adenocarcinoma. Previous studies have also shown that miR-1294 expression was reduced in epithelial ovarian cancer and gastric cancer (11, 25). It was also found that miR-1294 exerted a tumor suppressive effect in osteosarcoma (26). These findings are similar to our results. Besides, overexpression of circ_0005198 sponging miR-1294 promoted the proliferation, migration and invasion of glioma cells (27). In this study, LINC00473 also promoted cell proliferation and motility in lung adenocarcinoma by sponging miR-1294.

Table I. *Relationship between the expression of LINC00473 or miR 1294 and clinicopathological characteristics in lung adenocarcinoma patients.*

Characteristics	Cases	LINC00473		P-value	miR-1294		P-value
		High	Low		High	Low	
Age (years)				0.33			0.42
≥ 60	40	28	12		15	25	
<60	26	17	9		11	15	
Gender				0.24			0.31
Male	42	30	12		16	26	
Female	24	15	9		10	14	
Tumor size (mm)				0.08			0.09
⩽3	39	29	10		12	27	
>3	27	16	11		14	13	
Lymph nodes metastasis				0.04*			0.03*
Yes	25	15	10		10	15	
No	41	25	16		16	25	
Tumor stage				0.03*			0.04*
I-II	36	26	10		12	24	
III-IV	30	19	11		14	16	

Statistical analyses were performed by the χ^2 test.
**P<0.05 was considered significant.*

Furthermore, ROBO1 was confirmed to be a direct target of miR-1294. LINC00473 enhanced ROBO1 expression in lung adenocarcinoma by downregulating miR-1294. The relationship between ROBO1 and miR-1294 or LINC00473 has not been reported in previous studies. In addition, knockdown of ROBO1 suppressed cell proliferation, migration and invasion in lung adenocarcinoma. Consistent with our results, the carcinogenicity of ROBO1 has also been identified in gliomas and gastric cancer (28, 29). Additionally, miR-490-5p was found to inhibit the proliferation, migration and invasion of hepatocellular carcinoma cells by regulating ROBO1 (15). In our study, we found that miR-1294 can attenuate the carcinogenesis of ROBO1 in lung adenocarcinoma, which suggests that miR-1294 restrains the progression of lung adenocarcinoma by regulating ROBO1. More importantly, we found that LINC00473 promoted the development of lung adenocarcinoma by upregulating ROBO1.

In summary, this study reveals for the first time that LINC00473 promotes cell proliferation, migration and invasion in lung adenocarcinoma by regulating the miR-1294/ROBO1 axis. This study may provide a potential therapeutic target for lung adenocarcinoma.

REFERENCES

1. Martin P, Leighl NB. Review of the use of pretest probability for molecular testing in non-small cell lung cancer and overview of new mutations that may affect clinical practice. Ther Adv Med Oncol 2017; 9:405-14.
2. Liam CK, Andarini S, Lee P, Ho JC, Chau NQ, Tscheikuna J. Lung cancer staging now and in the future. Respirology 2015; 20:526-34.
3. Hong QY, Wu GM, Qian GS, et al. Prevention and management of lung cancer in China. Cancer 2015; 121 Suppl 17:3080-88.
4. Mayekar MK, Bivona TG. Current Landscape of Targeted Therapy in Lung Cancer. Clin Pharmacol Ther 2017; 102:757-64.
5. Zhang Q, Liang Y, Yuan H, et al. Integrated analysis of lncRNA, miRNA and mRNA expression profiling in patients with systemic lupus erythematosus. Arch Med Sci 2019; 15:872-79.
6. Yang S, Liu T, Sun Y, Liang X. The long noncoding RNA LINC00483 promotes lung adenocarcinoma progression by sponging miR-204-3p. Cell Mol Biol Lett 2019; 24:70.
7. Su C, Shi K, Cheng X, Han Y, Li Y, Yu D, Liu Z. Long noncoding RNA LINC00472 inhibits proliferation and promotes apoptosis of lung adenocarcinoma cells via regulating miR-24-3p/ DEDD. Technol Cancer Res Treat 2018; 17:1533033818790490.
8. Zhang Q, Wang G, Xu L, Yao Z, Song L. Long non-coding RNA LINC00473 promotes glioma cells proliferation and invasion by impairing miR-637/ CDK6 axis. Artif Cells Nanomed Biotechnol 2019; 47:3896-903.
9. Shi C, Yang Y, Yu J, Meng F, Zhang T, Gao Y. The long noncoding RNA LINC00473, a target of microRNA 34a, promotes tumorigenesis by inhibiting ILF2 degradation in cervical cancer. Am J Cancer Res 2017; 7:2157-68.
10. Wang Z, Yan J, Zou T, Gao H. MicroRNA-1294 inhibited oral squamous cell carcinoma growth by targeting c-Myc. Oncol Lett 2018; 16:2243-50.
11. Shi YX, Ye BL, Hu BR, Ruan XJ. Expression of miR-1294 is downregulated and predicts a poor prognosis in gastric cancer. Eur Rev Med Pharmacol Sci 2018; 22:5525-30.
12. Wang Y, Liu G, Sun S, Qin J. miR-1294 alleviates epithelial-mesenchymal transition by repressing FOXK1 in gastric cancer. Genes Genomics 2019; 42(2):217-24.
13. Chen H, Liu L, Li X, Shi Y, Liu N. MicroRNA-1294 inhibits the proliferation and enhances the chemosensitivity of glioma to temozolomide via the direct targeting of TPX2. Am J Cancer Res 2018; 8:291-301.
14. Parray A, Siddique HR, Kuriger JK, et al. ROBO1, a tumor suppressor and critical molecular barrier for localized tumor cells to acquire invasive phenotype: study in African-American and Caucasian prostate cancer models. Int J Cancer 2014; 135:2493-506.
15. Chen W, Ye L, Wen D, Chen F. MiR-490-5p inhibits hepatocellular carcinoma cell proliferation, migration and invasion by directly regulating ROBO1. Pathol Oncol Res 2019; 25:1-9.
16. Zhang X, Dong J, He Y, et al. miR-218 inhibited tumor angiogenesis by targeting ROBO1 in gastric cancer. Gene 2017; 615:42-49.
17. Li YJ, Zhang W, Xia H, Zhang BS, Chen P, Zhao

YL, Li J. miR-218 suppresses epithelial-to-mesenchymal transition by targeting Robo1 and Ecop in lung adenocarcinoma cells. Future Oncol 2017; 13:2571-82.
18. Zhao M, Xin XF, Zhang JY, Dai W, Lv TF, Song Y. LncRNA GMDS-AS1 inhibits lung adenocarcinoma development by regulating miR-96-5p/CYLD signaling. Cancer Med 2019; 9(3):1196-208.
19. Xu ZN, Wang ZX, Xu L, et al. Long noncoding RNA SNHG14 exerts oncogenic functions in lung adenocarcinoma through acting as a sponge to miR-613. Eur Rev Med Pharmacol Sci 2019; 23:10810-17.
20. Chen W, Zhang Y, Wang H, Pan T, Zhang Y, Li C. LINC00473/miR-374a-5p regulates esophageal squamous cell carcinoma via targeting SPIN1 to weaken the effect of radiotherapy. J Cell Biochem. 2019; 120:14562-72.
21. Shi X, Wang X. LINC00473 mediates cyclin D1 expression through a balance between activation and repression signals in breast cancer cells. FEBS Lett 2019; 593:751-59.
22. Chen H, Yang F, Li X, Gong ZJ, Wang LW. Long noncoding RNA LNC473 inhibits the ubiquitination of survivin via association with USP9X and enhances cell proliferation and invasion in hepatocellular carcinoma cells. Biochem Biophys Res Commun 2018; 499:702-10.
23. Zhang W, Song Y. LINC00473 predicts poor prognosis and regulates cell migration and invasion in gastric cancer. Biomed Pharmacother 2018; 107:1-6.
24. Mo J, Li B, Zhou Y, et al. LINC00473 promotes hepatocellular carcinoma progression via acting as a ceRNA for microRNA-195 and increasing HMGA2 expression. Biomed Pharmacother 2019; 120:109403.
25. Guo TY, Xu HY, Chen WJ, Wu MX, Dai X. Downregulation of miR-1294 associates with prognosis and tumor progression in epithelial ovarian cancer. Eur Rev Med Pharmacol Sci 2018; 22:7646-52.
26. Zhang ZF, Li GR, Cao CN, Xu Q, Wang GD, Jiang XF. MicroRNA-1294 targets HOXA9 and has a tumor suppressive role in osteosarcoma. Eur Rev Med Pharmacol Sci 2018; 22:8582-88.
27. Wang J, Li J, Wang H, Lv L, Sun J. Overexpression of circ_0005198 sponges miR-1294 to regulate cell proliferation, apoptosis, migration, and invasion in glioma. J Cell Biochem 2019; 120:15538-45.
28. Gu JJ, Gao GZ, Zhang SM. miR-218 inhibits the migration and invasion of glioma U87 cells through the Slit2-Robo1 pathway. Oncol Lett 2015; 9:1561-66.
29. Tie J, Pan Y, Zhao L, et al. MiR-218 inhibits invasion and metastasis of gastric cancer by targeting the Robo1 receptor. PLoS Genet 2010; 6:e1000879.

NARINGENIN INDUCES NEUROPROTECTION AGAINST HOMOCYSTEINE-INDUCED PC12 CELLS VIA THE UPREGULATION OF SUPEROXIDE DISMUTASE 1 EXPRESSION BY DECREASING miR-224-3p EXPRESSION

H. LI[1*], MW. LIU[2*], W. YANG[3], LJ. WAN[1], HL. YAN[4], J-C. LI[2], SY. TANG[5] and YQ. WANG[3]

[1]Intensive Care Unit, The Second Hospital Affiliated To Kunming Medical; University, Kunming, China; [2]Department of Emergency, The First Hospital Affiliated To Kunming Medical University, Wu Hua District, Kunming, China; [3]Department of Anesthesiology, The First Hospital Affiliated To Kunming Medical University, Wu Hua District, Kunming, China; [4]Trauma Medical Center, The First Hospital Affiliated To Kunming Medical University, Wu Hua District, Kunming, China; [5]Department of Anesthesiology, Yunnan Corps Hospital, Armed Police, Biji Town, Xishan District, Kunming, China

Received January 13, 2020 – Accepted March 27, 2020

[*]These Authors contributed equally to this work

Naringenin is a flavonoid compound with antioxidant effects. It is used to treat oxidative stress-related diseases, but its mechanism is unclear. In this experiment, we explored whether naringenin can increase the expression of superoxide dismutase 1(SOD1), reduce the oxidative stress of PC12 cells induced by homocysteine (Hcy), and decrease the apoptosis of PC12 cells induced by Hcy by inhibiting the expression of mir-224-3p. Different concentrations of Hcy (1, 3, 5, 8, and 10 mmol/L) was used to analyze effect of homocysteine on PC12 cells. A total of 5 mmol/L Hcy was used to induce the excitatory and neurotoxicity model of PC12 cells *in vitro*. The cells were divided into normal control, Hcy induction, Hcy + Naringenin (25 μM), Hcy + Naringenin (50 μM), Hcy + Naringenin (75 μM), Hcy + Naringenin (100 μM), and Hcy + Naringenin (150 μM) groups. The relative survival rate and activities of the PC12 cells were determined by the MTT method, and the apoptosis rate of the PC12 cells was determined by using flow cytometry. The Western blot method was used to determine the expressions of SOD1, Bax, Caspase-3, Caspase-8, and Bcl-2 in the PC12 cells induced by Hcy. The expressions of SOD1 mRNA and miR-224-3p in the Hcy-induced PC12 cells were determined by RT-PCR. Results found that Hcy increased the expression of miR-224-3p in a dose-dependent manner but decreased that of SOD1 mRNA and protein. Hcy also increased oxidative stress in the PC12 cells and the proapoptotic proteins Bax, Caspase-3, and Caspase-9. Furthermore, it decreased the expression of anti-apoptotic protein Bcl-2 and the activity and survival rate of the HT22 cells, but it increased the apoptosis of the PC12 cells. The treatment of Hcy-induced PC12 cells with different concentrations of naringenin for 24 h decreased the expression of miR-224-3p in a dose-dependent manner and increased the expressions of SOD1 mRNA and protein. The treatment also decreased the oxidative stress in the PC12 cells and the expressions of pro-apoptotic proteins Bax, Caspase-3, and Caspase-9; increased the expression of anti-apoptotic protein Bcl-2; decreased the apoptosis of the PC12 cells; and increased the PC12 cells.The results suggest that Naringenin

Key words: miR-224-3p; homocysteine; PC12 cells; SOD1; oxidative stress

Corresponding Author:
Dr Wang Yan-qiong,
Department of Anesthesiology,
The First Hospital, Affiliated To Kunming Medical University,
295, Xichang Road, Wu Hua District, Kunming,
Yunnan,650032,China
e-mail: xiaoyu750529@126.com

0393-974X (2020)
Copyright © by BIOLIFE, s.a.s.
This publication and/or article is for individual use only and may not be further reproduced without written permission from the copyright holder.
Unauthorized reproduction may result in financial and other penalties
DISCLOSURE: ALL AUTHORS REPORT NO CONFLICTS OF INTEREST RELEVANT TO THIS ARTICLE.

can decrease the apoptosis and oxidative stress of PC12 cells induced by Hcy and increase the activities and survival rates of PC12 cells. The mechanism may be related to naringenin decreasing the expression of miR-224-3p in PC12 cells induced by Hcy and increasing the expressions of SOD1 mRNA and protein.

The brain is one of the organs most sensitive to oxidative stress. As it is almost a single source of energy obtained through the aerobic metabolism of the mitochondrial respiratory chain, which generates a large number of free radicals, the brain is rich in unsaturated fatty acids and is highly vulnerable to oxidative stress for its weak antioxidant capacity (1). Increasing evidence shows that oxidative stress can be a major factor in cell damage in many neurological diseases, such as epilepsy, cerebral ischemia-reperfusion injury, Alzheimer's disease, and Parkinson's disease, and can lead to death by inducing neuronal apoptosis (2).

Reactive oxygen species (ROS) is a normal component of the body's aerobic respiration. ROS, including superoxide anion (O_2–), hydroxyl radical (–OH), and hydrogen peroxide (H_2O_2), are mainly produced by the mitochondria. The antioxidant systems in the body include superoxide dismutase (SOD), catalase (CAT), and glutathione peroxidase. Under normal circumstances, intracellular oxidation and antioxidation are in a dynamic balance. Oxidative stress occurs and leads to damage when intracellular oxidation increases and exceeds the level of antioxidation (2).

The current idea is that because homocysteine (Hcy) contains a sulfhydryl, auto-oxidation occurs in the presence of a large amount of O_2, generates superoxide anions and hydrogen peroxide, and ultimately increases the ROS in cells (3). Hcy can activate the glutamate binding site of the N-methyl-aspartic acid receptor, activate the oxidative stress of the ROS system, and enhance the sensitivity of nerve cells to excitotoxicity and oxidative stress injury. Ca_2+ overload and active oxygen production can cause neuronal damage (4). PC12 cells are single-gram drop cell lines isolated from rat adrenal chromaffin cells (5). PC12 and neural cells are derived from neural ridges through genesis and share many similarities in structure, functions, and nerves. PC12 cells are easier to culture than neural cells (5, 6). The study found that homocysteine induced oxidative stress response in PC12 cells (7). Therefore, they are widely used as *in vitro* cell models for studying the mechanisms of neuropharmacology, neuron differentiation and development, neural regeneration, and nervous system diseases.

MiRNAs are composed of a class of small non-coding RNAs that can control the expression of complementary target messenger RNA (8). In vertebrates, the expression of miRNAs in the brain is significantly higher than that in other organs. MiRNAs are expressed during embryonic and developmental maturity to participate in various physiological and pathological processes that determine cell fate. The role of nervous system development and various disease processes provide clues for further study. MiRNA is a type of endogenous, non-coding, single-stranded RNA with a length of about 19–22 nucleotides. At the post-transcriptional level, the 3'untranslated region (3′UTR) complementary sequence of the saturated gene leads to the degradation of the target gene in RNA or inhibits its translation (9). Studies confirmed that miRNAs are involved in cell proliferation, differentiation, and apoptosis and are closely related to the occurrence and development of diseases such as epilepsy, cerebral infarction, and Parkinson's disease (8–10). MiR-224-3p is a member of the miR-224 family. Relatively few studies on miR-224 are available, and they mainly focused on its role in tumor-related diseases. Several studies found that miR-224-3p expression is reduced in patients with colorectal cancer. Further research found that miR-224-3p can inhibit the proliferation of colorectal cancer cells and promote the apoptosis of cancer cells (11).

Naringenin is a dihydroflavone compound widely found in citrus fruits, such as grapefruit. Current pharmacological studies showed that naringenin has a wide range of biological activities, including anti-inflammatory, anti-apoptosis, antioxidant fibrosis, anticancer, antitumor, antibacterial, and antiviral activities; it also regulates arrhythmia and

glucose and fat metabolism in the body, improves atherosclerosis, protects liver functions, and exerts estrogen-like effects (12-17). At present, naringenin is widely used in food, medicine, and other fields.

In this study, we predicted through TargetScan that SOD1 may be a regulatory target of miR-382-3p. Therefore, we explored whether the inhibition of naringenin by miR-382-3p expression increases SOD1 expression and reduces the oxidative stress and apoptosis of PC12 cells by Hcy *in vitro*. The results should benefit the reduction of brain damage caused by oxidative stress.

MATERIALS AND METHODS

Cell culture and transfection

Murine adrenal pheochromocytoma PC12 cells were provided by the Medical Experiment Department of the Guangzhou General Hospital of the Guangzhou Military Region. The PC12 cells were removed from the cell bank, quickly thawed, and then transferred to a centrifuge tube on a clean bench. An appropriate amount of fresh medium was added, the mixture was subsequently centrifuged, and the sediments were removed. Then, fresh and DMEM medium was added and cultured in 10% fetal bovine serum. A total of 100 U/mL penicillin and 100 μg/ml streptomycin were used to culture the PC12 cells. The cells were routinely placed in a 37 °C humidified incubator containing 5% CO_2 and 95% air. The cells in the logarithmic growth phase were used for the subsequent experiments.

An appropriate amount of PC12 cells in the logarithmic growth phase were inoculated into six-well plates. According to the instructions of the Lipofectamine 2000 Transfection Reagent, the miR-224-3p mimic, miR-224-3p inhibitor, mimic control, and inhibitor control were transfected into the PC12 cells at a transfection concentration of 50 nmol/L when the cells adhered to the wall overnight reached 60%. After 6 h of transfection, the medium was replaced with a fresh one and cultured for 24 h. The cells were collected for real-time quantitative PCR (RT-qPCR) and Western blot detection.

3-(4,5-Dimethylthiazol-2-yl)-2,5-diphenyltetrazolium bromide (MTT) method to detect cell proliferation

The PC12 cells in the logarithmic growth phase were inoculated in a 96-well plate with a cell density of 5 × 10^7/L, and 100 μL of the cells were inoculated per well and cultured in a 5% CO_2 incubator to make the cells adhere to the wall. Before the next day of dosing, the old culture medium was removed, and five replicate wells were set up in each group. According to previously described[18,19], exactly 100 μL of each well in the experimental group was added with different concentrations of Hcy (1, 3, 5, 8, and 10 mmol/L) or naringenin (25, 50, 75, 100, and 150 μm) plus Hcy (5 mmol/L). The cells were cultured in 96-pore plates for 24 h, added with 20 μL of 5 g/L MTT solution, and cultured for 4 h. Then, the supernatant was discarded. A total of 150 μL DMSO was added into each pore, and the mixture was dissolved to dissolve the crystal. The cell absorbance (a) was measured at 490 nm.

CCK-8 to detect cell viability

The PC12 cells in the logarithmic growth phase were inoculated in a 96-well plate with a cell density of 5 × 10^7/L. Exactly 100 μL of cells per well were inoculated and placed in a 5% CO_2 incubator to make the cells adhere to the wall. Before the next day of dosing, the old culture medium was removed, and five replicate wells were set up in each group. In the experimental group, 100 μL of each well was added with different concentrations of Hcy (1, 3, 5, 8, and 10 mmol/L) or naringenin (25, 50, 75, 100, and 150 μM) for 24 h. The blank group only contained the medium without PC12 cells, and the control group was only added with the same medium. After dosing, PC12 cells was incubated in a 96-well plate for 24 h, and 20 μL of CCK-8 solution was added in each well. The PC12 cells were then incubated at 37°C for 1 h. While the culture was terminated, the blank well was set to zero and shaken on a microplate reader for 3 min. The OD value of each well was detected at the wavelength of 450 nm, and the cell activity was recorded and calculated.

Apoptosis detection

The PC12 cells were inoculated in six-well culture plates. They were then added with different concentrations of Hcy (1, 3, 5, 8, 10 and mmol/L) or naringenin (25, 50, 75, 100, and 150 μM) and cultured for 24 h. The cells were collected and washed thrice with PBS and centrifuged at 1200 r/min for 5 min. Afterward, 200 μL of binding buffer was added into the suspended cells. The mixture was then added with 5 μL of Annexin V-EGFP

and 5 μL of propidium iodide, which was protected from light for 15 min. Flow cytometry was used for detection with excitation and emission wavelengths of 488 and 530 nm, respectively. The green fluorescence of Annexin V-EGFP was detected via the FITC channel, whereas the red fluorescence of PI was detected via the PI channel. The fluorescence compensation adjustment used normal cells without apoptosis induction as a control to remove spectral overlap and set the position of the cross gate.

Detection of intracellular ROS

The cells in the logarithmic growth phase were selected and turned into a PC12 cell solution inoculated in 2×10^5/mL six-well culture plates. The solution was added with different concentrations of Hcy (1, 3, 5, 8, and 10 mmol/L) or naringenin (25, 50, 75, 100, and 150 μM) and then cultured for 24 h. The collected cells were suspended in a serum-free medium containing a final concentration of 10 μmol/L H2DCFDA. They were then incubated in a cell incubator at 37°C for 20 min and inverted and mixed every 3 to 5 minutes to ensure the full contact of the H2DCFDA fluorescent light probe and cells. The cells were washed once with a serum-free cell culture solution and washed twice with PBS solution to fully remove H2DCFD, which did not enter the cells. The cells were resuspended in 0.5–1 mL PBS solution, and the fluorescence intensity (OD value) of the cells was measured using a fluorescence spectrophotometer with excitation and emission wavelengths of 488 and 525 nm, respectively, to determine the intracellular ROS level. Each treatment was repeated at least thrice.

Detection of SOD activity and MDA content

The PC12 cells were seeded in six-well culture plates, added with different concentrations of Hcy (1, 3, 5, 8, and 10 mmol/L) or naringenin (25, 50, 75, 100, and 150 μM), and then cultured for 24 h. The cells from each group were collected, homogenized, and lysed on ice. The supernatant was collected through centrifugation. The SOD viability test was performed using an SOD viability detection kit. The MDA content was measured using an MDA content detection kit.

Protein extraction and Western blot

The PC12 cells were inoculated in six-well culture plates, added with different concentrations of Hcy (1, 3, 5, 8, and 10 mmol/L) or naringenin (25, 50, 75, 100, and 150 μM), and cultured for 24 h. The cells were collected and washed thrice with PBS. The cells were lysed by adding RIPA lysis buffer containing protease and phosphatase inhibitors. The BCA kit was used to determine the protein content and prepare the samples. SDS-PAGE gel was prepared, and the sample was loaded. After electrophoresis for 30 and 50 min at 70 and 140 V, the sample was transferred for 20 min by NC membrane 18 V 350 mA, and blocked with 5% PBS milk powder for 30 min. The membrane was washed with PBST thrice, and each washing lasted 5 min. Then, the membrane was cut with the 4 primary antibody (β-actin, SOD1, Bax, Caspase-3, Bcl-2, Caspase-9 diluted at 1:1 000) (Abcam, Cambridge, UK) and incubated overnight. The primary antibody was collected, that is, a secondary goat anti-rabbit IgG-horseradish peroxidase (HRP) antibody (1:2000) or goat anti-mouse IgG-HRP antibody (1:2000) obtained from Santa Cruz Biotechnology (Santa Cruz, CA, USA). The primary antibody was diluted in 5% (w/v) dry nonfat milk in TBST for 1 h at room temperature. Equal protein loadings of the samples were confirmed by β-actin. All Western blots were quantified using densitometry.

RT-qPCR

The PC12 cells were seeded in six-well culture plates, added with different concentrations of Hcy (1, 3, 5, 8, and 10 mmol/L) or naringenin (25, 50, 75, 100, and 150 μM), and cultured for 24 h. The cells were collected and centrifuged at 2000 g/min. After washing with PBS, the total RNA was extracted using the TRIzol method. According to the instructions of the PrimeScript TMRT reagent kit, mRNA was reverse transcribed into cDNA by M-MLV reverse transcriptase. Then, RT-qPCR was performed to detect the SOD1 mRNA expression in the cells. The reaction system was as follows: 10 μL of SYBR Premix Ex TaqTM II, 2 μL of PCR primer, 2 μL of DNA template, 6 μL of DEPC water, and 20 μL of total reaction system. Each sample was set up in three replicate wells. The reaction system was placed and completed on the PCR instrument. The amplification conditions were as follows: predenaturation at 94°C for 30 s, cycling reaction at 94°C for 10 s and 60°C for 30 s with 35 cycles, and cooling to 4°C. TaqMan MicroRNA assay kits (Applied Biosystems, Foster City, CA, USA) were used to determine the expression levels of miR-224-3p using the $2^{-\Delta\Delta Ct}$ method.

The reaction conditions were as follows: predenaturation at 95 °C for 30 s, reaction at 95 °C for 5 s, and annealing at 60 °C for 30 s with 40 cycles. The primer series are shown in Table I. U6 was used as an internal reference for miR-224-3p, whereas β-actin was used as an internal reference for SOD1 mRNA expression. After the reaction, the circulation threshold of each gene was calculated and compared with the internal reference gene U6 or β-actin to determine the expression levels.

Dual luciferase reporter assay

The target gene prediction software miR-Base (http://www.mirbase.org/), TargetScan (http://www.targetscan.org/), and PicTar (http://pictar.mdc-berlin.de/) were used to predict whether the target gene of miR-224-3p is SOD1 or not. According to the previous method (10), we constructed the wild-type (wt) SOD1 and mutant (mut) SOD1 luciferase gene vectors. These two plasmids were combined with miR-224-3p mimics, miR-224-3p inhibitor, mimic control, and inhibitor control. They were mixed and co-transfected into the PC12 cells induced by Hcy (5mmol / L) and counted as Wt + miR-224-3p mimics, Mut + miR-224-3p, Wt + negative control, and Mut + negative control. After incubation at 37°C for 48 h in an incubator within 5% CO_2, the dual luciferase reporter gene assay kit was used to detect the dual luciferase activity. The levels of SOD1 in the PC12 cells overexpressing miR-224-3p were detected using RT-qPCR and Western blot. The ratio of the luminous intensity of sea cucumber luciferase to that of firefly luciferase reflected the binding force of miR-224-3p to SOD1.

Statistical analysis

All data were analyzed using SPSS 17.00 software (San Diego, CA, USA). The measurement data were presented as normal distribution ($P > 0.05$), mean ± standard deviation ($P > 0.05$), and mean square deviation ($P > 0.05$). One-way ANOVA, SNK test, and LSD-t analysis were performed. The results were considered statistically significant when $P < 0.05$.

RESULTS

Hcy decreased PC12 cell activity and proliferation

To observe the effects of Hcy on PC12 cell activity and proliferation, we incubated the cells with various concentrations of Hcy (1, 3, 5, 8, and 10 mmol/L) for 24 h. The PC12 cell viability was measured using CCK-8, and the proliferation inhibition rate was determined using MTT assay. As shown in Fig. 1, Hcy attenuated the viability of the PC12 cells and increased their proliferation inhibition rate in a concentration-dependent manner. The Hcy concentrations of as low as 5 mmol/L effectively decreased PC12 cell viability and increased the proliferation inhibition rate.

Hcy increased the oxidative stress of PC12 cells

The PC12 cells were incubated with various concentrations of Hcy (1, 3, 5, 8, and 10 mmol/L) for 24 h to investigate the effects of Hcy on the oxidative stress of PC12 cells. The SOD activity and levels of ROS and MDA were determined. As shown in Fig. 2, the ROS and MDA levels were significantly increased, whereas the SOD activity was markedly decreased after Hcy administration for 24 h in a concentration-dependent manner. The Hcy concentrations of as low as 5 mmol/L effectively increased the PC12 cell oxidative stress and decreased mitochondrial membrane potential and ATP levels.

Hcy increased Bax, Caspase-3, and Caspase-8 expressions and suppressed Bcl-2 expression in PC12 cells

The PC12 cells were incubated with various concentrations of Hcy (1, 3, 5, 8, and 10 mmol/L) for 24 h to evaluate the effects of HCY on the Bax, Caspase-3, Bcl-2, and Caspase-9 expressions in PC12 cells. Bax, Caspase-3, Bcl-2, and Caspase-8 protein expression levels were measured using Western blot analysis. As shown in Fig. 3, Hcy increased Bax, Caspase-3, and Caspase-8 expressions and attenuated Bcl-2 expression in a concentration-dependent manner. The Hcy concentrations of as low as 5 mmol/L effectively increased Bax, Caspase-3, and Caspase-8 expression and attenuated Bcl-2 expression in PC12 cells.

Naringenin decreased Hcy-induced PC12 cell apoptosis

The PC12 cells were incubated with various concentrations of Hcy (1, 3, 5, 8, and 10 mmol/L) for 24 h to investigate the effects of Hcy on PC12

cell apoptosis, which was measured using flow cytometry. As shown in Fig. 4, PC12 cell apoptosis was significantly increased after Hcy administration for 24 h in a concentration-dependent manner. The effects of naringenin on Hcy-induced PC12 cell apoptosis were further evaluated by incubating the cells with Hcy (5 mmol/L) and various concentrations of naringenin (25, 50, 75, 100, and 150 μM) for 24 h. The naringenin concentrations of as low as 50 μM decreased Hcy-induced PC12 cell apoptosis (Fig. 4).

Naringenin increased Hcy-induced PC12 cell activity and proliferation

PC12 cells were incubated with Hcy (5 mmol/L) and various concentrations of naringenin (25, 50, 75,100, and 150 μM) for 24 h to analyze the

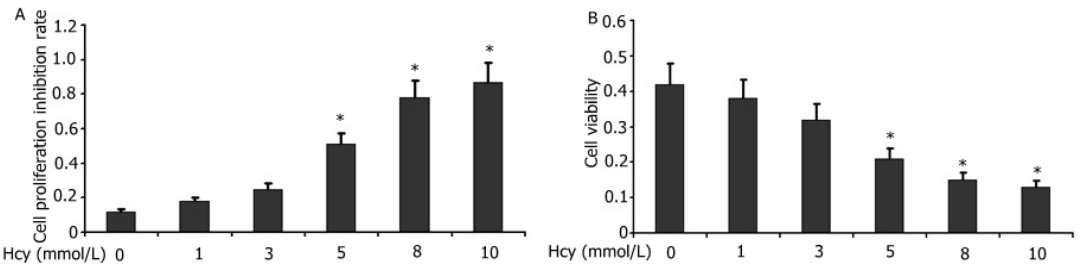


Fig. 1. *Effects of Hcy on PC12 cell activity and proliferation. After the PC12 cells were incubated with various concentrations of Hcy (1, 3, 5, 8, and 10 mmol/L) for 24 h, PC12 cell viability and proliferation inhibition rate were measured using CCK-8 and MTT, respectively. The data from three independent experiments are presented as mean ± SEM. *P < 0.05* vs *the control group.*

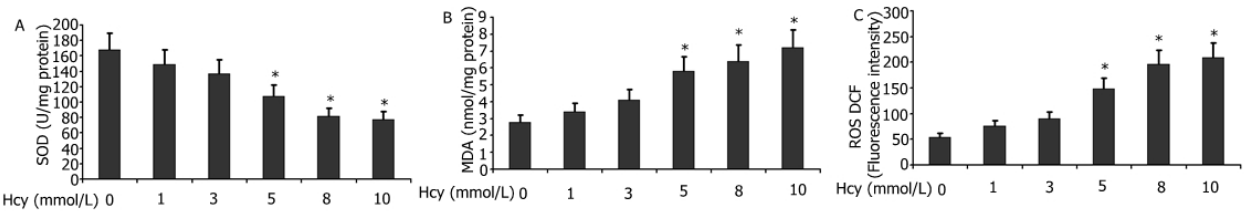


Fig. 2. *Effects of Hcy on PC12 cell oxidative stress. After the PC12 cells were incubated with various concentrations of Hcy (1, 3, 5, 8, and 10 mmol/L) for 24 h, the SOD activity, levels of MDA, and mitochondrial function were determined. The data from three independent experiments are presented as mean ± SEM. *P < 0.05* vs *the control group.*

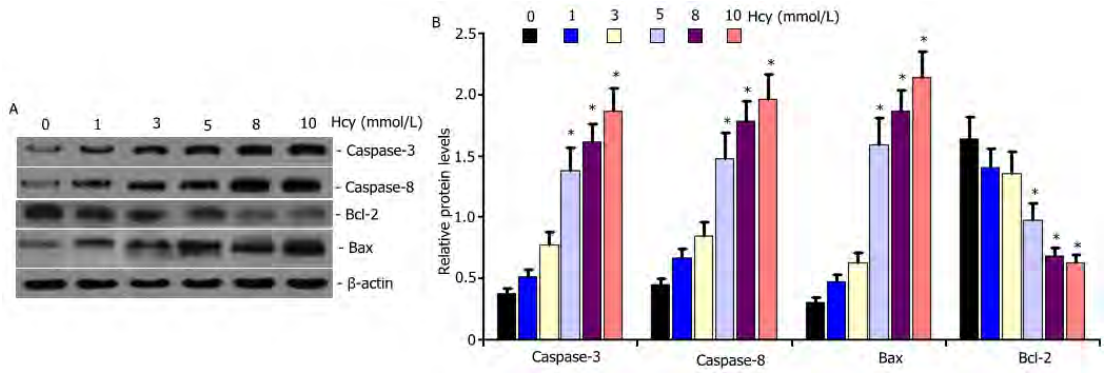


Fig. 3. *Effects of Hcy on Bax, Caspase-3, Caspase-8, and Bcl-2 expressions in PC12 cells. After the PC12 cells were incubated with various concentrations of HCY (1, 3, 5, 8, 10 mmol/L) for 24 h, the Bax, Caspase-3, Caspase-8, and Bcl-2 expressions were measured using Western blot. The data from three independent experiments are presented as mean ± SEM. *P < 0.05* vs *the control group.*

effects of naringenin on Hcy-induced PC12 cell viability and proliferation. PC12 cell viability and proliferation inhibition rate were determined using CCK-8 and MTT assay, respectively. As shown in Fig. 5, naringenin (as low as 50 μM) enhanced PC12 cell viability and decreased the proliferation inhibition rate in a concentration-dependent manner.

Naringenin decreased Hcy-induced PC12 cell oxidative stress

PC12 cells were incubated with Hcy (5 mmol/L) and various concentrations of naringenin (25, 50, 75, 100, and 150 μM) for 24 h to investigate the effects of naringenin on Hcy-induced PC12 cell oxidative stress. The SOD activity and levels of ROS and MDA were determined. As shown in Fig. 6, the ROS and MDA levels were significantly decreased, whereas the SOD activity markedly increased after naringenin administration (as low as 50 mmol/L) for 24 h in a concentration-dependent manner.

Naringenin increased SOD1 protein expression and attenuated miR-224-3p expression in Hcy-induced PC12 cells

PC12 cells were incubated with various concentrations of Hcy (1, 3, 5, 8, and 10 mmol/L) for 24 h to investigate the effects of Hcy on SOD1 gene and protein expression and miR-224-3p expression. The miR-224-3p expression and SOD1 protein expression were measured using RT-qPCR and Western blot, respectively. As shown in Fig. 7, the miR-224-3p expression was significantly

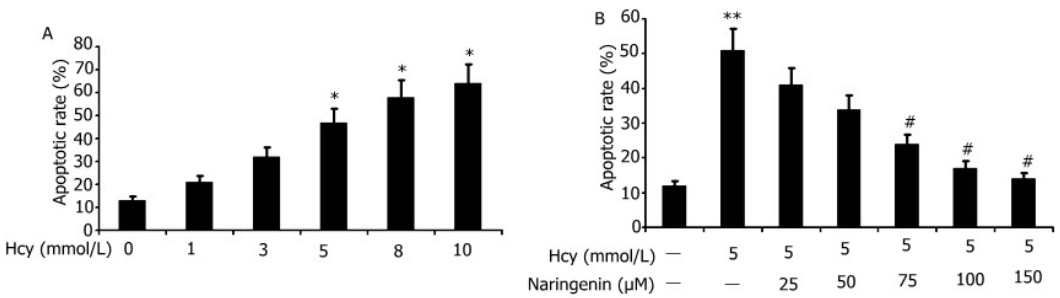


Fig. 4. *Effects of naringenin on Hcy-induced PC12 cell apoptosis. PC12 cells were incubated with various concentrations of Hcy (1, 3, 5, 8, and 10 mmol/L) for 24 h to investigate the effects of Hcy on PC12 cell apoptosis, which was measured using flow cytometry. To further evaluate the effects of naringenin on Hcy-induced PC12 cell apoptosis, we incubated the cells with Hcy (5 mmol/L) and various concentrations of naringenin (25, 50, 75, 100, and 150 μM) for 24 h. The data from three independent experiments are presented as mean ± SEM. *P < 0.05* vs *the control group. #P < 0.05 vs the Hcy (5 mmol/L) group.*

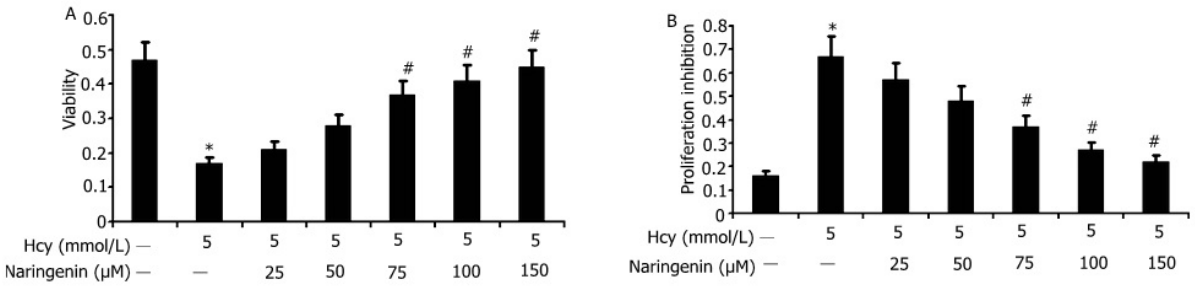


Fig. 5. *Effects of naringenin on Hcy-induced PC12 cell viability and proliferation. The PC12 cells were incubated with Hcy (5 mmol/L) and various concentrations of naringenin (25, 50, 75, 100, and 150 μM) for 24 h. PC12 cell viability and proliferation inhibition rate were determined using CCK-8 and MTT assay, respectively. The data from three independent experiments are presented as mean ± SEM. *P < 0.05* vs *the control group. #P < 0.05* vs *the Hcy (5 mmol/L) group.*

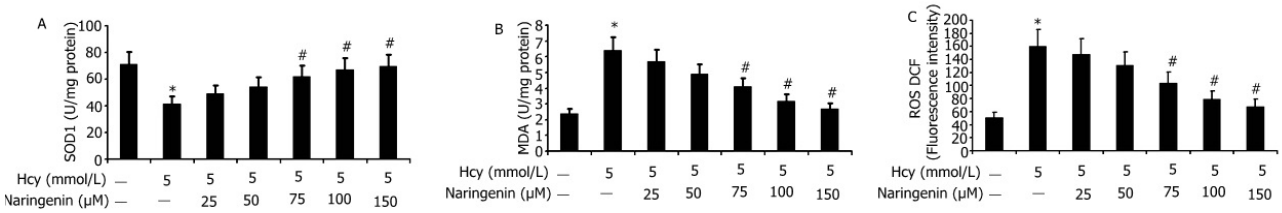


Fig. 6. *Effects of naringenin on Hcy-induced PC12 cell oxidative stress. The PC12 cells were incubated with Hcy (5 mmol/L) and various concentrations of naringenin (25, 50, 75, 100, and 150 μM) for 24 h. The SOD activity and levels of ROS and MDA were determined. The data from three independent experiments are presented as mean ± SEM. *P < 0.05* vs *the control group. #P < 0.05* vs *the Hcy (5 mmol/L) group.*

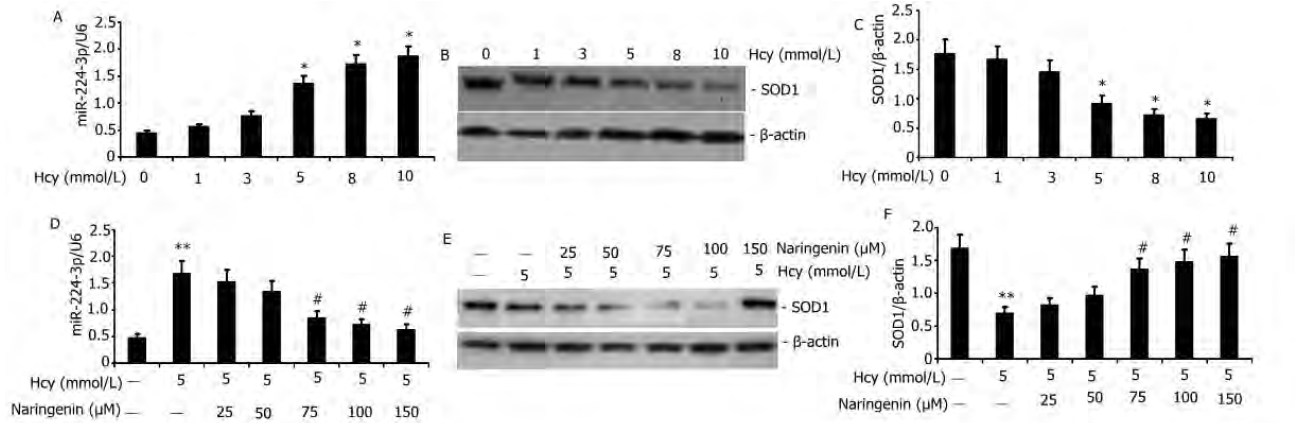


Fig. 7. *Effects of naringenin on SOD1 protein expression and miR-224-3p expression in Hcy-induced PC12 cells. The PC12 cells were incubated with various concentrations of Hcy (1, 3, 5, 8, and 10 mmol/L) for 24 h to investigate the effects of Hcy on SOD1 protein expression and miR-224-3p expression in PC12 cells. To further evaluate the effects of naringenin on SOD1 gene and protein expression and miR-224-3p expression in Hcy-induced PC12 cells, we incubated the cells with Hcy (5 mmol/L) and various concentrations of naringenin (25, 50, 75, 100, and 150 μM) for 24 h. The miR-224-3p expression and SOD1 protein expression were measured using RT-qPCR and Western blot, respectively. The data from three independent experiments are presented as mean ± SEM. *P < 0.05* vs *the control group. #P < 0.05* vs *the Hcy (5 mmol/L) group.*

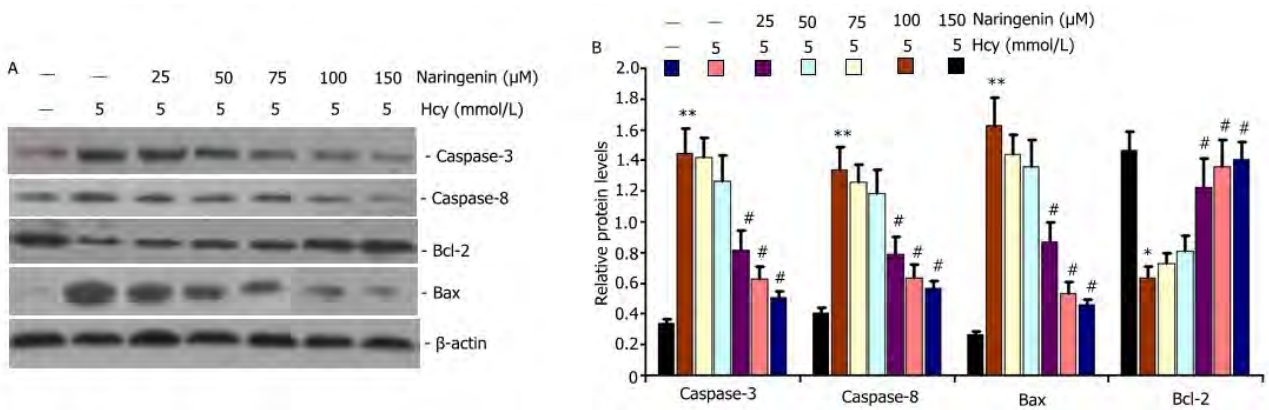


Fig. 8. *Effects of naringenin on Bax, Caspase-3, Caspase-8, and Bcl-2 expressions in Hcy-induced PC12 cells. The PC12 cells were incubated with Hcy (5 mmol/L) and various concentrations of naringenin (25, 50, 75, 100, and 150 μM) for 24 h. The Bax, Caspase-3, Caspase-8, and Bcl-2 expressions were measured using Western blot. The data from three independent experiments are presented as mean ± SEM. **P < 0.01, *P < 0.05 vs the control group. #P < 0.05 vs the Hcy (5 mmol/L) group.*

increased, whereas the SOD1 protein expression was significantly decreased after Hcy administration for 24 h in a concentration-dependent manner. Moreover, PC12 cells were incubated with Hcy (5 mmol/L) and various concentrations of naringenin (25, 50, 75, 100, and 150 μM) for 24 h to further evaluate effects of naringenin on SOD1 gene and protein expression and miR-224-3p expression in Hcy-induced PC12 cells. The miR-224-3p expression and SOD1 protein expression were measured using RT-qPCR and Western blot, respectively. As shown in Fig. 7, the miR-224-3p expression was significantly decreased, whereas the SOD1 protein expression was significantly increased after naringenin administration (as low as 50 μM) for 24 h in a concentration-dependent manner.

Naringenin decreased Bax, Caspase-3, and Caspase-8 expression and enhanced Bcl-2 expression in PC12 cells

The PC12 cells were incubated with Hcy (5 mmol/L) and various concentrations of naringenin (25, 50, 75,100, and 150 μM) for 24 h to evaluate the effects of naringenin on the Bax, Caspase-3, Bcl-2, and Caspase-8 expressions in Hcy-induced PC12 cells. The Bax, Caspase-3, Bcl-2, and Caspase-8 protein expression levels were measured using Western blot analysis. As shown in Fig. 8, naringenin (as low as 5 mmol/L) increased the Bax, Caspase-3, and Caspase-8 expressions and attenuated the Bcl-2 expression in a concentration-dependent manner.

SOD1 is a regulatory target of miR-224-3p

To determine how miR-224-3p mediated Hcy-induced PC12 cell apoptosis, we used TargetScan in predicting likely targets of miR-224-3p and found that SOD1 is an important regulator of Hcy-induced PC12 cell apoptosis. Analysis revealed that the SOD1 mRNA and protein levels were dramatically decreased after miR-224-3p overexpression (Figs. 9 A–B and D–E). To validate the interaction between miR-224-3p and SOD1, we constructed a wild-type and mutant SOD1 for dual luciferase reporter assay (Figs. 9 C and F). As hypothesized, miR-224-3p became bound to the wild-type SOD1 but not to the mutants (Fig. 9D).

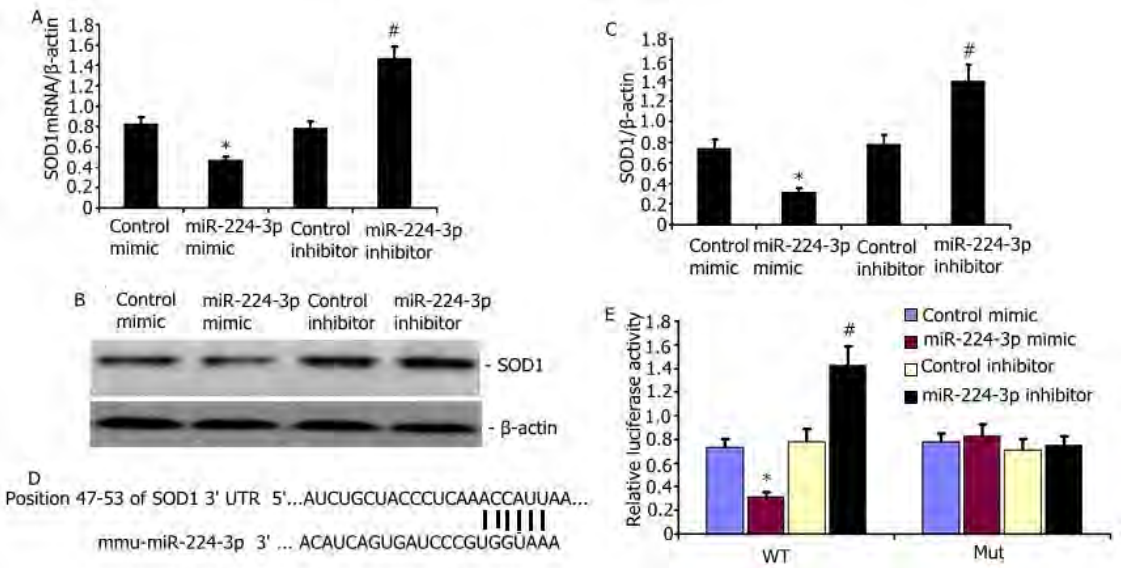


Fig. 9. *SOD1 is a downstream target of miR-224-3p.* ***A–B****) SOD1 was decreased in Hcy-induced PC12 cells with miR-224-3p overexpression relative to the empty vector control (P < 0.05). SOD1 was significantly increased in cells with miR-224-3p downregulation.* ***C–D****) The mRNA levels of SOD1 in Hcy-induced PC12 cells decreased after miR-224-3p overexpression (P < 0.05). The levels were enhanced after miR-224-3p upregulation (P < 0.05).* ***E****) miR-224-3p was bound to the 3'-UTR regions of SOD1. Binding was interrupted in mutant SOD1.* ***F****) Dual luciferase reporter assay indicated that miR-224-3p mimic was bound to the 3'-UTR region of wild-type SOD1 but not to the SOD1 mutants (P < 0.05).*

DISCUSSION

Recent studies showed that Hcy is closely related to a variety of neurological diseases and can cause oxidative stress injury, induce neurotoxicity, and promote apoptosis [4-6]. Naringenin has powerful antioxidant, anti-inflammatory, antimutation, and anti-ionizing activities [12–17]. In the present study, we studied the mechanism of Hcy-induced cellular oxidative stress and explored its protective effect on cell damage.

Xu et al. found that naringenin can increase the phosphorylation of Akt and promote the release of brain-derived neurotrophic factors by upregulating the Erk1/2 signaling pathway in hippocampal cells, thereby reducing the death of glutamate-induced dendritic cells (20). Lou H. et al. found that naringenin can reduce 6-OHDA-induced cell death and reduce behavioral changes by reducing the ROS content and increasing the number of tyrosine hydroxylase positive cells in the substantia nigra (21, 22). Muthaiah VPK et al. found that naringenin can protect neuro 2A cells by reducing the ROS content in neuro 2A cells exposed to menavir (23). Sachdeva AK et al. found that in the streptozotocin-induced AD model, naringenin could increase the activity of mitochondrial complex enzymes (I, II, and IV) in the cerebral cortex and hippocampus and increase the redox capacity, thereby reducing the damage caused by streptozotocin and improving the learning and memory functions of the AD model (24). In the present study, naringenin reduced the MDA and ROS activities and oxidative stress of PC12 cells induced by Hcy and increased the activity of PC12 cells.

SOD is a type of enzyme commonly found in animals, plants, and microorganisms and is the first line of defense in biological antioxidant systems. It is a type of metalloenzyme and is the only antioxidant enzyme in the body that can specifically remove oxygen free radicals. SODs are mainly divided into three types, namely, Cu/Zn-SOD (SOD1), Mn-SOD (SOD2), and Fe-SOD (SOD3). The internal and external compounds in the human body can generate oxygen free radicals under the action of various enzymes. Oxygen free radicals are converted to H_2O_2 under the catalysis of SOD. The CAT and peroxidase in the body immediately decompose H_2O_2 into completely harmless water. When the organism does not have enough SOD, active oxygen accumulates in large quantities; if not removed in time, it causes oxidative and body damage, including base mutation, DNA strand breaks, membrane lipid peroxidation, protein damage, accelerated aging, and diseases (25–28). In addition to its antioxidant effects, SOD also has anti-inflammatory (25), antitumor (26), and immunity regulation (27) functions; plays a role in killing viruses for immune defenses (28); balances the oxidation and antioxidant effects of the body; and protects cells from damage (29). In the present study, Hcy inhibited the expression of SOD1 mRNA and protein in PC12 cells, reduced the activity of SOD1, and increased the ROS and MDA activities and PC12 cell apoptosis. Treatment with naringenin could increase the expressions of mRNA and protein

Table I. *Primer sequences for RT-PCR analysis.*

Gene	Primers	Product
miR-224-3p	F-5'-CTGCAATCATTCACGGACAAC-3'	154
	R-5'-GTGTCGTCGAGTCGGCAATTC-3'	
U6	F-5'-CTCGCTTCGGCAGCACA-3'	192
	R-5'-AACGCTTCACGAATTTGCGT-3'	
SOD1mRNA	R-5'-AACGCTTCACGAATTTGCGT-3'	220
	R-5'-GTTTACTGCGCAATCCCAAT-3'	
β-actin	F-5'CGGGAAATCGTGAT-3'	167
	R-5'- GAACTTTGGGGGATGCTCGC-3'	

of SOD1 in PC12 cells and the SOD1 activity, reduce the activity of ROS and MDA, and improve Hcy-induced PC12 cell apoptosis.

Apoptosis is the body's self-regulation mechanism that plays an important role in cell maturation and differentiation. Oxidative stress can easily induce neuronal apoptosis in various environments. Apoptosis is a kind of programmed death, and bax, bcl-2, caspase-3, and caspase-8 are all apoptosis-regulating genes (30). Caspase-3 activates related signaling pathways by cleaving downstream effector molecules, leading to apoptosis. As an anti/pro-apoptotic gene, bcl-2/bax can be used as an upstream regulatory gene for caspase-3 and caspase-8. The overexpression of bax can activate downstream caspase-3 and caspase-8 proteases and mediate cell survival or death, whereas bcl-2 can form a dimer with bax to inhibit bax activity (31, 32). In the present study, when the PC12 cells were cultured for 24 h with Hcy, their oxidative stress; cell apoptosis; and bax, caspase-3, and caspase-8 expressions increased; by contrast, bcl-2 expression decreased. The administration of naringenin reduced the oxidative stress of the PC12 cells. The expressions of bax, caspase-3, and caspase-8 in the PC12 cells were reduced by treatment with naringenin, whereas the expression of bcl-2 was increased, thereby improving Hcy-induced PC12 cell apoptosis.

MiR-224 is located at the X chromosome of human beings. A large number of studies confirmed that miR-224 is upregulated in liver, breast, and pancreatic cancers and that it can regulate cell proliferation, apoptosis, migration, and invasion (33). A study found that miR-224 is highly expressed in and selectively regulates the autophagy of tumor cells by mediating the autophagosome degradation system (34). Another study found that hepatitis B virus-related hepatocellular carcinoma has abnormal cell autophagy and that miR-224 can reduce the expression of the target gene Smad4, thereby increasing cell migration and tumor formation (34). Moreover, miR-224-3p can target hypoxia-induced autophagy-related genes in human glioblastoma cells (35). MiR-224-3p affects the autophagy activity of glioblastoma cells, and its overexpression can inhibit hypoxia-induced autophagy-related protein expression in glioblastoma cells (35). Another research found that miR-224-3p can increase the apoptosis of glioblastoma cells induced by hypoxia (35). In the present study, Hcy increased the expression of miR-224-3p, inhibited the mRNA and protein expressions of SOD1, promoted oxidative stress in PC12 cells, and increased apoptosis in PC12 cells. By contrast, naringenin treatment reduced the expression of miR-224-3p, increased the expressions of SOD1 mRNA and protein, reduced Hcy-induced oxidative stress, and significantly reduced PC12 cell apoptosis.

We aimed to observe whether or not naringenin can regulate the expression of SOD1 in PC12 cells and regulate the apoptosis of these cells through miR-224-3p. Using the TargetScan database, we predicted that SOD1 is the regulatory target of miR-224-3p. We increased the expression of miR-224-3p and decreased the expressions of SOD1 mRNA and protein in the PC12 cells by increasing miR-224-3p mimic and inhibitor to transfect Hcy-induced PC12 cells. The dual luciferase reporter assay results suggested that SOD1 is a regulatory target for miR-224-3p, which regulates the oxidative stress of PC12 cells induced by Hcy through the expressions of SOD1 mRNA and protein and further regulates cell apoptosis. We further investigated the correlation between miR-224-3p and SOD1 mRNA and protein in regulating HcyA-induced PC12 cell apoptosis and found that miR-224-3p and SOD1 mRNA are negatively correlated with protein expression.

Therefore, Hcy could increase oxidative stress and the expression of miR-224-3p in PC12 cells to promote apoptosis. This study clearly demonstrated that naringenin could reduce the expression of miR-224-3p in Hcy-induced PC12 cells, increase the expressions of SOD1 mRNA and protein, reduce apoptosis and the oxidative stress of Hcy-induced PC12 cells, and increase the activity and survival rate of PC12 cells. SOD1 was found to be a regulatory target of miR-224-3p. The mRNA of miR-224-3p and SOD1 was inversely related to protein expression.

ACKNOWLEDGEMENTS

We thank Enpapers for its linguistic assistance

during the preparation of this manuscript.

This study received a Research Grant [Grant No. 2017FE468(-032)] from Yunnan Applied Basic Research Project-Union Foundation.

REFERENCES

1. Guzmán DC, Brizuela NO, Herrera MO, Peraza AV, Mejía GB, Olguín HJ, Jiménez FT. Sildenafil alters biogenic amines and increases oxidative damage in brain regions of insulin-hypoglycemic rats. Acta Pharm 2020; 70(1):121-27.
2. Scotton E, Colombo R, Reis JC, et al. BDNF prevents central oxidative damage in a chronic unpredictable mild stress model: The possible role of PRDX-1 in anhedonic behavior. Behav Brain Res 2020; 378:112245
3. Murray LK, Jadavji NM. The role of one-carbon metabolism and homocysteine in Parkinson's disease onset, pathology and mechanisms. Nutr Res Rev 2019; 32 (2):218-30.
4. Li J, Zhou F, Wu FX. Relationship between homocysteine level and prognosis of elderly patients with acute ischemic stroke treated by thrombolysis with recombinant tissue plasminogen activator. World J Clin Cases 2019; 7(22):3751-56.
5. Kalvala AK, Yerra VG, Kumar A . LONP1 induction by SRT1720 attenuates mitochondrial dysfunction against high glucose induced neurotoxicity in PC12 cells. Toxicol In Vitro 2020; 62:104695.
6. Liu B, Cao W, Xue J. LncRNA ANRIL protects against oxygen and glucose deprivation (OGD)-induced injury in PC-12 cells: potential role in ischaemic stroke. Artif Cells Nanomed Biotechnol 2019; 47(1):1384-95
7. Wang CY, Zou W, Liang XY, et al . Hydrogen sulfide prevents homocysteine-induced endoplasmic reticulum stress in PC12 cells by upregulating SIRT-1. Mol Med Rep 2017; 16 (3):3587-93.
8. You Q, Gong Q, Han YQ, Pi R, Du YJ, Dong SZ. Role of miR-124 in the regulation of retinoic acid-induced Neuro-2A cell differentiation. Neural Regen Res 2020; 15 (6):1133-39.
9. Wang Z, Zheng Y, Zheng M, Zhong J, Ma F, Zhou B, Zhu J. Neurogenic Niche Conversion Strategy Induces Migration and functional neuronal differentiation of Neural Precursor Cells following Brain Injury. Stem Cells Dev 2019; 12(6):1134-47.
10. Jaber VR, Zhao Y, Sharfman NM, Li W, Lukiw WJ. Addressing Alzheimer's Disease (AD) Neuropathology Using Anti-microRNA (AM) Strategies. Mol Neurobiol 2019; 56 (12):8101-8.
11. Amankwatia EB, Chakravarty P, Carey FA, et al. MicroRNA-224 is associated with colorectal cancer progression and response to 5-fluorouracil-based chemotherapy by KRAS-dependent and -independent mechanisms. Br J Cancer 2015; (112):1480-90.
12. Rebello CJ, Beyl RA, Lertora JJL, et al. Safety and pharmacokinetics of naringenin: A randomized, controlled, single-ascending-dose clinical trial. Diabetes Obes Metab 2020; 22(1):91-98.
13. Jin Y, Wang H. Naringenin inhibit the hydrogen peroxide-induced SH-SY5Y Cells Injury Through Nrf2/HO-1 Pathway. Neurotox Res 2019; 36(4):796-805.
14. Escribano-Ferrer E, Queralt Regué J, Garcia-Sala X, Boix Montañés A, Lamuela-Raventos RM. In vivo anti-inflammatory and antiallergic activity of pure naringenin, naringenin chalcone, and quercetin in mice. J Nat Prod 2019; 82 (2):177-82
15. Nguyen-Ngo C, Willcox JC, Lappas M. Anti-diabetic, anti-inflammatory, and anti-oxidant effects of naringenin in an in vitro human model and an in vivo murine model of gestational diabetes mellitus. Mol Nutr Food Res 2019; 63(19): e1900224.
16. Fouache A, Zabaiou N, De Joussineau C, et al. Flavonoids differentially modulate liver X receptors activity-structure-function relationship analysis. J Steroid Biochem Mol Biol 2019; 190:173-82
17. Parashar P, Tripathi CB, Arya M, et al. Biotinylated naringenin intensified anticancer effect of gefitinib in urethane-induced lung cancer in rats: favourable modulation of apoptotic regulators and serum metabolomics. Artif Cells Nanomed Biotechnol 2018; 46 (supl3):S598-S610.
18. Cheng J, Li F, Sun X, Liu S, et al. Low-dose alcohol ameliorated homocysteine-induced anxiety-related behavior via attenuating oxidative stress in mice. Neurosci Lett 2020; 714:134568.
19. Jin Y, Wang H. Naringenin Inhibit the Hydrogen Peroxide-Induced SH-SY5Y Cells Injury Through Nrf2/HO-1 Pathway. Neurotox Res 2019; 36(4):796-805.

20. Xu XH, Ma CM, Han YZ, et al. Protective effect of naringenin on glutamate-induced neurotoxicity in cultured hippocampal cells. Arch Biol Sci 2015; 67:639-46
21. Zbarsky V, Datla KP, Parkar S, Rain DK, Aruoma OI, Dexter DT. Neuroprotective properties of the natural phenolic antioxidants curcumin and naringenin but not quercetin and fisetin in a 6-OHDA model of Parkinson's disease. Free Radic Res, 2005; 39(10):1119-25.
22. Lou HY, Jing XJ, Wei X, Shi HY, Ren DM, Zhang XM. Naringenin protects against 6-OHDA-induced neurotoxicity via activation of the Nrf2/ARE signaling pathway. Neuropharmacology 2014; 79:380-88.
23. Muthaiah VPK, Venkitasamy L, Michael FM, Kirubhanand C, Sankar V. Neuroprotective role of naringenin on carbaryl induced neurotoxicity in mouse neuroblastoma cells. J Pharmacol Pharmacother 2013; 4(3):192.
24. Sachdeva AK, Kuhad A, Chopra K. Naringin ameliorates memory deficits in experimental paradigm of Alzheimer's disease by attenuating mitochondrial dysfunction. Pharmacol Biochem Behav 2014; 127:101-10.
25. Chen Y, Yang B, Ross RP, et al. Orally Administered CLA. Ameliorates DSS-induced colitis in mice via intestinal barrier improvement, oxidative stress reduction, and inflammatory cytokine and gut microbiota modulation. J Agric Food Chem 2019; 67(48):13282-98.
26. Sharma P, Kumar S. Metformin inhibits human breast cancer cell growth by promoting apoptosis via a ROS-independent pathway involving mitochondrial dysfunction: pivotal role of superoxide dismutase (SOD). Cell Oncol (Dordr) 2018; 41(6):637-50.
27. Aminzadeh A, Salarinejad A. Citicoline protects against lead-induced oxidative injury in neuronal PC12 cells. Biochem Cell Biol 2019; 97(6):715-21.
28. Wang MM, Lu M, Zhang CL, et al. Oxidative stress modulates the expression of toll-like receptor 3 during respiratory syncytial virus infection in human lung epithelial A549 cells. Mol Med Rep 2018; 18(2):1867-77.
29. Kang J, Sun Y, Deng Y, et al . Autophagy-endoplasmic reticulum stress inhibition mechanism of superoxide dismutase in the formation of calcium oxalate kidney stones. Biomed Pharmacother 2020; 121:109649.
30. Jiao C, Chen W, Tan X, et al. Ganoderma lucidum spore oil induces apoptosis of breast cancer cells in vitro and in vivo by activating caspase-3 and caspase-9. J Ethnopharmacol 2020; 247:112256.
31. Escobar ML, Echeverria OM, Palacios-Martínez S, Juárez-Chavero S, Sánchez-Sánchez L, Vázquez-Nin GH . Beclin 1 Interacts With Active Caspase-3 and Bax in Oocytes From Atretic Follicles in the Rat Ovary. J Histochem Cytochem 2019; 67(12):873-89.
32. Joseph L, Srinivasan KK. Triacontanoic ester of 5''-hydroxyjustisolin: Tumour suppressive role in cervical cancer via Bcl-2, BAX and caspase-3 mediated signalling. Toxicol Rep 2019; 6:1198-205.
33. Chen W, Fan XM, Mao L, Zhang JY, Li J, Wu JZ, Tang JH. MicroRNA-224: as a potential target for miR-based therapy of cancer. Tumour Biol 2015; 36:6645-52.
34. Lan SH, Wu SY, Zuchini R, et al. Autophagy suppresses tumorigenesis of hepatitis B virus-associated hepatocellular carcinoma through degradation of microRNA-224. Hepatology 2014; 59:505-17.
35. Guo X, Xue H, Guo XF, Guo XF. MiR224-3p inhibits hypoxia-induced autophagy by targeting autophagy-related genes in human glioblastoma cells. Oncotarget 2015; 6:41620-37.

PROPOFOL RELIEVES OXIDATIVE STRESS RESPONSE OF CEREBRAL ISCHEMIA-REPERFUSION INJURY THROUGH SIRT1 SIGNALING PATHWAY

X.-B. LIU[1*], H. XIA[2*], G. WANG[1], W. ZHANG[1], Y. HU[1] and J. ZHANG[3]

[1]Department of Anesthesiology, Beijing Jishuitan Hospital, Beijing, China; [2]Department of Anesthesiology, Dongfang Hospital Beijing University of Chinese Medicine, Beijing, China; [3]Department of Anesthesiology, Dongzhimen Hospital Beijing University of Chinese Medicine, Beijing, China

Received February 3, 2020 – Accepted March 27, 2020

[*]These Authors contributed equally to this work

This study explored the effects of propofol on the cognitive function and expressions of superoxide dismutase (SOD) and malondialdehyde (MDA) through the silent information regulator 1 (SIRT1) signaling pathway during cerebral ischemia-reperfusion (I/R) injury. C57BL/6J mice were used and divided into Sham group, I/R group (I/R model established *via* ligation of artery) and Treated group (peritoneal injection of propofol) according to different treatments. The memory ability of mice was evaluated using Morris water maze test, and the motor coordination was assessed using Rota rod test and oblique beam walking test. The brain tissues were prepared into embedded sections, and then the pathological changes in brain neurons were detected *via* hematoxylin-eosin (HE) staining, and the changes in apoptosis of brain tissues were detected *via* flow cytometry. Moreover, after the mice were anesthetized and sacrificed, the brain tissues were isolated and whole blood was collected. Then the changes in SIRT1 protein were determined using Western blotting, and the changes in MDA and SOD activity were determined through biochemical assays. The results of Morris water maze test and elevated plus-maze test revealed that transfer latency time (TLT) was significantly prolonged, and escape latency time (ELT) was significantly shortened in the I/R group compared with those in Sham group ($^{*}P<0.05$), indicating memory impairment after cerebral I/R injury. TLT was shortened, and ELT was significantly prolonged in the Treated group compared with those in I/R group ($^{\#}P<0.05$). In Rota rod test, the falling down time was obviously shorter in the I/R group than in the Sham group ($^{*}P<0.05$), while it was obviously longer in the Treated group than that in the I/R group ($^{\#}P<0.05$). Compared with the Sham group, the I/R group had neurological impairment, manifested as the evident increase in motor performance score ($^{*}P<0.05$), and the motor performance score in the Treated group was evidently lower than that in the I/R group ($^{\#}P<0.05$). The apoptosis was markedly enhanced in the I/R group ($^{*}P<0.05$), while it was markedly weakened in the Treated group ($^{\#}P<0.05$) compared with that in the Sham group. In addition, the results of Western blotting showed that the expression of SIRT1 was evidently higher in I the /R group than that in the Sham group, while it evidently declined after treatment with propofol ($^{\#}P<0.05$).

Key words: propofol; memory ability; motor performance; MDA; SOD; SIRT1

Corresponding Author:
Jie Zhang, MD
Department of Anesthesiology, Dongzhimen Hospital,
Beijing University of Chinese Medicine Hai Yun Cang on the 5th Zip,
Dongcheng District, Beijing 100700, China
Tel.: 86013810300482
e-mail: jiezhang19850113@163.com

0393-974X (2020)
Copyright © by BIOLIFE, s.a.s.
This publication and/or article is for individual use only and may not be further reproduced without written permission from the copyright holder.
Unauthorized reproduction may result in financial and other penalties
DISCLOSURE: ALL AUTHORS REPORT NO CONFLICTS OF INTEREST RELEVANT TO THIS ARTICLE.

The I/R group had remarkably higher MDA activity and remarkably lower SOD activity than the Sham group ($^{*}P<0.05$), while the Treated group had remarkably lower MDA activity and remarkably higher SOD activity than the I/R group ($^{\#}P<0.05$). Propofol can alleviate cerebral I/R injury through inhibiting the SIRT1 pathway, and also relieve the oxidative stress response of I/R injury.

Ischemia-reperfusion (I/R) injury is a major health problem occurring after stroke, cardiac arrest and resuscitation, and organ transplantation (1). Although several prevention strategies for I/R injury have been discovered in experimental studies, there are still no effective protective therapies for clinical I/R injury (2). Oxidative stress caused by mitochondrial dysfunction during reperfusion is a key pathogenic mechanism of cerebral I/R injury (3, 4). In a recent study, Chouchani et al. (5) proposed a new mechanical concept that could inspire novel therapeutic methods. They found that succinic acid is an intermediate molecule in the mitochondrial citric acid cycle and its level constantly rises in ischemic tissues, whose accumulation during I/R induces the production of reactive oxygen species (ROS) (6). It is also reported that the succinate dehydrogenase (SDH) inhibitors can reduce succinic acid accumulation during ischemia, and decrease tissue damage in the brain and heart after I/R injury (5-7). Propofol is an intravenous anesthetic widely used to reduce cerebral I/R injury and apoptosis (8-13). In a recent study, it was found that propofol can alleviate mitochondrial dysfunction *via* reducing the production of ROS in mitochondria (14). In another study, propofol can inhibit the activity of SDH in the cerebral cortex of immature pigs (15). Therefore, this study aims to evaluate the protective mechanism of propofol in cerebral I/R injury and its effects on the activity of oxidative stress markers superoxide dismutase (SOD) and malondialdehyde (MDA).

MATERIALS AND METHODS

Thirty male C57BL/6 mice (provided by the Laboratory Animal Center in our institute) of SPF grade, and 8 weeks old, weighing 18-22 g, were selected for this study. The following materials were used: sodium dodecyl sulfate polyacrylamide gel electrophoresis (SDS-PAGE) loading buffer (Beyotime, Shanghai, China), silent information regulator 1 (SIRT1), phosphorylated SIRT1 and GAPDH primary antibody (Abcam, Cambridge, MA, USA), horseradish peroxidase (HRP)-labeled secondary antibody (Santa Cruz Biotechnology, Santa Cruz, CA, USA), propofol (Kunming Nanjiang Pharmaceutical, Kunming, China), bicinchoninic acid (BCA) kit (Applygen, Beijing, China), and apoptosis assay kit (BD, Franklin Lakes, NJ, USA).

Mice were housed in a temperature controlled room (21±2°C) on a 12/12-h light/dark cycle (lights on at 06:00). All mice had free access to water and food. Then the mice were randomly selected and divided into a Sham group (no I/R, n=10), an I/R group (I/R model established *via* operation, n=10) and a Treated group (peritoneal injection of propofol, n=10). This study was approved by the Animal Ethics Committee of Beijing University of Chinese Medicine Animal Center (NO2018-002-03).

Mouse model of cerebral I/R

The mice were first anesthetized *via* intraperitoneal injection of chloral hydrate (400 mg/kg) according to the method of Himori et al. (16), followed by cerebral ischemia surgery (17). The ventral throat was cut along the midline, and it was observed that the carotid arteries on the left and right sides were located at and separated from adjacent tissues and vagus nerves. The cotton thread was passed under each carotid artery, and its end was pulled under the same strength to induce global cerebral ischemia for 17 min. After that, the thread was released for reperfusion for 24 h. Then the skin was sutured and disinfected. For reperfusion intervention, propofol (30 mg/kg) (i.e., pPoCo) was intraperitoneally injected for 5 min at 24 h before reperfusion, so that the drugs could circulate at the beginning of reperfusion. In the Sham group and I/R group, the same volume of normal saline was injected only.

Morris water maze (MWM) test

The test was performed for 4 days (4 times a day,

5 min/time) for each mouse, with relaxation between every 2 tests. Every day, the initial position of training was changed, and Q4 was the target quadrant in all tests. On the 4th day, escape latency time (ELT) (the time required for finding the hidden platform) was recorded to indicate the memory and learning ability, after which I/R injury was induced. On the 5th day, all mice explored the MWM without an escape platform for 120 s. The residence time in other quadrants besides Q4 was recorded, and the recovery time (the time of finding the missing platform in Q4) was also recorded. Moreover, the short-term memory was evaluated using elevated plus-maze (EPM) test, in which the mice were placed at the end of the open arm of the maze away from the central platform and passed through it. The first EPM test was performed on the 2nd day, the mice were re-exposed to EPM on the 3rd and 4th days, and the transfer latency time (TLT) (the time required for rodents coming from the open arm into the closed arm) was recorded. At 4 d ays after the 3rd training, mice had I/R injury. The memory and learning ability was assessed from the 4th day, and memory retrieval was detected from the 5th day.

Rota rod test

The Rota rod instrument helps evaluate the grip ability on the Rota rod, and it is able to assess the animal's motor coordination. The changes in falling down time indicate the motor coordination compared with control animals. On the 4th day, the test was performed for mice prior to I/R injury, and finally those that could remain on the Rota rod for 5 min were selected. At 5 d after I/R injury, the Rota rod test was conducted repeatedly.

Evaluation of motor coordination of fore and rear limbs using oblique beam walking test

The changes in coordination are expressed as grade 0-4. On the 4th day, the test was performed for mice prior to I/R injury, and finally those that could move easily on the beam (grade 0) were selected. At 5 days after I/R injury, the test was conducted repeatedly.

Western blotting

The brain samples were collected from the cortex around the contusion at 1 and 3 days after injury. After the blood was washed away, the cell lysis buffer was added. BCA method was used to detect the protein concentration of the sample according to the instruction. Then 60 μg of protein samples were separated *via* SDS-PAGE, transferred onto a membrane, sealed with blocking buffer (prepared by buffer A and B at 1:1) for 10 min, and incubated with the primary antibody for 15 h and with the secondary antibody for 1 h on the next day. Finally, the membrane was scanned.

Hematoxylin-eosin (HE) staining

After the mice were anesthetized and sacrificed, the head was quickly removed, and the brain tissues were washed and cut into an appropriate size of the tissue block. Then the block was fixed with fixative for 24 h, embedded in paraffin, sliced into sections of similar thickness, and placed in an oven at 65°C overnight. After deparaffinization and dehydration, the sections were stained with hematoxylin, rinsed with running water, dehydrated with alcohol for 1 h, stained again with eosin, decolorized with running water and alcohol, transparentized with xylene and sealed.

Determination of MDA and SOD activity

After the mice were anesthetized and sacrificed, the blood was collected and centrifuged at 3000 rpm for 10 min to obtain plasma. Then the plasma was detected using the automatic biochemical instrument and corresponding mixed solution on the machine.

Detection of brain cell apoptosis using flow cytometry

At 3 days after injury, the diseased hemisphere was harvested and homogenized using a 40 μm nylon mesh. The single cells were isolated using 5 mL of 30% Percoll solution (700 × g, 5 min). After rinsing with phosphate buffered saline, the cells were incubated with the dye in apoptosis assay kit according to the manufacturer's instructions, and detected using a flow cytometer.

Statistical analysis

Statistical Product and Service Solutions (SPSS) 17.0 (SPSS Inc., Chicago, IL, USA) software was used for statistics of experimental results. Comparison between multiple groups was carried

out using One-way ANOVA test followed by Post Hoc Test (Least Significant Difference). $P<0.05$ suggested the statistically significant difference.

RESULTS

Effect of propofol on memory of mice with cerebral I/R injury

The short-term memory impairment of mice with cerebral I/R injury was evaluated using the MWM and EPM tests. It was found that TLT was significantly prolonged, and ELT was significantly shortened in the I/R group compared with those in the Sham group ($^{*}P<0.05$), indicating the memory impairment after cerebral I/R injury. TLT was shortened, and ELT was significantly prolonged in the Treated group compared with those in the I/R group ($^{\#}P<0.05$) (Fig. 1).

Effect of propofol on motor performance of mice with cerebral I/R injury

The motor coordination of mice was assessed using the falling down time and motor performance score detected in the Rota rod test and oblique beam walking test. The results revealed that the falling down time was obviously shorter and the motor performance score was obviously higher in the I/R group than those in the Sham group ($^{*}P<0.05$), while the falling down time was obviously longer and the motor performance score was obviously lower in Treated group than those in I/R group ($^{\#}P<0.05$) (Fig. 2).

Propofol could alleviate apoptosis of brain tissues in cerebral I/R injury

The brain tissues were separated and the neuronal apoptosis was detected *via* flow cytometry. The results showed that the apoptosis ratio was below 6% in the Sham group and above 70% in the I/R group. It was found that the proportion of apoptotic cells was markedly increased in the I/R group ($^{*}P<0.05$), while it was markedly lower in the Treated group (<20%) than that in the I/R group ($^{\#}P<0.05$), suggesting that propofol can alleviate neuronal apoptosis caused by I/R (Fig. 3).

Pathological changes in mice with cerebral I/R injury

The stained brain tissues were observed under the microscope. Microscopically, the neurons in the Sham group were uniform in size and arranged regularly, and the brain tissues had normal morphology without vacuolization. In the I/R group, the neurons had irregular morphology with nuclear shrinkage, massive neutrophil infiltration could be seen under the microscope, the inflammatory response was obvious, and there were multiple lesions, with irregular cell arrangement. In the Treated group, neurons mostly had normal morphology, neutrophils could be seen under the microscope, and the number of lesions was evidently smaller than that in the I/R group (Fig. 4).

Effects of propofol on SIRT1 protein expression and SOD and MDA activity in mice with cerebral I/R injury

The changes in SIRT1 protein expression were determined using Western blotting, and the changes in MDA and SOD activity were determined through biochemical assays. The results manifested that the oxidative stress response was obvious in the I/R group, and the I/R group had remarkably higher SIRT1 protein expression than the Sham group, inhibited SOD activity and remarkably enhanced MDA activity ($^{*}P<0.05$). After propofol Treatment, the oxidative stress response declined, and the Treated group had remarkably lower SIRT1 protein expression than the I/R group, enhanced SOD activity and inhibited MDA activity ($^{\#}P<0.05$) (Fig. 5).

DISCUSSION

Reperfusion is a strategy to save the brain after ischemia, but rapid reperfusion can also cause damage to brain tissues, eventually leading to I/R injury (18). It has been proved in animal studies that various cerebral protective preconditioning (e.g., pharmacological or ischemic pre-conditioning) is effective (19, 20). However, ischemic episodes often fail to be exacted in clinical practice. Therefore, this preconditioning has extremely limited utility (21). Furthermore, ischemic post-conditioning has also been confirmed to be able to resist post-ischemic injury, but it is difficult to be initiated in clinical practice (22). Therefore, pPoCo involving the administration of bioactive agents

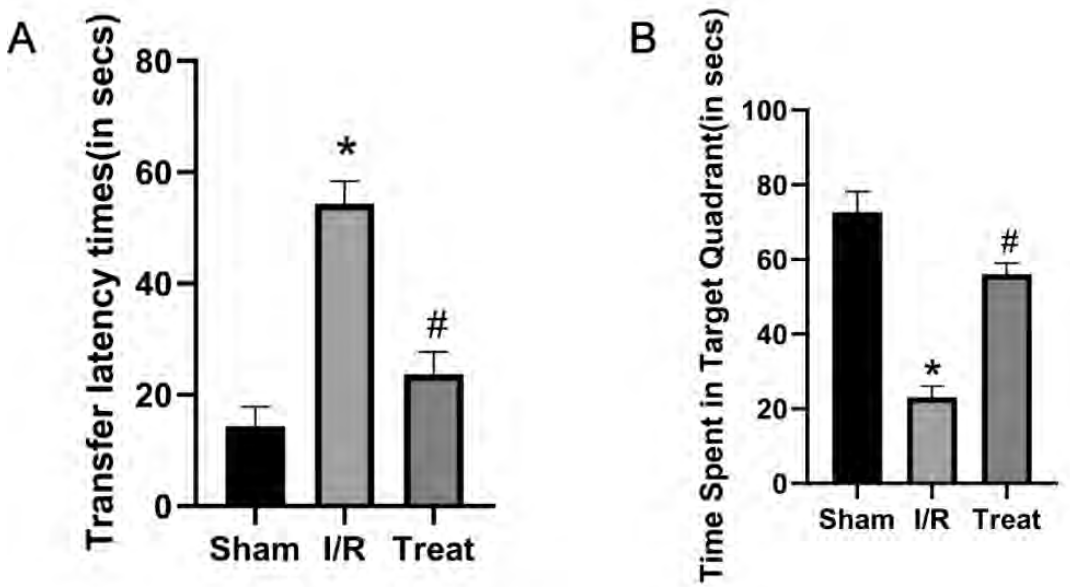


Fig. 1. *Changes in memory of mice evaluated using MWM test.* ***A)*** *TLT is significantly prolonged in the I/R group compared with that in the Sham group (*P<0.05), while it is substantially shortened in the Treated group in comparison with that in the I/R group (#P<0.05).* ***B)*** *ELT is notably shorter in the I/R group than that in the Sham group (*P<0.05), whereas it is significantly prolonged in the Treated group compared with that in the I/R group (#P<0.05). (*P<0.05 vs Sham group, #P<0.05 vs I/R group)*

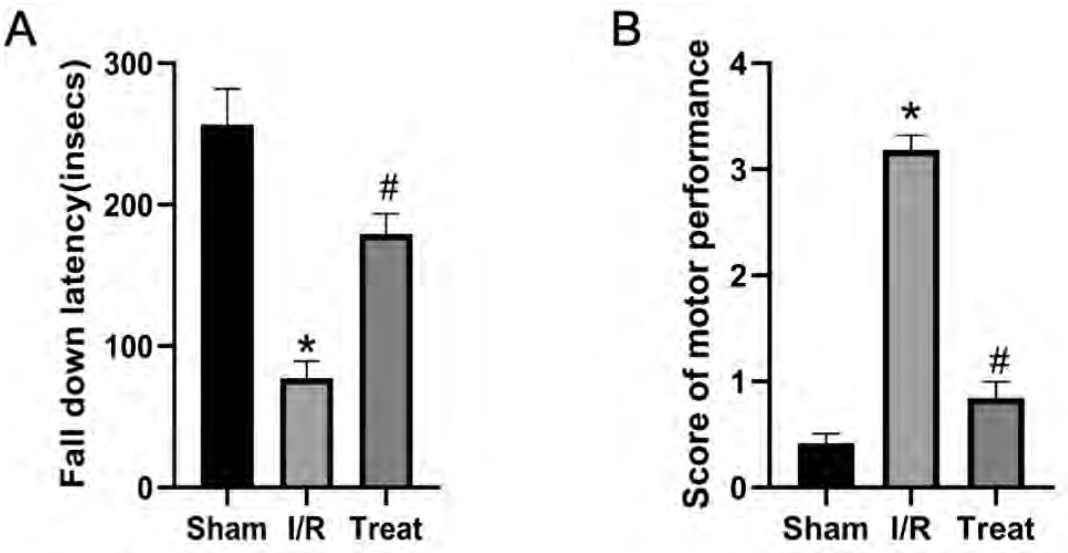


Fig. 2. *Changes in falling down time and motor performance score after cerebral I/R injury.* ***A)*** *Changes in falling down time of mice. The falling down time is obviously shorter in the I/R group than that in the Sham group (*P<0.05), while it is obviously longer in the Treated group than that in the I/R group (#P<0.05).* ***B)*** *Changes in motor performance score. The motor performance score is obviously higher in the I/R group than that in the Sham group (*P<0.05), while it is obviously lower in the Treated group than that in the I/R group (#P<0.05). (*P<0.05 vs Sham group, #P<0.05 vs I/R group).*

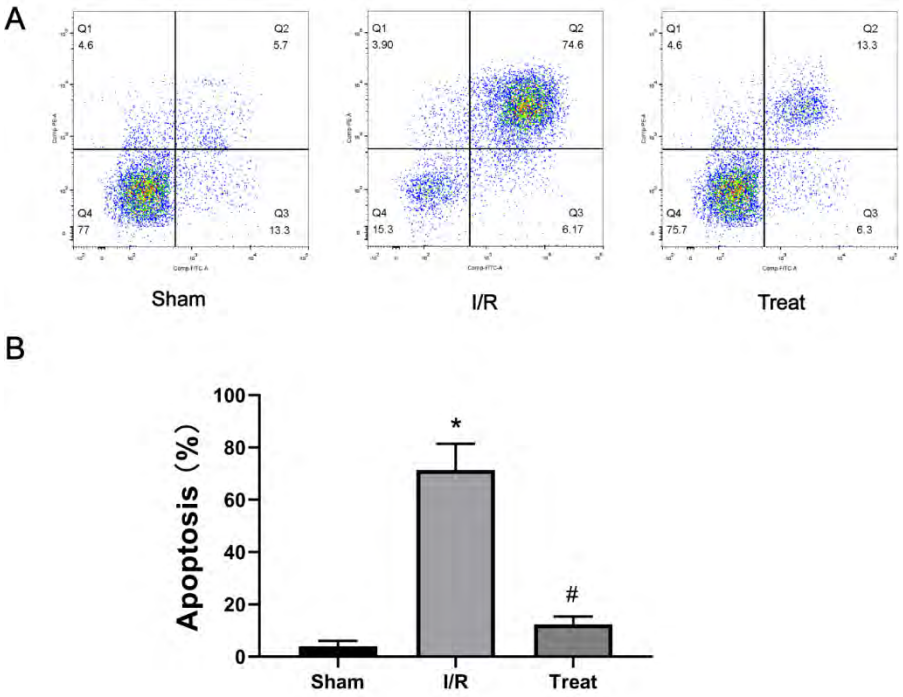


Fig. 3. *Effect of propofol on neuronal apoptosis caused by I/R.* ***A)*** *Neuronal apoptosis detected via flow cytometry.* ***B)*** *The proportion of apoptotic cells is markedly higher in the I/R group than that in the Sham group ($^{*}P<0.05$), while it is markedly lower in the Treated group than that in the I/R group ($^{\#}P<0.05$). ($^{*}P<0.05$ vs Sham group, $^{\#}P<0.05$ vs I/R group)*

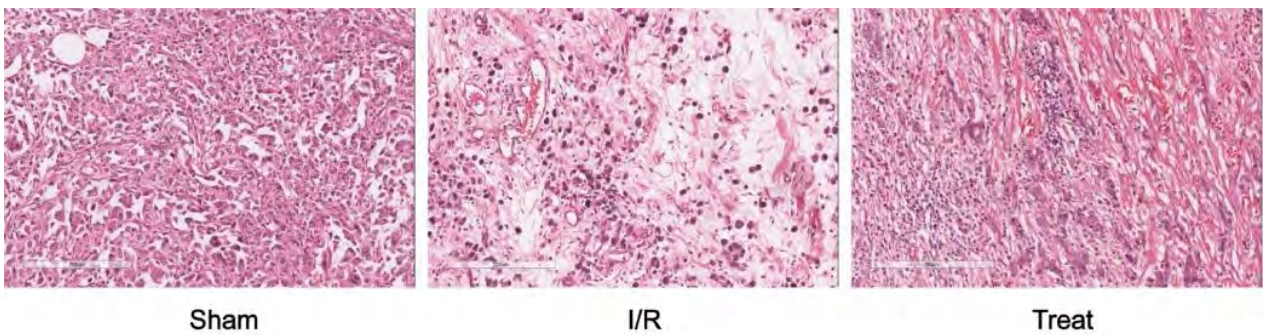


Fig. 4. *Pathological changes in brain tissues. (magnification: 200×)*

during or prior to reperfusion seems to be more practical and promising, as it is achievable, effective and safe in clinical practice (23).

In order to study the protective mechanism of propofol in cerebral I/R injury, C57BL/6J mice were used as study animals and divided into a Sham group (no I/R), an I/R group (I/R model established *via* ligation of artery) and a Treated group (peritoneal injection of propofol). The short-term memory impairment of mice with cerebral I/R injury was evaluated using the MWM and EPM tests. It was found that TLT was significantly prolonged, and ELT was significantly shortened in the I/R group compared with those in the Sham group (*P<0.05), indicating the

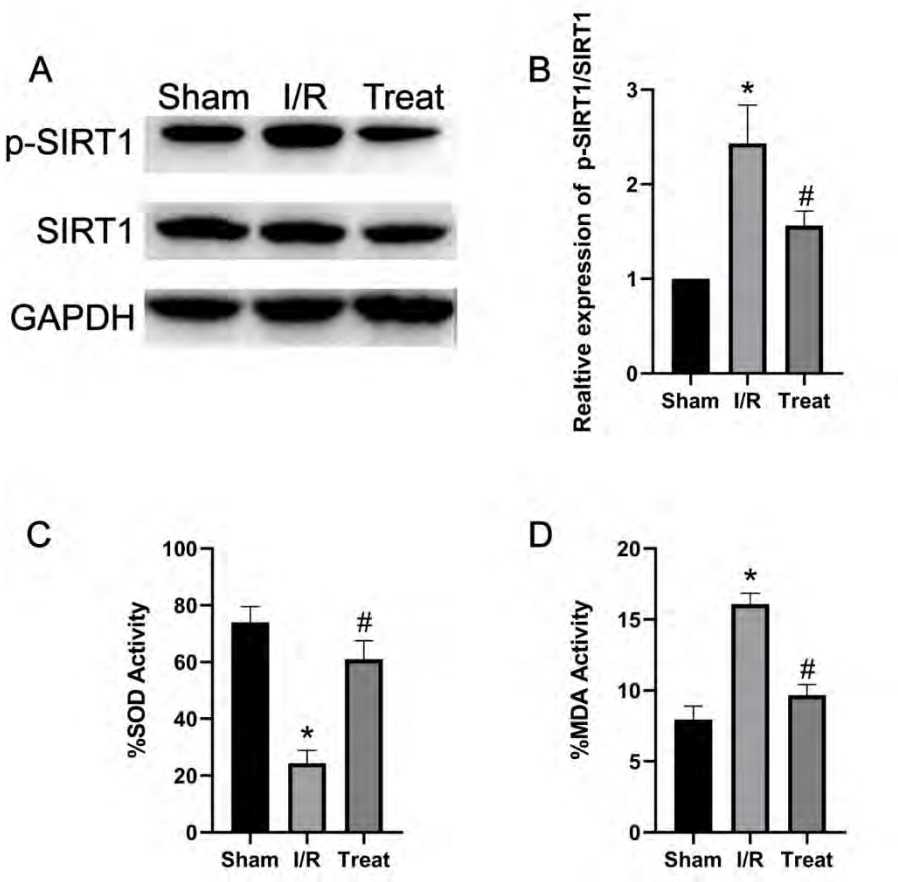


Fig. 5. *Effects of propofol on SIRT1 protein expression and SOD and MDA activity in mice with cerebral I/R injury.* ***A)*** *Changes in SIRT1 protein expression.* ***B)*** *The SIRT1 protein expression is evidently higher in the I/R group than that in the Sham group (*P<0.05), while it is evidently lower in the Treated group than that in the I/R group (#P<0.05).* ***C)*** *Changes in SOD activity.* ***D)*** *Changes in MDA activity.*

memory impairment after cerebral I/R injury. TLT was shortened, and ELT was significantly prolonged in the Treated group compared with the I/R group (#P<0.05), suggesting that propofol can improve the memory and learning ability of mice with cerebral I/R injury. Then the motor coordination of mice was assessed using the falling down time and motor performance score detected in Rota rod test and oblique beam walking test. The results revealed that the falling down time was obviously shorter in the I/R group than that in the Sham group (*P<0.05), while it was obviously longer in the Treated group than that in the I/R group (#P<0.05). Compared with the Sham group, the I/R group had neurological impairment, manifested as the evident increase in motor performance score (*P<0.05), and the motor performance score in the Treated group was evidently lower than that in the I/R group (#P<0.05), demonstrating that propofol can improve the motor coordination after cerebral I/R injury. The stained brain tissues were observed under a microscope. It was observed that the neurons in the Sham group were uniform in size and arranged regularly, and the brain tissues had normal morphology. In the I/R group, the neurons shrank and became smaller, the cells were non-uniform in size and arranged irregularly, massive neutrophil infiltration could be seen and there were markedly more lesions under the microscope. In the Treated group, neurons mostly had normal morphology, neutrophils could be seen under the microscope, and the number of lesions was evidently smaller than that in the I/R group. The above findings indicate that propofol can reverse the damage to brain neurons caused by I/R injury. Moreover, the results of flow cytometry manifested

that the apoptosis was markedly enhanced in the I/R group, while it was markedly weakened in the Treated group compared with that in the I/R group. It can be seen that the proportion of apoptotic cells significantly declines after propofol Treatment. It has been confirmed that the SIRT1 pathway is involved in oxidative stress and I/R. SOD and MDA are markers for oxidative stress. In this study, the blood was drawn from mice after cerebral injury, and the changes in SIRT1 protein expression were determined using Western blotting, and the changes in MDA and SOD activity were determined through biochemical assays. The results manifested that the I/R group had remarkably higher SIRT1 protein expression than the Sham group, inhibited SOD activity and enhanced MDA activity. The Treated group had remarkably lower SIRT1 protein expression than the I/R group, enhanced SOD activity and inhibited MDA activity. The above results suggest that SITR1 protein is highly expressed under stress conditions, SOD activity is inhibited and MDA activity is increased after cerebral I/R injury, but propofol can restore the expression levels of the three indexes in the normal human body.

In conclusion, propofol can alleviate cerebral I/R injury through inhibiting the SIRT1 pathway, and also relieve the oxidative stress response of I/R injury. However, there are still some deficiencies in this study. The SIRT1 pathway was not studied deeply enough, so it will be further explored in the future.

REFERENCES

1. Hausenloy DJ, Yellon DM. Myocardial ischemia-reperfusion injury: a neglected therapeutic target. J Clin Invest 2013; 123:92-100.
2. Hausenloy DJ, Barrabes JA, Botker HE, et al. Ischaemic conditioning and targeting reperfusion injury: a 30 year voyage of discovery. Basic Res Cardiol 2016; 111:70.
3. Suliman HB, Piantadosi CA. Mitochondrial Quality Control as a Therapeutic Target. Pharmacol Rev 2016; 68:20-48.
4. Eltzschig HK, Eckle T. Ischemia and reperfusion--from mechanism to translation. Nat Med 2011; 17:1391-101.
5. Chouchani ET, Pell VR, Gaude E, et al. Ischaemic accumulation of succinate controls reperfusion injury through mitochondrial ROS. Nature 2014; 515:431-45.
6. Chouchani ET, Pell VR, James AM, et al. A Unifying Mechanism for Mitochondrial Superoxide Production during Ischemia-Reperfusion Injury. Cell Metab 2016; 23:254-23.
7. Dhingra R, Kirshenbaum LA. Succinate dehydrogenase/complex II activity obligatorily links mitochondrial reserve respiratory capacity to cell survival in cardiac myocytes. Cell Death Dis 2015; 6:e1956.
8. Iijima T, Mishima T, Akagawa K, Iwao Y. Neuroprotective effect of propofol on necrosis and apoptosis following oxygen-glucose deprivation--relationship between mitochondrial membrane potential and mode of death. Brain Res 2006; 1099:25-32.
9. Shao H, Li J, Zhou Y, Ge Z, Fan J, Shao Z, Zeng Y. Dose-dependent protective effect of propofol against mitochondrial dysfunction in ischaemic/reperfused rat heart: role of cardiolipin. Br J Pharmacol 2008; 153:1641-16.
10. Adembri C, Venturi L, Tani A, et al. Neuroprotective effects of propofol in models of cerebral ischemia: inhibition of mitochondrial swelling as a possible mechanism. Anesthesiology 2006; 104:80-89.
11. Li J, Han B, Ma X, Qi S. The effects of propofol on hippocampal caspase-3 and Bcl-2 expression following forebrain ischemia-reperfusion in rats. Brain Res 2010; 1356:11-23.
12. Wang HY, Wang GL, Yu YH, Wang Y. The role of phosphoinositide-3-kinase/Akt pathway in propofol-induced postconditioning against focal cerebral ischemia-reperfusion injury in rats. Brain Res 2009; 1297:177-14.
13. Yano T, Nakayama R, Ushijima K. Intracerebroventricular propofol is neuroprotective against transient global ischemia in rats: extracellular glutamate level is not a major determinant. Brain Res 2000; 883:69-76.
14. Li J, Yu W, Li XT, Qi SH, Li B. The effects of propofol on mitochondrial dysfunction following focal cerebral ischemia-reperfusion in rats. Neuropharmacology 2014; 77:358-38.
15. Kajimoto M, Atkinson DB, Ledee DR, et al. Propofol compared with isoflurane inhibits mitochondrial metabolism in immature swine cerebral cortex. J Cereb Blood Flow Metab 2014; 34:514-51.
16. Himori N, Watanabe H, Akaike N, Kurasawa M, Itoh

J, Tanaka Y. Cerebral ischemia model with conscious mice. Involvement of NMDA receptor activation and derangement of learning and memory ability. J Pharmacol Methods 1990; 23:311-37.

17. Rehni AK, Singh TG, Jaggi AS, Singh N. Pharmacological preconditioning of the brain: a possible interplay between opioid and calcitonin gene related peptide transduction systems. Pharmacol Rep 2008; 60:904-93.
18. L L, X W, Z Y. Ischemia-reperfusion Injury in the Brain: Mechanisms and Potential Therapeutic Strategies. Biochem Pharmacol (Los Angel) 2016; 5.
19. Gidday JM. Cerebral preconditioning and ischaemic tolerance. Nat Rev Neurosci 2006; 7:437-48.
20. Altintas O, Kumas M, Altintas MO. Neuroprotective effect of ischemic preconditioning via modulating the expression of adropin and oxidative markers against transient cerebral ischemia in diabetic rats. Peptides 2016; 79:31-38.
21. Bansal S, Sangha KS, Khatri P. Drug Treatment of acute ischemic stroke. Am J Cardiovasc Drugs 2013; 13:57-69.
22. Leger PL, Bonnin P, Renolleau S, Baud O, Charriaut-Marlangue C. Ischemic postconditioning in cerebral ischemia: Differences between the immature and mature brain? Int J Dev Neurosci 2015; 45:39-43.
23. Esmaeeli-Nadimi A, Kennedy D, Allahtavakoli M. Opening the window: Ischemic postconditioning reduces the hyperemic response of delayed tissue plasminogen activator and extends its therapeutic time window in an embolic stroke model. Eur J Pharmacol 2015; 764:55-62.

TIR-DOMAIN-CONTAINING ADAPTER-INDUCING INTERFERON-β CONTRIBUTES TO TLR3/TLR4 TRIGGERED APOPTOSIS AND INFLAMMATION IN NUCLEUS PULPOSUS CELLS

H.-L. LV[1], J. YU[2], J.-F. PEI[3], H.-Y. WANG[4] and Z.-L. GUO[5]

[1]Department of Spinal Surgery, Yantai Yuhuangding Hospital, Yantai, China; [2]Department of Eastern Operation Room, Yantai Yuhuangding Hospital, Yantai, China; [3]Department of Medical Examination Center, Yantai Yuhuangding Hospital, Yantai, China; [4]Department of Central Laboratory, Yantai Yuhuangding Hospital, Yantai, China; [5]Department of Orthopedics, The 80th Group Army Hospital of Chinese PLA, Weifang, China

Received February 3, 2020 – Accepted March 27, 2020

The senescence and degeneration of the intervertebral disc are closely related to the reduction of nucleus pulposus (NP) cells caused by apoptosis. TIR-domain-containing adapter-inducing interferon-β (TRIF) is an adapter for Toll-like receptors 3/4 (TLR3/4), which involves in cell apoptosis. The aim of this study is to detect the role of TRIF in the apoptotic progress of NP cells. The expression of collagen II, aggrecan, TLR3/4, and TRIF were analyzed in different degrees of degenerated human NP samples from patients. NP cells were isolated from mild degenerated tissues and cultured with IL-1β to accelerate the degradation, and treated with TLR3/4 protein. siRNA was used to silence TRIF gene expression, and TRLF-plasmid was used to upregulate TRLF gene expression. We used flow cytometry assay to analyze cell apoptosis. The expression of collagen II, aggrecan, TLF3/4, TRIF, caspase-8/3, MMP-13, TNF-α was determined by immunofluorescence, Western blot, or RT-PCR. That the expression of collagen II and aggrecan markedly decreased, but TLF3/4, TRIF, caspase-8/3, MMP-3, TNF-α, and IL-1β were increased in severely degenerated disc tissues. IL-1β treatment induced NP cell degeneration and TLF3/4, TRIF, caspase-8/3, MMP-3, TNF-α overexpression. TLF3/4 protein treatment promoted NP cell degeneration and apoptosis by upregulation of TRIF, caspase-8/3, MMP-3, and TNF-α. Furthermore, TRIF silencing reversed the negative effect of TLF3/4 overexpression, and TRIF overexpression played the same role in NP cell apoptosis. Based on these results, we believe that TRIF is activated in a degenerated intervertebral disc. TLF3/4 promotes NP cell apoptosis and inflammation through the TRLF adaptor. TRLF expression is positively related to the apoptosis and inflammation in NP cells. These results suggest a therapeutic potential of the TRIF in the treatment of disc degeneration.

Intervertebral disc is composed of aggrecan, glycoprotein, collagen and elastic fiber, and the aggrecan acts in combination with water to resist pressure and thus has a dispersing effect on the load. Collagen constitutes the intercellular framework, the proportion of type I collagen in the annulus fibrosus (AF) is higher, and the outward-inward type I collagen is gradually decreasing, but the type II collagen and aggrecan are increasing (1). Type II collagen and aggrecan in the intervertebral disc

Key words:nNucleus pulposus cells; intervertebral disc degeneration; TRIF; TLFs; apoptosis

Corresponding Author:
Zhiliang Guo, MD
Department of Orthopedics, The 80th Group Army Hospital of Chinese PLA,
256 Beigong West Street, Weifang, Shandong Province, China.
Postal Code: 261021
Tel: 860536-8439403
e-mail: drzlguo@163.com

0393-974X (2020)
Copyright © by BIOLIFE, s.a.s.
This publication and/or article is for individual use only and may not be further reproduced without written permission from the copyright holder.
Unauthorized reproduction may result in financial and other penalties
DISCLOSURE: ALL AUTHORS REPORT NO CONFLICTS OF INTEREST RELEVANT TO THIS ARTICLE.

tissue are secreted by the NP cells, which balances the intervertebral disc ion concentration and osmotic pressure, thereby ensuring the viability of NP cells contributes to intervertebral disc continuously gain nutrients and maintain normal function (2).

As age increases, intervertebral disc degeneration (IDD) gradually worsens, and it usually begins with the degeneration as well as the apoptosis of NP cells. Apoptosis affects the synthesis and secretion function of NP cells, resulting in the reduction of type II collagen and aggrecan of the extracellular matrix (ECM) that affects functions to effectively bear the load. Therefore, excessive apoptosis of the NP cells is one of the most important pathological bases for IDD (3). Toll-like receptors (TLRs) serve as a bridge between natural and acquired immunity, and their signal transduction pathways have attracted much attention in recent years (4). MyD88 (Myeloid differentiation primary response protein 88)-dependent pathway is common for almost all TLR signaling pathways (5). In addition, the other is linked by TRIF, which is MyD88 non-dependent, mainly involved in TLR3 and TLR4 signaling pathway (6). TLR3 can be directly bound to TRIF, but TLR4 indirectly recruits TRIF using the TRAM (Trif-related adaptor molecule) as an adaptor (7).

Among the five known adaptor proteins containing the TIR domain, TRIF is the only one that mediates the apoptotic signaling pathway. It has been found that TRIF is involved in mediating several signaling pathways and takes part in the development of inflammatory reactions (8) and cell apoptosis (9). Kaiser et al. reported that TRIF induced apoptosis depending on interacting protein homotypic interaction motif (10). Peterson et al. (11) found TRIF signaling promoted Yersinia-induced apoptosis by collaborating with TNF. Increased levels of TLRs have been elucidating to accelerate IDD along with chronic inflammation and pain development (12, 13). What the previous studies mainly mentioned is the relationship between TLRs and the destruction of ECM of the intervertebral disc resulting from the activation of inflammation (14). However, the mechanism of TLR3/4 and TRIF in IDD based on apoptosis still remains unknown.

In this study, we aimed to detect the role of TRIF in the degeneration of human intervertebral disc through primary NP cells isolated from the tissue. We found that TLR3/4 upregulation induced degenerative changes in the NP cells with increased apoptosis and inflammation *via* TRIF. TLR3/4 and their adaptor TRIF may be potential therapeutic targets for slowing IDD.

MATERIALS AND METHODS

NP tissue collection

This project was supported by the Ethics Committee of Yantai Yuhuangding Hospital. From June to August 2018, a total of 16 patients (average age: 48 years; 9 males, 7 females.) undergoing lumbar disc herniation surgery in our department participated in the study. All the subjects gave informed, signed consent to participate in the study. The IDD degree in each surgical segment was determined based on the Pfirrmann score according to the Magnetic Resonance Imaging (MRI) before surgery, of which grades I suggests no significant IDD, while grades and II, III, IV, and V suggest varying degrees of IDD from mild to severe. We divided all NP tissues into two groups: i) Mild degenerated group (grades II or III), ii) Severe degenerated group (grades IV or V).

NP cells isolation and treatments

The NP samples were placed in a pre-prepared sterile culture flask containing a small amount of Dulbecco's modified eagle medium/F12 (DMEM/F12) (Invitrogen, Carlsbad, CA, USA) culture medium, which were quickly placed in an icebox and taken to the laboratory. Tissues were cut into equal pieces, digested with 0.2% type II collagenase in a 37°C water bath for 6 h, and the cells were collected by cell sieve at an appropriate density. All experimental cells were passaged to the first to third generations and grouped as following: i) Control group (without treatment); ii) IL-1β group (pretreated with 5 or 10 ng/mL IL-1β); iii) recombinant human (rh)-TLR3 group (pretreated with 10 μg/mL rh-TLR3 protein (15). ab73825, Abcam, Cambridge, MA, USA) ; iv) rh-TLR4 group (pretreated with 10 μg/ml rh-TLR4 protein (16). ab233665, Abcam, Cambridge, MA, USA); v) null-siRNA group (transfected with null-siRNA, as negative control, with 10 μg/mL rh-TLR3 or rh-TLR4); vi) TRIF-siRNA group (transfected with siRNA against TRIF, as

negative control, with 10 μg/mL rh-TLR3 or rh-TLR4); vii) TRIF-plasmid group (transfected with TRIF-plasmid)

Western blot analysis

The protein extraction was performed on ice. The reaction solution was pre-cooled with ice water. Phosphatase inhibitor and protease inhibitor were added in the lysate (Beyotime, Shanghai, China), and the protein content was determined by the bicinchoninic acid (BCA) protein concentration assay kit (Beyotime, Shanghai, China). Sample was boiled in 5× loading buffer to be denatured and then separated by electrophoresis on 10% sodium dodecyl sulphate-polyacrylamide gel electrophoresis (SDS-PAGE), electroporated onto a polyvinylidene fluoride (PVDF) membranes (Roche, Basel, Switzerland). Then, the membrane was blocked with 5% non-fat milk for 1 h. After that, membranes were incubated with primary antibodies against collagen II (Abcame, Cambridge, MA, USA), aggrecan (Abcam, Cambridge, MA, USA), TLR3 (Cell Signaling, Danvers, MA, USA), TLR4 (Cell Signaling, Danvers, MA, USA), TRIF (Cell Signaling, Danvers, MA, USA), and β-Actin (as loading control; Abcam, Cambridge, MA, USA) at 4°C overnight. After incubating with secondary antibody for 1 h, membranes were exposed with chemiluminescent electrochemiluminescence (ECL) (Beyotime, Shanghai, China).

Immunofluorescence (IF)

NP cells were seeded at 5×104 /mL on coverslips in 24-well plates. NP cells were fixed with 4% paraformaldehyde, permeabilized with 0.05% TritonX-100, and endogenous peroxide was added dropwise to the cells. After blocking with bovine serum albumin (BSA) for 15 min, coverslips were incubated with primary antibodies: collagen II (Cell Signaling, Danvers, MA, USA) at 4°C overnight; After rewarming, coverslips were added with fluorescein isothiocyanate (FITC)-labeled secondary antibody (Invitrogen, Carlsbad, CA, USA) and 4',6-diamidino-2-phenylindole (DAPI), incubated at 37°C for 30 min avoiding light. The staining intensity was measured using the ImageJ software.

Quantitative reverse-transcription polymerase chain reaction (RT-PCR)

Total RNA was isolated from the RNA extraction kit RNAiso Plus (TaKaRa, Dalian, China) according to the instruction. The mRNA was reverse transcribed into complementary deoxyribose nucleic acid (cDNA) using the PrimeScript RT reagent Kit with gDNA Eraser (TaKaRa, Dalian, China), and the SYBR Green Realtime PCR Master Mix reagent (TOYOBO, Shanghai, China) was used for the quantitative PCR reaction. Relative gene expression was achieved by normalization to the amount of glyceraldehyde 3-phosphate dehydrogenase (GAPDH) and calculated with the method of $2^{-\Delta\Delta Ct}$. The primers used for RT-PCR are listed in Table I.

siRNA and plasmid transfection

Double-stranded siRNA targeting the TRIF gene, and negative control-siRNA (null-siRNA) were designed and chemically synthesized by Invitrogen (Carlsbad, CA, USA). NP cells were seeded at 1.5×10^5 cells/well in a 6-well plate 24 h before transfection. When the cell fusion rate reached 60%-70% after seeding, the specific siRNA transfection reagent PepMute siRNA Transfection Reagent (SignaGen, Rockville, MD, USA) was transfected with TRIF-siRNA and null-siRNA for 36 h according to the instructions.

NP cells were seeded at 1.5×10^5 cells/well in a 6-well plate 24 h before transfection. When the cell fusion rate reached 60%-70% after seeding, 4 μg TRIF-plasmid (Invitrogen, Carlsbad, CA, USA) and 4 μL lipofectamine 2000 were diluted in 250 μL culture medium and mixed with NP cells for 30 min. The medium was changed, after 6 h incubation in a cell culture incubator.

Flow cytometry

Apoptosis was detected by Annexin VFITC/PI double staining apoptosis assay kit (Keygene, Nanjing, China). The cells were havested and washed with phosphate buffered saline (PBS), labeled with Annexin V-FITC and PI, and then detected by a FACS Calibur flow cytometer (BD, Franklin Lakes, NJ, USA). The cells in early apoptosis (Annexin V+, PI-) and late apoptosis (Annexin V+, PI+) were counted together.

Statistical analysis

Data were analyzed by Graph Pad Prism Version 7 (La Jolla, CA, USA) and expressed at mean ± standard deviation (SD). Band intensities were measured by ImageJ software. Differences between two groups were analyzed by using Student's *t*-test. Comparison between multiple

groups was carried out using One-way ANOVA test followed by Post Hoc Test (Least Significant Difference). $P<0.05$ was considered to be statistically significant.

RESULTS

TLR3/4 and TRIF levels in degenerated human NP tissues

To determine the relationship between TLR3/4, TRIF and the degree of intervertebral disc degeneration, we measured relevant gene expression of mild and severe degenerated disc tissues. As shown in Fig. 1 A, B, decreased collagen and aggrecan expression indicated the severe group had a greater significant degeneration than the mild group. With the development of IDD, MMP-3, TNF-α, and IL-1β and apoptotic markers such as caspase-8 and caspase-3 were upregulated compared with the mild group (Fig. 1C). TLR3, TLR4, and TRIF expression were increased in the severely degenerated group compared with the mild group both in protein and mRNA levels. These results indicated that TLR3, TLR4, and TRIF were associated with the progress of IDD, which might be related to the inflammatory and apoptotic response.

TLR3/4 and TRIF levels in IL-1β-treated NP cells in vitro

To confirm the TLR3/4 and TRIF levels in the degenerated NP cells *in vitro*, we used different concentrations of IL-1β to promote the development of NP cell degeneration. As shown in Fig. 2 A, B, the expression of collagen II was reduced resulting from IL-1β treatment in a dose-dependent manner, suggesting a degenerated phenotype of NP cells. Moreover, NP cell apoptosis was promoted due to

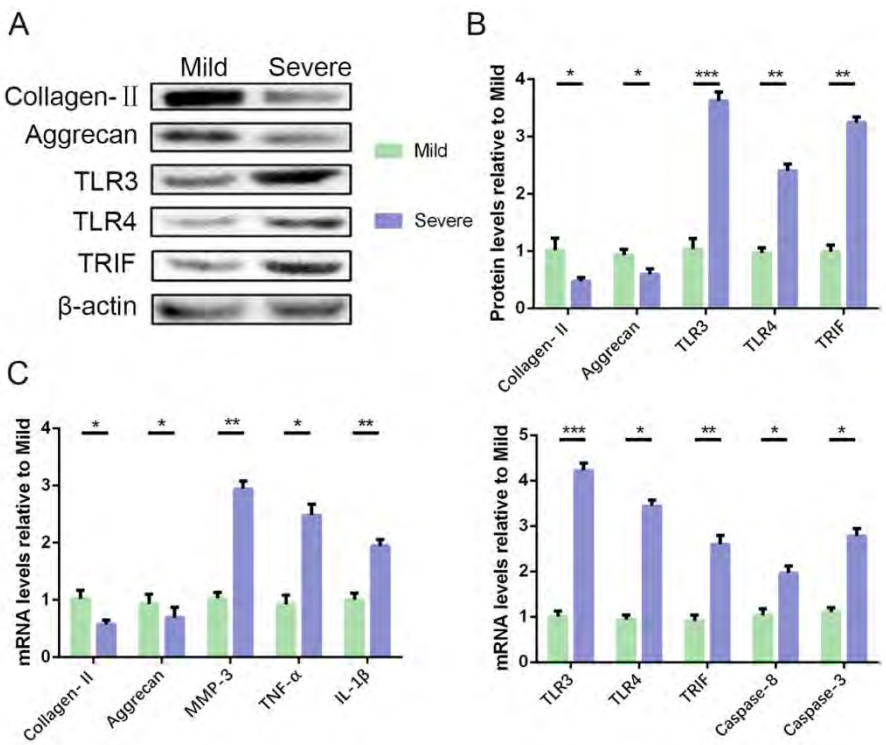


Fig. 1. *TLR3/4 and TRIF levels in human degenerated intervertebral disc tissues. Tissues were lysed and measured with Western blot and RT-PCR methods.* ***A, B****) The protein levels of collagen II, aggrecan, TLR3, TLR4, and TRIF were determined by Western blot (A) and quantification analysis (B).* ***C****) mRNA levels of collagen II, aggrecan, MMP-3, TNF-α, IL-1β, TLR3, TLR4, TRIF, caspase-8, and caspase-3 and were determined by RT-PCR. The values are mean ± SD of three independent experiments (n=3). (*P<0.05, **P<0.01, ***P<0.001)*

IL-1β treatment (Fig. 2C). The protein expression of TLR3, TLR4, and TRIF were upregulated in the degenerated NP cells compared with the controls (Fig. 2 D, E). The results of RT-PCR showed that

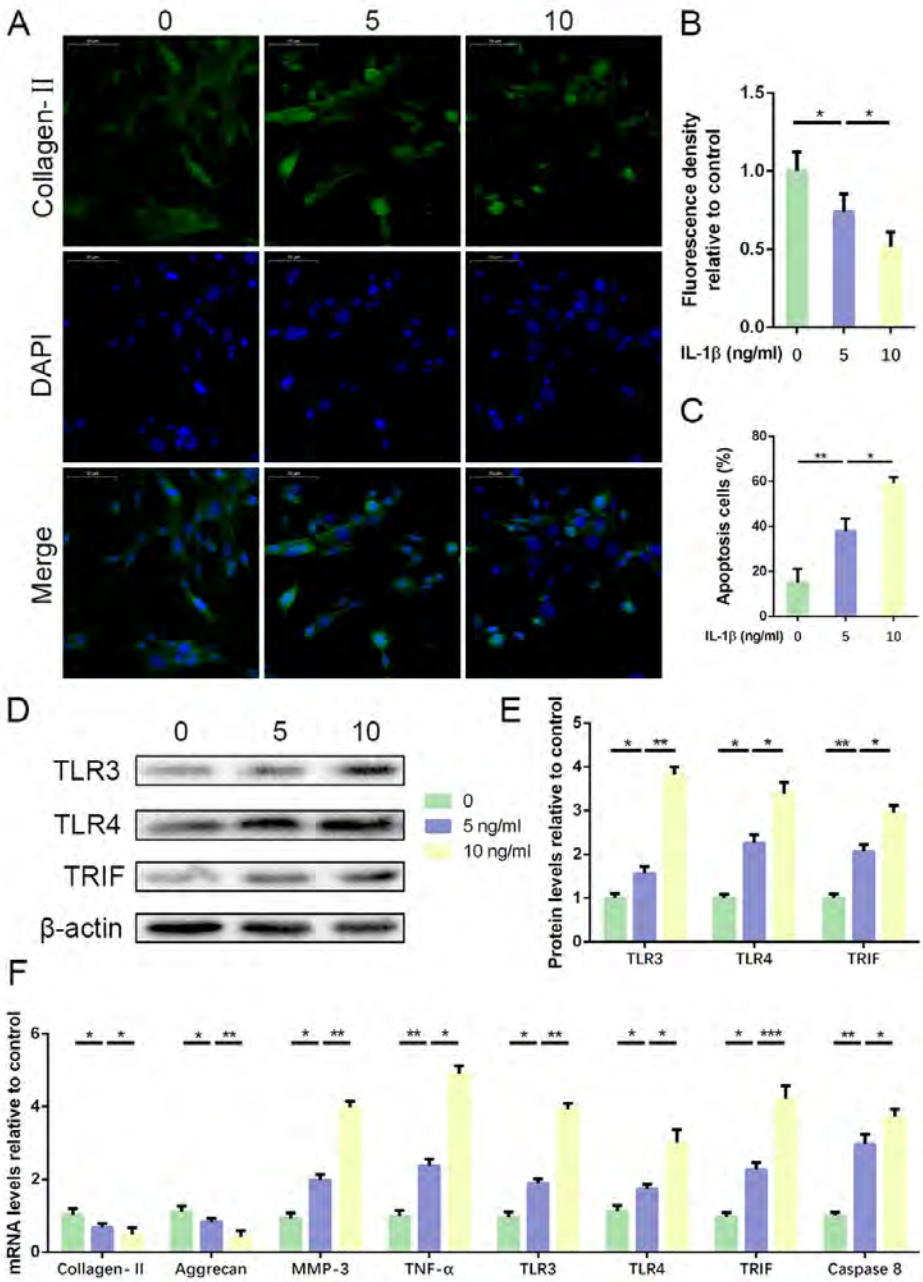


Fig. 2. *TLR3/4 and TRIF levels in IL-1β treated NP cells in vitro. NP cells isolated from mild degenerated tissues were pretreated with a low or high concentration of IL-1β (5 or 10 ng/ml) for 24 h.* ***A, B****) The protein expression level of collagen II was determined by immunofluorescence (A) and quantification analysis (B) (magnification×400).* ***C****) The ratio of apoptosis cells was analyzed by flow cytometry.* ***D, E****) The protein expression levels of TLR3, TLR4 and TRIF were determined by Western blot (D) and quantification analysis (E).* ***F****) The mRNA expression levels of collagen II, aggrecan, MMP-3, TNF-α, TLR3, TLR4, TRIF, and caspase-8 were assayed by RT-PCR. The values are mean ± SD of three independent experiments (n=3). (*P<0.05, **P<0.01, ***P<0.001)*

collagen II and aggrecan were suppressed, MMP-3 and TNF-α, caspase-8 and caspase-3 were unregulated. These results indicated that TLR3/4 and TRIF were overexpressed in degenerated NP cells *in vitro*, accompanied with active apoptosis and inflammatory response (Fig. 2F).

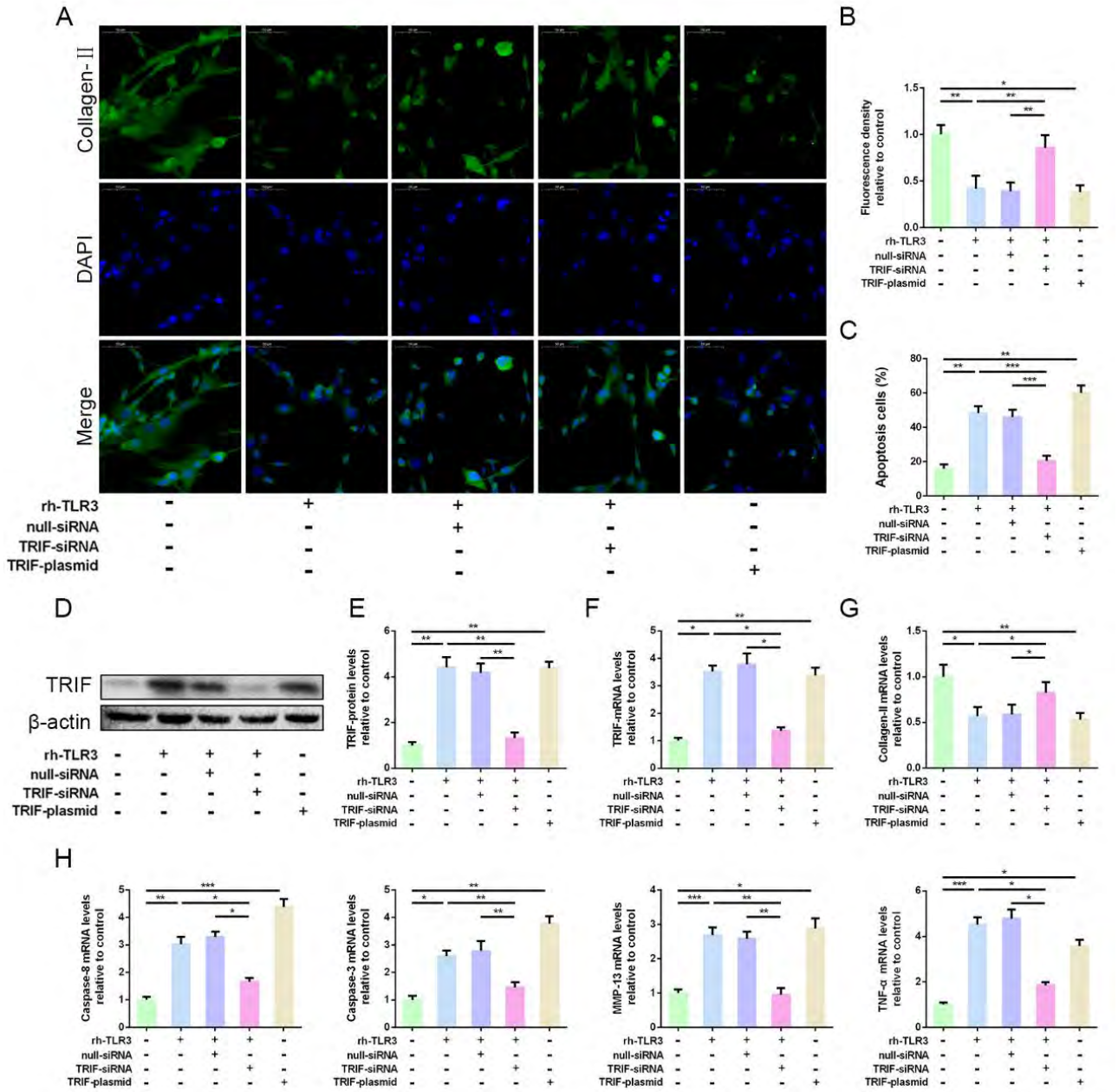


Fig. 3. *TLR3 induces NP cell degeneration through TRIF. NP cells were pretreated with 10 μg/mL of TLR3 for 24 h. Then, NP cells were transfected with null-siRNA and TRIF-siRNA, or TRIF-plasmid as well.* ***A, B****) The protein expression level of collagen II was determined by immunofluorescence (A) and quantification analysis (B) (magnification×400).* ***C****) The ratio of apoptosis cells was analyzed by flow cytometry.* ***D, E****) The protein expression levels of TRIF was determined by Western blot (D) and quantification analysis (E).* ***F-H****) The mRNA expression levels of TRIF (F) collagen II (G), caspase-8, caspase-3, MMP-13, and TNF-α were assayed by RT-PCR (H). The values are mean ± SD of three independent experiments (n=3). (*P<0.05, **P<0.01, ***P<0.001)*

TLR3 triggered NP cell degeneration through TRIF activation

To determine the role of TLR3 and its adaptor TRIF in the progress of NP cell degeneration, we treated NP cells with rh-TLR3 protein and changed the TRIF gene expression *via* siRNA or plasmid transfection. IF showed that TLR3 overexpression reduced the collagen II content compared with the control group, and the silencing of TRIF could reverse this effect, additionally, overexpression of

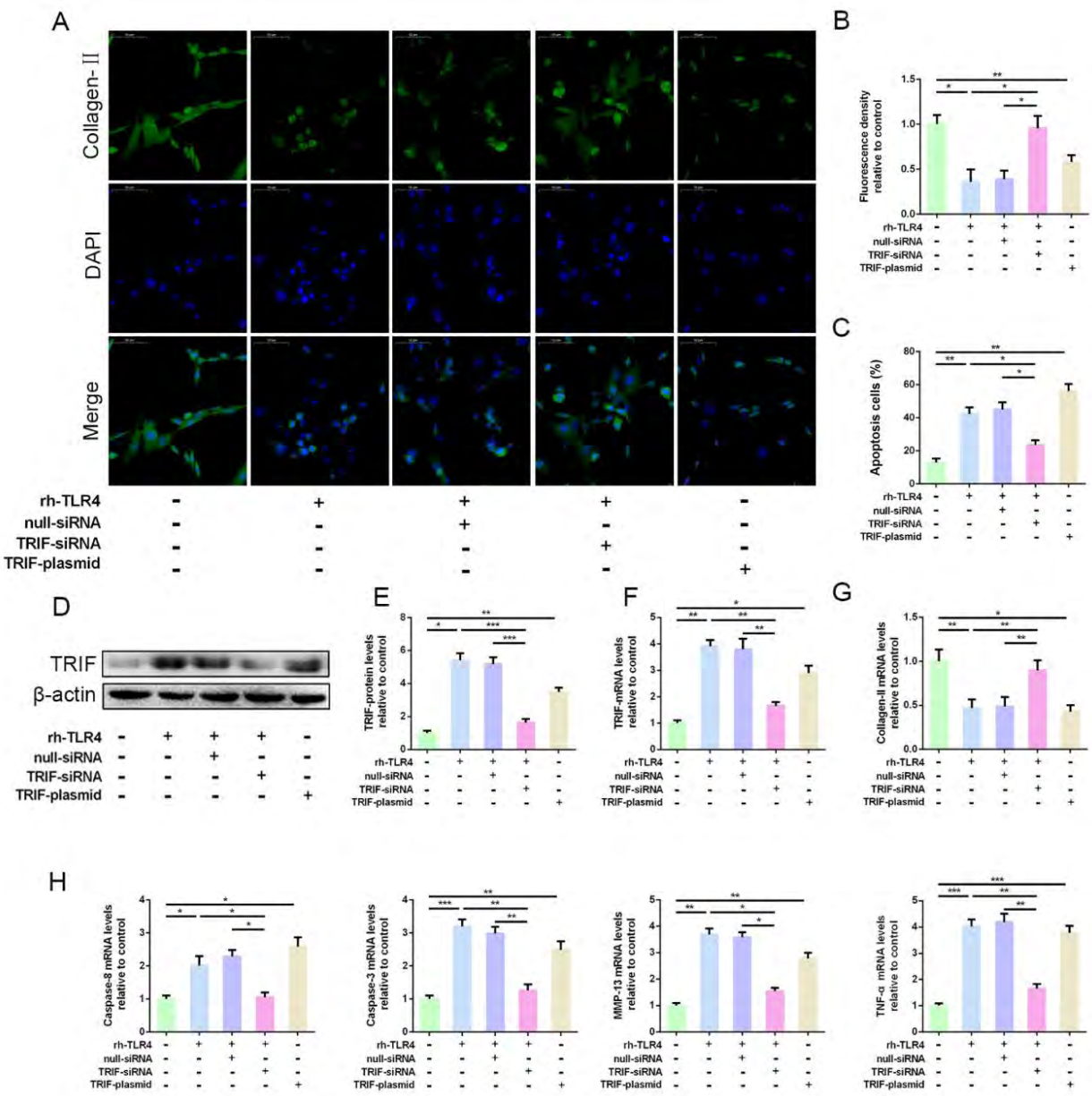


Fig. 4. *TLR4 induces NP cell degeneration through TRIF. NP cells were pretreated with 10 μg/mL of TLR4 for 24 h. Then, NP cells were transfected with null-siRNA and TRIF-siRNA, or TRIF-plasmid as well.* ***A, B****) The protein expression level of collagen II was determined by immunofluorescence (A) and quantification analysis (B) (magnification×400).* ***C****) The ratio of apoptosis cells was analyzed by flow cytometry.* ***D, E****) The protein expression levels of TRIF was determined by Western blot (D) and quantification analysis (E).* ***F-H****) The mRNA expression levels of TRIF (F) collagen II (G), caspase-8, caspase-3, MMP-13, and TNF-α were assayed by RT-PCR (H). The values are mean ± SD of three independent experiments (n=3). (*P<0.05, **P<0.01, ***P<0.001)*

TRIF contributed also to suppressing collagen II expression (Fig. 3A, 3B). We found the apoptotic cell population was significantly increased due to TLR3 and TRIF overexpression, however, TRIF deficiency blocked TLR3-induced NP cells apoptosis (Fig. 3C). Interestingly, rh-TLR3 induced upregulation of TRIF expression both in protein and mRNA levels (Fig. 3 D-F). In addition, we also analyzed the mRNA expression of inflammatory factors MMP-13 and TNF-α, and caspase-8 and caspase-3, which were all upregulated in the condition of TLR3 or TRIF overexpression. As expected, the silencing of TRIF also interrupted the side-effect of TLF3 to the NP cells (Fig. 3 G, H). Taken together, these results demonstrate that TLR3 triggers NP cell degeneration by promoting apoptosis and inflammation through TRIF activation, and the TRIF level is positively related to the apoptosis of NP cells.

TLR4 triggered NP cell degeneration through TRIF activation

To determine whether TLR4 affects the development of NP cell degeneration through TRIF as TLR3, rh-TLR4 protein was also used to stimuli NP cells, and siRNA or plasmid were also used to edit TRIF gene expression. As shown in Fig. 4 A, B, lyrh-TLR4 protein induced a reduction of collagen II expression compared with the control group, and TRIF silencing significantly dropped this effect, moreover, overexpression of TRIF also suppressed collagen II expression as TLR4 upregulation. Flow cytometry indicated the apoptotic cell population was significantly increased resulting from TLR4 and TRIF overexpression, however, silencing of TRIF reversed TLR4-induced NP cells apoptosis (Fig. 4C). As rh-TLR3, rh-TLR4 upregulated TRIF expression both in protein and mRNA levels (Fig. 4 D-F). Furthermore, mRNA expression of MMP-13, TNF-α, caspase-8, and caspase-3, were all upregulated in the condition of TLR3 or TRIF overexpression. As expected, the silencing of TRIF blocked the side-effect of TLF4 to the NP cells (Fig. 4 G, H). These results suggested that TLR4 triggers NP cell degeneration by promoting apoptosis and inflammation through TRIF activation.

Table I. *Primer sequences of the genes for RT-PCR*

Gene name	Forward (5'>3')	Reverse (5'>3')
Collagen II	TGGACGATCAGGCGAAACC	GCTGCGGATGCTCTCAATCT
Aggrecan	ACTCTGGGTTTTCGTGACTCT	ACACTCAGCGAGTTGTCATGG
TLR3	ATTGCCTTGTATCTACTTTTGGGG	TCAACACTGTTATGTTTGTGGGT
TLR4	AGACCTGTCCCTGAACCCTAT	CGATGGACTTCTAAACCAGCCA
TRIF	GCCAGCAACTTGGAAATCAGC	GGGGTCGTCACAGAGCTTG
MMP-13	ACTGAGAGGCTCCGAGAAATG	GAACCCCGCATCTTGGCTT
TNF-α	CCTCTCTCTAATCAGCCCTCTG	GAGGACCTGGGAGTAGATGAG
Caspase-8	CATCCAGTCACTTTGCCAGA	GCATCTGTTTCCCCATGTTT
Caspase-3	AGAACTGGACTGTGGCATTGAG	GCTTGTCGGCATACTGTTTCAG
GAPDH	ACAACTTTGGTATCGTGGAAGG	GCCATCACGCCACAGTTTC

RT-PCR: quantitative reverse-transcription polymerase chain reaction

DISCUSSION

Among the factors related to IDD, non-physiological loading stress, inflammation, and lack of nutrient supply are all associated with the apoptosis of NP cells (1, 17). As intervertebral disc tissues used for research are mainly obtained from patients with advanced degeneration, it is normal to observe the apoptosis of NP cells along with the IDD. Apoptosis causes a decrease in the number of functional NP cells, which seriously impairs the dynamic stability of the ECM, such as the presence of inflammatory factors, such as IL-1β, IL-6, IL-8, MMPs, TNF-α, and insufficient nutrient supply (18). TLRs are important natural immune receptors (19). They can play an important role in identifying pathogen-associated molecular pattern, initiating an early response to invading pathogens, and inducing an adaptive immune response. Both TLR3 and TLR4 were found to be expressed in NP cells (20). Therefore, in order to determine the effects of TLRs and TRIF on NP cells, we used rh-TLR3 protein and rh-TLR4 protein to treat NP cells, respectively.

From the samples collected from the patients, we found TLR3, TLR4, and TRIF were decreased as intervertebral disc got into severe degeneration, with an upregulation of inflammation and apoptosis. Substantial evidence has been supplied to prove TLR activation is responsible for the inflammation and apoptosis response during cell degradation (21, 22). The TRIF-dependent pathway, also known as the MyD88-independent pathway, is mainly found in the TLR3 and TLR4 pathways. TRIF induces apoptosis through the Fas-associated protein with death domain (FADD)/Caspase-8 pathway, and FADD binds to Caspase-8 *via* the death effector domain, which triggers a cascade of caspase reactions that mediate apoptosis (23).

To establish a degenerated cell model, we used IL-1β as an inducer to accelerate the degeneration of NP cells, in addition, IL-1β was also reported to be able to induce TLR upregulation (24). In our study, IL-1β degenerated NP cells in a dose-dependent, with an upregulation of TLR3, TLR4, TRIF, and a significant apoptotic and inflammatory response. To clear the interaction of TLR3, TLR4 and TRIF in the apoptosis of NP cells, NP cells were cultured with rh-TLR3 or -TLR4. The expression of TRIF was obviously increased and triggered the upregulation of caspase-8, caspase-3, inflammatory factors so as to promote the apoptosis and the degeneration of NP cells. Caspase-8 plays a key role in the process of apoptosis, mainly in two aspects. Firstly, caspase-8 activation initiates the caspase proteolytic cascade, and further chain-deactivate the downstream homologous enzymes, such as caspase-6, caspase-7, and finally activate caspase-3. Secondly, the death receptor pathway activates caspase-8, resulting in caspase precursor and cytochrome C (CytC) release. CytC releases from the mitochondrial membrane space to the cytosol in the early stage of apoptosis, involving in the activation of caspase-9, followed by activation of caspase-3, which ultimately causes DNA fragmentation and apoptosis. The TRIF/caspase-8-dependent pathway plays an important role in TLR3-mediated resistance to viral invasion and prevention of viral spread, that TLR3-mediated B cell proliferation is disordered in caspase-8 deficiency. The TRIF/caspase-8-dependent pathway is also present in the TLR4 pathway, which induces apoptosis in bacterially infected macrophages (25).

However, TRIF deficiency interrupted the negative function of TLR3 and TLR4 including apoptotic and inflammatory progress, which confirmed TRIF was the media of TLR3 and TLR4 in the NP cell apoptosis. Lin et al. (26) found TRIF deficiency inactivates NF-κB and reduces the release of harmful cytokines. Wu et al. (27) stated that deficiency of TRIF inhibits TLR3/4-mediated innate immune signaling. Apart from these, TRIF overexpression played the same role as upregulated TLR3 or TLR4 in the activation of apoptosis or inflammation in NP cells *via* caspase-8 and caspase-3. As in previous studies, TRIF activation induced chicken T-cell lymphoma apoptosis (28); TRIF-dependent activation of caspase-8 controls apoptosis proteins in melanoma cells (29), and TRIF-dependent caspase-8 pathway should contribute to the apoptosis of human NP cells.

In summary, our study elucidated that TRIF is critical for TLR3/4-mediated NP cell apoptosis in the development of NP cell degeneration, and TRIF

deficiency alleviates TLR3/4-induced apoptosis by caspase-8 inhibition. TRIF and its mediated signaling pathway are critical for us to understand the role of TLR3/4 in apoptotic and inflammatory responses. The role of TRIF in NP cell degeneration may become a novel topic of research, providing new theories and new ideas for IDD. Based on these results, we believe that TRIF is activated in a degenerated intervertebral disc. TLF3/4 promotes NP cell apoptosis and inflammation through the TRLF adaptor. TRLF expression is positively related to the apoptosis and inflammation in NP cells. These results suggest a therapeutic potential of the TRIF in the treatment of disc degeneration.

REFERENCES

1. Sampara P, Banala RR, Vemuri SK, Av GR, Gpv S. Understanding the molecular biology of intervertebral disc degeneration and potential gene therapy strategies for regeneration: a review. Gene Ther 2018; 25:67-82.
2. Vo NV, Hartman RA, Patil PR, et al. Molecular mechanisms of biological aging in intervertebral discs. J Orthop Res 2016; 34:1289-306.
3. Ding F, Shao ZW, Xiong LM. Cell death in intervertebral disc degeneration. Apoptosis 2013; 18:777-85.
4. Vidya MK, Kumar VG, Sejian V, Bagath M, Krishnan G, Bhatta R. Toll-like receptors: Significance, ligands, signaling pathways, and functions in mammals. Int Rev Immunol 2018; 37:20-36.
5. Kim AY, Shim HJ, Kim SY, Heo S, Youn HS. Differential regulation of MyD88- and TRIF-dependent signaling pathways of Toll-like receptors by cardamonin. Int Immunopharmacol 2018; 64:1-9.
6. Ho CC, Luo YH, Chuang TH, Lin P. Quantum dots induced interferon beta expression via TRIF-dependent signaling pathways by promoting endocytosis of TLR4. Toxicology 2016; 344-346:61-70.
7. Nilsen NJ, Vladimer GI, Stenvik J, et al. A role for the adaptor proteins TRAM and TRIF in toll-like receptor 2 signaling. J Biol Chem 2015; 290:3209-22.
8. Xia MZ, Liang YL, Wang H, et al. Melatonin modulates TLR4-mediated inflammatory genes through MyD88- and TRIF-dependent signaling pathways in lipopolysaccharide-stimulated RAW264.7 cells. J Pineal Res 2012; 53:325-34.
9. Mukherjee A, Morosky SA, Delorme-Axford E, Dybdahl-Sissoko N, Oberste MS, Wang T, Coyne CB. The coxsackievirus B 3C protease cleaves MAVS and TRIF to attenuate host type I interferon and apoptotic signaling. Plos Pathog 2011; 7:e1001311.
10. Kaiser WJ, Offermann MK. Apoptosis induced by the toll-like receptor adaptor TRIF is dependent on its receptor interacting protein homotypic interaction motif. J Immunol 2005; 174:4942-52.
11. Peterson LW, Philip NH, Dillon CP, Bertin J, Gough PJ, Green DR, Brodsky IE. Cell-Extrinsic TNF Collaborates with TRIF Signaling To Promote Yersinia-Induced Apoptosis. J Immunol 2016; 197:4110-17.
12. Klawitter M, Hakozaki M, Kobayashi H, et al. Expression and regulation of toll-like receptors (TLRs) in human intervertebral disc cells. Eur Spine J 2014; 23:1878-91.
13. Li Z, Wang X, Pan H, et al. Resistin promotes CCL4 expression through toll-like receptor-4 and activation of the p38-MAPK and NF-kappaB signaling pathways: implications for intervertebral disc degeneration. Osteoarthritis Cartilage 2017; 25:341-50.
14. Krock E, Rosenzweig DH, Currie JB, Bisson DG, Ouellet JA, Haglund L. Toll-like Receptor Activation Induces Degeneration of Human Intervertebral Discs. Sci Rep 2017; 7:17184.
15. Lee SM, Yip TF, Yan S, Jin DY, Wei HL, Guo RT, Peiris J. Recognition of Double-Stranded RNA and Regulation of Interferon Pathway by Toll-Like Receptor 10. Front Immunol 2018; 9:516.
16. Hulina-Tomašković A, Somborac-Bačura A, Grdić Rajković M, Bosnar M, Samaržija M and Rumora L. Effects of extracellular Hsp70 and cigarette smoke on differentiated THP-1 cells and human monocyte-derived macrophages. Molecular immunology 2019; 111:53-63.
17. Molinos M, Almeida CR, Caldeira J, Cunha C, Goncalves RM, Barbosa MA. Inflammation in intervertebral disc degeneration and regeneration. J R Soc Interface 2015; 12:20150429.

18. Jiang L, Zhang X, Zheng X, et al. Apoptosis, senescence, and autophagy in rat nucleus pulposus cells: Implications for diabetic intervertebral disc degeneration. J Orthop Res 2013; 31:692-702.
19. McCausland MR, Lebron AC, Pilch-Cooper HA, Howell S, Albert JM, Park YS and Levine AD. Toll-like receptor distribution in colonic epithelium and lamina propria is disrupted in HIV viremic, immune success and failure. AIDS (London, England) 2020 (DOI: 10.1097/QAD.0000000000002499).
20. Ellman MB, Kim JS, An HS, Chen D, KC R, An J, Dittakavi T, van Wijnen AJ, Cs-Szabo G, Li X, Xiao G, An S, Kim SG and Im HJ. Toll-like receptor adaptor signaling molecule MyD88 on intervertebral disk homeostasis: in vitro, ex vivo studies. Gene 2012; 505:283-90.
21. Michels KR, Lukacs NW, Fonseca W. TLR Activation and Allergic Disease: Early Life Microbiome and Treatment. Curr Allergy Asthma Rep 2018; 18:61.
22. Azam S, Jakaria M, Kim IS, Kim J, Haque ME, Choi DK. Regulation of Toll-Like Receptor (TLR) Signaling Pathway by Polyphenols in the Treatment of Age-Linked Neurodegenerative Diseases: Focus on TLR4 Signaling. Front Immunol 2019; 10:1000.
23. Kang S, Fernandes-Alnemri T, Rogers C, et al. Caspase-8 scaffolding function and MLKL regulate NLRP3 inflammasome activation downstream of TLR3. Nat Commun 2015; 6:7515.
24. Klawitter M, Quero L, Klasen J, Liebscher T, Nerlich A, Boos N, Wuertz K. Triptolide exhibits anti-inflammatory, anti-catabolic as well as anabolic effects and suppresses TLR expression and MAPK activity in IL-1beta treated human intervertebral disc cells. Eur Spine J 2012; 21 Suppl 6:S850-S859.
25. Maelfait J, Beyaert R. Non-apoptotic functions of caspase-8. Biochem Pharmacol 2008; 76:1365-73.
26. Lin S, Liang Y, Zhang J, et al. Microglial TIR-domain-containing adapter-inducing interferon-beta (TRIF) deficiency promotes retinal ganglion cell survival and axon regeneration via nuclear factor-kappaB. J Neuroinflammation 2012; 9:39.
27. Wu X, Lei C, Xia T, Zhong X, Yang Q, Shu HB. Regulation of TRIF-mediated innate immune response by K27-linked polyubiquitination and deubiquitination. Nat Commun 2019; 10:4115.
28. Zou H, Su R, Ruan J, et al. Double-stranded RNA induces chicken T-cell lymphoma apoptosis by TRIF and NF-kappaB. Sci Rep 2017; 7:7547.
29. Weber A, Kirejczyk Z, Besch R, Potthoff S, Leverkus M, Hacker G. Proapoptotic signalling through Toll-like receptor-3 involves TRIF-dependent activation of caspase-8 and is under the control of inhibitor of apoptosis proteins in melanoma cells. Cell Death Differ 2010; 17:942-51.

CAVEOLIN-1 IMPROVES LUNG INJURY IN RATS WITH CHRONIC OBSTRUCTIVE PULMONARY DISEASE PARTIALLY THROUGH Wnt/β-CATENIN SIGNALING PATHWAY

P. GUAN[1*], W.-T. CAI[2*], F. JIANG[1], W. LI[1], M. ZENG[1] and J. WU[1]

[1]Departments of Geriatrics, Hainan General Hospital, Hainan Affiliated Hospital of Hainan Medical University, Haikou, China; [2]Departments of Spinal surgery, Hainan General Hospital, Hainan Affiliated Hospital of Hainan Medical University, Haikou, China

Received February 5, 2020 – Accepted March 27, 2020

*These Authors contributed equally to this work

The aim of this study was to explore the effects of Caveolin-1 on lung injury in rats with chronic obstructive pulmonary disease (COPD). The forced expiratory volume in 0.3 s/forced vital capacity (FEV0.3/FVC) and peak expiratory flow (PEF) were determined. The total white blood cells (WBC), neutrophil ratio (NEUT%), mononuclear macrophage ratio (MNM%), lymphocyte ratio (LY%) and protein concentration in bronchoalveolar lavage fluid (BALF) were measured. Both FEV0.3/FVC and PEF significantly declined in the COPD group compared with those in the Control group, while they significantly rose in the IWR-1 group and Daidzin group compared with those in the COPD group. HE staining showed that there were alveolar dilatation and enlargement with obviously increased intercept in the COPD group, while there were basically no changes in the alveoli in the IWR-1 group and Daidzin group. Massive apoptosis of alveolar tissues was observed in COPD group, and there was only a little apoptosis in IWR-1 group and Daidzin group. In COPD group, WBC, NEUT% and protein concentration in BALF were obviously increased, MNM% was obviously decreased, and there was no obvious difference in LY% compared with those in the Control group. In the the IWR-1 group and Daidzin group, WBC, NEUT%, protein concentration, MNM% and LY% in BALF had no obvious differences compared with those in the Control group. In the IWR-1 group and Daidzin group, WBC, NEUT% and protein concentration evidently declined, MNM% evidently rose, and there was no obvious difference in LY% compared with those in the COPD group. Caveolin-1, Wnt-1 and β-catenin in lung tissues were remarkably higher in the COPD group than those in the Control group. Caveolin-1 was remarkably higher in the IWR-1 group than that in the Control group. And Wnt-1 and β-catenin were higher in the Daidzin group than those in the Control group. In addition, Wnt-1 and β-catenin in lung tissues markedly declined in the IWR-1 group compared with those in the COPD group. Caveolin-1, Wnt-1 and β-catenin in lung tissues also markedly declined in the Daidzin group compared with those in the COPD group. Caveolin-1 can improve lung injury in COPD rats through the Wnt/β-catenin signaling pathway.

Key words: Caveolin-1; chronic obstructive pulmonary disease; Wnt/β-catenin; signaling pathway

Corresponding Author:
Pin Guan, MD
Departments of Geriatrics, Hainan General Hospital,
Hainan Affiliated Hospital of Hainan Medical University,
No.19, Xiuhua Road, Xiuying District, Haikou,
Hainan, 570311 China
Tel.: +86 013519826648
e-mail: pinggu19770119@163.com

0393-974X (2020)
Copyright © by BIOLIFE, s.a.s.
This publication and/or article is for individual use only and may not be further reproduced without written permission from the copyright holder.
Unauthorized reproduction may result in financial and other penalties
DISCLOSURE: ALL AUTHORS REPORT NO CONFLICTS OF INTEREST RELEVANT TO THIS ARTICLE.

Chronic obstructive pulmonary disease (COPD) is a disease characterized by incomplete reversibility and persistent airflow obstruction (1), the pathological changes of which are chronic inflammation and structural damage in the airway wall and lung parenchyma, ultimately leading to airway stenosis, emphysema and increase in airflow resistance (2). Airway wall edema, smooth muscle contraction and secretion retention can cause partially reversible airflow obstruction (3). Different pathological changes in patients display different phenotypes in clinical conditions.

Caveolin is a 50-100 nm invaginated plasma membrane discovered in the 1950s, and is composed of Caveolin-1, Caveolin-2 and Caveolin-3. These proteins have specific functions and can exert various effects according to different cell types (4, 5). Caveolin-1 possesses a variety of biological functions in various diseases. After knockout of Caveolin-1 in the animal model of sepsis, the production of cytokines in mice is prolonged out of control. It can be seen that Caveolin-1 may be a key protective protein in sepsis animals (6). One study found that Caveolin is expressed in lung tissues (7), since when the role of Caveolin in lung tissue diseases has been increasingly studied year by year (8-10).

In recent years, there are increasingly more studies on Caveolin-1 and Wnt/β-catenin signaling pathways, but the association between Caveolin-1 and COPD through the Wnt/β-catenin signaling pathway has not been reported. Currently, the mechanism of action of Caveolin-1 in COPD remains unclear. In this study, therefore, the expression of Caveolin-1 was inhibited by IWR-1, and the effect of Wnt/β-catenin signaling pathway on COPD rats was studied, to provide a certain experimental basis for the treatment of COPD.

MATERIALS AND METHODS

Main reagents and instruments

Daidzin (cat.no 42926) and IWR-1 (cat.no I0161) were purchased from Sigma (St. Louis, MO, USA), the total RNA extraction kit from Beijing BioTeke Corporation (Beijing, China, the reverse transcription kit from TaKaRa (Dalian, China), Caveolin-1 (cat.no MA3-600), Wnt (cat. no PA5-96453), β-catenin (cat.no 71-2700) and β-actin (cat.no MA5-15739) antibodies from eBioscience (San Diego, CA, USA), the horseradish peroxidase (HRP)-labeled goat anti-rabbit IgG antibody from Proteintech (Wuhan, China), the ECL kit from Millipore (Billerica, MA, USA), low-temperature high-speed centrifuge, optical microscope, tissue embedding instrument, fluorescence quantitative polymerase chain reaction (qPCR) amplification instrument, gel imager, and small animal lung function tester.

Animal modeling and grouping

A total of 40 healthy adult male Sprague-Dawley rats weighing 260-300 g were purchased from the Laboratory Animal Center of Guangzhou Hospital of Traditional Chinese Medicine [animal license No.: SCXK (Guangdong) 2013-0020], and they were adaptively fed in a suitable environment at a temperature of 22±2°C and in 12/12 h light/dark cycle and had free access to food and water. The rats were divided into a Control group (n=10), COPD group (n=10), an IWR-1 group (n=10) and a Daidzin group (n=10). In the COPD group, IWR-1 group and Daidzin group, the rat model of COPD was established through airway infusion of lipopolysaccharide combined with smoking for 28 d according to a previous study (11). Briefly, the rats were placed in a glass box and exposed for 10 min to cigarette smoke twice per day, 10 cigarettes at a time. The rats were placed in the cage for routine feeding after each smoking time. On the 1st and 14th day, lipopolysaccharide (1.25 g/L, 1 mg/kg) was infused into the trachea of the rats. At 2 d after modeling, IWR-1 (inhibitor of Wnt/β-catenin signaling pathway, 10 μM, 2ml/kg) and Daidzin (inhibitor of Caveolin-1, 0.1 mg/kg) were injected *via* caudal vein into rats in the IWR-1 group and Daidzin group once a day for 3 d, the doses were determined by the preliminary experimental results (data not shown). This study was approved by the Animal Ethics Committee of Hainan Medical University Animal Center.

Detection of lung function

After modeling, the forced expiratory volume in 0.3 s/forced vital capacity (FEV0.3/FVC) and peak expiratory flow (PEF) in each group were determined using whole body plethysmography, as follows: the rats were placed in the plethysmograph of non-invasive lung function meter and connected to the sensor and data analysis system, and

then the above indexes were recorded after the breathing became quiet.

Bronchoalveolar lavage

The thoracic cavity of rats was cut open, the gavage needle was inserted through the organ and connected to the injector, and the bronchus was ligated, followed by bronchoalveolar lavage with pre-cooled normal saline for 3 times (2.5 mL/time). Then the bronchoalveolar lavage fluid (BALF) was collected, centrifuged using the low-temperature centrifuge at 2000 rpm and 4°C for 10 min, and stored at -20°C with the supernatant discarded.

Fluorescence qPCR

The total RNA was extracted from lung tissues using TRIzol reagent (Invitrogen, Carlsbad, CA, USA), and its concentration and purity were measured based on A_{260}/A_{280} using an ultra-micro spectrophotometer. Then the RNA was reversely transcribed into cDNA, followed by qRT-PCR using the AceQ qPCR SYBR Green Master Mix kit. The amplification conditions were as follows: 95°C for 5 min, 95°C for 10 s, 60°C for 30 s, 72°C for 1 min for a total of 40 cycles, 95°C for 10 min. The fluorescence qPCR system included 5 μL of qPCR Master Mix (2×), 1 μL of PCR reverse primers (Table I), 1 μL of cDNA and 12 μL of ddH_2O. Finally, the results were calculated using $2^{-\Delta\Delta ct}$.

Hematoxylin-eosin (HE) staining

The lung tissue samples fixed for 24 h were taken out, washed with water, dehydrated with ethanol, embedded in paraffin and sliced into sections, followed by hematoxylin staining at room temperature for 10 min. Then the sections were washed with water for 30 min, 1% hydrochloric acid for 30 s and water for 30 s, stained with eosin at room temperature for 5 min, dehydrated with ethanol and sealed with neutral gel in a ventilated environment, followed by observation of changes in lung tissues under a microscope.

Terminal deoxynucleotidyl transferase-mediated dUTP nick end labeling (TUNEL) staining

The apoptosis was detected using the *in situ* apoptosis assay kit in strict accordance with the instructions. After the sections were baked dry, they were deparaffinized with xylene twice (10 min/time), dehydrated with gradient alcohol (10 min/gradient), soaked in citrate (pH 6.0) for 1 min, sealed for 30 min, and washed with phosphate buffered saline (PBS) for 5 times (3 min/time), followed by color development using DAB and nuclear counterstaining with methyl green. The apoptotic nuclei were stained brown yellow, while the non-apoptotic nuclei were stained light dark green.

Western blotting

After the rats were sacrificed, the lung tissues were taken, washed twice with PBS, ground with liquid nitrogen in a pre-cooled mortar, and lysed with lysis buffer on ice for 1 h. The total protein was ultrasonically extracted and centrifuged at 13,000 rpm for 10 min, and the supernatant was taken to quantify the protein concentration using the bicinchoninic acid (BCA) method (Pierce, Rockford, IL, USA). After 12% sodium dodecyl sulphate-polyacrylamide gel electrophoresis (SDS-PAGE), 30 μg of protein samples were transferred onto a 0.45 μm polyvinylidene fluoride (PVDF) membranes (Millipore, Billerica, MA, USA), and the membrane was sealed with 3% bovine serum albumin and washed twice with phosphate buffered saline-tween (PBST) (5 min/time). Then the protein was incubated with primary antibodies diluted with the antibody diluent at 4°C overnight. After the membrane was washed again with PBST for 3 times (5 min/time), the protein was incubated again with horseradish peroxidase (HRP)-labeled secondary antibodies diluted with the antibody diluent at 37°C for 1 h. Finally, the electrochemiluminescence (ECL) developing solution was added dropwise for color development and quantification using the ChemiDoc MP gel imaging system.

Statistical analysis

Statistical Product and Service Solutions (SPSS) 20.0 software (IBM, Armonk, NY, USA) was used for the statistical analysis of all experimental results. All experiments were repeated for 3 times and the results were expressed as mean ± standard deviation. One-way analysis of variance for the intergroup comparison followed by Least Significant Difference as its Post Hoc Test. $P<0.05$ suggested the statistically significant difference.

RESULTS

Comparison of lung function in each group

As shown in Fig. 1, both FEV0.3/FVC and PEF significantly declined in the COPD group compared with those in the Control group ($P<0.01$), while they

had no significant differences in the IWR-1 group and Daidzin group compared with those in the Control group. FEV0.3/FVC and PEF significantly rose in the IWR-1 group and Daidzin group compared with those in the COPD group (P<0.01).

Pathological manifestations of lung tissues in each group

As shown in Fig. 2, compared with Control group, COPD group had alveolar dilatation and enlargement with obviously increased intercept (P<0.01), while there were basically no changes in the alveoli in the IWR-1 group and Daidzin group. Compared with the COPD group, the IWR-1 group and Daidzin group had alveolar atrophy and shrinking with decreased intercept (P<0.01).

TUNEL staining of lung tissues in each group

No apoptosis of alveolar tissues was found in the Control group. Compared with the Control group, most nuclei in alveolar tissues were stained brown yellow. The apoptosis of alveolar cells was obvious in the COPD group. Compared with the COPD group, the apoptosis of alveolar tissues was evidently improved, and the nuclei were not significantly stained brown yellow (Fig. 3).

Cell count and protein concentration in BALF

In the COPD group, total white blood cells (WBC), neutrophil ratio (NEUT%) and protein concentration in BALF were obviously increased (P<0.05), mononuclear macrophage ratio (MNM%) was obviously decreased (P<0.05), and there was no obvious difference in lymphocyte ratio (LY%) compared with those in the Control group. In the IWR-1 group and Daidzin group, WBC, NEUT%, protein concentration, MNM% and LY% in BALF

Table I. *qRT-PCR primer sequences*

Primer	Sequence
Caveolin-1	5'-GCAGACGAGGTGAATGAGAAG-3'
	5'-GGTAGACAGCAAGCGGTAAAA-3'
Wnt-1	5'-AGACCTTCGACTGCCTTTTC-3'
	5'-AGGAACTCAGGTAGTCACGGA-3'
β-catenin	5'-GTGCAATTCCTAGCTGACA-3'
	5'-CTTAAAGATGGCCAGCAAGC-3'
β-actin	5'-CTCTCCCTCACGCCATC-3'
	5'-ACGCACGATTTCCCTCTC-3'

Table II. *Cell count and protein concentration in BALF*

	Control group	COPD group	IWR-1 group	Daidzin group
WBC ($\times 10^8$/L)	1.36±0.23	2.34±1.08[a]	1.61±2.1[b]	1.83±4.3[b]
NEUT%	8.7±2.7	18.5±6.1[a]	9.4±3.8[b]	12.6±3.2[b]
MNM%	84.6±2.3	72.1±2.4[a]	83.4±3.1[b]	81.8±2.5[b]
LY%	7.4±1.8	8.5±1.5	7.3±1.0	7.8±1.5
Protein (mg/L)	194.24±34.15	367.91±43.54[a]	201.66±40.14[b]	264.86±36.72[b]

a :P<0.05 vs Control group; b: P<0.05 vs COPD group

had no obvious differences compared with those in the Control group. In the IWR-1 group and Daidzin group, WBC, NEUT% and protein concentration evidently declined (P<0.05), MNM% evidently rose (P<0.05), and there was no obvious difference in LY% compared with those in the COPD group (Table II).

MRNA levels of Caveolin-1, Wnt-1 and β-catenin in lung tissues in each group

The mRNA expressions of Caveolin-1, Wnt-1 and β-catenin in lung tissues were remarkably higher in the COPD group than those in the Control group, displaying extremely significant differences (P<0.01), they had no differences in the IWR-1 group and Daidzin group compared with those in the Control group, while they were lower in the IWR-1 group and Daidzin group than those in the COPD group, displaying extremely significant differences (P<0.01) (Fig. 4).

Protein levels of Caveolin-1, Wnt-1 and β-catenin in lung tissues in each group

The protein expressions of Caveolin-1, Wnt-1 and β-catenin in lung tissues were remarkably higher in the COPD group than those in the Control group (P<0.05), the protein expression of Caveolin-1 was remarkably higher without obvious changes in Wnt-1 and β-catenin proteins in IWR-1 group than that in the Control group (P<0.05), and the protein expressions of Wnt-1 and β-catenin were higher without obvious changes in Caveolin-1 protein in the Daidzin group than those in the Control group. In addition, the protein expressions of Wnt-1 and β-catenin in lung tissues markedly declined without obvious changes in Caveolin-1 protein in the IWR-1 group compared with those in the COPD group (P<0.05), and the protein expressions of Caveolin-1, Wnt-1 and β-catenin in lung tissues also markedly declined in the Daidzin group compared with those in the COPD group (P<0.05) (Fig. 5) (Table III).

DISCUSSION

COPD is a disease characterized by chronic inflammation and structural damage in the airway wall and lung parenchyma, ultimately leading to airway stenosis, emphysema and increase in airflow resistance (12). Studies have demonstrated that COPD is a systemic disease, and its multiple extrapulmonary manifestations also significantly affect the progression of disease (13). The characteristic pathological changes in COPD are small airway inflammation and lung parenchymal destruction. Chronic bronchitis occurs at the initial stage, and emphysema is caused ultimately with the aggravation of inflammation and increase in viscosity of mucus and airway resistance (14). Studies have shown that in the induced sputum, BALF and lung tissues of COPD patients, the expressions of pro-inflammatory factors IL-8, TNF-α, MCP-1 and IFN-γ markedly rise (15, 16). There are also studies proving that the overexpression of IFN-γ may be one of the causes of emphysema (17).

Caveolin is expressed in most tissues in the body.

Table III. *Optical density of Caveolin-1, Wnt-1 and β-catenin protein bands in each group*

Protein	Optical density	Control group	COPD group	IWR-1 group	Daidzin group
Caveolin-1	Target protein/β-actin	0.73±0.24	2.86±0.32a	2.46±0.24ab	1.21±0.46b
Wnt-1	Target protein/β-actin	1.56±0.24	5.48±0.34a	1.68±0.41b	2.69±0.2.7ab
β-catenin	Target protein/β-actin	1.34±0.29	6.32±0.42a	1.48±0.48b	2.78±0.48b

a: P<0.05 vs Control group; b: P<0.05 vs COPD group

Caveolin-1 can interact with many proteins and regulate the cell membrane transport and intracellular signal transduction pathway (18), which is involved in many pathological and physiological processes. In the study on inflammation, tissue damage and tumors, Caveolin-1 can function through regulating cell cycle, secretion of inflammatory factors and apoptotic pathway (19). The Wnt family, a kind of secretory glycoproteins, can participate in many cellular processes, such as cell proliferation, differentiation and apoptosis (20). β-catenin is a key molecule in the activation of the Wnt/β-catenin signaling pathway. Studies have confirmed that Caveolin-1 can regulate various diseases caused by inflammation through the Wnt/β-catenin signaling pathway (21).

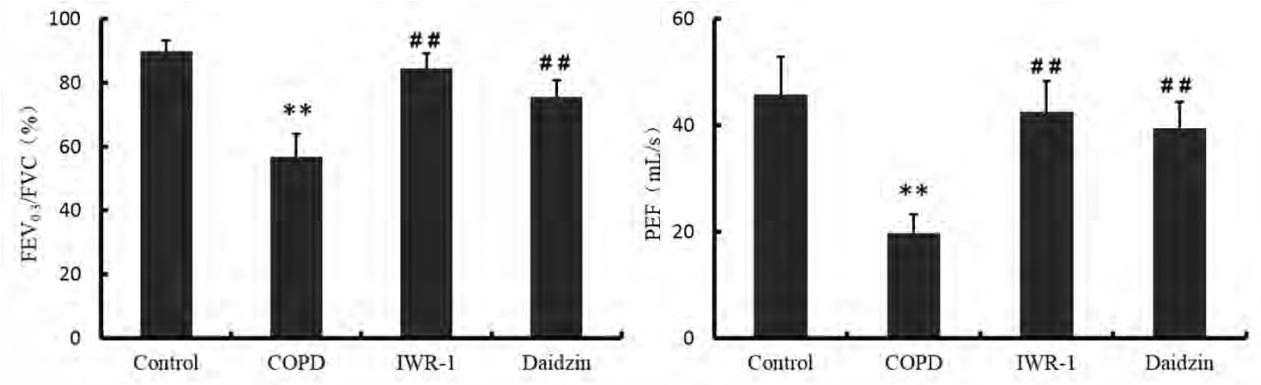


Fig. 1. *Comparison of lung function in each group. FEV0.3/FVC: forced expiratory volume in 0.3 s/forced vital capacity, PEF: peak expiratory flow. $^{**}P<0.01$ vs Control group; $^{\#\#}P<0.01$ vs COPD group.*

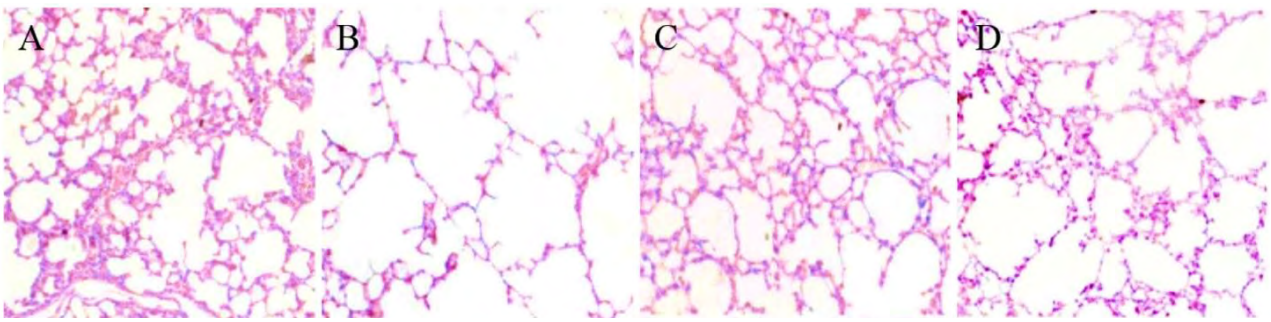


Fig. 2. *HE staining of alveoli in each group (magnification: 200×). **A**) Control group. **B**) COPD group. **C**) IWR-1 group. **D**) Daidzin group*

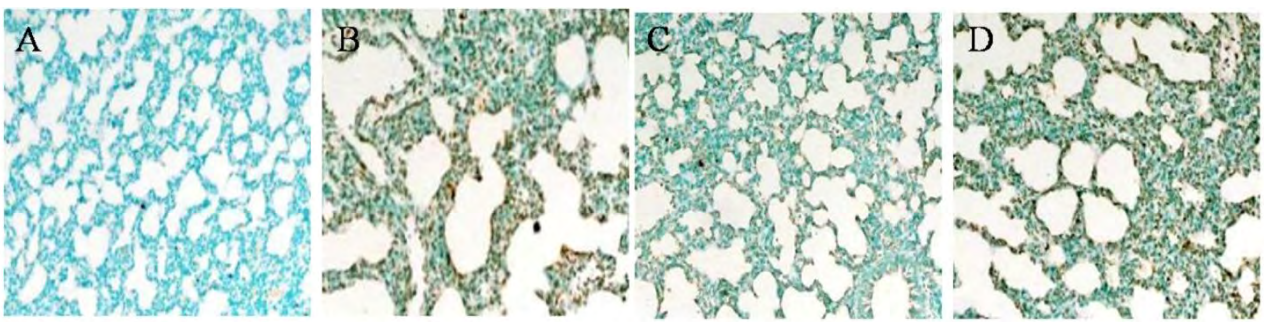


Fig. 3. *TUNEL staining of lung tissues in each group (magnification: 400×). **A**). Control group. **B**) COPD group) **C**) IWR-1 group. **D**) Daidzin group*

In the present study, the rat model of COPD was established through airway infusion of lipopolysaccharide combined with smoking. The Wnt/β-catenin pathway was inhibited by IWR-1, and the effect of Caveolin-1 on COPD was explored. Then the Caveolin-1 was suppressed by Daidzin, and the effect of Wnt/β-catenin pathway on COPD was also explored. It was found that in the COPD group, WBC, NEUT% and protein concentration in BALF were obviously increased (P<0.05), MNM% was obviously decreased (P<0.05), and there was no obvious difference in LY% compared with those in the Control group. In IWR-1 group and Daidzin group, WBC, NEUT%, protein concentration, MNM% and LY% in BALF had no obvious differences compared with those in the Control group. It can

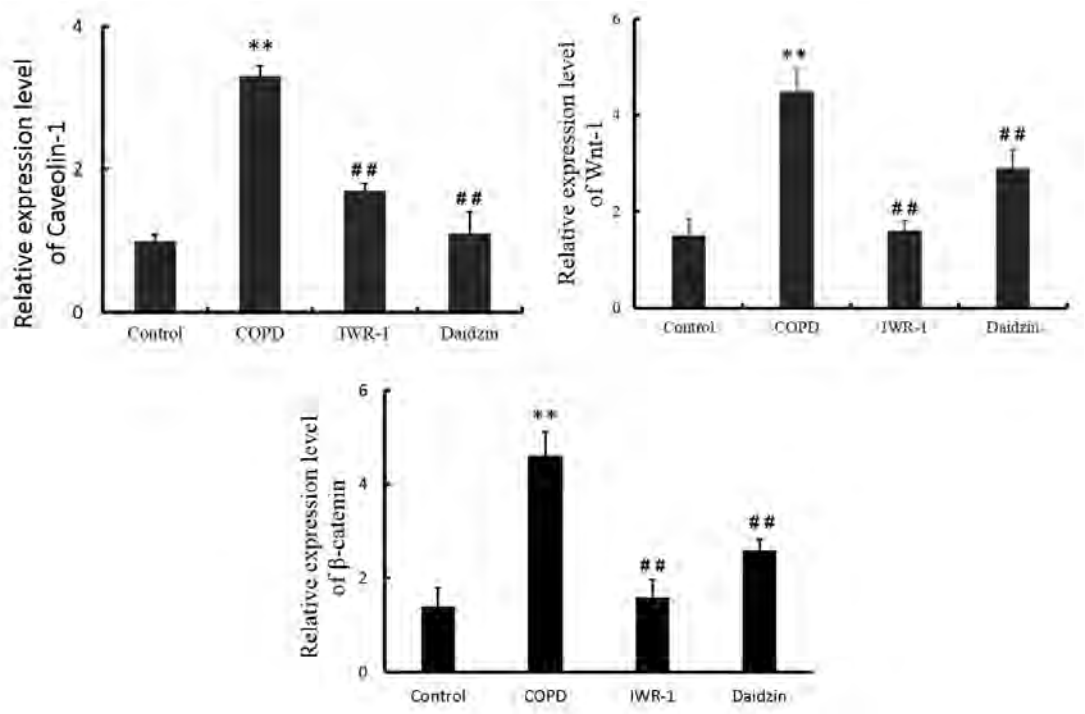


Fig. 4. *MRNA levels of Caveolin-1, Wnt-1 and β-catenin in lung tissues in each group. **P<0.01 vs Control group; ##P<0.01 vs COPD group.*

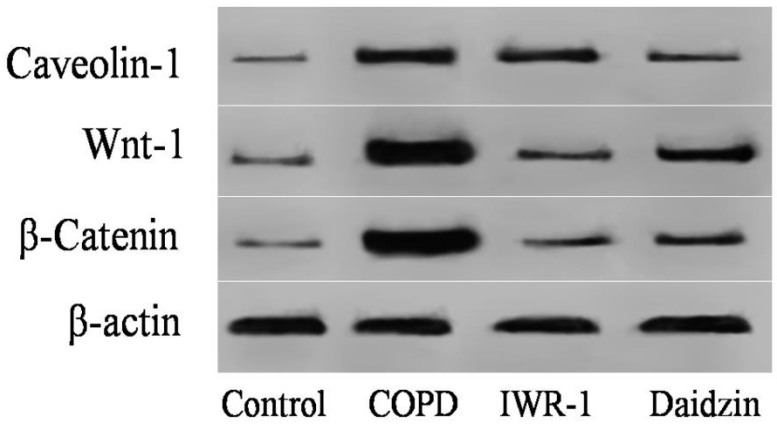


Fig. 5. *Protein levels of Caveolin-1, Wnt-1 and β-catenin in lung tissues in each group*

be seen that inhibiting the Wnt/β-catenin signaling pathway can markedly reduce the production of inflammatory factors in COPD. Moreover, the results of HE staining showed that there were alveolar dilatation and enlargement with obviously increased intercept in COPD group ($P<0.01$), while there were basically no changes in the alveoli in the IWR-1 group and Daidzin group, suggesting that suppressing Caveolin-1 and Wnt/β-catenin pathway can markedly improve the pathological changes in COPD in rats. According to the TUNEL staining, obvious apoptosis of alveolar tissues was observed in the COPD group, and apoptosis was effectively improved in the IWR-1 group and Daidzin group. Furthermore, the results of qRT-PCR showed that after the expression of Caveolin-1 was inhibited, the mRNA expressions of Wnt and β-catenin declined, which were also verified *via* Western blotting. To sum up, Caveolin-1 can improve COPD in rats through the Wnt/β-catenin signaling pathway. When lung injury occurs, Caveolin-1 is up-regulated by inflammatory factors, and then it activates the Wnt/β-catenin pathway, thus promoting inflammation and inducing apoptosis. On the contrary, inflammatory factors are significantly reduced to inhibit apoptosis when the Wnt/β-catenin signaling pathway is inhibited, and inflammatory factor-induced apoptosis is alleviated when Caveolin-1 is inhibited.

However, the exact mechanism of Caveolin-1 in affecting COPD may also be associated with other signaling pathways, and only the effect on the Wnt/β-catenin signaling pathway was verified without clarifying whether it has an effect on other signaling pathways. This study lays an experimental foundation for further research on the occurrence mechanism of COPD in the future.

In conclusion, caveolin-1 can improve lung injury in COPD rats through the Wnt/β-catenin signaling pathway.

REFERENCES

1. Yu X, Wang W, Zheng H, Qian XJ, Jiang P. Clinical efficacy of a series of Chinese herbal medicines in the treatment of stable chronic obstructive pulmonary disease based on syndrome differentiation. J Biol Regul Homeost Agents 2019; 33:1539-44.
2. Liu BH, Sun MX, Zhou N, Li YP, Wang MZ, Yu J, Zhou HS. Detection and study of plasma D-dimer change in patients with acute exacerbation of chronic obstructive pulmonary disease. J Biol Regul Homeost Agents 2016; 30:839-45.
3. Malerba M, Ragnoli B, Salameh M, Sennino G, Sorlini ML, Radaeli A, Clini E. Sub-clinical left ventricular diastolic dysfunction in early stage of chronic obstructive pulmonary disease. J Biol Regul Homeost Agents 2011; 25:443-51.
4. Aggarwal NR, King LS, D'Alessio FR. Diverse macrophage populations mediate acute lung inflammation and resolution. Am J Physiol Lung Cell Mol Physiol 2014; 306:L709-L725.
5. Qiaoli S, Yi S, Jie Z, Deyun C. KLF2 and caveolin-1 as early indicators of acute lung injury induced by paraquat. Eur Rev Med Pharmacol Sci 2016; 20:138-45.
6. Charles S, Raj V, Arokiaraj J, Mala K. Caveolin1/protein arginine methyltransferase1/sirtuin1 axis as a potential target against endothelial dysfunction. Pharmacol Res 2017; 119:1-11.
7. Hackett TL, de Bruin HG, Shaheen F, van den Berge M, van Oosterhout AJ, Postma DS, Heijink IH. Caveolin-1 controls airway epithelial barrier function. Implications for asthma. Am J Respir Cell Mol Biol 2013; 49:662-71.
8. Cai L, Yi F, Dai Z, et al. Loss of caveolin-1 and adiponectin induces severe inflammatory lung injury following LPS challenge through excessive oxidative/nitrative stress. Am J Physiol Lung Cell Mol Physiol 2014; 306:L566-L573.
9. Gilbert G, Ducret T, Savineau JP, Marthan R, Quignard JF. Caveolae are involved in mechanotransduction during pulmonary hypertension. Am J Physiol Lung Cell Mol Physiol 2016; 310:L1078-L1087.
10. Ludwig A, Nguyen TH, Leong D, et al. Caveolae provide a specialized membrane environment for respiratory syncytial virus assembly. J Cell Sci 2017; 130:1037-50.
11. Wang C, Ding H, Tang X, Li Z, Gan L. Effect of Liuweibuqi capsules in pulmonary alveolar epithelial cells and COPD through JAK/STAT pathway. Cell Physiol Biochem 2017; 43:743-56.
12. Yu Q, Chen X, Fang X, Chen Q, Hu C. Caveolin-1 aggravates cigarette smoke extract-induced MUC5AC secretion in human airway epithelial cells. Int J Mol Med 2015; 35:1435-42.

13. Hackett TL, de Bruin HG, Shaheen F, et al. Caveolin-1 controls airway epithelial barrier function. Implications for asthma. Am J Respir Cell Mol Biol 2013; 49:662-71.
14. Cai L, Yi F, Dai Z, et al. Loss of caveolin-1 and adiponectin induces severe inflammatory lung injury following LPS challenge through excessive oxidative/nitrative stress. Am J Physiol Lung Cell Mol Physiol 2014; 306:L566-L573.
15. Zhang M, Lin L, Lee SJ, Mo L, Cao J, Ifedigbo E, Jin Y. Deletion of caveolin-1 protects hyperoxia-induced apoptosis via survivin-mediated pathways. Am J Physiol Lung Cell Mol Physiol 2009; 297:L945-L953.
16. Jin Y, Lee SJ, Minshall RD, Choi AM. Caveolin-1: a critical regulator of lung injury. Am J Physiol Lung Cell Mol Physiol 2011; 300:L151-L160.
17. Shao M, Yue Y, Sun GY, You QH, Wang N, Zhang D. Caveolin-1 regulates Rac1 activation and rat pulmonary microvascular endothelial hyperpermeability induced by TNF-alpha. Plos One 2013; 8:e55213.
18. Moon RT, Kohn AD, De Ferrari GV, Kaykas A. WNT and beta-catenin signalling: diseases and therapies. Nat Rev Genet 2004; 5:691-701.
19. Baarsma HA, Konigshoff M, Gosens R. The WNT signaling pathway from ligand secretion to gene transcription: molecular mechanisms and pharmacological targets. Pharmacol Ther 2013; 138:66-83.
20. Bauer M, Willert K. Wnt signaling: the beta-cat(enin)'s meow. Genes Dev 2012; 26:105-109.
21. De Langhe SP, Reynolds SD. Wnt signaling in lung organogenesis. Organogenesis 2008; 4:100-108.

LINC00662 PROMOTES GLYCOLYSIS AND CELL SURVIVAL BY REGULATING miR-375/HIF-1α AXIS IN OVARIAN CANCER

L-M. TAO[1], Y-F. GONG[2], H-M. YANG[1], J-H. PEI[1], X-J. ZHAO[1] and S-S. LIU[1]

[1]Department of Obstetrics and Gynecology, The First Affiliated Hospital of Nanchang University, Nanchang, Jiangxi Province, China; [2]Department of Geriatrics, The First Affiliated Hospital of Nanchang University, Nanchang, Jiangxi Province, China

Received July 15, 2019 – Accepted December 10, 2019

Ovarian cancer (OC) is one of the most common gynecological malignancies, with the highest mortality rate in women worldwide. LINC00662, a long non-coding RNA (lncRNA), was shown to play a vital role in many malignancies, while little is known about its role in OC. Firstly, our study determined the expression of LINC00662 in OC tissues and cells. Upregulation or downregulation of LINC00662 were performed in OC cells to explore its effects on cell proliferation and glycolysis of OC. The interaction between LINC00662 and miR-375 was verified using luciferase assays and RNA immunoprecipitation. Results showed that LINC00662 was highly expressed in OC tissues and cells, and patients with increased expression of LINC00662 were associated with shorter overall survival. Furthermore, functional assays proved that LINC00662 was essential for OC cell proliferation and glycolysis. Subsequently, our study further revealed that LINC00662 acted as a competitive RNA and it could modulate the expression of HIF-1α through directly binding with miR-375. Collectively, upregulation of LINC00662 in ovarian cancer tissues is closely correlated to poor survival. LINC00662 might regulate HIF-1α expression via miR-375. These findings suggested that LINC00662 has the potential to be explored as a diagnostic biomarker for OC.

Ovarian cancer (OC) is the sixth most common and aggressive malignancy in women worldwide (1, 2). Because of the lack of specific symptoms and deficiencies in tumor screening procedure (1, 3), OC is frequently diagnosed at an advanced stage, which leads to poor survival rates. It is of great importance to explore novel methods or specific markers for OC early diagnosis.

LncRNAs are a type of transcribed RNAs with a length of more than 200 nucleotides that do not encode proteins. LncRNAs were reported to play important roles in participating in fundamental biological mechanisms and to have oncogenic or suppressive effects during tumor progression. Numerous studies demonstrated that lncRNA was involved in regulation of protein expression via directly binding with microRNAs (4-8), and this mechanism was also frequently found in various type of cancers (5, 9-11). LINC00662 is an lncRNA that was found to be aberrantly expressed in many cancer types. For example, LINC00662 competitively sponges miR-34a to promote the prostate cancer (12). High expression of LINC00662 also contributes to progressions of oral squamous cell carcinoma and lung cancer (8, 11). In addition, the expression of LINC00662 was closely correlated

Key words: LINC00662; miR-375; ovarian cancer; HIF-1α; glycolysis

Corresponding Author:
Dr Sisun Liu,
Department of Obstetrics and Gynecology,
The First Affiliated Hospital of Nanchang University,
17 Yongwai Zhengjie, Donghu District,
Nanchang City, Jiangxi Province, China
Tel.: +86 13767071017
e-mail: sisunliusdr@163.com

0393-974X (2020)
Copyright © by BIOLIFE, s.a.s.
This publication and/or article is for individual use only and may not be further reproduced without written permission from the copyright holder.
Unauthorized reproduction may result in financial and other penalties
DISCLOSURE: ALL AUTHORS REPORT NO CONFLICTS OF INTEREST RELEVANT TO THIS ARTICLE.

to clinicopathological characteristics (8). Therefore, LINC00662 exhibits as a promising diagnostic marker in diverse cancer types. However, the role of LINC00662 in OC remains largely unknown.

The most popular therapy used for cancer treatment was to inhibit the proliferation of tumor cells, and the metabolism of tumor cells has recently been recognized as a novel therapeutic target (13). Tumor environment is characterized with low oxygen (14). Glycolysis rather than oxidative phosphorylation is the major source of energy demand for rapidly proliferating tumor cells (15). Reversing glycolysis to oxidative phosphorylation is an efficient strategy to induce tumor cell death (16). A number of studies have explored methods to inhibit glycolysis as potential therapy for cancer treatment (17). Hypoxia-inducible factor-1α (HIF-1α) is the most studied transcription factor which can be activated under hypoxic conditions (18), and its activation importantly contributes to glycolysis (13). Therefore, HIF-1α is a promising target to inhibit glycolysis and reprogram the energy metabolism in tumor cells. Hence, a comprehensive knowledge of regulation mechanisms on HIF-1α is of great importance. Regulation of HIF-1α by lncRNA has been recently reported in several studies. Shih et al. demonstrated LncHIFCAR acted as an HIF-1α co-activator in promoting oral cancer progression (19). Luo et al. suggested that lncRNA MALAT1 was able to promote glycolysis via stabilizing HIF-1α (9).

In the present study, firstly the expression was determined of the pattern of LINC00662 in OC tissues and cells, and then its effects were explored on OC cell proliferation and glycolysis. Finally, the inherent mechanisms mediating LINC00662-associated effects were investigated.

MATERIALS AND METHODS

Tissue samples

A total of 40 tumor tissues and paired adjacent noncancerous tissues were collected from patients receiving surgical resection at The First Affiliated Hospital of Nanchang University (Approval no.2019-32). All OC patients were histologically diagnosed by staining with hematoxylin and eosin (H&E), and none had received any anti-tumor treatment prior to surgery. Written informed consent was obtained from all enrolled patients, and the study was approved by the ethics committee of The First Affiliated Hospital of Nanchang University.

Human OC cell lines (CAOV3, SKOV3, OVCAR3, A2780), one human ovarian epithelial cell (HOSEpiC) and HEK-293T cells were purchased from American Type Culture Collection (ATCC). SKOV3 were maintained in McCoy's 5A (GIBCO, USA). HOSEpiC and OVCAR3 were cultured in RPMI 1640 (GIBCO, USA). HEK293, CAOV3 and A2780 were routinely cultured in Dulbecco's Modified Eagle Medium (GIBCO, USA). Cells were all cultured in indicated medium supplemented with 10% fetal bovine serum (GIBCO, USA) in a humidified incubator at 37°C under 5% CO_2.

RNA extraction and qRT-PCR assay

Total RNA was extracted from tissue samples and OC cells using TRIzol reagent (Life Technologies Corporation, Carlsbad, CA, USA). Complementary DNA (cDNA) was then synthesized using a Reverse Transcription Kit (Takara, Japan). QRT-PCR was performed with a SYBR green Master Mix (Takara, Japan) in triplicate. The primers were designed by Primer 5.0 as shown in Table I and specificities of the primers were tested by Primer-BLAST (http://blast.ncbi.nlm.nih.gov/Blast.cgi). Relative expression levels of miRNA, mRNA and LINC00662 were normalized using $2^{-\Delta\Delta Ct}$ method. miRNA and LINC00662 expression were normalized to U6, while mRNA of protein was normalized to glyceraldehyde 3-phosphate dehydrogenase (GAPDH).

Western blot analysis

Cells were lysed by RIPA lysis buffer (Cell Signaling Technology, USA) supplemented with protease inhibitor to obtain total protein. Protein concentration was determined by bicinchoninic (BCA) protein assay. Western blot analysis was performed with the primary antibodies targeting human GAPDH, HIF-1α, Cyclin D1, and p21. All the antibodies were purchased from Abcam. An enhanced chemiluminescence kit was used to visualize the blots, and signal was measured by ChemiDoc™ XRS+ System (Bio-Rad, USA).

Vector construction and siRNA transfection

LINC00662 overexpression plasmid was constructed using

pcDNA3.1 vector (Invitrogene, USA). A scramble vector was used as control vector. LINC00662 interference RNA (si-LINC00662#1: 5'-GCAGGCGTACAACTAACAAdTdT-3', si-LINC00662#2: 5'-GGCTGATCTCACCTTGTAAdTdT-3') was designed and constructed by GenePharma Co., Ltd (Shanghai, China). The miR-375 mimics and inhibitors were purchased from RiboBio Co., Ltd. (Guangzhou, China). Transfections were performed using Lipofectamine 2000 (Invitrogen, Carlsbad, CA, USA) in serum-free medium according to the manufacturer's instructions.

Proliferation assay

For the cell proliferation assay, cells were plated into a flat bottom 96-well plate at 2.5×10^3 cells per well in triplicate with 100 µl medium. Ten µl of cell counting kit-8 (Dojindo, China) was added into each well at 0, 24, 48, 72 and 96 h. After incubation for 2 h, the absorbance at 450 nm was measured using a microplate reader (Bio-Rad, USA).

Cell-cycle distribution analysis

For cell cycle analysis, cells in log phase of growth were collected and fixed with 90% ethanol overnight at 4°C after being washed with phosphate-buffered saline. Then cells were treated with RNase for 30 min at 37°C, and then stained with PI (propidium iodide) for an another 30 min. Cells were examined in a FACS Calibur flow cytometer (Becton-Dickinson), and DNA histograms were analyzed using Modifit software.

Luciferase assay

The wild-type (WT) or mutant (MUT) miRNA response element of LINC00662 and 3'-untranslated region (3'-UTR) of HIF-1A were synthesized and inserted into multiple cloning site of the pmiRGOL vector (Promega, USA). HEK293 were co-transfected with mimics or control for miR-375 and pmiRGOL vectors carrying wild type or mutant target sequences using Lipofectamine 2000 reagent following instructions. Activities of firefly and renilla luciferases were measured using the Dual Luciferase Assay Kit (Promega, USA). All assays were designed in triplicate and repeated for three times.

RNA

RNA ISH was performed on formalin fixed paraffin-embedded (FFPE) tissue sections with the RNAscope® 2.0 HD Detection Kit (Advanced Cell Diagnostics) and custom probe set Hs-LINC00662 as per the instructions. The tissue sections were scanned using the Aperio Imagescope (Leica) after Hematoxylin counterstaining.

Cells were crosslinked with UV and then lysed in RIPA buffer containing the proteinase and RNase inhibitors. Cell lysates were collected for immunoprecipitation overnight at 4°C using anti-Ago2 antibodies (Abcam, UK) and IgG control (Abcam, UK), and protein A/G beads. The beads that binded with protein-RNA complex were then washed with RIPA buffer for 5 times and digested with Proteinase K at 45°C for 45 min to release the RNA from the beads. Then LINC00662 and miR-375 were determined by qRT-PCR.

Detection of glucose uptake, lactate production and cellular ATP level

The glucose uptake assay was performed using the Glucose Uptake Assay Kit (Abcam, #ab136955) and lactate production assay was performed using the l-Lactate Assay Kit (Abcam, #ab65331) according to the manufacturer's protocol. Cellular ATP levels were measured by using an ATP Assay Kit (Abcam, #ab83355) according to the manufacturer's protocol.

Statistical analysis

All statistical analyses were performed using SPSS 21.0 (SPSS, USA). Data are presented as mean ± standard deviation of parallel experiments. Paired Student's *t*-test was used for comparison of paired data. One-way ANOVA analysis was used for comparison of more than two groups, followed by Newman-Keuls post hoc test. Log-rank Test was performed to determine the associations between the LINC00662 expression and overall survival of patients.

RESULTS

Aberrant expression of LINC00662 *in ovarian cancer tissues and cell lines*

The expression levels of LINC00662 in OC tissues samples and cells were determined by qRT-PCR. The results showed that LINC00662 was dramatically higher in OC tissues compared with paired adjacent non-cancerous tissues (Fig. 1A). *In situ* expression of LINC00662 in OC tissues was also higher detected by *in situ* RNA hybridization (Fig. 1B). Further analysis of LINC00662 expression revealed that increased expression of LINC00662

was correlated with poor prognosis in OC patients, and patients with higher expression of LINC00662 tended to have shorter overall survival (Fig. 1C). LINC00662 expressions in all OC cells surveyed in our study were relatively higher than HOSEpiC, and OVCAR3 was detected to have the highest LINC00662 expression. Taken together, these results suggest that LINC00662 may be involved in the progression of OC.

Expression of LINC00662 was essential for proliferation of OC cells in vitro

To evaluate the effect of LINC00662 on proliferation of OC cells in vitro, CAOV3 cells were transfected with LINC00662 overexpression vector to increase LINC00662 expression, while OVCAR3 cells were transfected with si-LINC00662 (si-LINC00662 1#, si-LINC00662 2#) to silence endogenous LINC00662. The transfection efficacies of LINC00662 were confirmed by qRT-PCR assay. As a result, LINC00662 was successfully overexpressed in CAOV3 cells and silenced in OVCAR3 cells (Fig. 2A). si-LINC00662 2# was chosen in the following assays for its high silence efficacy. CCK-8 assay was used to evaluate the proliferation capacity of OC cells, and results suggested that ectopic expression of LINC00662 markedly enhanced cell viability of CAOV3, meanwhile, downregulation of LINC00662 by si-LINC00662 transfection significantly reduced the cell viability of OVCAR3

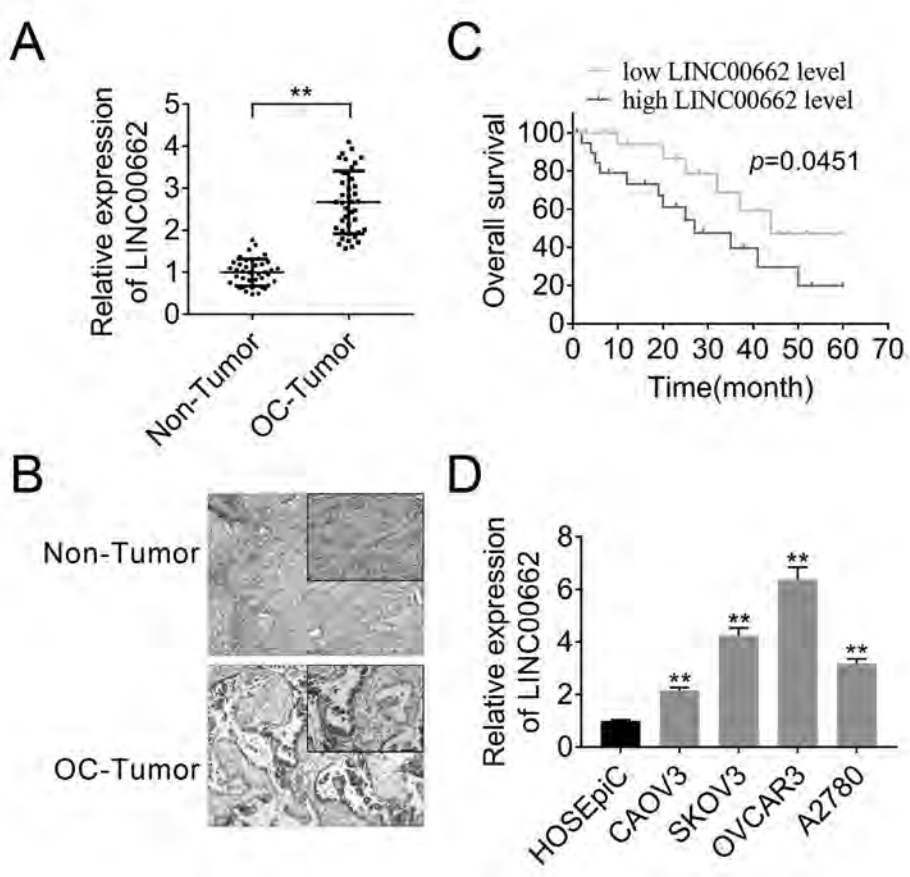


Fig. 1. *Elevated expression of LINC00662 expression in human OC tissues and cells.* ***A, B***) The expression of *LINC00662 in 40 pairs of OC tissue (OC-tumor) and adjacent noncancerous (non-tumor) tissue samples were analyzed by qRT-PCR and RNA in situ hybridization.* ***C***) Data from TCGA was collected and analyzed to dissect the correlation between *LINC00662 expression and overall survival.* ***D***) *LINC00662 expression was detected in OC cells by qRT-PCR.* ** $P < 0.01$.

after 96 hours of incubation (Fig. 2B). These results indicated LINC00662 played a promoting role in OC cells proliferation. In addition, cell cycle analysis suggested that overexpressed LINC00662 was conducive to transfer of OC cells from G0/G1 stage to S and G2/M stage, while cells were blocked in G0/G1 stage by LINC00662 silence (Fig. 2C). Proteins involved in cell cycle regulation were also detected by Western blot. Results showed that p21 was significantly upregulated by LINC00662 transfection while decreased by si-LINC00662 (Fig. 2D). Moreover, Cyclin D1 was obviously downregulated by LINC00662 transfection and increased by si-LINC00662 (Fig. 2D). Taken together, these results indicated that LINC00662 was involved in cell cycle regulation of OC cells via modulating p21 and Cyclin D1.

Influence of LINC00662 on glycolysis of OC cells

Since glycolysis is one the main characteristics in tumor cells (15), glucose uptake, lactate production and cellular ATP levels were determined to determine the effect of LINC00662 on glycolysis of OC cells. Results indicated that transfection of LINC00662 into CAOV3 cells significantly increased glucose uptake, lactate production and cellular ATP levels (Fig. 3), while these effects were obviously decreased by si-LINC00662 transfection in OVCAR3 cells (Fig. 3). These data demonstrate the important role of LINC00662 in metabolism regulation of OC cells.

LINC00662 expression negatively correlated with miR-375

Prediction using miRDB showed that LINC00662 contained an miRNA response element (MRE) as a putative binding site for miR-375 (Fig. 4A). To verify the predicted targeting relationship between LINC00662 and miR-375, miR-375 mimic, which was proved to increase miR-375 level, was used in luciferase reporter assays (Fig. 4B). As shown in Fig. 4C, data showed that the relative luciferase activity was evidently decreased in cells co-transfected with miR-375 mimic and vector inserted with wild type LINC00662 MRE sequence, while there was

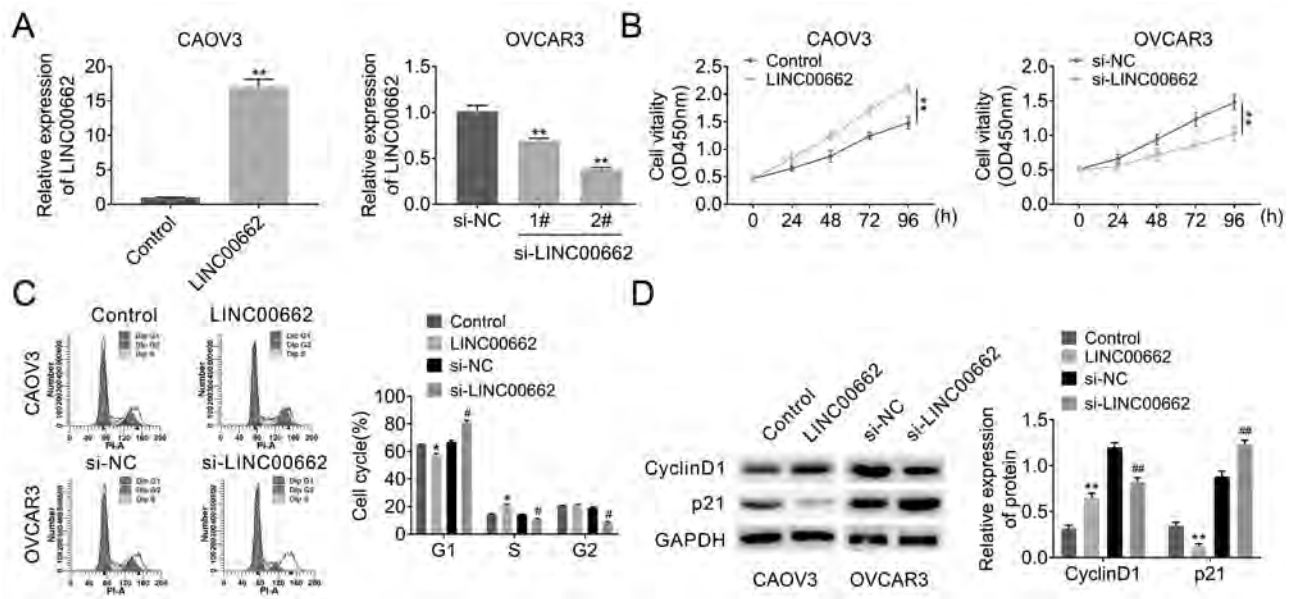


Fig. 2. *Effects of LINC00662 on proliferation* in *OC cells in vitro. **A**)* Two siRNAs (si-*LINC00662#1 and* si-*LINC00662#2) or vector carrying LINC00662 were designed to downregulate or overexpress LINC00662 in OC cells. ***B**) CCK-8 assay was used to measure the effects of LINC00662 on cell proliferation. **C**) Cell cycle distribution was analyzed in cells transfected with increased or downregulated LINC00662. **D**) Proteins associated with cell proliferation were determined by Western blot. Asterisk (*) indicated difference between control and LINC00662, hash (#) indicated difference between si-NC and si-LINC00662. * $P < 0.05$, ** $P < 0.01$, # $P < 0.05$, ## $P < 0.01$.*

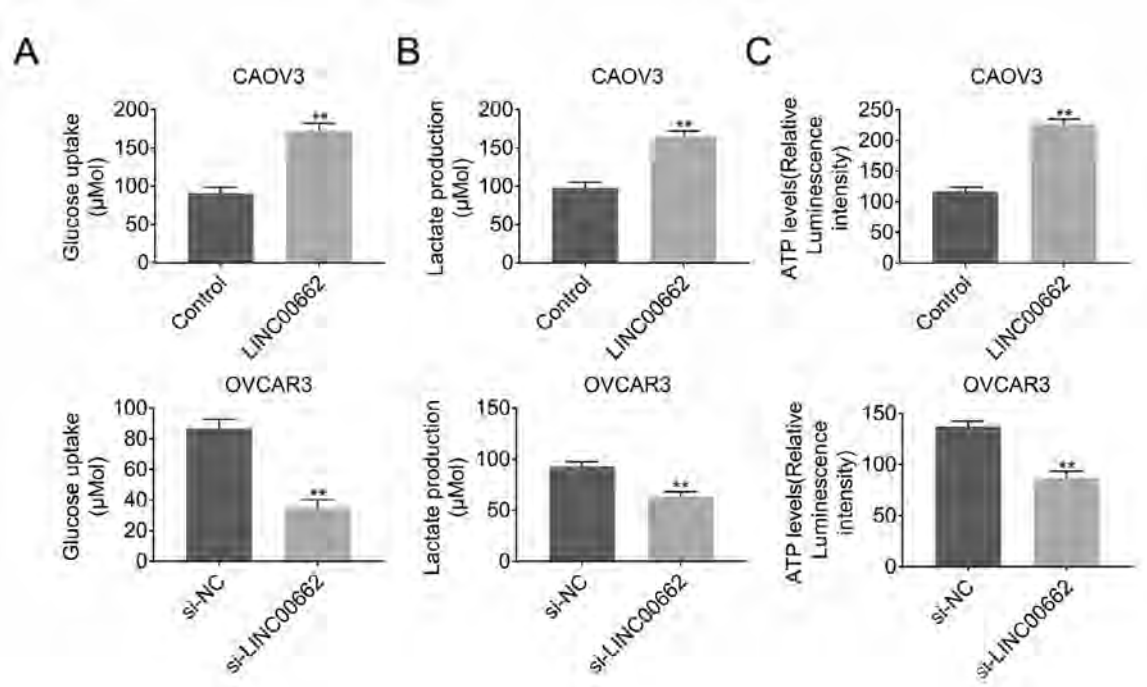


Fig. 3. *Effects of LINC00662 on glycolysis. LINC00662 vector were transfected to CAOV3, while si-LINC00662 was transfected to OVCAR3. Glucose uptake (**A**), lactate production (**B**) and ATP level (**C**) were measured to evaluate glycolysis.* ** $P<0.01$.

Table I. *Sequence information of primers*

Primer	Sequence 5'>3'
GAPDH_forward	GGTGAAGGTCGGAGTCAACG
GAPDH_reverse	ACCATGTAGTTGAGGTCAATGAAGG
LINC00662 _forward	CACGCTTCTGAAACTGGTGT
LINC00662 _reverse	GCCTGTAGAAGGGAAACGCT
U6 _ forward	AAAGCAAATCATCGGACGACC
U6 _ reverse	GTACAACACATTGTTTCCTCGGA
HIF-1α_ forward	GAACGTCGAAAAGAAAAGTCT
HIF-1α_ reverse	CCTTATCAAGATGCGAACTCA
MiR-375_ forward	*TGCGGTTTGTTCGTTCGGCT*
MiR-375_ reverse	*CAGTGCAGGGTCCGAGGT*

no significant difference in groups transfected with mutant LINC00662 MRE and control mimic. RIP assay was performed to further verify the direct interaction between LINC00662 and miR-375. A significant coexistence of LINC00662 and miR-375 was observed in fraction treated with the Ago2 antibody compared with IgG control (Fig. 4D). These findings revealed that LINC00662 directly interacted with miR-375 via the specific MRE. To investigate the regulation of LINC00662 on miR-375, we also

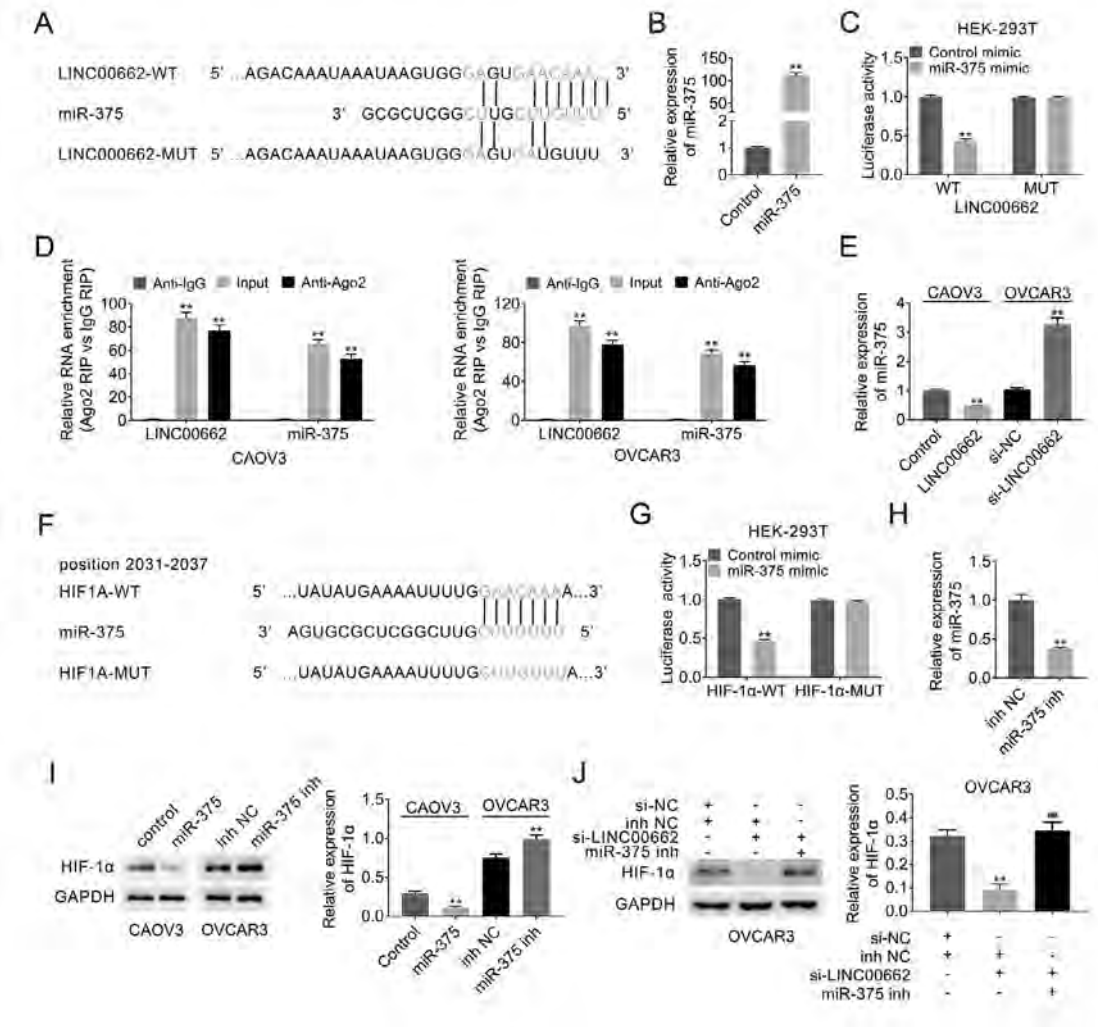


Fig. 4. *LINC00662 regulated HIF-1α expression via miR-375.* ***A***) *Prediction in miRDB suggested that a miRNA response element (MRE) for miR-375 was included in LINC00662.* ***B***) *MiR-375 mimics were used to elevate miR-375 level.* ***C***) *Luciferase reporter assays revealed that co-transfection of miR-375 mimics and vectors carrying the MRE decreased the relative luciferase activity, while no significant difference in cells transfected with MUT-MRE.* ***D***, ***E***) *RNA immunoprecipitation (RIP) assay was performed to further confirm the interaction between LINC00662 and miR-375, qRT-PCR results suggested that LINC00662 and miR-375 were mostly accumulated in groups treated with Ago2 antibody compared with IgG control.* ***F***) *Bioinformatics analysis showed that HIF-1α was a direct target of miR-375.* ***G)*** *Luciferase reporter assay was performed to verify the direct regulation of miR-375 on HIF-1α.* ***H***) *miR-375 inhibitor were used to successfully decrease the miR-375 level.* ***I***) Expression of *HIF-1α was detected in cells transfected with miR-375 inhibitor or miR-375 mimics using Western blot analysis.* ***J)*** *The effects of LINC00662 on HIF-1α were investigated using si-LINC00662 and miR-375 inhibitor, HIF-1α was detected using Western blot analysis.* * * $P<0.01$

determined the miR-375 expression in CAOV3 cells transfected with LINC00662 overexpression vector and in OVCAR3 cells transfected with si-LINC00662. Notably, miR-375 was shown to be downregulated by overexpressed LINC00662, while it was upregulated by LINC00662 silence (Fig. 4E).

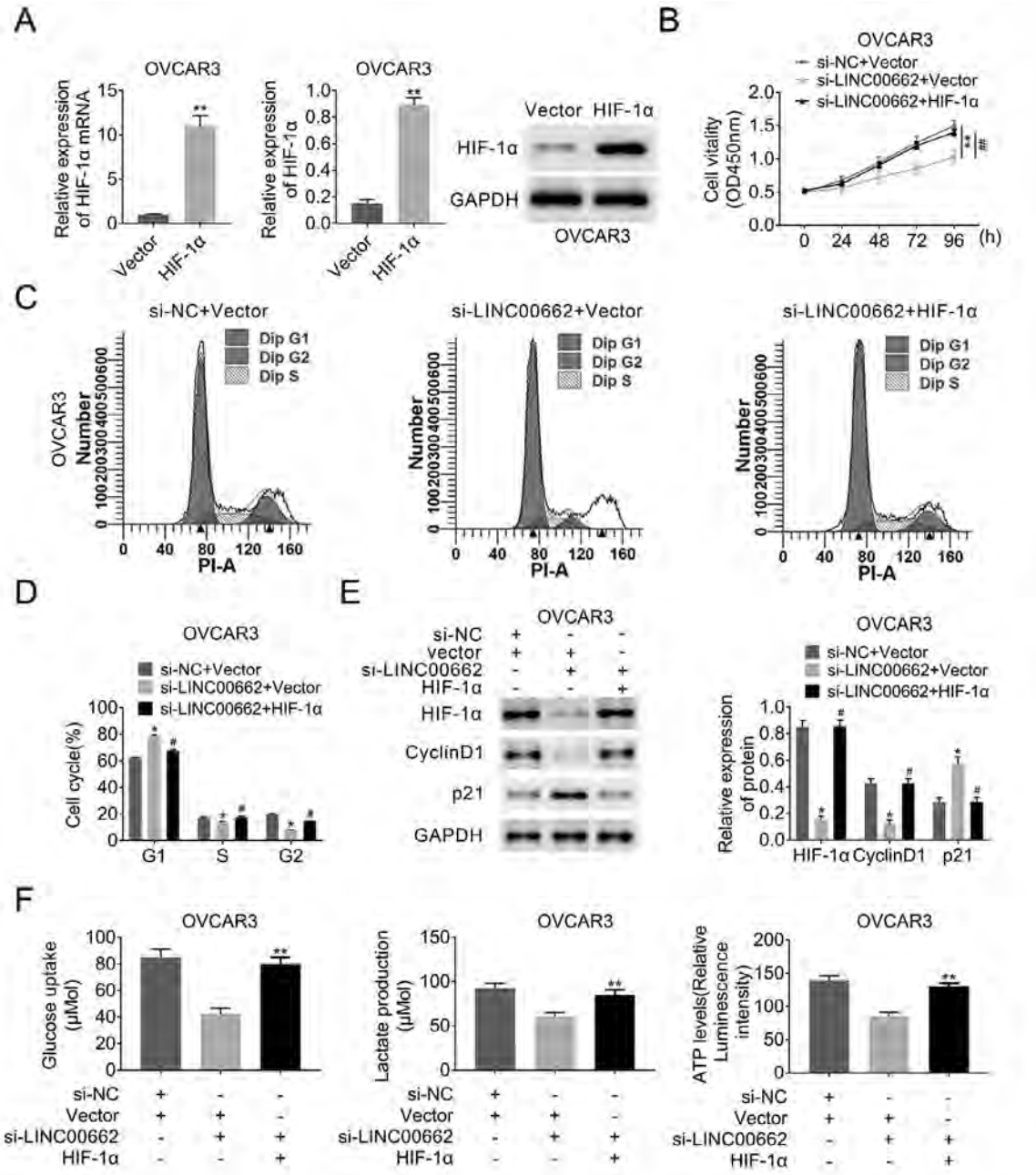


Fig. 5. *LINC00662 influenced cell proliferation and glycolysis via modulating HIF-1α expression.* ***A)*** *Plasmid carrying HIF-1α gene was constructed, qRT-PCR and* Western blot were performed to confirm the overexpression of *HIF-1α.* ***B)*** *Silenced LINC00662 induced inhibition effects on cell proliferation were compromised by* overexpression of *HIF-1α.* ***C, D)*** *Cell cycle distribution was analyzed in cells transfected with si-LINC00662 and HIF-1α vector.* ***E)*** *Proteins associated with cell proliferation were determined by Western blot. Asterisk (*) indicated difference between si-NC and si-LINC00662, hash (#) indicated difference between si-LINC00662&HIF-1α vector and si-LINC00662.* ** $P < 0.01$, ## $P < 0.01$.

LINC00662 was involved in regulation of HIF-1α expression by miR-375

Bioinformatics analysis using TargetScan predicted a putative binding site for miR-375 in 3'-UTR of HIF-1α gene (Fig. 4F). Based on the luciferase reporter assay performed in HEK293, we found that the relative luciferase activity was evidently decreased in cells co-transfected with miR-375 mimic and vector inserted with wild type 3'-UTR sequence of HIF-1α gene, while no significant difference existed in groups transfected with mutant 3'-UTR sequence of HIF-1α gene and control mimic (Fig. 4G). miR-375 inhibitor was used to successfully decrease the miR-375 level in CAOV3 cells (Fig. 4H). Meanwhile, results of Western blot analysis revealed that the expression of HIF-1α was elevated in miR-375 silencing cells, while HIF-1α expression was decreased in miR-37 upregulated cells (Fig. 4I). Since we found that miR-375 might be increased by si-LINC00662 transfection, Western blot assay further revealed that HIF-1α was downregulated in OVCAR3 cells transfected with si-LINC00662, which was subsequently reversed by an additional transfection of miR-375 inhibitor (Fig. 4J). All these results proved that HIF-1α was directly regulated by miR-375, and LINC00662 was involved in regulation of HIF-1α via miR-375.

LINC00662 promoted the proliferation and glycolysis of OC cells via upregulating HIF-1α

We have proved that LINC00662 might effectively influence the proliferation and glycolysis of OC cells. We next proposed that the effects induced by LINC00662 were mediated by its regulation on HIF-1α. Vector inserted with gene encoding HIF-1α was used to overexpress HIF-1α in OC cells. Results of qRT-PCR and Western blotting showed that HIF-1α was successfully upregulated in OVCAR3 cells (Fig. 5A). Subsequently, CCK-8 assays indicated the LINC00662 silencing induced inhibition effects on OVCAR3 cells were counteracted by upregulation of HIF-1α (Fig. 5B). The above findings suggested that osteosarcoma cells might be blocked in G0/G1 stage by LINC00662 silencing. Then, we co-transfected OVCAR3 cells with LINC00662 siRNA and HIF-1α. As a result, a lower proportion in G0/G1 stage and a higher proportion in S or G2/M stage were observed in cells cotransfected with LINC00662 siRNA and HIF-1α as compared to those of cells transfected with LINC00662 siRNA alone (Fig. 5C, D). These results suggested that LINC00662 silence-induced cell cycle arrest in G0/G1 stage was rescued by increasing HIF-1α expression. Furthermore, the decreased Cyclin D1 and increased p21 in LINC00662-silenced group were completely reversed by elevated HIF-1α expression (Fig. 5E). Also, the observed inhibitory effects of LINC00662 silence on glucose uptake, lactate production and ATP level were compromised by upregulated HIF-1α (Fig. 5F). Taken together, these results indicated that the effects of LINC00662 on cell proliferation and glycolysis of OC cells were presumably mediated through regulating HIF-1α.

DISCUSSION

LncRNAs have long been described as an important participant in tumor progression (20). This article mainly aimed to explore the effects of LINC00662 in OC progression and the relevant mechanisms.

The study demonstrated that the expression of LINC00662 was significantly upregulated in OC tissues and cell lines, which was in line with the results of published investigations on prostate cancer and oral squamous cell carcinoma (8, 12). Another study also reported that prostate cancer patients with higher level of LINC00662 had shorter overall survival (12). The expression of LINC00662 in patients with oral squamous cell carcinoma was closely correlated with clinicopathologic features such as tumor size, lymph node metastasis and TNM classification (8). Combining the results we obtained in current study on OC, it can be hypothesised that LINC00662 played a tumor promoter role during OC progression. The effects of LINC00662 on OC cell survival were also evaluated **in vitro**. Results showed that changes of LINC00662 expression significantly affected cell proliferation by regulating cell cycle. LncRNA has long been demonstrated as an important regulator involved in tumor progression including growth and metastasis (10, 11, 21). Because of the

close link between glycolysis and tumorigenesis, tumor glycolysis was a promising target for cancer treatment although the detailed mechanisms remain poorly understand (14, 15). In the present study, we demonstrated that LINC00662 closely regulated glycolysis characterized by increased glucose uptake, enhanced lactate production and high intracellular ATP level. A variety of lncRNAs have been reported in OC (20), while our study revealed for the first time a significant role of LINC00662 in OC.

The main mechanism by which lncRNAs participated in regulation of protein expression is to function as RNAs which can bind microRNAs and impair their modulation on corresponding mRNA targets (12, 20). Luciferase assay and RIP assay revealed that LINC00662 might directly bind to miR-375, and further experiments demonstrated that miR-375 was negatively regulated by LINC00662 in OC cells. MiR-375 has recently been investigated as a tumor suppressor in several cancers including colorectal cancer (22), prostate cancer (23), and laryngeal squamous cell carcinoma (24). Yan et al. summarized that miR-375 can target several key hallmarks of cancer including *AEG-1*, *YAP1*, *IGF1R* and *PDK1* (25). Here, we proved that HIF-1α was another novel target of miR-375. HIF-1α was frequently reported as a responder to hypoxia, activating various genes involving neoangiogenesis, glycolysis, resistance to therapeutics and metastasis (26, 27). HIF-1α expression can be induced in rapidly proliferating cells by hypoxia caused by insufficient oxygen supply (13). HIF-1α was found to be overexpressed in tumor cells, which would reprogram the metabolism of tumor cells towards glycolysis (28). Wang et al. reviewed that HIF-1α was involved in angiogenesis, metastasis and chemoresistance in glioblastoma multiforme (29). Based on the above findings, we hypothesized that LINC00662 might regulate the HIF-1α expression via acting as a completive RNA by competitively binding to miR-375. To confirm this hypothesis, si-LINC00662 and vector carrying HIF-1α gene were co-transfected to OVCAR3 cells. We found that the HIF-1α overexpression reversed si-LINC00662-induced inhibition effects on cell proliferation and glycolysis. The expression changes of Cyclin D1 and p21 caused by si-LINC00662 were all rescued by HIF-1α overexpression. Thus, the axis of LINC00662/miR-375/HIF-1α was established in OC cells. The relationship between HIF-1α and lncRNA has previously been reported in several studies. LncRNA MALAT1 was able to cause accumulation of HIF-1α via alleviating ubiquitination of HIF-1α (9). An investigation on oral cancer revealed that LncHIFCAR might form complexes with HIF-1α, further recruiting p300 cofactor to the target promoter (19). The influences of LINC006622 on glycolysis were demonstrated to be mediated by HIF-1α, however, whether LINC006622 is involved in regulation of glycolysis associated proteins including glycolysis-associated enzymes and transport protein were of great significance to mechanistically dissect LINC006622-related OC progression.

In summary, our study revealed that LINC00662 was involved in cell survival and glycolysis of OC cells and exerted as a repressor of miR-375. These findings from our study contribute to further exploring the application of LINC006622 as a promising target for OC treatment.

REFERENCES

1. Chiyoda T, Hart PC, Eckert MA, et al. Loss of BRCA1 in the cells of origin of ovarian cancer induces glycolysis: a window of opportunity for ovarian cancer chemoprevention. Cancer Prev Res (Phila) 2017; 10:255-66.
2. Han RL, Wang FP, Zhang PA, Zhou XY, Li Y. miR-383 inhibits ovarian cancer cell proliferation, invasion and aerobic glycolysis by targeting LDHA. Neoplasma 2017; 64:244-52.
3. Chakraborty PK, Mustafi SB, Xiong X, et al. MICU1 drives glycolysis and chemoresistance in ovarian cancer. Nat Commun 2017; 8:14634.
4. Kuang D, Zhang X, Hua S, Dong W, Li Z. Long non-coding RNA TUG1 regulates ovarian cancer proliferation and metastasis via affecting epithelial-mesenchymal transition. Exp Mol Pathol 2016; 101:267-73.
5. Mitra R, Chen X, Greenawalt EJ, et al. Decoding critical long non-coding RNA in ovarian cancer epithelial-to-mesenchymal transition. Nat Commun 2017; 8:1604.

6. Liu D, Li H. Long non-coding RNA GEHT1 promoted the proliferation of ovarian cancer cells via modulating the protein stability of HIF1alpha. Biosci Rep 2019; 39.
7. Huang S, Qing C, Huang Z, Zhu Y. The long non-coding RNA CCAT2 is up-regulated in ovarian cancer and associated with poor prognosis. Diagn Pathol 2016; 11:49.
8. Xu D, Chen Y, Yuan C, Zhang S, Peng W. Long non-coding RNA LINC00662 promotes proliferation and migration in oral squamous cell carcinoma. Onco Targets Ther 2019; 12:647-56.
9. Luo F, Liu X, Ling M, et al. The lncRNA MALAT1, acting through HIF-1alpha stabilization, enhances arsenite-induced glycolysis in human hepatic L-02 cells. Biochim Biophys Acta 2016; 1862:1685-95.
10. Liu X, Zhu Q, Guo Y, Xiao Z, Hu L, Xu Q. LncRNA LINC00689 promotes the growth, metastasis and glycolysis of glioma cells by targeting miR-338-3p/PKM2 axis. Biomed Pharmacother 2019; 117:109069.
11. Gong W, Su Y, Liu Y, Sun P, Wang X. Long non-coding RNA Linc00662 promotes cell invasion and contributes to cancer stem cell-like phenotypes in lung cancer cells. J Biochem 2018; 164:461-69.
12. Li N, Zhang L-Y, Qiao Y-H, Song R-J. Long noncoding RNA LINC00662 functions as miRNA sponge to promote the prostate cancer tumorigenesis through targeting miR-34a. European Review for Medical and Pharmacological Sciences 2019; 23:11.
13. Courtnay R, Ngo DC, Malik N, Ververis K, Tortorella SM, Karagiannis TC. Cancer metabolism and the Warburg effect: the role of HIF-1 and PI3K. Mol Biol Rep 2015; 42:841851.
14. Akram M. Mini-review on glycolysis and cancer. J Cancer Educ 2013; 28:454-57.
15. Ganapathy-Kanniappan S, Geschwind J-FH. Tumor glycolysis as a target for cancer therapy_ progress and prospects. Molecular Cancer 2013; 12:11.
16. Warmoes MO, Locasale JW. Heterogeneity of glycolysis in cancers and therapeutic opportunities. Biochem Pharmacol 2014; 92:12-21.
17. Sun L, Yin Y, Clark LH, Sun W. Dual inhibition of glycolysis and glutaminolysis as a therapeutic strategy in the treatment of ovarian cancer. Oncotarget 2017; 8:11.
18. Gabriely G, Wheeler MA, Takenaka MC, Quintana FJ. Role of AHR and HIF-1alpha in Glioblastoma Metabolism. Trends Endocrinol Metab 2017; 28:428-36.
19. Shih JW, Chiang WF, Wu ATH, et al. Long noncoding RNA LncHIFCAR/MIR31HG is a HIF-1alpha co-activator driving oral cancer progression. Nat Commun 2017; 8:15874.
20. Nikpayam E, Tasharrofi B, Sarrafzadeh S, Ghafouri-Fard S. The role of long non-coding RNAs in ovarian cancer. Iranian Biomedical Journal 2017; 21:13.
21. Lou Y, Jiang H, Cui Z, Wang L. Linc-ROR induces epithelial-to-mesenchymal transition in ovarian cancer by increasing Wnt_β-catenin signaling. Oncotarget 2017; 8.
22. Liu X-H, Wang J, Dong Y-H. The inhibitory effect of miR-375 targeting sp1 in colorectal cancer cell proliferation. Eur Rev Med Pharmacol Sci 2018; 22:7.
23. Selth LA, Das R, Townley SL, et al. A ZEB1-miR-375-YAP1 pathway regulates epithelial plasticity in prostate cancer. Oncogene 2016; 36:24-34.
24. Wang B, Lv K, Chen W, et al. miR-375 and miR-205 Regulate the Invasion and Migration of Laryngeal Squamous Cell Carcinoma Synergistically via AKT-Mediated EMT. BioMed Research International 2016; 2016:1-11.
25. Yan JW, Lin JS, He XX. The emerging role of miR-375 in cancer. Int J Cancer 2014; 135:1011-18.
26. Ma Q, Zhang Y, Liu T, et al. Hypoxia promotes chemotherapy resistance by down-regulating SKA1 gene expression in human osteosarcoma. Cancer Biol Ther 2017; 18:177-85.
27. Sowa T, Menju T, Chen-Yoshikawa TF, et al. Hypoxia-inducible factor 1 promotes chemoresistance of lung cancer by inducing carbonic anhydrase IX expression. Cancer Med 2017; 6:288-97.
28. Zhang W, Tong D, Liu F, Li D, Li J. RPS7 inhibits colorectal cancer growth via decreasing HIF-1α-mediated glycolysis. Oncotarget 2015; 7:15.
29. Wang G, Wang JJ, Fu XL, Guang R, To ST. Advances in the targeting of HIF-1alpha and future therapeutic strategies for glioblastoma multiforme (Review). Oncol Rep 2017; 37:657-70.

MicroRNA-206 INHIBITS TUMOR METASTASIS OF NASOPHARYNGEAL CARCINOMA THROUGH TARGETING G6PD

Q. GUO[1*], X-H. REN[1*], C-P. ZHAO[1] and B-H. ZHANG[2]

[1]Department of Ear-nose-throat (ENT), Yidu Central Hospital of Weifang, Qingzhou, Weifang, Shandong, China; [2]Department of Pathology, Zibo Central Hospital, Zhangdian, Zibo, Shandong, China

Received January 15, 2020 – Accepted April 1, 2020

[*]These authors contributed equally to this study and share first authorship

Nasopharyngeal carcinoma (NPC) is a main type of otolaryngological malignancy. In many cancers, miR-206 functions as a tumor suppressor, suppressing cell proliferation, migration and invasion. The purpose of this study was to explore how miR-206 worked on cell metastasis in NPC. The mRNA levels of miR-206 and G6PD were determined in NPC tissues and cell lines by RT-qPCR and Western blot. Transwell assay was applied to evaluate the migratory and invasive capacities. Dual luciferase reporter assay was employed to confirm that miR-206 mediated the expression of G6PD in C666-1 cells. In this study, miR-206 was downregulated, whereas G6PD was upregulated in NPC tissues and cell lines. In addition, G6PD was identified as a direct target gene of miR-206 in C666-1 cells. The expression of G6PD was mediated by miR-206, which could partially reverse the inhibitory effects of miR-206 on the migration, invasion and EMT in C666-1 cells. In conclusion, miR-206 regulated the migratory, invasive and EMT abilities through directly targeting the 3'-UTR of G6PD mRNA in C666-1 cells. The newly identified miR-206/G6PD axis provides novel insight into the pathogenesis of nasopharyngeal carcinoma.

Nasopharyngeal carcinoma (NPC) is a malignant tumor on the upper and lateral walls of the nasopharyngeal cavity, and is prevalent in northern Africa, Southeast Asia, and southern China (1, 2). Therefore, it is crucial to investigate the molecular markers for the strategy of NPC.

MicroRNAs (miRNAs) suppress genes expression through directly binding to the 3'-UTR or cleaving the target mRNA at post-transcriptional level (3, 4). It is thought that miRNAs regulated a variety of biological phenomena, such as cell growth, proliferation, differentiation, and death (5-7). Previous studies have revealed that miR-206 was downregulated and played a tumor suppressive role in many tumors, including lung adenocarcinoma, glioblastoma and triple negative breast cancer (8-10). miR-206 acted as a tumor suppressor by inhibiting cell proliferation, colony formation, migration, invasion and induced cell cycle arrest at G0/G1 phase in bladder cancer (11). miR-206 inhibited cisplatin resistance and facilitated cell apoptosis in gastric cancer by directly targeting MAPK2 (12). In addition, miR-206 suppressed cell viability and migration by targeting LIM and SH3 protein 1 in medulloblastoma (13). Similarly, miR-206 impaired the proliferation and migration, and

Key words: miR-206; G6PD; EMT; nasopharyngeal carcinoma; invasion

Corresponding Author:
Dr Baohua Zhang,
Department of Pathology,
Zibo Central Hospital, 54 Gongqing Tuanxi Road,
Zhangdian District 255022, Zibo, Shandong Province, China
Tel.: +86 0533 2881510,
e-mail: baopoyexian33573@163.com

0393-974X (2020)
Copyright © by BIOLIFE, s.a.s.
This publication and/or article is for individual use only and may not be further reproduced without written permission from the copyright holder.
Unauthorized reproduction may result in financial and other penalties
DISCLOSURE: ALL AUTHORS REPORT NO CONFLICTS OF INTEREST RELEVANT TO THIS ARTICLE.

enhanced cell apoptosis in hepatocellular carcinoma (14). Considering these articles, miR-206 was found to be downregulated and suppressed the migration, invasion and EMT in nasopharyngeal carcinoma.

Glucose-6-phosphate dehydrogenase (G6PD) is a metabolic enzyme, present in eukaryotes and prokaryotes, which catalyses the first reaction in the pentose phosphate pathway and provides reductive capacity in forming NADPH to all cells (15). Although G6PD plays a key role in cells, G6PD deficiency is the second most common human enzymatic disease (16). Nowadays, G6PD has emerged as a prognosis marker for a variety of tumors, including glioma, breast cancer and lung adenocarcinoma (17-19). Moreover, suppression of G6PD could enhanced recovery of cisplatin sensitivity via impacting redox homeostasis in lung cancer (20). Inhibition of G6PD suppressed cancer growth and metastasis in head and neck squamous cell carcinoma (21). In this study, miR-206 was first proposed to inhibit the migration, invasion and EMT through directly targeting G6PD in C666-1 cells.

MATERIALS AND METHODS

Patients and clinical samples

From 2014 to 2016, 49 pairs of nasopharyngeal carcinoma and the adjacent paracancerous esophageal tissues were obtained from Yidu Central Hospital of Weifang. The patients had not undergone adjuvant chemotherapy or radiotherapy preoperatively prior to surgery. The specimens were immediately frozen in liquid nitrogen and then stored at -80°C. For all the specimens of this study, informed consent was given by te patients and the study was approved by the Ethics Committee of Yidu Central Hospital of Weifang.

Cell lines and culture condition

Two human nasopharyngeal carcinomas (SUNE1 and C666-1) and a normal human nasopharyngeal epithelial cell NP69 were obtained from the American Type Culture Collection (ATCC, Rockville, USA). All the cells were incubated in RPMI-1640 medium (Thermo, Beijing, China) supplemented with 10% fetal bovine serum (FBS; Gibco Life Technologies, Carlsbad, USA) at 37°C in a humidified atmosphere of 5% CO_2.

RNA isolation and RT-qPCR

Total mRNAs and miRNAs were extracted using TRIzol Reagent (Invitrogen, Carlsbad, USA) or MIRcute and Separation of miRNAs Kit (Tiangen, Beijing, China). Reverse transcription was performed using the OneStep PrimeScript® cDNA Synthesis kit (Takara, Dalian, China) to synthesized the first cDNA chain. Afterwards, the level of G6PD and miR-206 were determined using the SYBR Prime Script miRNA RT-PCR Kit (Takara, Otsu, Japan) and SYBR Premix Kit (Takara, Otsu, Japan) in the ABI PRISM StepOnePlus real-time PCR system (Applied Biosystems, Foster City, CA, USA). GAPDH and U6 small nuclear RNA were acted as normalization for G6PD and miR-206. The relative quantification of mRNA and miRNA was calculated using the $2^{-\Delta\Delta Ct}$ method. The sequences of primers were shown as follows: miR-206, forward primer: 5'-CGATGGAATGTAAGGAAGT-3' and reverse primer: 5'-GTGCAGGGTCCGAGGT-3'; U6, forward primer: 5'-CTCGCTTCGGCAGCACA-3' and reverse primer: 5'-AACGCTTCACGAATTTGCGT-3'; G6PD, forward primer: 5'-ACGTGAAGCTCCCTGACGC-3' and reverse primer: 5'- GTGAAAATACGCCAGGCCTTA-3'; GAPDH, forwardprimer:5'-TGGAGAATGAGAGGTGGGATG-3'and reverse primer: 5'- GAGCTTCACGTTCTTGTATCTGT-3'.

Protein extraction and Western blotting

For Western blotting, proteins were extracted from tissues and cells using an RIPA Lysis Buffer (Beyotime, Shanghai, China) containing the protease inhibitor PMSF (Beyotime, Shanghai, China). The concentration was determined using a BCA Reagent Kit (Solarbio, Beijing, China), and an equal amount of protein was separated using 12% Sodium dodecylsulphate polyacrylamide gel electrophoresis (SDS-PAGE). The blots were transferred onto a PVDF membrane and blocked with 5% non-fat milk for 1 h. The membrane was then incubated with rabbit anti-G6PD monoclonal antibody (1:1,000; Abcam, Cambridge, USA) overnight at 4°C, which normalized by glyceraldehyde-phosphate dehydrogenase (GAPDH). Thereafter, the membranes were incubated with horseradish peroxidase (HRP) goat anti-rabbit IgG (1:3000, Santa Cruz, CA, USA), and chemiluminescence signal was carried out using the Image-Pro Plus software 6.0 (Media Cybernetics, Silver Spring, MD, USA).

Transwell assay

Cell invasive ability was calculated using Transwell

chamber (8 μm, Biosciences, San Jose, CA, USA), which was covered with Matrigel (Clontech, Mountain View, CA, USA). The Transwell chamber was put into a 24-well plate, and the cells were suspended in serum-free RPMI-1640 medium, and 100 μl of the cell suspension was seeded into the upper chamber, after which 600 μl RPMI-1640 medium with 15% FBS was placed into the lower chamber. After incubation for 48 h at 37°C in 5% CO_2, the cells still at the upper surface were removed with a cotton swab, and then the cells moved to the lower surface were fixed and stained using methanol and 0.1% crystal violet. The ability of cells to invade is represented by the number of cells crossing the membrane.

Transfection

Vectors (miR-206 mimic, miR-206 inhibitor or pcDNA3.1-G6PD as well as their negative control) were purchased from GenePharma (Shanghai, China). The miR-206 mimic or inhibitor were used for up/down regulated miR-206, while pcDNA3.1-G6PD was utilized to overexpress G6PD. SUNE1 cells were seeded in a 6-well plate and cultured overnight before transfection. 4 μg vectors and 8 μL Lipofectamin 2000 reagent (Invitrogen, Carlsbad, CA, USA) were mixed in 1.5 mL microcentrifuge tube and let stand for 20 min. The mix was then added into cells and shaken. The cells were harvested after transfection of 48 h.

Luciferase reporter assay

TargetScan was employed to predict possible targets of miR-206 and G6PD was selected as a target of miR-206. The 3'UTR of G6PD mRNA containing binding sites was cloned and inserted into a pmirGlo luciferase vector (wild type, WT). The binding sequences were mutated using the QuickChange Multi Site-Directed Mutagenesis Kit (Stratagene, Santa Clara, CA, USA), and the mutant was inserted in pmirGlo luciferase vector (mutant, MUT). The miR-206 mimic or negative control and wild type or mutant G6PD were co-transfected into TR-2 cells, and the transfection was performed utilized Lipofectamine 2000 (Invitrogen, Carlsbad, CA, USA). Subsequently, the luciferase activity was measured using the Dual-Luciferase Reporter Assay System (Promega, USA).

Statistical analysis

Student's *t*-test or one-way ANOVA were performed to analyze the data using SPSS 16.0 (Chicago, IL, USA). The correlation between miR-206 and the mRNA level of G6PD was evaluated used Spearman's correlation analysis. $P< 0.05$ was considered to indicate statistically differences.

RESULTS

Overexpression of miR-206 predicted poor prognosis of NPC tissues

The expression of miR-206 was lower in NPC tissues than that of corresponding normal tissues ($P< 0.05$) (Fig. 1A). The association between the expression of miR-206 and the 5-year overall survival were calculated, and downregulation of miR-206 was predicted to be associated with poor prognosis of NPC patients ($P< 0.05$) (Fig. 1B). Meanwhile, the expression of miR-206 was inspected in three cells in our laboratory, including a normal nasopharyngeal epithelial cell NP69 and two NPC cells SUNE1 and C666-1. As expected, miR-206 was overexpressed relative to NP69 in NPC cell lines SUNE1 ($P< 0.05$) and C666-1 ($P< 0.05$) (Fig. 1C). To explore the roles of miR-206 in NPC, the miR-206 mimic or miR-206 inhibitor was utilized to overexpress ($P< 0.05$) or knockdown of miR-206 ($P< 0.05$) in C666-1 cells (Fig. 1D).

miR-206 suppressed migration, invasion and the EMT of NPC cells

To explore the roles of miR-206 in NPC cells, Transwell assay was employed to evaluate the migratory and invasive abilities. Cell migration was reduced by transfecting miR-206 mimic in C666-1 cells ($P< 0.05$), and it had consistent result with the cell invasion ($P< 0.05$) (Fig. 2A). On the contrary, the cell number of migration ($P< 0.05$) and invasion ($P< 0.05$) were enhanced when transfected with miR-206 inhibitor in C666-1 cells ($P< 0.05$) (Fig. 2B). Additionally, Western blot was used to assess the expression of EMT markers, including E-cadherin and N-cadherin. The expression of E-cadherin was decreased by miR-206 mimic, while it was increased by miR-206 inhibitor. Inversely, miR-206 mimic enhanced the expression of N-cadherin, which was impaired by miR-206

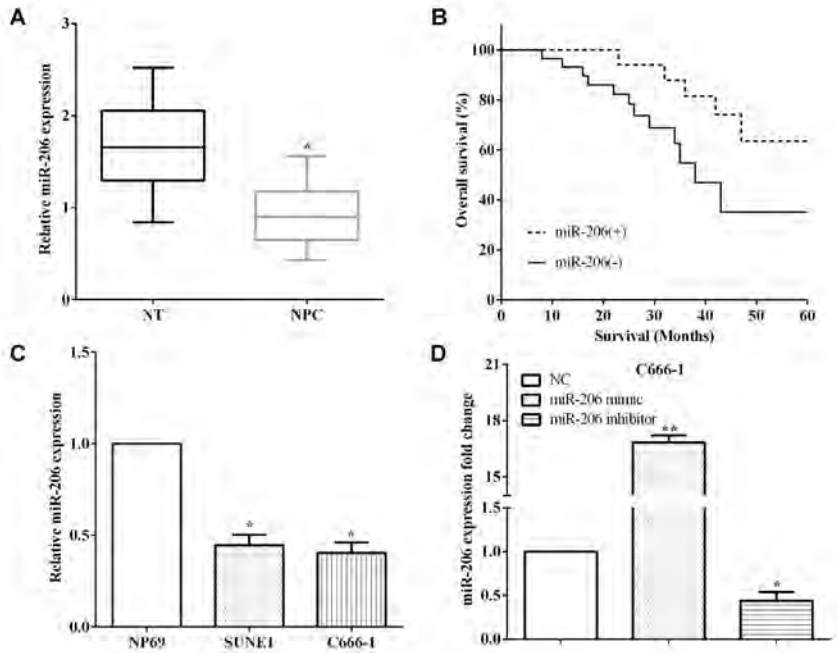


Fig. 1. *Overexpression of miR-206 predicted poor prognosis of NPC patients.* ***A****) The expression of miR-206 was lower in NPC tissues than that of corresponding normal tissues.* ***B****) Downregulation of miR-206 predicted poor prognosis of NPC patients.* ***C****) miR-206 was low expressed in NPC cells SUNE1 and C666-1 versus NP69.* ***D****) miR-206 mimic or miR-206 inhibitor was utilized to overexpress or knockdown of miR-206 in C666-1 cells.*

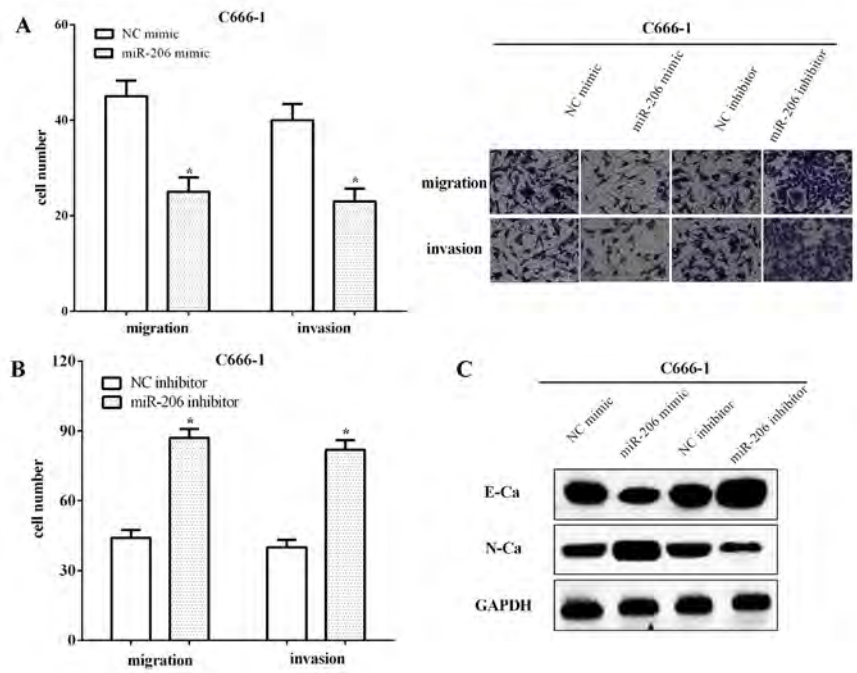


Fig. 2. *miR-206 suppressed the migration, invasion and EMT of C666-1 cells.* ***A****) Cell migration was reduced by the miR-206 mimic, and it had similar findings with the cell invasion.* ***B****) The cell number of migration and invasion were enhanced when transfected with miR-206 inhibitor.* ***C****) miR-206 inhibited the EMT ability in C666-1 cells.*

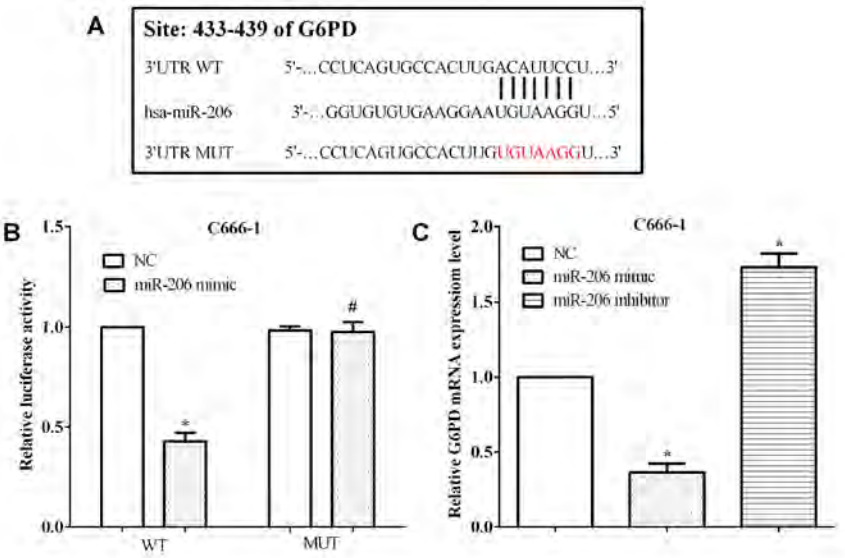


Fig. 3. *miR-206 regulated the expression of G6PD by directly targeting its mRNA 3'UTR.* ***A)*** *G6PD was predicted by TargetScan as a target of miR-206.* ***B)*** *miR-206 mimic repressed the luciferase activity of wild type G6PD in C666-1 cells.* ***C)*** *In C666-1 cells, miR-206 mimic suppressed the mRNA level of G6PD, whereas miR-206 inhibitor promoted its expression.*

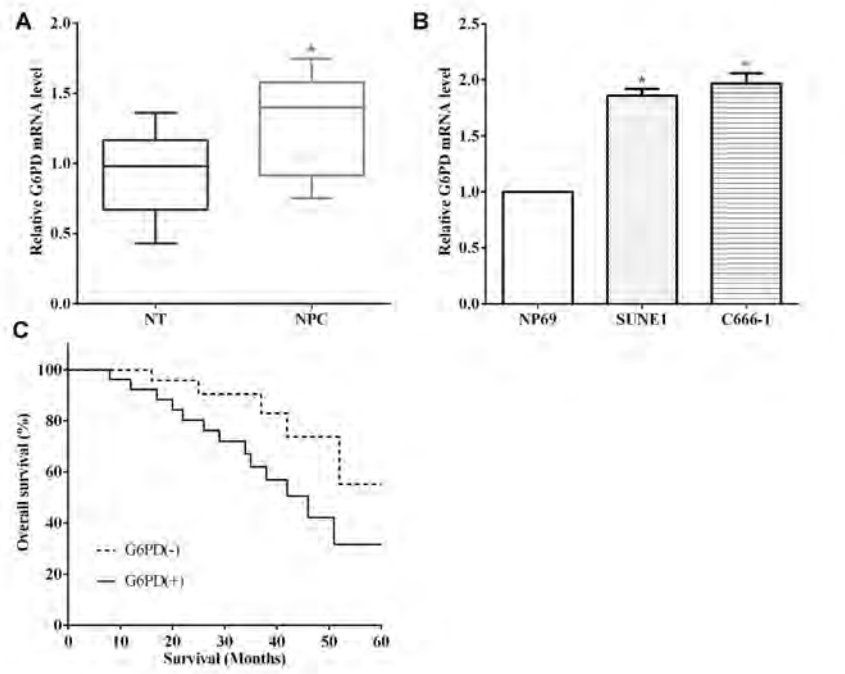


Fig. 4. *Overexpression of G6PD predicted poor prognosis in NPC.* ***A)*** *The expression of G6PD was higher in NPC tissues than that of the corresponding normal tissues.* ***B)*** *G6PD was overexpressed in NPC cell lines SUNE1 and C666-1 versus normal cell line NP69.* ***C)*** *Overexpression of NP69 was associated to worse outcome of NPC patients.*

inhibitor (Fig. 2C). All the findings suggested that miR-206 inhibited the migration, invasion and the EMT ability in C666-1 cells.

miR-206 regulated the expression of G6PD by directly targeting its mRNA 3'UTR

TargetScan predicted several target genes of miR-206, and G6PD was selected as a candidate target gene of miR-206, and the binding sequences were located at 433-439 on its mRNA 3'-UTR. To confirm whether miR-206 directly binds to G6PD, the binding site was mutated from 5'-ACAUUCC-3' (wide type, WT) to 5'-UGUAAGG-3' (mutant, MUT), both of which were inserted in pmirGlo vector (Fig. 3A). The luciferase activity was measured after co-transfection with the miR-206 mimic or negative control and WT or MUT into C666-1 cells. miR-206 mimic repressed the luciferase activity of wild type G6PD in C666-1 cells ($P< 0.05$), whereas it had no change of the mutant G6PD ($P< 0.05$) (Fig. 3B). Next, the influence of miR-206 on the expression of G6PD was examined by RT-qPCR, and the mRNA level of G6PD was discovered to be suppressed by the miR-206 mimic ($P< 0.05$), whereas it was promoted by the miR-206 inhibitor in C666-1 cells ($P< 0.05$) (Fig. 3C).

Overexpression of G6PD predicted poor prognosis in NPC

The mRNA level of G6PD was measured in NPC tissues and cells using RT-qPCR. The expression of G6PD was higher in NPC tissues in comparison with the corresponding normal tissues ($P< 0.05$) (Fig. 4A). Meanwhile, the expression of G6PD was also calculated in C666-1 cells, and G6PD was discovered to be overexpressed in NPC cells SUNE1 ($P< 0.05$) and C666-1 ($P< 0.05$) *versus* normal cells NP69 (Fig. 4B). In addition, overexpression of NP69 was associated to a worse outcome of NPC patients (Fig. 4C).

G6PD partially suppressed the tumor suppressive roles of miR-206

To verify whether G6PD is involved in miR-

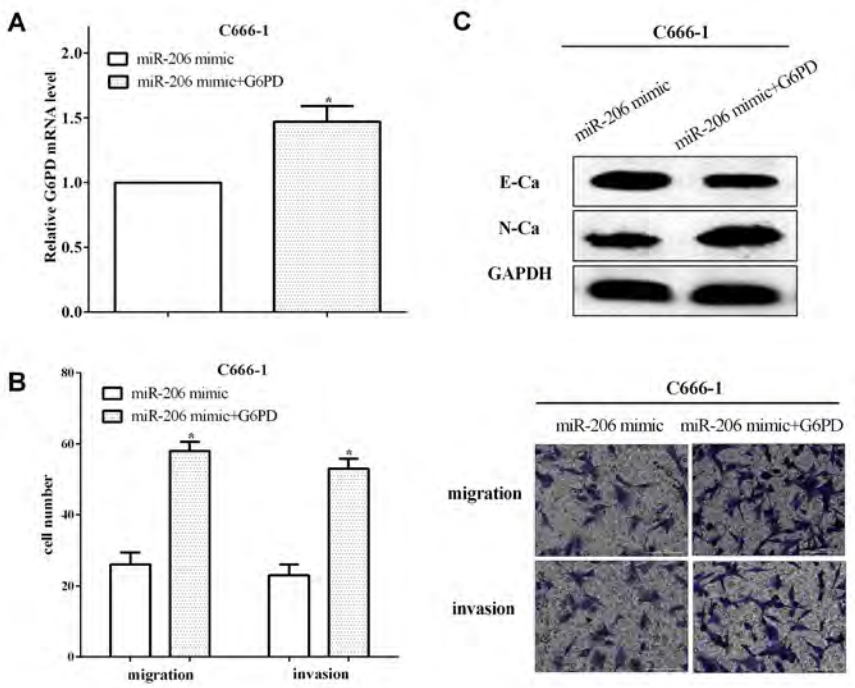


Fig. 5. *G6PD partially suppressed tumor suppressive roles of miR-206.* ***A)*** *RT-qPCR elucidated that G6PD was re-expressed by transfecting pcDNA3.1-G6PD in C666-1 cells.* ***B)*** *Re-expression of G6PD could rescue the inhibition of miR-206 on C666-1 cell migration and invasion.* ***C)*** *G6PD could partially reverse the suppression of miR-206 on the EMT.*

206-mediated tumor suppression on cell metastasis, miR-206 mimic and pcDNA3.1-G6PD plasmid were co-transfected into C666-1 cells. As expected, RT-qPCR elucidated that G6PD was re-expressed by transfecting pcDNA3.1-G6PD in C666-1 cells ($P< 0.05$) (Fig. 5A). Moreover, re-expression of G6PD could rescue the inhibition of miR-206 on C666-1 cell migration ($P< 0.05$) and invasion ($P< 0.05$) (Fig. 5B). Upregulation of G6PD also enhanced the expression of E-cadherin, while it inhibited the expression of N-cadherin in C666-1 cells (Fig. 5C). All the results revealed that G6PD could partially reverse the suppression of miR-206 on the migration, invasion and EMT

DISCUSSION

MicroRNAs (miRNAs) bind to 3'-UTR or cleave the target mRNA to suppress gene expression at post-transcriptional level, which was thought to regulate a variety of biological phenomena (22, 23). miR-206 was downregulated and inhibited cell viability and migration via MET in lung adenocarcinoma (24). Consistent with previous findings, miR-206 was found to be low expressed in NPC tissues, meanwhile, it was also downregulated in NPC cell lines SUNE1 and C666-1. miR-206 was also found to act as a prognosis marker in nasopharyngeal carcinoma. Downregulation of miR-206 predicted worse prognosis of NPC patients, which was consistent with the findings of cervical cancer (25). miR-206 impaired cell growth, migration and invasion, and enhanced cell apoptosis in osteosarcoma (26). Our results were consistent with the findings in osteocarcinoma, we found miR-206 reduced cell migratory and invasive abilities in C666-1 cells. In addition, miR-206 was first proposed to inhibit EMT ability by regulating the expression of E-cadherin and N-cadherin in C666-1 cells, which was consistent with the findings of Ning Yang in prostate cancer (27). In addition, G6PD was discovered to be a target of miR-206 and its expression was regulated by miR-206.

Overexpression of G6PD was connected with poor prognosis of clear cell renal cell carcinoma patients (28). Also, G6PD promoted the proliferation via p-STAT3 in renal cell carcinoma (29). G6PD was overexpressed in NPC tissues and cell lines *versus* normal tissues and normal cell lines. It was also discovered that upregulation of G6PD predicted worse outcome of NPC patients. G6PD was found to be a target of miR-206 and its expression was mediated by miR-206, which was consistent with the findings in cervical cancer (25).. Furthermore, G6PD enhanced the migration, invasion and EMT in hepatocellular carcinoma (30). G6PD could partially reverse the inhibitory effects of miR-206 on migratory, invasive and EMT ability in C666-1 cells.

In conclusion, miR-206 was downregulated in NPC tissues and NPC cells, whereas G6PD was upregulated in NPC tissues. miR-206 could impair cell migratory, invasive and EMT capacities via directly targeting G6PD. The current findings promote our understanding of the molecular pathogenesis of nasopharyngeal carcinoma and support the potential of miR-206 as an effective new therapeutic target for nasopharyngeal carcinoma.

REFERENCES

1. Tang LL, Chen WQ, Xue WQ, He YQ, Zheng RS, Zeng YX, Jia WH. Global trends in incidence and mortality of nasopharyngeal carcinoma. Cancer Lett 2016; 374:22-30.
2. Wei KR, Zheng RS, Zhang SW, Liang ZH, Ou ZX, Chen WQ. Nasopharyngeal carcinoma incidence and mortality in China in 2010. Chin J Cancer 2014; 33:381-87.
3. Bartel DP. MicroRNAs: genomics, biogenesis, mechanism, and function. Cell 2004; 116:281-97.
4. Bartel DP. MicroRNAs: target recognition and regulatory functions. Cell 2009; 136:215-33.
5. Ambros V. The functions of animal microRNAs. Nature 2004; 431:350-5.
6. He L, Hannon GJ. MicroRNAs: small RNAs with a big role in gene regulation. Nat Rev Genet 2004; 5:522-31.
7. Schickel R, Boyerinas B, Park SM, Peter ME. MicroRNAs: key players in the immune system, differentiation, tumorigenesis and cell death. Oncogene 2008; 27:5959-74.
8. Watt K, Newsted D, Voorand E, et al. MicroRNA-206 suppresses TGF-beta signalling to limit tumor growth and metastasis in lung adenocarcinoma. Cell Signal

2018; 50:25-36.
9. Hao W, Luo W, Bai M, et al. MicroRNA-206 inhibited the progression of glioblastoma through BCL-2. J Mol Neurosci 2016; 60:531-38.
10. Liang Z, Bian X, Shim H. Downregulation of microRNA-206 promotes invasion and angiogenesis of triple negative breast cancer. Biochem Biophys Res Commun 2016; 477:461-66.
11. Huang B, Zhai W, Hu G, Huang C, Xie T, Zhang J, Xu Y. MicroRNA-206 acts as a tumor suppressor in bladder cancer via targeting YRDC. Am J Transl Res 2016; 8:4705-15.
12. Chen Z, Gao YJ, Hou RZ, et al. MicroRNA-206 facilitates gastric cancer cell apoptosis and suppresses cisplatin resistance by targeting MAPK2 signaling pathway. Eur Rev Med Pharmacol Sci 2019; 23:171-80.
13. Pan X, Wang Z, Wan B, Zheng Z. MicroRNA-206 inhibits the viability and migration of medulloblastoma cells by targeting LIM and SH3 protein 1. Exp Ther Med 2017; 14:3894-900.
14. Wang Y, Tai Q, Zhang J, et al. MiRNA-206 inhibits hepatocellular carcinoma cell proliferation and migration but promotes apoptosis by modulating cMET expression. Acta Biochim Biophys Sin (Shanghai) 2019; 51:243-53.
15. Cappellini MD, Fiorelli G. Glucose-6-phosphate dehydrogenase deficiency. Lancet 2008; 371:64-74.
16. Cunningham AD, Hwang S, Mochly-Rosen D. Glucose-6-phosphate dehydrogenase deficiency and the need for a novel treatment to prevent kernicterus. Clin Perinatol 2016; 43:341-54.
17. Yang CA, Huang HY, Lin CL, Chang JG. G6PD as a predictive marker for glioma risk, prognosis and chemosensitivity. J Neurooncol 2018; 139:661-70.
18. Benito A, Polat IH, Noe V, Ciudad CJ, Marin S, Cascante M. Glucose-6-phosphate dehydrogenase and transketolase modulate breast cancer cell metabolic reprogramming and correlate with poor patient outcome. Oncotarget 2017; 8:106693-706.
19. Nagashio R, Oikawa S, Yanagita K, et al. Prognostic significance of G6PD expression and localization in lung adenocarcinoma. Biochim Biophys Acta Proteins Proteom 2019; 1867:38-46.
20. Hong W, Cai P, Xu C, et al. Inhibition of Glucose-6-phosphate dehydrogenase reverses cisplatin resistance in lung cancer cells via the redox system. Front Pharmacol 2018; 9:43.
21. Mele L, Paino F, Papaccio F, et al. A new inhibitor of glucose-6-phosphate dehydrogenase blocks pentose phosphate pathway and suppresses malignant proliferation and metastasis in vivo. Cell Death Dis 2018; 9:572.
22. Luan X, Zhou X, Trombetta-eSilva J, Francis M, Gaharwar AK, Atsawasuwan P, Diekwisch TGH. MicroRNAs and Periodontal Homeostasis. J Dent Res 2017; 96:491-500.
23. Hartig SM, Hamilton MP, Bader DA, McGuire SE. The miRNA Interactome in Metabolic Homeostasis. Trends Endocrinol Metab 2015; 26:733-45.
24. Chen X, Tong ZK, Zhou JY, Yao YK, Zhang SM, Zhou JY. MicroRNA-206 inhibits the viability and migration of human lung adenocarcinoma cells partly by targeting MET. Oncol Lett 2016; 12:1171-77.
25. Cui J, Pan Y, Wang J, Liu Y, Wang H, Li H. MicroRNA-206 suppresses proliferation and predicts poor prognosis of HR-HPV-positive cervical cancer cells by targeting G6PD. Oncol Lett 2018; 16:5946-52.
26. Pan BL, Tong ZW, Wu L, et al. Effects of MicroRNA-206 on osteosarcoma cell proliferation, apoptosis, migration and invasion by targeting ANXA2 through the AKT signaling pathway. Cell Physiol Biochem 2018; 45:1410-22.
27. Yang N, Wang L, Liu J, Liu L, Huang J, Chen X, Luo Z. MicroRNA-206 regulates the epithelial-mesenchymal transition and inhibits the invasion and metastasis of prostate cancer cells by targeting Annexin A2. Oncol Lett 2018; 15:8295-302.
28. Zhang Q, Yi X, Yang Z, et al. Overexpression of G6PD represents a potential prognostic factor in clear cell renal cell carcinoma. J Cancer 2017; 8:665-73.
29. Zhang Q, Yang Z, Han Q, et al. G6PD promotes renal cell carcinoma proliferation through positive feedback regulation of p-STAT3. Oncotarget 2017; 8:109043-60.
30. Lu M, Lu L, Dong Q, et al. Elevated G6PD expression contributes to migration and invasion of hepatocellular carcinoma cells by inducing epithelial-mesenchymal transition. Acta Biochim Biophys Sin (Shanghai) 2018; 50:370-80.

MiR-20a PROMOTES LUNG TUMORIGENESIS BY TARGETING RUNX3 VIA TGF-β SIGNALING PATHWAY

X. QIN[1*], XY. WANG[2*], JW. FEI[1], FH. LI[1], J. HAN[1] and HX. WANG[1]

[1]Department of Respiratory Medicine, Yantaishan Hospital, Yantai, China; [2]Department of Clinical Laboratory, Jinan Zhangqiu District Hospital of TCM, Jinan, China

Received January 10, 2020 – Accepted April 2, 2020

*These Authors contributed equally to this work

MiR-20a shows a significant role in the development of various human tumors. However, its specific biological function in non-small-cell lung cancer (NSCLC) is still not clear. qRT-PCR was applied for detecting miR-20a expression. The analysis of cell growth and apoptosis were performed by MTT, xenograft models, Western blot assays. Dual luciferase reporter, Western blotting and qRT-PCR were carried out to verify the potential target of miR-20a. In NSCLC tissues and cells, miR-20a was highly expressed and RUNX3 was lowly expressed. Moreover, up-regulation of miR-20a expression promoted NSCLC cell proliferation, invasion and migration, while low-expression of miR-20a showed the converse case on cell proliferation, invasion and migration. RUNX3 was verified as the direct target of miR-20a and it could overturn its biological function in NSCLC cells. Moreover, miR-20a negatively regulated RUNX3 expression. Mechanistically, increasing miR-20a expression inhibited RUNX3 expression and then activated the TGF-β signaling pathway. Taken together, our results demonstrated that re-expression of miR-20a promoted lung tumorigenesis by down-regulation of RUNX3 and facilitating the activation of TGF-β signaling pathway.

Lung cancer is the leading cause of cancer deaths worldwide, killing 1.4 million people each year. Lung tumors are often found as metastatic diseases, and although the molecular diagnosis and targeted therapy have been improved, the 5-year survival rate remains 10-20% (1, 2). Non-small cell lung cancer (NSCLC) is the most common subtype of lung cancer, accounting for about 80% of all the new lung cancer cases (3). Therefore, it is prerequisite to explore the molecular mechanisms participated in NSCLC progression and provide a basis for the treatment of patients.

MicroRNAs (miRNAs), as long as 18-25 nucleotides in length, are small endogenous non-coding RNAs, negatively regulating gene expression through targeting the 3'UTR of mRNA (4). Genome-genome analysis of miRNAs expression revealed significant differences between tumor samples and their corresponding normal tissues, which usually indicates that miRNAs are associated with tumor development and progression (5-8). MiRNAs could contribute to cancer development via modulating cell proliferation, invasion and migration. MiR-20a belongs to the miR-17-92 cluster, located in the

Key words: miR-20a; lung; RUNX3; TGF-β signaling pathway

Corresponding Author:
Dr Haixia Wang,
Department of Respiratory Medicine,
Yantaishan Hospital, 91 Jiefang Road,
Yantai 264000, China
Tel.: +86 18366198692 - Fax: 0535 6602028
e-mail: juhkrtc4564@163.com

0393-974X (2020)
Copyright © by BIOLIFE, s.a.s.
This publication and/or article is for individual use only and may not be further reproduced without written permission from the copyright holder.
Unauthorized reproduction may result in financial and other penalties
DISCLOSURE: ALL AUTHORS REPORT NO CONFLICTS OF INTEREST RELEVANT TO THIS ARTICLE.

13q31.1 chromosomal region (9). Recently, miR-20a has been reported exhibiting different functions in human cancers and diseases. For example, miR-20a regulated colon cancer metastasis by targeting WTX (10). Also, dowregulation of miR-20a suppressed cervical cancer cell proliferation and promoted cell apoptosis via regulating THBS2 (11). Moreover, Bai X. et al showed that miR-20a facilitated breast cancer cells growth via targeting RUNX3 (12). In addition, miR-20a expression was higher in lung cancer and served as the promising prognostic biomarker of NSCLC patients (13-15). However, miR-20a molecular mechanism in regulating NSCLC progression was not well understood.

The runt-related transcription factor 3 (RUNX3) has been reported to be associated with tumors progression (16). The low expression of RUNX3 was found in multiple cancers. For example, it was down-regulated in tongue squamous cell carcinomas and served as a potential prognostic biomarker (17). Moreover, Chen et al. revealed that RUNX3 took part in hepatocellular carcinoma progression regulated by miR-761 (18). Zhang et al. showed that RUNX3 took part in cell growth and migration of colorectal cancer as the target of miR-301a (19). Furthermore, some studies have displayed that RUNX3 was lower in lung tissues (20-22). However, the function of RUNX3 in the development of NSCLC and whether RUNX3 served as the target of miR-20a was not fully elucidated. Furthermore, previous studies showed that RUNX family proteins affected TGF-β signaling through a variety of mechanisms in many cancers (23).

In the present study, our goal was to investigate the functional role of miR-20a and its molecular mechanism in regulating NSCLC tumorigenesis. The results demonstrated that miR-20a enhanced NSCLC tumorigenesis by inhibiting RUNX3 via TGF-β signaling pathway.

MATERIALS AND METHODS

Clinical specimens and cell culture

The tissue specimens were extracted from NSCLC patients and the patients were underwen surgery at Yantaishan Hospital. Informed written consent was obtained from all of the patients. Pathological examination confirmed that at least 80% of the tumor tissue was present in the cancer samples, while the corresponding benign area showed no cancerous tissue at all. The tissue specimens were stored at –80°C until further analysis. The research process was reviewed and approved by the ethic committee of Yantaishan Hospital.

NSCLC cell lines (H1299, H1650, H460 and H23) and normal cell line (16HBE) were purchased from ATCC. All cells were cultured into RPMI-1640 medium (Gibco, NY, USA) containing 10% FBS. Cell cultures were incubated in a humidified atmosphere containing 5% of CO_2 at 37°C.

Cell transfection

MiR-20a mimic, miR-20a inhibitor or control purchased from GenePharma (Shanghai, China) was used to increase or decrease miR-20a expression. The transfection procedures were performed by Lipofectamine 2000™ reagent. After transfection for 48 h, the cells were harvested for further use.

QRT–PCR

Total RNA was isolated from the tissues and cell lines using Trizol Reagent (Beyotime). Reverse transcription of the isolated RNA was first performed using the TaqMan miRNA Reverse Transcription Kit (Thermo, MA, USA). Then, complementary DNA was synthesized using the Reverse Transcriptase M-MLV kit with random primers (TaKaRa, Dalian, China). The TaqMan miRNA assay (Thermo, MA, USA) was carried out to perform the quantitative PCR. GAPDH or U6 was used as an internal control. All reactions were performed three times and the $2^{™\Delta\Delta Ct}$ method was applied for detecting the differential expression levels.

Cell viability assay

3-(4, 5-dimethylthiazol-2-yl)-2, 5-diphenyltetrazolium bromide (MTT) assay was applied for monitoring cell viability. Cells with different transfection were seeded into 48-well plates at 2×10^3 cells/well and incubated for 24 h, 48 h, 72 h and 96 h at 37°C. Then 20 µl MTT solution were added to each well and incubated for another 4 h at 37°C. Finally, 200 mL DMSO were added to each well and the

absorbance at a wavelength of 490 nm was detected by a microplate reader.

Cell migration and invasion assay

A Transwell with 8 μm PET track-etched membrane insert (Corning, NY, USA) was applied to measure the migratory and invasive ability of NSCLC cells. For invasion assay, Matrigel (Franklin Lakes, NJ, USA) was spread over the upper chamber and then incubated for 2 h at 37°C, while for migration assay, there has no matrigel coverage. Then, $5x10^4$ cells were seeded on the upper chamber and DMEM medium supplementing with 10% FBS was added in the lower chamber as a chemoattractant. After incubation for 24 h, cells on the top side were moved to the lower side, and the cells on the upper chamber were removed with a cotton swab. Cells that migrated through the pores and adhered to the lower surface of the filter were fixed with 4% paraformaldehyde, stained with 0.1% crystal violet. Finally, we counted the migratory and invasive cells by a microscope (×200). Five fields of view were randomly selected for analysis from each chamber.

Protein analysis

Firstly, we used RIPA buffer (Solarbio, Beijing, China) to lyse the cells on ice and then added the cell lysates onto the SDS-polyacrylamide gels. The protein concentration was determined using the BCA assay. After the proteins were separated, they were transferred onto NC membrane. Subsequently, 5% diluted milk in TBST was used for blocking the membrane for 2 h and then the primary antibodies at 4°C overnight. After washing three times with TBST, second antibodies were added and incubated for 2 h. Finally, the chemiluminescence of membranes was detected by ECL chemiluminescence reagents. The expression level of RUNX3 was normalized to GAPDH and measured using Quantity One software.

Animal model and tumorigenesis

The BALBc nude mice (4 weeks old, weighing 20–25g) were purchased from Shanghai Laboratory Animal Center (Shanghai, China). The flanks of the mice were subcutaneously injected with H460 cells that stably expressed miR-20a mimic to conduct animal model. Tumor volumes were measured weekly and calculated using the formula: Volume (mm3) = 1/2 (length × width)^2. The animal experiments were approved by the Laboratory Animal Ethics Committee of Yantaishan Hospital (Yantai, China) and followed the Regulations for the Administration of Affairs Concerning Experimental Animals approved by the State Council and promulgated by Decree No 2 of the State Science and Technology Commission (1988).

Luciferase assay

The wild type of RUNX3 3' UTR (RUNX3 3' UTR-WT) or mutational type (RUNX3 3' UTR-MUT) was inserted into the downstream of the pGL3 reporter vector (Promega, Madison, USA). MiR-20a mimic or inhibitor and 3' UTR RUNX3-pGL3 reporter were con-transfected into cells for 48 h and then incubated for 24 h, followed by measuring the luciferase activity by a Dual-Luciferase Reporter System (Promega, Madison, USA).

Immunohistochemistry (IHC) and staining evaluation

After the NSCLC tissues fixed with 4% paraformaldehyde, paraffin sections (6 μm) were obtained. Then, sections were blocked with 5% goat milk for 2 h at room temperature, subsequently incubated with the primary antibody anti-MTDH for 48 h at 4°C and biotinylated goat anti-rabbit IgG secondary antibody (Santa Cruz) for 2 h. The sections were stained by DAB mixture. Then, a graded alcohol series was used to dehydrate the stain sections, the xylene to clear sections and neutral balsam to coverslip sections. Finally, the protein density of per section was determined by the Image Pros Plus 5.0 software (USA).

Statistical analysis

All experiments were conducted at least 3 times. SPSS software was carried out to perform the statistical analysis of data and data was expressed as mean±and *Chi*-squared test was used to analyze the correlation between miR-20a expression and clinicopathological features. Student's *t*-test was used to analyze the difference between two groups. Multiple group comparisons were tested by one-way

ANOVA and Tukey test. P< 0.05 was considered statistically significant.

RESULTS

MiR-20a expression and prognostic value in NSCLC patients

To examine miR-20a expression in NSCLC, 50 pairs of NSCLC tissues and matched noncancerous tissues were obtained from NSCLC patients. As shown in Fig. 1A, miR-20a level was higher in NSCLC tissues than that in adjacent normal tissues. We then detected the relevance of miR-20a expression with the survival rate of NSCLC patients. As presented in Fig. 1B, the patients with high miR-20a expression had clearly shorter 5-year survival time compared with those with low miR-20a expression. Also, the data in Table I showed that miR-20a was highly related to stage and tumor size. All the above results indicated that high expression of miR-20a represent poor prognostic of lung cancer.

Overexpression of miR-20a enhanced cancer cell functions

Four NSCLC cell lines (H1299, H1650, H460 and H23) exhibited significantly upregulated miR-20a levels compared with the normal control 16HBE cell line (Fig. 2A). These data suggested that miR-20a may serve as a prognostic marker for patients with NSCLC. H460 cells were transfected with miR-20a-inhibitor, control inhibitor, miR-20a mimic, and control mimic, respectively. The expression levels of miR-20a were assessed by RT-qPCR. The expression of miR-20a in the miR-20a-inhibitor cells was decreased compared with that in the control inhibitor cells, while the expression of miR-20a in the miR-20a-mimic cells was increased compared with that in the control mimic cells (Fig. 2B). Overexpression of miR-20a resulted in an obvious increase of the proliferative, migratory and invasive ability of NSCLC cells, but inhibiting miR-20a exhibited the inverse effect (Fig. 2 C-E).

MiR-20a facilitated xenograft tumor growth

Since we found that miR-20a is increased in NSCLC tissues and cell lines, the potential role of miR-20a in tumor growth was evaluated in mice. H460 cells transfected with miR-20a mimic were injected into the nude mice subcutaneously and we examined the tumor volume weekly for 28 days by a caliper. Results displayed that miR-20a mimic boosted the tumor volumes (Fig. 3A) and its tumor cell xenografts grew more quickly (Fig. 3B).

RUNX3 was the direct target of miR-20a

To explore miR-20a mechanism in NSCLC, TargetScan 7.0 was used to predict miR-20a target genes. As shown in Fig. 4A, it was found that RUNX3 contains a putative binding site for miR-20a. Furthermore, RUNX3 was further confirmed as miR-20a direct target using the luciferase reporter assay (Fig. 4B). Results showed that increasing miR-20a

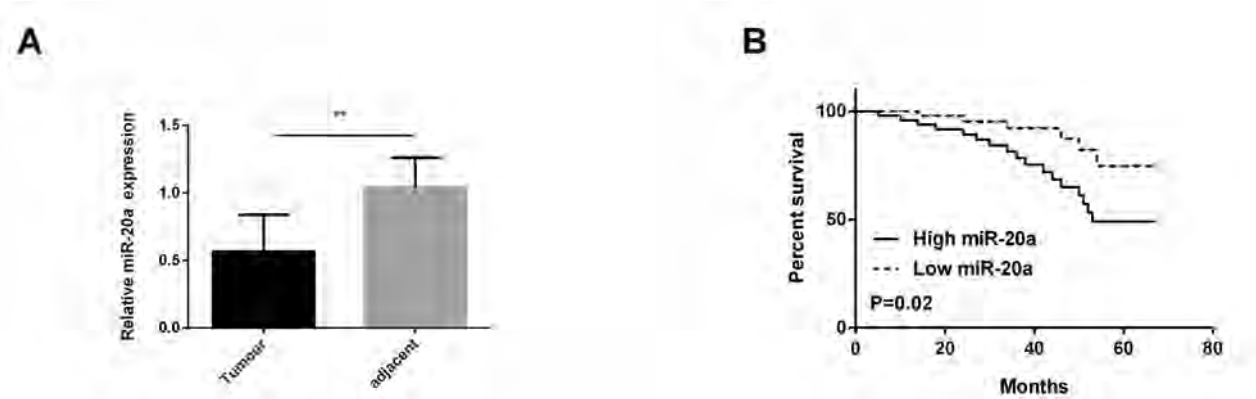


Fig. 1. *High expression of miR-20a in NSCLC. **A)** miR-20a expression detected in NSCLC tissue specimens. **B)** Overall survival correlation analysis the association of NSCLC patients with miR-20a expression. **P < 0.01.*

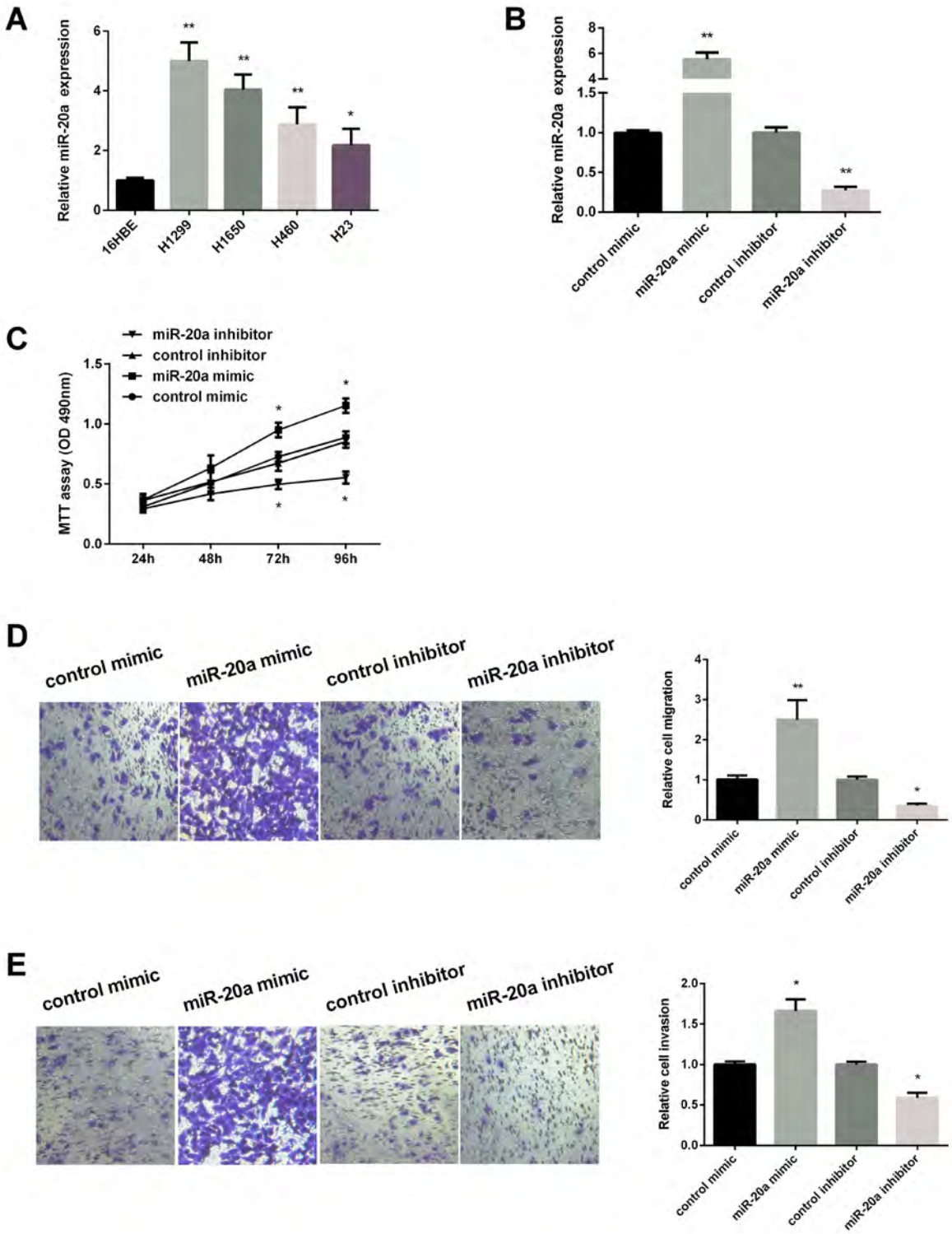


Fig. 2. *Facilitating effect of miR-20a on NSCLC progression.* ***A)*** *MiR-20a expression detected in NSCLC cell lines (H1299, H1650, H460, H23) and normal cells (16HBE).* ***B)*** *MiR-20a expression tested in H460 cells after increasing or decreasing miR-20a.* ***C)*** *H460 cells viability measured after increasing or decreasing miR-20a.* ***D)*** *H460 cells migration rate examined after increasing or decreasing miR-20a.* ***E)*** *H460 cells invasion rate examined after increasing or decreasing miR-20a.* P <0.05, ** P <0.01.*

made RUNX3 3′-UTR-WT activity decreased, while RUNX3 3′-UTR-MuT activity had no significant change. Then, the expressional level of RUNX3 changed by miR-20a was detected by qRT-PCR. The results showed that there was a decreased expression of RUNX3 in miR-20a mimic group, whereas an increased expression of RUNX3 in miR-20a inhibitor group (Fig. 4C). Moreover, overexpression analysis demonstrated that the relationship between RUNX3 and miR-20a was negative (Fig. 4D). In brief, we determined that RUNX3 was a direct target of miR-20a.

Prognostic value of RUNX3 in NSCLC

To understand the functional role of RUNX3 in NSCLC, IHC staining was applied for examining its expression in NSCLC tissues. As presented in Fig. 5A, the positive RUNX3 protein was expressed in the nucleus of tissues, and the protein intensity of RUNX3 was obviously lower in NSCLC tissues than that in the adjacent normal tissues (Fig. 5B). Besides, Kaplan-Meier survival curve displayed that down-regulation of RUNX3 predicted poor prognosis of NSCLC (P= 0.0087, Fig. 5C).

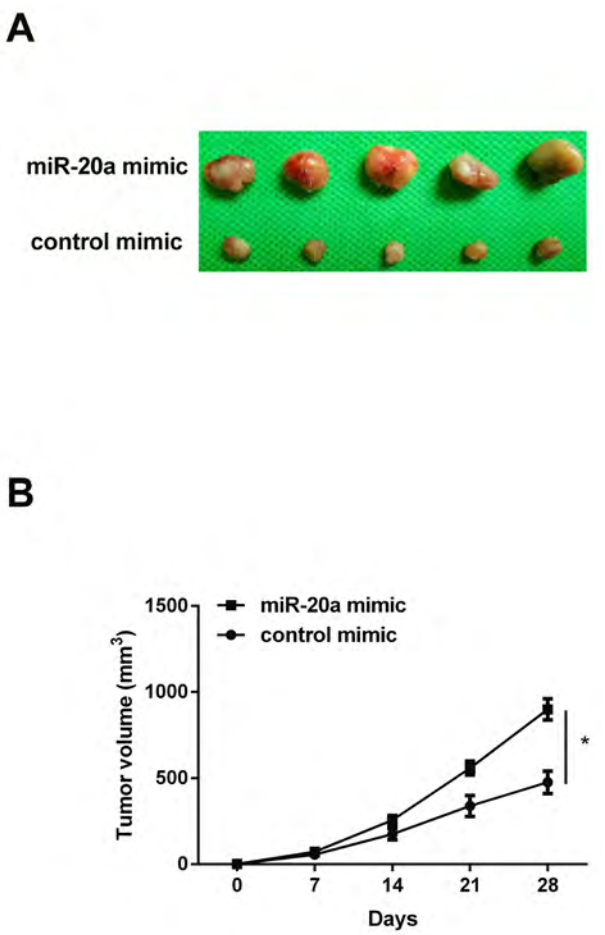


Fig. 3. *Increased effect of miR-20a on tumor growth in vivo.* ***A****) The tumorigenic ability detected after treated with miR-20a mimic.* ***B****) The growth rate of tumors measured after treated with miR-20a mimic. * P < 0.05, ** P < 0.01.*

MiR-20a facilitated EMT and TGF-β signaling pathway in NSCLC

To test whether miR-20a regulated the EMT and TGF-β pathway via RUNX3 in NSCLC, E-cadherin, N-cadherin, Vimentin, RUNX3 and Smad3, p-Smad3 protein levels were examined by Western blot in H460 cells after overexpression of miR-20a or TGF-β or both miR-20a and TGF-β, respectively. As shown in Fig. 6, increasing miR-20a reduced E-cadherin expression, while TGF-β upregulation raised its expression. However, miR-20a has the opposite effect on N-cadherin and Vimentin expression. Besides, RUNX3 was decreased by miR-20a mimic whereas raised by TGF-β stimulation. Furthermore, P-Smad3 expression was increased by miR-20a mimic and reduced by stimulating TGF-β. Moreover, TGF-β stimulation could overturn miR-20a effect on EMT and TGF-β/Smad3 pathway in H460 cells, indicating that TGF-β/Smad3 pathway took part in NSCLC progression regulated by miR-20a. In general, we concluded that miR-20a enhanced NSCLC progression via TGF-β/Smad3 pathway by targeting RUNX3.

DISCUSSION

MiRNAs participate in the pathogenesis of NSCLC by negatively regulating their target mRNA as oncogenes or tumor suppressors. MiRNAs are used as therapeutic agents in NSCLC basing on the following hypothesis: they play important roles in NSCLC development and their expression is imbalanced in cancer patients. Also, regulating the miRNA expression *in vivo* and *in vitro* can change the phenotype of cancer. In this study, the findings showed that miR-20a was up-regulated in NSCLC. MiR-20a downregulation inhibited NSCLC cell progression *in vivo* and *in vitro*. Moreover, we

Table I. *Associations between miR-20a expression and clinicopathological characteristics*

Characteristics	n=100	miR-20a		P-value
		High (n=50)	Low (n=50)	
Age (years)				0.423
≥ 60	48	26	22	
< 60	52	24	28	
Gender				0.677
Male	64	33	31	
Female	36	17	19	
Smoker				0.137
Yes	33	13	20	
No	67	37	30	
Histology				0.529
LSC	35	19	16	
LAC	65	31	34	
Tumor size				0.004*
<5cm	62	38	24	
⩾5cm	38	12	26	
TNM stage				0.041*
I-II	60	25	35	
III-IV	40	25	15	
Lymph node metastasis				0.019*
Absence	24	17	7	
Presence	76	33	43	

Statistical analyses were performed by the χ^2 test.
**P<0.05 was considered significant.*

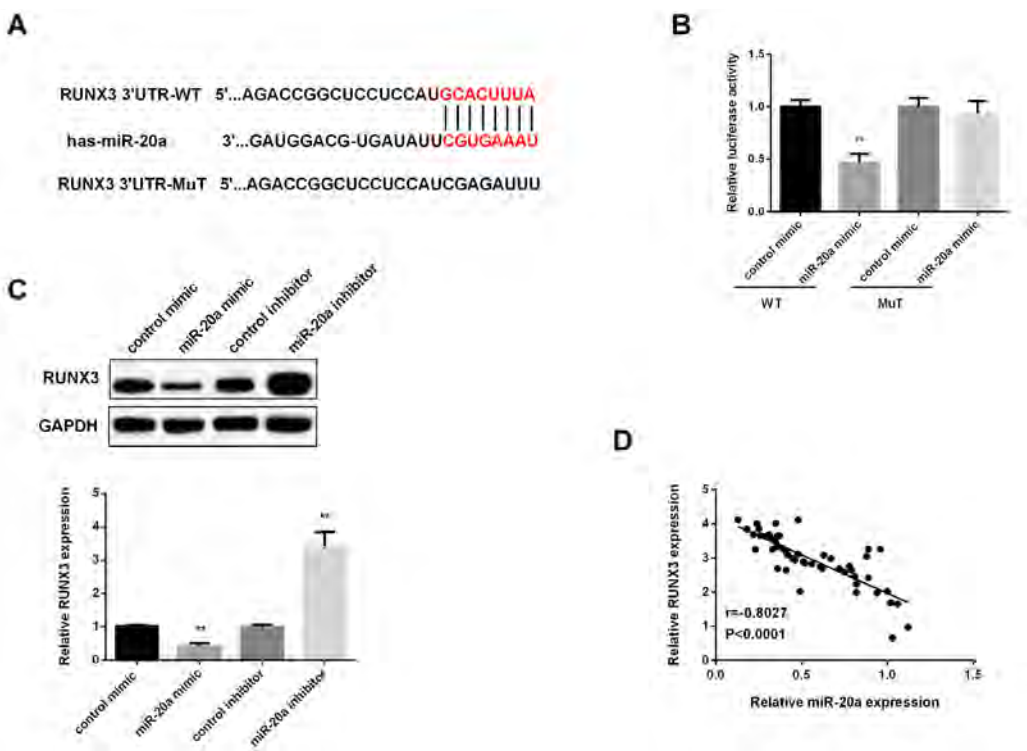


Fig. 4. *RUNX3 was the target of miR-20a. **A**) The binding site of miR-20a with RUNX3 shown in A. **B**) Luciferase activities measured in H460 cells after increasing miR-20a. **C**) RUNX3 expression tested in H460 cells after increasing or decreasing miR-20a. **D**) The relationship between miR-20a and RUNX3 expression tested in NSCLC tissues. ** P <0.01*

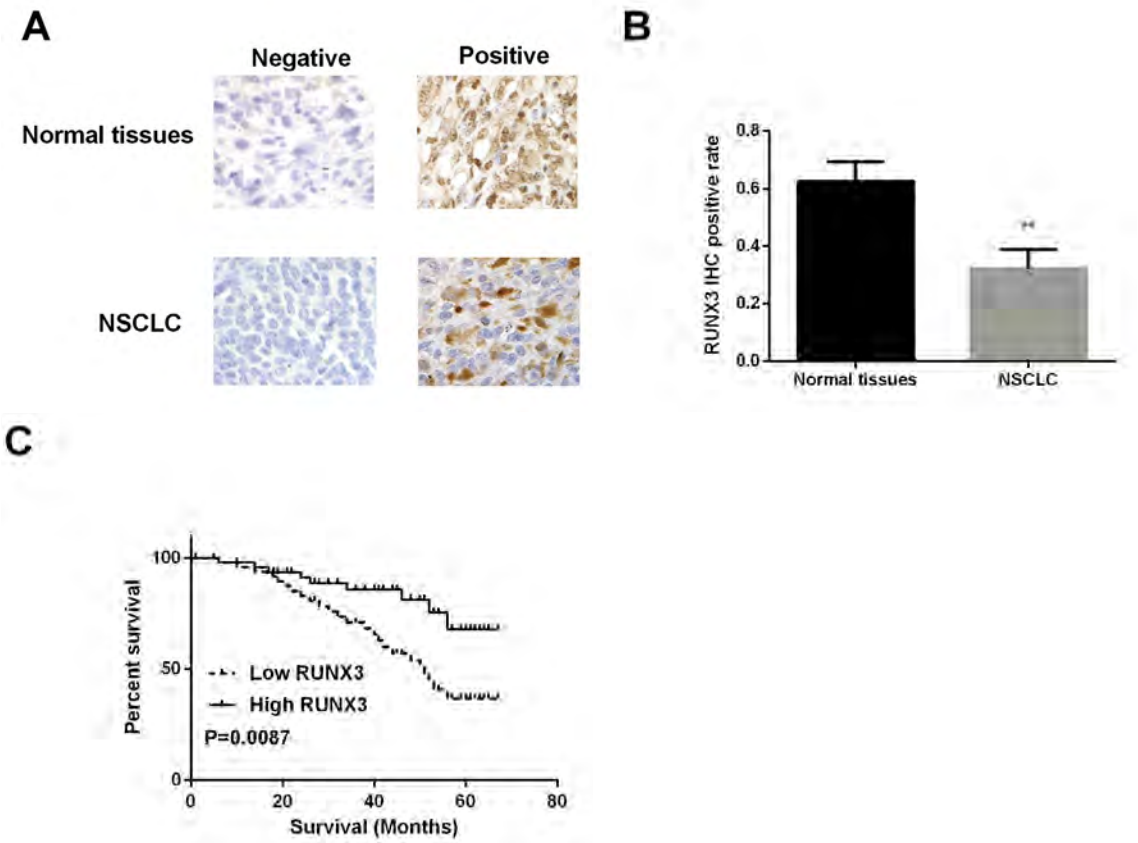


Fig. 5. *Low expression of RUNX3 in NSCLC tissues.* ***A)*** *RUNX3 protein expression localization in NSCLC cells.* ***B)*** *RUNX3 expression tested in H460 cells.* ***C)*** *The correlation of RUNX3 expression with overall survival measured in NSCLC patients. **P < 0.01.*

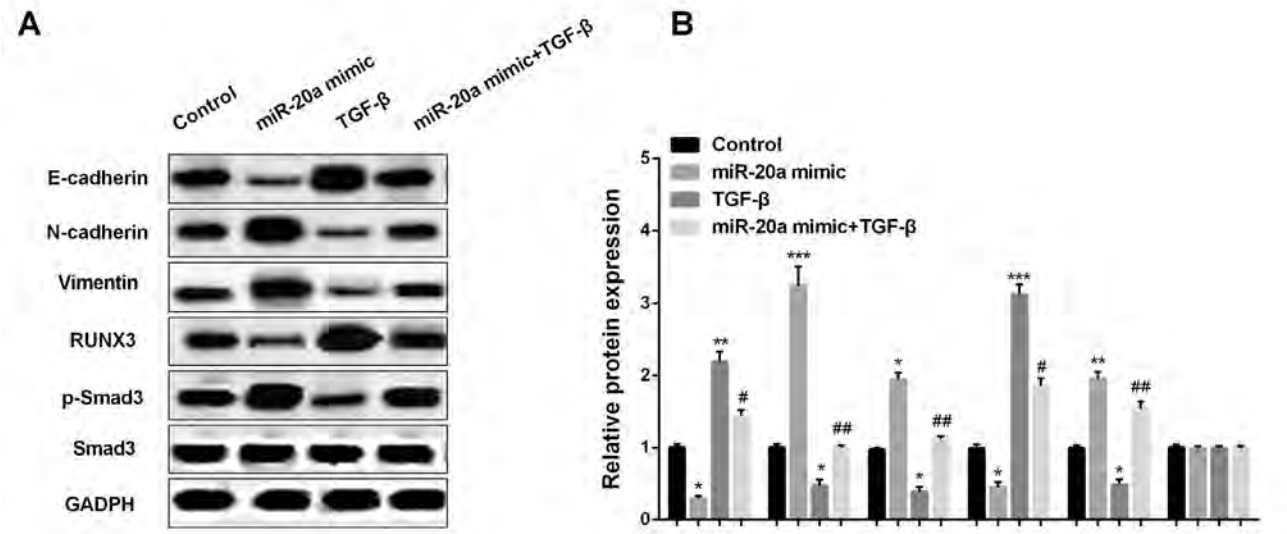


Fig. 6. *MiR-20a enhanced EMT and TGF-β/Smad3 pathway in NSCLC cell progression.* ***A)*** *Western blot analysis of E-cadherin, N-cadherin, Vimentin, RUNX3, SMAD3, p-SMAD3 expression levels in H460 cells after increasing miR-20a or stimulated by TGF-β.* ***B)*** *The protein levels of E-cadherin, N-cadherin, Vimentin, RUNX3, SMAD3, p-SMAD3 in H460 cells. * P < 0.05, **P < 0.01, ***P < 0.001* vs *control group; # P < 0.05, ##P < 0.01* vs *TGF-β group*

identified RUNX3 as the direct target of miR-20a and miR-20a regulated TGF-β/Smad3 signaling pathway subsequently.

Previous studies showed that many miRNAs took part in NSCLC progression. For example, miR-1260b, miR-593, miR-653 and miR-193a expression was imbalanced in NSCLC patients (24-26). Moreover, the expression of miR-20a was found to be abnormal in NSCLC (13). In addition, miR-20a also played an important role in multiple tumor development. For instance, a previous study verified the mechanism of miR-20a in regulating colon cancer progression which provided a potential target for treating colon cancer patients (10). Also, miR-20a regulated glioma progression via targeting CELF2 (27). Xin et al. showed that miR-20a was associated with gastric cancer cell apoptosis and autophagy (28). It is important to note that a single miRNA could regulate many target genes. For example, miR-20a modulated pancreatic ductal adenocarcinoma development by targeting ULK1 (29). miR-20a was over-expressed in colorectal cancer cells and downregulation of miR-20a promoted the sensitivity to cisplatin via targeting ASK1 (30). Also, RUNX3 was proved as the direct target of miR-20a and involved in regulating the triple-negative breast cancer cell growth (12). In our study, miR-20a was raised in NSCLC, and we first proved that miR-20a facilitated cell progression via targeting RUNX3, which which is in agreement with a previous study (31). Therefore, the results of the present study were convincing.

Accumulating studies have proved that RUNX3 took part in tumor cellular biological progressions. Sun and coll. showed that over-expression of RUNX3 suppressed glioma cell viability and invasion, and enhanced apoptosis (32). Moreover, one research showed that RUNX3 was a direct target of miR-20a in triple-negative breast cancer and hepatocellular carcinoma (12, 33). In our study, we revealed that RUNX3 was the target of miR-20a in NSCLC cells. RUNX3 was low expressed in NSCLC tissues and was associated with the survival of NSCLC patients (21, 34), which is consistent with our research that RUNX3 expressional level was decreased in NSCLC. Moreover, the result confirmed that RUNX3 could overturn the miR-20a promotion effect on NSCLC cell proliferation, migration and invasion. RUNX3 was also reported to regulate TGF-β axis in tumor progression and TGF-β suppressed tumor cell growth and promoted cell apoptosis, while it accelerated tumor angiogenesis, EMT and advanced cancer metastasis (35). Here, our study determined that TGF-β reversed miR-20a effect on EMT and Smad3 pathway in NSCLC, suggesting that miR-20a showed promoted effect by negatively regulating the TGF-β/Smad3 pathway.

In conclusion, miR-20a expression was raised in NSCLC while RUNX3 was decreased, and over-expression of miR-20a enhanced NSCLC progression. RUNX3 was a target of miR-20a in regulating NSCLC progression, and miR-20a achieved the promotion effect on NSCLC by regulating TGF-β/Smad3 signaling pathway.

REFERENCES

1. Chen Z, Li JL, Lin S, et al. cAMP/CREB-regulated LINC00473 marks LKB1-inactivated lung cancer and mediates tumor growth. J Clin Invest 2016; 126:2267-79.
2. Siegel R, Ma J, Zou Z, Jemal A. Cancer statistics, 2014. CA Cancer J Clin 2014; 64:9-29.
3. Chen Z, Fillmore CM, Hammerman PS, Kim CF, Wong KK. Non-small-cell lung cancers: a heterogeneous set of diseases. Nat Rev Cancer 2014; 14:535-46.
4. Bartel DP. MicroRNAs: genomics, biogenesis, mechanism, and function. Cell 2004; 116:281-97.
5. Volinia S, Calin GA, Liu CG, et al. A microRNA expression signature of human solid tumors defines cancer gene targets. Proc Natl Acad Sci U S A 2006; 103:2257-61.
6. Lu J, Getz G, Miska EA, et al. MicroRNA expression profiles classify human cancers. Nature 2005; 435:834-38.
7. Iorio MV, Ferracin M, Liu CG, et al. MicroRNA gene expression deregulation in human breast cancer. Cancer Res 2005; 65:7065-70.
8. Yanaihara N, Caplen N, Bowman E, et al. Unique microRNA molecular profiles in lung cancer diagnosis and prognosis. Cancer Cell 2006; 9:189-98.
9. Tsuchida A, Ohno S, Wu W, et al. miR-92 is a key

oncogenic component of the miR-17-92 cluster in colon cancer. Cancer Sci 2011; 102:2264-71.
10. Zhu GF, Xu YW, Li J, et al. Mir20a/106a-WTX axis regulates RhoGDIa/CDC42 signaling and colon cancer progression. Nat Commun 2019; 10:112.
11. Zhou Q, Dong J, Luo R, Zhou X, Wang J and Chen F. MicroRNA-20a regulates cell proliferation, apoptosis and autophagy by targeting thrombospondin 2 in cervical cancer. Eur J Pharmacol 2019; 844:102-9.
12. Bai X, Han G, Liu Y, Jiang H, He Q. MiRNA-20a-5p promotes the growth of triple-negative breast cancer cells through targeting RUNX3. Biomed Pharmacother 2018; 103:1482-89.
13. Wei L, Ran F. MicroRNA-20a promotes proliferation and invasion by directly targeting early growth response 2 in non-small cell lung carcinoma. Oncol Lett 2018; 15:271-77.
14. Li C, Qin F, Hu F, et al. Characterization and selective incorporation of small non-coding RNAs in non-small cell lung cancer extracellular vesicles. Cell Biosci 2018; 8:2.
15. Xu X, Zhu S, Tao Z, Ye S. High circulating miR-18a, miR-20a, and miR-92a expression correlates with poor prognosis in patients with non-small cell lung cancer. Cancer Med 2018; 7:21-31.
16. Ito Y. Oncogenic potential of the RUNX gene family: 'overview'. Oncogene 2004; 23:4198-208.
17. Zhou WN, Du YF, Zheng Y, Zhang W, Wu YN, Song XM, Bai J. Inactivation of RUNX3 protein expression in tongue squamous cell carcinoma and its association with clinicopathological characteristics. Mol Med Rep 2018; 19(2):885-94.
18. Chen Z, Zuo X, Pu L. circLARP4 induces cellular senescence through regulating miR-761/RUNX3/p53/p21 signaling in hepatocellular carcinoma. Cancer Sci 2018; 110(2):568-81.
19. Zhang L, Zhang Y, Zhu H, Sun X, Wang X, Wu P, Xu X. Overexpression of miR-301a-3p promotes colorectal cancer cell proliferation and metastasis by targeting deleted in liver cancer-1 and runt-related transcription factor 3. J Cell Biochem 2018; 120(4):6078-89.
20. Chen K, Liu H, Liu Z, et al. Genetic variants in RUNX3, AMD1 and MSRA in the methionine metabolic pathway and survival in non-small cell lung cancer patients. Int J Cancer 2019; 145(3):621-31.
21. Wang Y, Li Y, Wu B, Shi C, Li C. MicroRNA-661 promotes non-small cell lung cancer progression by directly targeting RUNX3. Mol Med Rep 2017; 16:2113-20.
22. Kim HJ, Park J, Lee SK, Kim KR, Park KK, Chung WY. Loss of RUNX3 expression promotes cancer-associated bone destruction by regulating CCL5, CCL19 and CXCL11 in non-small cell lung cancer. J Pathol 2015; 237:520-31.
23. Krishnan V, Ito Y. RUNX3 loss turns on the dark side of TGF-beta signaling. Oncoscience 2017; 4:156-57.
24. Xia Y, Wei K, Yang FM, et al. miR-1260b, mediated by YY1, activates KIT signaling by targeting SOCS6 to regulate cell proliferation and apoptosis in NSCLC. Cell Death Dis 2019; 10:112.
25. Han W, Wang L, Zhang L, Wang Y, Li Y. Circular RNA circ-RAD23B promotes cell growth and invasion by miR-593-3p/CCND2 and miR-653-5p/TIAM1 pathways in non-small cell lung cancer. Biochem Biophys Res Commun 2019; 510:462-66.
26. Liu X, Min S, Wu N, et al. miR-193a-3p inhibition of the Slug activator PAK4 suppresses non-small cell lung cancer aggressiveness via the p53/Slug/L1CAM pathway. Cancer Lett 2019; 447:56-65.
27. Yang HL, Thiyagarajan V, Shen PC, et al. Anti-EMT properties of CoQ0 attributed to PI3K/AKT/NFKB/MMP-9 signaling pathway through ROS-mediated apoptosis. J Exp Clin Cancer Res 2019; 38:186.
28. Xin L, Zhou LQ, Liu L, Yuan YW, Zhang HT, Zeng F. METase promotes cell autophagy via promoting SNHG5 and suppressing miR-20a in gastric cancer. Int J Biol Macromol 2019; 122:1046-52.
29. Huang F, Chen W, Peng J, et al. LncRNA PVT1 triggers Cyto-protective autophagy and promotes pancreatic ductal adenocarcinoma development via the miR-20a-5p/ULK1 Axis. Mol Cancer 2018; 17:98.
30. Zhang L, He L, Zhang H, Chen Y. Knockdown of MiR-20a Enhances Sensitivity of Colorectal Cancer Cells to Cisplatin by Increasing ASK1 Expression. Cell Physiol Biochem 2018; 47:1432-41.
31. Fan L, Sha J, Teng J, et al. Evaluation of serum paired MicroRNA ratios for differential diagnosis of non-small cell lung cancer and benign pulmonary diseases. Mol Diagn Ther 2018; 22(4):493-502.
32. Sun J, Li B, Jia Z, et al. RUNX3 inhibits glioma survival and invasion via suppression of the beta-

catenin/TCF-4 signaling pathway. J Neurooncol 2018; 140:15-26.
33. Chen Y, Wang X, Cheng J, et al. MicroRNA-20a-5p targets RUNX3 to regulate proliferation and migration of human hepatocellular cancer cells. Oncol Rep 2016; 36:3379-86.
34. Chen Z, Wei H, Zhao X, et al. Metformin treatment alleviates polycystic ovary syndrome by decreasing the expression of MMP-2 and MMP-9 via H19/miR-29b-3p and AKT/mTOR/autophagy signaling pathways. J Cell Physiol 2019; 234(11):19964-76.
35. Jin Y, Chen W, Yang H, et al. Scutellaria barbata D. Don inhibits migration and invasion of colorectal cancer cells via suppression of PI3K/AKT and TGF-beta/Smad signaling pathways. Exp Ther Med 2017; 14:5527-34.

SILENCING LncRNA LINC01305 INHIBITS EPITHELIAL MESENCHYMAL TRANSITION IN LUNG CANCER CELLS BY REGULATING TNXB-MEDIATED PI3K/Akt SIGNALING PATHWAY

F. YAN*, S-W. LIU*, X-Y. LI, C-C. LI and Y. WU

Jiangsu Cancer Hospital & Jiangsu Institute of Cancer Research & The Affiliated Cancer Hospital of Nanjing Medical University, Nanjing, China

Received February 5, 2020 – Accepted April 2, 2020

*These Authors contributed equally to this work

The aim of this study was to investigate whether LINC01305 can regulate TNXB-mediated phosphatidilinositol 3-kinase (PI3K)/protein kinase B (Akt) signaling pathway and therefore affect epithelial mesenchymal transition in lung cancer cells. Quantitative real-time polymerase chain reaction (qRT-PCR) was conducted to detect LINC01305 level in 52 non-small cell lung cancer (NSCLC) tissues and paracancerous normal lung tissues, and the relationship between LINC01305 expression and clinical pathological parameters of these subjects was analyzed. After LINC01305 was knocked down in PC9 cell and overexpressed in A549 cells, qRT-PCR was used to verify the transfection efficiency, and nuclear fractionation technique, cell counting kit-8 (CCK-8), plate cloning assay and Transwell test were used to detect the effect of LINC01305 on cell viability. LINC01305 had an obviously higher expression in NSCLC tissues, and the expression in lung cancer patients with tumor size >3 cm was higher than those with tumor ≤3 cm. LINC01305 expression in tumor tissues in T3-T4 stage was obviously higher than those in T1-T2 stage, and the overall survival rate of lung cancer patients with high expression of LINC01305 was lower than those with low expression. Moreover, clinical analysis revealed that LINC01305 level was related to tumor size, TNM stage and lymph node metastasis of patients with lung cancer, but not related to age or gender. Silencing LINC01305 can inhibit the epithelial mesenchymal transition-induced transformation of lung cancer cells through regulating TNXB-mediated PI3K/Akt signaling pathway, which in turn affects the progression of lung cancer.

As one of the most common malignant tumors in the world, lung cancer ranks first among all malignant tumors in men. In women, its incidence rate ranks fourth, and mortality ranks second (1). Current standard therapies for lung cancer include surgical resection, platinum-based dual chemotherapy, and radiation therapy. However, these therapies rarely achieve the goal of complete cure, and the 5-year survival rate is still only 17% (2). Therefore, we must actively seek sensitive markers for early diagnosis and effective treatment strategies.

Epithelial mesenchymal transition (EMT) is a process in which epithelial cells are gradually transformed into mesenchymal-like cells (3). It

Key words: lung cancer; epithelial mesenchymal transition; LINC01305; PI3K/Akt signaling pathway; TNXB

Corresponding Author:
Yuan Wu, MM
Jiangsu Cancer Hospital & Jiangsu Institute of Cancer Research & The Affiliated Cancer Hospital of Nanjing Medical University, Baiziting42, Nanjing 210009, China
Tel.: +86 025 83283312
e-mail: yuanwudui19960719@163.com

0393-974X (2020)
Copyright © by BIOLIFE, s.a.s.
This publication and/or article is for individual use only and may not be further reproduced without written permission from the copyright holder. Unauthorized reproduction may result in financial and other penalties
DISCLOSURE: ALL AUTHORS REPORT NO CONFLICTS OF INTEREST RELEVANT TO THIS ARTICLE.

is generally believed that EMT is involved in the pathogenesis of many lung diseases, such as lung tissue hypoplasia, fibrosis, cancer, etc. (4). Epithelial cells lose cell polarity and adhesion during EMT and become an interstitial phenotype with migration and invasiveness properties, which is an important factor leading to metastasis of tumors. Therefore, early detection and inhibition of tumor invasion and metastasis is of great significance for the clinical diagnosis and treatment of lung cancer.

Long-chain non-coding RNA (lncRNA) is a type of non-coding RNA with a transcript of more than 200 nucleotides in length (5). Some lncRNAs are closely related to EMT, such as MALAT1, and H19 (6, 7), which provide new ideas for the diagnosis and prognosis of lung cancer, as well as a new strategy for treatment. To date, it has been reported that LINC01305 can promote the development of cervical cancer, however, there is no report on the correlation between LINC01305 and lung cancer (8).

Tenascin XB (TNXB) is a macromolecular extracellular matrix protein expressed in human connective tissue but its function is still unclear. Some researchers believe that this gene is an essential regulator of collagen deposition in skin fibroblasts. The disorder of connective tissue is the main cause of human Ehlers-Danlos syndrome (9). At present, there are no reports on the related mechanisms of TNXB in the occurrence and progression of lung cancer.

The phosphatidilinositol 3-kinase (PI3K)/protein kinase B (Akt) signaling pathway is closely relevant to the development of different human tumors (10). Studies indicated that lung cancer metastasis and drug resistance are closely related to the PI3K/Akt signal transduction pathway (11). Other researchers have reported that this pathway is relevant to the induction of EMT in squamous cell carcinoma cells (12). Meanwhile, LINC01305 silencing was confirmed to be able to affect the development of cervical cancer by regulating TNXB-mediated PI3K/Akt signaling pathway (13). Therefore, this study investigated whether LINC01305 can inhibit lung cancer cells also by regulating TNXB-mediated PI3K/Akt signaling pathway. The occurrence of EMT provides new clinical ideas for finding potential targets for lung cancer treatment.

MATERIALS AND METHODS

Clinical tissue collection

All the clinical tissue samples in this study were collected from patients suffering from histopathologically-confirmed lung cancer during surgical excision. The tissues were stored at -80°C for RNA isolation. All the participants signed the informed consent form for this research.

Cell culture and transfection

Normal lung cell line (BEAS2B) and lung cancer cell lines (PC9, H460 and A549) were cultured in Roswell Park Memorial Institute (RPMI1640) medium (Gibco, Grand Island, NY, USA) supplemented with 10% fetal bovine serum (FBS) (HyClone, South Logan, UT, USA) and penicillin/streptomycin at 37°C in an incubator with 5% CO_2. Cells with good growth and proliferation were selected for the study. Transfection was performed with Lipofectamine 2000 (Invitrogen, Carlsbad, CA, USA) when the cell density reached approximately 80%. Si-LINC01305 was transfected into PC9 cells, and LINC01305 or LINC01305&TNXB were transfected into A549 cells for 24 h.

Quantitative real-time polymerase chain reaction (qRT-PCR)

The total RNA of the cells was extracted with TRIzol (Invitrogen, Carlsbad, CA, USA), and the expression levels of LINC01305 and TNXB were detected using a PCR detection kit (TaKaRa, Tokyo, Japan). Primer sequences are as follows: LINC01305: F: 5'-CCACGCAGCTCTCCAACACTC-3', R: 5'-TTTGGGCGACTACAGAATCCA-3'; TNXB: F: 5'-GTGGTCCAGTATGAGGACACG-3', R: 5'-CTGGTGGTCACGTCAGTCAC-3'; Glyceraldheyde 3-phosphate dehydrogenase (GAPDH): F: 5'-CAGGGCTGCTTTTAACTCTGGTAA-3', R: 5'-GGGTGGAATCATATTGGAACATGT-3'

Nuclear separation

Nuclear separation was performed following the instructions of the nuclear protein and cytoplasmic protein extraction kit. The cells were scraped off, centrifuged to obtain a precipitate, and cytoplasmic protein extracting reagent A containing phenylmethanesulfonyl fluoride

(PMSF) was added. After the mixture was shaken vigorously then underwent an ice-bath, cytoplasmic protein extracting reagent B was added, and then the mixture was again shaken vigorously, ice bathed, and centrifuged. After the precipitate was obtained, the nuclear protein extracting reagent containing PMSF was added, and the mixture was dissolved in an ice bath, centrifuged, and the supernatant was transferredd to a pre-cooled Eppendorf (EP) tube for storage.

Cell counting kit-8 (CCK-8) test

In a 96-well plate (Corning, Corning, NY, USA), approximately 1×10^3 cells were plated per well and cultured for 5 days. 10 μL of CCK-8 (Beyotime, Shanghai, China) was added to each well after 6, 24, 48, 72 and 96 h of culture. The optical density (OD) value was measured at 450 nm after incubation at 37°C with 5% CO_2 for 1 h, and each group was subjected to 5 replicate wells.

Plate clone formation

After the cells were stably transfected, digested, and centrifuged, about 5×10^2 cells were seeded per well in a 6-well plate. After two weeks of culture at 37°C, they were counted after having been stained with crystal violet, and 3 wells were repeated for each experiment.

Transwell invasion

After the Matrigel gel was diluted 1:6, 50 μL of the diluent was used to coat the bottom membrane of the Transwell upper chamber. 600 μL of medium with 10% FBS was added into the lower chamber, and 200 μL of serum-free medium was added to the upper chamber. The cells in each group were added to the upper chamber with 1×10^5 per well and incubated for 24 h at 37°C. Then the Matrigel gel was wiped with a cotton swab, and the Transwell upper chamber was fixed in 4% paraformaldehyde and stained with 0.1% crystal violet for 10 min and then observed under an inverted microscope.

Transwell migration assay

600 μL of medium containing 10% FBS was added to the lower chamber, and the treated cells were added to the upper chamber. The number of cells was 1×10^5 cells/room, the cell suspension volume was 200 μL, and the culture was carried out at 37°C. After the cells above the chamber were wiped with a cotton, the upper chamber was placed in 4% paraformaldehyde and stained with 0.1% crystal violet for 10 min, and then they were observed.

Dual-luciferase reporting assay

After 24 h of transfection, the cell culture medium was removed, and the appropriate amount of lysate was added to fully lyse the cells according to the requirements of the kit. After centrifugation at 10,000 g for 5 min, 100 μL of the supernatant of the lysate was taken for measurement. The Renal luciferase was used as an internal reference, and the RLU value obtained by the firefly luciferase assay was divided by the RLU value obtained by the Renilla luciferase assay. The degree of activation of the reporter gene for different samples was compared based on the ratio obtained.

RNA immunoprecipitation (RIP) experiment

The cells were lysed using RNA-binding protein immunoprecipitation kit (Beyotime, Shanghai, China) and lysed with RNA lysis buffer. Whole cell lysates were collected and incubated with RIP buffer containing magnetic beads and antibody against Ago2 overnight for gentle shaking. After the incubated sample was treated with proteinase K, the RNA concentration was measured with a spectrophotometer. The purified RNA was subjected to qRT-PCR reaction to verify the presence of binding.

Western blot

The collected protein sample was lysed with an appropriate amount of protein loading buffer and heated in a boiling water bath at 100°C for 3-5 min to fully denature the protein. After dodecyl sulfate, sodium salt-polyacrylamide gel electrophoresis (SDS-PAGE), transferring, blocking, incubating with primary antibody, secondary antibody (Cell Signaling Technology, Danvers, MA, USA) and enhanced chemiluminescence (ECL) developer, respectively, the protein image was developed by Bio-Rad (Hercules, CA, USA) Chemiluminescence Imager.

Statistical analysis

Data analysis was performed using Statistical Product and Service Solutions (SPSS) 22.0 (SPSS, Chicago, IL, USA) statistical software. The *t*-test was used to compare the difference between the two groups. The measurement data were expressed as mean ± standard deviation ($\bar{x}\pm s$).

Comparison between groups was carried out using One-way ANOVA test followed by Post Hoc Test (Least Significant Difference). P<0.05 was considered to be statistically significant**.**

RESULTS

High expression of LINC01305 in NSCLC and analysis of clinical data

QRT-PCR revealed that LINC00511 in 52 NSCLC tissue specimens was obviously higher than that in the normal ones (Fig. 1A). The LINC01305 level in patients with tumors size >3 cm was obviously higher than in those with tumor size ≤3 cm (Fig. 1B), and its expression in patients with tumors in T3-T4 stage was also obviously higher than that those in T1-T2 (Fig. 1C). We also found that LINC01305 was significantly higher in patients with lymph node metastasis than in patients without lymph node metastasis (Fig. 1D). Further analysis suggested the prognosis of patients with high expression of LINC00511 was obviously worse than those with low expression. (Fig. 1E HR=2.536, P=0.0362). In addition, clinical research revealed the LINC01305 level was correlated with tumor size, TNM stage and lymph node metastasis of patients with lung cancer, but not obviously correlated with patient's age and gender (Table I). The above results indicated that LINC01305 was relevant to the occurrence of this cancer and might promote its progression.

High expression of LINC01305 promotes migration of NSCLC cells

LINC01305 levels in normal lung cells (BEAS2B) and lung tumor cell lines (PC9, H460 and A549)

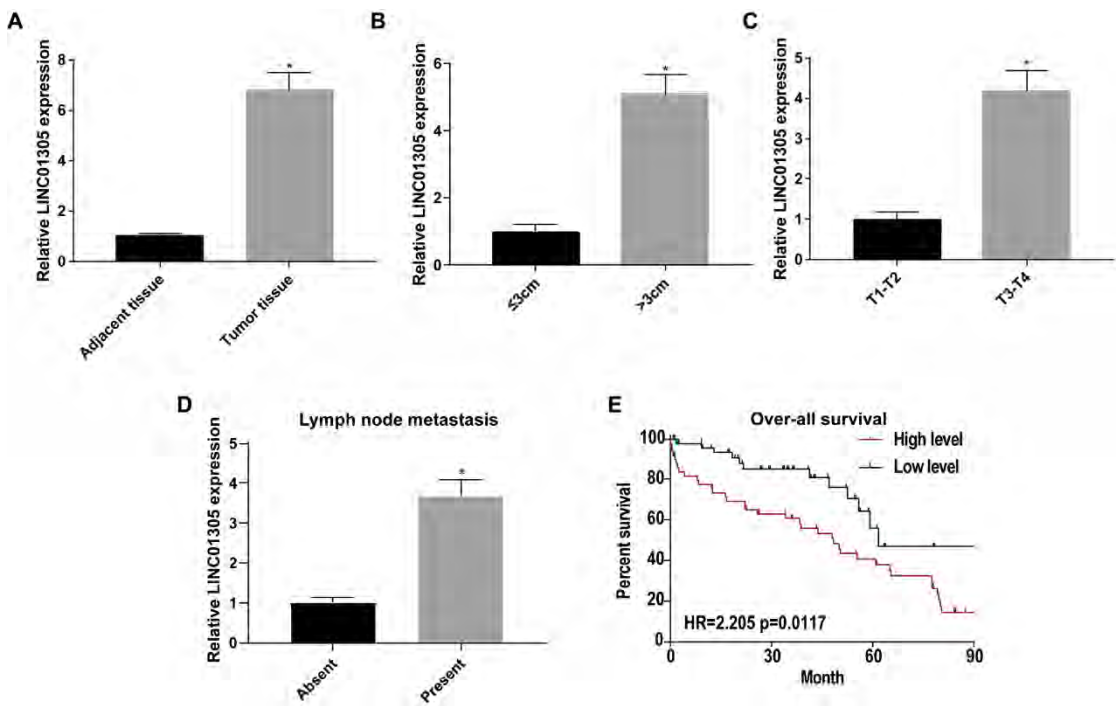


Fig. 1. *LINC01305 is highly expressed in non-small cell carcinoma. **A)** qRT-PCR detection showed that LINC00511 expression in 52 non-small cell lung cancer tissues was obviously higher than the normal control group. **B)** qRT-PCR detection suggested that LINC01305 in patients with >3 cm tumors was obviously higher than patients with tumor size ≤3 cm. **C)** qRT-PCR detection showed that LINC01305 in T3-T4 tumor patients was obviously higher than those in T1-T2 phase. **D**). qRT-PCR detection showed that LINC01305 was significantly higher in patients with lymph node metastasis than in patients without lymph node metastasis. **E)** The overall survival rate of LINC01305 in patients with high expression of LINC01305 in non-small cell carcinoma was obviously lower than those with low expression.*

were detected by qRT-PCR, and the expression of LINC01305 was found highest in PC9 cells and lowest in A549 cells (Fig. 2A). Therefore, PC9 and A549 cells were selected for subsequent experiment. In PC9 cells, the expression of LINC01305 was obviously decreased after knockdown of LINC01305. In A549 cells, the expression of LINC01305 was obviously increased after overexpression of LINC01305, proving that the transfection efficiency was successful (Fig. 2B). In PC9 and A549 cells, it was found that LINC01305 was more abundant in the cytoplasm according to the result of nuclear separation assay (Fig. 2C). CCK-8 test revealed that knockdown of LINC01305 in PC9 cells inhibited cell viability, while after overexpression of LINC01305 in A549 cells enhanced cell viability (Fig. 2D), which indicated that up-regulation of LINC01305 could increase cell viability. The results of plate cloning experiment showed that knockdown of LINC01305 obviously reduced the colony forming ability of PC9 cells, while overexpression of LINC01305 enhanced cloned ability of A549 cells (Fig. 2E), indicating that LINC01305 could promote cell proliferation. Transwell experiments indicated that knockdown of LINC01305 in PC9 cells obviously reduced cell migration ability and invasiveness, while the opposite result was observed after overexpression of LINC01305 in A549 cells (Fig. 2F). The above results indicated that LINC01305 could increase the viability, proliferation, migration and invasiveness of lung cancer cells.

LINC01305 can target TNXB

Bioinformatics analysis revealed a binding site for LINC01305 and TNXB (Fig. 3A). Luciferase reporter gene assay indicated that wild-type TNXB was capable of quenching fluorescence of LINC01305 (Fig. 3B), RIP assay result showed that LINC01305 was able to bind to TNXB 3'-UTR (Fig. 3C), suggesting that TNXB can be targeted and combined. In order to verify whether there is regulation between the two, after knocking down LINC01305 in PC9 cells, the mRNA and protein expression levels of TNXB were detected and found obviously increased. However, after overexpression of LINC01305 in A549 cells, the expression of TNXB was observed obviously reduced (Fig. 3 D, E). The above results indicated that LINC01305 could indeed target TNXB and regulate its expression.

Table I. *Correlation between the expression of LINC01305 and clinicopathological features in lung cancer patients (n = 52).*

Clinicopathologic features	Number of cases	LINC01305 expression		P-value
		Low (n=26)	High (n=26)	
Age (years)				
≤56	31	16	15	0.7775
>56	21	10	11	
Gender				
Male	22	12	10	0.5745
Female	30	14	16	
Tumor size				
≤3CM	27	18	9	0.0487
>3CM	25	8	17	
TNM stage				
I~II	31	20	11	0.0110
III~IV	21	6	15	
Lymph node metastasis				
Absent	24	17	7	0.0054
Present	28	9	19	

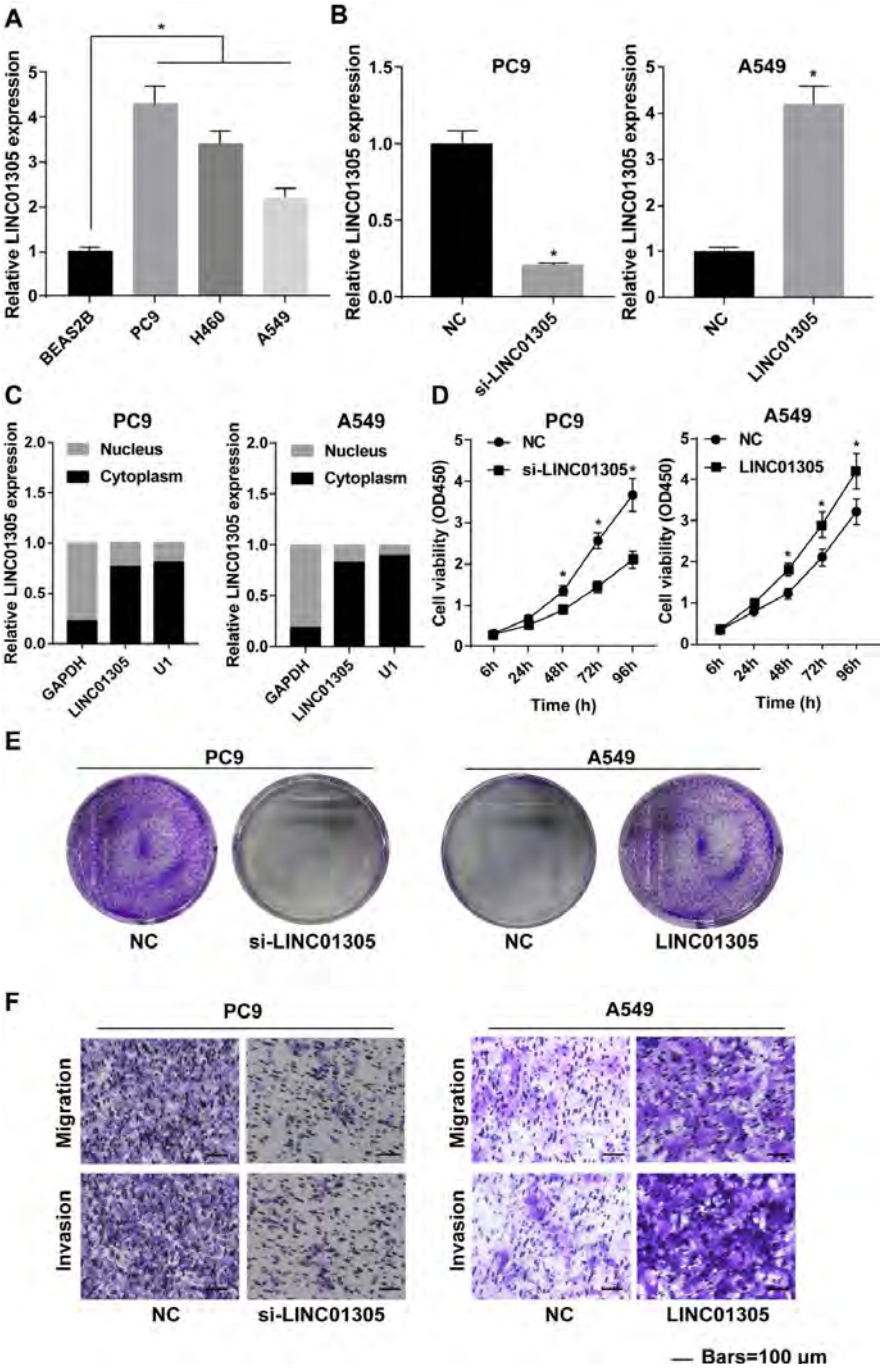


Fig. 2. *High expression of LINC01305 promotes migration and invasiveness of lung cancer cells.* ***A****) qRT-PCR detected the expression level of LINC01305 in normal lung cells (BEAS2B) and lung cancer cell lines (PC9, H460 and A549).* ***B****) In PC9 cells, the expression of LINC01305 was obviously decreased in cells after knockdown of LINC01305. In A549 cells, the expression of LINC01305 was obviously increased in cells after overexpression of LINC01305.* ***C****) In PC9 and A549 cells, LINC01305 is more abundant in the cytoplasm according to nuclear separation assay.* ***D****) In PC9 cells, knocking down LINC01305 reduced the activity of CCK-8 cells, while in A549 cells, overexpression of LINC01305 enhanced cell viability.* ***E****) In PC9 cells, after knocking down LINC01305, the cloning ability of the cells was obviously reduced; in A549 cells, after overexpressing LINC01305, the cell cloning ability was obviously enhanced.* ***F****) In PC9 cells, after knocking down LINC01305, Transwell assay showed that the migration ability and invasiveness of cells was obviously reduced; in A549 cells, after overexpressing LINC01305, the migration ability and invasiveness of cells was obviously enhanced (magnifications: 400 X).*

TNXB reverses the impact of LINC01305 on lung cancer cells via PI3K/Akt pathway

In order to clarify the regulatory interplay between LINC01305 and TNXB in the process of EMT in lung cancer cells, we divided the cells into three groups, the control group, the overexpressed LINC01305 group, and simultaneous overexpressed LINC01305&TNXB group. It was found that overexpression of TNXB with LINC01305 reversed the promoting impact of overexpression of LINC01305 alone on p-PI3K and p-Akt (Fig. 4A) expression, cell viability (Fig. 4B) and cell invasiveness (Fig. 4C). These results suggested that TNXB could inhibit the promoting role of LINC01305 in lung cancer through the PI3K/Akt pathway.

DISCUSSION

Lung cancer is one of the world's most serious threats to human health and life. Its morbidity and mortality have led to the forefront of various malignant tumors, and more than 80% of malignant tumor deaths are caused by NSCLC (14). Researches have shown that EMT can play a pivotal part in the progression of this cancer (15). Sulzer et al. (16)

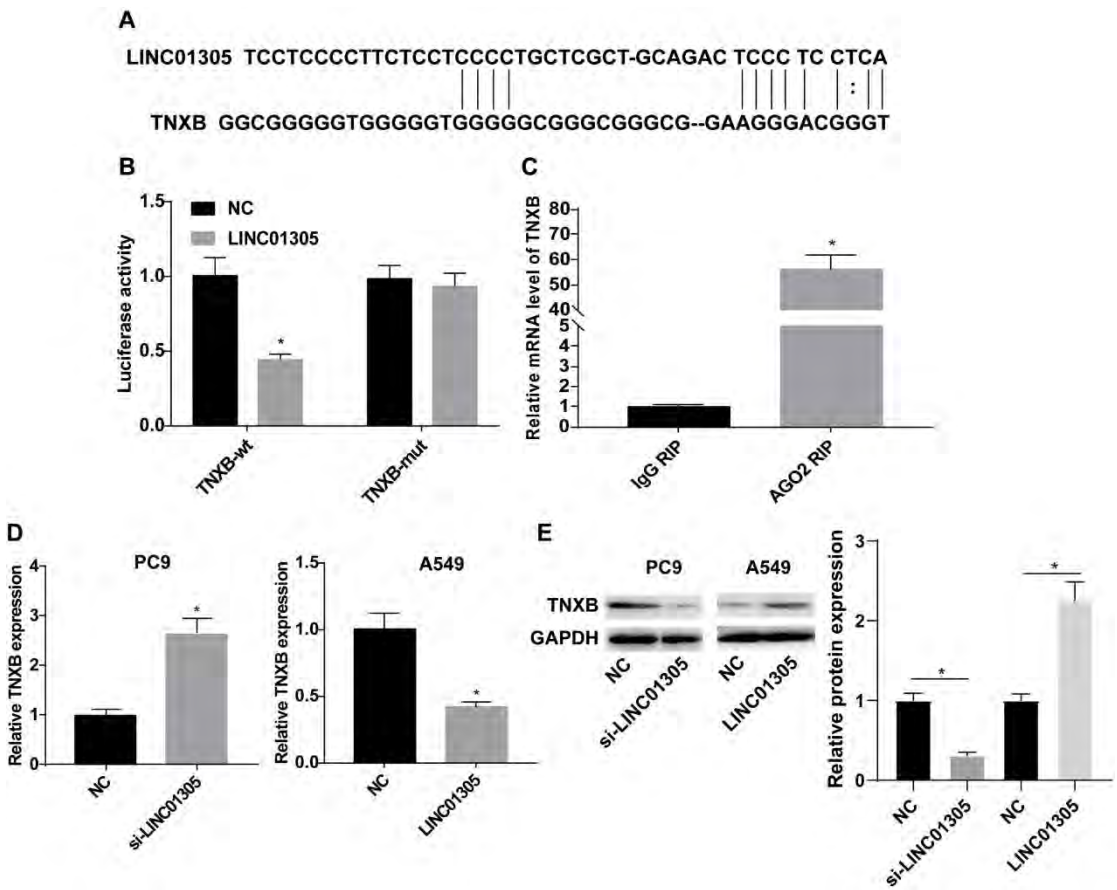


Fig. 3. *TNXB is a target gene for LINC01305.* ***A****) Binding site of LINC01305 and TNXB was predicted.* ***B****) Luciferase reporter assay showed that wild-type TNXB is capable of fluorescent quenching of LINC01305.* ***C****) RIP experimental indicated that LINC01305 is capable of binding to the TNXB 3'-UTR.* ***D****). qRT-PCR detection suggested that TNXB expression was obviously increased after knockdown of LINC01305 in PC9 cells and was obviously decreased after overexpression of LINC01305 in A549 cells.* ***E****) Western blot analysis showed that the expression of TNXB was obviously increased after knockdown of LINC01305 in PC9 cells and obviously decreased after overexpression of LINC01305.*

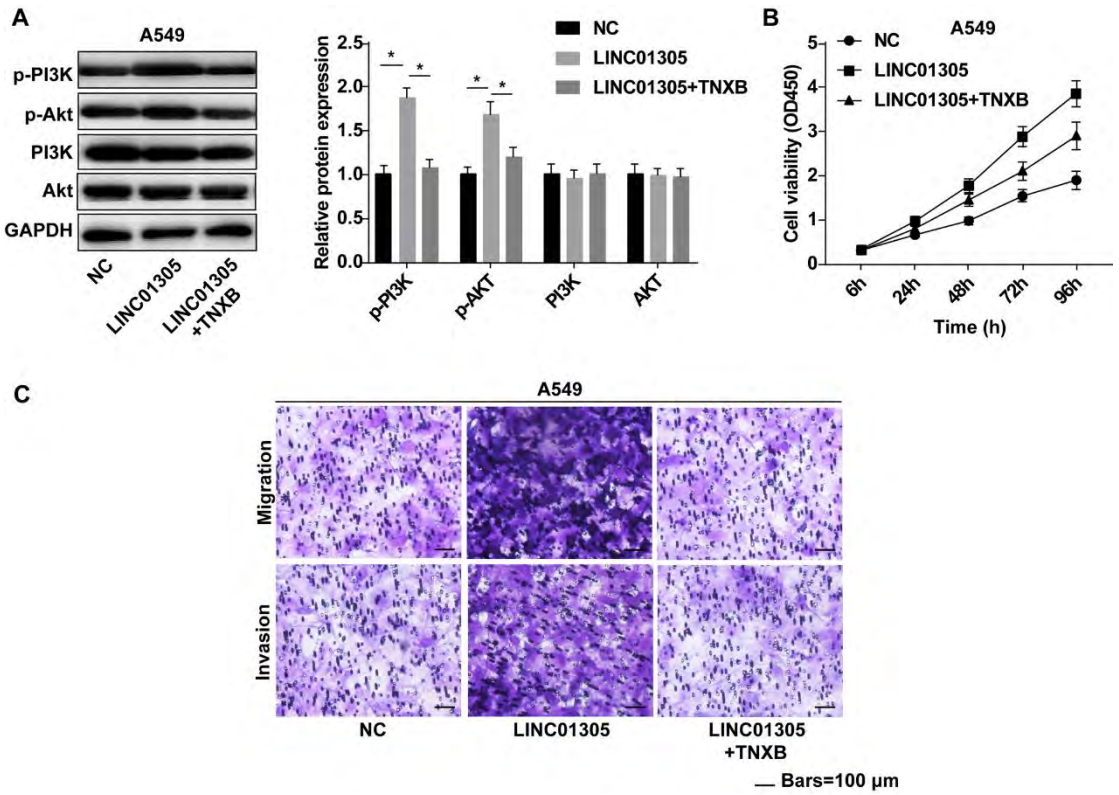


Fig. 4. *TNXB reverses the effect of LINC01305 on lung cancer cells via the PI3K/Akt pathway.* ***A****) In A549 cells, overexpression of TNXB and LINC01305 in A549 cells reversed the effect of overexpression of LINC01305 alone on p-PI3K and p-Akt.* ***B****) CCK-8 assay showed that overexpression of TNXB and LINC01305 can reverse the promoting effect of overexpression of LINC01305 on the viability of A549 cells.* ***C****) Transwell assay showed that overexpression of TNXB could reverse the promoting effect of overexpression of LINC01305 on the migration and invasiveness of A549 cells (magnifications: 400 X).*

found that the survival rate of patients with lung cancer is closely associated with the expression of E-cadherin, one of the EMT marker. In recent years, related research has found another EMT-related marker, Vimentin, is also associated with distant metastasis of lung cancer (17). Therefore, further research on the relationship between lung cancer and EMT may contribute to the prevention and treatment.

As a transcriptional by-product of RNA polymerase II, LncRNA plays a critical role in regulating gene expression. Some LncRNAs can influence the expression of downstream proteins by regulating the activity of intracellular signaling pathways (18). lncRNA ANRIL is shown to promote proliferation and inhibit apoptosis of NSCLC cells through silencing KLF2 and P21 expression and low expression of TUBA4B increases cell proliferation in NSCLC and predicts poor prognosis (19). The lung cancer-associated LncRNAs serving as the oncogenes are known to have metastasis-associated lung adenocarcinoma transcript 1 (MALAT1), HOX transcriptional antisense RNA (HOTAIR), and CCAT1, which can activate the expression of related transcripts through signaling pathways. It affects the expression of epithelial and mesenchymal cell markers and regulates the EMT process (20-22). Similar to the above conclusions, in this study, we found that LINC01305 was overexpressed in lung

cancer tissues and cells. Moreover, LINC01305 could prompt the migration of lung cancer cells.

PI3K/Akt pathway can regulate various functions such as cell survival, proliferation and differentiation (23), and is regulated by multiple factors. The molecules involved in regulation are mainly negative feedback molecules, including tumor suppressor proteins such as PTEN, CTMP, PHLPP and SHP2 (24, 25). Studies (26) have reported that activated PI3K produces a second messenger PIP3 to activate downstream Akt, which in turn activates or inhibits downstream target proteins by phosphorylation, so as to regulate cell survival, proliferation and differentiation, cytoskeletal composition, and EMT induction. Activation of the PI3K/Akt signaling pathway can enhance the invasiveness and metastasis of tumor cells. Steelman et al. (27) believe that the sustained activation and high activity of PI3K/Akt are closely relevant to EMT in the progression of lung cancer. TNXB was down-regulated in cervical cancer, and overexpression of TNXB could be a positive indicator for cervical cancer (7), Tenascin-X has been previously reported to affect the activation of the TGF-β signaling, 31with studies suggesting that TGF-β could potentially interact with the PI3K-Akt signaling (28, 29). In the present study, overexpression of TNXB depressed the enhanced activation of PI3K-Akt pathway induced by LINC01305. In addition, highly expressed TNXB reversed the increase in viability and enhanced cell migration and invasion caused by high expression of LINC01305.

In summary, this experiment revealed that silencing LINC01305 can inhibit TNXB-mediated PI3K/Akt signaling pathway, thereby inhibiting epithelial mesenchymal transition in lung cancer cells, which provides a theoretical basis for the pathogenesis of lung cancer and broadens the thinking for further research on the disease.

In conclusion, LINC01305 was found highly expressed in non-small cell carcinoma and could target and modulate TNXB expression. In addition, downregulation of LINC01305 may inhibit epithelial mesenchymal transition in lung cancer cells through the PI3K/Akt signaling pathway, which can provide a new idea for the targeted diagnosis and treatment of lung cancer. However, the function and molecular of the identified lncRNAs in tumorigenesis and their expression in human lung cancer tissues need further investigation.

ACKNOWLEDGEMENTS

This study was supported by CSCO-CSPC Cancer Research Fund (Y-sy2018-069); Project of Jiangsu Cancer Hospital (ZM201909); National Natural Science Foundation of China (81871873) and Scientific Research Foundation of Jiangsu Health and Health Committee (H2018087).

REFERENCES

1. Jemal A, Bray F, Center MM, Ferlay J, Ward E, Forman D. Global cancer statistics. CA Cancer J Clin 2011; 61:69-90.
2. Siegel RL, Miller KD, Jemal A. Cancer Statistics, 2017. CA Cancer J Clin 2017; 67:7-30.
3. Nieto MA. The ins and outs of the epithelial to mesenchymal transition in health and disease. Annu Rev Cell Dev Biol 2011; 27:347-76.
4. Bartis D, Mise N, Mahida RY, Eickelberg O, Thickett DR. Epithelial-mesenchymal transition in lung development and disease: does it exist and is it important? Thorax 2014; 69:760-765.
5. Ponting CP, Oliver PL, Reik W. Evolution and functions of long noncoding RNAs. Cell 2009; 136:629-41.
6. Huarte M, Guttman M, Feldser D, et al. A large intergenic noncoding RNA induced by p53 mediates global gene repression in the p53 response. Cell 2010; 142:409-19.
7. Yan SP, Chu DX, Qiu HF, et al. LncRNA LINC01305 silencing inhibits cell epithelial-mesenchymal transition in cervical cancer by inhibiting TNXB-mediated PI3K/Akt signalling pathway. J Cell Mol Med 2019; 23:2656-66.
8. Barsyte-Lovejoy D, Lau SK, Boutros PC, et al. The c-Myc oncogene directly induces the H19 noncoding RNA by allele-specific binding to potentiate tumorigenesis. Cancer Res 2006; 66:5330-37.
9. Mao JR, Taylor G, Dean WB, et al. Tenascin-X deficiency mimics Ehlers-Danlos syndrome in mice through alteration

of collagen deposition. Nat Genet 2002; 30:421-25.
10. Pisick E, Jagadeesh S, Salgia R. Receptor tyrosine kinases and inhibitors in lung cancer. ScientificWorldJournal 2004; 4:589-604.
11. Samuels Y, Wang Z, Bardelli A, et al. High frequency of mutations of the PIK3CA gene in human cancers. Science 2004; 304:554.
12. Yan W, Fu Y, Tian D, et al. PI3 kinase/Akt signaling mediates epithelial-mesenchymal transition in hypoxic hepatocellular carcinoma cells. Biochem Biophys Res Commun 2009; 382:631-36.
13. Yan SP, Chu DX, Qiu HF, et al. LncRNA LINC01305 silencing inhibits cell epithelial-mesenchymal transition in cervical cancer by inhibiting TNXB-mediated PI3K/Akt signalling pathway. J Cell Mol Med 2019; 23:2656-66.
14. Jemal A, Bray F, Center MM, Ferlay J, Ward E, Forman D. Global cancer statistics. CA Cancer J Clin 2011; 61:69-90.
15. Kajiyama H, Shibata K, Terauchi M, Yamashita M, Ino K, Nawa A, Kikkawa F. Chemoresistance to paclitaxel induces epithelial-mesenchymal transition and enhances metastatic potential for epithelial ovarian carcinoma cells. Int J Oncol 2007; 31:277-283.
16. Sulzer MA, Leers MP, van Noord JA, Bollen EC, Theunissen PH. Reduced E-cadherin expression is associated with increased lymph node metastasis and unfavorable prognosis in non-small cell lung cancer. Am J Respir Crit Care Med 1998; 157:1319-23.
17. Dauphin M, Barbe C, Lemaire S, et al. Vimentin expression predicts the occurrence of metastases in non small cell lung carcinomas. Lung Cancer 2013; 81:117-22.
18. Ulitsky I, Bartel DP. lincRNAs: genomics, evolution, and mechanisms. Cell 2013; 154:26-46.
19. Wei S, Liu J, Li X, Liu X. Repression of lncRNA-SVUGP2 mediated by EZH2 contributes to the development of non-small cell lung cancer via brisking Wnt/beta-catenin signal. Artif Cells Nanomed Biotechnol 2019; 47:3400-409.
20. Enriquez AD, Goldman ME. Management of hypertrophic cardiomyopathy. Ann Glob Health 2014; 80:35-45.
21. Wang Y, Shi J, Chai K, Ying X, Zhou BP. The Role of Snail in EMT and Tumorigenesis. Curr Cancer Drug Targets 2013; 13:963-72.
22. Ye Z, Zhou M, Tian B, Wu B, Li J. Expression of lncRNA-CCAT1, E-cadherin and N-cadherin in colorectal cancer and its clinical significance. Int J Clin Exp Med 2015; 8:3707-715.
23. Brozovic A, Osmak M. Activation of mitogen-activated protein kinases by cisplatin and their role in cisplatin-resistance. Cancer Lett 2007; 251:1-16.
24. Rosivatz E. Inhibiting PTEN. Biochem Soc Trans 2007; 35:257-59.
25. Downes CP, Perera N, Ross S, Leslie NR. Substrate specificity and acute regulation of the tumour suppressor phosphatase, PTEN. Biochem Soc Symp 2007:69-80.
26. Grille SJ, Bellacosa A, Upson J, et al. The protein kinase Akt induces epithelial mesenchymal transition and promotes enhanced motility and invasiveness of squamous cell carcinoma lines. Cancer Res 2003; 63:2172-78.
27. Steelman LS, Stadelman KM, Chappell WH, et al. Akt as a therapeutic target in cancer. Expert Opin Ther Targets 2008; 12:1139-65.
28. Sanchez-Antolin G, Almohalla-Alvarez C, Bueno P, et al. Evidence of Active Pro-Fibrotic Response in Blood of Patients with Cirrhosis. Plos One 2015; 10:e137128.
29. Hamidi A, Song J, Thakur N, et al. TGF-beta promotes PI3K-AKT signaling and prostate cancer cell migration through the TRAF6-mediated ubiquitylation of p85alpha. Sci Signal 2017; 10.

MiR-19a INHIBITOR IMPROVES DIABETIC RETINOPATHY IN RATS THROUGH PTEN/Akt/P-Akt SIGNALING PATHWAY

X.-L. ZHANG and Z. LIU

Department of Ophthalmology, First Affilated Hospital of Xi'an Jiaotong University, Xi'an, China

Received February 6, 2020 – Accepted April 3, 2020

The aim of this study is to explore the regulatory effect of micro ribonucleic acid (miR)-19a on diabetic retinopathy (DR) through mediating the phosphatase and tensin homolog deleted on chromosome ten (PTEN)/protein kinase B (Akt) signaling pathway. Thirty male Sprague-Dawley rats were first divided into Healthy group, DR group and miR-19a inhibitor group. The DR model was induced by intraperitoneal injection of streptozotocin (STZ) (60 mg/kg). The retinal tissues were dissected and RGCs were isolated. The expression level of miR-19a therein was determined using quantitative polymerase chain reaction (qPCR). The pathological changes were observed through hematoxylin-eosin staining (HE) staining. The apoptosis was detected by flow cytometry. PTEN was predicted as a target gene of miR-19a through TargetScan biological software. The protein expression of PTEN was detected via immunofluorescence assay. The changes in the phosphatidylinositol 3-hydroxy kinase (PI3K)/Akt pathway-associated proteins were detected using Western blotting. The expression of miR-19a declined substantially in DR rats injected with miR-19a inhibitor (P<0.05). RGCs were arranged regularly, showing apoptosis and milder necrosis in miR-19a inhibitor group. The proportion of apoptotic cells was substantially decreased in miR-19a inhibitor group (P<0.05). It was found that miR-19a inhibitor group exhibited an evidently lower protein expression of PTEN and a higher activation degree of the Akt pathway than DR group (P<0.05). MiR-19a binds to PTEN protein in a targeted manner to mediate the PI3K/Akt pathway, thereby affecting the progression of DR.

Diabetic retinopathy (DR), a complication of diabetes, can result in blindness of patients if not controlled (1-5). About 33% of diabetes patients experience retinopathy (6). DR is mainly characterized by the aberrant growth of retinal blood vessels and retinal edema as well as exudates and edema in the middle edema due to vessel leakage (2). The pathogenesis of DR involves genetic and epigenetic factors (7), increase in the production of free radicals (8), advanced glycation end products (9), the release of inflammatory factors (10) and pro-angiogenetic vascular epidermal growth factors (11, 12) in retinal tissues. Literature has shown that the higher the concentration of released interleukin (IL)-10, the likelier DR will occur (13), but its potential mechanism remains to be further explored. Inflammatory factors serve as the risk factors to accelerate the development and progression of DR (14-18). Micro nucleic acid (miR)-19a is up-regulated in the T-cells of asthma subjects and can bind to phosphatase and tensin homolog deleted on chromosome ten (PTEN) protein to facilitate

Key words: miR-19a; diabetic retinopathy; PTEN protein; Akt pathway

Corresponding Author:
Zhao Liu, MD
Department of Ophthalmology,
First Affiliated Hospital of Xi'an Jiaotong University,
No. 277 Yanta West Road, Xi'An, Shaanxi, 710061China
Tel.: +86 018729040161
e-mail: dr.liuzhao@foxmail.com

0393-974X (2020)
Copyright © by BIOLIFE, s.a.s.
This publication and/or article is for individual use only and may not be further reproduced without written permission from the copyright holder.
Unauthorized reproduction may result in financial and other penalties
DISCLOSURE: ALL AUTHORS REPORT NO CONFLICTS OF INTEREST RELEVANT TO THIS ARTICLE.

the production of cytokines and pro-inflammatory factors by T helper cells (1). PTEN has been extensively identified as the crucial gene involved in tumor cell initiation, proliferation and metastasis (4). In addition, miR-19a targets PTEN to regulate the proliferation and migration of airway smooth muscle cells in asthma patients (1). Therefore, it was hypothesised in this study that miR-19a can regulate the progression of DR through the targeted binding to PTEN protein.

MATERIALS AND METHODS

Animals

In the present study, a total of 30 Sprague-Dawley (SD) rats (Male, 6-8 weeks old, weighing 180-240 g, fom the Laboratory Animal Center of our hospital) were housed in a temperature controlled room (21±2°C) on a 12:12-h light/dark cycle (lights on at 06:00). All rats had free access to water and food. The SD rats and retinal ganglion cells (RGCs) isolated from the retinal tissues of rats in each group were used in this study. The rats were first divided into Healthy group, DR group and miR-19a inhibitor group, and the retinal tissues of the rats were dissected in the three groups to isolate RGCs. This study was approved by the Animal Ethics Committee of Xi'an Jiaotong University Animal Center.

Isolation of RGCs in DR rats

After adapting to the environment, the SD rats were injected with 60 mg/kg STZ or miR-19a inhibitor at the same time, and after feeding for 1 week, the RGCs were extracted from 4 rats in each group according to the following steps: The newborn rats were immersed in 75% alcohol, and the retinas were dissected aseptically. Then, the retinal tissues were cut and digested in Hank's balanced salt solution containing 15 U/mL papain solution and 70 U/mL collagenase for 30 min. Subsequently, a Pasteur pipette was used to slightly pipette and dissociate cells in the Dulbecco's modified Eagle's medium (DMEM)/F12 medium (Gibco, Rockville, MD, USA) containing 2 mg/mL ovomucoid solution, 1 mg/mL bovine serum albumin (BSA) and 0.004% deoxyribonuclease, and the resulting cell suspension was elutriated using anti-macrophage reagent to remove macrophages. Then, anti-Thy1.1 antibody was utilized to elutriate the resulting cells so as to selectively bind to RGCs. Finally, the harvested RGCs were cultured with serum-free DMEM supplemented with 10 ng/mL eyelash neurotrophic factor, 50 ng/mL brain-derived neurotrophic factor and 5 ng/mL Forskolin in a 25 mm^2 culture flask with poly-D-lysine and mouse laminin at 37°C, and normally subcultured, during which the medium was regularly replaced.

Immunofluorescence assay

To observe the expression and position of PTEN protein, the isolated RGCs were seeded into a 6-well plate at a density of 2.0×10^4 cells/mL, fixed in methanol and sealed using 5% BSA. The resulting cells were first stained with rabbit anti-PTEN antibody and then with Cy3-coupled goat anti-mouse IgG, and they were washed thoroughly using phosphate buffered saline (PBS) for at least 3 times, added with rabbit anti-PTEN antibody and incubated with fluorescein-labeled rabbit secondary antibody. Finally, 4',6-diamidino-2-phenylindole (DAPI) staining solution was added dropwise to stain cells, and 5 min later, images were captured.

Western blotting

The cryopreserved retinal tissues were taken out, thawed, cut into small pieces for the convenience of lysis, added with cell lysis buffer, shaken using a vortexer and ultrasonically smashed. The lysate was centrifuged and quantified using Bradford reagent according to the manufacturer's specifications. The protein samples (10 μg) of the same molecular mass were separated in the prepared 10% sodium dodecyl sulphate-polyacrylamide gel electrophoresis (SDS-PAGE) gel at 4°C overnight, and the protein bands were blotted onto a membrane and sealed using BSA for 1 h. Then the phosphorylated protein kinase B (p-Akt), Akt, p-phosphatidylinositol 3-hydroxy kinase (p-PI3K), PI3K and glyceraldehyde-3-phosphate dehydrogenase (GAPDH) antibodies were used for Western blotting analysis. After the membrane was washed for 3 times (5 min/time), the secondary antibodies were added. Finally, electrochemiluminescence (ECL) was used for color development of protein bands.

Hematoxylin-eosin (HE) staining

Following successful modeling, the rats were sacrificed through anesthesia, and their retinal tissues were anatomized, fixed in the fixation fluid for 48 h, embedded

in paraffin, sliced and stained with hematoxylin twice (the next step was started when each staining was terminated), dehydrated and transparentized. Finally, the sections were sealed.

Detection of cell apoptosis via flow cytometry

The retinal tissues were first prepared into tissue suspension, and then RGCs were isolated and extracted. Subsequently, the cells were made into suspension, centrifuged at 1,000 rpm for 5 min, and with the supernatant discarded, the resulting cells were washed using phosphate buffered saline (PBS) once, and stained with propidium iodide and anti-Annexin-V antibody at 4°C for 1 h. Finally, the cells were washed with PBS once and analyzed using a flow cytometer (Partec AG, Arlesheim, Switzerland).

Real-time fluorescence quantitative polymerase chain reaction (PCR)

Total RNAs were separated from the retinal tissues of rats. The quality of the RNAs was verified through calculating the ratio of optical density $(OD)_{260}/OD_{280}$, and the expression of miR-19a was evaluated using the stem-loop real-time PCR-based Bulge-Loop™ miRNA qRT-PCR kit as specified by the manufacturer. The real-time PCR was conducted using SYBR Green and the following primers on the ABI 7900 instrument. miR-19a stem-loop primer: TCGTATCCAGTGCAGGGCCTG AGGTATTCGCACTGGATACGA-CTCAGTT, miR-19a-F: CCTCTGTTAGTTTTGCATAGTTGC, and U6-F: GCGCGTCGTGAAGCGTTC, U6-R: GTGCAGGGTC-CGAGGT. U6 small nucleolar RNAs were used to normalize the measurement of miRNAs. Finally, the relative expression level of miR-19a was normalized into that of U6, and calculated using ΔΔCt.

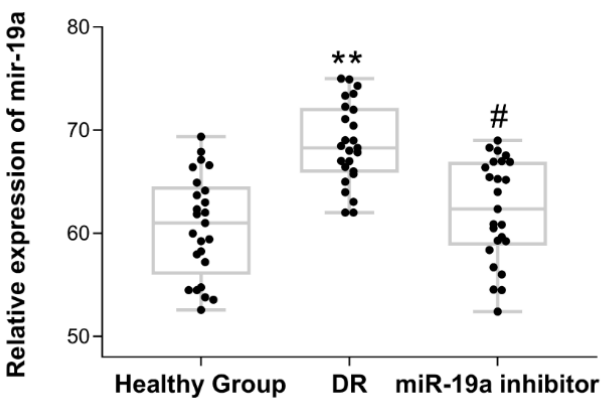


Fig. 1. *Expression level of miR-19a in the peripheral blood of DR rats (**P<0.01* vs *Healthy group, #P<0.05* vs *DR group).*

Statistical analysis

Statistical Product and Service Solutions (SPSS) 17.0 software (SPSS Inc., Chicago, IL, USA) was used to process the research data in experiments and the *p*-value was analyzed. Comparison between groups was carried ut using One-way ANOVA test followed by Post Hoc Test (Least Significant Difference). P<0.05 represented that the experimental results were statistically significantly different.

RESULTS

MiR-19a was highly expressed in the peripheral blood of DR rats

The changes in the expression of miR-19a in the peripheral blood were detected using the real-time fluorescence PCR in 30 rats, and the results showed that the expression of miR-19a was remarkably raised in DR group (P<0.01), while its expression substantially declined in miR-19a inhibitor group (P<0.05), suggesting the high expression of miR-19a in the peripheral blood of DR rats (Fig. 1).

Pathological changes in RGCs

The Healthy group exhibited regularly arranged RGCs with fewer apoptotic cells and normal tissue morphology. The RGCs in DR group had a swollen soma and were irregularly sized and arranged, with more apoptotic cells. Compared with those in DR group, the RGCs in miR-19a inhibitor group were arranged regularly, and the soma size was more uniform, with a notably decreased proportion of apoptotic cells. The microscopic observation manifested obvious pathological changes and severe tissue damage in DR rats (Fig. 2).

Inhibiting miR-19a could improve the apoptosis of RGCs

The proportion of apoptotic cells in the retinal tissue homogenate was determined via flow cytometry, and according to the experimental results,

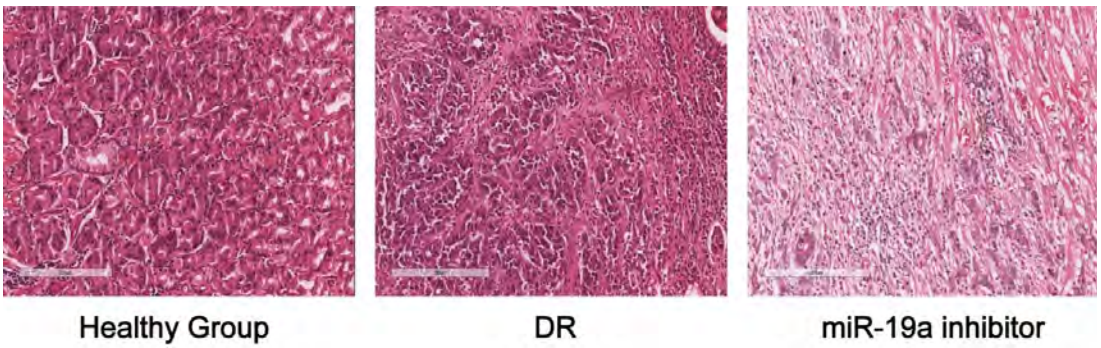


Fig. 2. *Pathological changes in rat retinas. (magnification: 200×)*

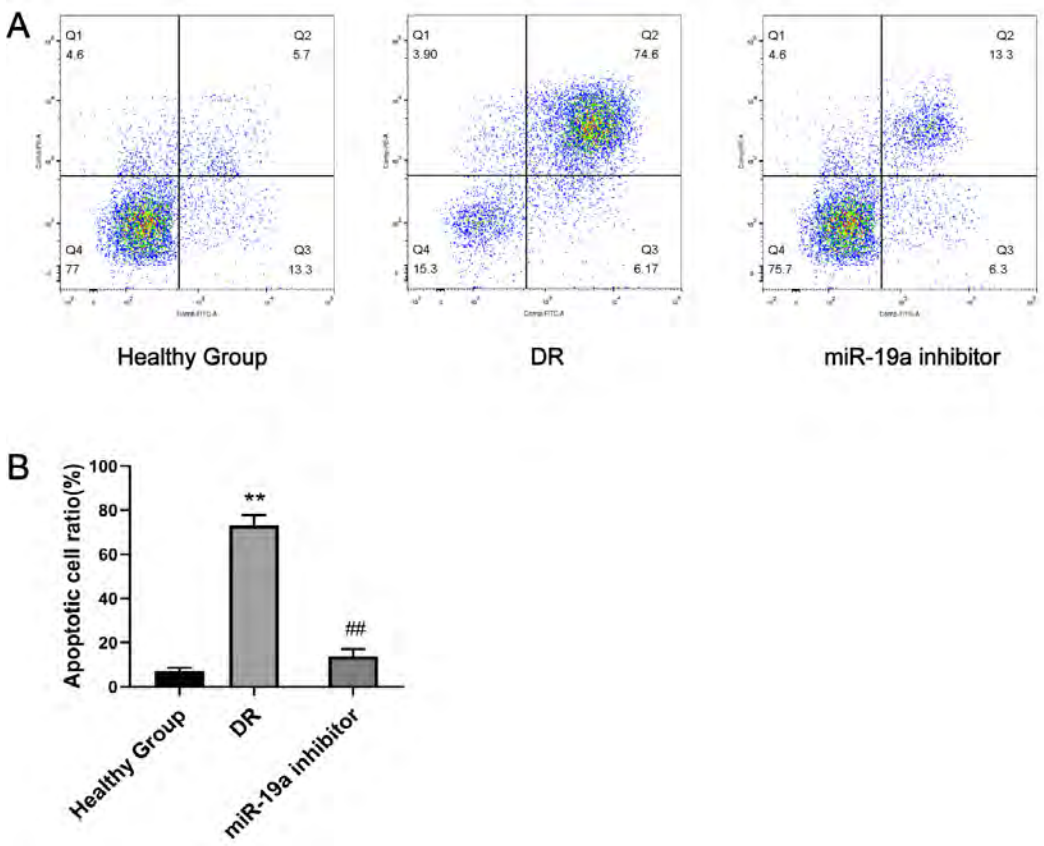


Fig. 3. *Changes in the apoptosis of RGCs.* ***A)*** *Cell apoptosis in Healthy group, DR group and miR-19a inhibitor group according to the flow cytometry results.* ***B)*** *Changes in the proportion of cell apoptosis. (*$^{**}P<0.01$ vs *Healthy group,* $^{\#\#}P<0.01$ vs *DR group).*

there was an obvious difference in the proportion of apoptotic cells between the Healthy group and DR group (less than 10% *vs* more 70%, P<0.01), and the proportion of apoptotic cells in the miR-19a inhibitor group (about 13%) was significantly different from that in the DR group (P<0.01). The above results suggest that inhibiting the miR-19a expression will reduce the proportion of apoptotic RGCs (Fig. 3).

Inhibition on miR-19a expression could down-regulate the protein expression of PTEN in a targeted manner

The PTEN protein was predicted by the biological prediction software TargetScan as a downstream protein of miR-19a, and the immunofluorescence assay results revealed that PTEN protein was mainly expressed in the cytoplasm. Based on the observation results of fluorescence intensity, DR group showed brighter red fluorescence of PTEN, and more expressed proteins, and the differences were statistically significant (P<0.05). Compared with that in DR group, the protein expression of PTEN was decreased in the miR-19a inhibitor group, with a statistically significant difference (P<0.05). The above results demonstrate that miR-19a can positively regulate PTEN protein expression in a targeted manner (Fig. 4).

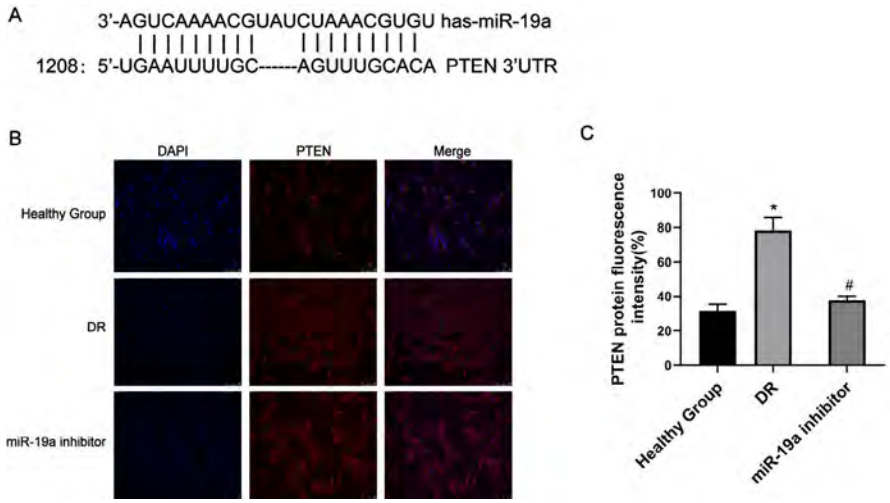


Fig. 4. *Changes in PTEN protein expression in RGCs.* ***A****) PTEN protein predicted by the TargetScan software as the downstream target protein of miR-19a.* ***B****) PTEN expression in RGCs detected using immunofluorescence assay: PTEN protein is mainly present in the cytoplasm, and the red fluorescence is brighter in DR group. (magnification: 400×)* ***C****) Statistical results of PTEN protein expression (*P<0.05* vs *Healthy group, #P<0.05* vs *DR group).*

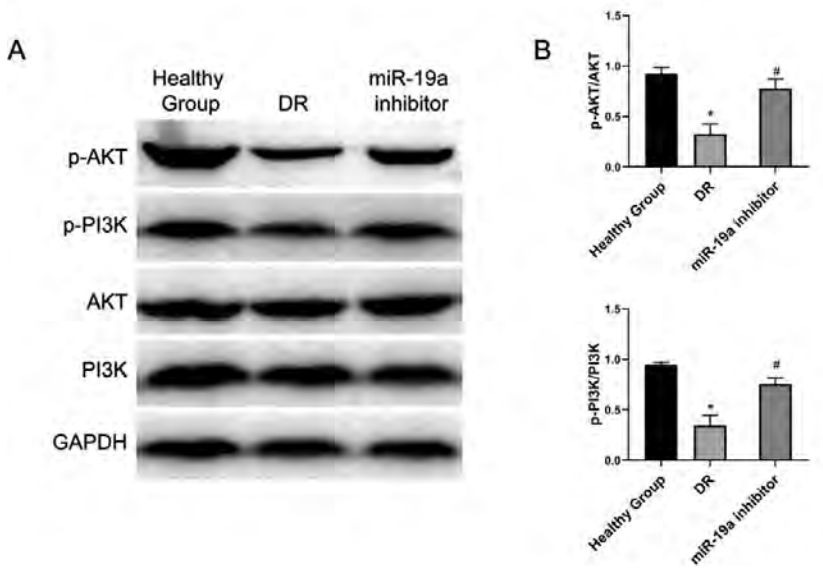


Fig. 5. *Changes in the expressions of active proteins in the PI3K/Akt pathway.* ***A****) Western blots analysis reveals the expression of active proteins in the PI3K/Akt pathway.* ***B****) Semi quantitative analysis of active proteins in the PI3K/Akt pathway. (*P<0.05* vs *Healthy group, #P<0.05* vs *DR group).*

Repressing miR-19a expression activated the Akt pathway

Western blotting revealed that the PI3K/Akt pathway was inactivated and the expression of the phosphorylated proteins declined considerably inthe DR group ($P<0.05$), while the expression levels of phosphorylated proteins in the PI3K/Akt pathway were raised in the miR-19a inhibitor group, suggesting that inhibiting miR-19a can activate PI3K and Akt (Fig. 5).

DISCUSSION

Diabetes is an increasingly common chronic disease that is characterized by absolute or relative lack of insulin, high blood glucose, dyslipidemia and neurovascular injury. Such a disease can affect each organ system in the body of patients, damage their quality of life and pose economic burdens to the local and global communities. DR, the common complication of types 1 and 2 diabetes, causes high individual and social economic cost. Diabetes occurs at an increasingly young age, with a gradually increasing mortality rate (19, 20), and it is far likelier to induce blindness than other diseases (20). DR is caused by many factors of which genetic and epigenetic factors have gradually become the important inducing factors. These factors are also the current treatment targets, while some factors, such as pigment epithelium-derived factor (21) and miRNAs (22), may be taken as the potential therapeutic agents in the future. The knowledge of conventional and novel biomarkers can probably improve the prognosis of DR and promote the development and individuation of primary and secondary prevention strategies, including new and even more efficacious treatment methods. Therefore, the treatment methods of diabetes are searched for to improve the quality of life of people. The high expression of miR-19a in DR patients has be focused on, so the present study mainly aims to explore the role of miR-19a in DR and its mechanism of action.

In this study, the changes in the expression of miR-19a in the peripheral blood of rats were first detected, and it was found that its expression rose remarkably in the DR group, and after intravitreal injection of miR-19a inhibitor, the expression of miR-19a in the peripheral blood was substantially lower. The retinal tissues were then dissected, and their pathological changes were observed via HE staining. According to the results,the healthy group exhibited regularly arranged RGCs with fewer apoptotic cells and normal tissue morphology, the DR group had irregularly sized and arranged RGCs, with a swollen soma, of which there were more apoptotic cells, and compared with those in the DR group, the RGCs in the miR-19a inhibitor group were arranged regularly, with a notably decreased proportion of apoptotic cells and more uniform soma size. Moreover, it was microscopically observed that the DR rats had obvious pathological changes and severe tissue damage. When miR-19a expression was inhibited, the inflammatory responses in the retinal tissues were alleviated. According to the flow cytometry results, the proportion of apoptotic cells was raised notably in the DR group compared with Healthy group (more than 70% *vs* less than 10%), showing an obvious difference, while the DR group had fewer apoptotic cells (about 13%) after the inhibition on the expression of miR-19a. To further explore the mechanism of miR-19a in DR, the target proteins of miR-19a were predicted using the TargetScan biological software in this study, and it was found that the PTEN protein was one of the downstream target proteins of miR-19a. RGCs were isolated from the three groups of retinal tissues, and the position and expression changes of PTEN protein were detected *via* immunofluorescence assay. Based on the experimental results, PTEN protein was mainly expressed in the cytoplasm, and its fluorescence intensity in the DR group was higher than that in the miR-19a inhibitor group, illustrating that miR-19a can up-regulate PTEN protein expression, and that the PTEN/Akt pathway plays a pivotal role in DR. Finally, the protein expressions of p-Akt/Akt and p-PI3K/PI3K were detected using Western blotting to investigate the influences of miR-19a on the changes in the PTEN/Akt pathway, and it was found that their expressions declined considerably in the DR group.

In summary, the results of the present study demonstratel that miR-19a can mediate PTEN protein to inhibit the activation of the Akt pathway.

REFERENCES

1. Jotheeswaran AT, Lovakanth N, Nadiga S, Anchala R, Murthy GV, Gilbert CE. Estimating the proportion of persons with diabetes developing diabetic retinopathy in India: A systematic review and meta-analysis. Indian J Endocrinol Metab 2016; 20:S51-S58.
2. Nigro E, Scudiero O, Monaco ML, et al. New insight into adiponectin role in obesity and obesity-related diseases. Biomed Res Int 2014; 2014:658913.
3. Ostenson CG. The pathophysiology of type 2 diabetes mellitus: an overview. Acta Physiol Scand 2001; 171:241-47.
4. Knip M, Siljander H. The role of the intestinal microbiota in type 1 diabetes mellitus. Nat Rev Endocrinol 2016; 12:154-67.
5. Harcourt BE, Penfold SA, Forbes JM. Coming full circle in diabetes mellitus: from complications to initiation. Nat Rev Endocrinol 2013; 9:113-23.
6. Wong TY, Cheung CM, Larsen M, Sharma S, Simo R. Diabetic retinopathy. Nat Rev Dis Primers 2016; 2:16012.
7. Kowluru RA, Mishra M. Contribution of epigenetics in diabetic retinopathy. Sci China Life Sci 2015; 58:556-63.
8. Kowluru RA, Kowluru A, Mishra M, Kumar B. Oxidative stress and epigenetic modifications in the pathogenesis of diabetic retinopathy. Prog Retin Eye Res 2015; 48:40-61.
9. Eshaq RS, Wright WS, Harris NR. Oxygen delivery, consumption, and conversion to reactive oxygen species in experimental models of diabetic retinopathy. Redox Biol 2014; 2:661-666.
10. Yu Y, Chen H, Su SB. Neuroinflammatory responses in diabetic retinopathy. J Neuroinflammation 2015; 12:141.
11. Ajlan RS, Silva PS, Sun JK. Vascular Endothelial Growth Factor and Diabetic Retinal Disease. Semin Ophthalmol 2016; 31:40-48.
12. Hausenloy DJ, Yellon DM. Myocardial ischemia-reperfusion injury: a neglected therapeutic target. J Clin Invest 2013; 123:92-100.
13. Dong H, Li Q, Wang M, Wan G. Association Between IL-10 Gene Polymorphism and Diabetic Retinopathy. Med Sci Monit 2015; 21:3203-8.
14. Velloso LA, Eizirik DL, Cnop M. Type 2 diabetes mellitus--an autoimmune disease? Nat Rev Endocrinol 2013; 9:750-55.
15. Chouchani ET, Pell VR, James AM, et al. A Unifying Mechanism for Mitochondrial Superoxide Production during Ischemia-Reperfusion Injury. Cell Metab 2016; 23:254-263.
16. Serr I, Furst RW, Achenbach P, et al. Type 1 diabetes vaccine candidates promote human Foxp3(+)Treg induction in humanized mice. Nat Commun 2016; 7:10991.
17. de Waal MR, Haanen J, Spits H, et al. Interleukin 10 (IL-10) and viral IL-10 strongly reduce antigen-specific human T cell proliferation by diminishing the antigen-presenting capacity of monocytes via downregulation of class II major histocompatibility complex expression. J Exp Med 1991; 174:915-24.
18. Olkkola KT, Kontinen VK, Saari TI, Kalso EA. Does the pharmacology of oxycodone justify its increasing use as an analgesic? Trends Pharmacol Sci 2013; 34:206-14.
19. Simpson LJ, Patel S, Bhakta NR, et al. A microRNA upregulated in asthma airway T cells promotes TH2 cytokine production. Nat Immunol 2014; 15:1162-70.
20. Di Cristofano A, Pandolfi PP. The multiple roles of PTEN in tumor suppression. Cell 2000; 100:387-390.
21. Elahy M, Baindur-Hudson S, Cruzat VF, Newsholme P, Dass CR. Mechanisms of PEDF-mediated protection against reactive oxygen species damage in diabetic retinopathy and neuropathy. J Endocrinol 2014; 222:R129-R139.
22. Qing S, Yuan S, Yun C, et al. Serum miRNA biomarkers serve as a fingerprint for proliferative diabetic retinopathy. Cell Physiol Biochem 2014; 34:1733-40.

LONG NONCODING RNA SNHG8 PROMOTES THE PROLIFERATION OF OSTEOSARCOMA CELLS BY DOWNREGULATING miR-542-3p

G-B. ZHONG[1], C-Q. JIANG[2], X-S. YU[2], Z-D. LIU[2], W-L. WANG[3] and R-D. XU[3]

[1]Baoshan Branch, Ren Ji Hospital, School of Medicine, Shanghai Jiao Tong University. Shanghai, China; [2]Department of Orthopaedics, Ren Ji Hospital, School of Medicine, Shanghai Jiao Tong University, Shanghai, China; [3]Department of Orthopaedics, South Campus, Ren Ji Hospital, School of Medicine, Shanghai Jiao Tong University, Shanghai, China

Received February 15, 2020 – Accepted April 6, 2020

Small nucleolar RNA host genes (SNHGs) as a subset of long noncoding RNAs (lncRNAs) have critical roles in the pathogenesis of multiple malignancies, however, the role and molecular mechanisms of lncRNA SNHG8 in osteosarcoma (OS) remain unclear. In the present study, the correlation of SNHG8 or miR-542-3p with clinicopathological elements and prognosis in OS patents was estimated by TCGA cohort. Cell viability and invasion were assessed by MTT and Transwell assays. The interplay between SNHG8 and miR-542-3p was affirmed by a luciferase report assay. The effects of SNHG8 on miR-542-3p expression were examined in MG-63 and SW-1353 cells by qRT-PCR analysis. The results showed that incremental expression of SNHG8 or reduced expression of miR-542-3p was related to poor survival and tumor recurrence in OS patients. Overexpressing SNHG8 accelerated the growth and invasion of MG-63 cells, but silencing SNHG8 harbored an opposite effect in SW-1353 cells. Additionally, SNHG8 could negatively regulate miR-542-3p expression and bind with miR-542-3p, which attenuated SNHG8 induced cell proliferation. Taken together, these findings indicate that lncRNA SNHG8 promotes the proliferation of OS cells by downregulating miR-542-3p.

Osteosarcoma (OS) remains one of the most common kinds of pernicious bone sarcomas in young persons (1). Despite the tremendous progress made for OS treatment, tis disease has worse outcomes owing to tumor invasion and metastasis (2). Substantial data have indicated that the dysregulation of noncoding RNAs (ncRNAs) have vital roles in the pathogenesis and progression of OS (3-5), therefore, the identification of candidate ncRNAs may offer early diagnosis of OS patients.

Small nucleolar RNA host genes (SNHGs), as a subgroup of long non-coding RNAs (lncRNAs), possess a relationship with the prognosis and progression of OS (6-8). Increasing studies show that the expression of SNHG8 is upregulated in cervical cancer (9), pancreatic adenocarcinoma (10), gastric cancer (11, 12), esophageal squamous cell carcinoma (ESCC) (13), colorectal cancer (CRC) (14), endometrial carcinoma (EC) (15), and non-small-cell lung cancer (NSCLC) (16). The enhancive expression of SNHG8 is also correlated with tumor differentiation, tumor size, distant metastasis, TNM stage and poor survival in multiple cancers (10, 11, 13, 16). Moreover, incremental SNHG8 expression

Key words: lncRNA; SNHG8; miR-542-3p; prognosis; osteosarcoma

Corresponding Author:
Dr. Ruida Xu,
Department of Orthopaedics,
South Campus, Ren Ji Hospital, School of Medicine,
Shanghai Jiao Tong University,
Shanghai, China
e-mail: renjispine02@163.com

0393-974X (2020)
Copyright © by BIOLIFE, s.a.s.
This publication and/or article is for individual use only and may not be further reproduced without written permission from the copyright holder.
Unauthorized reproduction may result in financial and other penalties
DISCLOSURE: ALL AUTHORS REPORT NO CONFLICTS OF INTEREST RELEVANT TO THIS ARTICLE.

facilitates the proliferation, cycle progression, cell invasion, chemo-resistance and arrests cell apoptosis in cancers (9, 10, 12, 14-16). These studies suggest that SNHG8 may be a prognostic and tumor-promoting factor in cancer.

In addition, SNHG8 can act as sponges of microRNAs (miRNAs, favoring the progression of malignant tumors. Accumulating data indicate that SNHG8 functions as an oncogenic factor by sponging miR-411 in ESCC (13), miR-663 in CRC (14), miR-152 in EC (15), and miR-542-3p in NSCLC (16). These studies indicate that SNHG8 can mediate miRNA regulatory networks to participate in cancer progression.

However, the association of SNHG8 with OS has not yet been reported. In the present study, it was found that high SNHG8 expression or low miR-542-3p expression was linked to a poor survival and tumor recurrence in OS patients. SNHG8 promoted the growth and invasion of OS cells by downregulating miR-542-3p and providing a potential candidate biomarker for OS.

MATERIALS AND METHODS

Clinical samples

The clinical information containing the patients' survival/recurrence time or status from 126 cases of OS samples as well as SNHG8 and miR-542-3p expression levels were collected from the Cancer Genome Atlas (TCGA) database (https://genome-cancer.ucsc.edu). Eight paired OS tissues were provided by our laboratory. All subjects gave informed and signed consent to participate in the study, and the protocols used were approved by the Ethics Committee of South Campus of Ren Ji Hospital.

Normal tissues and OS cell lines (MG-63, Saos-2, SW-1353) were stored in our laboratory. SNHG8 plasmids/pcDNA3.1, SNHG8 siRNA (si-SNHG8)/si-NC, miR-542-3p mimic/inhibitor or miR-NC/negative control (NC) were from GenePharma (Shanghai, China).

Methods

Wild type (WT) or mutant (Mut) SNHG8 3' UTR vectors were established by annealing double-strand DNA and inserted into the pmirGLO vector at the BamHI and EcoRI sites. Their luciferase activity was detected when co-transfected into MG-63 or SW-1353 cell line for 48 h.

OS cells (MG-63 and SW-1353) were cultured in DMEM medium supplemented with 10% heat-inactivated FBS, 100U/ml of penicillin, and 100 μg/ml of streptomycin. Cells in this medium were placed in a humidified atmosphere containing 5% CO2 at 37°C. MG-63 was an osteosarcoma cell line obtained from a 14-year-old boy with interferon expression. SW-1353 was na osteosarcoma cell line from a 72-year-old white woman with primary grade II osteosarcoma.

To assess the expression of SNHG8 and miR-542-3p in OS cell lines, qRT-PCR was conducted. Total RNA was extracted using TRIzol (Invitrogen, Karlsruhe, Germany) or a High Pure miRNA isolation kit (Roche) according to the manufacturer's protocol. Reverse transcription was performed by using PrimeScript RT Reagent Kit and cDNA amplification by using SYBR Premix Ex Taq (TaKaRa, Dalian, China). β-actin or U6 gene was used as an endogenous control. MTT and Transwell assays were conducted as previously described (5). OS cells were seeded into 24-well plates. After 24-h incubation, luciferase report vector carrying WT or Mut SNHG8 3'UTR was co-transfected with miR-542-3p mimic or inhibitor into MG-63 or SW-1353 cells. 48 h after transfection, luciferase activities were examined with a Dual-luciferase Reporter System (Promega).

Statistical analysis

Statistical analyses were carried out by SPSS 20.0 (IBM, SPSS, Chicago, IL, USA) and GraphPad Prism. Student's *t*-test or *Chi*-squared test was used to assess the statistical significance for comparisons of two groups. Pearson correlation analysis was used to analyze the correlations. Overall survival curves were analyzed with the Kaplan-Meier method and log-rank test. Univariate and multivariate analysis was conducted by a Cox proportional hazard regression model. $P < 0.05$ was considered statistically significant.

RESULTS

Upregulation of SNHG8 was an independent prognostic factor of poor survival in OS patients

We examined the expression of SNHG8 in 8 paired OS tissues by qRT-PCR analysis and found that SNHG8 expression was markedly elevated in OS

tissues (Fig. 1A). This result was validated in TCGA cohort in paired (n = 15) and unpaired OS tissues (n = 126, Fig. 1B). According to SNHG8 expression levels, the patients' survival time and survival status, a cutoff value (10.52) of SNHG8 was acquired in OS by a cutoff Finder (http://molpath.charite.de/cutoff/load.jsp), and divided the patients into high SNHG8 expression and low SNHG8 expression groups (Fig. 1C). SNHG8 had an association with age in OS patients. Kaplan-Meier analysis revealed that the patients with high SNHG8 expression harbored a poorer survival as compared with those with low SNHG8 expression (Fig. 1D). Univariate and Multivariate Cox regression analysis uncovered SNHG8 as an independent prognostic factor of poor survival in OS (Table I).

Table I. *Cox regression analysis of SNHG8 expression as a survival predictor*

Variables	Univariate Cox regression analysis		Multivariate Cox regression analysis	
	RR (95% CI)	*P* value	RR (95% CI)	*P* value
Age (years)				
≥60 *vs* <60	1.460 (0.644 to 3.313)	0.365	NA	NA
Gender				
Male *vs* Female	0.775 (0.333 to 1.802)	0.553	NA	NA
Tumor size(cm)				
>5 *vs* ≤5	4.176 (0.563 to 30.991)	0.162	NA	NA
Distant metastases				
Yes *vs* No	1.746 (0.750 to 4.066)	0.196	1.676 (0.717 to 3.916)	0.233
SNHG8 expression				
High *vs* Low	3.309 (1.240 to 8.833)	0.017	3.202 (1.197 to 8.563)	0.020

NA: not analyzed

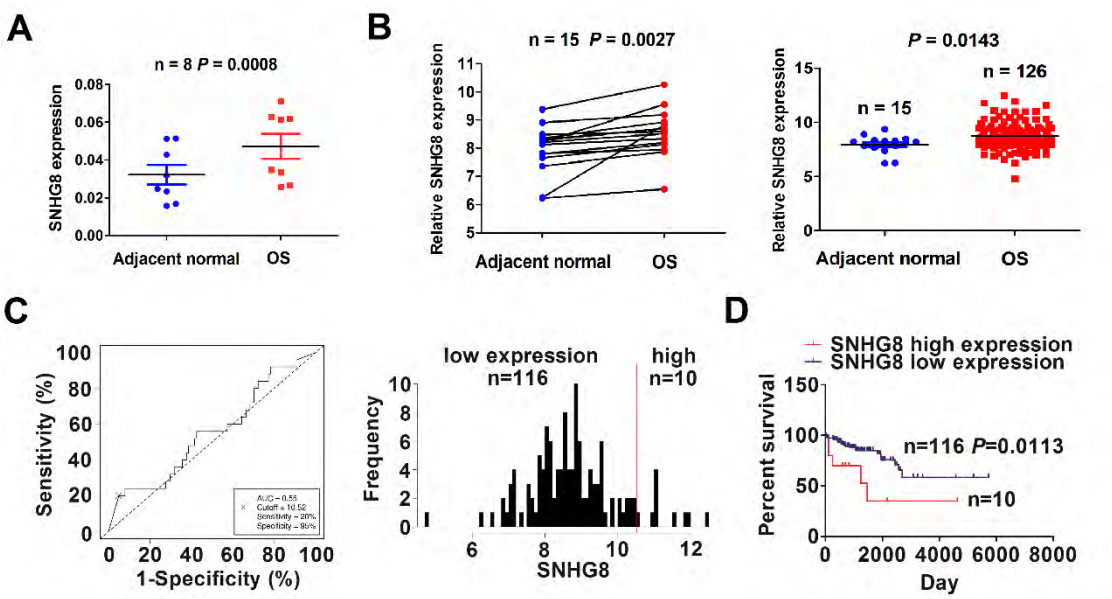


Fig. 1. *Increased expression of lncRNA SNHG8 was associated with poor survival in OS patients.* ***A****) qRT-PCR analysis of the expression of SNHG8 in 8 paired OS tissues.* ***B****) TCGA cohort validated the increased expression of SNHG8 in 15 paired and 126 unpaired OS tissues.* ***C****) The cutoff value of SNHG8 was acquired by a ROC curve. and divided the patients into SNHG8 high expression group and low expression groups.* ***D****) Kaplan-Meier analysis of the association of high or low SNHG8 expression with overall survival in OS patients.*

Table II. *Cox regression analysis of miR-542-3p expression as a survival predictor*

Variables	Univariate Cox regression analysis		Multivariate Cox regression analysis	
	RR (95% CI)	*P* value	RR (95% CI)	*P* value
Age (years)				
≥60 *vs* <60	1.369 (0.597 to 3.136)	0.458	NA	NA
Gender				
Male *vs* Female	0.799 (0.340 to 1.875)	0.606	NA	NA
Tumor size(cm)				
>5 vs ≤5	3.787 (0.509 to 28.167)	0.193	NA	NA
Distant metastases				
Yes *vs* No	1.797 (0.765 to 4.220)	0.179	2.017 (0.857 to 4.745)	0.108
miR-542-3p expression				
Low *vs* High	3.115 (1.064 to 9.120)	0.038	3.343 (1.136 to 9.840)	0.028

NA: not analyzed

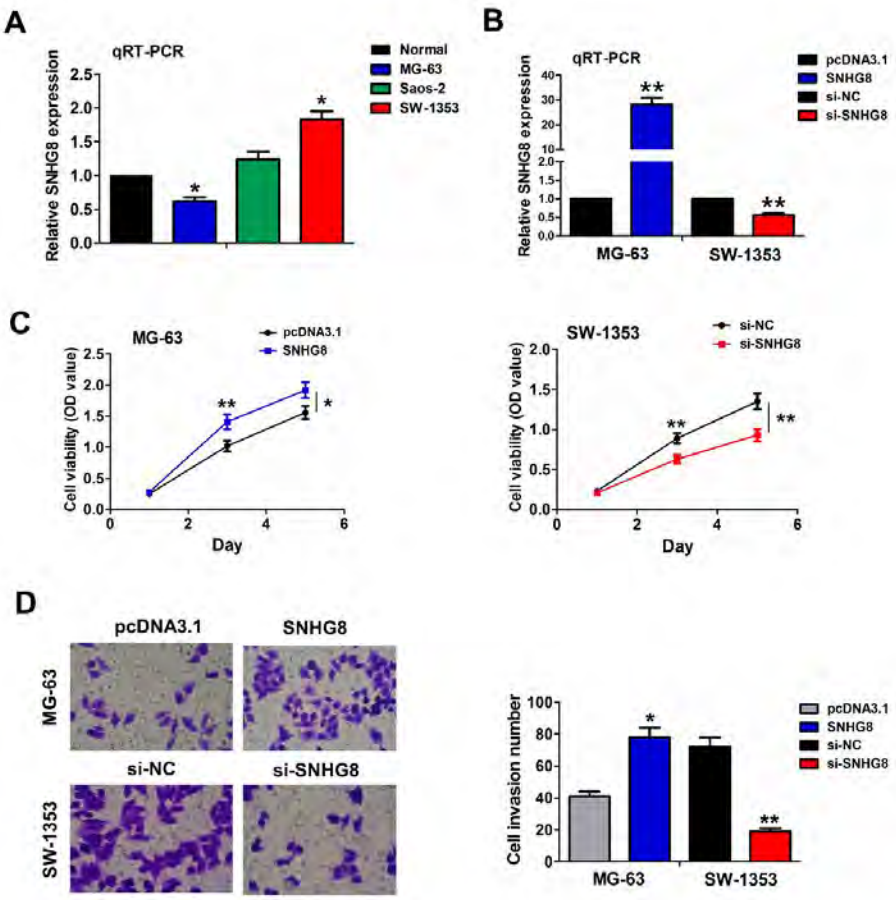


Fig. 2. *SNHG8 promoted the proliferation and invasion of OS cells.* ***A)*** *qRT-PCR analysis of the expression levels of SNHG8 in various OS cell lines.* ***B)*** *qRT-PCR analysis of the overexpression efficiencies of SNHG8 plasmids in MG-63 cell line or knockdown efficiency of si-SNHG8 in SW-1353 cell line.* ***C, D)*** *MTT and Transwell analysis of the effects of SNHG8 overexpression or knockdown on cell proliferation and invasion in MG-63 and SW-1353 cells. *P<0.05; **P<0.01.*

SNHG8 enhanced the proliferation and invasion of OS cells

The expression of SNHG8 in different OS cell lines was examined by qRT-PCR analysis, which indicated that SNHG8 harbored a higher expression in SW1353 cell line but a lower expression in MG-63 cell line (Fig. 2A). The overexpression efficiencies of SNHG8 plasmids in MG-63 cell line or the knockdown efficiency of si-SNHG8 in SW1353 cell line was verified by qRT-PCR analysis (Fig.2B). The ectopic expression of SNHG8 favored cell viability and cell invasion in MG-63 cell line as compared with the control group, but knockdown of SNHG8 reversed these effects (Fig. 2 C, D).

SNHG8 negatively regulated miR-542-3p expression in OS cells

The correlation analysis indicated that SNHG8 had a negative correlation with miR-542-3p expression in 123 OS tissue samples (Fig. 3A). The binding sites between miR-542-3p and the WT or Mut SNHG8 3'UTR are shown in Fig. 3B. WT or Mut SNHG8 3'UTR and miR-542-3p mimic or inhibitor was co-transfected into MG-63 or SW-1353 cells and it was

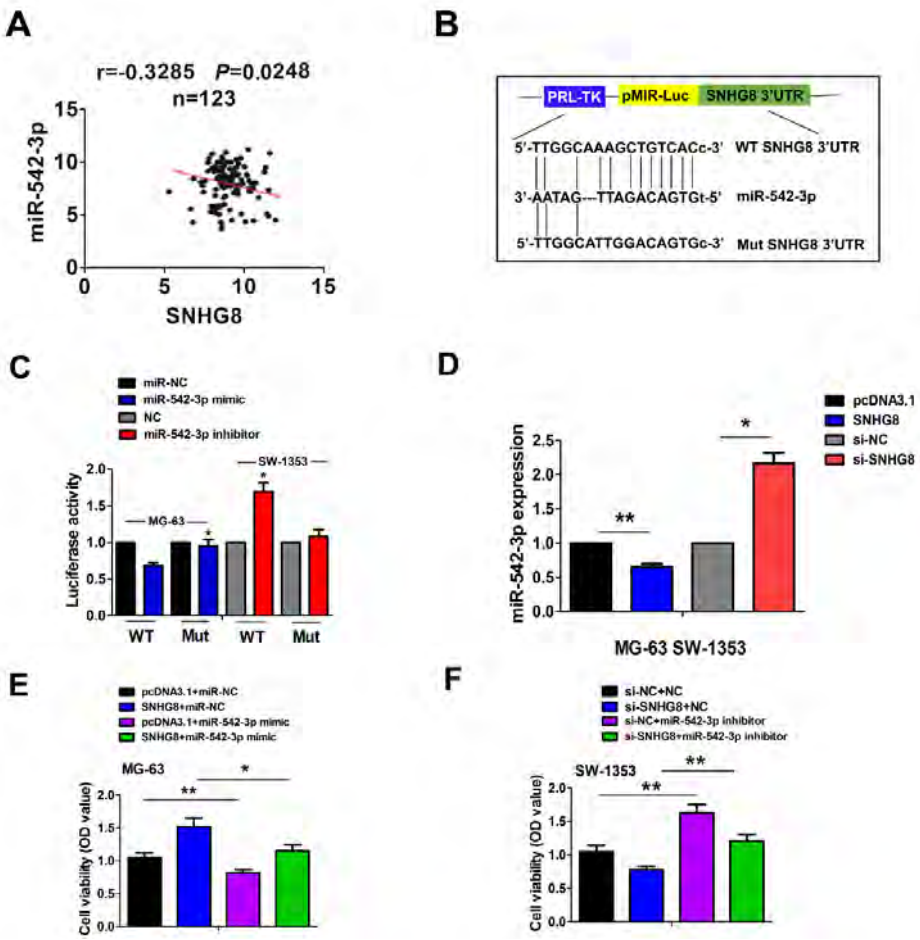


Fig. 3. *SNHG8 negatively regulated miR-542-3p expression in OS cells.* ***A****) The correlation of SNHG8 with miR-542-3p expression in OS tissues was analyzed.* ***B****) The binding sites between miR-542-3p and WT or Mut SNHG8 3'UTR.* ***C****) The luciferase activity of WT SNHG8 3'UTR was decreased by miR-542-3p mimic and increased by miR-542-3p inhibitor) but the luciferase activity of Mut SNHG8 3'UTR was unaffected by miR-542-3p mimic or inhibitor in MG-63 and SW-1353 cells.* ***D****) qRT-PCR analysis of the effects of SNHG8 overexpression or knockdown on miR-542-3p expression in MG-63 or SW-1353 cell line.* ***E, F****) MTT analysis of the cell viability after co-transfection with SNHG8 plasmids and miR-542-3p mimic in mg-63 cell line or si-SNHG8 and miR-542-3p inhibitor in SW-1353 cell line. *P<0.05, **P<0.01.*

found that miR-542-3p mimic reduced the luciferase activity of WT SNHG8 3'UTR, and its inhibitor reversed this effect, but they had no effects on that of Mut SNHG8 3'UTR compared to the control group (Fig. 3C). qRT-PCR analysis indicated that overexpressing SNHG8 repressed the expression of miR-542-3p, and silencing SNHG8 increased its expression (Fig. 3D). However, miR-542-3p mimic or inhibitor had no effect on the expression of SNHG8 in OS cells In addition, after co-transfection with SNHG8 plasmids and miR-542-3p mimic in MG-63 cells or si-SNHG8 and miR-542-3p inhibitor in SW-1353 cells, MTT assay indicated that miR-542-3p inhibited the cell viability and reversed SNHG8-induced cell proliferation in MG-63 cells, but miR-542-3p inhibitor had the opposite effects (Fig. 3E, F).

Downregulation of miR-542-3p was an independent prognostic factor of poor survival in OS patients

The expression of miR-542-3p in OS tissue samples was examined by TCGA cohort, which indicated that miR-542-3p expression was markedly lowered in paired (n = 15) and unpaired OS tissues (n = 123, Fig. 4 A). According to miR-542-3p expression levels, the patients' survival time and survival status,

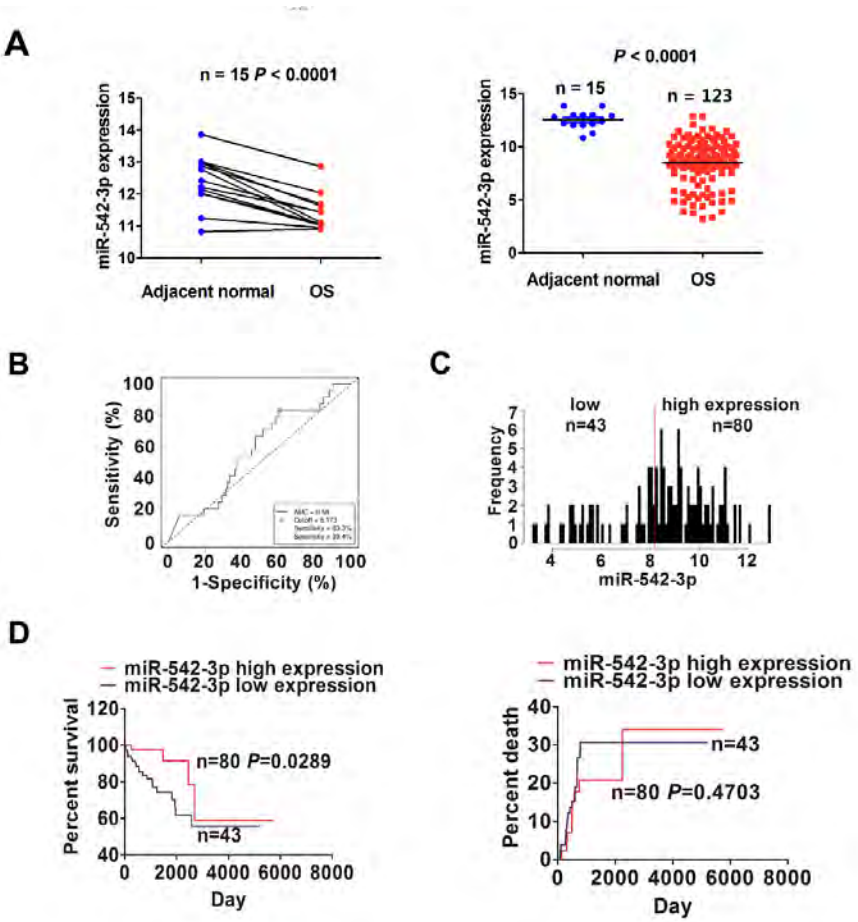


Fig. 4. *Downregulation of miR-542-3p was associated with poor survival in OS patients.* ***A****) TCGA analysis of the expression levels of miR-542-3p in 15 paired and 123 unpaired OS tissues.* ***B****) The cutoff value of miR-542-3p was acquired by a ROC curve in OS.* ***C****) The cutoff value of miR-542-3p divided the patients into miR-542-3p high expression and low expression groups.* ***D****) Kaplan-Meier analysis of the association of high or low miR-542-3p expression with overall survival and tumor recurrence in OS patients.*

a cutoff value (8.173) of miR-542-3p was gained in OS by a cutoff Finder (Fig. 4B), and divided the patients into high miR-542-3p expression and low miR-542-3p expression groups (Fig. 4C). miR-542-3p had no association with the clinicopathological characteristics in OS patients. Kaplan-Meier analysis showed that the patients with high miR-542-3p expression possessed a better survival but had no difference in tumor recurrence as compared with those with low miR-542-3p expression (Fig. 4D). Univariate and Multivariate Cox regression analysis demonstrated that low expression of miR-542-3p was an independent prognostic factor of poor survival in OS (Table II).

DISCUSSION

Increasing data have indicated that the upregulation of SNHG8 is a common event in cancers and is correlated with tumor metastasis and poor survival in cancer patients (10, 11, 13, 16). However, the prognostic value of SNHG8 in OS patients is unknown. In coinciding with previous reports in other cancers (11, 13), our results in TCGA cohort showed that SNHG8 expression was elevated in OS tissue samples. High expression of SNHG8 was associated with age and poor survival, and acted as an independent prognostic factor of poor survival in OS patients.

Previous studies indicated that SNHG8 acts as a cancer promoter in a variety of cancers (9, 10, 12). In consistence with these studies, we also found that ectopic expression of SNHG8 boosted the proliferation and invasion of OS cells, and knockdown of SNHG8 had the opposite effect. Mechanically, SNHG8 can recruit EZH2 to inhibit RECK expression in OS cells (9). More studies are focused on the interaction of SNHG8 with miRNAs in cancer (14-16). Herein, we identified SNHG8 specific binding with miR-542-3p and found that SNHG8 could negatively regulate and bind with miR-542-3p in OS cells. SNHG8 can also sponge miR-542-3p to promote the progression of NSCLC (16). These findings indicated that SNHG8 acted by regulating miR-542-3p in OS cells.

Some studies have shown that miR-542-3p expression is downregulated in hepatocellular carcinoma (HCC) (17), CRC (18, 19) and NSCLC (20), and associated with a better survival in HCC (17) and CRC (19). MiR-542-3p suppresses the growth and invasion of multiple cancers (18-20). In addition, low expression of miR-542-3p is associated with advanced tumor stage and poor survival in OS patients and miR-542-3p inhibits the proliferation of OS cells (21, 22). In our study, we found that miR-542-3p was dramatically downregulated in OS and its low expression was an independent prognostic factor of poor survival in OS patients. MiR-542-3p repressed cell proliferation and reversed SNHG8 induced cell proliferation in OS cells.

Taken together, our findings indicted that upregulated SNHG8 expression or downregulated miR-542-3p expression acted as an independent prognostic factor of poor survival in OS patients. SNHG8 facilitated the proliferation and invasion of OS cells by downregulating miR-542-3p expression and provided a candidate biomarker for OS patients.

ACKNOWLEDGEMENTS

This work was supported by the funding from Shanghai Municipal Commission of Health and Family Planning Foundation (20184Y0249).

REFERENCES

1. Harrison DJ, Schwartz CL. Osteogenic sarcoma: systemic chemotherapy options for localized disease. Curr Treat Options Oncol 2017; 18(4):24.
2. Huang JF, Du WX, Chen JJ. Elevated expression of matrix metalloproteinase-3 in human osteosarcoma and its association with tumor metastasis. J BUON 2016; 21(1):235-43.
3. Xiao X, Zhang Y, Pan W, Chen F. miR-139-mediated NOTCH1 regulation is crucial for the inhibition of osteosarcoma progression caused by resveratrol. Life Sci 2020; 242:117215.
4. Sheng K, Li Y. LncRNA TUG1 promotes the development of osteosarcoma through RUNX2. Exp Ther Med 2019; 18(4):3002-8.
5. Yang Y, Fei M, Zhou X, Li Y, Jin D. The potential value of lncRNA-BC050642 in osteosarcoma

origination and outcomes. Artif Cells Nanomed Biotechnol 2019; 47(1):1859-66.
6. Chen J, Wu Z, Zhang Y. LncRNA SNHG3 promotes cell growth by sponging miR-196a-5p and indicates the poor survival in osteosarcoma. Int J Immunopathol Pharmacol 2019; 33:2058738418820743.
7. Xu R, Feng F, Yu X, Liu Z, Lao L. LncRNA SNHG4 promotes tumour growth by sponging miR-224-3p and predicts poor survival and recurrence in human osteosarcoma. Cell Prolif 2018; 51(6):e12515.
8. Wang J, Cao L, Wu J, Wang Q. Long non-coding RNA SNHG1 regulates NOB1 expression by sponging miR-326 and promotes tumorigenesis in osteosarcoma. Int J Oncol 2018; 52(1):77-88.
9. Qu X, Li Y, Wang L, Yuan N, Ma M, Chen Y. LncRNA SNHG8 accelerates proliferation and inhibits apoptosis in HPV-induced cervical cancer through recruiting EZH2 to epigenetically silence RECK expression. J Cell Biochem 2020. doi: 10.1002/jcb.29646. [Epub ahead of print]
10. Song Y, Zou L, Li J, Shen ZP, Cai YL, Wu XD. LncRNA SNHG8 promotes the development and chemo-resistance of pancreatic adenocarcinoma. Eur Rev Med Pharmacol Sci 2018; 22(23):8161-68.
11. Lin Y, Hu D, Zhou Q, Lin X, Lin J, Peng F. The fasting blood glucose and long non-coding RNA SNHG8 predict poor prognosis in patients with gastric carcinoma after radical gastrectomy. Aging (Albany NY) 2018; 10(10):2646-56.
12. Liu J, Yang C, Gu Y, et al. Knockdown of the lncRNA SNHG8 inhibits cell growth in Epstein-Barr virus-associated gastric carcinoma. Cell Mol Biol Lett 2018; 23:17.
13. Song H, Song J, Lu L, Li S. SNHG8 is upregulated in esophageal squamous cell carcinoma and directly sponges microRNA-411 to increase oncogenicity by upregulating KPNA2. Onco Targets Ther 2019; 12:6991-7004.
14. Zhen Y, Ye Y, Wang H, et al. Knockdown of SNHG8 repressed the growth, migration, and invasion of colorectal cancer cells by directly sponging with miR-663. Biomed Pharmacother 2019; 116:109000.
15. Yang CH, Zhang XY, Zhou LN, et al. LncRNA SNHG8 participates in the development of endometrial carcinoma through regulating c-MET expression by miR-152. Eur Rev Med Pharmacol Sci 2018; 22(6):1629-37.
16. Chen C, Zhang Z, Li J, Sun Y. SNHG8 is identified as a key regulator in non-small-cell lung cancer progression sponging to miR-542-3p by targeting CCND1/CDK6. Onco Targets Ther 2018; 11:6081-90.
17. Chen X, Zhang Q, Ma W, Lan T, Hong Z, Yuan Y. Serum miR-542-3p as a prognostic biomarker in osteosarcoma. Cancer Biomark 2018; 21:521-26.
18. Yang C, Wang MH, Zhou JD, Chi Q. Upregulation of miR-542-3p inhibits the growth and invasion of human colon cancer cells through PI3K/AKT/survivin signaling .Oncol. Rep 2017; 38:3545-53.
19. Yuan L, Yuan P, Yuan H, et al. miR-542-3p inhibits colorectal cancer cell proliferation, migration and invasion by targeting OTUB1. Am J Cancer Res 2017; 7:159-72.
20. Liu B, Li J, Zheng M, Ge J, Li J, Yu P. MiR-542-3p exerts tumor suppressive functions in non-small cell lung cancer cells by upregulating FTSJ2. Life Sci 2017; 188:87-95.
21. Li Q, Song S, Ni G, Li Y, Wang X. Serum miR-542-3p as a prognostic biomarker in osteosarcoma. Cancer Biomark 2018; 21:521-26.
22. Wu Y, You J, Li F, Wang F, Wang Y. MicroRNA-542-3p suppresses tumor cell proliferation via targeting Smad2 inhuman osteosarcoma. Oncol Lett 2018; 15:6895-902.

EFFECTS OF sDR5-Fc FUSION PROTEIN ON INFANT MICE WITH ULCERATIVE COLITIS VIA THE TRAIL-DR5 PATHWAY

LJ. CAI[1], MF. WANG[1], XL. WANG[1,2], HF. ZHU[3,4] and XZ. CHEN[5]

[1]Department of Pediatric Gastroenterology, Hubei Maternal and Child Health Hospital, Wuhan, Hubei Province, China; [2]Hubei Province Key Laboratory of Occupational Hazard Identification and Control, Wuhan University of Science and Technology, Wuhan, Hubei Province, China; [3]Hubei Provincial Hospital of Traditional Chinese Medicine, Wuhan, China; [4]Hubei Province Academy of Traditional Chinese Medicine, Wuhan, China; [5]Department of Pediatrics, Fourth Hospital of Wuhan, Hubei Province, Wuhan, China

Received September 3, 2019 – Accepted January 28, 2020

To explore effects of the sDR5-Fc fusion protein on ulcerative colitis of infant mice via the TRAIL-DR5 pathway, 50 female mice were randomly divided into 5 groups, i.e., control group (group A), dextran sulfate sodium group (group B), hIgG group (group C), 10 mg/kg sDR5-Fc group (group D), and 20 mg/kg sDR5-Fc group (group E). The acute ulcerative colitis models were established. The weights and disease activity index (DAI) of each group were monitored daily. In addition, the pathological changes of colon tissues were observed by Hematoxylin-Eosin staining. The number of macrophages in colon tissues was detected by immunohistochemistry assay. Changes in the expression of inflammatory factors in colon tissues were detected by quantitative real-time polymerase chain reaction (PCR). Lipopolysaccharide (LPS) of different concentrations was utilized alone or in combination with TRAIL to stimulate the NCM460 cells. The activation of NLRP3 inflammasomes was detected by Western blot. The apoptosis of NCM460 cells was detected by flow cytometry. The results showed that in groups B and C, the body weights decreased, the DAI increased, the colon epithelial cells were injured, the inflammatory cells were infiltrated, and the macrophages in colon tissues increased significantly. In groups D and E, the body weights increased, the DAI decreased, the inflammation was significantly improved, the macrophages decreased significantly, and the gene expression levels of NLRP3, Caspase-1, and IL-1β decreased significantly. Thus, sDR5-Fc could inhibit the activation of NLRP3 inflammasomes induced by TRAIL, thereby decreasing the apoptosis of NCM460 cells. In conclusion, the sDR5-Fc fusion protein could block the TRAIL-DR5 pathway to reduce the expression of NLRP3 inflammasomes, thereby improving ulcerative colitis.

Ulcerative colitis (UC), a non-specific chronic inflammatory disease in colon and rectum, is a type of inflammatory bowel disease (1). The pathogenesis of UC is complicated and traditional treatments have a relatively high recurrence rate, and some patients have developed drug tolerance. Therefore, it is necessary to explore the pathogenesis of UC for more effective drugs. Currently, most researchers suggest

Key words: sDR5-Fc fusion protein; ulcerative colitis; NLRP3 inflammasome; macrophage; TRAIL-DR5 pathway

Corresponding Author:
Dr Xiaoli Wang,
Department of Pediatric Gastroenterology,
Hubei Maternal and Child Health Hospital,
745 Wuluo Road, Hongshan District,
Wuhan, Hubei Province, 430070, China
e-mail: wxli86965816@163.com

0393-974X (2020)
Copyright © by BIOLIFE, s.a.s.
This publication and/or article is for individual use only and may not be further reproduced without written permission from the copyright holder.
Unauthorized reproduction may result in financial and other penalties
DISCLOSURE: ALL AUTHORS REPORT NO CONFLICTS OF INTEREST RELEVANT TO THIS ARTICLE.

that the etiology of UC is related to some factors such as genetic and immune dysfunctions, mental status, and infections (2, 3). The extreme activation and imbalance of immune function, especially the activated macrophages, have an important impact on the progression of the disease (4). Scholars have targeted the inhibition of the activation of NLRP3 inflammasomes, suggesting that their activation is the key in the pathogenesis (5-7). Tumor necrosis factor-related apoptosis-inducing ligand (TRAIL) is expressed in various tissues such as colon tissues, and is probably involved in the onset of inflammatory bowel diseases (8). Under inflammatory conditions, inflammatory factors promote the expression of TRAIL in isolated intestinal epithelial cells and induce the apoptosis of intestinal epithelial cells by paracrine or autocrine pathways, while the macrophages induce the apoptosis of intestinal epithelial cells by secreting TRAIL. TRAIL can bind to DR4/DR5 (cytoplasmic region, including death domain) to induce cellular apoptosis. Moreover, it can bind to DcR1/DcR2 (deficient of the cytoplasmic region, or incomplete death domain) to inhibit the apoptosis of positive DR4/DR5 cells induced by TRAIL (9). It has been shown that TRAIL could bind to DR5 to form the TRAIL-DR5 pathway, resulting in a remarkable decrease in apoptosis of cerebral ischemic bodies (10). Other studies have shown that TRAIL was increased in patients with inflammatory bowel diseases and promoted the expression of inflammatory factors (11, 12). sDR5-Fc is a soluble fusion protein produced by the recombination of the extracellular domain of DR5 with human Fc. It has been shown that sDR5-Fc can bind to TRAIL and inhibit the secretion of TRAIL-induced macrophage pro-inflammatory factors under hypoxia-reoxygenation conditions (13). Therefore, it is hypothesised that sDR5-Fc plays a role in improving acute UC in mice. Thus, is the TRAIL-DR5 pathway involved in the regulation of epithelial cell apoptosis in UC and the activation of macrophage NLRP3 inflammasomes?

In summary, to verify whether sDR5-Fc plays a role in improving acute UC in mice, it is necessary to elucidate the pro-apoptotic effect of TRAIL on colon epithelial cells under inflammatory conditions and explore the relationship between TRAIL and inflammation. Therefore, the effects of the sDR5-Fc fusion protein on infant mice with UC mediated by the TRAIL-DR5 pathway were explored, providing a scientific basis for the clinical treatment of UC.

MATERIALS AND METHODS

Animals and cells

Fifty healthy female C57BL/6 mice, aged 6-8 weeks and weighing approximately 18-25 g, were purchased from Nanjing Junke Bioengineering Co., Ltd., China. The animal experiments were conducted in accordance with the Chinese Experimental Animal Protection and Management Regulations and were approved by the ethics committee of Hubei Maternal and Child Health Hospital.

The human normal colon epithelial cell line (NCM460, Shanghai BinSui Biotech, China) was kept in a liquid nitrogen tank.

Grouping and establishment of infant mouse UC models

Fifty female C57BL/6 mice were randomly divided into 5 groups, 10 in each group, i.e., control group (group A), dextran sulfate sodium group (group B), hIgG group (group C), 10 mg/kg sDR5-Fc group (group D), and 20 mg/kg sDR5-Fc group (group E).

Mice in group A were given pure water every day, and mice in groups B, C, D, and E were given oral dextran sulfate sodium (DSS) (3%, Beijing ZEPING Bioscience & Technology, China) for 6 consecutive days. On the 2nd day and the 4th day, mice in group C were injected intraperitoneally with 0.1 mL hIgG protein (2 mg/mL, Sigma, USA), mice in group D with sDR5-Fc fusion protein (10 mg/kg, Beijing LvYuan BoDe Biotech, China), and mice in group E with sDR5-Fc fusion protein (20 mg/kg), respectively. After model establishment, the mice were then sacrificed. The distal colon in each mouse was divided into 3 parts for Hematoxylin & Eosin (H&E) staining, immunohistochemistry (IHC) assay, and quantitative real-time PCR (qPCR), respectively.

Monitoring of weights and disease activity index

During the period of model establishment, the changes in weights and the disease activity index (DAI) scores of mice were recorded daily.

Assessment criteria: Body weight scores: 0, Less than

1% weight loss; 1, 1%-5% weight loss; 2, 5%-10% weight loss; 3, 10%-20% weight loss; 4, more than 20% weight loss. Feces scores: 0, normal viscosity of feces; 1, loose feces; 4, diarrhea. Hemorrhage scores: 0, no hemorrhage in feces; 1, positive occult blood; 4, obvious hemorrhage. The calculation equation: DAI = (body weight scores + feces scores + hemorrhage scores) /3.

Pathological changes in mouse colon tissues via H&E staining

The mouse colon tissues were fixed with paraformaldehyde (4%, Shanghai MACKLIN Reagent, China). After 24 h, the tissues were routinely dehydrated and decolored. The tissues were conventionally embedded with paraffin and fixed at room temperature for 2 h. The colon tissues were serially sectioned with a thickness of 4 μm each. After being cooled at room temperature, the sections were dewaxed in xylene for 10 min and dehydrated. The sections were then stained with H&E solution, followed by dehydration, decoloration, and sealing with neutral gum (Shanghai Yantuo Biotechnology, China). By using a full-automatic microscope (Leica, Germany), pathological changes in colon tissues were observed, scored, photographed, and preserved.

Detection of macrophages in mouse colon tissues by IHC assay

The mouse colon tissues were fixed with paraformaldehyde. After 24 h, the tissues were routinely dehydrated and decolored. The sections were dewaxed with xylene, dehydrated, rinsed with ddH_2O, and added with 3% H_2O_2 at room temperature (in the dark). After 20 min, the sections were washed with PBS for 3 times, 5 min each time. The sections were heated with citric acid buffer solution (pH 6.0, Xiamen YANKE Biotechnology, China). The heating process was not terminated until the mixture was boiled. Then, the mixture was heated to 95°C for 2 s every 2 min, and the heating was repeated 6 times. The sections were blocked with 50 μL bovine serum albumin (BSA, 5%, Shanghai HENGFEI Biotechnology, China) for 30 min. The primary antibody was added and cultured overnight at 4°C. The biotinylated secondary antibody was added and cultured at room temperature for 1 h. The horseradish peroxidase-labeled streptavidin-biotin complex (SABC) was added and cultured at room temperature for 30 min, followed by PBS washing. After 50 μL AEC colorimetric solution (Beijing Biodragon Immunotechnologies, China) was added, the sections were stained with Hematoxylin (Shanghai Baomanbio, China) for 5 s, rinsed with running water for 10 min, and sealed with neutral gum. By using a fully automatic microscope, the sections were observed, photographed, and preserved.

Extraction of total RNA from mouse colon tissues by Trizol

The mouse colon tissues were harvested and placed in a glass grinder to obtain the homogenate. Afterwards, the homogenate was added with 500 μL of Trizol (Jiaozuo LFFBio, China) and mixed evenly. It stood for 10 min at room temperature, and underwent centrifugation at 12000 rpm and 4□ for 10 min. Then, the upper solution was pipetted and added with trichloromethane (200 μL, Sinopharm Chemical Reagent, China) and kept for 5 min at room temperature. The tube was centrifuged for 10 min, added with isopropanol (500 μL, Tianjin Guangcheng Chemical Reagent, China), and mixed evenly and kept at room temperature for 10 min, and the supernatant was discarded. The precipitate was added with 75% ethanol (1 mL, Tianjin Guangcheng Chemical Reagent, China), and centrifuged for 10 min. The supernatant was discarded. The precipitate was added with 75% ethanol (1 mL), and centrifuged for 10 min. The supernatant was discarded. After the precipitate had dried naturally, it was fully dissolved in DEPC water (50 μL, Shanghai Huyu Biological Technology, China).

The RNA concentration was determined by an ultra-micro full-wavelength spectrophotometer (NANODROP 2000, Thermo Fisher Scientific, USA). The RNA was stored at -80°C.

Detection of inflammatory factor expressions in mouse colon tissues by QPCR

1 μg total RNA extracted from tissues was selected as the template for reverse transcription; 1 μL Random Primer, 10 μL 2×P-Mix, 1 μL E-mix, and 1 μL gDNA Remover were used. The total volume reached 20 μL after DEPC water was added and fully mixed.

The reverse transcription reaction was carried out at 42°C for 30 min and 85°C for 5 s by a Q-PCR instrument (Stepone Plus, Applied Biosystems, USA).

For the PCR reaction solution, NLRP3, Caspase-1, and IL-1β, as well as internal reference β-actin primer sequence were designed. 5 μL 2×SYBR Mix, 0.25

μL Sense primer, and 0.25 μL Anti-sense primer were selected. The total volume reached 10 μL after DEPC water was added.

The reaction was carried out at 95°C for 10 min each time. The pre-denaturation was carried out at 95°C for 15 s, and the reaction was carried out at 60°C for 1 min. The cycle was repeated for 40 times. The relative value of gene expressions was calculated using the $2^{-\Delta\Delta CT}$ formula.

Culture of NCM460 cells

The NCM460 cells were transferred to a biosafety cabinet (Wuhan YIPU Biotechnology, China). After the medium was discarded, the cells were washed with PBS and trypsinized (0.25% trypsin, Zhongshan Latterson Biotechnology, China). After 3 min, the cells were added with complete medium containing 10% fetal bovine serum (1 mL, Beijing DG Biotech, China) and centrifuged (500 g) for 5 min. The supernatant was discarded, and the cells were cultured with 1640 complete medium (Beijing Huaxiatech, China) in a culture dish. When the cell confluency reached 90%, 6 groups were set: normal group, 100 ng/mL LPS group, 100 ng/mL LPS and 50 ng/mL TRAIL group, 100 ng/mL LPS and 100 ng/mL TRAIL group, 100 ng/mL LPS and 200 ng/mL TRAIL group, and 100 ng/mL LPS and 400 ng/mL TRAIL group, in which TRAIL was added 6 h after LPS was added and cultured for 6 h.

Detection of NLRP3 inflammasome activation by Western Blot

After the culture medium was discarded, the cells were rinsed with PBS, lysed with 100 μL RIPA lysate (Shanghai Zhenyu Biotechnology, China) on ice. After 10 min, the cells were centrifuged (4°C, 12000 rpm) for 10 min, and the supernatant was transferred into a new EP tube. Then, the cells were added with 5×Loading Buffer, boiled for 10 min, and centrifuged (12000 rpm) for 3 min. The 10% separation gel and 5% stacking gel were prepared, and the samples were loaded. The constant voltage for stacking gel was 80V and the electrophoresis was carried out for 30 min. Then the constant voltage for separation gel was changed to 120V. The Bio-Rad standard wet membrane transfer device was utilized. The membrane transfer was carried out at a constant current of 250 mA for 2 h. The membrane was blocked for 1 hour with 5% skimmed milk on a shaker. The primary antibody was added, and the cells were cultured overnight on a shaker at 4°C and washed with TBST solution on a shaker for 3 times, 10 min each time. The secondary antibody was added, and the cells were cultured on a shaker for 1 hour and washed with TBST solution on a shaker for 3 times. With the application of the Chemi Doc XRS gel image capture system (Bio-Rad, USA), the membranes were scanned and photographed, and the gray values were calculated.

Detection of NCM460 cell apoptosis by flow cytometry

NCM460 cells treated with LPS and TRAIL were removed from the incubator. The medium was discarded and the cells were washed with PBS. After trypsinizing for 5 min, the cells were transferred into a tube and centrifuged (800 g) for 5 min. With the supernatant discarded, the cells were washed with PBS and centrifuged twice. Then, the binding buffer, Annexin V-FITC, and propidium iodide were added and cultured with the cells at room temperature for 10 min in the darkness. NCM460 cell apoptosis was determined by flow cytometry.

Statistical analysis

The SPSS 21.0 statistical software package was used for data processing and analysis. The quantitative data in normal distribution were presented as mean ± standard deviation (x±s). Intra-group comparisons were tested by independent sample *t*-test or the Rank-sum test. Inter-group comparisons were tested by *Chi*-squared test. $P<0.05$ indicated significant difference.

RESULTS

Changes of weights and DAI

Changes of weights and DAI are shown in Tables I and II. The weights of mice in group A were stable with a slight increase. Compared with group A, the weights in groups B, C, D, and E were relatively stable in the first 3 days. However, from the 4th day, the weights decreased remarkably. There were no significant differences in the decrease of weights between groups C and B ($P>0.05$). Compared with groups B and C, the weights in groups D and E increased obviously, and the differences were statistically significant ($P<0.05$). The DAI in group A was stable. Compared with group A, the DAI in groups B, C, D, and E increased from the 3rd day. The increase in weights was not significantly different between groups C and B ($P>0.05$). Compared with

groups B and C, the DAI in groups D and E decreased obviously, and the differences were statistically significant ($P<0.05$).

Pathological results of colon tissues

The pathological results of colon tissues are shown in Fig. 1. In group A, the colon tissues were intact, the mucosa was not defective, the lamina propria of mucosa was not infiltrated by inflammatory cells, and the glands were arranged neatly. In group B, the colon epithelial cells were damaged, the lamina propria of mucosa was infiltrated by inflammatory cells, and the glands were arranged disorderly, atrophic, and even disappeared. In group C, the pathology scores were not significantly different from those of group B. Compared with groups B and C, the glands in lamina propria of mucosa were relatively neatly arranged, the number of inflammatory cells reduced obviously, and the pathology scores decreased in groups D and E.

Macrophages infiltration in mouse colon tissues

Macrophage infiltration in mouse colon tissues is shown in Fig. 1. Compared with group A, the number of macrophages in mouse colon tissues

Table I. *Changes in weight*

Percentage of weight changes (%)	Group A	Group B	Group C	Group D	Group E
Day 0	100	100	100	100	100
1st day	100.86±0.09	102.44±0.13	101.10±0.11	99.76±0.66	99.02±0.57
2nd day	102.44±0.23	102.20±0.54	101.22±0.51	102.93±0.96	101.59±0.83
3rd day	104.03±0.78	100.00±0.96	100.49±1.01	102.44±1.31	100.98±1.24
4th day	105.74±1.68	93.66±1.73	95.86±1.74	102.08±2.35	100.25±2.08
5th day	106.59±2.06	82.45±2.28	85.37±2.32	97.33±2.66	95.01±2.55
6th day	107.81±2.35	73.42±3.07	76.59±3.08	89.00±3.87	88.42±3.46

Note: x±s indicated the mean number ± standard deviation.

Table II. *Changes in DAI*

Percentage of weight changes (%)	Group A	Group B	Group C	Group D	Group E
Day 0	100	100	100	100	100
1st day	100.86±0.09	102.44±0.13	101.10±0.11	99.76±0.66	99.02±0.57
2nd day	102.44±0.23	102.20±0.54	101.22±0.51	102.93±0.96	101.59±0.83
3rd day	104.03±0.78	100.00±0.96	100.49±1.01	102.44±1.31	100.98±1.24
4th day	105.74±1.68	93.66±1.73	95.86±1.74	102.08±2.35	100.25±2.08
5th day	106.59±2.06	82.45±2.28	85.37±2.32	97.33±2.66	95.01±2.55
6th day	107.81±2.35	73.42±3.07	76.59±3.08	89.00±3.87	88.42±3.46

x±s indicates the mean number ± standard deviation

significantly increased in groups B and C (P<0.05). Compared with groups B and C, the body weights of mice decreased obviously in groups D and E, and the differences were statistically significant (P<0.05).

Inflammatory factor expressions in colon tissues

Expressions of inflammatory factors in colon tissues are shown in Fig. 2. Compared with groups B and C, the gene expressions of NLRP3, Caspase-1, and IL-1β significantly decreased in groups D and E (P<0.05).

The activation of NLRP3 inflammasomes

The activation of NLRP3 inflammasomes is shown

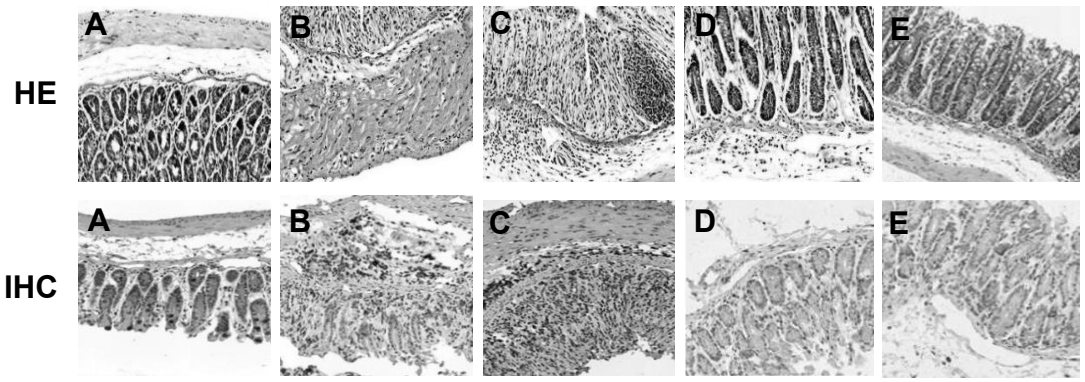


Fig. 1. *Pathological results and macrophage count in mouse colon tissues. HE showed the pathological results of mouse colon tissues; IHC showed the results of macrophage count.*

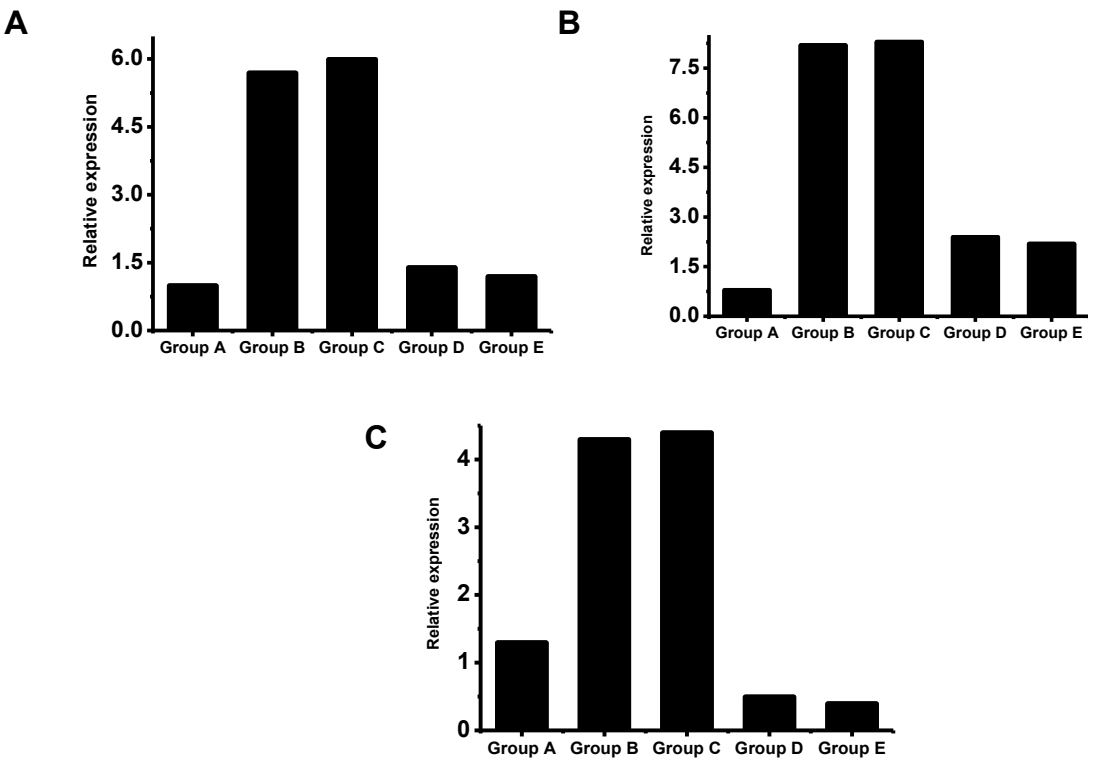


Fig. 2. *Expressions of inflammatory factors in colon tissues. **A**, **B** and **C** represent the expression of NLRP3, Caspase-1, and IL-1β, respectively.*

in Fig. 3. Compared with the group of NCM460 cells treated solely by LPS, NLRP3 and p-p65 expressions increased in the group with combined treatment of LPS and 50 ng/mL or 100 ng/mL TRAIL. When the concentration of sDR5-Fc was 400ng/mL, the expressions of NLPR3, pro-caspase1, and cleaved-casp1 decreased (Fig. 3B). As seen in Fig. 3C, when the concentration of TRAIL was 100 ng/mL, the expression of DR5 in NCM460 cells increased, while 400 ng/mL sDR5-Fc inhibited the effects of TRAIL and decreased the expression of DR5.

Apoptosis of NCM460 cells

The apoptosis of NCM460 cells is shown in Fig. 4. The activity of caspase3/7 in NCM460 cells treated by LPS and TRAIL was enhanced, and the apoptosis increased. After being treated by sDR5-Fc, the activity of caspase 3/7 in NCM460 cells and the apoptosis decreased.

DISCUSSION

In the progression of UC, the epithelial injuries

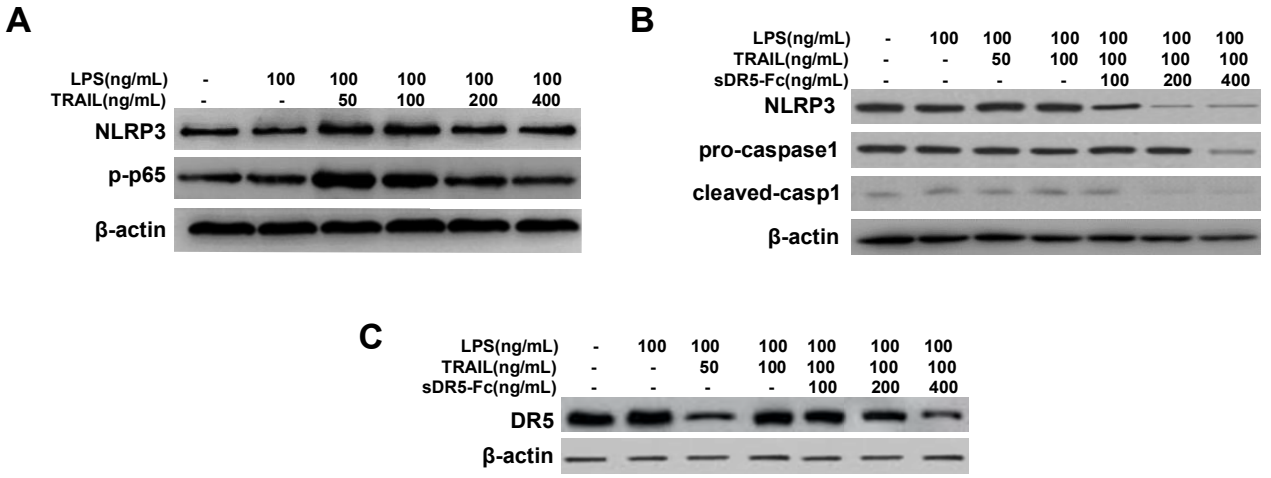


Fig. 3. *Activation of NLRP3 inflammasomes. **A**) Expressions of NLRP3 and p-p65 in NCM460 cells treated solely by LPS. **B**) Expressions of NLPR3, pro-caspase1, and cleaved-casp1 in NCM460 cells treated by sDR5-Fc. **C**) Expression of DR5, wherein β-actin acted as the internal reference.*

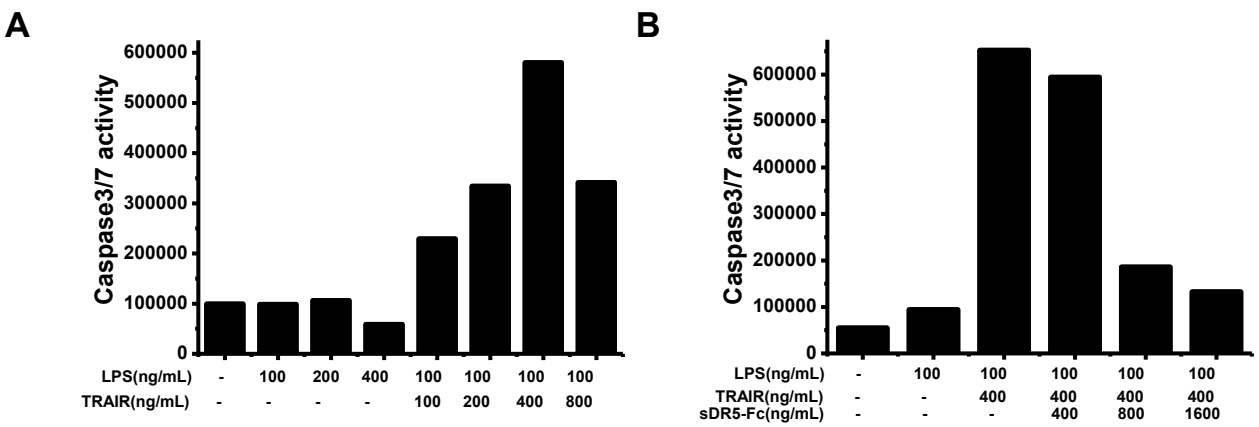


Fig. 4. *Apoptosis of NCM460 cells. **A**) NCM460 cells treated by LPS and TRAIL. **B**) NCM460 cells treated by sDR5-Fc.*

of colon and inflammation played essential roles (14, 15). The injured colon epithelial cells promoted the generation of macrophages. Meanwhile, the injured colon epithelial cells secreted various cytokines and activated other inflammatory cells to induce the production of pro-inflammatory factors, participating in the disease progression of UC (16, 17). In the present study, the infant mouse models of acute ulcerative colitis were established. The results showed that the sDR5-Fc fusion protein can reduce the infiltration of inflammatory cells and the number of macrophages in colon tissues of mice with ulcerative colitis. It was indicated that sDR5-Fc was effective in improving acute UC in mice. The expressions of NLRP3, Caspase-1, and IL-1β in groups D and E significantly decreased compared with those in groups B and C, thereby suggesting that the sDR5-Fc fusion protein can inhibit the activation of NLRP3 inflammasomes. It was consistent with the findings that tissue-infiltration colon macrophages would secrete pro-inflammatory factors (18).

TRAIL plays an important role in innate immunity (19). It has been shown that there is a significant upward trend of TRAIL in patients with UC (20). Scholars have suggested that the gene polymorphism of TRAIL was associated with UC, while the serum sTRAIL level was positively correlated with UC onset (21). Other scholars have constructed mouse obesity models and mouse insulin resistance models, and it was found that knocking out the TRAIL-R in mice showed protective effects on these two disease models, which inhibited the accumulation of activated macrophages in the liver and adipose tissues (22). In this study, NCM460 cells were stimulated with different concentrations of LPS solely or in combination with TRAIL. The results showed that 50 ng/mL and 100 ng/mL TRAIL could induce the activation of NLRP3 inflammasomes in the presence of LPS, while 400 ng/mL sDR5- Fc can inhibit the effects of TRAIL and reduce the activation of NLRP3 inflammasomes and the DR5 expression. In the presence of LPS, TRAIL can promote the apoptosis of NCM460 cells. After the treatment with sDR5-Fc, the induction of apoptosis by TRAIL on NCM460 cells was inhibited. It was suggested that TRAIL and its receptor DR5 were involved in the induction of apoptosis in colon epithelial cells under inflammatory conditions. Furthermore, sDR5-Fc could competitively inhibit the binding of TRAIL to its receptor in combination with TRAIL to improve the symptoms of UC.

In conclusion, sDR5-Fc can reduce the infiltration of inflammatory cells in colon tissues of UC mice and improve UC, which could be achieved by blocking the TRAIL-DR5 pathway to reduce the expression of NLRP3 inflammasomes. However, the mechanism of sDR5-Fc reducing the number of macrophages still requires further investigation.

ACKNOWLEDGEMENTS

This work was supported by Health Commission of Hubei Province Scientific Research Project (No. WJ2019H189); The Hubei Provincial Natural Science Foundation Project Fund (No. 2018CFB736 and 2018CFC819); The Hubei Province Science and Technology Department (Project of Scientific Research Condition and Resource Research Development Fund (No. 2015BCE099).

REFERENCES

1. Loftus EV Jr, Colombel JF, Feagan BG, et al. Long-term Efficacy of vedolizumab for ulcerative colitis. J Crohns Colitis 2017; 11(4):400-411.
2. Colombel JF, Sands BE, Rutgeerts P, et al. The safety of vedolizumab for ulcerative colitis and Crohn's disease. Gut 2017; 66(5):839-51.
3. Lipov E, Candido K. Efficacy and safety of stellate ganglion block in chronic ulcerative colitis. World J Gastroenterol 2017; 23(17):3193-94.
4. Lazaridis LD, Pistiki A, Giamarellos-Bourboulis EJ, et al. Activation of NLRP3 inflammasome in inflammatory bowel disease: differences between Crohn's disease and ulcerative colitis. Dig Dis Sci 2017; 62(9):2348-56.
5. Magro F, Gionchetti P, Eliakim R, et al. Third European Evidence-based Consensus on Diagnosis and Management of Ulcerative Colitis. Part 1: Definitions, Diagnosis, Extra-intestinal Manifestations, Pregnancy, Cancer Surveillance, Surgery, and Ileo-anal Pouch Disorders. J

Crohns Colitis 2017; 11(6):649-70.
6. Sandborn WJ, Su C, Sands BE, et al. Tofacitinib as induction and maintenance therapy for ulcerative colitis. N Engl J Med 2017; 376(18):1723-36.
7. Bopanna S, Ananthakrishnan AN, Kedia S, Yajnik V, Ahuja V. Risk of colorectal cancer in Asian patients with ulcerative colitis: a systematic review and meta-analysis. Lancet Gastroenterol Hepatol 2017; 2(4):269-76.
8. Ślebioda TJ, Kmieć Z. Tumour necrosis factor superfamily members in the pathogenesis of inflammatory bowel disease. Mediators Inflamm 2014; 2014:325129.
9. Hu D, Xia SL, Shao XX, et al. Association of ulcerative colitis with TNF-related apoptosis inducing ligand (TRAIL) gene polymorphisms and plasma soluble TRAIL levels in Chinese Han population. Eur Rev Med Pharmacol Sci 2015; 19(3):467-76.
10. Huang G, Chen X, Cai Y, Wang X, Xing C. miR-20a-directed regulation of BID is associated with the TRAIL sensitivity in colorectal cancer. Oncol Rep 2017; 37(1):571-78.
11. Begue B, Wajant H, Bambou JC, et al. Implication of TNF-related apoptosis-inducing ligand in inflammatory intestinal epithelial lesions. Gastroenterology 2006; 130(7):1962-74.
12. Brost S, Koschny R, Sykora J, Stremmel W, Lasitschka F, Walczak H, Ganten TM. Differential expression of the TRAIL/TRAIL-receptor system in patients with inflammatory bowel disease. Pathol Res Pract 2010; 206(1):43-50.
13. Tsai H F, Hsu P N. Modulation of tumor necrosis factor-related apoptosis-inducing ligand (TRAIL)-mediated apoptosis by Helicobacter pylori in immune pathogenesis of gastric mucosal damage. J Microbiol Immunol Infect 2017; 50(1):4-9.
14. Boal Carvalho P, Cotter J. Mucosal healing in ulcerative colitis: a comprehensive review. Drugs 2017; 77(2):159-73.
15. Ungaro R, Mehandru S, Allen PB, Peyrin-Biroulet L, Colombel JF. Ulcerative colitis. Lancet 2017; 389(10080):1756-70.
16. Maul J, Zeitz M. Ulcerative colitis: immune function, tissue fibrosis and current therapeutic considerations. Langenbecks Arch Surg 2012; 397(1):1-10.
17. Immune response and inflammatory pathway of ulcerative colitis. Immune response and inflammatory pathway of ulcerative colitis. J Basic Clin Physiol Pharmacol 2018; 30(1):1-10.
18. Liu L, Dong Y, Ye M, et al. The pathogenic role of NLRP3 inflammasome activation in inflammatory bowel diseases of both mice and humans. J Crohns Colitis 2017; 11(6):737-50.
19. Manzo F, Nebbioso A, Miceli M, et al. TRAIL plays an important role in innate immunity. Int J Biochem Cell Biol 2009; 41(3):460-66.
20. Hu D, Xia SL, Shao XX, et al. Association of ulcerative colitis with TNF-related apoptosis inducing ligand (TRAIL) gene polymorphisms and plasma soluble TRAIL levels in Chinese Han population. Eur Rev Med Pharmacol Sci 2015; 19(3):467-76.
21. Lazaridis LD, Pistiki A, Giamarellos-Bourboulis EJ, et al. Activation of NLRP3 Inflammasome in Inflammatory Bowel Disease: Differences Between Crohn's Disease and Ulcerative Colitis. Dig Dis Sci 2017; 62(9):2348-56.
22. Afonina IS, Zhong Z, Karin M, Beyaert R. Limiting inflammation—the negative regulation of NF-κB and the NLRP3 inflammasome. Nat Immunol 2017; 18(8):861-69.

LETTER TO THE EDITOR

CORRELATION OF MATERNAL COMPONENTS AND BLOOD LIPIDS DURING PREGNANCY WITH THE ONSET OF PREECLAMPSIA

KL. LIU[1*], HX. CHEN[2*], Y. LIU[1] and QM. FU[1]

[1]Department of Obstetrics & Gynecology, People's Hospital of Baoan District, Shenzhen City, China; [2]Department of Obstetrics & Gynecology, The Third People's Hospital of Longgang District, Shenzhen City, China

Received September 2, 2019 – Accepted January 24, 2020

[#]These authors contributed equally to this work

To the Editor,

Preeclampsia (PE) is an idiopathic disease common in pregnancy (1). Severe preeclampsia is divided into two subtypes according to the weeks of pregnancy when the disease occurs: early-onset severe preeclampsia (ESPE) (2) and late-onset severe preeclampsia (LSPE) (3). Typical clinical manifestations of PE include hypertension, edema and proteinuria, which are related to or can bring change to human body components (such as water, minerals, protein, and fat) (4). One study (5) suggested that there was also an abnormal increase in body water of pregnant women with PE in late pregnancy, i.e., after weight correction, the body water content was significantly higher than that of healthy pregnant women. Bio-electrical impedance analysis (BIA) can evaluate the changes in body contents, and has been widely applied (6, 7) as it could reveal the proportions of protein, fat, total water, inorganic salts and other components of the human body.

MATERIALS AND METHODS

Patients

A total of 76 PE patients who had regular prenatal examinations and gave birth in the People's Hospital of Baoan District between May 2017 and January 2019 were included in the PE group. Thirty-nine of these cases were categorized as the ESPE group and 37 cases fell into the LSPE group. For the control group, 35 healthy women in the late stage of pregnancy who went for prenatal examinations at the same hospital during the same period were selected. The maternal components and blood lipid indicators of the subjects in both early and late stages of pregnancies were detected and analyzed. Informed written consent was provided by all participants, and the study was approved by the Ethics Committee of People's Hospital of Baoan District.

The diagnostic criteria of severe preeclampsia (SPE) followed the Diagnostic Guidelines for Pregnancy-Induced Hypertension Diseases (2015 version) published in the Chinese Journal of Obstetrics and Gynecology.

The body component detection test was carried out in strict accordance with the instructions of Inbody 720 Body Component Analyzer (Biospace, South Korea). Subjects went through fasting and clearing of urine and stool before the exam. Electrolyte wet wipes were used to wipe the subjects feet and hands. After inputting basic information into the Inbody720 Body Component Analyzer, subjects were told to stand on the foot-shaped electrodes with their thumbs pressed on top of and the other 4 fingers under the

Key words: preeclampsia; pregnancy; maternal component; blood lipid levels

Corresponding Author:
Dr Qingmei Fu,
Department of Obstetrics & Gynecology,
People's Hospital of Baoan District,
No.118 Longjing 2nd road, Baocheng District,
Shenzhen City, 518101, China
e-mail: fuqingmei2004@126.com

0393-974X (2020)
Copyright © by BIOLIFE, s.a.s.
This publication and/or article is for individual use only and may not be further reproduced without written permission from the copyright holder.
Unauthorized reproduction may result in financial and other penalties
DISCLOSURE: ALL AUTHORS REPORT NO CONFLICTS OF INTEREST RELEVANT TO THIS ARTICLE.

handle. The arms were kept straight for a certain distance from the torso and the whole test took around 1 to 2 min. The Inbody 720 Body Component Analyzer detected height, weight, intracellular water (ICW), extracellular water (ECW), total body water (TBW), proteins mass, fat-free mass (FFM), fat mass (FM), minerals, percentage of body fat (PBF), and gestational weight gain (GWG).

Detection methods of blood lipid

All subjects started fasting at 20:00 the day before blood lipid detection. On the day of blood lipid detection (the fasting time should be at least 10 hours), 4 mL of venous blood samples were collected from each subject in fasting and resting state. The blood samples stood for 30 min before being centrifuged for 8 minat 4000 g/min to separate the serum. A 7600-020 Automatic Biochemical Analyzer (Hitachi, Japan) was used to detect the levels of total cholesterol (TC), triglyceride (TG), high-density lipoprotein-cholesterol (HDL-C), and low-density lipoprotein-cholesterol (LDL-C).

Statistics analysis

All the data were processed by the Statistical Package for the Social Science (SPSS) 22.0 statistics software (IBM, USA), and the continuous variables in normal distribution were shown as $(\bar{x}\pm s)$. The comparison of early pregnancy and late pregnancy was conducted by paired-samples *t*-test and the correlation between blood lipid and PE was analyzed by Spearman correlation analysis. $P<0.05$ indicated significant difference.

RESULTS

General clinical indicators

In early pregnancy, there was no significant difference between the age, height, weeks of pregnancy and body mass index (BMI) of pregnant women in the PE group sand the control group ($P>0.05$); however, the systolic blood pressure (SBP) and diastolic blood pressure (DBP) of those in the PE groups were significantly higher ($P<0.05$). In late pregnancy, the current body weight, BMI, SBP, and DBP in the PE group were significantly higher than those in the control group ($P<0.05$). The details are shown in Table I.

Detection results of body components and blood lipid in early pregnancy

It is shown in Table II that in terms of maternal components, the detected levels of GWG, FM, PBF,

Table I. *General clinical indicators of the study subjects*

Indicators		The control group	The ESPE group	The LSPE group	F Values	P Value
Height (m)		1.66±0.15	1.64±0.13	1.67±0.11	2.334	0.101
Age (years old)		33.24±5.14	34.29±4.59	34.14±4.35	1.242	0.283
Weight before pregnancy (Kg)		64.32±8.27	63.14±7.55	65.85±6.24	0.626	0.504
Early pregnancy	Weeks of pregnancy	10.21±1.02	10.82±0.85	9.84±0.93	0.819	0.173
	Weight (Kg)	65.44±10.09	65.32±9.07	67.97±7.67	0.723	0.504
	BMI (kg/m^2)	24.43±2.35	24.33±2.35	24.53±2.35	0.412	0.665
	SBP (mmHg)	111.95±9.64	122.67±10.73*	128.47±9.17*#	11.516	<0.001
	DBP (mmHg)	68.03±8.93	73.19±8.28*	78.82±9.03*#	17.927	<0.001
Late pregnancy	Weeks of pregnancy	32.23±1.55	31.56±1.43	32.11±1.24	0.434	0.632
	Weight (Kg)	75.68±13.72	79.42±12.66 *	83.68±11.01*#	25.921	<0.001
	BMI (kg/m^2)	28.52±2.25	31.35±1.24*	31.68±1.52*	31.353	<0.001
	SBP (mmHg)	109.19±10.27	122.71±11.28*	130.28±11.34*#	13.012	<0.001
	DBP (mmHg)	67.92±8.28	73.18±7.29*	80.28±9.17*#	18.292	<0.001

*Note: * P<0.05, compared to the control group; # P<0.05, compared to the ESPE group.*

Table II. *Comparison of body components and blood lipid between each group in early pregnancy*

Periods	Indicators		The control group	The ESPE group	The LSPE group	F Values	P Value
Early pregnancy	Body components	ICW (Kg)	16.35±1.45	17.13±1.66	16.64±1.85	4.553	0.127
		ECW (Kg)	12.93±1.36	14.71±1.26*#	13.83±1.28*	1.924	0.013
		TBW (Kg)	29.64±1.85	31.83±2.74*#	30.84±2.75*	3.613	0.028
		Protein (Kg)	7.43±1.34	8.02±1.02	7.88±1.12	0.073	0.918
		FFM (Kg)	43.58±5.52	43.91±3.31	44.12±3.26	0.976	0.342
		FM (Kg)	21.02±6.28	23.07±5.27 *	23.65±4.35*	1.724	0.168
		Minerals (Kg)	3.02±0.21	3.07±0.24	3.03±0.34	0.452	0.611
		PBF (%)	31.65±4.34	34.58±3.94 *	34.73±3.15*	5.724	0.004
		GWG (Kg)	1.12±0.82	2.18±1.52 *	2.12±1.43 *	0.735	0.005
	Blood lipid	TC (mmoL/L)	4.43±0.73	4.48±0.65	4.53±0.61	0.093	0.902
		TG (mmoL/L)	1.32±0.25	1.29±0.19	1.26±0.14	2.119	0.115
		HDL-C (mmoL/L)	1.31±0.22	1.32±0.12	1.28±0.16	1.453	0.233
		LDL-C (mmoL/L)	2.07±0.27	1.96±0.25	1.96±0.22	1.512	0.222
Late pregnancy	Body components	ICE (Kg)	21.03±1.27	22.41±1.82*	23.28±1.33*#	13.025	<0.001
		ECW (Kg)	14.01±1.31	16.72±1.85*	16.83±0.85*#	32.434	<0.001
		TBW (Kg)	35.63±1.73	39.38±2.24*	40.02±1.66*#	25.542	<0.001
		Protein (Kg)	8.38±1.19	8.95±0.46	8.83±0.42	0.475	0.613
		FFM (Kg)	50.04±4.12	52.93±3.51*	53.44±1.92*	7.423	<0.001
		FM (Kg)	25.18±4.39	29.37±3.23*	31.48±2.32*#	24.523	<0.001
		Minerals (Kg)	3.00±0.27	3.06±0.29	3.04±0.31	0.432	0.602
		PBF (%)	33.22±3.88	35.72±2.49*	39.03±2.14*#	14.224	<0.001
		GWG (Kg)	11.36±5.45	16.28±5.11	17.83±4.77	26.95	<0.001
	Blood lipid	TC (mmoL/L)	5.14±0.25	6.86±0.65*	6.96±0.61*	45.034	<0.001
		TG (mmoL/L)	3.64±0.34	5.22±0.53*	5.35±0.43*	48.498	<0.001
		HDL-C (mmoL/L)	1.87±0.24	1.43±0.36*	1.47±0.29*	43.540	<0.001
		LDL-C (mmoL/L)	3.08±0.22	4.18±0.51*	4.36±0.37	34.32	<0.001

*Note: * P<0.05, compared to the control group; # P<0.05, compared to the ESPE group. FFM: Fat Free Mass; TBW: Total Body Water; ECW: Extracellular Water; ICW: Intracellular Water; FM: Fat Mass; GWG: Gestational Weight Gain; PBF: Percent Body Fat.*

and TBW in the PE groups were significantly higher compared to controls (P<0.05), while the difference in levels of protein, minerals, FFM between the PE groups and control was insignificant(P>0.05). TBW of the ESPE group was significantly higher than that of the LSPE group (P<0.05). The results of correlation analysis showed that weight gain, FM and TBW were correlated with PBF and PE. In terms of the blood lipid levels, there was no significant difference between the PE groups and the control group.

Detection results of body components and blood lipid in late pregnancy

As seen in Table II, the FFM, TBW, FM and PBF of the PE groups were all significantly higher than those in the control group (P<0.05). In terms of blood lipid indicators in late pregnancy, the levels of TC,

Table III. *Changes in body components of the three groups*

Indicators		The control group	The ESPE group	The LSPE group	F Value	P Value
Body components	ICW (Kg)	4.68±1.18	5.28±2.16*	6.64±2.52	3.454	0.037
	ECW (Kg)	1.08±0.75	2.01±0.59*	3.00±0.43*	32.543	<0.001
	TBW (Kg)	5.99±2.12	7.55±3.50*	9.18±4.09*	15.242	<0.001
	Protein (Kg)	0.95±0.75	0.93±0.56	0.95±0.70	0.234	0.845
	FFM (Kg)	6.46±3.40	9.02±4.23*	9.32±4.34*	18.954	<0.001
	FM (Kg)	4.16±1.89	6.30±2.04*	7.83±2.03*	15.365	<0.001
	Minerals (Kg)	0.02±0.02	0.01±0.01*	0.01±0.01*	15.452	<0.001
	GWG (Kg)	1.57±0.84	1.14±1.04*	2.30±1.01*	28.023	<0.001
	PBF (%)	10.24±4.34	14.10±3.59*	17.71±3.34*#	0.718	<0.05
Blood lipid	TC	0.71±0.48	2.38±0.43*	2.43±0.68*	54.823	<0.001
	TG	2.32±1.79	3.93±2.34*	4.09±2.29*	41.277	<0.001
	HDL-C	0.56±0.42	0.11±0.08*	0.19±0.13*	24.142	<0.001
	LDL-C	1.01±0.85	2.22±1.26*	2.40±1.15*	43.623	<0.001

*Note: * P<0.05, compared to the control group; # P<0.05, compared to the ESPE group.*

TG and LDL-C of the PE groups were significantly higher than those in the control group (P<0.05), and the HDL-C of the PE groups was significantly lower than that in the control group (P<0.05). No significant difference was found in blood lipid indicators among the PE groups. The ECW, TBW, FM and PBF of pregnant women in the LSPE group were all significantly higher than those in the ESPE group (P<0.05). The correlation analysis showed that in late pregnancy, body components TBW, FM, PBF and GWG of the PE groups were correlated with PE.

Changes in body components and blood lipid of three groups

In terms of blood lipid changes, the levels of TC, TG, and LDL-C in the PE groups not only increased, but also were significantly higher compared to the control group (Table III). For changes in maternal components, FFM, TBW, FM and PBF of the PE groups were significantly higher compared to controls.

DISCUSSION

Past studies have proposed a variety of human body component models (8), however, the 2-element, 3-element, and 4-element models are currently the most widely used. Compared with other models, the 4-element model can describe the components of the human body more accurately, and has been widely applied. In the present study, the 4-element model was applied (9) where the body components were protein, mineral, water and fat. The results showed that the body components of PE patients had changed in early pregnancy, manifested as the increases in TBW, FM, and PBF. Changes of body components in ESPE patients were more significant.

During pregnancy, healthy pregnant women experience metabolic changes in blood lipids (10) as, in order to protect the growth and development of the fetus and guarantee postpartum breastfeeding, a large amount of fat must be stored (11). The results indicated that blood lipid levels increase with the progression of pregnancy. No significant difference in blood lipids between the LSPE and the ESPE groups was found in late pregnancy. Lipometabolism disorder, not the timing of onset, is usually related to the severity of PE. Thus, it is not surprising that no significant difference was found in blood lipids changes between the ESPE group and the LSPE group.

In summary, body component analysis could reflect the content and distribution of fat *in vivo*, as well as the changes in lipometabolism. By monitoring the changes in body components and

blood lipid indicators during pregnancy, the pregnant women with abnormal lipometabolism could be screened, thereby reducing the risks of early PE. Meanwhile, in late pregnancy, the early conditions of PE could be evaluated by jointly monitoring the body components and blood lipid levels.

ACKNOWLEDGEMENTS

This work was supported by The Shenzhen Bao'an Medical & Health Science Project Foundation (No.2016CX162 and 2018JD189) and the Young People Fund of Affiliated Bao'an Hospital of Shenzhen (No.20170908 and No.2018B004).

REFERENCES

1. Sween LK, Althouse AD, Roberts JM. Early-pregnancy percent body fat in relation to preeclampsia risk in obese women. Am J Obstet Gynecol 2015; 212(1):84.e1-7.
2. Lecarpentier E, Gris JC, Cochery-Nouvellon E, et al. Angiogenic factor profiles in pregnant women with a history of early-onset severe preeclampsia receiving low-molecular-weight heparin prophylaxis. Obstet Gynecol 2018; 131(1):63-69.
3. Alpoim PN, Perucci LO, Godoi LC, Goulart COL, Dusse LMS. Oxidative stress markers and thrombomodulin plasma levels in women with early and late severe preeclampsia. Clin Chim Acta 2018; 483:234-38.
4. Staelens AS, Vonck S, Molenberghs G, Malbrain ML, Gyselaers W. Maternal body fluid composition in uncomplicated pregnancies and preeclampsia: a bioelectrical impedance analysis. Eur J Obstet Gynecol Reprod Biol 2016; 204:69-73.
5. da Silva EG, Carvalhaes MA, Hirakawa HS, da Silva EG, Peraçoli JC. Bioimpedance in pregnant women with preeclampsia. Hypertens Pregnancy 2010; 29(4):357-65.
6. Yasuda R, Takeuchi K, Funakoshi T, Maruo T. Bioelectrical impedance analysis in the clinical management of preeclamptic women with edema. J Perinat Med 2003; 31(4):275-80.
7. Staelens AS, Vonck S, Molenberghs G, Malbrain ML, Gyselaers W. Maternal body fluid composition in uncomplicated pregnancies and preeclampsia: a bioelectrical impedance analysis. Eur J Obstet Gynecol Reprod Biol 2016; 204:69-73.
8. Wells JC, Haroun D, Williams JE, et al. Evaluation of DXA against the four-component model of body composition in obese children and adolescents aged 5-21 years. Int J Obes (Lond) 2010; 34(4):649-55.
9. Devakumar D, Grijalva-Eternod C, Cortina-Borja M, Williams J, Fewtrell M, Wells J. Disentangling the associations between parental BMI and offspring body composition using the four-component model. Am J Hum Biol 2016; 28(4):524-33.
10. Ephraim R, Doe P, Amoah S, Antoh E. Lipid Profile and High Maternal Body Mass Index is Associated with Preeclampsia: A Case-Control Study of the Cape Coast Metropolis. Ann Med Health Sci Res 2014; 4(5):746-50.
11. El Khouly NI, Sanad ZF, Saleh SA, Shabana AA, Elhalaby AF, Badr EE. Value of first-trimester serum lipid profile in early prediction of preeclampsia and its severity: A prospective cohort study. Hypertens Pregnancy 2016; 35(1):73-78.

LETTER TO THE EDITOR

EXPRESSIONS OF Kif2c AND Ki-67 IN NON-SMALL CELL LUNG CANCER AND THEIR RELATIONSHIP WITH INVASION AND METASTASIS

LF. XIONG, YM. LOU and L. WANG

Department of Integrative Oncology, The First People's Hospital of Fuyang, Hangzhou, Zhejiang, China

Received November 27, 2019 – Accepted February 18, 2020

To the Editor,

Lung cancer can be divided into non-small cell lung cancer (NSCLC) (1) and small cell lung cancer (SCLC) (2), of which NSCLC is the main subtype, accounting for 80-85% (3). Kinesin family member 2C (Kif2c), also known as mitotic centromere associated kinesin (MCAK) (4), is the most typical member of the Kinesin-13 family. Kif2c is a mitotic centromere-related driving protein (5) which reduces the stability of microtubules in interphase cells. Inhibition of Kif2c can cause various defects in the microtubule attachment, and abnormal connection between the movement point and microtubule attachment contributes to aneuploidy cells. In addition, the reduction or deletion of the Kif2c expression leads to abnormal arrangement of mitotic S-phase chromosomes and incorrect separation of G2 chromosomes, which disrupts the normal mitotic process (6). It is considered as a potential factor of tumorigenesis. Ki-67 (Ki-67 antigen) is a cell proliferation marker and changes of Ki-67 can cause abnormal signal transduction, and promote the evolution of tumors (7). In this study, we aimed to analyze the expression of Kif2c and Ki-67 in NSCLC tissues from a molecular point of view to help improve the clinical diagnosis and treatment of lung cancer.

MATERIALS AND METHODS

Ninety-six NSCLC specimens were collected from The First People's Hospital of Fuyang from November 2017 to May 2019, while 40 paracancerous tissues (at least 5 cm away from the tumor) were collected. All specimens met the following criteria. Firstly, none of the patients with NSCLC had undergone radiotherapy, chemotherapy, immunotherapy or any other cancer treatment before surgery. Secondly, all cases were confirmed by pathological examination after surgery. According to the revised pTNM staging standard of the Union for International Cancer Control in 2009, 60 cases were of stage I + II and 36 cases of stage III. According to WHO classification of lung cancer, 51 cases were of squamous cell carcinoma and 45 cases of adenocarcinoma. There were 46 cases of low differentiation and 50 cases of high differentiation. Lymph node metastasis was found in 59 cases while absent in 37 cases. The study was approved by the Ethics Committee of The First People's Hospital of Fuyang and each patient signed an informed consent to participate in the study.

Western blot

Samples which had been stored at -80°C before use were placed on ice to melt naturally and then weighed. Each EP tube contained 100 mg tissues. Tissue fragments were ground with liquid nitrogen and mortar; 100 uL of cracking solution was added. PMSF (30 uL, 10mg/mL PMSF per gram of tissue) was added and shaken once every 10 min on ice for 30

Key words: Non-small cell lung cancer; invasion and metastasis; Kfi2c; Ki-67

Corresponding author:
Dr Lifeng Xiong,
Department of Integrative Oncology,
The First People's Hospital of Fuyang,
429 Bei Huan Road, Fuyang District, Hangzhou,
311400, Zhejiang, China
e-mail: xionglifeng2001@163.com

0393-974X (2020)
Copyright © by BIOLIFE, s.a.s.
This publication and/or article is for individual use only and may not be further reproduced without written permission from the copyright holder.
Unauthorized reproduction may result in financial and other penalties
DISCLOSURE: ALL AUTHORS REPORT NO CONFLICTS OF INTEREST RELEVANT TO THIS ARTICLE.

min before being centrifuged at 20,000g and 4°C for 15 min. The supernatant was absorbed into another EP tube and centrifuged at 4°C and 20,000g for 15 min. The protein concentration was determined by BCA. According to the protein concentration, samples with the same protein content (10-40 ug) were added with 5 x SDS loading buffer. The total volume of the sample generally did not exceed 20 uL, with the maximum volume of the sample hole being 30 uL. The protein was denatured by heating for 5 min at 100°C before being cooled at room temperature and stored at -20°C for reserve. SDS-PAGE gel was prepared according to the molecular weight of the target protein. After gelling, the comb was pulled out. The gel was fixed on the electrophoretic device, and 1 x Tris-Gly electrophoresis buffer was added to the internal and external groove. A microinjector was used for sampling. The marker sample size was 5 uL and protein sample size was 20uL~30uL. 50V voltage was first used for the electrophoresis device. After the dye ran out of the concentrate (about 50 min), the voltage was increased to 75V. The electrophoresis lasted until the bromophenol blue entered the bottom of the separation gel. The protein was then transferred to the PVDF membrane after 2 h of electroporation at a constant current of 80mA. The PVDF membrane was removed and sealed at room temperature for 1 h with TBST solution containing 5% skimmed milk. The antibody was diluted with TBST solution containing 5% skimmed milk for multiple times according to the instructions. The closed PVDF film was then left overnight at 4°C before recovering tbe first reactant the next day. The membrane was then washed three times with TBST solution for 10 min each time. The secondary antibody was diluted with TBST solution containing 5% skimmed milk and incubated at room temperature for 2 h. It was then recovered and washed three times with TBST solution for 10 min each. The PVDF film was finally taken out and placed on a paved fresh-keeping film. The dark room of ECL light-emitting kit fixed the film, and Image J image analysis system was used for analysis.

Immunohistochemical staining

The slides were immersed in potassium dichromate concentrated sulfuric acid solution for 24 h. After 24 h of flushing with flowing tap water, they were baked in a 60°C oven. The dried slides were immersed in 10% poly-L-lysine solution for several seconds before being removed. After being drained, they were baked in a 60°C oven for 1 h. The prepared tissue wax blocks were cut into paraffin slices with a thickness of 4 microns by a microtome, and the paraffin slices were placed in a constant temperature box at 60°C for 1 h. Paraffin sections were dewaxed to hydration. A drop of 3% H_2O_2 solution was added to each slice and incubated at room temperature for 10 min. PBS was used to rinse 3 times, 3 to 5 min each time. After antigen repair, 5% BSA solution was sealed at room temperature for 20 min. Appropriate dilution of the primary antibody left at 4°C overnight. PBS was used to rinse 3 times, 3 to 5 min each time. The residual PBS solution on the section was discarded. After drying, reagent A was added to each slice and incubated at room temperature for 20 min. PBS was used to wash for three times, 3 to 5 min each time, and the residual PBS solution on the slices was discarded. After drying, reagent B was added to each slice and incubated at room temperature for 30 min. PBS was used to rinse 3 times, 3 to 5 min each time. DAB was used for staining, hematoxylin was used for re-staining, and 0.1% hydrochloric acid was used for differentiation. After washing with tap water for 15 min, the PBS buffer was used to wash the water back to blue. Finally, dehydration, transparent and sealing were carried out.

Statistical analysis

SPSS 22.0 statistical software was used for statistical analysis. Statistical methods included variance analysis, *chi*-squared test and Spearman correlation analysis. $P < 0.05$ was considered statistically significant.

RESULTS

Expressions of Kif2c and Ki-67

Immunohistochemical results showed that Kif2c protein was mainly expressed in cytoplasm and nuclei. Kif2c was positive in 73 of 96 NSCLC

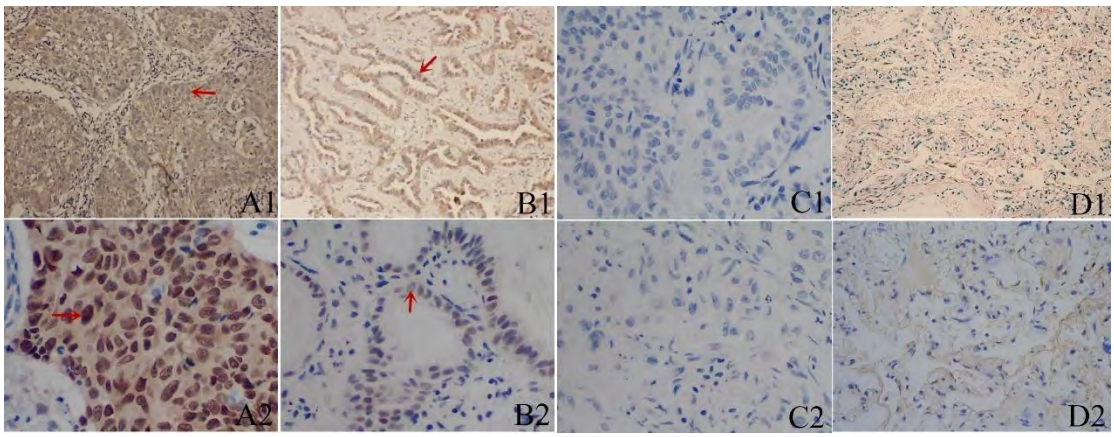


Fig. 1. *Immunohistochemical results (A1: Kif2c positive expression in lung squamous cell carcinoma, ×200; B1: Kif2c positive expression in lung adenocarcinoma, ×200; C1: Kif2c negative expression in lung cancer, ×400; D1: Kif2c negative expression in paracancerous lung cancer, ×200; A2: Ki-67 positive expression in lung squamous cell carcinoma, ×400; B2: Ki-67 positive expression in lung adenocarcinoma, ×400; C2: Ki-67 negative expression in lung cancer, ×400; D2: Ki-67 expression in paracancerous tissues, ×400).*

Table I. *Relationship between Kif2c and clinicopathological parameters*

Clinical parameters		Cases (n)	Positive expression n (%)	Negative expression n (%)	χ^2 value	P value
Gender	Male	60	45(75.00)	15(25.00)	0.132	0.733
	Female	36	28(77.78)	8(22.22)		
Age	≥60 years	45	33(73.33)	12(26.67)	0.351	0.563
	<60 years	51	40(78.43)	11(21.57)		
Smoking history	Yes	84	65(77.38)	19(22.62)	0.892	0.321
	No	12	8(66.67)	4(33.33)		
Pathological type	Squamous cell carcinoma	51	37(72.55)	14(27.45)	0.374	0.538
	Adenocarcinoma	45	36(80.00)	9(20.00)		
Degree of tumor differentiation	Low	46	32(69.57)	14(30.43)	1.037	0.298
	Middle-high	50	41(82.00)	9(18.00)		
Lesion size	T1+T2	56	39(69.64)	17(30.36)	1.884	0.172
	T3+T4	40	34(85.00)	6(15.00)		
Lymph node metastasis	N0	37	20(54.05)	17(45.95)	10.037	0.002
	N1+N2	59	53(89.83)	6(10.17)		
Clinical stages	I+II	60	39(65.00)	21(35.00)	7.947	0.005
	III	36	34(94.44)	2(5.56)		

patients (76.04%). Kif2c was positive in 11 out of 40 specimens (27.5%). There was a significant difference between the two groups (P=0.002 < 0.01). The results showed that the positive expression rate of Kif2c in NSCLC was significantly higher than that in normal lung tissues adjacent to cancer. It can be considered that the expression of Kif2c in NSCLC was up-regulated (Fig. 1 A1-D1).

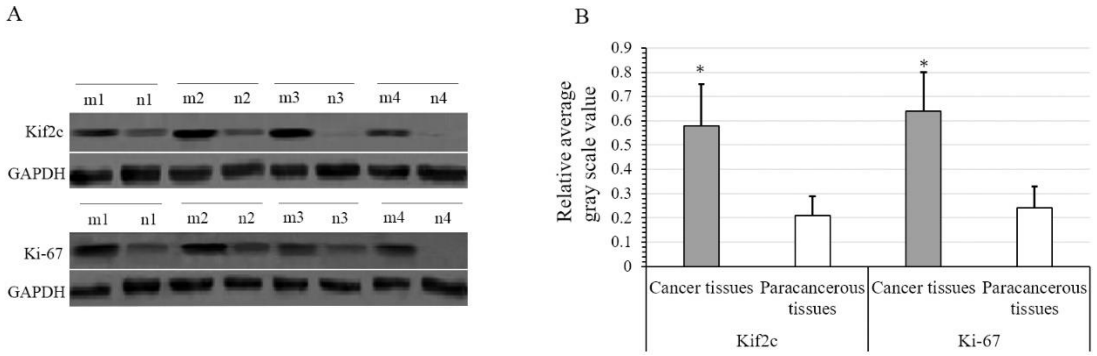


Fig. 2. *The expression of Kif2c and Ki-67 in cancer tissues (m) and paracancerous tissues (n) in NSCLC (A: tissue immunoblotting band; B: relative gray value statistics, GAPDH as internal reference, * P < 0.05, compared with paracancerous tissues).*

Table II. *Relationship between Ki-67 and clinicopathological parameters*

Clinical parameters		Cases (n)	Positive expression n (%)	Negative expression n (%)	χ^2 value	P value
Gender	Male	60	32(53.33)	28(46.67)	0.563	0.621
	Female	36	21(58.33)	15(41.67)		
Age	≥60 years	45	28(62.22)	17(37.78)	2.012	0.162
	<60 years	51	25(49.02)	26(50.98)		
Smoking history	Yes	84	48(57.14)	36(42.86)	2.385	0.127
	No	12	5(41.67)	7(58.33)		
Pathological type	Squamous cell carcinoma	51	36(70.59)	15(29.41)	6.193	0.012
	Adenocarcinoma	45	17(37.78)	28(62.22)		
Degree of tumor differentiation	Low	46	15(32.61)	31(67.39)	7.846	0.006
	Middle-high	50	38(76.00)	12(24.00)		
Lesion size	T1+T2	56	31(55.36)	25(44.64)	0.265	0.826
	T3+T4	40	22(55.00)	18(45.00)		
Lymph node metastasis	N0	37	13(35.14)	24(64.86)	4.947	0.027
	N1+N2	59	40(67.80)	19(32.20)		
Clinical stages	I+II	60	27(45.00)	33(55.00)	3.193	0.046
	III	36	26(72.22)	10(27.78)		

The positive expression of Ki-67 was a brown-yellow color in nuclei. Out of 96 NSCLC patients, 53 (55.21%) were Ki-67 positive. Ki-67 positive expression was found in none of the paracancerous tissues. The expression of Ki-67 in NSCLC and adjacent tissues was significantly different ($P < 0.05$) (Fig. 1 A2-D2).

In order to study the relationship between the expression of Kif2c protein and the clinical data of patients, the immunohistochemical results of Kif2c protein were graded and analyzed according to the patients' gender, age, tumor size, clinical stage, pathological grade and lymph node metastasis. The results showed that the positive expression of Kif2c was correlated with lymph node metastasis and clinical stage ($P < 0.05$), but not with gender, age, smoking history, pathological type, degree of differentiation of tumors and size of lesions ($P > 0.05$) (Table I).

The clinicopathological parameters of 96 NSCLC patients showed that the positive expression of Ki-67 was not related to gender, age, smoking history and lesion size ($P > 0.05$), but was related to pathological type, degree of differentiation, lymph node metastasis and clinical stage ($P < 0.05$), as shown in Table II.

Western blot detection of protein expressions

Four pairs of NSCLC cancer tissues and adjacent normal tissues were randomly selected. The expression of Kif2c and Ki-67 protein was detected by Western blot. The results showed that the expression levels of Kif2c and Ki-67 in cancer tissues were significantly higher than those in adjacent normal tissues ($P < 0.05$) (Fig. 2).

Correlation between expressions of kif2c and Ki-67 in NSCLC

The expression of Kif2c in NSCLC tissues was compared with that of Ki-67. Statistical results showed that there was a correlation between the two ($R = 0.342$, $P < 0.05$). The expression levels of Kif2c and Ki-67 in cancer tissues were positively correlated (Table III).

DISCUSSION

Abnormal expression of Kif2c in cells can cause imbalance of the microtubule dynamic system (8). However, disorders of mitotic kinase and phosphatase can lead to mitotic abnormalities, chromosomal instability and transcriptional disorders (9). Therefore, the abnormality of Kif2c may play an important role in the occurrence and development of cancer. However, Shimo et al. (10) found that Kif2c is one of the genes that transactivate breast cancer tissues. Further studies have shown that Kif2c is highly expressed in breast cancer tissues and cell lines. Nakamura et al. (11) suggested that the high expression of Kif2c is associated with lymph node invasion, lymph node metastasis and poor prognosis of gastric cancer. Our results showed that the high expression of Kif2c in cancer tissues promoted tumor progression. From the perspective of biological proliferation, it directly affected cell proliferation and participated in cell mitosis. Kif2c, as a motor protein on microtubules, was closely related not only to the division and proliferation of NSCLC cells, but also to the distant metastasis of tumor cells. Therefore, it can be regarded as a proto-oncogene.

Table III. *Correlation between Kif2c and Ki-67 expressions in NSCLC tissues*

		Kif2c		Total
		Positive	Negative	
Ki-67	Positive	45	8	53
	Negative	28	15	43
	Total	73	23	96

Ki-67 is a marker of proliferative nuclei. It can reflect the growth rate, malignancy and invasiveness of cancer cells (12). The results showed that Ki-67 can reflect the occurrence, development and metastasis of NSCLC, and that the expression of Ki-67 in metastatic lung adenocarcinoma was consistent with that in primary lung cancer. In addition, the results of this study suggested that the expression of Kif2c and Ki-67 may play a synergistic role in the invasion and metastasis of cancer cells., however, more theoretical and experimental data are needed to support the relationship.

In summary, Kfi2c and Ki-67 are highly expressed in NSCLC tissues, and the expression of Kfi2c protein is positively correlated with Ki-67, suggesting that they may play synergistic roles in the occurrence, development, invasion, and metastasis of NSCLC.

REFERENCES

1. Na II, du Choe H, Kim CH, Park SH, Park JH, Lee JC. CT findings in non-small-cell lung cancer patients treated with gefitinib or erlotinib. J Cancer Res Ther 2012; 8(2):247-53.
2. Camidge DR, Bang YJ, Kwak EL, et al. Activity and safety of crizotinib in patients with ALK-positive non-small-cell lung cancer: updated results from a phase 1 study. Lancet Oncol 2012; 13(10):1011-19.
3. Fehrenbacher L, Spira A, Ballinger M, et al. Atezolizumab versus docetaxel for patients with previously treated non-small-cell lung cancer (POPLAR): a multicentre, open-label, phase 2 randomised controlled trial. Lancet 2016; 387(10030):1837-46.
4. Gan H, Lin L, Hu N, et al. KIF2C exerts an oncogenic role in nonsmall cell lung cancer and is negatively regulated by miR-325-3p. Cell Biochem Funct 2019; 37(6):424-31.
5. Bie L, Zhao G, Wang YP, Zhang B. Kinesin family member 2C (KIF2C/MCAK) is a novel marker for prognosis in human gliomas. Clin Neurol Neurosurg 2012; 114(4):356-60.
6. Manning AL, Ganem NJ, Bakhoum SF, Wagenbach M, Wordeman L, Compton DA.. The kinesin-13 proteins Kif2a, Kif2b, and Kif2c/MCAK have distinct roles during mitosis in human cells. Mol Biol Cell 2007; 18(8):2970-79.
7. Yamamoto Y, Nishiyama Y, Ishikawa S, et al. Correlation of 18F-FLT and 18F-FDG uptake on PET with Ki-67 immunohistochemistry in non-small cell lung cancer. Eur J Nucl Med Mol Imaging 2007; 34(10):1610-16.
8. Wang W, Cantos-Fernandes S, Lv Y, Kuerban H, Ahmad S, Wang C, Gigant B. Insight into microtubule disassembly by kinesin-13s from the structure of Kif2C bound to tubulin. Nat Commun 2017; 8(1):70.
9. Wang W, Jiang Q, Argentini M, Cornu D, Gigant B, Knossow M, Wang C. Kif2C minimal functional domain has unusual nucleotide binding properties that are adapted to microtubule depolymerization. J Biol Chem 2012; 287(18):15143-53.
10. Shimo A, Tanikawa C, Nishidate T, et al. Involvement of kinesin family member 2C/mitotic centromere-associated kinesin overexpression in mammary carcinogenesis. Cancer Sci 2008; 99(1):62-70.
11. Nakamura Y, Tanaka F, Haraguchi N, et al. Clinicopathological and biological significance of mitotic centromere-associated kinesin overexpression in human gastric cancer. Br J Cancer 2007; 97(4):543-49.
12. Vesselle H, Salskov A, Turcotte E, et al. Relationship between non-small cell lung cancer FDG uptake at PET, tumor histology, and Ki-67 proliferation index. J Thorac Oncol 2008; 3(9):971-78.

LETTER TO THE EDITOR

THE IMPLICATION OF INTERLEUKIN-1β IN THE DEVELOPMENT AND PROGRESSION OF MULTIPLE MYELOMA

H. JIANG[1], XF. YIN[1], JY. Yu[1] and CY. SU[2]

[1]Department of Hematology, Sir Run Run Shaw Hospital, Zhejiang University School of Medicine, Hangzhou, China; [2]Department of Hematology, Tongde Hospital of Zhejiang Province, Hangzhou, China

Received February 3, 2020 – Accepted February 20, 2020

To the Editor,

Multiple myeloma (MM) is a malignant hematological disease produced mainly by clonal expansion of plasma cells in bone marrow (1). Osteolytic lesions appear in more than 80% of the myeloma patients and are responsible for the most devastating characteristics of the disease (1). The bone marrow microenvironment plays an essential role in supporting the growth and survival of MM cells (2). Bone marrow mesenchymal stem cells (BMMSCs) are one of the important components of bone marrow microenvironment (3). The complex interactions between MM cells and BMMSCs lead to the activation of multiple signaling pathways on MM cells, which support their proliferation, migration, anti-apoptosis, and drug resistance (4). In the bone marrow microenvironment of MM patients, an increased expression was observed of Inter leukin (IL)-1β and IL-6 correlated with the occurrence, development and drug resistance of MM (5). IL-1β participates in acute and chronic inflammation and plays a crucial role in the innate immune response.

Moreover, many diseases involving immune system disorders are clinically accompanied by the abnormal expression of IL-1β, so targeting the inhibition of IL-1β expression is used in the treatment of many diseases. IL-1β is a potent osteoclast activating factor and has a significant role in the development of osteolytic lesions (6). The activity of osteoclast activating factor in MM patients is correlated with IL-1β, which indicates that IL-1β plays a key role in the pathogenesis of MM osteopathy (7). Based on all these findings, this study evaluates the effect of IL-1β on BMMSC osteogenesis *in vitro* and on the expression of stem cell genes such as NANOG and chemotaxis related chemokine receptors, including CCR1, and CCR2 by multiple myeloma NCI-H929 cells in co-culture with BMMSCs.

MATERIALS AND METHODS

Human bone marrow was obtained from patients diagnosed with iron deficiency anemia (IDA) in Sir Run Run Shaw Hospital. All subjects participating in the study signed written informed consent. Bone marrow mononuclear cells were isolated by Ficoll, and then inoculated into low-glucose Dulbecco's modified eagle medium (DMEM) (Suzhou Vita Chemistry Co., Ltd., China) containing 10% fetal bovine serum at a density of 2 x10^6/mL. After 24 h, cell adherence was followed by fluid exchange for primary culture. Myeloma cell line NCI-H929 was purchased from Nanjing Kebai Biological Technology Co., Ltd. of China. Three groups of BMMSC cells were used in the study: control Group

Key words: IL-1β; multiple myeloma; bone marrow mesenchymal stem cells; NCI-H929 cells

Corresponding Author:
Dr Chuanyong Su,
Department of Hematology,
Tongde Hospital of Zhejiang Province,
No.234 Gucui Road,
Hangzhou, 310012, China
e-mail: suchuanyongtd0203@163.com

0393-974X (2020)
Copyright © by BIOLIFE, s.a.s.
This publication and/or article is for individual use only and may not be further reproduced without written permission from the copyright holder.
Unauthorized reproduction may result in financial and other penalties
DISCLOSURE: ALL AUTHORS REPORT NO CONFLICTS OF INTEREST RELEVANT TO THIS ARTICLE.

A which included cells without any treatment; Group B in which the cells were treated with IL-1β (10 ng/mL) for 24 hours; and Group C where cells were treated with IL-1β (10 ng/mL) once a day for 7 days. After 7 days of culture, myeloma cells NCI-H929 were added to each group and co-cultured with the BMMSCs for 3 days. 3-5 mL bone marrow fluid from IDA patients was extracted and mixed in an anticoagulant tube. Mononuclear cells were isolated and prepared into a single-cell suspension. Primary cell culture was carried out after the concentration was adjusted to 10 mL with L-DMEM medium containing 10% fetal bovine serum (FBS). After 24-48 h of culture, the liquid was changed entirely and the non-adherent cells were removed; 10 mL L-DMEM culture medium containing 10% FBS was added, and half of the liquid was replaced every 2-3 days. Moreover, BMMSCs were subcultured, and cell growth was observed under an inverted microscope every day during the culture.

Cryopreserved NCI-H929 cells were resuscitated in an incubator at 37°C and 5% CO_2. During the culture, the growth of cells was observed under an inverted microscope every day.

P_3~P_6 BMMSCs with good growth were obtained and inoculated into three dishes with 8 x 10^4 cells per dish. After 7 days of treatment the old culture medium was removed. Each dish was supplemented with 2 x 10^6 NCI-H929 cells and 10% FBS-RPMI-1640 medium (GIBCO company, USA). After 3 days of culture, suspended NCI-H929 cells were carefully sucked out. NCI-H929 cells with right cell concentration were cultivated in H4034 medium at 37°C for 30 min and inoculated in a small dish with a diameter of 3.5 cm in concentrations of 1x104 cells per dish. The cells were counted under an inverted microscope. Clusters of more than 40 cells were recorded as a colony. After cultivation, NCI-H929 cells were collected for subsequent polymerase chain reaction (PCR) and Western blot experiments.

NCI-H929 cell suspension was absorbed into different centrifugal tubes, labeled, and centrifuged at room temperature at 80 r/min for 5 min. After centrifugation, the supernatant was discarded, and PBS was added to blow evenly, then again centrifuged. After that, the supernatant was discarded. Then, 150 UL RIPA + PMSF (250:1) cell lysate (RIPA, PMSF: Nanjing Vazyme Biotech Co., Ltd) was added to each tube. When thoroughly mixed with cells, it was sucked out and placed in a 1.5 ml EP tube and labeled. Each step was carried out on ice. Each EP tube oscillated once every 60 seconds, then cracked on ice for 5 min. After the operation was repeated five times, it was centrifuged at 4°C at 12,000 g, for 15 min. After centrifugation, the supernatant was absorbed into the new EP tube and labeled, and the volume of supernatant was recorded. The supernatants obtained from 1.5 mL EP tubes were detected and recorded on an Eppendorf Nucleic Acid Protein Quantitative Instrument (Eppendorf Corporation, USA). Loading buffer (1/4 protein volume) was added, boiled in water for 5 to 10 min, and stored at -20°C.

Separation glue (12%) is configured to penetrate into the glass gap, and the upper layer is added with ddH_2O to the top. After 30~40 min, the gel was removed and ddH2O was discarded and dried with filter paper. The laminating glue was configured and added to the upper layer of the separating glue and reached the top. The comb was inserted to remove bubbles, and it was kept at room temperature for 30 to 40 min.

Protein Electrophoresis was performed using a BioRad electrophoresis device.

Fresh transfer solution was prepared, PVDF membrane of appropriate size was cut, and marks were made to distinguish the positive and negative sides. The separating glue was removed from the glass plate and the filter paper was immersed in the transfer solution for at least 30 s. The cut PVDF film was immersed in methanol for 60 s, then translucent, then moved to the transfer solution for 5 min. The membrane transfer device was placed on ice, and the transfer took place at 90 mA overnight or at 350 mA for 2 h. Then, the PVDF membranes were placed in the sealed liquid and sealed at room temperature on the shaking table for 1 h (or 4°C overnight). The sealing liquid was prepared as follows using 1g skimmed milk powder (or bovine serum albumin) dissolved in 20 ml TBST solution and formulated as a sealing solution with a concentration of 5%. Sealing solution was used to dilute rabbit anti-

sheep antibodies: NANOG (1:500) (Cell Signaling Company, USA), SOX2 (1:1000) (Cell Signaling Company, USA) and OCT-4 (1:1000) (Epitomics Company, USA) and mouse anti-sheep antibodies: GAPDH (1:2000) (Cell Signaling Company, USA). After overnight incubation at 4°C, on a shaking bed, the membranes were washed with the TBS-T solution for 10 min, 3-5 times. The rabbit anti-sheep IgG antibody was diluted in a 1:2000 ratio with the sealing solution and incubated at 37°C for 1 h. The above steps were repeated. The PVDF films were colored with the exposure liquid and then exposed to the Western scanner.

In order to detect whether the increase of BMP-2 expression after IL-1β pretreatment was related to the NF-κB signaling pathway, cellular immunohistochemistry was used to detect the expression of BMP-2 in short-term (24h) and long-term (7 days) BMMSCs cultured with IL-1β pretreatment, and to detect the expression of BMP-2 in short-term (24h) and long-term (7days). BMMSCs cultured with PDTC (Pyrrolidine dithiocarbamate) (150 micromol/L), an inhibitor of NF-κB. BMMSCs were cultured in 24-well culture plate until more than 70% of cells fusioned, and the culture medium was exhausted. The cells were washed three times with PBS and fixed with 4% paraformaldehyde for 20 min at room temperature. Then, the fixative solution was removed and rewashed with PBS for 3 consecutive times. Then the cells were incubated with 3% hydrogen peroxide deionized water for 15 min. After incubation, the cells were washed with PBS three times and permeabilized with 0.3%Triton X-100 for 30 min. Afterwards the cells were washed with PBS three times and sealed with 5% sheep serum for 10 min. Subsequently, the cells were incubated with anti-bone morphogenetic protein (BMP)-2 (sterile PBS: BMP-2 = 730:1) (Abcam, China) overnight at 4°C. After culture, the cells were washed with PBS three times and then incubated, with the second anti-goat anti-mouse IgG (AmyJet Scientific Co., Ltd., China) for 30 min at room temperature. Finally, the cells were colored with 3,3'-diaminobenzidine tetrahydrochloride (DAB) for 5-10 min, washed for 10 min with deionized water and after 2 min restained with hematoxylin. After dehydration with gradient alcohol, neutral gum seals were prepared. After drying, the cells were observed under inverted microscope, photographed, and accessed. Image-Pro Plus 6.0 analysis software was used for image analysis. Five visual fields were selected for each slice to determine the Integrated Optical Density (IOD). The larger the IOD was, the stronger the positive expression was.

Total RNA was isolated using TRIzol reagent (Thermo Fisher Scientific, USA) according to the manufacturer's protocol. 1 μg of total RNA was reversed transcribed into cDNA using RevertAidTM First-Strand cDNA Synthesis Kit RNA (a reverse transcription kit) (Nanjing Vazyme Biotech Co., Ltd., China) according to the manufacturer instruction. The synthesized cDNAs were subjected to PCR using Raindrop digital PCR System (Beijing YimeiTongde Technology Development Co., Ltd., China) for the determination of the following genes: CCR1, CCR2, MIP-1α, and MCP-1.

Statistical analysis

Image-Pro Plus 6.0 (media cybernetics Image Technology Company, USA) was used to process the gray value of Western Blot, and Graph Pad Prism 5 software (Beijing Huanzhongruichi Technology Co., Ltd., China) was used for statistical analysis. The measured data were expressed as mean ± standard deviation $(\bar{x}\pm s)$. One-way analysis of variance was used for comparison between groups, and the difference was considered statistically significant when $P<0.05$.

RESULTS

BMMSC and NCI-H929 cell morphology

It could be seen that the growth rate of primary BMMSCs was accelerated after going down to the next generation. At 24 h after inoculation, BMMSCs grew in a long spindle shape with uniform distribution and there was no obvious change in cell morphology. Furthermore, there were no significant differences in morphology and growth characteristics of BMMSCs among groups A, B, and C (Fig. 1 A, B and C). Moreover, the morphology and growth characteristics of BMMSCs co-cultured with

NCI-H929 did not change significantly. NCI-H929 cells grew in suspension and some of them could aggregate into grape-like beads. Therefore, the number of cell colonies in NCI-H929 co-cultured with group A (Fig. 1D) and NCI-H929 co-cultured with group B (Fig. 1E) was increased compared to that in NCI-H929 co-culture with group C (Fig. 1F) observed under an inverted microscope.

The expression of BMP-2 in groups B and C obviously decreased after pretreatment with PDTC, an inhibitor of NF-κB ($P<0.05$) (Fig. 2).

The expression of SOX2 in groups B and C was significantly increased compared with group A ($P < 0.05$) (Fig. 3 A and B). However, there was no significant difference in the expression of NANOG and OCT-4 in the three groups ($P> 0.05$) (Fig. 3 A and B).

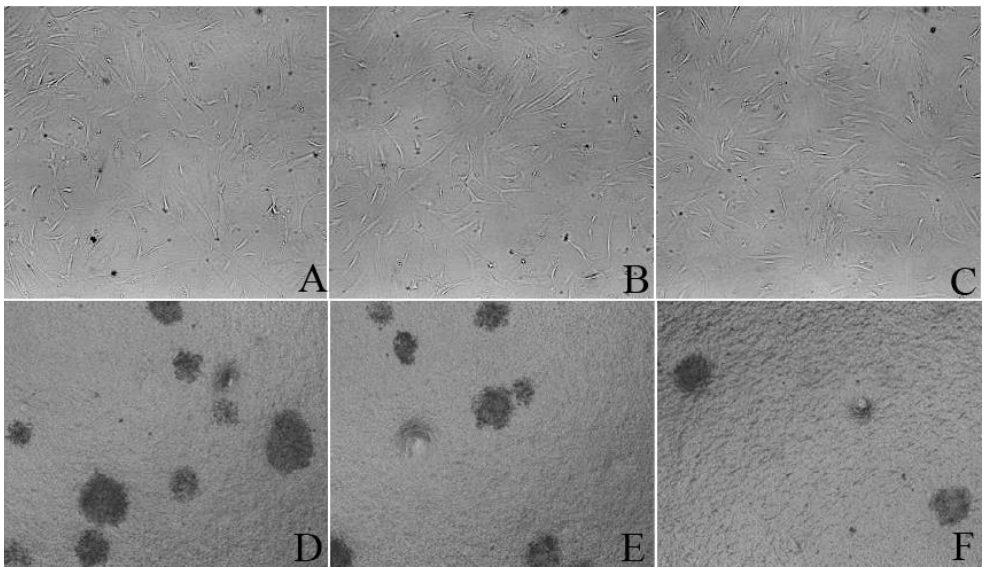


Fig. 1. *Morphological characteristics of BMMSCs and NCI-H929 (×40).* ***A****) BMMSCs in group A;* ***B****) BMMSCs in group B;* ***C****) BMMSCs in group C;* ***D****) NCI-H929 co-culture with group A;* ***E****) NCI-H929 co-culture with group B;* ***F****) NCI-H929 co-culture with group C.*

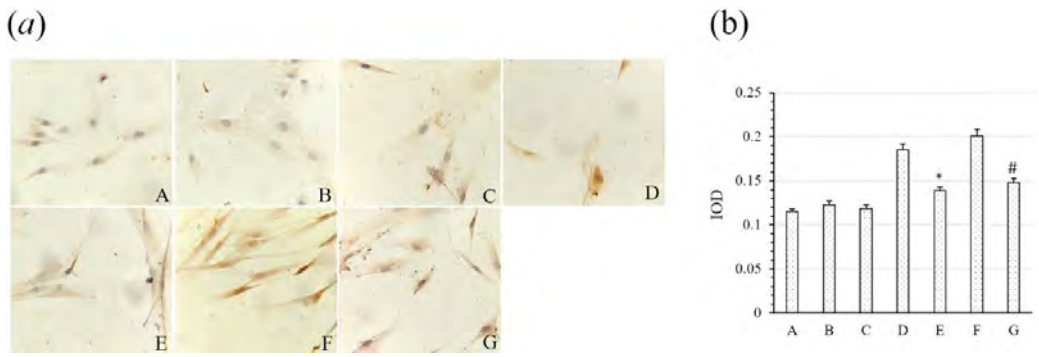


Fig. 2. *Detection of BMP-2 expression in the BMMSC cells by immunohistochemistry.* ***a****) Immunohistochemical images, ×200.* ***b****) Quantitative analysis * $P < 0.05$, E compared with D; #$P < 0.05$, G compared with F. (A: No anti-negative control group; B: group A; C: PDTC pretreatment group A; D: group B; E: PDTC pretreatment group B; F: group C; G: Group C pretreated with PDTC).*

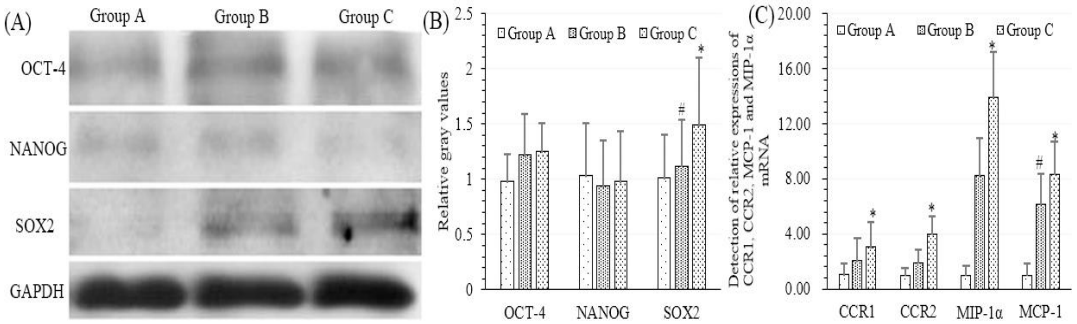


Fig. 3. ***A****) Expressions of NANOG, SOX2 and OCT-4 in NCI-H929 cells by Western blot;* ***B****) Relative gray values of NANOG, SOX2 and OCT-4 expression in NCI-H929 cells;* ***C****) Relative expressions of CCR1, CCR2, MCP-1, and MIP-1α mRNA in NCI-H929 cells by RT-PCR (*P < 0.05 group C compared with group A; # P< 0.05 group B and group A.*

Chemokine receptors CCR1, and CCR2, and chemokines MCP-1 and MIP-1α were detected in NCI-H929 cells from the groups A, B, and C. The expression levels of CCR1, CCR2, MCP-1, and MIP-1a in NCI-H929 cells were significantly increased in group C compared with group A ($P < 0.05$). The expression of MCP-1 in group B was significantly increased compared to group A ($p< 0.05$), as shown in Fig. 3C.

DISCUSSION

BMMSCs have many functions, such as self-renewal, multilineage differentiation, and immune regulation. Furthermore, BMMSCs can differentiate into osteoblasts under specific conditions (8). BMP/Smad signaling pathway is one of the related pathways involved in bone formation (9). BMPs belong to the superfamily of transforming growth factor-β proteins that can promote BMMSCs to differentiate into osteoblasts by activating the Smad signal transduction pathway. A previous study showed that after pretreatment of BMMSCs with IL-1β, the expression of phosphorylated Smad1/5/8 did not change significantly, however, increasing the expression of BMP-2 indicated that IL-1β cannot activate BMP/Smad signaling pathway (10). In this study, it was shown that the NF-κB signaling pathway was involved, as the expression of BMP-2 in single and multiple pretreatment groups of IL-1β decreased after pretreatment with PDTC, an inhibitor of NF-κB. MM cells express and secrete a variety of chemokines and chemokine receptors. These chemokine receptors interact with their ligands to participate in and influence the migration of plasma cells in the bone marrow and chemotaxis in the bone marrow microenvironment (11, 12). Chemokine receptors (such as CCR1, CCR2) in MM can bind to chemokines MIP-1α and MCP-1, regulate the proliferation, differentiation, and migration of tumor cells and prevent apoptosis of MM cells. The results of this study showed that BMMSC cells from normal bone marrow could affect the gene expression of stem cells in myeloma cells after single or multiple stimulations with IL-1β, especially the expression of CCR1, CCR2, MCP-1, and MIP-1a. In conclusion, this study demonstrates that IL-1β could be a possible therapeutic target for the treatment of multiple myeloma. Further studies should be carried out to certify these findings.

REFERENCES

1. Vincent R S. Multiple myeloma: 2014 Update on diagnosis, risk-stratification, and management. Am J Hematol 2014; 89(10):998-1009.
2. Huang JM, Bao Y, Xiang W, et al. Icariin regulates the bidirectional differentiation of bone marrow

mesenchymal stem cells through canonical wnt signaling pathway. Evid Based Complement Alternat Med 2017; 2017:12.
3. Guo J, Fei C, Zhao Y, et al. Lenalidomide restores the osteogenic differentiation of bone marrow mesenchymal stem cells from multiple myeloma patients via deactivating Notch signaling pathway. Oncotarget 2017; 8(33):55405-21.
4. Fu J, Wang P, Zhang X, et al. Myeloma cells inhibit osteogenic differentiation of mesenchymal stem cells and kill osteoblasts via TRAIL-induced apoptosis. Arch Med Sci 2010; 6(4):496-504.
5. Lust JA, Lacy MQ, Zeldenrust SR, et al. Induction of a chronic disease state in patients with smoldering or indolent multiple myeloma by targeting interleukin 1{beta}-induced interleukin 6 production and the myeloma proliferative component. Mayo Clin Proc 2009; 84(2):114-22.
6. Takagi S, Tsukamoto S, Park J, et al. Platelets enhance multiple myeloma progression via IL-1β upregulation. Clin Cancer Res 2018; 24(10):2430-39.
7. Suzuki A, Takahashi T, Okuno Y, et al. Production of parathyroid hormone-related protein by cultured human myeloma cells. Am J Hematol 1994; 45(1):88-90.
8. Huang C, Zhang G F, Han J, Liao GJ, Zou BG. Mechanism of age-related changes of bone marrow mesenchymal stem cells in senile osteoporosis. J Biol Regul Homeost Agents 2016; 30(2):565-69.
9. Wu M, Chen G, Li YP. TGF-β and BMP signaling in osteoblast, skeletal development, and bone formation, homeostasis and disease. Bone Res 2016; 4:16009.
10. Ye W, Fei XM, Tang Y, Xu XX, Zhu Y. [IL-1β-treated bone marrow mesenchymal stem cells enhances osteogenetic potential via NF-ϰB pathway]. Zhongguo Shi Yan Xue Ye Xue Za Zhi 2017; 25(3):890.
11. Wright N, de Lera TL, García-Moruja C, et al. Transforming growth factor-β1 down-regulates expression of chemokine stromal cell-derived factor-1: functional consequences in cell migration and adhesion. Blood 2003; 102(6):1978.
12. Yin Y. Cytocompatibility evaluation of grafted IKVAV PLEOF hydrogels with bone marrow mesenchymal stem cells. J Wuhan Uni Technol 2014; 29(4):824-31.

LETTER TO THE EDITOR

miR-130a INHIBITS CELL VIABILITY AND MIGRATION THROUGH FOSL1 IN LUNG CANCER

Y. XU[1], L. WANG[2] and J. LIU[1]

[1]Department of Respiratory Medicine, Zibo Central Hospital, Zhangdian, Zibo, China; [2]Zibo Municipal Government Hospital Century Garden Internal Medicine Ward, Zhangdian, Zibo, China

Received January 10, 2020 – Accepted February 25, 2020

To the Editor,

Lung cancer, the most frequent malignant tumor, is the leading cause of cancer deaths worldwide, and its 5-year survival rate is less than 17% (1). Despite advances in treatment and early diagnosis, the prognosis for lung cancer is still poor, therefore, identifying new biomarkers for therapies is urgently needed. MicroRNAs (miRNAs) are non-coding small RNAs, 19-25 nucleotides in length. miRNAs could regulate gene expression by binding to the 3'-UTR of target mRNAs, thereby inhibiting the translation or leading to mRNA degradation (2). Kong et al. indicated that miR-130a suppressed metastasis and induced G0/G1 arrest in breast cancer (3). Similarly, Wang et al. elucidated that miR-130a inhibited the metastasis and epithelial-mesenchymal transition (EMT), and suppressed the growth of gastric cancer xenografts (4). Thus, we conducted this study in order to explore the expression and the roles of miR-130a in lung cancer.

FOS like 1, AP-1 transcription factor subunit (FOSL1) encodes a leucine zipper protein that can dimerize with proteins of the JUN family, thereby forming the transcription factor complex AP-1 (5). Maurus et al. reported that FOSL1 was a novel reprogramming factor with potent tumor transformation potential for melanocytes (6). In the present study, we discovered that FOSL1 was overexpressed in lung cancer and re-expression of FOSL1could partially reversed the inhibition of miR-130a on viability and migration.

MATERIALS AND METHODS

From January 2016 to December 2018, we screened 52 lung cancer patients diagnosed at the People's Hospital of Zhangqiu Area, and obtained 52 lung cancer tissues and 52 samples of normal tissue specimens from adjacent regions. Among the 52 lung cancer patients, 47 patients were non-small cell lung and 5 patients were small cell carcinoma. The samples were frozen in liquid nitrogen immediately after surgery and stored at -80°C prior to analysis. Before the curative resection, none of the patients had undergone chemotherapy or radiotherapy. We obtained written informed consent from all the patients and the Ethics Committees of the People's Hospital of Zhangqiu Area approved this study.

Cell line and cell transfection

the Lung carcinoma cell lines (A549 and H1299) and a normal lung cell line MRC-5 were obtained from the Cobioer (Shanghai, China). All the cells were cultured in DMEM medium (Gibco, Carlsbad, CA, USA) supplement with 10% FBS at 37°C in a 5% CO2 humidified atmosphere.

For the transfection, the miR-130a mimic or the

Key words: miR-130a; FOSL1; lung cancer; viability; migration

Corresponding Author:
Dr Jing Liu,
Department of Respiratory Medicine,
Zibo Central Hospital, No. 54 Gongqingtuan West Road,
Zhangdian 255000, Zibo, China
Tel.: +86 13305332190
e-mail: donglujiaoyi86605@163.com

0393-974X (2020)
Copyright © by BIOLIFE, s.a.s.
This publication and/or article is for individual use only and may not be further reproduced without written permission from the copyright holder.
Unauthorized reproduction may result in financial and other penalties
DISCLOSURE: ALL AUTHORS REPORT NO CONFLICTS OF INTEREST RELEVANT TO THIS ARTICLE.

miR-130a inhibitor, as well as the control vectors were purchased from GenePharma Company (Shanghai, China), while the pcDNA3.1-FOSL1 vectors were from RiboBio Biotechnology (Guangzhou, China). The confluence of A549 cells in 6-well plate was cultured at 60% and then the transfection was performed using Lipofectamine 2000 (Invitrogen, Carlsbad, CA, USA). The lipofectamine 2000 and the vectors were diluted with Opti-MEM/Reduced serum medium (Thermo Scientific, Shanghai, China), respectively, and then the two solutions were mixed. The cells were harvested and analyzed 48 h after transfection.

RNA isolation and RT-qPCR

TRIzol reagent (Invitrogen, Carlsbad, CA, USA) or miRNeasy Mini Kit (Qiagen, Valencia, CA, USA) was used to isolate and purify the total miRNAs or mRNAs. Initially, the RT Real-Time SYBR Green (Bio-Rad Laboratories, Berkeley, CA, USA) was conducted to carry out the reverse transcription to produce the first cDNA chain. Subsequently, SYBR Green PCR master mix (Takara Biotechnology) or TaqMan miRNA Assay Kit (Applied Biosystems) were conducted to perform the quantitative PCR. The U6 and GAPDH were used as the normalization for miRNA and mRNA, respectively. The $2^{-\Delta\Delta Cq}$ method was applied to assess the relative mRNA levels of miRNA and mRNA.

Western blot

The proteins levels of E-cadherin (E-Ca), N-cadherin (N-Ca) and GAPDH were assessed by Western blot analysis. In brief, the cells were lysed using the lysis buffer. After centrifugation, the lysates were denatured by boiling in loading buffer. Thereafter, the denatured proteins were separated by 10% SDS-PAGE, and electro-transferred to a PVDF membrane. Then, after blocking with 5% non-fat milk for 2 h at room temperature, the membrane was incubated with primary antibodies at 4°C overnight. After washing away the primary antibody, the membrane was incubated with an HRP-conjugated secondary antibody (1:5,000) at room temperature for 1 h. The blots were visualized using a Western Lightning Chemiluminescent Detection Reagent (Amersham, Freiburg, Germany).

Cell Counting Kit-8

Cell Counting Kit-8 (CCK-8) (Dojindo Laboratories, Kumamoto, Japan) was used to calculate proliferative ability. A549 cells were placed in a 96-well plate and incubated at 37°C. The proliferative ability was determined at 24, 48, 72 and 96 h. After shaking for 10 min, the absorbance at 490nm was calculated used a microplate reader (Bio Teke, Winooski, USA).

Transwell assay

The migratory ability was evaluated through performing Transwell assay (24 wells, 8 μM pore size). The upper chamber coated with Matrigel (BD Biosciences, Franklin Lakes, NJ, USA) was filled with 200 μm A549 cell suspension, which were re-suspended by serum-free media. Meanwhile, 500 μm normal DMEM medium (HyClone, South Logan, UT, USA) with 15% FBS was added in the lower chamber. After incubating for 24 h at 37°C, the unmigrated cells were removed by a cotton swab. At the same time, 4% paraformaldehyde and 10% crystal violet were utilized to fix and stain the invasive cells, respectively. Finally, the invasive cells were photographed and counted under a microscope.

Luciferase reporter assay

Through TargetScan, we predicted the potential downstream targets of miR-130a, and FOSL1 was predicted as a candidate gene. To verify FOSL1 was a target of miR-130a in lung cancer cells, the binding sequences on the FOSL1 3'-UTR were mutated from UUGCACUA to AACGUGAC. Thereafter, the wide type and the mutant 3'-UTRs of FOSL1 mRNA were cloned into the dual luciferase reporter vectors. After A549 cells co-transfected with the miR-130a mimic/NC mimic and the WT/MUT, the luciferase activity was measured applying Dual Luciferase Reporter Assay System (Beyotime Biotechnology, Beijing, China).

Statistical analysis

All the data was analyzed by Statistical Product and Service Solutions (SPSS) 16.0 (IBM, Armonk, NY, USA). The results are expressed as mean ± SEM in bar graphs and line graphs. Kaplan-Meier curve was performed to evaluate the association between the expression of miR-130a and the overall survival for lung cancer patients. The comparisons between two or more groups were performed through Student's *t*-test or one-way ANOVA, followed by Student-Newman-Keuls post hoc test. Results were considered statistically significant if $P<0.05$.

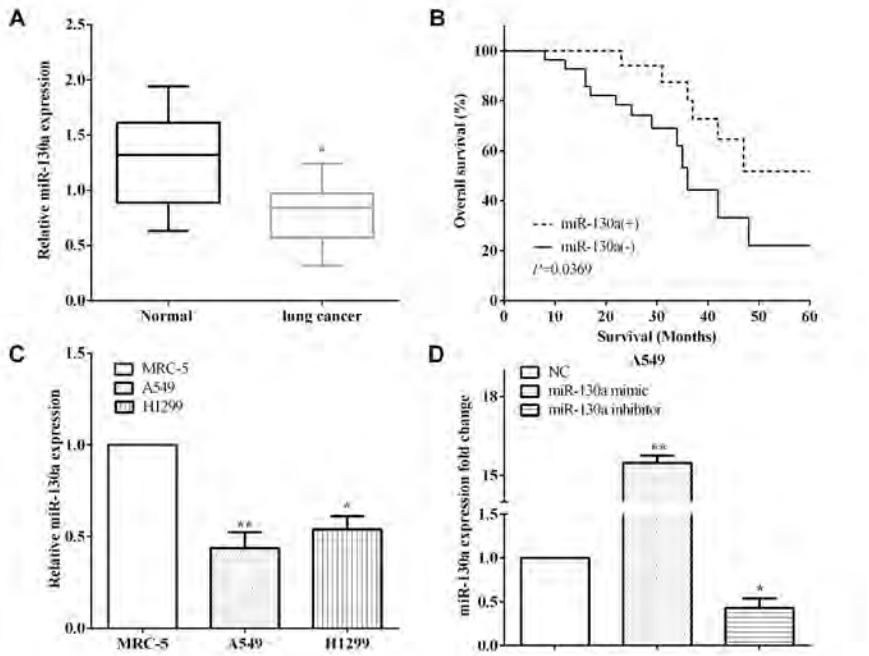


Fig. 1. *Low expression of miR-130a is associated with worse prognosis of lung cancer patients.* ***A)*** *MiR-130a was low expressed in the lung cancer tissues vs the corresponding normal tissues.* ***B)*** *Kaplan-Meier method revealed that upregulation of miR-130a predicted poor 5-year overall survival of lung cancer.* ***C)*** *MiR-130a was lower expressed in A549 and H1299 cells than that in MRC-5 cells.* ***D)*** *miR-130a was increased after the cells were transfected with miR-103a mimic while decreased after in A549 cells.*

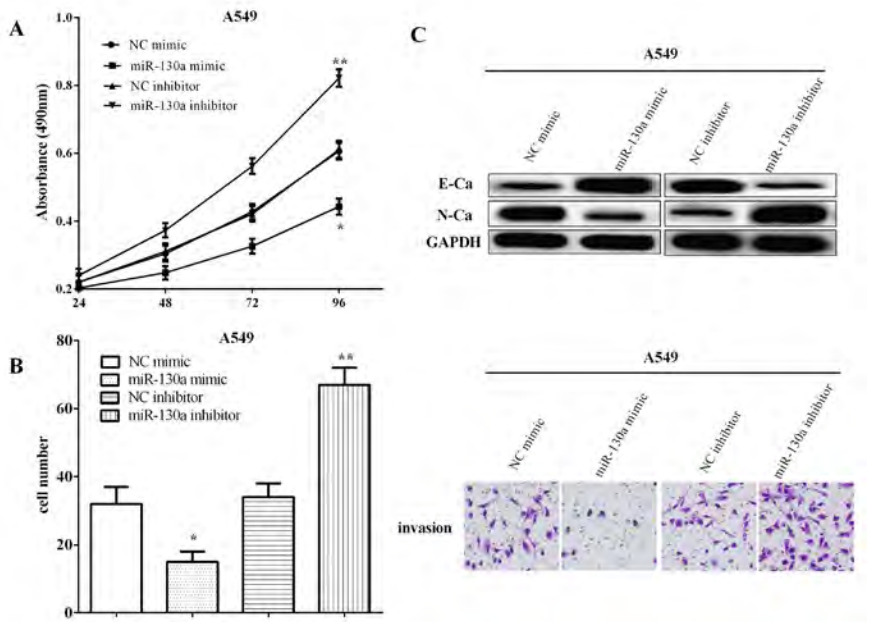


Fig. 2. *MiR-130a suppresses the proliferation, invasion and EMT of lung cancer.* ***A)*** *The proliferation of A549 cells transfected miR-130a mimic was inhibited, but elevated after transfection with miR-130a inhibitor.* ***B)*** *Transwell assay demonstrated that upregulating miR-130a reduced the number of invasive A549 cells, while downregulating miR-130a increased cell invasion.* ***C)*** *MiR-130a could inhibit the EMT of lung cancer cells.*

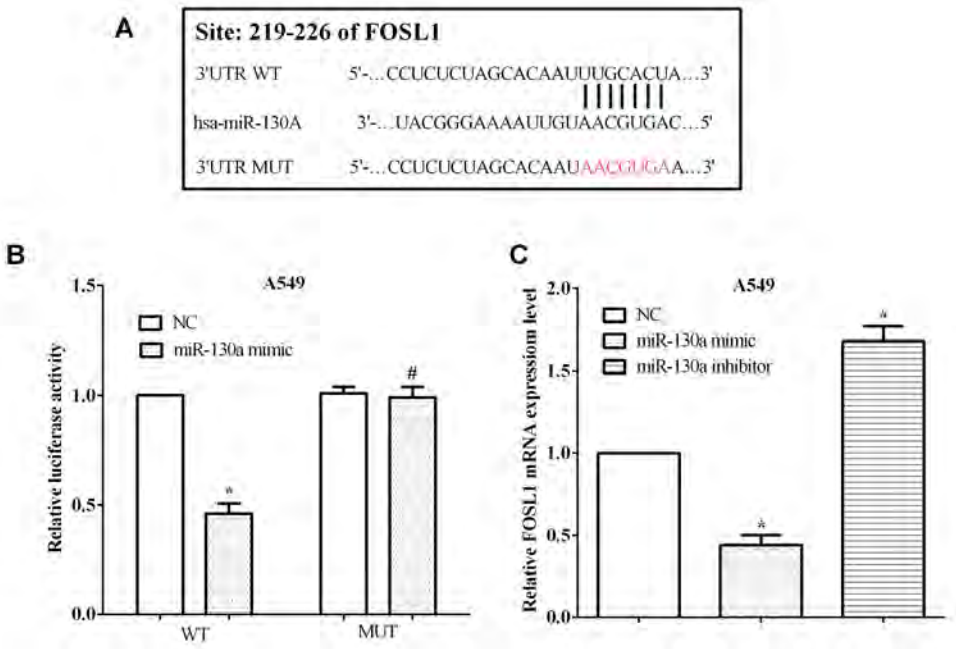


Fig. 3. *MiR-130a targets FOSL1 in lung cancer.* ***A****) FOSL1 was selected as the candidate target of miR-130a for further analysis.* ***B****) The miR-130a mimic reduced the cell luciferase activity that tranfected with wild type mRNA.* ***C****) Transfection of miR-130a mimic impaired the mRNA level of FOSL1 in A549 cells, but on the contrary, miR-130a inhibitor facilitated the FOSL1 expression.*

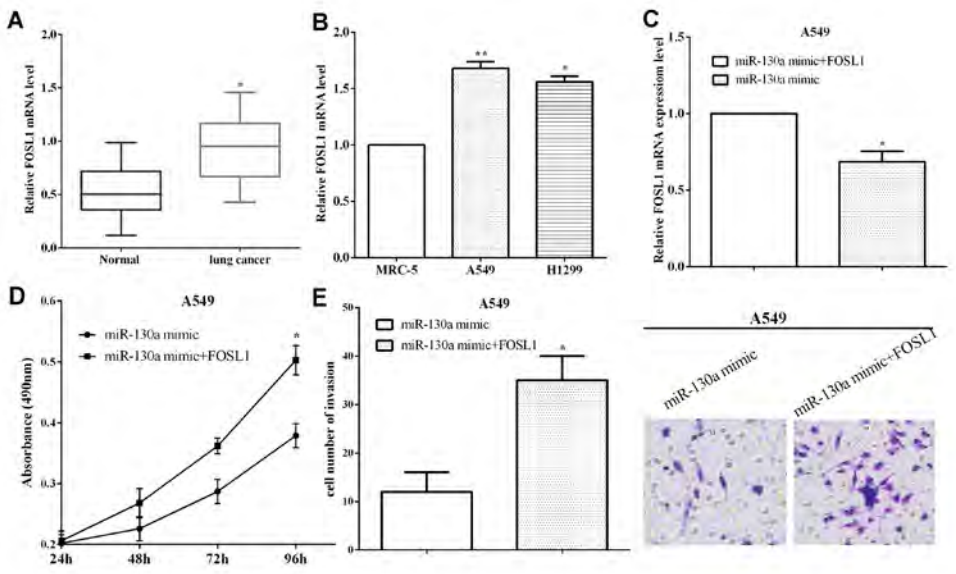


Fig. 4. *FOSL1 partially reversed the tumor-suppressive role of miR-130a on proliferation and metastasis in lung cancer cells.* ***A****) The expression of FOSL1 was higher in lung cancer tissues than that of corresponding normal tissues. B) FOSL1 was overexpressed in lung cancer cell lines compared with normal cell line.* ***C****) Transfection efficiency of co-transfection of miR-130a and FOSL1.* ***D****) FOSL1 reversed partial tumor-suppressive role of miR-130a on the proliferation.* ***E****) FOSL1 reversed partial function of miR-130a on lung cancer cell invasion.*

DISCUSSION

Lung cancer is the most death-causing cancer worldwide, therefore it is important to explore novel biomarkers for its treatment. Accumulating evidence elucidated that miRNAs functioned as oncogenes or tumor-suppressors in tumors (7). miR-130a, acted as tumor suppressor, impaired the migratory and invasive capacity of liver cancer (8). Consistent with all the previous findings, we discovered that miR-130a inhibited the proliferative, migratory and EMT abilities in lung cancer. Furthermore, downregulation of miR-130a predicted poor 5-year overall survival of lung cancer patients. However, in osteosarcoma, miR-130a enhanced cell metastasis and EMT (9). Thus, we deduced that miR-130a may be tissue-specific.

FOSL1 is a member of the Fos gene family, and could activate the trophoblast-specific gene expression in embryonic stem cells (10). FOSL1 has been reported to promote the growth, metastasis and EMT of prostate cancer (11). Consistent with Yu Han, we discovered that FOSL1 was overexpressed in lung cancer tissues and cells. Chen et al. elucidated that FOSL1 was a target gene of miR-130a, and miR-130a suppressed the metastasis of breast cancer through FOSL1 (12). Our results were consistent with the findings in breast cancer, where we found that miR-130a directly targeted FOSL1 and the expression of FOSL1 was mediated by altering miR-130a in A549 cells. We also discovered that miR-130a mediated the viability and migration through FOSL1. FOSL1 partially revealed the functions of miR-130a on the proliferation and migration in lung cancer.

In conclusion, miR-130a was downregulated in lung cancer and the downregulation predicted poor prognosis of lung cancer patients. miR-130a inhibited the viability, migration and EMT by directly binding to FOSL1 in A549 cells. Additionally, FOSL1 reversed partial roles of miR-130a on lung cancer cell viability and metastasis.

REFERENCES

1. Torre LA, F Bray, Siegel RL, Ferlay J, Lortet-Tieulent J, Jemal A. Global cancer statistics, 2012. CA Cancer J Clin 2015; 65(2):87-108.
2. Kloosterman WP, Plasterk RH. The diverse functions of microRNAs in animal development and disease. Dev Cell 2006; 11(4):441-50.
3. Kong X, J Zhang, Li J, Shao J, Fang L. MiR-130a-3p inhibits migration and invasion by regulating RAB5B in human breast cancer stem cell-like cells. Biochem Biophys Res Commun 2018; 501(2):486-93.
4. Wang S, H Han, Hu Y, et al. MicroRNA-130a-3p suppresses cell migration and invasion by inhibition of TBL1XR1-mediated EMT in human gastric carcinoma. Mol Carcinog 2018; 57(3):383-92.
5. Renaud SJ, K Kubota, Rumi MA, Soares MJ. The FOS transcription factor family differentially controls trophoblast migration and invasion. J Biol Chem 2014; 289(8):5025-39.
6. Maurus K, A Hufnagel, Geiger F, et al. The AP-1 transcription factor FOSL1 causes melanocyte reprogramming and transformation. Oncogene 2017; 36(36):5110-21.
7. Lee YS, A Dutta. MicroRNAs in cancer. Annu Rev Pathol 2009; 4:199-227.
8. Liu Y, Y Li, R Wang, et al. MiR-130a-3p regulates cell migration and invasion via inhibition of Smad4 in gemcitabine resistant hepatoma cells. J Exp Clin Cancer Res 2016; 35:19.
9. Chen J, D Yan, Wu W, Zhu J, Ye W, Shu Q. MicroRNA-130a promotes the metastasis and epithelial-mesenchymal transition of osteosarcoma by targeting PTEN. Oncol Rep 2016; 35(6):3285-92.
10. Lee BK, N Uprety, Jang YJ, et al. Fosl1 overexpression directly activates trophoblast-specific gene expression programs in embryonic stem cells. Stem Cell Res 2018; 26:95-102.
11. Luo YZ, P He, Qiu MX. FOSL1 enhances growth and metastasis of human prostate cancer cells through epithelial mesenchymal transition pathway. Eur Rev Med Pharmacol Sci 2018; 22(24):8609-15.
12. Chen X, M Zhao, Huang J, et al. microRNA-130a suppresses breast cancer cell migration and invasion by targeting FOSL1 and upregulating ZO-1. J Cell Biochem 2018; 119(6):4945-56.

LETTER TO THE EDITOR

EFFECTS OF NEGATIVE PRESSURE WOUND THERAPY ASSOCIATED WITH LOCAL INSULIN INJECTION ON TGF-β1 EXPRESSION IN DIABETIC FOOT WOUNDS

YL. HUANG, F. JU, SC. LAI, ZC. CHEN, XY. CHEN, LH. ZHOU and MX. FU

Department of Endocrinology, Second Affiliated Hospital of Hainan Medical College, Haikou City, Hainan Province, China

Received January 13, 2020 – Accepted February 25, 2020

To the Editor,

Diabetic foot (DF) is the most common complication in diabetic patients (1). Currently, the main treatment of DF consists of blood glucose control with debridement, blood flow-improving therapy, and dressing. This treatment procedure is complex and has to be undertaken for a long period, with many disadvantages (1). Ulcerations expose the deep tissues to bacterial colonization with Gram-positive aerobic bacteria, especially *Staphylococcus aureus* and beta-hemolytic *Streptococcus,* which are challenging to eradicate (2). Negative-pressure wound therapy (NPWT) can effectively promote wound healing and prevent wound infection (3). Wang et al. (3) showed that NPWT could promote the growth of granulation tissues filling the wound surface and wound healing. Moreover, clinical studies and animal experiments (4) showed that local insulin injection to DF also improved wound healing. Transforming growth factor-β1 (TGF-β1) is a key cytokine promoting wound healing (5), and mainly acts on the fibroblasts on the wound surface, stimulating the transformation of fibroblasts to myofibroblasts and causing wound shrinkage. In this study, we aimed to investigate the clinical efficacy of NPWT plus local insulin injection for DF, and to study whether the combined treatment promotes wound healing by upregulation of TGF-β1.

MATERIALS AND METHODS

Patients

Thirty-six DF patients were recruited from the Second Affiliated Hospital of Hainan Medical College between May 2018 and May 2019. All cases were randomly divided into an experimental group, that received NPWT plus local insulin injection, and a control group that received NPWT alone, 18 cases in each group. The study was approved by the Ethics Committee of the Second Affiliated Hospital of Hainan Medical College, and each patient signed a consent form to participate in the study. The following indicators were recorded for each patient: age, gender, body mass index (BMI), percentage of patients with hypertension, the evolution of DF, blood glucose levels and glycosylated hemoglobin levels upon admission, ankle-brachial index (ABI), transcutaneous oxygen pressure ($TcPO_2$), fasting blood glucose (FBG), hemoglobin A1c (HbA1c), time of ulceration, liver and kidney functions (serum creatinine and alanine aminotransferase), and the percentage of patients with or without nervous lesions.

Treatment

The wound surface of the feet was debrided in order to be able to remove the tissues without blood supply. For the experimental group, 3 Units of Isophane Protamine Biosynthetic Human Insulin Injection (Novo Nordisk (China) Pharmaceutical Co., Ltd., China) was mixed with

Key words: diabetic foot; negative-pressure wound therapy; insulin; transforming growth factor-β1

Corresponding Author:
Maoxiong Fu,
Department of Endocrinology,
Second Affiliated Hospital of Hainan Medical College,
Longhua District, Haikou City, 5
70311, Hainan Province, China
e-mail: fumaoxiong_haikmd@163.com

0393-974X (2020)
Copyright © by BIOLIFE, s.a.s.
This publication and/or article is for individual use only and may not be further reproduced without written permission from the copyright holder.
Unauthorized reproduction may result in financial and other penalties
DISCLOSURE: ALL AUTHORS REPORT NO CONFLICTS OF INTEREST RELEVANT TO THIS ARTICLE.

5 mL of normal saline and was injected subcutaneously in multi-points at the base and around the wound surface. The control group received the same multi-point injections but with only normal saline. Depending on the dressing used, the vacuum sealing drainage equipment was trimmed to the shape and size of the wound surface. The margin of the drainage equipment was sutured and immobilized to the skin. The drainage equipment was sealed with a semipermeable membrane. The treatment was applied for two weeks when the vacuum sealing drainage equipment was removed. Dressing change was performed for the wound surface until the wound healed.

Sample collection

Samples of granulation tissues were taken from the wound surface in the two groups before and after treatment, respectively. Granulation tissues with a diameter of 6 mm and thickness of 5 mm were collected from the wound surface using a corneal trephine and tissue scissors. Each sample was equally divided into three groups: groups A, B, and C, respectively. Tissues in group A were fixed in 4% paraformaldehyde and preserved at 4°C. The tissues were routinely embedded in paraffin and used for hematoxylin and eosin (HE) staining and immunohistochemistry. Tissues in group B were preserved at -80°C and used for Western blot analysis. Tissues in group C were immediately placed into liquid nitrogen, preserved at -80°C, and directly used for real-time PCR determinations.

HE staining

The paraffin-embedded tissue blocks were dewaxed in xylene (Jiangsu Victory Chemical Co., Ltd., China) for 5-10 min 2 consecutive times. Then the tissue blocks were treated with absolute ethyl alcohol (Shanghai Beyotime Institute of Biotechnology Co., Ltd., China) for 5 min, followed by 90% ethanol for 1 min, 70% ethanol for 2 min and finally with distilled water for 2 min. Next, the tissue blocks were stained with hematoxylin (Chengdu Biyang Biotechnology Co., Ltd., China) for 5-10 min, washed for 2 min in running water and then for 3 min with distilled water and dehydrated in 2 successive baths of 95% ethanol for 20 and 2 min, respectively. After dehydration, the blocks were passed in 2 successive xylene baths for 5 and 5 min. Finally, the sections were sealed with neutral balsam (Beijing Baiaolaibo Technology Co., Ltd., China) and the blocks were analyzed under a microscope (Shanghai Difeng new materials Co., Ltd., China).

Immunohistochemistry

The tissue sections were dewaxed and rehydrated according to the classical protocol. The tissue sections were kept for 5-10 min at room temperature in a mixture of 30% H_2O_2 (Shanghai Yuanxiang Medical Equipment Co., Ltd., China) and distilled water (1:10) and then washed for 3 consecutive times with distilled water. After antigen retrieval (GeneTex, Inc, Irvine, CA, USA), the sections were sealed with 5% BSA (Albumin from bovine serum) sealing solution (Guangzhou Tianjun Biotechnology Co., Ltd., China) at room temperature for 20 min, incubated with primary antibody (rabbit polyclonal TGF - β1 antibody, Beijing zhongshanjinqiao biological Co., Ltd., China), (1:500) at 37°C for 1 h, washed with PBS (Phosphate buffer saline) (Gibco Company, USA) for 3 consecutive times and incubated with the second antibody, biotinylated goat anti-rabbit IgG (Beijing zhongshanjinqiao biological Co., Ltd., China) at 35°C for 20 min. After incubation, the samples were washed with twice with PBS for 2 min each time, SABC (Streptavidin biotin complex) (Beijing baiaolaibo Technology Co., Ltd., China) was added in drops at 35°C for 20 min, followed by washing with PBS (pH 7.2-7.6) for four times, 5 min each time. The samples were colored with DAB (Diaminobenzidine) (Shanghai Xinyu Biotechnology Co., Ltd., China) and counterstained with hematoxylin, dehydrated, transparentized and sealed. The sections were observed under the optical microscope (Shanghai Difeng new materials Co., Ltd., China). Optical density (OD) was analyzed using the digital medical image analysis system (MoticMedical 6.0, Xiamen Motic Software Engineering Co., Ltd). Average OD was used to determine the TGF-β1 levels.

Western blot

100 mg of tissue was homogenized and centrifuged with 500 μL of pre-cooled RIPA lysis buffer (Shanghai Xinyu Biotechnology Co., Ltd., China) and the supernatant was collected. The protein levels were quantified using BCA (Bicinchoninic acid) method. For each channel, 50 μg of protein was taken and sodium dodecyl sulfate-polyacrylamide gel (Beijing Pulilai Gene Technology

Co., Ltd., China) electrophoresis (SDS-PAGE) was performed. The proteins were transferred to the PVDF (Polyvinylidene fluoride) membrane (Beijing baiaolaibo Technology Co., Ltd., China), sealed and incubated with the primary antibodies, rabbit polyclonal TGF - β1 antibody, Rabbit anti-mouse β-actin antibody (Beijing zhongshanjinqiao biological Co., Ltd., China) and then with horseradish peroxidase (HRP)-labeled secondary antibodies (Hefei white shark Biotechnology Co., Ltd., China). Finally, the PVDF membrane was detected by ECL kit (Shanghai Yanxi Biotechnology Co., Ltd., China), exposed and developed in the gel image analyzer.

Real-time Polymerase Chain Reaction

Total RNA extraction was performed from the tissues using the Trizol RNA reagent (Invitrogen Company, USA). Then reverse transcription was performed using All-in-One First-Strand cDNA Synthesis Kit (Gene Copoeia Company, USA) in accordance with the instruction of the manufacturer. The conditions for the reverse transcription were 37°C for 60 min, 85°C for 5 min and followed by storage at 4°C for subsequent use. Finally, Platinum SYBR Greenq PCR SuperMix-UDG (Life Technologies, USA) was used for real-time quantitative PCR, under the following conditions: predenaturation at 95°C for 10 min followed by 95°C for 15 s, 60°C for 1 min, 72°C for 30 s repeated for 4 cycles. Each determination was made in triplicate and the value was calculated as the average of the three determinations. After amplification, SDS V1.3 software (Thermo Fisher Technology Co., Ltd. China) interface was used to set the baseline as the 3rd to the 15th cycles. GAPDH was taken as an internal reference. The first sample of the control group was set as standard 1, and the Ct value of each target gene was calculated in each sample. Relative mRNA expressions were calculated using the $2^{-\Delta\Delta CT}$ method.

Statistical analysis

All experimental data were processed using SPSS 17.0 software (IBM Company, USA), and the results were

Table I. *Baseline information of the patients*

Indicators	Control group	Experimental group	T-value	P-value
Age (year)	63.16±7.41	61.93±8.28	0.131	0.916
Gender (male/female)	11/7	10/8	1.035	0.265
BMI (kg/m^2)	22.78±1.32	23.13±1.76	1.126	0.224
Blood pressure (%)	4(22.22)	6(33.33)	1.732	0.192
Course of disease of DF (week)	4.41±1.64	4.83±2.03	0.474	0.634
Blood glucose level upon admission (mmol/L)	8.74±2.12	9.03±2.25	0.453	0.655
Glycosylated hemoglobin level (%)	6.74±0.36	6.91±0.51	0.514	0.525
ABI	0.61±0.06	0.65±0.03	0.485	0.624
$TcPO_2$(mmHg)	28.23±5.54	29.13±4.41	0.315	0.767
FBG(mM)	8.23±3.84	9.05±3.53	1.822	0.113
HbA_{1c}(%)	10.18±1.87	9.93±2.13	0.635	0.523
Ulcer course(day)	56.17±15.34	58.13±14.57	0.643	0.511
Scr (μM)	57.24±10.24	61.19±11.28	0.812	0.64
ALT (U/L)	11.84±10.18	13.29±11.26	0.662	0.504
Number of patients with neuropathy	15	13	0.28	0.842

ABI: ankle-brachial index; $TcPO_2$: transcutaneous oxygen pressure; Scr: serum creatinine; ALT: alanine aminotransferase.

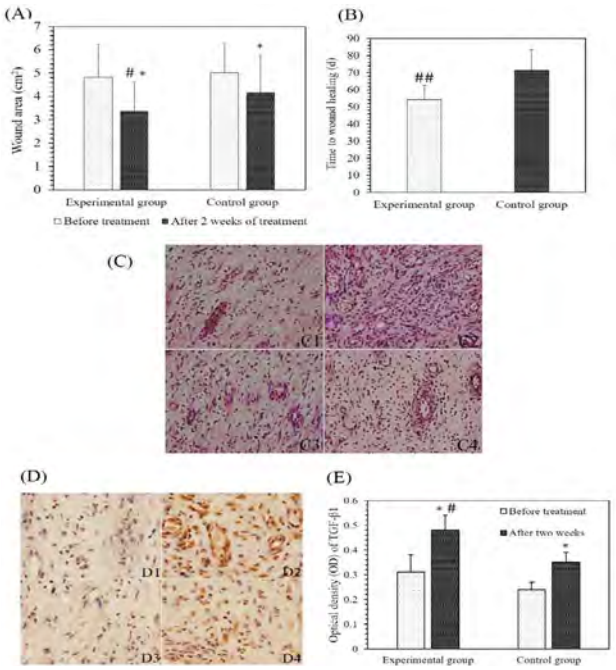


Fig. 1. ***A)*** *The wound area of the two groups before and after treatment, * P < 0.05 compared with the value before the treatment, #P < 0.05 compared with the control group.* ***B)*** *Wound healing time of the two groups, ##P < 0.01 compared with the control group;* ***C)*** *HE staining results: (C1) before treatment in experimental group; C2) two weeks of treatment in experimental group; C3) before treatment in control group; C4) two weeks of treatment in control group; × 400)* ***D)*** *immunohistochemistry chart: (D1) before treatment in experimental group; D2) two weeks of treatment in experimental group; D3) before treatment in control group; D4) two weeks of treatment in control group; × 400).* ***E)*** *Statistical chart of average optical density value, *P < 0.05 compared with the value before treatment, # P < 0.05 compared with the control group.*

expressed as mean±standard deviation. The means of two groups were compared by the independent-samples *t*-test, and P<0.05 was considered for a significant difference.

RESULTS

The two groups of patients showed no significant difference in baseline indicators (P>0.05) (Table I).

Healing of wound surface

The wound area was not significantly different in DF of the two groups before the treatment (P>0.05). After two weeks of treatment, the wound area of the experimental group was significantly decreased compared to the control group (P<0.05). In addition, the average time to wound healing in the experimental group was much shorter than that in the control group (P<0.05) (Fig. 1A and 1B).

HE staining

HE staining of wound surface in DF patients of the two groups before treatment indicated few fresh granulation tissues, few fibroblasts, and few new vessels, but many inflammatory cells. After two weeks of treatment, fresh granulation tissues filled the wound surface, especially in the experimental group, and there were abundant new vessels and fibroblasts (Fig. 1C).

Immunohistochemical detection of TGF-β1 protein expressions

As shown in Fig. 1 D and E, there were few granules indicating positive TGF-β1 expressions in the granulation tissues filling the wound surface in both two groups before treatment. After two weeks of treatment, there were more granulation tissues filling the wound surface, especially in the experimental group. Moreover, the OD of TGF-β1 in the two groups was increased after the treatment compared to the values before the treatment (P<0.05), with a significant increase in the experimental group compared to the control group (P<0.05).

Detection of TGF-β1 protein expressions by Western blot

As shown in Fig. 2 A and B, after two weeks of treatment, the relative TGF-β1 protein expression in the experimental group was significantly increased compared to the expression before treatment (P<0.05). The upregulation was also observed in the control group which received NPWT alone for two weeks (P<0.05). The relative TGF-β1 protein expression in the experimental group changed more significantly than in the control group (P<0.05).

Real-time PCR detection of the TGF-β1 mRNA expression

After two weeks of combined treatment, the relative TGF-β1 mRNA expression in the experimental group was significantly increased

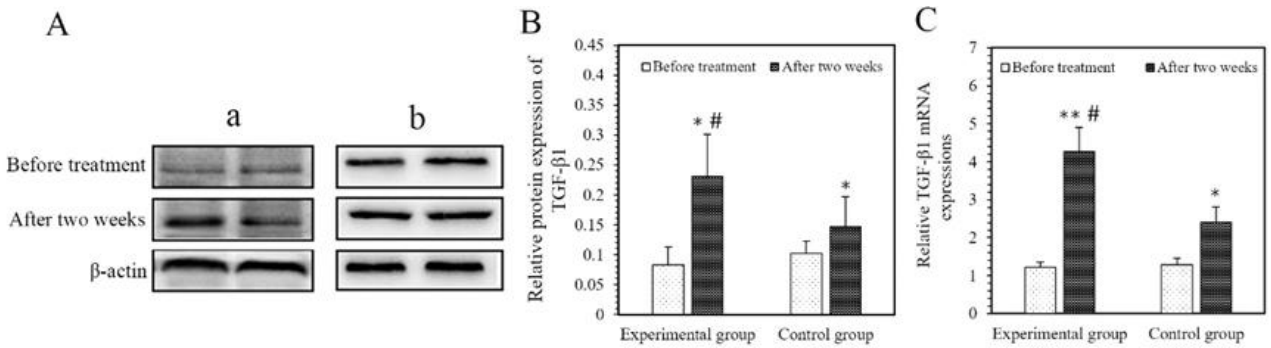


Fig. 2. *Western Blot detection of the TGF-β1 protein expression.* ***A****) Western blot diagram (a) Experimental group; b) Control group);* ***B****) Statistics of the relative TGF-β1 protein expression, *P<0.05, compared with the value before the treatment; #P < 0.05 compared with the control group);* ***C****) Relative TGF-β1 mRNA expressions. *P<0.05, compared with the value before the treatment; #P < 0.05 compared with the control group.*

compared with the value before the treatment (P<0.05). In the control group, after two weeks of treatment only with NPWT, the relative TGF-β1 mRNA expression in the control group was also significantly upregulated (P<0.01), but the increase was significantly higher in the experimental group compared to the control group (P<0.05).

DISCUSSION

Delayed wound healing in DF patients involves a very complex mechanism. Giangreco et al. (6) showed that the degree of re-epithelization of skin wounds during the healing process mainly depended on the normal proliferation of epithelial cells. Branski et al. (7) found that after glycation of type I and IV collagen, the adhesion and proliferative capacities of the epidermal stem cells is inhibited. TGF-β1 downregulation, functional abnormalities, and irregular signal expressions were observed during wound repair in DF (5).

NPWT can promote the growth of granulation tissues and wound healing in DF by facilitating local cytokine synthesis and cell proliferation of the wound surface, relieving local wound edema and bacterial load, and improving the local wound microenvironment (8).

Insulin, as one of the most important hormones in humans, not only facilitates the oxygenation and glycolysis of glucose but also promotes matter synthesis and storage in the liver. In addition, insulin also has an anti-inflammatory effect and promotes cell proliferation and differentiation (9). Local insulin use regulates glucose metabolism, generates energy, accelerates local vascularization, and promotes fibroblast growth and collagen synthesis and can promote wound healing.

We showed that NPWT plus local insulin had a much better clinical effect than NPWT alone in facilitating wound healing in DF patients. Moreover, the combined treatment increased the form of the new granulation tissues and increased the local TGF-β1 expression in both the protein and gene levels. The above findings provide specific theoretical support for the clinical use of NPWT with local insulin injection for the wound surface of DF.

REFERENCES

1. Zhang P, Lu J, Jing Y, Tang S, Zhu D, Bi Y. Global epidemiology of diabetic foot ulceration: a systematic review and meta-analysis (dagger). Ann Med 2017; 49(2):106-16.
2. Calina D, Docea AO, Rosu L, et al. Antimicrobial resistance development following surgical site infections. Mol Med Rep 2017; 15(2):681-88.
3. Wang J, Zhang H, Wang S. Application of vacuum sealing drainage in the treatment of internal fixation instrument exposure after early postoperative infection. Minerva chirurgica 2015; 70(1):17-22.

4. Lima MH, Caricilli AM, de Abreu LL, et al. Topical insulin accelerates wound healing in diabetes by enhancing the AKT and ERK pathways: a double-blind placebo-controlled clinical trial. PLoS One 2012; 7(5):e36974.
5. Wang L, Qin W, Zhou Y, et al. Transforming growth factor beta plays an important role in enhancing wound healing by topical application of Povidone-iodine. Sci Rep 2017; 7(1):991.
6. Giangreco A, Goldie SJ, Failla V, Saintigny G, Watt FM. Human skin aging is associated with reduced expression of the stem cell markers beta1 integrin and MCSP. J Invest Dermatol 2010; 130(2):604-8.
7. Branski LK, Gauglitz GG, Herndon DN, Jeschke MG. A review of gene and stem cell therapy in cutaneous wound healing. Burns 2009; 35(2):171-80.
8. Sepulveda G, Espindola M, Maureira M, et al. [Negative-pressure wound therapy versus standard wound dressing in the treatment of diabetic foot amputation. A randomised controlled trial]. Cir Esp 2009; 86(3):171-77.
9. Wentworth JM, Naselli G, Brown WA, et al. Pro-inflammatory CD11c+CD206+ adipose tissue macrophages are associated with insulin resistance in human obesity. Diabetes 2010; 59(7):1648-56.

JOURNAL OF BIOLOGICAL REGULATORS & HOMEOSTATIC AGENTS Vol. 34, no. 2, 565-570 (2020)

LETTER TO THE EDITOR

INFLUENCE OF DIABETES MELLITUS ON TOOTH ERUPTION AND OCCURRENCE OF MALOCCLUSION

A. ALMOUSA, M.A. KAMRAN, A. ALSHAHRANI and I. ALSHAHRANI

Department of Pedodontics and Orthodontics Sciences, College of Dentistry, King Khalid University, Abha, Saudi Arabia

Received February 7, 2020 – Accepted February 27, 2020

To the Editor,

According to the American Diabetes Association, Diabetes mellitus (DM) is a group of metabolic diseases characterized by hyperglycemia resulting from defects in insulin secretion, insulin action, or both (1). The chronic hyperglycemia of diabetes is associated with long-term damage, dysfunction, and failure of organs, especially the eyes, kidneys, nerves, heart, and blood vessels (1). DM is a growing public health concern throughout the world and is a common chronic metabolic disease worldwide (1). Moreover, the World Health Organization (WHO) has recently declared it to be a pandemic (2). Periodontal diseases have been proposed as the sixth most prevalent complication of DM (3).

Oral manifestations of DM includes salivary dysfunction leading to a reduction in salivary flow and changes in saliva composition and taste dysfunction (4). Oral mucosa lesions, such as stomatitis, geographic tongue, benign migratory glossitis, fissured tongue, traumatic ulcers, lichen planus, lichenoid reaction and angular cheilitis, are not uncommon in diabetic patients (3). There is conclusive evidence on the role of hyperglycemia-associated periodontal destruction documented in the medical and dental literature, however, little information is available about the effects of diabetes on tooth eruption and prevalence of malocclusion (4). A recent study by Sarmamy et al. reported accelerated dental development in diabetic children who were younger than 11.5 years, whereas older children with diabetes exhibited a delay in dental development (5). Moreover, a study by Zeigler and Neu observed a similar dual effect of the diabetes on tooth development and eruption (6). Lal et al. found a small and non-significant influence of diabetes on dental development and tooth eruption (7). Most of the available data on diabetes and malocclusion is heterogenous and there are no studies carried out in the region of the Kingdom of Saudi Arabia (KSA). Therefore, the present study was designed with the intention to evaluate tooth eruption and prevalence of malocclusion in children with diabetes in the region of Abha KSA.

MATERIALS AND METHODS

The present study was approved by the ethics committee of King Khalid University with ethical approval project no. E-158747. A case-control study was conducted to evaluate the effect of diabetes on tooth eruption and prevalence of malocclusion in 8 to 16-year-old children with Type I Diabetes Mellitus in the Asir region of Saudi Arabia. Tooth eruption and malocclusion were assessed for 100 children with mixed dentition: 50 with Type I diabetes (25 males, 25 females) and 50 controls without

Key words: diabetes mellitus; tooth eruption; malocclusion; children

Corresponding Author:
Dr. Ibrahim Alshahrani,
Department of Pedodontic and Orthodontic Sciences,
College of Dentistry,
King Khalid University,
Abha, Saudi Arabia
e-mail: ishahrani@kku.edu.sa

0393-974X (2020)
Copyright © by BIOLIFE, s.a.s.
This publication and/or article is for individual use only and may not be further reproduced without written permission from the copyright holder.
Unauthorized reproduction may result in financial and other penalties
DISCLOSURE: ALL AUTHORS REPORT NO CONFLICTS OF INTEREST RELEVANT TO THIS ARTICLE.

diabetes (20 males, 30 females), examined at King Khalid University, College of Dentistry, Abha, KSA. Subjects undergoing active orthodontic treatment and those with missing teeth were excluded from the study. The chronological age of each child was determined from the actual date of birth as per school records. The medical record provided necessary data regarding the type of diabetes, blood glucose levels, and mean glycosylated hemoglobin (HbA1c). Each participant (subject/legal guardian/parent) provided informed consent before participation. The study was conducted over a period of four months from May 2019 to September 2019. To access the eruption status, orthopantomogram (OPG) was taken for each of the children to measure the position of the second premolar. Occlusal plane and the mandibular plane were used as lines of reference and the buccal cusp tip of the premolar as the point of measurement by using the same X-ray machine emitting radiation level which was within the permissible level (Fig. I). To access the prevalence of malocclusion, data was collected from clinical examination by using a diagnostic form (Table I) and from diagnostic casts which were made with an irreversible hydrocolloid and poured with type III dental stone for each patient. Molar and canine relationship, presence of spacing, crowding, open bite (anterior) and cross bite (anterior and posterior), as well as measurement of overjet and overbite were noted for each subject. At the end of the examination, each patient received dental advice, an oral prophylaxis, and was offered the necessary oral care. Statistical analysis was carried out using SPSS and Student's *t*-test for significant differences between case and control populations. The data of the study were tabulated and analyzed using Student's *t*-test at a confidence level of 95%. Significance was seen in cases where the p-value was less than 0.05.

RESULTS

Effect on eruption

When the distance of the premolar cusp tip from the occlusal plane was analyzed in both normal and diabetic patients for tooth #35 (p=0.49) and tooth #45 (p=0.53), there was no statistically significant difference seen (Table II). When the distance of the premolar cusp tip from the occlusal plane was analyzed in both the male (p=0.08) and female (p=0.16) patients, there was no statistically significant difference (Table III). When the distance of the premolar cusp tip from the mandibular plane was analyzed between normal and diabetic patients for tooth #35 (26.29±6.8mm and 34.36±7.8mm) (p=0.00) and #45 (26.99±7.5mm and 34.43±7.4mm) (p=0.00) a statistically significant difference was seen. As per this statistical data, teeth of diabetic patients (premolars in this study) were far away from the mandibular plane and thus closer to eruption. Therefore, children with diabetes exhibited accelerated tooth eruption in the late mixed dentition period and were ahead of healthy children (Table III). When the distance of the premolar cusp tip from the mandibular plane was analyzed between male and female patients for tooth #35 (p=0.51) and # 45 (p=0.27), no statistically significant difference was seen (Table III).

Prevalence of malocclusion

The first set of analyses compared the difference in the molar and canine relationship between the two groups. The diabetic group reported significantly more class I molar/canine relationship than the control groups. Class II and class III molar/canine relationship were found to be more in control group than in the diabetic group (Table III). Statistical analysis of overjet and overbite bite showed insignificant association (p value>0.05) between diabetic and control groups (Table IV). Insignificant statistical association was found (p>0.05) when comparing anterior open bite in diabetic patient and control group as shown in Table IV. Anterior cross bite is a malocclusion resulting from lingual positioning of maxillary anterior teeth in relation to the mandibular anterior teeth. The anterior cross bite was presented equally in diabetic patients and the control group and no statistical significance was found (p=1) as presented in Table IV.

The posterior crossbite is an inadequate transversal relationship of maxillary and mandibular teeth. Statistical analysis of posterior crossbite depicted insignificant association between the two groups (p>0.05) (Table IV). The last dental malocclusion examined was spacing and crowding. Statistical analysis revealed insignificant association

between the diabetic and control groups ($p>0.05$) (Table IV). Statistical data analyzing the prevalence of malocclusion in diabetic and control groups suggested that there was no association between the acceleration of dentition in the diabetic patient and the development of malocclusion.

DISCUSSION

In the present study, children with diabetes showed accelerated tooth eruption as compared to the control group. These results are in agreement with Ferizi et al., (8) who reported accelerated tooth eruption among 6-14-year-old diabetic children as well as an increased gingival inflammation. Moreover, Carneiro et al. (9) also found accelerated tooth eruption among diabetic patients accompanied by increased gingival calculus and plaque indices among type I diabetes mellitus children compared to the control group. Furthermore, Novotna et al. (10) found accelerated tooth eruption in the late mixed dentition period (10-14 years of age) compared to healthy

Table I. *Classification of Diabetes according to the American Diabetes Association*

Type of Diabetes	Pathogenesis
Type 1 Diabetes Mellitus	Autoimmune β-cell destruction, usually leading to absolute insulin deficiency. The manifestations are seen in children, adolescents and young adults.
Type 2 Diabetes Mellitus	Progressive insulin secretory defect on the background of insulin resistance). The manifestations are mainly seen in middle and old age.
Gestational Diabetes Mellitus (GDM)	Hormonal change. GDM is diagnosed in the second or third trimester of pregnancy; usually resolves after pregnancy.
Specific types of diabetes due to other causes	• Monogenic diabetes syndromes (such as neonatal diabetes and maturity-onset diabetes of the young [MODY]) • Diseases of the exocrine pancreas (such as cystic fibrosis) • Drug- or chemical-induced diabetes (such as in the treatment of HIV/AIDS or after organ transplantation

Table II. *Diagnostic form for clinical examination*

Molar Relationship	Canine Relationship	Spacing and Crowding	Overjet and Overbite	Anterior open bite	Anterior cross bite	Posterior cross bite
Class I Class II Class III	Class I Class II Class III	Maxilla (anterior and posterior segment) Mandible (anterior and posterior segment	0 mm 1-3 mm 4-6 mm >6 mm	No open bite 1-3 mm 4-6mm >6 mm	Present Absent	No crossbite Unilateral Bilateral Scissor bite

Table III. *Distances between second premolars from the occlusal plane and from the mandibular plane in males and females in the diabetic and control groups.*

Premolar	Condition	n	Mean	SD	df	t-value	p-value
35-Occlusal	Normal	50	9.949	6.7339	97	0.69	0.492
	Diabetic	49	8.9143	8.14072			
45-Occlusal	Normal	50	9.3454	5.92628	97	0.631	0.530
	Diabetic	49	8.451	8.03944			
Premolar	**Gender**						
35-Occlusal	Male	44	10.9002	6.40901	97	1.769	0.080
	Female	55	8.2662	8.0434			
45-Occlusal	Male	44	9.993	6.36574	97	1.387	0.169
	Female	55	8.0305	7.46159			
Premolar	**Condition**						
35-Mandibular	Normal	50	26.2932	6.87182	97	-5.429	0.000*
	Diabetic	49	34.3653	7.89719			
45-Mandibular	Normal	50	26.9972	7.55743	97	-4.934	0.000*
	Diabetic	49	34.4347	7.43907			
Premolar	**Gender**						
35-Mandibular	Male	44	29.6684	8.42771	97	-0.655	0.514
	Female	55	30.7845	8.42765			
45-Mandibular	Male	44	29.6395	8.77234	97	-1.109	0.270
	Female	55	31.5095	7.96913			

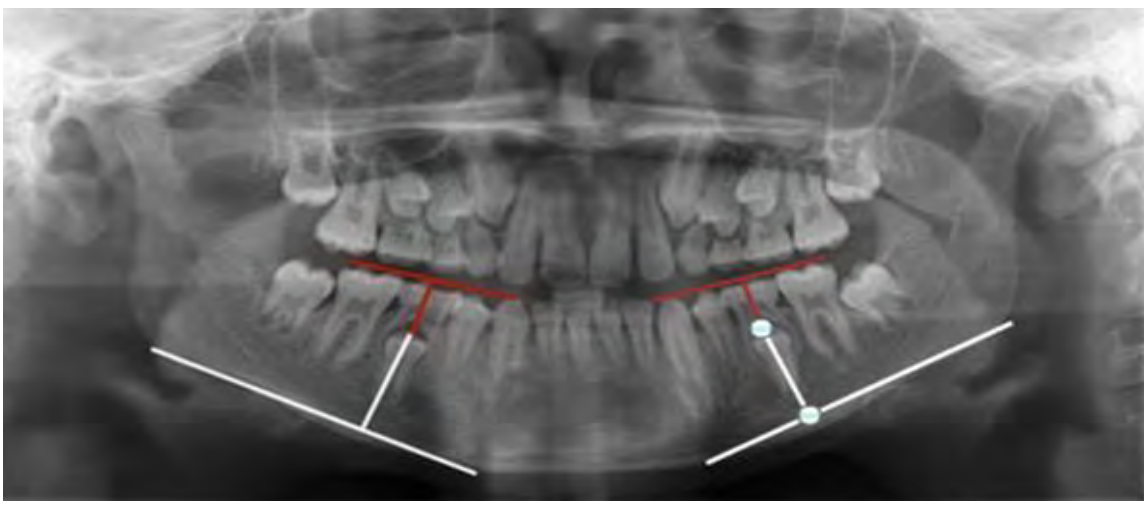


Fig. I. *OPG showing position of right mandibular second premolar from the occlusal and mandibular plane*

Table IV. *Comparison of molar and canine relationship, and different bites between the diabetic group and control group.*

Premolar	Condition	n	Mean	SD	df	t-value	p-value
35-Occlusal	Normal	50	9.949	6.7339	97	0.69	0.492
	Diabetic	49	8.9143	8.14072			
45-Occlusal	Normal	50	9.3454	5.92628	97	0.631	0.530
	Diabetic	49	8.451	8.03944			
Premolar	**Gender**						
35-Occlusal	Male	44	10.9002	6.40901	97	1.769	0.080
	Female	55	8.2662	8.0434			
45-Occlusal	Male	44	9.993	6.36574	97	1.387	0.169
	Female	55	8.0305	7.46159			
Premolar	**Condition**						
35-Mandibular	Normal	50	26.2932	6.87182	97	-5.429	0.000*
	Diabetic	49	34.3653	7.89719			
45-Mandibular	Normal	50	26.9972	7.55743	97	-4.934	0.000*
	Diabetic	49	34.4347	7.43907			
Premolar	**Gender**						
35-Mandibular	Male	44	29.6684	8.42771	97	-0.655	0.514
	Female	55	30.7845	8.42765			
45-Mandibular	Male	44	29.6395	8.77234	97	-1.109	0.270
	Female	55	31.5095	7.96913			

children. The reason for accelerated tooth eruption might be due to increased gingival inflammation in diabetic patients, which diminish the mass of bones supporting the tissues, shortening the distance that developing teeth need to progress to erupt through the gums. Malocclusion has a significant effect on oral functions such as swallowing, chewing and speech, as well as less esthetic facial appearances and increased risk for oral disease such as trauma, tooth decay, and periodontal disease (11). Although some minor malocclusions might be an esthetic concern, this may have a strong psychosocial effect on the individual, including altered self-esteem, social and interaction responses, and increased awareness of people's perceptions (12). The current study showed no association between the acceleration of dentition in the diabetic patient and the malocclusion. Future studies with a higher sample size and limited age group need to ascertain the role of diabetes in the development of such aberrations. Within the limitations of the study, better understanding of the biological and clinical effects of diabetes mellitus on the prevalence of malocclusion is something worth pursuing. Moreover, studies should be directed on the influence of other systemic diseases and their effect on malocclusion.

In conclusion, children with diabetes exhibit accelerated tooth eruption. Type I DM is more often encountered in younger patients who more frequently need orthodontic, restorative and periodontal treatment. It is of paramount importance for a pediatric dentist to diagnose altered eruption pattern in order to preserve such teeth on a long-term basis thus preventing untimely extractions and future orthodontic treatment. More *in-vivo* studies determining the effects of accelerated dental

development on complications such as malocclusion, crowding, impaired oral hygiene, and periodontal disease need to be ascertained

ACKNOWLEDGEMENT

The authors extend their appreciation to the Deanship of Scientific Research at King Khalid University for funding this work through General Research Project under grant number (G.R.P 159-41).

REFERENCES

1. Punthakee Z, Goldenberg R, Katz P. Definition, classification and diagnosis of diabetes, prediabetes and metabolic syndrome. Can J Diabetes 2018; 42:S10-S15. doi:10.1016/j.jcjd.2017.10.003
2. American Diabetes Association. Diagnosis and classification of diabetes mellitus, ADA Clinical Practice Recommendations. Diabetes Care 2013; 36(Suppl 1):S67-74. doi:10.2337/dc13-S067
3. Barceló A, Rajpathak S. Incidence and prevalence of diabetes mellitus in the Americas. Rev Panam Salud Publica/Pan Am J Public Heal 2001; 10(5):300-308. doi:10.1590/S1020-49892001001100002
4. Saini R, Saini S, Sugandha R. Periodontal disease: The sixth complication of diabetes. J Fam Community Med 2011; 18(1):31. doi:10.4103/1319-1683.78636
5. Sarmamy H, Saber S, Majeed V. The influence of type I diabetes mellitus on dentition and oral health of children and adolescents attending two diabetic centers in Erbil city. Zanco J Med Sci 2012; 16(3):204-212. doi:10.15218/zjms.2012.0036
6. Ziegler R, Neu A. Diabetes in childhood and adolescence - A guideline-based approach to diagnosis, treatment, and follow-up. Dtsch Arztebl Int 2018; 115(9):146-56. doi:10.3238/arztebl.2018.0146
7. Lal S, Cheng B, Kaplan S, et al. Accelerated tooth eruption in children with diabetes mellitus. Pediatrics 2008; 121(5). doi:10.1542/peds.2007-1486
8. Ferizi L, Dragidella F, Spahiu L, Begzati A, Kotori V. The influence of type 1 diabetes mellitus on dental caries and salivary composition. Int J Dent 2018; 18(4). doi:10.1155/2018/5780916
9. Carneiro VL, Fraiz FC, Ferreira F de M, Pintarelli TP, Oliveira ACB, Boguszewski MC da S. The influence of glycemic control on the oral health of children and adolescents with diabetes mellitus type 1. Arch Endocrinol Metab 2015; 59(6):535-40. doi:10.1590/2359-3997000000117
10. Novotna M, Podzimek S, Broukal Z, Lencova E, Duskova J. periodontal diseases and dental caries in children with type 1 diabetes mellitus. Mediators Inflamm 2015; 25(5). doi:10.1155/2015/379626
11. González-Serrano J, Serrano J, López-Pintor RM, Paredes VM, Casañas E, Hernández G. Prevalence of oral mucosal disorders in diabetes mellitus patients compared with a control group. J Diabetes Res 2016; 2016. doi:10.1155/2016/5048967
12. Raghavan S, Philip K, Batra P, Marcusson A. Aesthetic perceptions and psychosocial impact of malocclusion: Comparison between cleft and non-cleft patients and their parents. Eur J Orthod 2019; 41(1):38-45. doi:10.1093/ejo/cjy022.

EXPRESSION LEVELS OF ALPHA-SMOOTH MUSCLE ACTIN IN INTRARENAL ARTERIOLES OF PATIENTS WIT INTRARENAL ARTERIOLES OF PATIENTS WITH DIFFERENT STAGES OF CHRONIC KIDNEY DISEASE

ZQ. ZHOU, HH. YANG, GZ. CUI, CF. WANG, XF. ZHENG, XF. WANG, J. LIU and HL. LI

Department of Nephrology, Xixi Hospital of Hangzhou (Hangzhou Xixi Affiliated Hospital of Zhejiang Chinese Medical University), Hangzhou, Zhejiang Province, China

Received November 27, 2019 – Accepted February 28, 2020

To the Editor,

In recent years, the incidence of chronic kidney disease (CKD) has been gradually rising yearly due to the increased prevalence of obesity, hypertension, and diabetes (1). Renal fibrosis is the main pathological basis for CKD, while chronic renal failure (CRF) is the final result of CKD. Renal fibrosis includes glomerular sclerosis and renal interstitial fibrosis (RIF) (2). A large number of studies have shown that RIF contributes more to the progression of CKD compared to glomerular lesions (3). However, renal interstitium, tubules, and glomeruli are all involved in the process of fibrosis, in which inflammatory factors, growth factors, adhesion molecules, and other active substances induce phenotypic transformation of renal mesenchymal fibroblasts, tubular epithelial cells, or mesangial cells, and produce myofibroblasts (MyoF) positive for alpha-smooth muscle actin (α-SMA) (4). MyoF can proliferate massively, synthesize collagen I, secrete a large amount of extracellular matrix (ECM), and suppress the degradation of ECM, leading to excessive accumulation of ECM, which plays a key role in the development of renal fibrosis (5). α-SMA is a marker of damaged activation and phenotypic transformation of fibroblasts. As a specific marker of MyoF, α-SMA may also be a predicting factor of RIF progression (6). Some data showed that in normal blood vessels without obvious calcium salt deposition, the expression of α-SMA was high and mainly distributed throughout the entire vascular layer, but was significantly decreased in blood vessels with obvious calcium salt deposition (7). Carotid intima thickening is a marker for the occurrence of cardiovascular diseases. In the present study, different expression levels of α-SMA in intrarenal arterioles of patients with CKD at different stages were detected, and the relationship between intima-media thickness (IMT) and the expression of α-SMA in intrarenal arterioles was analyzed. Moreover, cardiovascular events were predicted by detecting α-SMA levels in renal tissues during renal biopsy.

MATERIALS AND METHODS

From February 2018 to July 2019, 76 CKD patients were admitted to Xixi Hospital of Hangzhou hospital and CKD was diagnosed by renal biopsy, including 25 patients with stage 1, 22 patients with stage 2, 18 patients with stage 3, and 11 patients with stage 4. Kidney tissues were collected from each patient and the paraffin-embedded sections were prepared and preserved

Key words: chronic kidney disease; intrarenal arterioles; renal interstitial; α-SMA; fibrosis

Corresponding Author:
Dr Huili Li,
Department of Nephrology,
Xixi Hospital of Hangzhou (Hangzhou Xixi Affiliated Hospital of Zhejiang Chinese Medical University),
Hangzhou, 310023, Zhejiang Province, China
e-mail: lihuililhl7078@163.com

0393-974X (2020)
Copyright © by BIOLIFE, s.a.s.
This publication and/or article is for individual use only and may not be further reproduced without written permission from the copyright holder.
Unauthorized reproduction may result in financial and other penalties
DISCLOSURE: ALL AUTHORS REPORT NO CONFLICTS OF INTEREST RELEVANT TO THIS ARTICLE.

for subsequent use. All patients in this study signed an informed consent and the study was approved by the Ethics Committee of Xixi Hospital of Hangzhou.

The height and fasting weight of the subjects were measured to calculate their body mass index (BMI). Within 24 h after admission, hematuria samples were collected for determination of corresponding biochemical indicators. After at least 10 min of quiet rest, the blood pressure of the brachial artery in the right upper arm was measured and the systolic and diastolic blood pressure was recorded. PHLIP SIE33 ultrasonic doppler probe with a frequency of 8-14 MHz and high resolution was used to determine the maximum mean intima-media thickness at the bifurcation of the common carotid artery. According to the reference standard, IMT>1.0mm was judged as arterial wall thickening.

Specimen processing

After formalin-aceto-alcohol (FAA) fixation, the kidney tissues were continuously sectioned by a paraffin embedding slicer to a thickness of 2 μm, and the slices were placed in a water bath. The slices were retrieved and placed in a thermostatic oven for baking at 60°C.

PAS staining

Xylene was used for dewaxing and gradient alcohol was used for hydration, after which the slides were rinsed with tap water. Periodate was added onto the slides for 10 min of oxidization reaction, and the samples were washed with tap water for 3 min. Schiff reagent was added dropwise for 10 min of incubation, and the samples were washed with tap water for 3 min. The samples were then stained with Mayers hematoxylin for 6 min and washed with tap water for 3 min. Then, the samples were differentiated with 1% hydrochloric acid alcohol for 2 s and washed with tap water for 3 min. In the next step, the samples were stained blue for 20 s in 1% ammonia water and washed with tap water for 3 min, after which they were dehydrated with gradient alcohol, treated with xylene for 1-2 min, and sealed in a neutral gum; their pathological changes were observed under a light microscope.

Expression of a-SMA in renal tissues detected by immunohistochemical staining

Sections were routinely dewaxed by water, treated with hydrogen peroxide in a light-proof wet box for 10 min, and washed with phosphate buffered saline (PBS) for 3 times ×5min/each. The sections were then placed in a specimen box containing a citric acid repair solution, boiled for 1 min and cooled to room temperature. A goat serum blocking solution was added to the slices to block them at room temperature for 15 min. The excess liquid was removed, and the diluted primary antibody was added and incubated at 25°C for 2 h. After PBS washing three times, 5 min each time, the biotinylated secondary antibody was added to the samples and incubated at 37°C for 15 min before the samples were washed with PBS for 3 times × 5min/each time. Then, a horseradish peroxidase-labeled streptomycin working solution was added to the samples and incubated at 37°C for 20 min, and washed with PBS for 3 times × 5min/each time. The samples were developed with a 3,3'-diaminobenzidine (DAB) color developer for 6 min and washed with tap water for 5 min. The nucleus was counterstained with hematoxylin for 5 min and washed thoroughly with water. Then, the samples were differentiated with 1% hydrochloric acid alcohol, stained blue with 1% amine water, and fully washed. They were then dehydrated, made transparent, and mounted. The samples were observed under a microscope, and the expression levels of α-SMA in the arterial wall and interstitial renal tissues were quantitatively analyzed by Image-Pro Plus 6.0.

Expression of a-SMA in renal tissues detected by immunoblotting

Total protein of renal tissues was extracted, and the protein concentration was determined by the bicinchoninic acid (BCA) method. According to the protein concentration, a suitable amount of concentrated 4 × sodium dodecyl sulfate polyacrylamide gel electrophoresis (SDS-PAGE) protein loading buffer was added to the protein samples before protein boiling and denaturation. After cooling to room temperature, the same amounts of protein samples were loaded into the sample wells of

an SDS-PAGE gel, followed by 90 min of SDS-PAGE electrophoresis and 30 min of membrane transfer. After being blocked in a 5% skim milk powder/TBST (TBS+Tween, TBS: Tris-Buffered Saline) blocking solution for 1 h, the membranes were incubated with α-SMA antibody overnight, followed by incubation with horseradish peroxidase (HRP) secondary antibody and electro-chemi-luminescence (ECL) development. After film exposure, an Image J Image analysis system was used for analysis.

Statistical analysis

SPSS 19.0 statistical software was used and the measurement data were expressed as ($\bar{x}$±s). *t*-test was used for the comparison between two groups, and analysis of variance was used for the comparison among multiple groups. Rank sum test was used for data that could not be analyzed by the analysis of variance. The correlation between two parameters was analyzed by Pearson correlation and $P<0.05$ was considered statistically significant.

RESULTS

General clinical data of patients in each period are shown in Table I.

Immunohistochemistry and PAS staining

As seen in Fig. 1 and Table II, there were significant differences in optical density (AOD)

Table I. *Statistics of general clinical data of patients in each group*

Index	CKD1	CKD2	CKD3	CKD4
BMI (kg/m^2)	23.92±1.23	24.14±1.15	24.34±1.64	23.41±1.35
FBG (mmol/L)	4.74±1.08	4.63±0.95	4.75±1.15	4.96±0.97
TG (mmol/L)	2.90±0.63	2.65±0.49*	2.28±0.52$^{*\#}$	1.41±0.68$^{**\#\&\&}$
TC (mmol/L)	5.88±1.36	5.27±1.38*	4.62±1.65$^{*\#}$	4.15±1.83$^{**\#\&\&}$
HDL-C (mmol/L)	1.17±0.25	1.32±0.33	1.12±0.41	0.96±0.38
Systolic blood pressure (mmHg)	127.24±14.29	140.15±11.43*	154.19±10.38$^{**\#\#}$	165.74±14.39$^{**\#\#\&\&}$
Diastolic blood pressure (mmHg)	75.84±9.25	86.28±7.95*	99.04±8.49$^{**\#\#}$	110.37±10.04$^{**\#\#\&\&}$
Serum creatinine (μmol)	68.75±6.46	137.28±16.39**	284.29±23.48$^{**\#\#}$	403.28±28.73$^{**\#\#\&\&}$
24h urine protein quantification (g/d)	5.18±2.22	3.38±2.15**	3.81±1.05$^{**\#}$	2.31±1.53$^{**\#\#\&\&}$
Blood potassium (mmol/L)	4.38±1.16	4.71±1.18*	4.99±1.27$^{*\#}$	5.78±1.53$^{**\#\#\&}$

Note: $^{*}P<0.05$, $^{**}P<0.01$, compared to CKD1 group; $^{\#}P<0.05$, $^{\#\#}P<0.01$, compared to CKD2 group; $^{\&}P<0.05$, $^{\&\&}P<0.01$, compared to CKD3 group

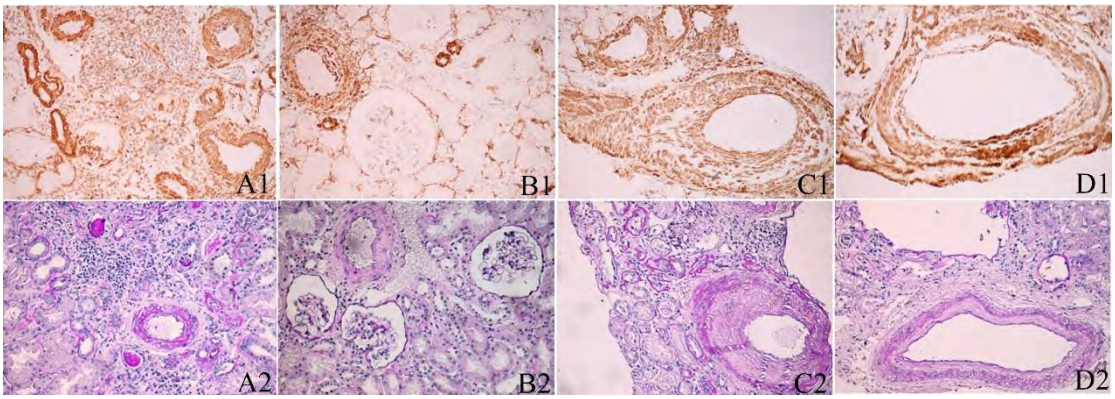


Fig. 1. *Results of immunohistochemistry and PAS staining. 1) immunohistochemical staining results, ×100; 2) results of PAS staining, ×100; **A**) CKD1 group; **B**) CKD2 group; **C**) CKD3 group; **D**) CKD4 group.*

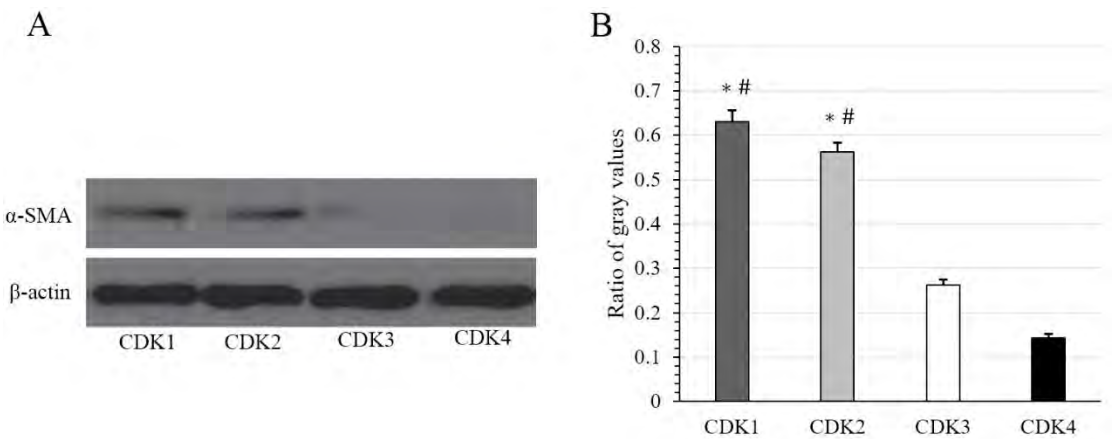


Fig. 2. *The expression of α-SMA protein in renal tissues of patients with CKD. **A**) Western blot results; **B**) statistical figure of relative gray value, *P<0.05, compared with CDK3 group, and #P<0.05, compared with CDK4 group*

and positive staining area percentage (APSAP) of α-SMA in the arterial wall among CKD groups (P<0.05). (P<0.05). It was also found that with the progression of kidney disease, the expression of α-SMA in the arterial wall decreased gradually. After pairwise comparison of CKD groups at each stage of kidney disease, it was found that there were significant differences in AOD and APSAP values in the expression of α-SMA in the renal interstitium (P<0.05). With the development of renal disease, the expression of α-SMA in the renal interstitium gradually increased.

Expression of α-SMA protein in renal tissues detected by Western blot

The results of Western blot (Fig. 2) showed that the expression of α-SMA protein in intrarenal arterioles of different groups was also different, and the expression levels of α-SMA protein in CDK1 and CDK2 groups were significantly higher than those of CDK3 and CDK4 groups (P<0.05).

Correlation between 100% positive α-SMA area of renal tissues and various indicators

The correlation analysis results showed that the

Table II. *AOD and APSAP values of α-SMA in renal tissues of each group*

Group		AOD value	APSAP (%)
Intrarenal arteriole wall	CDK1	0.283 ± 0.017	22.244 ± 7.543
	CDK2	0.270 ± 0.102	19.324 ± 9.345
	CDK3	0.218±0.053	14.353±12.353
	CDK4	0.193±0.034	10.415±11.703
	P value	0.032	0.041
Renal interstitium	CDK1	0.024±0.327	2.910±1.103
	CDK2	0.165±0.491	4.312±1.621
	CDK3	0.202±0.513	13.508±1.254
	CDK4	0.302±0.382	20.292±0.907
	P value	0.025	0.013

Table III. *Correlation between APSAP value of α-SMA in renal tissues and various indicators*

Index	APSAP value of α-SMA in intrarenal arterioles		APSAP value of renal interstitium	
	r value	P value	r value	P value
Creatinine	-0.491	0.001	0.717	0.001
Diastolic blood pressure	-0.203	0.015	0.311	0.001
Systolic blood pressure	-0.403	0.001	0.504	0.001
Serum potassium	-0.148	0.053	0.263	0.041
TG	0.131	0.062	-0.283	0.017
TC	0.302	0.005	-0.351	0.001
IMT	-0.337	0.001	0.433	0.001

APSAP value of α-SMA in intrarenal arterioles was negatively correlated with the levels of creatinine, blood pressure, serum potassium, and cIMT, and positively correlated with the levels of triglyceride (TG) and total cholesterol (TC) ($P<0.05$) (Table III). In addition, APSAP value of renal interstitium was positively correlated with the levels of creatinine, blood pressure, serum potassium, and IMT, and negatively correlated with the levels of TG and TC ($P<0.05$).

DISCUSSION

Studies have shown that epithelial cells can undergo phenotypic trans-differentiation and express α-SMA (8). Some scholars (9) analyzed rat fibrosis models after most parts of their kidneys were removed. It was found that the expression of α-SMA in renal tubular epithelial cells was positively correlated with the severity of renal tubular interstitial fibrosis, and α-SMA could be used as an important indicator to evaluate the transformation of renal tubular epithelial cells and the degree of renal interstitial fibrosis. In this research, it was found that the expression of α-SMA was positively correlated with the severity of CKD, suggesting that monitoring α-SMA in patients with CKD could help

to determine severity of the kidney disease.

IMT is the distance between the inner intimal surface of vessel lumen and the outer intimal surface of the tunica media (10). Detection of IMT is a good non-invasive method to clearly reveal the degree of atherosclerosis (11, 12). The results of this study showed that with the deterioration of renal functions in CKD patients, cIMT gradually increased and the degree of cIMT increase was positively correlated with the severity of CKD. It was suggested that the severity of CKD was closely related to the severity of carotid intima lesions.

The results of this study showed that the expression levels of α-SMA in different tissues of the kidney were quite different, and the change in the α-SMA expression in kidney tissues might be involved in the development of CKD. In addition, the APSAP value of α-SMA in intrarenal arterioles was negatively correlated with serum potassium levels ($P<0.05$), and the APSAP value in renal interstitium was positively correlated with potassium levels ($P<0.05$), which might be attributed to the increased serum potassium levels caused by the release of intracellular potassium ions during metabolic acidosis.

In conclusion, the combined detection of α-SMA in intrarenal arterioles and IMT can help the evaluation of CKD. At the same time, the expression level of α-SMA in renal tissues can be used to predict cardiovascular incidents in patients with CKD.

REFERENCES

1. Wu Y, Hou J, Li J, Luo Y, Wu S. Correlation between carotid intima–media thickness and early-stage chronic kidney disease: results from asymptomatic polyvascular abnormalities in community study. J Stroke Cerebrovasc Dis 2016; 25(2):259-65.
2. Chen L, Sha ML, Li D, et al. Relaxin abrogates renal interstitial fibrosis by regulating macrophage polarization via inhibition of Toll-like receptor 4 signaling. Oncotarget 2017; 8(13):21044-53.
3. Negri AL. Prevention of progressive fibrosis in chronic renal diseases: antifibrotic agents. J Nephrol 2004; 17(4):496-503.
4. Yin Q, Liu H. Connective tissue growth factor and renal fibrosis. Adv Exp Med Biol 2019; 1165:365-80.
5. Sun YB, Qu X, Caruana G, Li J. The origin of renal fibroblasts/myofibroblasts and the signals that trigger fibrosis. Differentiation 2016; 92(3):102-107.
6. Liu Y. Epithelial to mesenchymal transition in renal fibrogenesis: pathologic significance, molecular mechanism, and therapeutic intervention. J Am Soc Nephrol 2004; 15(1):1-12.
7. Takeji M, Moriyama T, Oseto S, Kawada N, Hori M, Imai E, Miwa T. Smooth muscle alpha-actin deficiency in myofibroblasts leads to enhanced renal tissue fibrosis. J Biol Chem 2006; 281(52):40193-200.
8. Elberg G, Chen L, Elberg D, Chan MD, Logan CJ, Turman MA. MKL1 mediates TGF-beta1-induced alpha-smooth muscle actin expression in human renal epithelial cells. Am J Physiol Renal Physiol 2008; 294(5):F1116-28.
9. Jercan O, Penescu M, Traşcă DM. Implications of tubulo-interstitial epithelial and mesenchymal relation in chronic kidney disease. Rom J Morphol Embryol 2012; 53(3 Suppl):713-17.
10. Khandelwal P, Murugan V, Hari S, Lakshmy R, Sinha A, Hari P, Bagga A. Dyslipidemia, carotid intima-media thickness and endothelial dysfunction in children with chronic kidney disease. Pediatr Nephrol 2016; 31(8):1313-20.
11. Roumeliotis A, Roumeliotis S, Panagoutsos S, Theodoridis M, Argyriou C, Tavridou A, Georgiadis GS. Carotid intima-media thickness is an independent predictor of all-cause mortality and cardiovascular morbidity in patients with diabetes mellitus type 2 and chronic kidney disease. Ren Fail 2019; 41(1):131-38.
12. Ziolkowska H, Brzewski M, Roszkowska-Blaim M. Determinants of the intima–media thickness in children and adolescents with chronic kidney disease. Pediatr Nephrol 2008; 23(5):805-11.

LETTER TO THE EDITOR

DNA MICROARRAY ANALYSIS OF DENDRITIC CELLS INFECTED BY *ENTEROVIRUS 71*

YJ. YANG[1,2*], Z. WANG[2*], RX. ZHENG[3*], Y. LI[2], L. WANG[4], YM. LIU[2], X. WANG[2], R. SU[5], QH. DAI[5] and C. LIU[5]

[1]Graduate School, Tianjin Medical University, Tianjin, China; [2]Department of Infectious Diseases, Tianjin Second People's Hospital, Tianjin, China; [3]Department of Pediatric, Tianjin Medical University General Hospital, Tianjin, China; [4]Department of Pharmacy, Tianjin Second People's Hospital, Tianjin, China; [5]Viral immunology Laboratory, Tianjin Second People's Hospital and Tianjin Institute of Hepatology, Tianjin, China

Received September 23, 2019 – Accepted March 4, 2020

[*]These authors contributed equally to this work

To the Editor,

Enterovirus 71 (EV71), a member of the *Picornaviridae* family, is one of the major causes of hand foot and mouth disease (HFMD) (1). It is associated with severe central nervous system complications, leading to high morbidity and mortality (2, 3). EV71 is harmful to the health of young children, and is a significant public health issue. Understanding the specific molecular mechanism of EV71 infection could help to develop new therapies against EV71.

Dendritic cells (DCs) are the main antigen-presenting cells, which play a central role in the invasion of EV71 (4). Previous studies show that EV71 bind to DCs through DC-specific intercellular adhesion molecule-3 grabbing nonintegrin (DC-SIGN) which leads to EV71 infection (5). However, the detailed mechanisms of how DCs interact with EV71 and what cellular signal transduction pathways play a role during EV71 invasion into host cells remains unclear. Gene microarray technique is widely used in the study of interaction between host cells and pathogens, including viruses. By detecting the alterations of gene expression profiles in virus-infected hosts, the intracellular molecular response in host cells can be discovered. This provides new targets for the clinical treatment of viral diseases.

In this study, we investigated the DC maturation after EV71 treatment *in vitro*. DCs 2.4 cell line, an immature dendritic cell line derived from mouse bone marrow (6), was used for this study. DNA microarray analysis was applied to screen the dysregulated genes in DCs after EV71 infection. Gene ontology enrichment analysis (GO) and KEGG analysis were performed to bioinformatically analyze the DNA microarray data to identify possible mechanisms of EV71 infection of DCs.

MATERIALS AND METHODS

Mouse DC 2.4 cell lines were provided by the Laboratory of Immunology and Pathogen Biology of Tianjin University of Traditional Chinese Medicine. EV71 virus and RD cells were obtained from Tianjin Center for Disease Control and Prevention. DMEM medium, special fetal calf serum (FCS), RPMI1640 medium, MEM-a, Trypsin, FITC-labeled anti-

Key words: enterovirus 71; dendritic cells; microarray; GO analysis; pathway analysis

Corresponding Author:
Dr Rongxiu Zheng,
Department of Pediatric,
Tianjin Medical University General Hospital,
No.154 Anshan Road,
Heping District, Tianjin,300052, China
e-mail: zhengrongxiu4086@163.com

0393-974X (2020)
Copyright © by BIOLIFE, s.a.s.
This publication and/or article is for individual use only and may not be further reproduced without written permission from the copyright holder.
Unauthorized reproduction may result in financial and other penalties
DISCLOSURE: ALL AUTHORS REPORT NO CONFLICTS OF INTEREST RELEVANT TO THIS ARTICLE.

mouse CD80 antibody, and APC-labeled anti-mouse CD86 antibody were purchased from Tianjin Zhongao Tianyuan Company (Tianjin, China).

Cell culture

DCs 2.4 cell lines were cultured and passaged with conventional methods. The cells were grown in a 6-well cell culture plate, and maintained in RPMI1640 medium containing FCS, in a cell incubator at 37°C and 5% CO_2. The medium was refreshed every 24 hours.

Infection of DCs with EV71

The EV71 virus were routinely expanded in RD cells (7). The median tissue culture infectious dose of virus was calculated according to the Reed-Muench method (Tissue Culture Infectious Dose, TCID50). When 80% ~ 90% confluency was reached, the DCs cells were infection virus at multiplicity of infection (MOI) = 5. After incubation for 1.5 h at 37°C and 5% CO_2, the maintenance solution was added to the cells and maintained for 24 h. A non-infection group was used as a control. Each group were carried out with three replicates.

Flow cytometry assay

After treatment, DCs were stained with FITC anti-mouse CD80 (bs-2211R-FITC Biosynthesis Biotechnology Co., Ltd., Beijing, China) and PE anti-mouse CD86 (bs-1035R-PE, Biosynthesis Biotechnology Co., Ltd., Beijing, China) for flow cytometry analysis. The data were collected with FACSCalibur and analyzed with Cell Quest-Pro software.

Isolation of RNAs and microarray assay

The Agilent SurePrint G3 Mouse GE V2.0 Microarray (8*60K, Design ID:074809) was used in this experiment, and data analyses of the six samples were completed. After DCs were cultured for 24 hours, total RNAs in the control group and EV71 group were isolated using RNA isolation kit following the manufacturer's protocol. The RNAs were quantitated by the NanoDrop ND-2000 (Thermo Scientific, USA), and the RNA integrity was assessed with Agilent Bioanalyzer 2100 (Agilent Technologies, USA). The sample labeling, microarray hybridization and washing were performed based on the manufacturer's standard protocols. Feature Extraction software (version10.7.1.1, Agilent Technologies) was used to analyze array images and obtain raw data, followed by analysis with Genespring (Version13.1, Agilent Technologies, USA).

GO analysis and KEGG analysis of data

Differentially expressed genes were identified through fold change and P value was calculated with Student's *t*-test. Dysregulated genes (fold change>= 2.0 and a P value<= 0.05) were chosen for further analyses. Afterwards, GO analysis and KEGG analysis were applied to determine the roles of these differentially expressed mRNAs. Three types of results were generated by GO analysis, including analysis of biological process, cellular component, and molecular function. Counting the number of differential genes were included in each GO entry. The significance of the differential gene enrichment in each GO entry was calculated using statistical testing. The result of the calculation returns as a significant P value for enrichment. A small p value indicated that the differential genes were enriched in the GO entry. Pathway analysis was performed in the differential genes using the KEGG database. The significance of differential gene enrichment in each Pathway entry was statistically analyzed. Lastly, Hierarchical Clustering was performed to display the distinct genes' expression panel among samples. The microarray dataset was deposited in the NCBI Gene Expression Omnibus (GEO) database (https://www.ncbi.nlm.nih.gov/geo/query/acc.cgi?acc=GSE142260).

Validation of microarray data by real-time quantitative polymerase chain reaction

Real time quantitative polymerase chain reaction (RT-PCR) was performed to confirm the microarray data. Six genes (Arap1, cb1c, jun, Thbs1, cdc37 and ubtd1) were chosen based on the microarray analysis data and confirmed with RT-PCR. β-actin was used as the internal control. 0.8 μg of total RNA of each sample was reverse-transcripted with a PrimeScript RT reagent Kit (TaKaRa Bio Inc., Shiga, Japan). The reaction program was 37°C for 15 min, then 85°C for 5 s. Quantitative RT-PCR was performed using SYBR® Green PCR Master Mix (Applied Biosystems., Warrington, UK). The reaction was performed on ABI7300 Real Time PCR System with program: 50°C for 2 min, 95°C for 10 min, then 40 cycles of 95°C for 10 s and 60°C for 30 s, and after the cycles, it was 95°C for 15 s, 60°C for 30 s, 95°C for 30 s, 95°C for 15 s using the ABI7300 Real Time PCR System.

Each gene expression was carried out in triplicate. Data were calculated and analyzed with formula $2^{-\Delta\Delta Ct}$. Ct is the threshold cycle. The ΔΔCt is ΔCt (drug treatment) −ΔCt (background), and the ΔCt is Ct (target gene) − Ct (β-actin). The sequences of all primers are listed in Table I.

RESULTS

EV71 induce DCs maturation in vitro

Flow cytometry analysis was used to observe the effect of EV71 on DC maturation. In comparison to the control group, the proportion of CD80 + CD86 + DC increased from 4.17% (control group) to 9.61% in the EV71 infected group (Fig. 1a). EV71 treatment significantly increased the proportion of CD80+CD86+DCs (Fig.1b), indicating that EV71 treatment could induce DC maturation.

Identification of differentially expressed genes in DCs treated with EV71

Generally, RNAs were sequenced in control group (n=3) and EV71 group (n=3). There were 87 differentially expressed genes (fold change ≥ 2.0) between control and EV71 groups as shown by Volcano Plot (Fig. 2A), including 66 upregulated genes and 21 downregulated genes.

Table I. *Primer sequences used in this study.*

Genes	primer sequence	
β-actin	forward	5'GGCTCCTAGCACCATGAAGA 3'
	reverse	5'AGCTCAGTAACAGTCCGCC 3'
Arap1	forward	5'TGTCCCAGAGTCAGAACG3'
	reverse	5'ACAGGCAGCAGAACAAGGAT3'
cb1c	forward	5'AGCGTTCAGCAAGAAGTC3'
	reverse	5'CCCTCTTCCTGGGAGAATC3'
jun	forward	5'CTGCATGGACCTAACATTCG3'
	reverse	5'GGAGCACTACAGAAGCAATC3'
Thbs1	forward	5'ACTGTCCCTATGTGCCTAA3'
	reverse	5'GCATCTCCTTTGCCATCTT3'
cdc37	forward	5'GGAAACTTAGCCACCATGTC3'
	reverse	5'GATGTGAGGAGCAGCACAA3'
ubtd1	forward	5'GAGATCTGGGATGCCCTC3'
	reverse	5'AGCCAGCTCATGGTCATTA3'

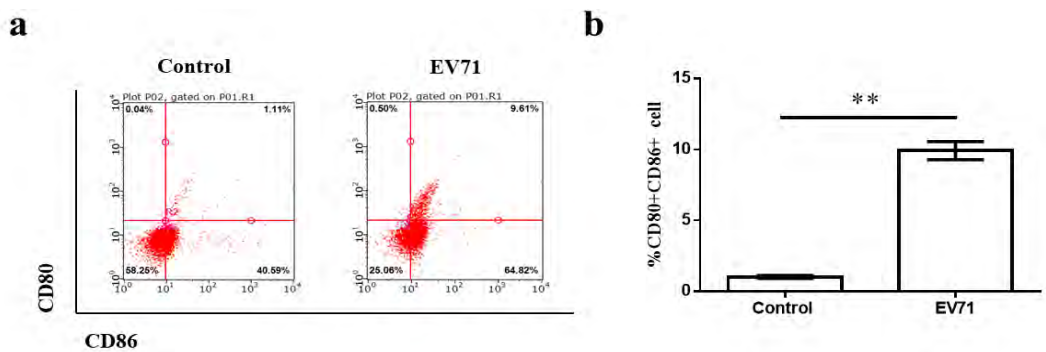


Fig. 1. *Flow cytometry assay indicated that EV71 treatment could significantly increase the proportion of CD80+CD86+DCs in comparison to the control.* ***a****) plot;* ***b****) graph. Control group (n=3), EV71 group (n=3); *: P<0.05; **: P<0.01.*

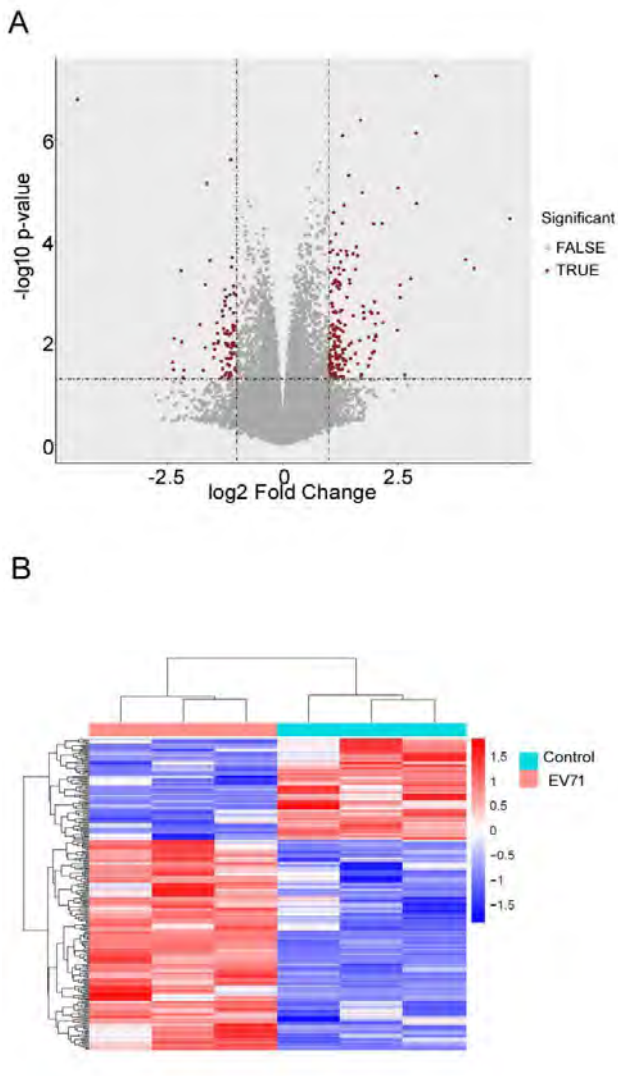


Fig. 2. ***A)*** *Fold changes of differentially expressed genes between control group and EV71 group were visualized in volcano plot. Differentially expressed genes with fold change ≥ 2.0, P≤0.05 were shown. Control group(n=3), EV71 group(n=3);* ***B)*** *Clustering analysis of differential gene expression in each sample indicated that differential gene expression grouping of microarray data was consistent with the experimental groups. Control group(n=3), EV71 group(n=3).*

Cluster analysis shows that differential gene expression grouping of microarray data was consistent with the experimental groups

Clustering analysis was conducted to detect signal values of differential gene expression in each sample. The signal values of differential gene expression were divided into control group and EV71 group (Fig. 2B), indicating that differential gene expression grouping of microarray data was in agreement with the experimental groups.

GO analysis and Pathway analysis show the most enriched molecular biological processes and pathways

GO analysis was conducted to predict the biological process, cellular component and molecular function in which EV71 may affect DCs. Among biological process analysis, up-regulated genes in the EV71 group were compared with the control group and they were mainly crucial for negative regulation of epidermal growth factor-activated receptor activity (GO:0007175), positive regulation by host of viral transcription (GO:0043922), with the fold enrichment scores of 99.90598 and 89.91538, respectively. For down-regulated genes, the closely related GO terms were reproductive process (GO:0022414), integrin activation (GO:0033622), with the fold enrichment scores of 311.7067, 259.7556, and 259.7556, respectively. Cellular component analysis suggested that neuronal cell body membrane (GO:0032809) and extracellular space (GO:0005615) were the top 2 terms among up-regulated genes with the fold enrichment score of 35.04525 and 3.285492, respectively, whereas spectrin (GO:0008091) and small nuclear ribonucleoprotein complex (GO:0030532) were top 2 terms among down-regulated genes with the enrichment score of 309.8 and 221.2857, respectively. Molecular function analysis suggested that hormone activity (GO:0005179), epidermal growth factor receptor binding (GO:0005154) were top 2 terms among up-regulated genes with the enrichment score of 11.9764 and 27.44591, respectively. Protein kinase A regulatory subunit binding (GO:0034237), ARF guanyl-nucleotide exchange factor activity (GO:0005086) were top 2 terms among down-regulated genes with the enrichment score of 95.14583 and 89.54902 respectively (Table II).

KEGG analysis showed that Endocytosis pathway (pathway ID: mmu04144), Riboflavin metabolism pathway (pathway ID: mmu00740), ErbB signaling pathway (pathway ID: mmu04012), TGF-beta signaling pathway(pathway ID: mmu04350) and T cell receptor signaling pathway (pathway ID:

Table II. *Up-regulated genes and down-regulated genes in DCs infected by EV71(top 5 P value in GO analysis).*

GO:ID	Term	Fold Enrichment	P-value
Biological Process (up)			
GO:0007175	negative regulation of epidermal growth factor-activated receptor activity	99.90598	0.000283
GO:0043922	positive regulation by host of viral transcription	89.91538	0.000339
GO:0061029	eyelid development in camera-type eye	69.16568	0.000536
GO:0042059	negative regulation of epidermal growth factor receptor signaling pathway	64.22527	0.000612
GO:0010763	positive regulation of fibroblast migration	64.22527	0.000612
Cellular Component (up)			
GO:0032809	neuronal cell body membrane	35.04525	0.001845
GO:0005615	extracellular space	3.285492	0.003298
GO:0005576	extracellular region	2.562684	0.014385
GO:0031464	Cul4A-RING E3 ubiquitin ligase complex	65.08403	0.017722
GO:0005577	fibrinogen complex	65.08403	0.017722
Molecular Function (up)			
GO:0005179	hormone activity	11.9764	0.002516
GO:0005154	epidermal growth factor receptor binding	27.44591	0.002912
GO:0003690	double-stranded DNA binding	11.07062	0.003121
GO:0017017	MAP kinase tyrosine/serine/threonine phosphatase activity	23.73701	0.003816
GO:0008201	heparin binding	10.05652	0.004056
Biological Process (down)			
GO:0022414	reproductive process	311.7067	0.004096
GO:0033622	integrin activation	259.7556	0.004777
GO:0045162	clustering of voltage-gated sodium channels	259.7556	0.004777
GO:0033135	regulation of peptidyl-serine phosphorylation	259.7556	0.004777
GO:0061337	cardiac conduction	173.1704	0.006817
Cellular Component (down)			
GO:0008091	spectrin	309.8	0.004121
GO:0030532	small nuclear ribonucleoprotein complex	221.2857	0.005491
GO:0043203	axon hillock	193.625	0.006175
GO:0070852	cell body fiber	140.8182	0.008225
GO:0043194	axon initial segment	119.1538	0.009588
Molecular Function (down)			
GO:0034237	protein kinase A regulatory subunit binding	95.14583	0.011833
GO:0005086	ARF guanyl-nucleotide exchange factor activity	89.54902	0.012524
GO:0004890	GABA-A receptor activity	84.57407	0.013215
GO:0008289	lipid binding	12.63347	0.013515
GO:0030506	ankyrin binding	76.11667	0.014595

mmu04660) were associated with differentially expressed genes with the fold enrichment score of 4.34965, 38.875, 7.317647, 7.317647 and 6.0388351 respectively (Table III).

Validation of DNA microarray results using Real-time RT-PCR

RT-PCR was conducted to further verify the dysregulated genes in DCs after EV71 infection. Six genes (Arap1, cb1c, jun, Thbs1, cdc37 and ubtd1) were selected and the relative expression of these genes was investigated. As shown in Fig. 3, the RT-PCR data supports the microarray results, indicating that the microarray results were reliable.

DISCUSSION

The host response to viral infection represents complex orchestration of divergent pathways to eliminate the virus and protect the host. Viruses affect many aspects of host cell biology and gene expression. Microarray, a high throughput assay, has been widely used in genomic studies. In our study, we investigated the DC maturation after being treated

Table III. *KEGG pathway enrichment analysis of dysregulated genes.*

Pathway ID	Term	Fold Enrichment	Genes	P value
mmu04144	Endocytosis	4.34965	Adrb2;Arfgef1; Arap1;Cblc	0.018782
mmu00740	Riboflavin metabolism	38.875	Flad1	0.029542
mmu04012	ErbB signaling pathway	7.317647	Cblc;Jun	0.035195
mmu04350	TGF-beta signaling pathway	7.317647	Thbs1;Inhba	0.035195
mmu04660	T cell receptor signaling pathway	6.038835	Cblc;Jun	0.049286

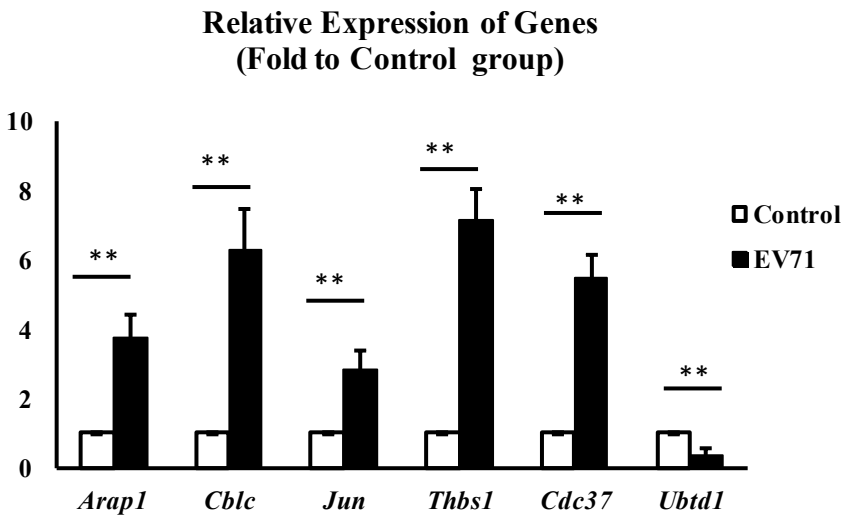


Fig. 3. *Expressions of 6 genes between control group and EV71 group were measured using qRT-PCR. qRT-PCR results were in agreement with the microarray data. Control group (n=3), EV71 group (n=3).* P<0.05; ** P<0.01.*

with EV71 *in vitro*, the gene expression signatures were screened using microarray. In agreement with previous studies, our flow cytometry assay showed that EV71 could significantly induce DC maturation, reflecting in inducing CD80 and CD86 expression on the cell surfaces.

However, how EV71 promotes the maturation of DCs, and what cellular signaling pathways are involved in the interaction between EV71 and DCs are not clear. Previous studies indicated the possible role of DCs during EV71 invasion. EV71 could induce DC maturation through TLR4 signaling pathways (8). Shi et al. (9) showed that the MEK/ERK signaling pathway plays an important role in the replication of immature DCs after EV71 infection. Our microarray data showed that a total of 87 differentially expressed genes were altered in EV71-treated DCs, including 66 upregulated genes and 21 downregulated genes.

Among the 252 GO-classified biological processes related to differential genes, 114 are critical biological processes ($P < 0.05$). These biological processes involve important life activities in the cell. Among the 37 GO-classified cellular components related to differential genes, 24 are important biological processes ($P < 0.05$). Among the 113 GO-classified molecular functions related to differential genes, 44 are crucial biological processes ($P < 0.05$). Many studies show MAP kinase tyrosine/serine/threonine phosphatase activity as an important biological process in DCs after being treated with EV71.

Interestingly, KEGG analysis revealed that endocytosis and TGF-beta signaling pathways are crucial for DCs during EV71 infection. Endocytosis of DCs consists of various cellular processes, including receptors, signaling and movements of viruses on the cell surface, endocytic uptake and trafficking, and finally penetration and genome uncoating (10, 11).

We analyzed the gene expression of DCs cells infected with EV71 by microarray technology and obtained preliminary data. In our future study we need to conduct in-depth analysis of the screening results of the microarray data to verify the most significant signal pathways and analyze the function of genes, the biological processes and signal transduction. This will help to elucidate the complex interaction mechanism of the pathogen and host, and will be helpful for investigating new targets for developing novel treatment options.

REFERENCES

1. Wong SS, Yip CC, Lau SK, Yuen KY. Human enterovirus 71 and hand, foot and mouth disease. Epidemiol Infect 2010; 138(8):1071-89.
2. Chen L, Mou X, Zhang Q, et al. Detection of human enterovirus 71 and coxsackievirus A16 in children with hand, foot and mouth disease in China. Mol Med Rep 2012; 5(4):1001-4.
3. Mcminn PC. Recent advances in the molecular epidemiology and control of human enterovirus 71 infection. Curr Opin Virol 2012; 2(2):199-205.
4. Lin YW, Wang SW, Tung YY, Chen SH. Enterovirus 71 infection of human dendritic cells. Exp Biol Med (Maywood) 2009; 234(10):1166-73.
5. Ren XX, Ma L, Liu QW, et al. The molecule of DC-SIGN captures enterovirus 71 and confers dendritic cell-mediated viral trans-infection. Virol J 2014; 11:47.
6. Lai CY, Yang LC, Lin WC. Type II arabinogalactan from Anoectochilus formosanus induced dendritic cell maturation through TLR2 and TLR4. Phytomedicine 2015; 22(14):1207-14.
7. Liu Q, Huang X, Ku Z, et al. Characterization of enterovirus 71 capsids using subunit protein-specific polyclonal antibodies. J Virol Methods 2013; 187(1):127-31.
8. Lin YL, Hu YC, Liang CC, Lin SY, Liang YC, Yuan HP, Chiang BL. Enterovirus-71 virus-like particles induce the activation and maturation of human monocyte-derived dendritic cells through TLR4 signaling. PLoS One 2014; 9(10):e111496.
9. Shi W, Hou X, Peng H, et al. MEK/ERK signaling pathway is required for entervirus 71 replication in immature dendric cells. Virol J 2014; 11:227.
10. Suomalainen M, Greber UF. Uncoating of non-enveloped viruses. Curr Opin Virol 2013; 3(1):27-33.
11. Takeuchi O, Akira S. Pattern recognition receptors and inflammation. Cell 2010; 140(6):805-20.

LETTER TO THE EDITOR

A RAT MODEL OF BUCCAL ORTHODONTIC FORCE ON PERIODONTAL TISSUES

Y. LIU[1,2], Z. WANG[1], R. WANG[2],Y. LIU[1], X. YU[1], Y. ZHANG[2], Y. LI[2] and Q. XU[1]

[1]The Affiliated Hospital of Qingdao University, Qingdao, China; [2]School of Stomatology of Qingdao University, Qingdao, China

Received February 1, 2020 – Accepted March 16, 2020

To the Editor,

Orthodontic tooth movement is a process of histological and biomechanical changes in teeth under the action of orthodontic forces (1). It is mainly dependent upon the reconstruction of periodontal tissues among which the most plastic and active part is the alveolar bone. When orthodontic forces transfer from teeth to the alveolar bone, resorption of the bone occurs at the compression side, and proliferation occurs on the tension side. This leads to constant renewal, thereby causing a movement in the teeth (2). Dental arch expansion is an important orthodontic treatment option to compensate skeletal discrepancies or to resolve crowding. Experimental animal models are critical to investigate mechanisms of periodontal pathogenesis and to test new therapeutic approaches (3). In previous studies on orthodontic forces, the first maxillary molar was applied with force to observe its movement in both the near and far directions (4). However, few studies on the horizontal movement of the teeth in the buccal and lingual directions have been reported. In a previous study, Danz J.C. successfully created a rat model of the buccal movement of teeth after orthodontic forces (5). Based upon the design principle of the model, a tiny adjustment was made to the appliances in this experiment to establish an animal model for buccal translational tooth movement for research on the effect of different duration on periodontal tissue.

MATERIALS AND METHODS

Thirty 2-month-old, male Wistar rats with a bodyweight of 253±12 g were used. All the rats were kept in pairs in cages under controlled temperatures (24±1°C),and humidity in a 12 h light/dark cycle and were fed a diet of finely ground laboratory food ad libitum. Soft food minimizes discomfort to the animal after installation of the orthodontic appliance and also reduces the risk of escaping. The body weights of all rats were measured every week. This study was conducted in conformity with the Animal Care and Use Committee of Qingdao University (Qingdao, Shandong Province, China).

The rats were randomly divided into two groups: 27 animals in a loading appliance group where resin was used to bond the orthodontic appliances onto the lingual of the first molar, and three animals in the control group were without any orthodontic appliances. The experimental group was divided into 3 subgroups (7d, 28d, 56d) according to the duration of the orthodontic force applied. During the experiment, animals with loosening or breakage of the force were excluded.

Key words: buccal orthodontic force; periodontal tissues; rat model

Corresponding Author:
Dr Quanchen Xu,
The Affiliated Hospital of Qingdao University,
No. 16, Jiangsu Road, Shinan District, Qingdao City,
Shandong Province, 266003, China
Tel.: +86 532 82911213
e-mail: qyfyxqc@126.com

0393-974X (2020)
Copyright © by BIOLIFE, s.a.s.
This publication and/or article is for individual use only and may not be further reproduced without written permission from the copyright holder.
Unauthorized reproduction may result in financial and other penalties
DISCLOSURE: ALL AUTHORS REPORT NO CONFLICTS OF INTEREST RELEVANT TO THIS ARTICLE.

Orthodontic appliances

The rats were anesthetized according to their weight by intraperitoneal injection with 10% chloral hydrate (0.35ml/100 g). As per the maxillary morphology of the rat, a personalized impression tray was prepared using a resin sheet (Fig. 1A). A rat maxillary model was prepared using alginate along with a super-hard plaster for filling in. An orthodontic force device was fabricated on the plaster model using a round 0.016″ b-titanium wire following a pre-designed model (Fig. 1B). The initial force applied to the rat's teeth was measured using an electronic dynamometer adjusted to provide a two-way force of 30±1.5 cN over a 5 mm range. This study used a modified biomechanical approach as described by Rebellato (6) to achieve translational tooth movement with torque control by expansive force and to minimize facial tipping movement of the teeth.

Establishment of the rat model

Rats were fixed on the experimental animal plates and gauze strips were placed under the rat head to protect their eyes. The appliances were bonded with resin (origin, 3M) directly on the lingual of the first molar. Transpalatal bars extending to the buccal surface of M2 and M3 were placed to retain the tooth position and to prevent the skeletal widening of the maxilla due to the opening of the mid-palatal suture (Fig. 1C).

Tissue preparation and histopathological analysis

Following perfusion fixation with 4% paraformaldehyde, the maxillae were dissected. The samples were decalcified in 10% EDTA for 3- 4 weeks and embedded in paraffin. Tissue sections of 3 μm thickness were obtained in vertical direction, and the central area of the first molars was stained with Hematoxylin and Eosin (H&E) staining.

We placed the Tartrate-resistant acid phosphatase (TRAP) staining solution mix in a staining dish and used a water bath to pre-warm it to 37°C. Slides were deparaffinized and rehydrated through gradient ethanol treatment. The slides were placed in the pre-warmed TRAP Staining solution and incubated at 37°C for 30 min. after which the slides were rinsed with distilled water. Each section randomly selected 5 clear fields with TRAP-positive cells under a high-power objective. The same person counted the number of osteoclasts in each field. The total number of TRAP-positive cells of the section was taken as the final result.

The left maxillae were defleshed and stained with an aqueous methylene blue solution (1%) to differentiate the bone from teeth. Image-pro plus 6.0 was used to measure the distance between the cementoenamel junction (CEJ) and the alveolar bone (AB) at 2 buccal and 2 palatal sites on the upper left first molar in each maxilla figure. All the measurements were made along the long axis of the roots of the upper left first molar. The sum of the 4 sites on both sides was identified as the alveolar bone resorption level of the maxillary first molar of the rat.

Statistical analysis

All the data were expressed as mean±SD. Statistical analysis was performed using a statistical package (SPSS

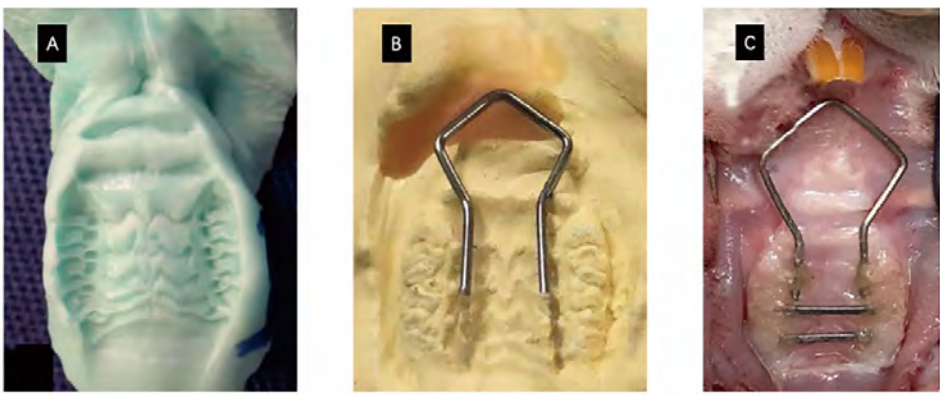


Fig. 1. *Establishment of the rat model.* ***A****) As per the maxillary morphology of the rat, a personalized impression tray was prepared using a resin sheet.* ***B****) An orthodontic force device was fabricated on the plaster model.* ***C****) The appliances were bonded with resin directly onto the lingual of the first molar.*

17.0, SPSS Inc, USA). Data were analyzed using one-way analysis of variance followed by the Bonferroni correction for multiple comparisons. P-value lower than 0.05 was considered as statistically significant. For morphometric analysis, the data were expressed as mean and standard deviation (mm). The independent sample *t*-test ($\alpha = 0.05$) was used for comparisons of alveolar bone loss between different groups.

RESULTS

All the rats in the experimental group were able to tolerate the whole surgical process. All of them woke up 1-2 h after anesthesia and resumed free activities on the second day after surgery. Consistent with the findings of Brudvik and Rygh (7), all the animals showed a temporary weight loss after the installation of the appliances. No feeding difficulties or death occurred during the sustained increase. During the whole observation period, there was no change in the direction of the force applied by the device. It should be noted that the distance between the maxillary first molar near the middle buccal tip and the palate was found to increase the teeth buccal movement but

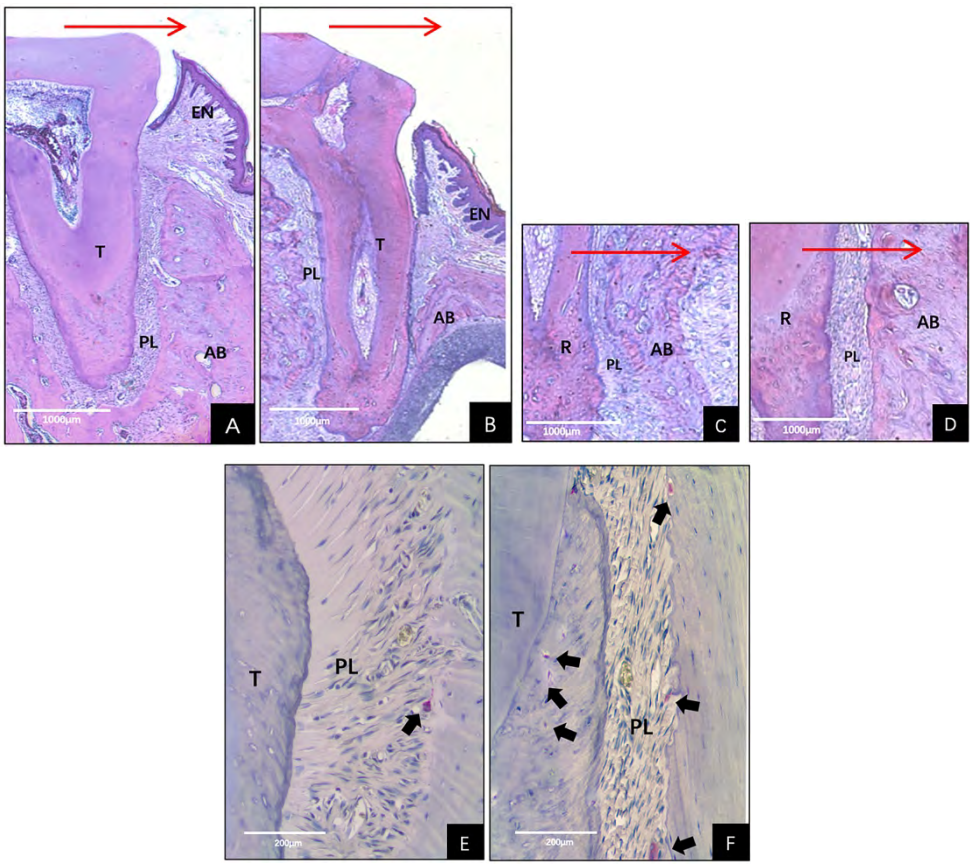


Fig. 2. *Histological observation of periodontal tissue (H&E staining) and histochemical reaction for tartrate-resistant acid phosphatase (TRAP). The periodontal tissue sections of the control group illustrated the width of the periodontal membrane was similar and the root surface was complete (**A**). In the 7d and 28d loading appliance group, the cementum was absorbed and the periodontal tissue became wide on the tension side, and at the pressure areas the periodontal tissue narrowed (**B**,**C**). In the 56d, the width of periodontal membrane was close to the normal level (**D**). The histochemical reaction for TRAP illustrated numerous TRAP-positive cells at the pressure areas. Section from the control group showing few TRAP-positive cells (**E**). Section from a 7d specimen; TRAP activity was significantly elevated in periodontal ligament and tooth surface (**F**). The red arrow indicates the direction of the force, the black arrow indicates the TRAP-positive cells. T: tooth; PL: periodontal ligament; AB: alveolar bone; R: root surface; EN: epithelial nail.*

no changes in the maxillary width were observed. Three of 27 rats in the loading appliance group lost the appliance, these were considered as failures and were excluded from further analysis.

The periodontal tissue sections of the control rats revealed an orderly and regular arrangement of the periodontal membrane fibers. The width of the periodontal membrane was similar, the edge of alveolar bone was continuous, the height of the alveolar crest on the buccal side was at the CEJ level without any obvious resorption and visual changes, and the root surface was complete. In the loading appliance group, by day 7 of loading, HE staining suggested that the epithelial nail protruding was thick, the arrangement of the periodontal membrane fibers was disordered, the periodontal membrane on the stressed side had narrowed, hyaline changes occurred, and the gap between the periodontal membrane on the tension side had widened. Compared with the control group, there were significant bone resorption pits such as silkworm erosion at the edge of the alveolar bone on the pressure side, also the number of collagen fibers has significantly increased. The alveolar crest was located in the root square of CEJ, and the cementum was absorbed to different degrees. By day 28 of loading, H&E staining demonstrated that the direction of the periodontal fiber bundle was in a transitional state and the tension side had transitional new bone deposition. The bone surface was covered with a layer of pink osteoid. and a well-arranged layer of columnar osteoblast cells was found in the periodontal membrane near the edge of the osteoid. By day 56, H&E staining showed that the width of the periodontal membrane was close to the normal level without any bone resorption lacunae. The distribution of osteoclasts and osteoblasts and the number of collagen fibers were significantly reduced. However, the expression level was slightly higher than that of the control group, suggesting that the process of osteoresorption and new bone formation may be over.

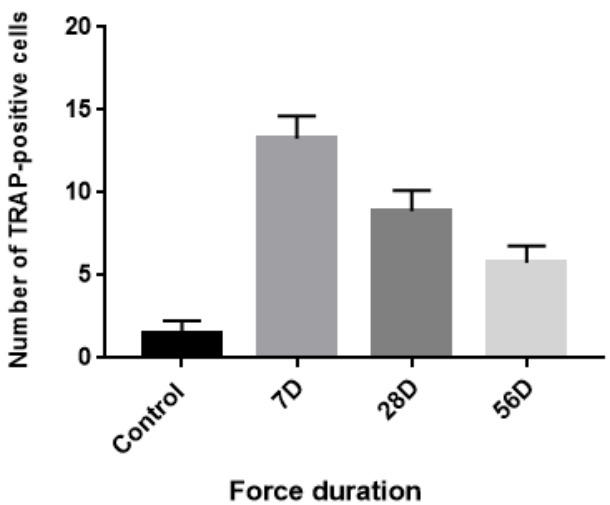


Fig. 3. *Number of osteoclasts in periodontal tissue. The number of osteoclasts reached the peak on the 7d and then gradually started to decrease.*

Sections from controls were negative for TRAP activity. Very few sections had the occasional TRAP-positive cells. At the pressure areas, most of the TRAP-positive cells appeared over the tooth and alveolar bone surface. By day 7 of loading appliances, TRAP activity was significantly elevated in periodontal ligament and root surface. By day 28, TRAP activity had decreased. By day 56, TRAP activity was indistinguishable from the control group. With the increase of time, the number of osteoclasts decreased gradually.

Alveolar bone loss determination

The distances from CEJ to AB at 4 sites bilaterally of the maxillary first molar were measured and calculated together to represent the alveolar bone loss level (Fig. 4 A, B). Morphometric analysis suggests a direct relationship between the duration of the appliances with the amount of alveolar bone resorption. The study observed higher alveolar bone destruction in the rats loading 56 days (teeth: 2.91±0.12; buccal sites: 1.51±0.12; palatal sites: 1.39±0.11 mm) than in the rats loading 28 days (teeth: 1.85±0.11; buccal sites: 0.97±0.11; palatal sites: 0.88±0.09 mm) than in the rats loading 7days (teeth: 1.21±0.07; buccal sites: 0.63±0.07; palatal sites: 0.58±0.07 mm) (Fig.5).

DISCUSSION

As an experimental animal, the rat has the advantages of low price, short growth cycle, easy standardization, and abundance of mouse-derived

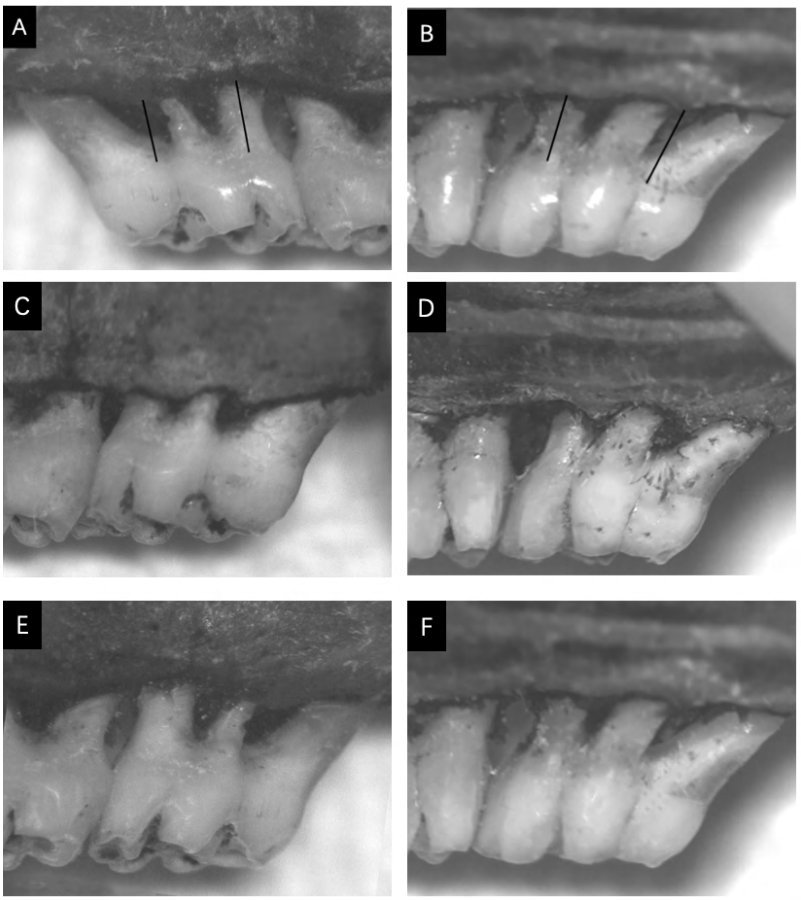


Fig. 4. A*lveolar bone loss evaluated morphometrically by measuring the distance between the cementoenamel junction (CEJ) and alveolar bone crest at 2 palatal (**A**) and 2 buccal (**B**) sites on the upper left first molar in each maxilla figure. The black lines indicate the four distances that were measured on each tooth. Photograph representative of the control group, without loading appliance (**C**) and illustrating the 7d (**D**), 28d (**E**), 56d (**F**) loading group, buccal site of the first molar.*

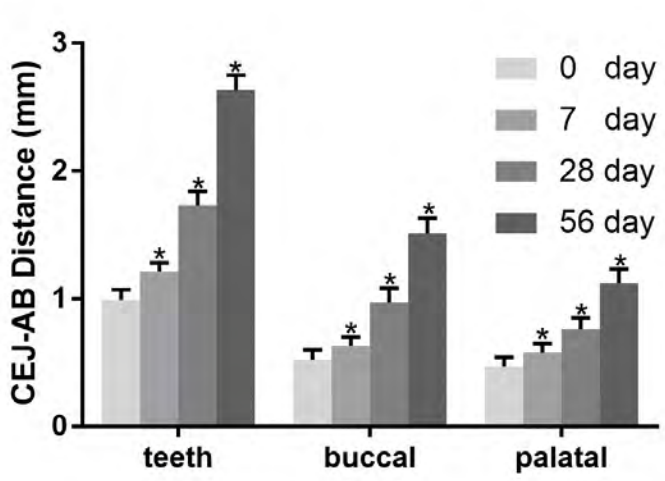


Fig. 5. *The distances from CEJ to AB at 4 sites bilaterally were measured and calculated together (n=8). *: P<0.05. **E)** The alveolar bone resorption level of day 56, day 28 and day 7 were significantly higher than control group.*

antibodies, making it more suitable for large-scale observations. Therefore, it is one of the most widely used models in orthodontic tooth movement research .(8) The molars of rats are multi-root teeth whose structure and characteristics are very similar to human teeth (9), Considering the oral and physical characteristics of rats and minimal interference of the adjacent teeth, the selected observation index in this experiment was the first maxillary molar.

The experiments reported in this study confirmed that the continuous application of constant orthodontic forces can lead to bone resorption and bone reconstruction in the compressed molar areas in rats. As per the classical theory in the presence of the orthodontic forces, the periodontal membrane on the pressure side is compressed while that on the tension side is stretched. Under the stimulation of the external forces, osteoclasts go into a polarized state and play an important role in demineralization, degradation of organic matter, secretion, and phagocytosis. Similarly, mesenchymal stem cells under external stimulation can differentiate into osteoblasts, regulating bone formation and resorption. A combination of these factors can eventually lead to bone resorption at the pressure side and bone formation at the tension side (10, 11). Orthodontic forces can cause the alveolar bone resorption along with ischemia in the periodontal ligament, influence cells to undergo apoptosis, and accelerate the periodontal tissue reconstruction (12). During tooth movement, with their ability to synthesize and decompose collagen, the fibroblasts in the periodontal membrane control the collagen metabolism and play a direct role in the reconstruction. In addition, they can also initiate the renewal of alveolar bone. After peaking the bone resorption, the periodontal tissues produce adaptive reparation and eventually tend to move into a stable state.

In conclusion, this study established a buccal force-model in rats from the perspective of clinical phenomena and the orthodontic loading method. The establishment of an animal model of buccal tooth movement is expected to provide a new outlook for the study on gingival recession, bone-cracking and bone fenestration in clinical treatment. It has been proved that the body can adjust itself under the action of proper orthodontic forces. With the increase of the duration of the orthodontic force, the periodontal tissues can be reconditioned physiologically. However, the mechanism of buccal force on the reconstruction of periodontal tissue still needs to be further studied.

ACKNOWLEDGEMENTS

This research was supported by Shandong Provincial Natural Science Foundation (ZR2017MH083) to Zhiguo Wang and Shandong Province Key Research Plan (2018GSF118150) to Quanchen Xu.

REFERENCES

1. Tengku BS, Joseph BK, Harbrow D, et al. Effect of a static magnetic field on orthodontic tooth movement in the rat. Eur J Orthod 2000; 22(5):475-87.
2. Ruf S, Hansen K, Pancherz H. Does orthodontic proclination of lower incisors in children and adolescents cause gingival recession? Am J Orthod Dentofacial Orthop 1998; 114(1):100-6.
3. Abe T, Hajishengallis G. Optimization of the ligature-induced periodontitis model in mice. J Immunol Methods 2013; 394(1-2):49-54.
4. Ibrahim AY, Gudhimella S, Pandruvada SN, et al. Resolving differences between animal models for expedited orthodontic tooth movement. Orthod Craniofac Res 2017; 20(Suppl 1):72-6.
5. Danz JC, Dalstra M, Bosshardt DD, et al. A rat model for orthodontic translational expansive tooth movement. Orthod Craniofac Res 2013; 16(4):223-33.
6. Rebellato J. Two-couple orthodontic appliance systems: transpalatal arches. Semin Orthod 1995; 1(1):44-54.
7. Brudvik P, Rygh P. Root resorption beneath the main hyalinized zone. Eur J Orthod 1994; 16(4):249-63.
8. Ren Y, Maltha JC, Kuijpers-Jagtman AM. The rat as a model for orthodontic tooth movement--a critical review and a proposed solution. Eur J Orthod 2004; 26(5):483-90.
9. Shirakata Y, Eliezer M, Nemcovsky CE, et al. Periodontal healing after application of enamel matrix

derivative in surgical supra/infrabony periodontal defects in rats with streptozotocin-induced diabetes. J Periodontal Res 2014; 49(1):93-101.
10. Wise GE, King GJ. Mechanisms of tooth eruption and orthodontic tooth movement. J Dent Res 2008; 87(5):414-34.
11. Nguyen PD, Lin CD, Allori AC, et al. Scaffold-based rhBMP-2 therapy in a rat alveolar defect model: implications for human gingivoperiosteoplasty. Plast Reconstr Surg 2009; 124(6):1829-39.
12. Nemcovsky CE, Sasson M, Beny L, et al. Periodontal healing following orthodontic movement of rat molars with intact versus damaged periodontia towards a bony defect. Eur J Orthod 2007; 29(4):338-44.

LETTER TO THE EDITOR

IMPROVING MODEL OF CORNEAL FUNGAL-INDUCED ULCER IN RABBIT

M. LI[1,2*], CY. ZHANG[3*], WJ. LI[3], CF. ZHU[3] and WH. ZHANG[3]

[1]School of Medicine, Shandong University, Jinan, Shandong, China; [2]Department of Ophthalmology, Qilu Hospital of Shandong University, Jinan, Shandong, China; [3]Department of Ophthalmology, Jinan second People's Hospital, Jinan, Shandong, China

Received February 13, 2020 - Accepted March 18, 2020

*These Authors contributed equally to this work

To the Editor,

Candida albicans, *Fusarium*, and *Aspergillus* are the primary focus of current fungal corneal ulcer research. Fungal corneal ulcer is an infectious disease with a very high rate of blindness. It is also an important cause of corneal blindness. Corneal trauma presents the opportunity for fungal infections. The extensive application of antibiotics, corticosteroids, antiviral drugs, and contact lenses has caused an increasing trend of ocular fungal disorders. Establishing a successful animal model of fungal corneal ulcer is key to observe the characteristics of fungal corneal ulcer and to assess the effectiveness of treatment. Injecting fungal spores into the rabbit deep corneal stroma is currently a widely used animal model for fungal corneal ulcer. This method has a high success rate of infection, low probability of a combined infection of the cornea, and is easy to perform at a low cost. However, the rate of corneal perforation and an intraocular infection is high using this method. It is also difficult to obtain infected tissue from the deep corneal stroma using a corneal scraping test.

The aim of the present study was to provide an improved method for establishing a rabbit fungal corneal ulcer model. The effectiveness of the model was compared with the method currently used in the field.

MATERIALS AND METHODS

Twenty-four healthy adult New Zealand white rabbits, weighing 2.5-3.0 kg, male or female, were purchased from the Shandong province Animal Laboratory Center. All of the rabbits were examined by slit lamp microscopy to exclude anterior segment disorders and were raised in an environment at 20 ~ 25°C and 40-70% humidity. The rabbits were acclimatised for two weeks and then randomly divided into group 1 (new method) and group 2 (control group, the widely used method). The study protocol was approved by the Institutional Ethics Committee of Experimental Animals of Liaocheng People's Hospital (2018069) and conformed to the national animal welfare and ethics regulations.

Preparation of Candida albicans *samples*

The concentration of fungal sample to ensure a successful corneal infection is from 10^6 to 10^{10} CFU/ml (colony-forming units) (1). However, the amount of fungi inoculated is very limited (0.05 ml-0.1 ml). The concentration of *Candida albicans* used in the present study was 10^6 CFU/ml according to the report by Zhong et al. (2). *Candida albicans* strain ATCC10231 was purchased from the clinical laboratory center of the National Health and Family Commission of China.

Key words: Candida albicans; fungal corneal ulcer; rabbit; confocal microscopy

Corresponding Author:
Dr Cuiying Zhang,
Department of Ophthalmology, Liaocheng People's Hospital in Shandong Province, No.67 Dongchang West Road,
Liaocheng 252000,
Shandong, China
e-mail: zhangcuiying80@126.com

0393-974X (2020)
Copyright © by BIOLIFE, s.a.s.
This publication and/or article is for individual use only and may not be further reproduced without written permission from the copyright holder.
Unauthorized reproduction may result in financial and other penalties
DISCLOSURE: ALL AUTHORS REPORT NO CONFLICTS OF INTEREST RELEVANT TO THIS ARTICLE.

Specimens were inoculated directly into Sabouraud's agar medium and incubated at 25°C for 48 h to produce gray cheese-like colonies. The smear was observed under a microscope, and oval-shaped budded cells on the surface with pseudohyphae on the bottom could be observed. YST identification card of the VITEK 2 automatic microbial identification system (Vite-2 compact, Merieux, France) was used to identify fungal species. The test colony was picked by an inoculation loop and diluted in normal saline to 0.5 standard units of wheat, which is equivalent to 10^8 CFU /ml, and then diluted 1:100 in normal saline to 10^6 CFU/ml.

Establishing rabbit Candida albicans *fungal cornear ulcer model*

The right eyes of the rabbits were used as the experimental eye. The rabbits were anesthetized intraperitoneally with 10% chloral hydrate (3ml/kg or 0.3g/kg). The right eyes were anesthetized three times using 0.4% oxybuprocaine hydrochloride eye drops. The chloral hydrate is similar to barbiturates, the central inhibito can quickly induce drowsiness, sedation, with anesthesia induction and rapid awakening (3). In the present study, 0.4% oxybuprocaine hydrochloride as the surface anesthetic was used to completely eliminate the cornea pain (4). The operation can be carried out within 2 min, and chloral hydrate together with 0.4% oxybuprocaine hydrochloride eye drops is the best choice for anesthesia. Their rabbits' heads were fixed and the eyelids were opened using an eye speculum. The conjunctival sacs were flushed with normal saline. In group 1, a total of 0.1 ml *Candida albicans* liquid was exacted using a new-style 1-ml disposable injection syringe (needle external diameter 0.4 mm, the bevel of the needle was 1 mm). About 5 mm of the forepart of the needle was bent to 30°, The procedure was performed under an ophthalmic surgical microscope (OPML Lumerai, Carl-Zeiss Meditec AG, Oberkochen, Germany) with an injection angle of approximately 5° to the surface of the central cornea, at the same time keeping the bevel of the needle upward. When the half bevel of the needle is put into the shallow corneal stroma (1/3 depth or less), the needle was pushed in horizontally until the bevel was completely into the cornea. Then *Candida albicans* was injected to produce an approximate 4-mm-diameter circular gray-white change at the shallow cornea. In group 2, 0.1 ml of the prepared *Candida albicans* liquid was injected directly into the central corneal stroma using an old-style 1-ml sterile syringe (needle external diameter 0.5 mm, the bevel of the needle was 1.2 mm) (Fig.1B) by the same method without the microscope, until an approximate 4-mm circular gray-white color change was observed (Fig. 1A). One rabbit

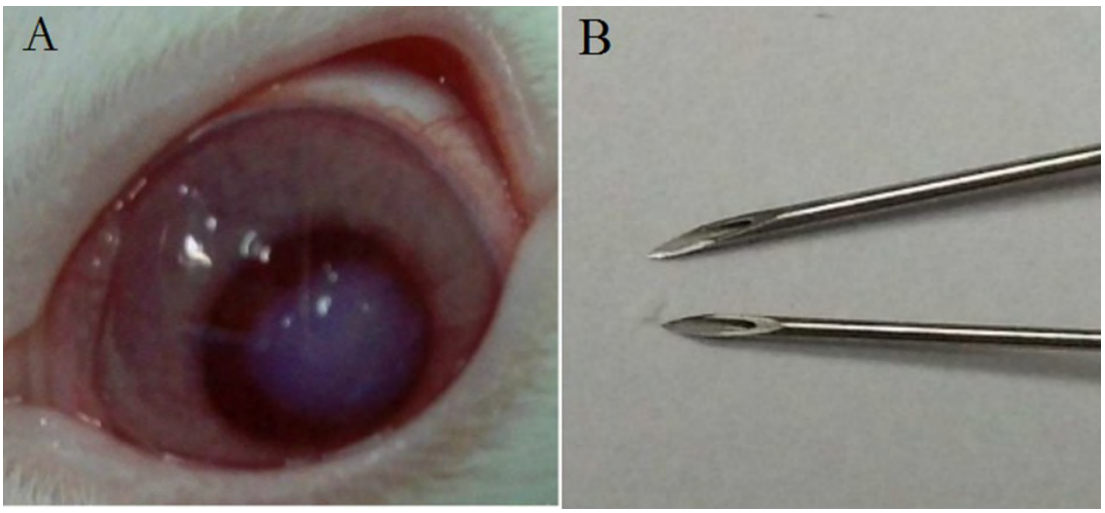


Fig. 1. ***A****) An approximately 4 mm circular gray-white area formed in the rabbit cornea after the* Candida albicans *injection.* ***B****) I syringes. The top (old-style) needle external diameter is 0.5 mm, the bevel of the needle is 1.2 mm; the lower (new-style) needle external diameter is 0.4 mm, the bevel of the needle is1 mm.*

demonstrated a lack of appetite and energy. It was thought to be suffering from peritonitis, therefore euthanasia was performed.

Slit-lamp microscopy (SL-1E, TOPCON Corporation, Tokyo, Japan) was performed in all the experimental eyes (the right eyes) to observe and evaluate the conjunctiva, cornea and anterior chamber at 1, 3, and 5 days after the injection. Corneal scraping, fungi culture, and the identification of fungi were performed at 3 and 5 days after the injection. The procedures were as follows. The right eyes were anesthetized three times using 0.4% oxybuprocaine hydrochloride eye drops. Their heads were fixed and the eyelids were opened using an eye speculum. A sterile blade was used to gently scrape the corneal ulcer tissues. The ulcer tissues were directly inoculated on Sabouraud medium and incubated overnight at 25°C. The suspicious colonies were chosen for a smear test under a microscope (BX41, Olympus, Japan). Fungi were confirmed if spores or mycelia were observed under the microscope. A YST identification card of the VITEK 2 automatic microbial identification system was used to identify fungal species.

The eyes of the rabbits were observed using a confocal microscope (Heidelberg Engineering, Germany) at 3 and 5 days after the models were established. The procedures were as follows. The right eyes were anesthetized three times using 0.4% oxybuprocaine hydrochloride eye drops. Their heads were fixed and the eyelids were opened using an eye speculum. Carbomer eye drops (10 g, 0.2%, Gerhard Mann Chem.-Pharm, Fabrik) were dripped on the surface of the objective lens of the confocal microscope. The corneas were covered with a disposable sterile glass lens. The objective lens was moved forward to touch the corneal glass lens on the cornea. The default depth of the focal plane was 0 μm. Images of the different depths of the cornea were captured by adjusting the focus button. Hyphae and spores were looked for in these corneal tissues. The images were captured multiple times and saved in the computer.

Finally, the rabbits were sacrificed through inhaling carbon dioxide together with nitrous oxide (20% and 60% of the chamber volume.min-1 respectively) (5).

Statistical analysis

Results were analyzed using SPSS22.0 (SPSS Inc., Chicago, IL, USA) software. Description statistics analysis was used to describe the rate of positive .

RESULTS

Slit lamp examinations were performed on days 1, 3 and 5 after the corneal *Candida albicans*

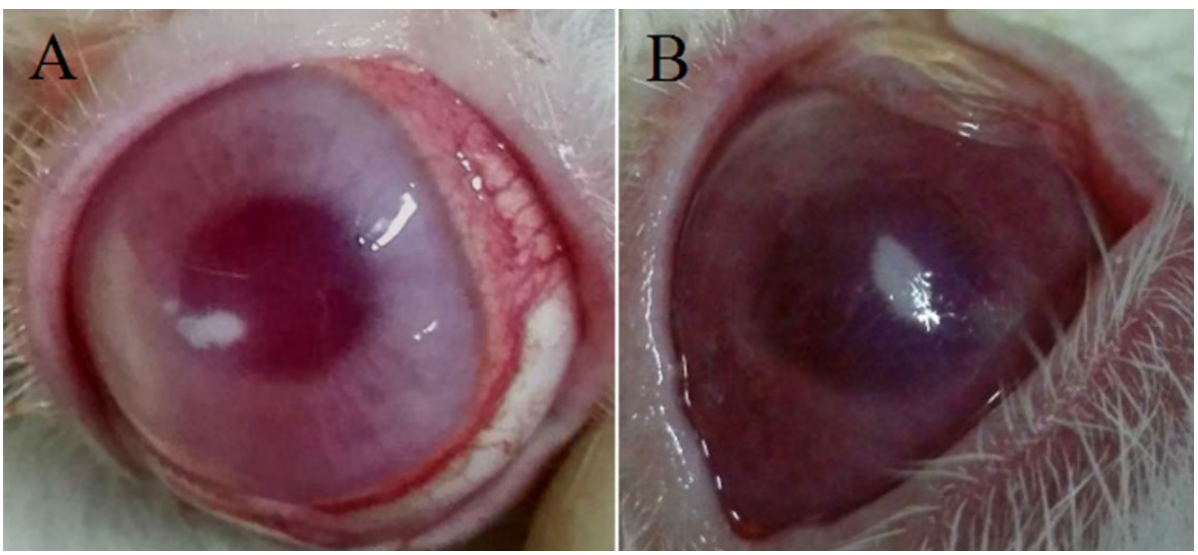


Fig. 2. ***A****) An eye from group 1;* ***(B)*** *an eye from group 2. One day after infection, corneal ulcer formation could be observed in both groups. The corneas had mild edema. The iris was visible and no hypopyon was observed in the anterior chamber.*

infection. On day 1 after the infection, no difference was observed between the two groups. They all had corneal ulceration and mild edema of the cornea. The irises were visible without hypopyon (Fig. 2). Three days after the infection, the area of corneal ulcers increased with several satellite spots around the lesions observed in group 1. The iris could not be seen in group 1 due to the diffusely corneal edema (Fig. 3A). However, in group 2, the corneal ulcers were deeper than those in group 1 and the corneal endothelium was involved (Fig. 3B). Five days after the infection, the area of the ulcer lesions in group 1 further expanded, and the fusion of the ulcer lesion and the satellite lesion was observed. The lesions were adhered to the necrotic tissues of the moss-like necrosis. The edges of the ulcers were

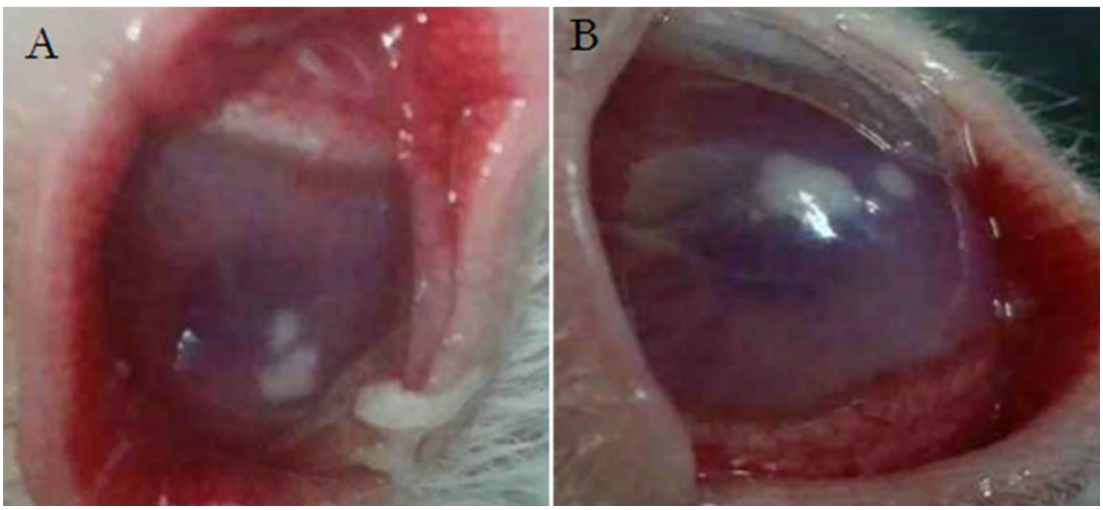


Fig. 3. *Three days after infection, the lesion area of the corneal ulcer increased in group 1, and satellite lesions were observed around the main lesion with a diffused corneal edema. The iris cannot be clearly observed (**A**). In group 2, the corneal ulcer was in the deeper layer of the corneal stroma and the corneal endothelium was involved (**B**).*

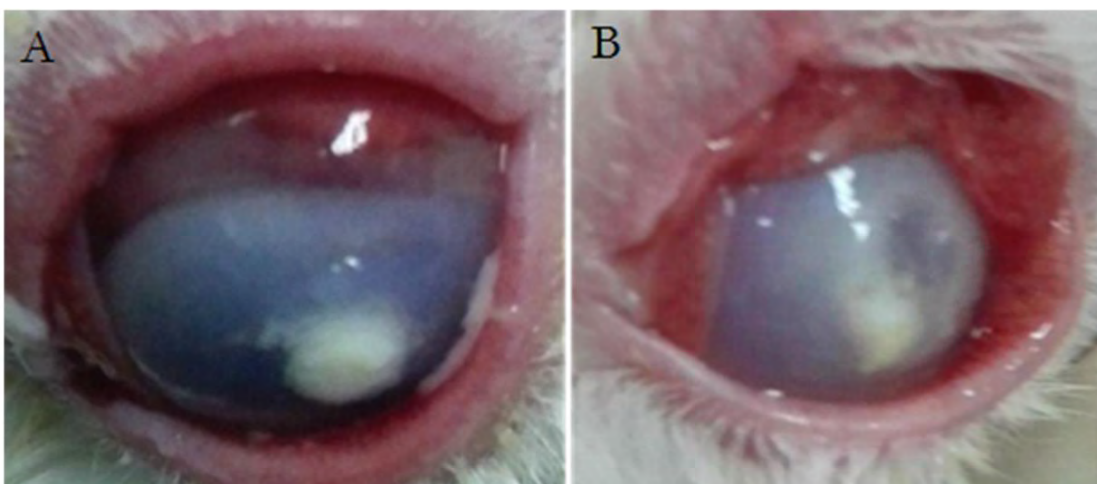


Fig. 4. *Five days after the infection, the area of the ulcer lesions in group 1 further expanded, and the fusion of the ulcer lesion and the satellite lesion was observed. The lesions were adhered to the necrotic tissues of the moss-like necrosis. The edge of the ulcers were irregular and slightly higher than the surface of the lesions. The cornea was diffusely edemic. **A**) In group 2, the corneal ulcers expanded to the deep stroma of the cornea. No obvious necrotic tissue was found on the corneal surface. The diffuse edema of the cornea was serious (**B**).*

irregular and slightly higher than the surface of the lesions. The corneas were diffusely edematous, and the hypopyon was barely seen.(Fig. 4A). In group 2, the corneal ulcers extended in the deep stroma of the cornea. No obvious necrotic tissue was found on the corneal surface. The diffuse edema of the cornea was serious, and hypopyon could be observed in the anterior chamber in 3 rabbits (Fig. 4B). Corneal perforation and the disappearance of the anterior chamber were observed in 3 rabbits.

Corneal ulcers were formed after the 3-5 days of infection. Growth of *Candida albicans* colonies was observed in the cultures of the corneal scraping samples. The colonies had typical manifestations of yeast including a large round shape, rough and wrinkled surface, and pseudohyphae immersed in the medium. The culture results are shown in Table I and Table II. There were significant differences of the positive rate between the two groups after 3 and 5 days following infection. The positive rates of group 1 were higher than those in group 2.

There was no significant difference between group 1 and group 2 regarding fungal species. Positive Gram staining with uneven staining and round or oval cells with pseudohyphae could be observed in both groups. The fungal cells with varied lengths of non-branched pseudohyphae were observed under high magnification of a microscope without staining. This is a typical manifestation of *Candida albicans*.

Corneal ulcers were formed after 3-5 days following the infection in the two groups. Mycelia or spores were found by confocal microscopy. A large number of fungal mycelia and inflammatory cells were observed. The mycelia were slender and curved into a cable-like shape with a high refractive index .

DISCUSSION

The wound healing process of the corneal stroma in rabbit eyes resembled that of the human eye (6). New Zealand white and Dutch band rabbits are commonly used (7), therefore, New Zealand white rabbits were used in the present study.

In the present study, the risk of corneal perforation was lower and the success rate of the model was higher. With this method, it was easier to obtain the infective corneal ulcer sample and increase the positive rate of the samples. Traditional methods to establish rabbit fungal keratitis models include the corneal surface scarification method, corneal stroma injection

Table I. *Culture results of the corneal scraping samples after three days of infection*

Group	Positive eyes	Negative eyes	Total eyes	Rate of positive %
Group 1	9	3	12	75.00
Group 2	7	5	12	58.33
Total eyes	16	8	24	66.67

Table II. *Culture results of the corneal scraping samples after five days of infection*

Group	Positive eyes	Negative eyes	Total eyes	Rate of positive %
Group 1	11	1	12	91.67
Group 2	6	3	9	66.67
Total eyes	17	4	21	80.95

method, contact lens method and acupuncture method. Postoperative subconjunctival injection or systemic use of hormones or immunosuppressive agents can induce the establishment of the model (8). The success rate of the scratch method or acupuncture is low. The current common fungal keratitis animal model injects fungal spores into the corneal stroma of the rabbit to induce a deep corneal fungal infection model (9). A confocal microscope could observe normal corneal cells and abnormal substances such as fungi, bacteria, and inflammatory cells. It also has the ability to quantitatively assess the cornea and surgical outcomes in normal corneas and disease states (10, 11).

In conclusion, the method demonstrated has the advantages of simple operation, high success rate of infection, low cost, easy to obtain ulcer tissue, and a significantly reduced risk of corneal perforation.

REFERENCES

1. Pinnock A, Shivshetty N, Roy S, et al. Ex vivo rabbit and human corneas as models for bacterial and fungal keratitis. Graefes Arch Clin Exp Ophthalmol 2017; 255:333-42.
2. Zhong W, Yin H,Xie L. Expression and potential role of major inflammatory cytokines in experimental keratomycosis. Mol Vis 2009; 15:1303-11.
3. Jiang X, Gao L, Zhang Y, et al. A comparison of the effects of ketamine, chloral hydrate and pentobarbital sodium anesthesia on isolated rat hearts and cardiomyocytes. J Cardiovasc Med (Hagerstown) 2011; 12:732-5.
4. Little WB, Jean GS, Sithole F, Little E, Jean KY. Degree of corneal anaesthesia after topical application of 0.4% oxybuprocaine hydrochloride and 0.5% proparacaine hydrochloride ophthalmic solution in clinically normal cattle. Aust Vet J 2016; 94:181-5.
5. Boivin GP, Hickman DL, Creamer-Hente MA, Pritchett-Corning KR, Bratcher NA. Review of CO(2) as a euthanasia agent for laboratory rats and mice. J Am Assoc Lab Anim Sci 2017; 56:491-99.
6. Dong CJ, Agey P, Hare WA. Origins of the electroretinogram oscillatory potentials in the rabbit retina. Vis Neurosci 2004; 21:533-43.
7. Kalkanci A, Bilgihan K, Ozdemir HB, Yar Saglam AS, Karakurt F, Erdogan M. Corneal cross-linking has no effect on matrix metalloproteinase 9 and 13 levels during fungal keratitis on the early stage. Mycopathologia 2018; 183:329-36.
8. Sauer A, Letscher-Bru V, Speeg-Schatz C, et al. In vitro efficacy of antifungal treatment using riboflavin/UV-A (365 nm) combination and amphotericin B. Invest Ophthalmol Vis Sci 2010; 51:3950-53.
9. Leal SM, Jr.,Pearlman E. The role of cytokines and pathogen recognition molecules in fungal keratitis - Insights from human disease and animal models. Cytokine 2012; 58:107-11.
10. Kumar RL, Cruzat A,Hamrah P. Current state of in vivo confocal microscopy in management of microbial keratitis. Semin Ophthalmol 2010; 25:166-70.
11. Wu XL, Tao Y, Qiu QC. Application of image recognition-based automatic hyphae detection in fungal keratitis. Australas Phys Eng Sci Med 2017; 28:1-9.

LETTER TO THE EDITOR

EXPRESSION LEVELS OF FILAMIN A IN PREECLAMPSIA PLACENTA

LL. ZHENG, XY. ZHANG, H. ZHANG, Y. WANG and Y. ZHOU

Department of Obstetrics, Second Affiliated Hospital of Shandong First Medical University, Taian City, China

Received September 16, 2019 – Accepted March 18, 2020

To the Editor,

Preeclampsia, a specific syndrome during pregnancy, is a complication that does not manifest until the 20th week of gestation. The main characteristics are hypertension, proteinuria and systemic dysfunction of multiple organs. Patients with severe symptoms may suffer from heart failure, coma and other serious conditions (1). At present, the pathogenesis of preeclampsia has not been clarified, but there is no doubt that the placenta plays a crucial role (2).

FLNA (Filamin A), also known as ABP-280 (actin binding protein 280), provides cytoskeletons with the filaments of cross-linking actin and contributes to cell movement, such as the normal movement of cells in placental tissues (3). Chen et al. studied the proteins related to CHDs (congenital heart defects) in prenatal diagnosis, and the results indicated that the FLNA expression may play an important part in late pregnancy (4). Hasan et al. explored the related gene editing sites in pregnant women with preeclampsia. The expression of FLNA was found abnormal but the mechanism was not clear. According to the studies above, FLNA is a multi-functional protein whose role in preeclampsia has not yet been clarified (5). Pregnant women were enrolled in this study in order to explore the expression of FLNA in placental tissues of patients with preeclampsia. After grouping, FLNA in the tissues of subjects was detected and statistically analyzed, providing new ideas for the remission and treatment of patients with preeclampsia.

MATERIALS AND METHODS

Patients

One hundred pregnant women who had undergone regular prenatal examinations and deliveries or miscarriages in the Second Affiliated Hospital of Shandong First Medical University from January to December 2018 were selected. All subjects had singleton pregnancies and were aged 23- 42 years. They were assigned into 5 groups: early pregnancy group (20 cases), preterm labor group (20 cases), full-term pregnancy group (20 cases), early-onset preeclampsia group (20 cases), and late-onset preeclampsia group (20 cases). All the subjects completed follow-up from enrollment until delivery. Informed consent forms were obtained from all the subjects and their family members. This experiment was approved by the ethics committee of Second Affiliated Hospital of Shandong First Medical University.

Inclusion criteria: the subjects experienced gestation for 1 to 5 times without other surgical procedures; all subjects conceived naturally; no smoking or drinking habits; no history of radiotherapy/chemotherapy; and the pregnancy was terminated by cesarean section. Exclusion criteria: the subjects had diabetes, immune, liver or other diseases; the subjects had autoimmune disease or infection.

Key words: preeclampsia; filamin A; placental tissues; gestation period

Corresponding Author:
Dr Yan Zhou,
Department of Obstetrics,
Second Affiliated Hospital of Shandong
First Medical University, Taian City 271000,
Shandong Province, China.
e-mail: zhouyanyis1816@163.com

0393-974X (2020)
Copyright © by BIOLIFE, s.a.s.
This publication and/or article is for individual use only and may not be further reproduced without written permission from the copyright holder.
Unauthorized reproduction may result in financial and other penalties
DISCLOSURE: ALL AUTHORS REPORT NO CONFLICTS OF INTEREST RELEVANT TO THIS ARTICLE.

Diagnostic criteria: preeclampsia was diagnosed if blood pressure increased in the second and third trimester of pregnancy, accompanied by 24--h urine protein over 0.3g, systolic blood pressure not less than 140mmHg or diastolic blood pressure not less than 90mmHg. This period could be divided into early onset (less than 34 weeks) and late onset (more than 34 weeks).

Sample collection

The placenta tissues were collected immediately after the placenta was identified during surgeries, and the placental maternal surfaces with no calcification and necrosis were selected. At the same time, the umbilical cord was avoided. Three-layer tissues (1 cm^3) from the middle part of the placenta were selected and washed repeatedly with sterilized saline, and finally dried by gauzes. Two of them were placed in two hyper-thermic sterilization tubes, respectively, and stored at -80°C for the following real-time PCR and protein detection. The rest of the tissues were labeled appropriately and fixed with paraformaldehyde (4%; Shanghai Reagent Factory, China) for ELISA.

Villous tissues from early pregnancy patients were collected. Entire villi were collected immediately after induced abortion. The samples were washed repeatedly with sterilized saline, and then dried by gauzes. The collected tissues were equally divided into three parts, two of which were put into two hyper-thermic sterilization freezing tubes and storedat a -80°C for the following real-time PCR and protein detection. The rest of the tissues were labeled appropriately and fixed with paraformaldehyde (4%) for ELISA.

ELISA

After thorough washing, the sections were immersed in dichromate sulfate solution for one day. They were removed with tweezers, rinsed with dd H_2O cycle, and dried. Then they were placed in anhydrous ethanol for 24 h, removed, dried, and coated with 10% poly-amino acid (Beijing Zhongshan Jinqiao Biotechnology Co., Ltd., China) anti-stripping tablets. Sections were embedded in paraffin. The sections were cut into slices (5 μm) by a slicer (Leica, Germany). The slices were prepared by baking, dewaxing, hydration and microwave antigen thermal repair. Afterwards, the slices were cultured with 10% goat serum sealing solution (Shanghai Solarbio Bioscience & Technology Co., Ltd., China) in a 37°C incubator and incubated with primary antibody, secondary antibody and stained with 3, 3-aminobenzidine (Shanghai Solarbio Bioscience & Technology Co., Ltd., China). The staining results were observed with an electron microscope, and the sections were rinsed with water. Then, the sections were re-dyed with hematoxylin (Zhuhai Baso Biotechnology Co., Ltd., China) for 2 min. Finally, the sections were rinsed with water and sealed with neutral gum. Five different visual fields were observed in each section, and the expression of FLNA was measured by Image-Pro Plus Image analysis software with an average optical density.

RT-PCR

Total RNA in the tissue was extracted first. Frozen placenta or villi (60~100 mg) from early pregnancy patients were added in EP (Eppendorf) tubes containing inactivated RNA enzymes, and 1 mL Trizol solution was added (Invitrogen, USA) to obtain total RNA by the Trizol method. RNA concentrations and OD (optical density) value of 1 μL samples were measured with an ultra-micro ultraviolet spectrophotometer. The samples were stored at -80°C refrigerator. The gene sequences were then obtained by reverse transcription. 50 μL reverse transcription reaction system was prepared (Total RNA: 2 μL; 5×first-strand Buffer: 4 μL; M-Mu LV Reverse Transcriptase (200U/μL): 0.8 μL; Oligo dT Primer (50μM): 2 μL; dNTP Mixture (10mM each): 2 μL; RNase Inhibitor (40U/μL): 0.5 μL; RNase Free ddH_2O was added until the total volume reached 50 μL; reverse transcription program: the samples were placed on a PCR machine (BIO-RAD, USA) at 42°C for 30 min and then maintained at 4°C for 10 min and finally cooled on ice. The cDNA could directly react with an ABI Stepone plus fluorescent quantitative PCR instrument (BIO-RAD, USA) in a 96-well plate containing the samples. The Rotor-gene Q software was adopted. β-actin was used as internal reference, and the real-time quantitative FLNA mRNA level was determined by $2^{-\Delta\Delta Ct}$ method. Each experiment was repeated 3 times.

Western blot

Placenta tissues or villi (50-100 mg) from early pregnancy patients were obtained, chopped into small pieces, and lysed on ice. After sufficient mixing, the mixture was centrifuged at 15,000rpm in 4°C for 15 min, and the supernatant was obtained. The protein

concentrations were measured with a BCA (bicinchoninic acid) protein kit (Pierces, USA). Then the proteins were added (10-30 μg), and the SDS-PAGE (sodium dodecyl sulfate polyacrylamide gel electrophoresis) electrophoresis was conducted under the constant pressure of 60V. When the proteins reached the separation gels, the voltage was increased to 120V. After electrophoresis, the membrane was transferred and sealed in turn. Then the membrane was washed with 1×TBST (TBS+Tween, TBS: Tris-Buffered Saline) (2.4 g Tris base, 8 g sodium chloride, double distilled water and concentrated HCl were added to adjust the pH to 7.6) for 4 times, 10 min each time. The corresponding horseradish peroxidase-labeled secondary antibody was added to the membranes (1: 2000 dilution) and incubated at room temperature for 1 h. Afterwards, the membranes were washed with 1×TBST for 10 min for 4 times. Liquid A (luminol) and B (hydrogen peroxide) of the developer were mixed at a ratio (1:1) and added to the surface of PVDF (polyvinylidene fluoride) membranes evenly. Digital multi-functional image enhanced chemiluminescence system was used for image exposure and storage (Shanghai Tianneng Technology Co., Ltd., China). The FLNA protein expression level was determined by the FLNA/β- actin ratio.

Statistical analysis

All data were obtained from three independent experiments, and expressed as mean±standard deviation.

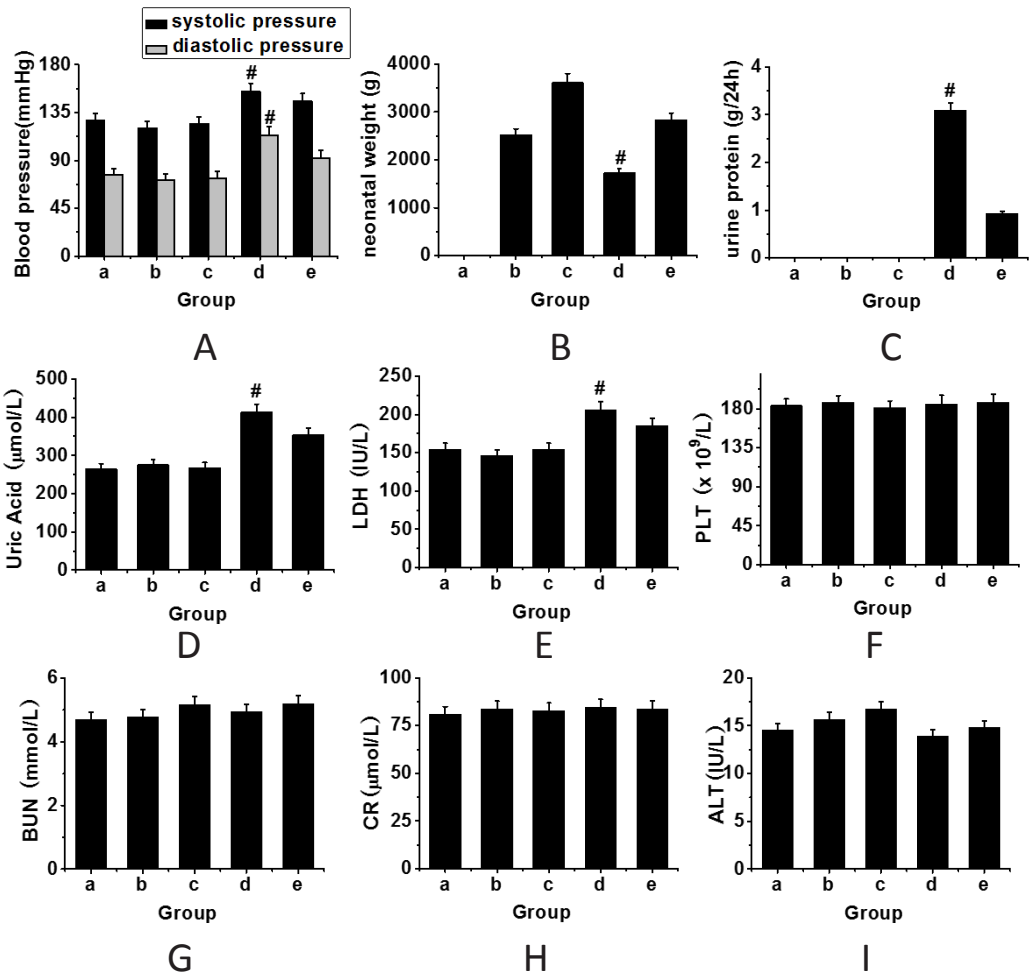


Fig. 1. *Comparison and analysis of the general clinical data of each group. a: early pregnancy group; b: premature birth group; c: full-term pregnancy group; d: early-onset preeclampsia group; e: late-onset preeclampsia group.* ***A)*** *systolic and diastolic blood pressure;* ***B)*** *newborn body weight;* ***C)*** *urine proteins;* ***D)*** *uric acid;* ***E)*** *LDH;* ***F)*** *PLT;* ***G)*** *BUN;* ***H)*** *Cr;* ***I)*** *ALT; compared with full-term pregnancy group and late-onset preeclampsia group, #P<0.01 indicated statistical significance.*

SPSS 22.0 statistical software was used for *t*-test, and Pearson correlation analysis was employed. $P < 0.05$ indicated statistical significance.

RESULTS

As shown in Fig. 1, the clinical parameters in each group were analyzed. It was found that the systolic blood pressure and diastolic blood pressure in the early-onset preeclampsia group were significantly higher than those in the late-onset preeclampsia group and the normal pregnancy group ($P<0.01$). The neonatal body weight in the early-onset preeclampsia group was significantly lower than that in the late-onset preeclampsia group and the normal pregnancy group ($P<0.01$) (Fig. 1B). In Fig. 1 C D, E, proteins, uric acid and LDH (lactate dehydrogenase) in early-onset preeclampsia group were significantly higher than those in the late-onset preeclampsia group and normal pregnancy group ($P<0.01$). Fig. 1 F, G, H and I show there was no significant difference in PLT (platelet), BUN (urea nitrogen), Cr (muscular intoxication), ALT (glutamic-pyruvic transaminase) among the groups ($P >0.05$).

Enzyme-linked immunoassay was performed using placenta or villi tissues from each group (Fig. 2). Tissues from all the groups showed positive expressions of the proteins. FLNA expressions in placenta were found to be localized in cells, most of which were located at the cytoplasmic borders, and a few appeared in the nucleus. FLNA staining in the early pregnancy group was shallow and the count of positive cells was low (Fig. 2). In the early-onset preeclampsia group, FLNA staining was the deepest and the count of positive cells was the highest.

The analysis diagram of FLNA mRNA expression in placenta or villi of each group determined by RT-PCR is shown in Fig.3. Compared with the preterm delivery group and the full-term pregnancy group, the FLNA mRNA expression level in the early pregnancy group was statistically lower ($P<0.01$). Compared with the late-onset preeclampsia group

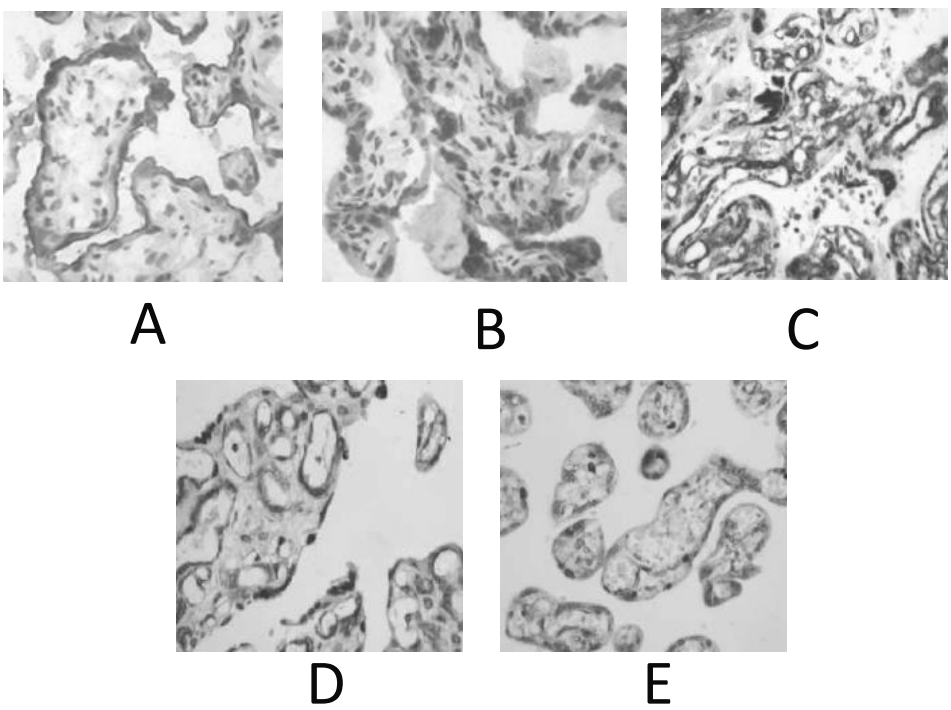


Fig. 2. *FLNA expressions in placenta or villi from early pregnancy patients in each group (×400).* ***A****) early pregnancy group;* ***B****) premature birth group;* ***C****) full-term pregnancy group;* ***D****) early-onset preeclampsia group;* ***E****) late-onset preeclampsia group.*

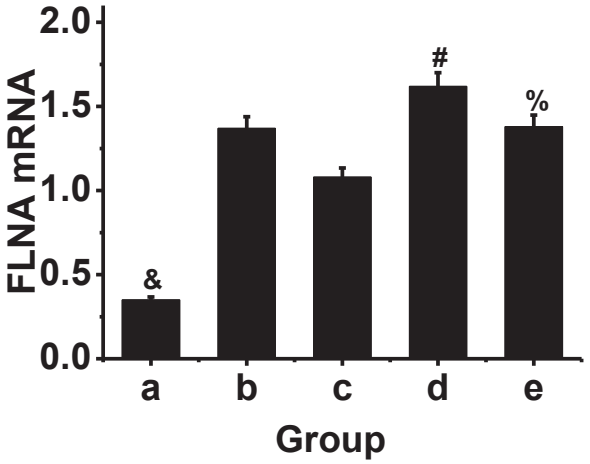


Fig. 3. *Expressions of FLNA mRNA in placenta or villi from early pregnancy patients in each group a: early pregnancy group; b: premature birth group; c: full-term pregnancy group; d: early-onset preeclampsia group; e: late-onset preeclampsia group. Compared with preterm delivery group and full-term pregnancy group, &P<0.01 indicated significant difference; compared with the late-onset preeclampsia group and the preterm labor group, #P<0.01 indicated significant difference; compared with the full-term pregnancy group, %P<0.01 indicated significant difference.*

and the preterm delivery group, the FLNA mRNA expression level was statistically higher in the early-onset preeclampsia group (P<0.01). Compared with the full-term pregnancy group, the FLNA mRNA expression level was statistically higher in the late-onset preeclampsia group (P<0.01).

As shown in Fig.4, the expression of FLNA expressions in placenta or villi from early pregnancy patients in each group was detected by Western blot. Compared with the preterm delivery group and full-term pregnancy group, the FLNA protein expression level in the early pregnancy group was statistical lower (P<0.01). Compared with the late-onset preeclampsia group and the preterm delivery group, the FLNA expressions level in the early-onset preeclampsia group was statistically higher (P<0.01). Compared with the full-term pregnancy group, the expression level of FLNA was statistically higher in the late-onset preeclampsia group (P<0.01).

DISCUSSION

Studies have demonstrated that the most obvious symptoms in pre-eclampsia are increased blood pressure and a significant drop in the body weight of fetuses (6). By comparing and analyzing the general clinical data in each group, it was found that the systolic blood pressure, diastolic blood pressure and newborn body weight in early-onset preeclampsia group were significantly different from those in the late-onset preeclampsia group and normal pregnancy group (P<0.01), which was basically consistent with the research of Li et al. (7).

At present, three members of the filament protein family have been found, namely FLNA, FLNB and

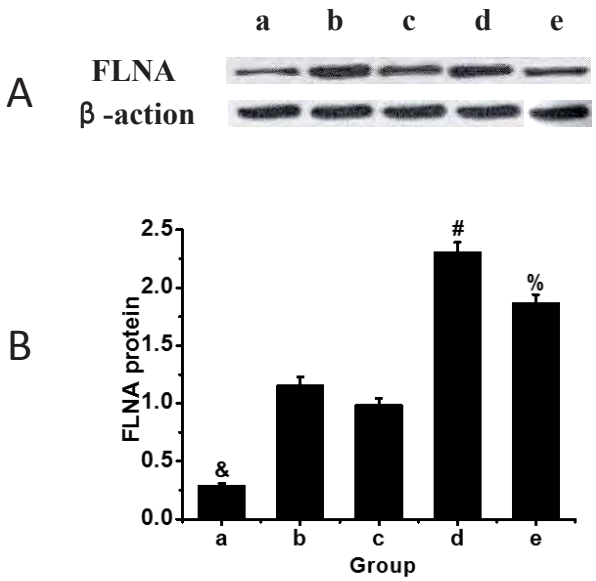


Fig. 4. *The FLNA expressions in the placenta or villus from early pregnancy patients detected by Western blot. a: early pregnancy group; b: premature birth group; c: full-term pregnancy group; d: early-onset preeclampsia group; e: late-onset preeclampsia group.* ***A****)the expression level of FLNA protein detected by Western blot in placenta or villi from early pregnancy patients in each group;* ***B****) quantitative analysis of the FLNA protein expression in placenta or villi from early pregnancy patients in each group. Compared with preterm delivery group and full-term pregnancy group, &P<0.01 indicated significant difference; compared with the late-onset preeclampsia group and the preterm labor group, #P<0.01 indicated significant difference; compared with the full-term pregnancy group, %P<0.01 indicated significant difference.*

FLNC. Among them, FLNA can be found in multiple organs. Through binding with dozens of proteins, it is involved in the forming of channels, receptors, intracellular signal molecules and transcription factors, etc. FLNA can also form cytoskeleton with cross-linked actin (8). Results of RT-PCR and Western blot showed that compared with the preterm delivery group and the full-term pregnancy group, the FLNA protein expression level was statistically lower in the early pregnancy group ($P<0.01$). Compared with the full-term pregnancy group, the FLNA protein expression was statistically higher in the late-onset preeclampsia group ($P<0.01$), which was basically consistent with the result of Urra et al. (9). However, it was inferred that FLNA was involved in the pathophysiological process of preeclampsia in the early stage, and was related to the severity of preeclampsia in the early stage, which was not indicated in previous studies.

In conclusion, it can be found that intervening the expression of FLNA in cells can alleviate the symptoms of pregnant patients with preeclampsia and achieve the desired effect, thereby providing a new idea for clinical relief and treatment of patients with preeclampsia.

REFERENCES

1. Ramos JGL, Sass N, Costa SHM. Preeclampsia. Rev Bras Ginecol Obstet 2017; 39(9):496-512.
2. Motawea HKB, Chotani MA, Ali M, et al. Human placenta expresses α2-Adrenergic receptors and may be implicated in pathogenesis of preeclampsia and fetal growth restriction. The Am J Pathol 2018; 188(12):2774-85.
3. Toomer K, Sauls K, Fulmer D, et al. FilaminA as a balance between Erk/Smad activities during cardiac valve development. Anat Rec (Hoboken) 2019; 302(1):117-124.
4. Chen L, Gu H, Li J, et al. Comprehensive maternal serum proteomics identifies the cytoskeletal proteins as non-invasive biomarkers in prenatal diagnosis of congenital heart defects. Sci Rep 2016; 6:19248.
5. Wei J, Fu Y, Mao X, Jing Y, Guo J, Ye Y. Decreased Filamin b expression regulates trophoblastic cells invasion through ERK/MMP-9 pathway in pre-eclampsia. Ginekol Pol 2019; 90(1):39-45.
6. Guedes-Martins L. Superimposed preeclampsia. Adv Exp Med Biol 2017; 956:409-17.
7. Li Fraine S, Patel A, Duprat F, Sharif-Naeini R. Dynamic regulation of TREK1 gating by Polycystin 2 via a Filamin A-mediated cytoskeletal mechanism. Sci Rep 2017; 7(1):17403.
8. Guo Y, Li M, Bai G, et al. Filamin A inhibits tumor progression through regulating BRCA1 expression in human breast cancer. Oncol Lett 2018; 16(5):6261-66.
9. Urra H, Henriquez DR, Cánovas J, et al. IRE1α governs cytoskeleton remodelling and cell migration through a direct interaction with filamin A. Nat Cell Biol 2018; 20(8):942-53.

LETTER TO THE EDITOR

ROLE OF LYMPHOCYTE SUBSETS AND IL-17 IN NON-SMALL CELL LUNG CANCER

C. DENG, BY. REN, XP. HUANG, JJ. TAN, JJ. WU, W. WANG and C. ZHU

Department of Oncology, Chongqing Three Gorges Central Hospital, Wanzhou District, Chongqing, China

Received October 10, 2019 – Accepted January 24, 2020

To the Editor,

Some studies have shown that the mortality due to primary lung cancer is the highest among malignant tumors, of which more than 80% are non-small cell lung cancer (NSCLC) (1), and death is mainly attributed to advanced lymph node metastasis (bleeding, pain, and other symptoms) (2). Systemic chemotherapy is the main choice for the treatment of advanced NSCLC. However, chemotherapeutic drugs destroy normal immune systems. Therefore, changes in the immune status of patients with advanced NSCLC before and after chemotherapy have become the focus of research in recent years.

Lymphocyte subsets are believed to play an important role in maintaining the balance of the immune system, killing tumor cells and immune monitoring. It has been shown that when lung cancer cells lose human leukocyte antigen (HLA) - I cell molecules, cloning of CTL ceases. When immune responses fail over time, deterioration of lung cancer occurs (3). In recent years, natural killer cells (NK) have been found to have a strong immunomodulatory effect (4). IL-17 can stimulate cells to secrete and release pro-inflammatory cytokines under certain conditions, thus promoting inflammation and tumors in the body (5, 6). Therefore, through determination of peripheral lymphocyte subsets and cytokine IL-17 in NSCLC patients, the immune function, especially its clinical significance before and after tumor treatment, is worthy of further study and discussion. However, there are few relevant studies in this field.

Based on the above facts, in this study, the changes of lymphocyte subsets and IL-17 levels in advanced NSCLC patients after chemotherapy were observed and the correlation was analyzed.

MATERIALS AND METHODS

Subjects

Seventy-eight advanced NSCLC patients admitted to Chongqing Three Gorges Central Hospital from May 2017 to October 2018 were selected as the experimental group, including 50 males and 28 females. Their ages ranged from 41 to 79 (average 63.51±7.68) years. According to their pathological types, they were divided into 46 patients with adenocarcinoma and 32 patients with squamous cell carcinoma. According to the TNM staging system, there were 4 cases of stage III and 64 cases of stage IV. Seventy-eight healthy subjects (47 males and 31 females) were selected as the control group. Their ages ranged from 43 to 80 (average 62.48±10.62) years. None of the subjects had major visceral diseases, liver or kidney dysfunctions, or family tumor history. The two groups were comparable in age, gender and other basic data, and the differences were not statistically significant ($P > 0.05$). All participants signed informed consents prior to the study which was approved by the Ethics Committee of Chongqing Three Gorges Central Hospital.

Key words: NSCLC; Lymphocyte subsets; IL-17; CTL; CD8+CD28- cells

Corresponding Author:
Dr Chuan Zhu,
Department of Oncology,
Chongqing Three Gorges Central Hospital,
165 Xincheng Road, Wanzhou District,
Chongqing, 404100, China
e-mail: zhuchuansky201@126.com

0393-974X (2020)
Copyright © by BIOLIFE, s.a.s.
This publication and/or article is for individual use only and may not be further reproduced without written permission from the copyright holder.
Unauthorized reproduction may result in financial and other penalties
DISCLOSURE: ALL AUTHORS REPORT NO CONFLICTS OF INTEREST RELEVANT TO THIS ARTICLE.

Five mL of fasting venous blood was collected from both groups and placed in EDTA anticoagulation tubes (Becton, Dickinson and Company, USA), and sent to the oncology laboratory for testing.

Patients in the experimental group received 2 cycles of platinum-containing drugs combined with chemotherapy. Blood samples were taken before and after chemotherapy.

Lymphocyte subsets were detected by flow cytometry: 100 μL of anticoagulant whole blood and 20 μL of corresponding fluorescent antibody were added to 4 test tubes before being shaken and mixed, and incubated in the dark for 20 min. Each tube was then added with 2 mL hemolysin, shaken and mixed, and incubated in the dark for 15 min. The samples were centrifuged at 2000r/min for 10 min (Hunan Xiang Yi Laboratory Instrument Development Co. Ltd., China), and the supernatant was discarded. After washing with PBS, they were centrifuged again for 10 min at 2000r/min and the supernatant was discarded. PBS was added once more and the mixture was thoroughly shaken. The proportions of CD3+, CD4+, CD8+, CD28+, NK and Treg cells were determined by FACS Caliber flow cytometry (Becton, Dickinson and Company, USA).

Enzyme-linked immunosorbent assay (ELISA) (TianJin Annorikang Biotechnology Co. Ltd., China) was used for the detection of IL-17; 2 mL of anticoagulant whole blood was taken and centrifuged at 3500r/min for 10 min for separation of the serum. A standard sample was acquired for testing with the blank well, standard well and sample well set. 50 μL of standard substance was added to the standard well first. 40 μL of the processed sample was then added to the sample well to be tested with 10 μL of sample balance liquid added to make it evenly balanced for 30 min. 100 μL of horseradish peroxidase antibody was added and thoroughly mixed into the standard well and the sample well. The coated microplate was incubated smoothly in a 37°C incubator for 60 min and repeatedly rinsed with the diluted washing solution to completely discard the remaining residue in the well. 50 μL of TMBI was added into the blank well, the standard well, and the sample well followed by adding and mixing 50 μL of TMBII in the dark for 20 min. Finally, 50 μL of termination liquid was added and fully mixed to each well to terminate the reaction. The absorbance value of each well was read with a microplate reader (China University of Science and Technology Innovation Co. Ltd., China) at 450 nm, and the standard curve was drawn with the concentration curve value of standard substance to obtain the data.

Statistical analysis

Data obtained by flow cytometry were analyzed by Cell Quest software. The measurement data were normally distributed and expressed as $(\bar{x}\pm s)$. SPSS17.0 statistical software was used for statistical analysis of the experimental data, and paired *t*-test was used to compare the differences between groups. Pearson correlation analysis was used, and the significance level was $\alpha=0.05$, and $P < 0.05$ was considered statistically significant.

RESULTS

Changes of IL-17 levels in peripheral blood of patients in the experimental group

The results (Table I) showed that there was no significant correlation between IL-17 levels in peripheral blood of the patients and clinicopathological data such as gender, age, smoking, and pathological type ($P > 0.05$). The level of IL-17 of the control group was 31.56±7.95, but in the experimental group increased significantly to 43.78±6.55 ($P<0.05$). Before and after treatment the levels of IL-17 showed that after 2 cycles of chemotherapy, the levels decreased significantly from 43.78±6.55 to 40.29±7.07 ($P < 0.05$). The results showed that IL-17 levels in patients with stage III and IV were higher than those in the control group, and the difference was statistically significant ($P<0.05$). However, there was no significant difference in IL-17 levels between stage IV and stage III patients ($P>0.05$).

Changes in the number of peripheral blood lymphocyte subsets in the experimental group

The number of peripheral blood lymphocyte subsets in the experimental group and the control group was analyzed. The results showed that

compared with the control group, the proportion of CD3+ cells, CD3+CD4+ cells, CD4+/CD8+ ratio, CD8+CD28+ cells and NK cells in the peripheral blood of the experimental group was significantly reduced. While the proportion of CD3+CD8+ cells, CD8+CD28- cells and CD4+CD25Hi CD127Lo Treg cells was significantly increased ($P < 0.05$).

In the experimental group, the changes of the number of peripheral blood lymphocyte subsets before and after treatment were analyzed. The results (Table II) showed that the proportion of CD3+ cells, CD3+CD4+ cells, CD4+/CD8+ ratio, NK cells and CD8+CD28+ cells increased after treatment in patients with advanced NSCLC, while the proportion of CD8+CD28- cells and CD4+CD25Hi CD127Lo Treg cells significantly decreased.

The number of peripheral blood lymphocyte subsets in different stages of the experimental group was analyzed. The results showed that, compared with the control group, the proportion of CD3+CD4+ cells, CD4+/CD8+ ratio and NK cells decreased in patients with stage III NSCLC, while

Table I. *Comparison of the number of peripheral blood lymphocyte subsets between experimental group and control group ($\bar{x}\pm s$)*

Groups	Control group	Experimental group	t value	P value
CD3+(%)	64.94±4.76	61.27±5.01	10.78	0.00
CD3+CD4(%)	34.56±3.71	24.87±4.71	102.98	0.00
CD3+CD8(%)	27.71±4.38	33.49±5.21	27.05	0.00
CD4+/CD8+ ratio	1.21±0.33	0.78±0.23	69.82	0.00
CD3-CD56+(%)	26.46±4.32	18.56±3.56	77.07	0.00
CD8+CD28+(%)	20.78±4.39	18.89±4.67	2.67	0.01
CD8+CD28-(%)	15.84±3.27	26.75±2.01	306.87	0.00
CD4+CD25Hi CD127Lo Treg (%)	3.76±0.85	6.56±0.98	261.76	0.00

Table II. *Comparison of the number of peripheral blood lymphocyte subsets before and after treatment in NSCLC patients ($\bar{x}\pm s$)*

Group	Control group	Experimental group	t value	P value
CD3+(%)	60.26±5.01	66.38±4.71	-12.84	0.00
CD3+CD4(%)	25.43±4.35	30.79±3.75	-12.22	0.00
CD3+CD8(%)	33.46±5.04	32.89±4.32	1.36	0.23
CD4+/CD8+ ratio	0.78±0.24	0.98±0.19	-6.46	0.00
CD3-CD56+(%)	18.57±3.71	21.03±4.11	-7.28	0.00
CD8+CD28+(%)	18.97±4.54	21.62±4.72	-5.17	0.00
CD8+CD28-(%)	25.29±2.57	22.45±3.62	8.31	0.00
CD4+CD25Hi CD127Lo Treg (%)	6.59±0.78	5.31±0.87	10.33	0.00

the proportion of CD3+CD8+ cells, CD8+CD28- cells, CD4+CD25Hi CD127Lo Treg cells increased significantly ($P < 0.05$). CD3+ cells, CD3+CD4+ cells, CD4+/CD8+ ratio, NK cells and CD8+CD28+ cells were reduced in stage IV NSCLC patients while the proportion of CD3+CD8+ cells, CD8+CD28- cells, CD4+CD25Hi CD127Lo Treg cells increased significantly ($P < 0.05$). There was no significant difference in lymphocyte subsets between the patients in stage III and those in stage IV ($P>0.05$), as shown in Fig.1. The quantitative changes of peripheral blood lymphocyte subsets of different pathological types in the experimental group were analyzed. The results showed that there was no significant difference between the peripheral blood lymphocyte subsets of different pathological types in patients with advanced NSCLC ($P > 0.05$), as shown in Figs. 1 and 2.

Pearson correlation analysis showed that the IL-17 level was negatively correlated with CTL

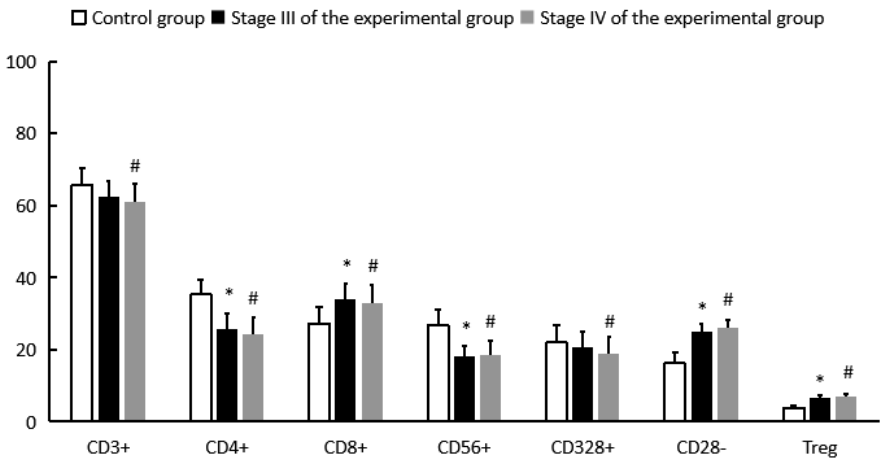


Fig. 1. *Comparison of the number of peripheral blood lymphocyte subsets in different stages of NSCLC ($\bar{x}\pm s$). $^{*}P < 0.05$, compared with the control group; $^{\#}P < 0.05$, compared with the control group.*

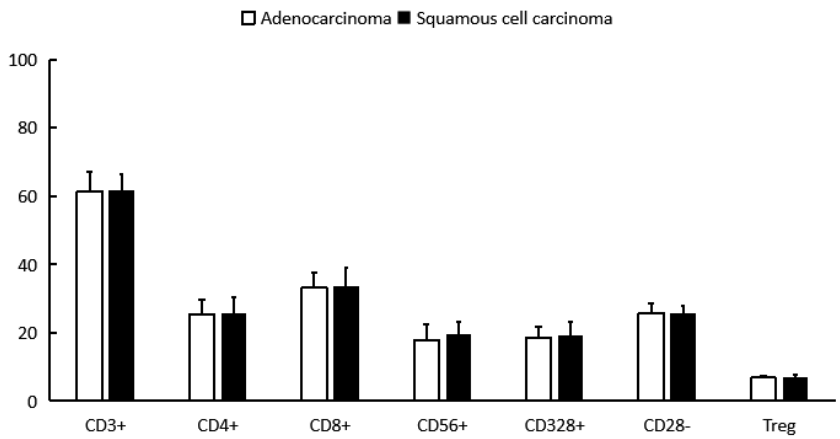


Fig. 2. *Comparison of the number of peripheral blood lymphocyte subsets of different pathological types in NSCLC ($\bar{x}\pm s$).*

ratio in advanced NSCLC patients (r=-0.660, P < 0.05), while the IL-17 level was not correlated with CD8+CD28- cell ratio (r=-0.037, P > 0.05).

DISCUSSION

Previous studies have confirmed that cellular immunity mechanism plays a powerful role in the process of anti-tumor immunity of the body, the most important of which is the cellular immunity mediated by T lymphocytes (7). The results of this study demonstrated that the effects of chemotherapy on T lymphocyte subsets are non-ignorable. Meanwhile, the experimental results were consistent with those of Hald et al. (8) and Meloni et al. (9), suggesting that CD3+T cells, CD4+T cells, and CD4+/CD8+ ratio may be independent factors for monitoring the immune function of lung cancer patients.

One study found significantly increased CD4+CD25+Treg cells in the peripheral blood of NSCLC patients (10). In this study, Treg cells in the experimental group were significantly higher than those in the control group, which indicated that Treg, as a negative regulatory factor, was significant in affecting the occurrence and development of lung cancer, especially advanced NSCLC. After 2 weeks of chemotherapy, Treg cells decreased compared with the initial stage, which proved that the imbalance in the immune mechanism of lung cancer can be improved after treatment.

The results of the present study show that IL-17 in the experimental group was significantly higher than that in the control group and also decreased after treatment. The analysis results were consistent with those of Wang et al. (11) where the number of Treg cells in the peripheral blood of NSCLC patients and the level of IL-17 increased, while the proportion of CD8+CTL decreased. Our correlation analysis suggested that there was a negative correlation between IL-17 and CTL. This also implied that IL-17, CD8+CTL and Treg cells were all involved in the occurrence of NSCLC.

In summary, monitoring immune cells in NSCLC patients can provide an insight to disease changes in patients as well as the immune status of the body, thereby providing information for treatment and prognosis.

REFERENCES

1. Akhtari IM, Bernicker EH, Teh BS. Chemotherapy in nonsmall cell lung cancer:opportunities for advancement. Chin J Cancer 2016; 35(1):56.
2. Kocher F, Lunger F, Seeber A, et al. Incidental diagnosis of asymptomatic non-small-cell lung cancer: a registry-based analysis. Clin Lung Cancer 2016; 17:62-67.
3. Baba T, Hanagiri T, Takenoyama M, et al. Identification of a lung cancer antigen evading CTL attack due to loss of human leukocyte antigen (HLA) class I expression. Cancer Sci 2010; 101(10):2115-20.
4. Aktaş ON, Öztürk AB, Erman B, Erus S, Tanju S, Dilege Ş. Role of natural killer cells in lung cancer. J Cancer Res Clin Oncol 2018; 144(6):997-1003.
5. Harrington LE Hatton RD Mangan PR et al Interleukin 17-producing CD4+ effector T cells develop via a lineage distinct from the T helper type 1 and 2 lineages. Nat Immunol 2005; 6(11):1123-32.
6. McGeachy MJ, Cua DJ, Gaffen SL. The IL-17 Family of cytokines in health and disease. Immunity 2019; 50(4):892-906.
7. Ho PC, Kaech SM. Reenergizing T cell anti-tumor immunity by harnessing immunometabolic checkpoints and machineries. Curr Opin Immunol 2017; 46:38-44.
8. Hald SM, Bremnes RM, Al-Shibli K, et al.CD4/CD8 co-expression shows independent prognostic impact in resected non-small cell lung cancer patients treated with adjuvant radiotherapy. Lung Cancer 2013; 80(2):209-15.
9. Meloni F, Morosini M, Solari N, et al. Foxp3 expressing CD4+CD25+ and CD8+CD28- T regulatory cells in the peripheral blood of patients with lung cancer and pleural mesothelioma. Hum Immunol 2006; 67(1-2):1-12.
10. Okita R, Saeki T, Takashima S, et al. CD4CD25 regulatory T cells in the peripheral blood of patients with breast cancer and non-small cell lung cancer. Oncol Rep 2005; 14(5):1269-73.
11. Wang XF, Zhu YT, Wang JJ, et al. The prognostic value of interleukin-17 in lung cancer: A systematic review with meta-analysis based on Chinese patients. PLo S One 2017; 12(9):e0185168.

LETTER TO THE EDITOR

PLASMA RICH IN GROWTH FACTORS IN THE MANAGEMENT OF MEDICALLY COMPROMISED PATIENTS IN ORAL SURGERY

E. ANITUA[1,2] and M.H. ALKHRAISAT[2,3]

[1]Private practice in oral implantology, Clínica Eduardo Anitua, Vitoria, Spain; [2]University Institute for Regenerative Medicine and Oral Implantology UIRMI (UPV/EHU-Fundación Eduardo Anitua), Vitoria, Spain; [3]BTI Biotechnology Institute, Vitoria, Spain

Received October 29, 2018 – Accepted February 4, 2019

To the Editor,

In 2015, the life expectancy at birth in Europe and USA was 80.6 and 78.8 years, respectively. The prevalence of chronic diseases is associated with ageing. By 2050, it is estimated to have 89 million USA inhabitants with an age ≥ 65 years (1). It has also been reported that 92.2% of the population aged ≥ 65 years will suffer from one or more chronic diseases (1). These figures would emphasize the need to develop cost-effective therapies for the treatment of medically compromised patients, being at higher risk to develop complications. Although there are no studies that assess the cost associated with oral surgical complications, Healy et al. have assessed this aspect in general surgery, vascular surgery and gynecology (2). At an overall complication rate of 14.5%, the mean hospital costs have been $19,626 higher for patients with complications. The mean third-party reimbursement have been $18,497 higher. Finding therapies that are effective in preventing and/or treating surgical complications would increase the cost-effectiveness of the national health systems.

The use of autologous growth factors would be of value to potentiate the healing in medically compromised patients who undergo surgical intervention (3-8). Plasma rich in growth factors (PRGF) allows the delivery of platelet- and plasma-derived proteins via different formulations to enhance tissue healing (9). Several clinical trials have shown significant positive clinical benefits from the use of plasma rich in growth factors in medically compromised patients. In a randomized controlled clinical trial (3), Mozzati et al. compared the effectiveness of autologous PRGF against fibrin glue (Tisseel) as a local measure in the management of patients with bleeding disorders and in need of dental extractions. PRGF has been effective as a local haemostatic preventing bleeding events, as well as treating it once occurred. Another randomized clinical trial (RCT) recruited patients affected by insulin-dependent diabetes mellitus (4). The study concluded that PRGF is significantly efficient in improving tissue healing (closure of the extraction socket). In a controlled split-mouth clinical trial (5), the capacity of PRGF in the prevention of osteoradionecrosis (ORN) due to tooth extraction in patients who received radiotherpay was tested. PRGF improved the socket healing without any postoperative complications. However, in the control side, slower healing and 2 cases of bone exposure were observed. In another study (6), 10 patients with ORN were treated by debridement of the necrotic bone using an ultrasound device followed by the application of PRGF to im-

Corresponding Author:
Dr. Eduardo Anitua,
Eduardo Anitua Foundation
C/ Jose Maria Cagigal 19,
01007 Vitoria, Spain
Tel: +34 945160653,
e-mail: eduardo@fundacioneduardoanitua.org

0393-974X (2020)
Copyright © by BIOLIFE, s.a.s.
This publication and/or article is for individual use only and may not be further reproduced without written permission from the copyright holder. Unauthorized reproduction may result in financial and other penalties

prove and accelerate soft-tissue healing. The clinical and radiographic evaluations showed uneventful healing achieving complete closure of the defect.

Tooth extraction is the main risk factor in the occurrence of medication-related osteonecrosis of the jaw (MRONJ). This motivated Mozzati et al. to study the efficacy of PRGF in the prevention of MRONJ in patients treated with zoledronic acid (7). One hundred seventy six patients were recruited and randomized to either a PRGF group or a control (blood clot) group. The results showed the occurrence of MRONJ in 5 patients in the control group where 267 tooth extractions were performed. PRGF was effective in preventing the occurrence of MRONJ in all patients where 542 extractions had been performed (7). The efficacy of PRGF in the treatment of MRONJ due to intravenous bisphosphonates was evaluated in 32 patients (8). The treatment protocol included the surgical resection of the necrotic bone and the bio-stimulation of tissue regeneration with PRGF (8). The patients had been followed-up for 48-50 months, confirming the efficacy of PRGF to stimulate the closure of the defect and the absence of intra- and post-operative complications (8).

It is obvious that there is a need to do more randomized clinical trials that assess PRGF as a tool for the management of patients with systematic diseases receiving a surgical intervention. However, the reported findings are encouraging for the use of PRGF to prevent and treat surgical complications in this group of patients. Probably this autologous and versatile tool would increase the effectiveness of health care providers and affect positively in the quality of life of the patients.

CONFLICT OF INTERESTS: EA is the Scientific Director of BTI Biotechnology Institute (Vitoria, Spain). He is the head of the Foundation Eduardo Anitua, Vitoria, Spain. MHA is a scientist at BTI Biotechnology Institute (Vitoria, Spain).

REFERENCES

1. Dall TM, Gallo PD, Chakrabarti R, West T, Semilla AP, Storm MV. An aging population and growing disease burden will require a large and specialized health care workforce by 2025. Health Aff (Millwood) 2013; 32(11):2013-20.
2. Healy MA, Mullard AJ, Campbell DA Jr, Dimick JB. Hospital and payer costs associated with surgical complications. JAMA Surg 2016; 151:823-30.
3. Cocero N, Pucci F, Messina M, Pollio B, Mozzati M, Bergamasco L. Autologous plasma rich in growth factors in the prevention of severe bleeding after teeth extractions in patients with bleeding disorders: a controlled comparison with fibrin glue. Blood Transfus 2015; 13:287-94.
4. Mozzati M, Gallesio G, di Romana S, Bergamasco L, Pol R. Efficacy of plasma-rich growth factor in the healing of postextraction sockets in patients affected by insulin-dependent diabetes mellitus. J Oral Maxillofac Surg 2014; 72:456-62.
5. Mozzati M, Gallesio G, Gassino G, Palomba A, Bergamasco L. Can plasma rich in growth factors improve healing in patients who underwent radiotherapy for head and neck cancer? A split-mouth study. J Craniofac Surg 2014; 25:938-43.
6. Gallesio G, Del Fabbro M, Pol R, Mortellaro C, Mozzati M. Conservative treatment with plasma rich in growth factors-Endoret for osteoradionecrosis. J Craniofac Surg 2015; 26:731-36.
7. Mozzati M, Arata V, Gallesio G. Tooth extraction in patients on zoledronic acid therapy. Oral Oncol 2012; 48:817-21.
8. Mozzati M, Gallesio G, Arata V, Pol R, Scoletta M. Platelet-rich therapies in the treatment of intravenous bisphosphonate-related osteonecrosis of the jaw: a report of 32 cases. Oral Oncol 2012; 48:469-74.
9. Anitua E, Alkhraisat MH, Orive G. Perspectives and challenges in regenerative medicine using plasma rich in growth factors. J Control Release 2012; 157(1):29-38.

LETTER TO THE EDITOR

GINSENOSIDE Rb1 ATTENUATES LPS-INDUCED MUC5AC EXPRESSION VIA THE TLR4-MEDIATED ERK1/2 AND NF-κB PATHWAY IN HUMAN AIRWAY EPITHELIAL NCI-H292 CELLS

YD. KIM[1,2], YS. CHOI[1], HG. NA[1], SY. SONG[1] and CH. BAE[1]

[1]Department of Otorhinolaryngology-Head and Neck Surgery, College of Medicine, Yeungnam University, Daegu, Republic of Korea; [2]Regional Center for Respiratory Diseases, Yeungnam University Medical Center, Daegu, Republic of Korea

Received October 3, 2019 – Accepted March 10, 2020

To the Editor,

Mucus plays a biological role in maintaining humidity, lubricating, and removing inhaled substances in the respiratory tract. Mucins mainly determine the properties of mucus. Among mucins, MUC5AC is chiefly produced in goblet cells of the airway epithelium and is the predominant secreted mucin, which contributes to the formation of gel in the mucus layer. MUC5AC expression is increased by inflammatory mediators such as lipopolysaccharide (LPS), transforming growth factor, and interleukin (IL)-1β in human airway epithelial cells (1). Clinically, MUC5AC expression is notably increased in chronic inflammatory airway diseases, such as asthma and chronic obstructive pulmonary disease, which are associated with the stasis of mucus, declined lung function, and increased severity of infection (1).

Panax ginseng has long been used medicinally for many diseases in Asia. Ginsenoside is a saponin contained in *Panax ginseng* that plays the most important role in the pharmacological properties exhibited by the plant. Ginsenosides are classified into three types: protopanaxadiol, protopanaxatriol, and oleanolic acid (2). Ginsenoside Rb1 is the most abundant protopanaxadiol-type ginsenoside in the root of *Panax ginseng,* and it possesses various biological roles that are involved in anti-inflammatory, antioxidant, anti-diabetic, and anti-tumor activity in various tissues of the human body (3-6). Recently, several studies have reported that that ginsenoside Rb1 displays anti-inflammatory effects in the respiratory tract (3, 6). But the effect of ginsenoside Rb1 on inflammation-induced mucin expression in human airway epithelial cells has not been studied yet. Therefore, the effect of ginsenoside Rb1 on MUC5AC expression and the corresponding brief signaling pathway were investigated in human airway epithelial NCI-H292 cells.

MATERIALS AND METHODS

Materials

Mucin-producing human airway epithelial NCI-H292 cells were purchased from the American Type Culture Collection (Manassas, VA, USA). Ginsenoside Rb1 (G0777) from the root of *Panax ginseng* (Korean ginseng),

Key words: ginsenoside Rb1; MUC5AC; TLR4; ERK1/2; NF-κB; airway epithelial cells

Corresponding Author:
Dr Chang Hoon Bae,
Department of Otorhinolaryngology-Head and Neck Surgery,
College of Medicine, Yeungnam University,
170, Hyeonchung-ro, Nam-gu, Daegu,
42415, Republic of Korea
Tel.: +82 53 620 3784 - Fax: +82 53 628 7884
e-mail: baich@med.yu.ac.kr

0393-974X (2020)
Copyright © by BIOLIFE, s.a.s.
This publication and/or article is for individual use only and may not be further reproduced without written permission from the copyright holder.
Unauthorized reproduction may result in financial and other penalties
DISCLOSURE: ALL AUTHORS REPORT NO CONFLICTS OF INTEREST RELEVANT TO THIS ARTICLE.

LPS (L8643) from *Pseudomonas aeruginosa* 10, and dexamethasone (D8893) were obtained from Sigma-Aldrich (St. Louis, MO, USA). Fetal bovine serum (FBS) was obtained from Hyclone Laboratories, Inc. (Logan, UT, USA). TRIzol and Roswell Park Memorial Institute (RPMI) 1640 medium were purchased from Life technologies (Carlsbad, CA, USA). For cell viability analysis using water-soluble tetrazolium salt (WST-1) assay, the EZ-Cytox Cell Viability Assay Kit was obtained from the Daeil Lab (Seoul, Korea). For polymerase chain reaction (PCR) analysis, reverse transcription PCR (RT-PCR) kit was obtained from Thermo Fisher Scientific (Foster City, CA, USA) and real-time PCR kit was obtained Bio-Rad Lab (Hercules, CA, USA). For enzyme-linked immunosorbent assay (ELISA), the primary antibody of MUC5AC (sc-20118) and goat anti-rabbit immunoglobulin G (IgG)-horseradish peroxidase (HRP) secondary antibody (sc-2004) were obtained from Santa Cruz Biotechnology (Santa Cruz, CA, USA). Bovine serum albumin (BSA) was purchased from Hyclone Laboratories, Inc. For Western blot analysis, the primary antibody of phospho-extracellular signal regulated kinase 1/2 (ERK1/2) (#9101S), ERK1/2 (#9102S), phospho-p38 (#9211S), p38 (#9212S), phospho-nuclear factor-kappa-light-chain-enhancer of activated B cells (NF-κB) (#3033S), and NF-κB (#4764S) were obtained from Cell Signaling Technology (Danvers, MA, USA). Donkey anti-rabbit IgG HRP secondary antibody (NB7185) was obtained from Novus Biologicals (Littleton, CO, USA).

Cell culture, treatment, and viability

Human airway epithelial NCI-H292 cells were cultured in RPMI 1640 medium supplemented with 2 mM L-glutamine, 100 U/mL penicillin, 100 μg/mL streptomycin, and 10% FBS in a humidified atmosphere with 5% CO_2 at 37°C, and subcultured twice weekly. When cultures were 80-90% confluent, cells were incubated in RPMI 1640 medium containing 0.5% FBS for 24 h. Cells were then rinsed with serum-free RPMI 1640 medium and phosphate-buffered saline (PBS), and treated with LPS (100 ng/mL). For the controls, human airway epithelial NCI-H292 cells were incubated with cultured medium alone for the same amount of time. Cell viability was examined using the EZ-Cytox Cell Viability Assay Kit for WST-1 assay, and changes in cell morphology were observed microscopically.

RT-PCR and real-time PCR for MUC5AC, Toll-like receptor 4 (TLR4), myeloid differentiation primary response 88 (MyD88), and Toll/interleukin-1 receptor-domain-containing adapter-inducing interferon-β (TRIF) mRNA expression

Total RNA was isolated from human airway epithelial NCI-H292 cells. RT-PCR was performed using the GeneAmp RNA PCR Core Kit and real-time PCR was performed using the iQ SYBR Green Supermix (Bio-Rad Lab) in conformity with the manufacturer's instructions. The primer sequences, amplification conditions, and representation of results were conducted according to previously published protocols for MUC5AC, TLR4, MyD88, and TRIF (7, 8). As a positive control, PCR amplification of glyceraldehyde-3-phosphate dehydrogenase (GAPDH) was also conducted for each sample in order to normalize all values to their respective GAPDH values.

ELISA for MUC5AC glycoprotein production

Cell lysates and supernatants were extracted from human airway epithelial NCI-H292 cells. Samples of the cell lysates and supernatants were diluted with PBS, and incubated at 4°C in F96 Cert. Maxisorp Nunc-Immunoplate (Fisher scientific, Lenexa, KS, USA) overnight. Subsequently, samples were blocked with 2% BSA for 1 h at room temperature, and incubated with the primary antibody of MUC5AC which was diluted at 1:200 in PBS containing 0.05% Tween 20 for 1 hour. Then, samples were incubated with HRP conjugated secondary antibody of MUC5AC which was diluted at 1:5,000 in PBS containing 0.05% Tween 20. After 1 h, color was generated using 3,3',5,5'-tetramethylbenzidine peroxidase solution, and the reaction was stopped with 2 N H_2SO_4. Optical densities were determined using an EL800 ELISA reader (BIO-TEK Instruments, Winooski, VT, USA) at 450 nm. The findings were presented as percentages of baseline controls.

Western blot analysis for the phosphorylation of ERK1/2, p38, and NF-κB

Human airway epithelial NCI-H292 cells were seeded in a 6-well plate, and treated with LPS (100 ng/mL). Cells were harvested in 200 μL of radioimmunoprecipitation assay buffer (Thermo scientific, Rockford, IL, USA) with phosphatase inhibitor cocktail (Roche, Mannheim, Germany), and incubated for 20 min at 4°C. Subsequently,

the samples were centrifuged at 2,500 × g for 10 minutes at 4°C, and the supernatant was saved as a whole-cell lysate, and used to estimate total protein. Proteins (20 μg) were separated using 10% reducing sodium dodecyl sulfate–polyacrylamide gel electrophoresis, and electroblotted onto a polyvinylidene difluoride membrane. The membrane was blocked with 5% nonfat dry milk in Tris-buffered saline with 0.1% Tween 20, and subsequently incubated with a primary antibody at 4°C overnight, followed by HRP conjugated secondary antibody for 1 h. The protein bound to the antibody was visualized using enhanced West Pico chemiluminescent substrate (Thermo Fisher Scientific) and a chemiluminescence image system (FUSION FX7 system, Vilber Lourmat, Marnela-Vallée, France). The findings were presented as fold change from the baseline control.

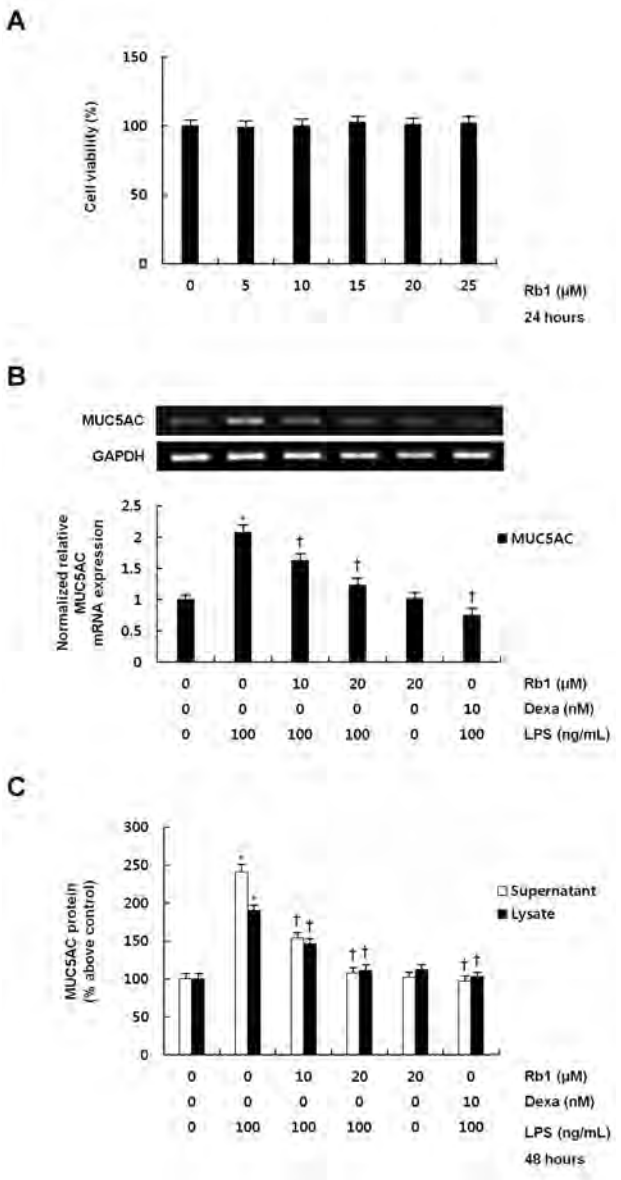


Fig. 1. *Effect of ginsenoside Rb1 on LPS-induced MUC5AC expression. **A**) Cell viability; **B**) LPS induced MUC5AC expression; **C**) Ginsenoside Rb1 and dexamethasone inhibited LPS-induced MUC5AC expression. *p<0.05 compared with zero value; †p<0.05 compared with LPS alone.*

Statistical analysis

All experimental values are expressed as the mean ± standard deviation of three independent experiments performed in triplicate. Statistical analysis was performed using commercially available software (SPSS version 12.0; SPSS Inc., Chicago, IL, USA). Data comparisons were conducted with Kruskal-Wallis one-way analysis of variance followed by the Mann-Whitney test or unpaired *t*-test. For all tests, a *p* value of less than 0.05 was considered statistically significant.

RESULTS

Cell viability assay

To investigate the effects of ginsenoside Rb1 on the cell viability of human airway epithelial NCI-H292 cells, cells were treated with different concentrations of ginsenoside Rb1 for 24 h. WST-1 assay found that cell viability was unaffected by ginsenoside Rb1 at all tested concentrations (up to 25 μM) (Fig. 1A).

Ginsenoside Rb1 on LPS-induced MUC5AC expression

To investigate the effect of ginsenoside Rb1 on inflammation-induced MUC5AC expression in human airway epithelial NCI-H292 cells, cells were incubated with LPS (100 ng/mL) for 1 h following 1 h of pretreatment with ginsenoside Rb1 (10 and 20 μM) or dexamethasone (10 nM). Results of RT-PCR, real-time PCR, and ELISA showed that LPS induced MUC5AC mRNA expression and glycoprotein production significantly. Ginsenoside Rb1 and dexamethasone inhibited LPS-induced MUC5AC mRNA expression and glycoprotein production significantly; ginsenoside Rb1 (20 μM) displayed an inhibitory effect on LPS-induced MUC5AC

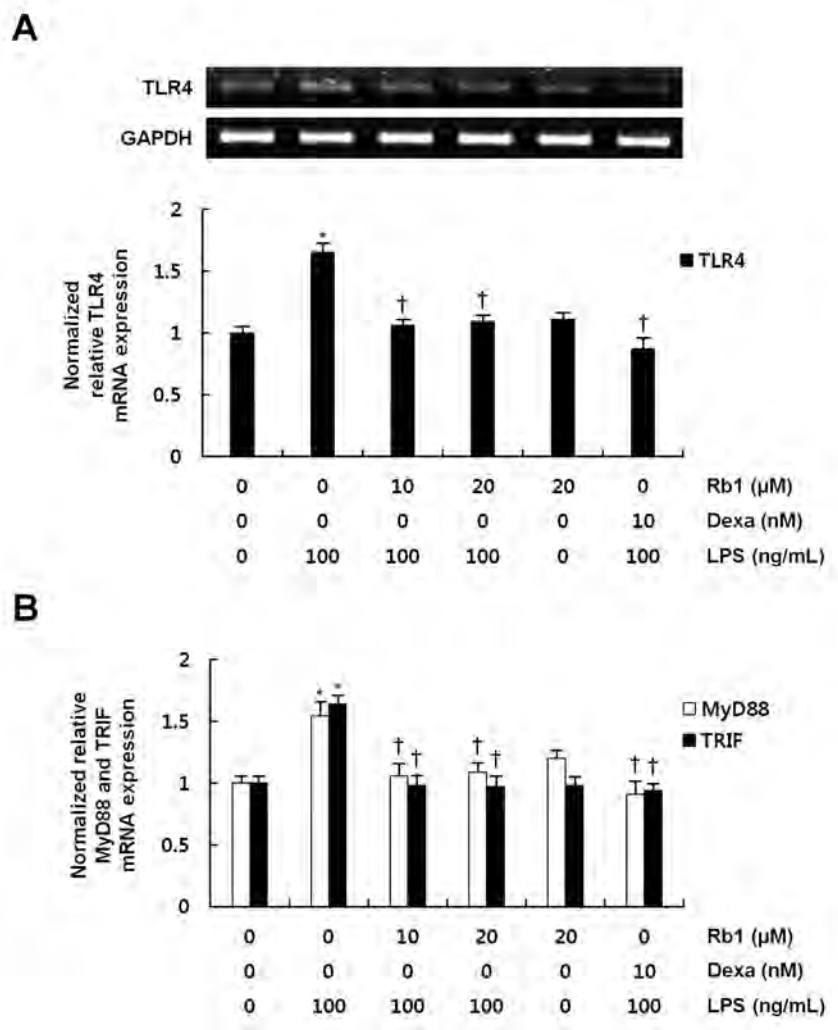


Fig. 2. *Effect of ginsenoside Rb1 on LPS-induced TLR4, MyD88, and TRIF mRNA expression.* ***A*** *and* ***B****) Ginsenoside Rb1 and dexamethasone inhibited LPS-induced TLR4, MyD88, and TRIF mRNA expression. *p<0.05 compared with zero value.* †*p<0.05 compared with LPS alone.*

expression similar to that of dexamethasone (10 nM) (Fig. 1 B and C).

Ginsenoside Rb1 on LPS-induced TLR4 expression

To investigate the effect of ginsenoside Rb1 on LPS-induced TLR4 expression in human airway epithelial NCI-H292 cells, cells were incubated with LPS (100 ng/mL) for 1 h following 1 h of pretreatment with ginsenoside Rb1 (10 and 20 μM) or dexamethasone (10 nM). Results of RT-PCR and real-time PCR showed that LPS increased TLR4, MyD88, and TRIF mRNA expression significantly. Ginsenoside Rb1 and dexamethasone inhibited LPS-induced TLR4, MyD88, and TRIF mRNA expression significantly; ginsenoside Rb1 (20 μM) exhibited a similar inhibitory effect on LPS-induced TLR4, MyD88, and TRIF mRNA expression as that of dexamethasone (10 nM) (Fig. 2A and B).

Ginsenoside Rb1 on LPS-induced phosphorylation of ERK1/2, p38, and NF-κB

To investigate the brief intracellular mechanisms involved in the effect of ginsenoside Rb1 on LPS-activated phosphorylation of ERK1/2, p38, and

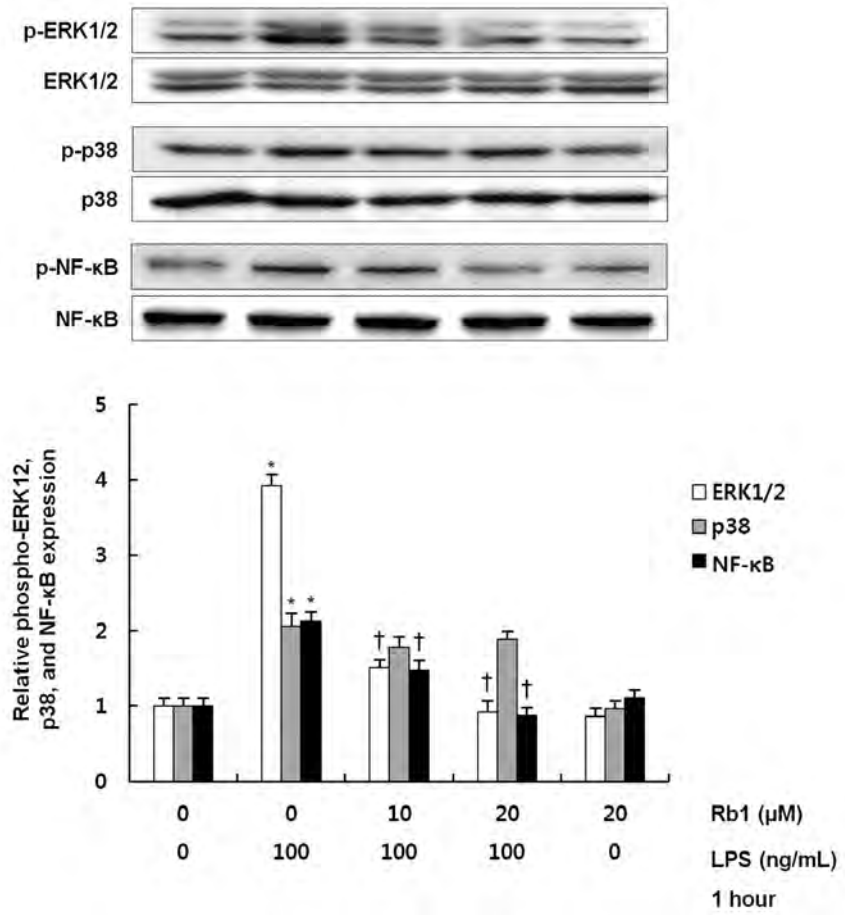


Fig. 3. *Effect of ginsenoside Rb1 on LPS-induced phosphorylation of ERK1/2, p38, and NF-κB. Ginsenoside Rb1 inhibited LPS-induced phosphorylation of ERK1/2 and NF-κB but did not inhibit that of p38. *p<0.05 compared with zero value. †p<0.05 compared with LPS alone.*

NF-κB in human airway epithelial NCI-H292 cells, cells were incubated with LPS (100 ng/mL) for 1 h following 1 hof pretreatment with ginsenoside Rb1 (10 and 20 μM). Western blot analysis found that LPS induced the phosphorylation of ERK1/2, p38, and NF-κB significantly. Ginsenoside Rb1 inhibited LPS-induced phosphorylation of ERK1/2 and NF-κB significantly but did not inhibit that of p38 (Fig. 3).

DISCUSSION

As to the various pharmacological effects of ginsenoside Rb1, several studies concerning anti-inflammatory effects exerted by ginsenoside Rb1 in the respiratory tract have been reported (3, 6, 9, 10). Therefore, it could be hypothesized that ginsenoside Rb1 may inhibit the production of inflammatory mediators, which could decrease inflammation-induced mucin expression in human airway epithelial cells. The results of this study demonstrated that ginsenoside Rb1 inhibited LPS-induced MUC5AC expression; this inhibition was similar to the effect of dexamethasone.

Regarding the signaling pathway for LPS-

induced MUC5AC expression, LPS is well known to activate TLR4-mediated intracellular signaling pathway through the MyD88-dependent and TRIF-dependent pathways (11, 12). The results of this study suggest that ginsenoside Rb1 inhibits LPS-induced MUC5AC expression via the TLR4-mediated ERK1/2 and NF-κB signaling pathway.

However, a few limitations exist in this study that must be considered when interpreting results. To overcome the limitations, additional ginsenoside Rb1-related experiments that investigate the expression of other mucins with time-dependent effect and various signaling pathways using additional human airway epithelial cell lines and animal models including the measurements of the dosage and blood concentration are needed.

In conclusion, the results of this study provide important data regarding the role of ginsenoside Rb1 on the regulation of mucin secretion in human airway epithelial cells, and ginsenoside Rb1 may be used as a therapeutic agent to inhibit mucus production in inflammatory airway diseases.

ACKNOWLEDGEMENT

This work was supported by the 2016 Yeungnam University Research Grant.

REFERENCES

1. Ma J, Rubin BK, Voynow JA. Mucins, mucus, and goblet cells. Chest 2018; 154:169-76.
2. Oh SJ, Kim K, Lim CJ. Suppressive properties of ginsenoside Rb2, a protopanaxadiol-type ginseng saponin, on reactive oxygen species and matrix metalloproteinase-2 in UV-B-irradiated human dermal keratinocytes. Biosci Biotechnol Biochem 2015; 79:1075-81.
3. Chen T, Xiao L, Zhu L, Ma S, Yan T, Ji H. Anti-asthmatic effects of ginsenoside Rb1 in a mouse model of allergic asthma through relegating Th1/Th2. Inflammation 2015; 38:1814-22.
4. Zhou P, Xie W, He S, Sun Y, Meng X, Sun G, Sun X. Ginsenoside Rb1 as an anti-diabetic agent and its underlying mechanism analysis. Cells 2019; 8:E204.
5. Liu D, Liu T, Teng Y, Chen W, Zhao L, Li X. Ginsenoside Rb1 inhibits hypoxia-induced epithelial-mesenchymal transition in ovarian cancer cells by regulating microRNA-25. Exp Ther Med 2017; 14:2895-902.
6. Yu S, Zhou X, Li F, et al. Microbial transformation of ginsenoside Rb1, Re and Rg1 and its contribution to the improved anti-inflammatory activity of ginseng. Sci Rep 2017; 7:138.
7. Kim MH, Bae CH, Choi YS, Na HG, Song SY, Kim YD. Endoplasmic reticulum stress induces MUC5AC and MUC5B expression in human nasal airway epithelial cells. Clin Exp Otorhinolaryngol 2019; 12:181-89.
8. Karnati HK, Pasupuleti SR, Kandi R, et al. TLR-4 signalling pathway: MyD88 independent pathway up-regulation in chicken breeds upon LPS treatment. Vet Res Commun 2015; 39:73-78.
9. Shaukat A, Guo YF, Jiang K, et al. Ginsenoside Rb1 ameliorates Staphylococcus aureus induced Acute Lung Injury through attenuating NF-κB and MAPK activation. Microb Pathog 2019; 132:302-12.
10. Yuan Q, Jiang YW, Ma TT, Fang QH, Pan L. Attenuating effect of ginsenoside Rb1 on LPS-induced lung injury in rats. J Inflamm (Lond) 2014; 11:40.
11. Hu H, Li H. Prunetin inhibits lipopolysaccharide-induced inflammatory cytokine production and MUC5AC expression by inactivating the TLR4/MyD88 pathway in human nasal epithelial cells. Biomed Pharmacother 2018; 106:1469-77.
12. Ma C, Ma W. Plantamajoside inhibits lipopolysaccharide-induced MUC5AC expression and inflammation through suppressing the PI3K/Akt and NF-κB signaling pathways in human airway epithelial cells. Inflammation 2018; 41:795-802.

LETTER TO THE EDITOR

CHROMOSOME 14-LINKED DISEASE MISDIAGNOSED AS PRADER-WILLI SYNDROME

WJ. LIAN[1], P. DUAN[1], XP. LU[2], TT. LU[2] and H. ZHENG[2]

[1]Henan University of Chinese Medicine, Zhengzhou, China; [2]Department of Pediatrics, the First Affiliated Hospital of Henan University of Chinese Medicine, Zhengzhou, China

Received November 12, 2019 – Accepted March 19, 2020

To the Editor,

The incidence of chromosomal disorders ranges from 1/200,000 to 1/4,000 (1). Chromosomal disorders are usually misdiagnosed as brain damage, cerebral palsy and mental retardation (2). However, it is rare to misdiagnose chromosomal disorders as Prader-Willi syndrome (PWS). In this paper, we reported and analysed a patient with chromosome 14-linked disease, who had been misdiagnosed with PWS.

Case presentation

A fourteen-month-old girl was admitted to our hospital with her mother complaining about the child's 'retarded growth'. The patient was the product of a full-term pregnancy, delivered by caesarean section. Her post-birth response was poor, with low body weight and feeding difficulty. Thus, after birth, she received treatment in the Division of Neonatology at our hospital. At the age of two months, she was admitted to our hospital again for severe pneumonia. An atrial septal defect of 6.3 mm was subsequently found. The suspected diagnosis of 'low birth weight, congenital heart disease, and hereditary metabolic disease' was drawn based on clinical signs and symptoms. However, no pathogenic mutation was found in the whole-genome exon sequencing at this time.

During our last consultation, when the patient was aged fourteen months, her symptoms were short stature, unable to sit or stand, and weakness of the limbs. The legal guardian provided written, informed consent to publish this paper. On physical examinations, the child weighed 6 kg (<-2SD), was 70 cm tall (<-2 SD), and had a head circumference of 40 cm (<-2SD). Her hands (long axis, 7.5 cm) and feet (long axis, 8 cm) were small. The ulnar margins of both hands were absent, and the fingers were slender. Her skin was white, and her hair sparse. Her subcutaneous fat layer was thin. Other distinctive features included almond-shaped eyes, a narrow forehead, high palatine arch and globular nose. Additionally, cardiac colour ultrasound revealed that she had an atrial septal defect, and a blowing noise could be heard in her heart area. Full spine X-ray revealed that she had scoliosis. The karyotype was 46XY.

On cranial nerve examination, the patient's pursuit eye and gaze movements to auditory targets were sluggish, motor function was disordered, limb muscle strength and muscle tension were weak, shallow reflections could be normally provoked, tendon reflex of both knees was active, and the pathological sign was negative. The Gesell development assessment revealed the following: adaptability was equivalent to infants aged 4.2 months old; gross motor skills

Key words: Prader-Willi Syndrome; chromosome 14; genetic testing; intellectual disability

Corresponding Author:
Hong Zheng,
Department of Pediatrics,The First Affiliated Hospital of Henan University of Chinese Medicine,
No. 19 Renmin Road, Zhengzhou 450000, China
Tel.: +86 18937153029 - Fax: +86 0371 66211093
e-mail: hzdr_789@163.com

0393-974X (2020)
Copyright © by BIOLIFE, s.a.s.
This publication and/or article is for individual use only and may not be further reproduced without written permission from the copyright holder.
Unauthorized reproduction may result in financial and other penalties
DISCLOSURE: ALL AUTHORS REPORT NO CONFLICTS OF INTEREST RELEVANT TO THIS ARTICLE.

were equivalent to infants aged 1.5 months old; fine motor skills were equivalent to 4.6-month old infants; verbal ability was equivalent to 6.3-month old infants; the comprehensive development quotient was 30.4 points, and overall development was retarded.

Based on the medical history and clinical characteristics of the child, a suspected preliminary clinical diagnosis of PWS was drawn. Therefore, the girl received growth hormone and nutritional therapy treatments. The girl was followed-up after three months, but there was no significant improvement in muscle tension. The malnutritional appearance and feeding difficulties were not improved. The MS-MLPA test revealed a negative result. With a suspected chromosome-linked disease (chromosome microdeletion syndrome), copy number variation (CNV) detection was further performed. The result revealed that in the pathogenic CNV, the patient carried a heterozygous deletion variant on chromosome 14 at the q32.2-q32.33 position, with a length of approximately 6.24 Mb (Fig. 1). CNV tests were also carried out on the patient's parents, which revealed a normal phenotype. Therefore, the final diagnoses are as follows: (1) microdeletion syndrome on chromosome 14 (heterozygous deletion at chromosome 14 q32.2-q32.33 with a length of approximately 6.24 Mb); (2) nutritional disorders.

DISCUSSION

PWS is a genetic disease associated with genomic imprinting. Its main pathogenesis is caused by lack of expression of the paternal allele in the 15q11.2-q13 region (3). The main manifestations of PWS in early childhood are difficulty in feeding, central hypotonia and developmental retardation, which can easily be misdiagnosed as hypoxic-ischemic encephalopathy and congenital muscular dystrophy (4). Chromosome 14 microdeletion syndrome is a rare chromosomal disease. Its deletions are mainly located at the end of the long arm of chromosome 14. The appearance characteristics are as follows: microcephaly, prominent forehead, high palate arch, narrow cleft eye, epicanthus, bulbous nose, low set ears, thin upper lip, deformity of the hands and feet, and teeth dysplasia. The misdiagnosis of chromosome 14-linked disease as PWS is rare and

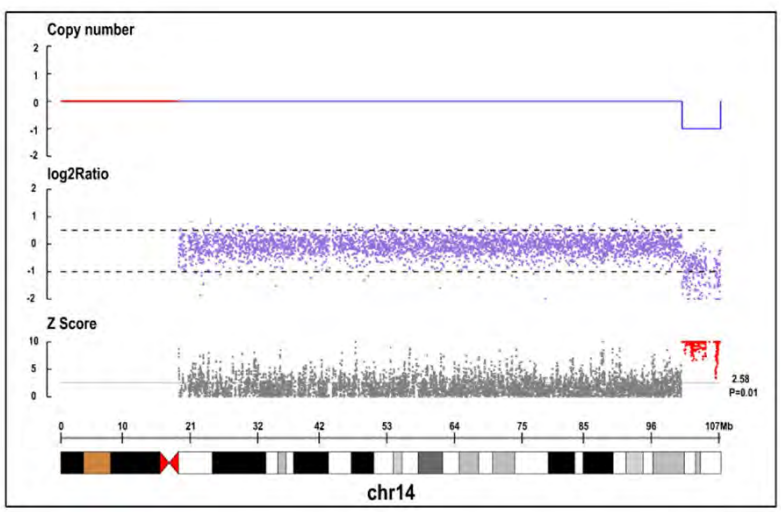


Fig. 1. *Copy number variation (CNV) detection revealed that the patient carried a heterozygous deletion variant on chromosome 14 at the q32.2-q32.33 position, with a length of approximately 6.24 Mb.*

Table I. *Similarities and differences in clinical characteristics between chromosome 14 microdeletion syndrome and PWS*

	Chromosome 14 microdeletion syndrome	PWS
Similarities	1. Feeding difficulties and central hypotonia at birth 2. Small micrognathia, thin upper lip, and teeth dysplasia 3. Slow increase in body weight during the neonatal period 4. Short stature, hypogonadism	
Differences	1. Amniotic fluid abnormalities during pregnancy and developmental retardation from pregnancy to birth 2. Microcephaly, protruding forehead, narrow cleft eye, high palate arch, and bulbous nose 3. Continuously slow growth of body weight, no complications of overfeeding and behavioral disorders 4. Complications: visual and hearing disorders, malformation signs of heart, intestinal tract, hands and feet.	1. Few fetal motilities during pregnancy 2. Long skull, narrow face, white skin, shallow hair, almond eyes, small hands and feet 3. Overfeeding, obesity and compulsive behavior 4. Complications: adenoidal hypertrophy and thyroid dysfunction

PWS: Prader-Willi syndrome

has not been previously reported in China. The similarities and differences in clinical characteristics between chromosome 14 microdeletion syndrome and PWS are shown in Table I (5-8).

In this case, the patient's main characteristics were similar to those of PWS. However, PWS-related MS-MLPA revealed no pathogenic 15q11.2-q13 mutation. The pathogenic CNV detection confirmed that a heterozygous deletion mutation of approximately 6.24 Mb was on chromosome 14 q32.2-q32.33. Thus, the diagnosis of chromosome 14 microdeletion syndrome was finally made.

In conclusion, the clinical characteristics of a child with chromosome 14 microdeletion syndrome were described. The final diagnosis of this disease depended on a genetic diagnosis. Therefore, chromosome microarray or CNV detection should be performed on children with apparent abnormalities and multiple malformations. Additionally, before reproduction, families with chromosome 14 microdeletion need to undergo amniocentesis to assist prenatal diagnosis.

ACKNOWLEDGEMENTS

This study was supported by National Key Research and Development Program of China (2017YFC1001704) and Jin Lei Pediatric Endocrinology Growth Research Fund for Young Physicians (PEGRF-CR-20171007).

REFERENCES

1. Wang ZG, Guo QW, Zhou YL. Current status and prospect of genetic testing for chromosomal microduplication. Chin J Lab 2016; 39(6):407-9.
2. The Subspecialty Group of Endocinologic, Hereditary and Metabolic Diseases, The Society of Pediatrics, Chinese Medical Association. Expert consensus on diagnosis and treatment of Prader-

Willi syndrome in China (2015). Chin J Pediatrics 2015; 53(6):419-24.
3. Holm VA, Cassidy SB, Butler MG, et al. Prader-Willi Syndrome: Consensus Diagnostic Criteria. Pediatrics 1993; 91(2):398-402.
4. Bar C, Diene G, Molinas C, Bieth E, Casper C, Tauber M. Early diagnosis and care is achieved but should be improved in infants with Prader-Willi syndrome. Orphanet J Rare Dis 2017; 12(1):118.
5. Maurin ML, Brisset S, Le Lorc'h M, et al. Terminal 14q32.33 deletion: genotype-phenotype correlation. Am J Med Genet A 2006; 140(21):2324-29.
6. Schlade-Bartusiak K, Ardinger H, Cox DW. A child with terminal 14q deletion syndrome: Consideration of genotype–phenotype correlations. Am J Med Genet A 2009; 149A(5):1012-18.
7. Schneider A, Benzacken B, Guichet A, et al. Molecular cytogenetic characterization of terminal 14q32 deletions in two children with an abnormal phenotype and corpus callosum hypoplasia. Eur J Hum Genet 2008; 16(6):680-87.
8. Engels H, Schüler HM, Zink AM, et al. A phenotype map for 14q32.3 terminal deletions. Am J Med Genet A 2012; 158A(4):695-706.

LETTER TO THE EDITOR

DOUBLE KIRSCHNER-WIRES PERCUTANEOUS ANTEGRADE INTRAMEDULLARY FIXATION FOR TREATMENT OF UNSTABLE PHALANGEAL NECK FRACTURES IN ADULTS

F. GAO[1], J-Y. REN[1], B-J. BI[1], L-J. LU[2], Z. HAN[1] and Y-H. PAN[1]

[1]Department of Hand and Foot Surgery, The Affiliated Hospital of Qingdao University; Shandong, China: [2]Department of Hand Surgery, The First Hospital of Jilin University, Jilin, China

Received January 8, 2020 – Accepted March 24, 2020

To the Editor,

Phalangeal neck fractures are usually observed in children and only rarely in adults. The incidence ratio between adults and children is 1:10 (1). The fractures often occur in the proximal and middle phalanges. At present, the most commonly used classification method for phalangeal neck fractures is that suggested by Al-Qattan (2). According to this system, type I fracture is a non-displaced fracture, type II fractures exhibit a displaced distal fragment maintaining bone-to-bone contact with the proximal fragment, and type III fractures are characterized by displaced distal fragment with no bone-to-bone contact with proximal fragment. The type I phalangeal neck fractures can be fixed with interphalangeal joint extension within 4 weeks of injury. However, the displaced fracture is generally unstable. Among the displaced fractures, the distal fractures of type II and type III are often accompanied by rotational deformity due to the traction of the lateral collateral ligament. Internal fixation by Kirschner wire (K-wire) is required to maintain a good reduction. The traditional surgical method uses the interdigital joint extension position and the Kirschner needle to retrograde and fix the interphalangeal joint. Although the stability is good, there are obvious shortcomings, as the long-term fixation of the interphalangeal joint can easily lead to the flexion and extension dysfunction of the interphalangeal joint. If the fracture line is located in or around the joint capsule, open reduction can easily lead to the joint capsule ligament adhesion. Closed reduction with percutaneous retrograde needle and K−wire through the joint capsule interfere with the collateral ligament, often causing joint stiffness (3).

From February 2016 to March 2018, we treated 10 adult patients with phalangeal neck fractures using closed reduction and double K−wire for the percutaneous transluminal intramedullary fixation of the basal ganglia and achieved satisfactory results. This article describes the clinical outcomes of this procedure.

MATERIALS AND METHODS

Data were collected and analyzed retrospectively for patients diagnosed with phalangeal neck fractures between February 2016 and March 2018 in our hospital. A total of 10 patients with 13 fractured fingers were included. The fractures were located at proximal phalanges of index fingers (2 fractures), proximal phalanges of middle fingers (3 fractures), middle neck of ring fingers (2 fractures),

Key words: phalangeal neck fracture; antegrade intramedullary fixation; unstable fracture

Corresponding Author:
Dr Yue-Hai Pan,
Department of Hand and Foot Surgery,
The Affiliated Hospital of Qingdao University,
No.16 Jiangsu Road, Shinan District,
Qingdao, Shandong, China 266071
e-mail: pan_yhai@aliyun.com

0393-974X (2020)
Copyright © by BIOLIFE, s.a.s.
This publication and/or article is for individual use only and may not be further reproduced without written permission from the copyright holder.
Unauthorized reproduction may result in financial and other penalties
DISCLOSURE: ALL AUTHORS REPORT NO CONFLICTS OF INTEREST RELEVANT TO THIS ARTICLE.

proximal section of ring finger (2 fractures), neck section of middle finger (2 fractures), proximal section of little finger (1 fracture), and middle section of middle finger (1 fracture). There were 9 male and one female patients. The age of patients was in the range between 25 and 59 years, with the average age of 36.5 years. The cause of fractures was crush injury in all cases. According to the Al-Qattan's classification (1), 10 fractures were identified as type II and 3 fractures as type III. Patients meeting the following criteria were excluded: a flexor and extensor tendon injury around the interphalangeal joint; completely and incompletely disconnected fingers; other parts of the hand injury, affecting hand function recovery. All included subjects gave informed, signed consent to participate in the study.

Surgical methods

All patients underwent preoperative lateral X-ray examination, and the fracture displacement was evaluated. The classification was performed according to the criteria of Al-Qattan (1). All patients underwent surgery under anesthesia with internal nerve block. Patients were in supine position, with the injured limb extending outwards. Two ordinary K−wires with a diameter of 1 mm were selected, the needle tip was pre-bend at about 20º, the tail end was cut off, and the K-wire was fixed to the electric drill bit. Then, a 5 ml syringe needle was used to position the base of the phalanx under the C-arm fluoroscope. After accurate positioning, the proximal interphalangeal joint or the metacarpophalangeal joint was flexed to avoid the K−wire needle tail interfering with the joint capsule and tendon and causing joint distraction. Hand-held electric drill bit was used to percutaneously puncture the needle from the proximal end to the distal end in a direction of 45º with the long axis of the phalanx. The needle tip of the K−wire was turned down. After breaking through the cortex, the needle tip was turned to the side or the back, and the medullary cavity was sent distally along the long axis of the phalanx. When the C-arm perspective showed that the K−wire is located in the medullary cavity, the handle was rotated left and right to keep the K−wire distally. When the distal end of the K−wire was close to the fracture line, the C-arm was examined on the positive and lateral X-ray films, and the direction of the needle tip was clearly defined. The operator used one hand to slowly pull the distal finger axially of the fracture. Another hand pushed the distal end from the dorsal side to the volar side. During the operation, according to the direction of the fracture displacement, the lateral displacement was corrected by one hand. Another hand was holding the drill to pass the K−wire through the fracture line into the phalanx. The C-arm was used to obtain the front position perspective, and the lateral and oblique 45° X-ray films - to observe the fracture reduction and the position of Kirschner wire. The Kirschner needle tip was placed distally to reach the subchondral bone level without crossing the articular surface. In this group of patients, only 1 patient could not successfully regain the manipulative abilities, and the volar movement of the volar bone was obvious. The accurate reset was achieved by rotating the tip of the Kirschner needle from the palm side to the back side by 180°. The same method was used to insert another K-wire. Finally, the tail end was pre-bent and left out of the skin.

Surgical treatment of all patients was performed by the same hand surgeon. No specific individual difficulties were encountered in different patients during the operation.

Postoperative management

The patients underwent metacarpophalangeal flexion and interphalangeal joint extension for 2 weeks after surgery. Two weeks after operation, the brace was separately extended to fix the interphalangeal joint (the type I fractures were not fixed, and the early interphalangeal joint flexion and extension exercises were prescribed). The metacarpophalangeal joint flexion and extension exercises were administered, and the brace was removed four weeks after surgery. Patients were educated about the active flexion and extension exercise. Depending on the fracture healing and rehabilitation of the finger function, the K−wires were pulled out 4−6 weeks after surgery. At the last follow-up visit to the hospital, the activity of the interphalangeal joint or metacarpophalangeal joint was measured, and the incidence of infection, pain, finger deformity, nonunion of the fracture, malunion, and avascular necrosis of the phalanges were noted.

RESULTS

Ten patients were followed-up for 6−12 months (mean 9 months). All patients were splinted for 2

weeks, after which the rehabilitation exercises were initiated. The K-wires were removed 4-6 weeks after operation, and the fractures were healed. The joints of the finger and metacarpophalangeal joints had good flexion and extension. According to Barton's and Al-Qattan's grades (1), excellent results were achieved for 4 fingers, good for 8 fingers, and fair for 1 finger. The excellent-to-good rate was 92.3%, with no infection or joint pain, no tendon rupture or finger deformity, and no skeletal ischemic necrosis or other complications noted in the patients.

Typical case

One patient, a 52-year-old male, had a history of proximal interphalangeal joint trauma of the left finger, and his left index finger was limited in flexion and extension of the proximal interphalangeal joint. The patient was referred with the pain, bleeding, and limited activity of the distal joint of the left middle finger and ring finger due to a machine crushing injury. The patient was admitted to the emergency room 1 hour after injury and underwent examination (Fig. 1). The skin of the left middle finger and ring finger was bruised and contused. The fingers were bleeding, the tenderness in the distal interphalangeal joint was obvious, and the active flexion and extension were limited. Debridement was performed under the local anesthesia, and the fracture closure and reduction of K-wire was used for intramedullary fixation. After the operation, splint fixation was given for 2 weeks, followed by the rehabilitation exercise. The K-wires were pulled out 6 weeks after the operation, and the fracture healed well. The flexion and extension of the distal finger joint of the middle finger were good, with no infection or joint stiffness.

DISCUSSION

Phalangeal neck fractures typically occur in children and are rarely observed in adult patients. In the group of adult patients described in this study, the fractures occurred due to hand crush injury, often

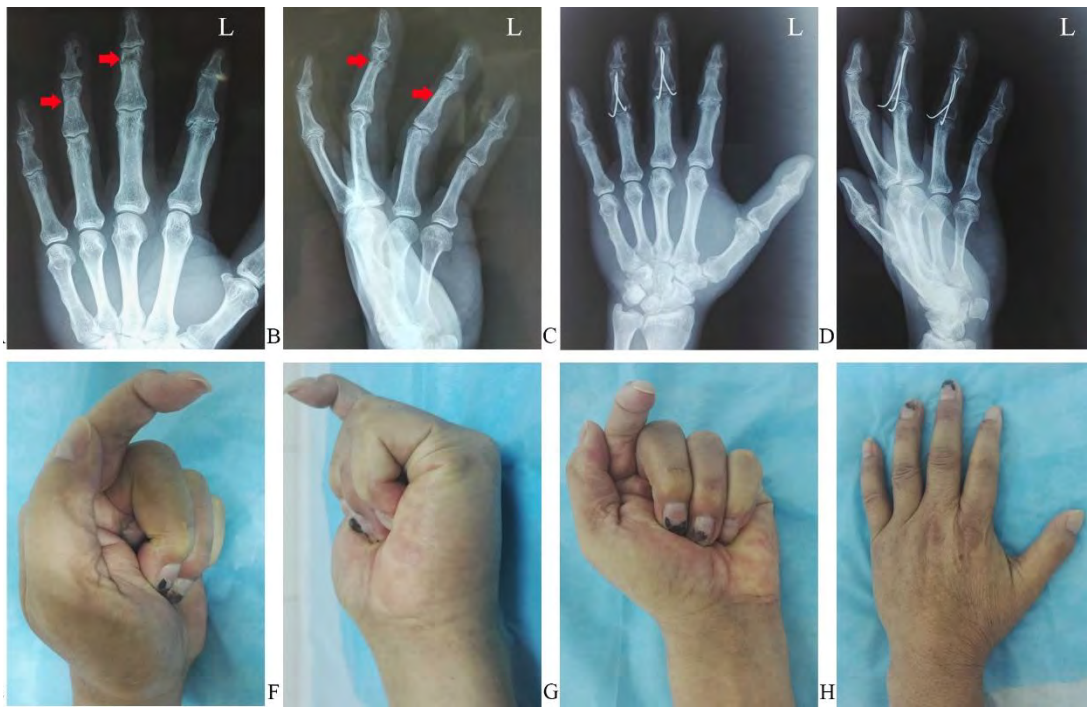


Fig. 1. ***A, B****) Preoperative radiographs showing the phalangeal neck fractures in the left middle finger and the ring finger joints. The fracture in the middle finger is Al-Qattan's type III, while the fracture in the ring finger is Al-Qattan's type I.* ***C, D****) X-ray film 6 weeks after surgery. The fractures were well restored and healed.* ***E-H****) Three months after surgery, the flexion and extension functions of the middle and ring finger recovered. Arrows: fracture lines.*

involving multiple finger injuries and the damage to the finger skin with varying degrees of contusion and exfoliation. Due to the instability of the phalangeal neck fractures, closed reduction and percutaneous K-wire are currently used for retrograde cross fixation. This procedure is demanding for operators who often need to repeatedly apply the needle to obtain the ideal strong fixation. Since the needle insertion point is adjacent to the lateral collateral ligament and the articular surface, the procedure is associated with an increased risk of damage to articular cartilage and joint capsule, extensor tendon and collateral ligament of the phalanx. In addition, the repeated needle insertions lead to iatrogenic fractures of the articular surface, which may result in joint stiffness, delayed healing, and ischemic necrosis of the phalanx, eventually leading to limited flexion and extension of the finger joints (4). How to avoid the iatrogenic injury of the interphalangeal joint and surrounding tissue and achieve the accurate reduction and strong fixation is a clinical problem to be solved urgently.

Al-Qattan (2) reported 15 cases of type II phalangeal neck fractures in children fixed with closed reset splint. Only 5 patients achieved good therapeutic effect, while 5 other patients developed malformation resulting in finger deformity, and the fractures in 5 remaining patients did not heal. For the displaced type II/III phalangeal neck fracture, the simple splint fixation cannot maintain the fracture reduction due to the traction of the collateral ligament. The risk of loss after the reduction of the fracture end is extremely high. The K-wire through interphalangeal joint fixation and the K-wire needle fixing method have been often used in children and achieved satisfactory results (5). However, the articular fixation for the treatment of phalangeal neck fractures in adults often leads to joint stiffness. Gonzalez et al. (6) reported in 1995 that K-wire intramedullary fixation for the treatment of phalangeal fractures without fixing finger joints achieved good finger function recovery, and complications were rare. The treatment of intramedullary fixation of phalangeal neck fractures has rarely been reported. In 2010, Al-Qattan (4) reported a method of antegrade intramedullary fixation with K-wire for the treatment of proximal phalanx and phalangeal neck fractures without disturbing the tissues around the joint. The effect was satisfactory. However, for the single Kirschner wire fixation, the anti-rotation performance remains poor despite the improvements in bending resistance, and there is still a risk of loss of fracture reduction (7). We used double K-wire intramedullary fixation to solve the shortcomings of rotational instability. The fixation was stronger, allowing early inter-finger joint flexion and extension exercises, which significantly improved the flexion and extension function of the fingers.

We designed a method of antegrade intramedullary fixation of the phalanges to treat the fracture of the phalanges, without interfering with the joint capsule and collateral ligaments around the interphalangeal joints and without the need to fix these joints. This method uses double Kirschner needle intramedullary fixation to solve the problem of rotation instability. The resulting biomechanical stability is better than that of K-wire cross fixation (8, 9), which greatly enhances the stability of the fracture end and significantly improves the function of the finger. The operation is simple, inexpensive, requires no incision, involves minimal trauma, and greatly shortens the hospitalization period, making it an ideal surgical method.

REFERENCES

1. Al-Qattan MM, Al-Qattan AM. A review of phalangeal neck fractures in children. Injury 2015; 46(6):935-44.
2. Al-Qattan MM. Phalangeal neck fractures in children: classification and outcome in 66 cases. J Hand Surg Br 2001; 26(2):112-21.
3. Al-Qattan MM. Phalangeal neck fractures in adults. J Hand Surg Br 2006; 31(5):484-88.
4. Al-Qattan MM. Phalangeal neck fractures of the proximal phalanx of the fingers in adults. Injury 2010; 41(10):1084-89.
5. Londner J, Salazard B, Gay A, et al. A new technique of intrafocal pinning for phalangeal neck fractures in children. Chir Main 2008; 27(1):20-25.
6. Gonzalez MH, Igram CM, Hall RF. Intramedullary nailing of proximal phalangeal fractures. J Hand

Surg Am 1995; 20(5):808-12.
7. Sharma H, Taylor GR, Clarke NM. A review of K-wire related complications in the emergency management of paediatric upper extremity trauma. Ann R Coll Surg Engl 2007; 89(3):252-58.
8. Wong TC, Ip FK, Yeung SH. Comparison between percutaneous transverse fixation and intramedullary K-wires in treating closed fractures of the metacarpal neck of the little finger. J Hand Surg Br 2006; 31(1):61-65.
9. Shi L, Liangfu J, Jixin X, et al. Double Kirschner wire via phalangeal base insertion for intramedullary fixation of proximal phalangeal fractures. Chin J Hand Surg 2015; 31(6):410-12.

JOURNAL OF BIOLOGICAL REGULATORS & HOMEOSTATIC AGENTS Vol. 34, no. 2, 629-633 (2020)

LETTER TO THE EDITOR

EFFECTS OF PROPOFOL AND GAS ANESTHESIA ON COGNITIVE IMPAIRMENT IN ELDERLY PATIENTS AFTER SURGERY

JW. DAI[1*], LQ. HONG[1*], MF. HAN[2], L. LIN[1] and ZW. DUAN[3]

[1]Department of Anesthesiology, the First Affiliated Hospital of Xiamen University, China; [2]Anesthesiology Department of Operation Room (III), Binzhou People's Hospital, China; [3]Embo Hospital of Xiamen, China

Received September 18, 2019 – Accepted March 30, 2020

[*]These Authors contributed equally to this study

To the Editor

Anesthesia, one of the important components of modern surgical treatment, eliminates or effectively reduces pain in patients (1, 2). However, for elderly patients, due to the slowdown of metabolism and the deterioration of cholinergic nerve function, anesthetics are often retained *in vivo*, resulting in inhibition of the function of the central nervous system, which may lead to postoperative cognitive dysfunction (3, 4). Cognitive impairment manifests mainly in changes in social behavior, mental activities and cognitive abilities (5). This complication affects the physical and mental health of elderly patients, and also reduces their quality of life. Currently, clinical studies have shown that cognitive impairment is associated with disorders in the endocrine system, immune system and central nervous system, as well as anesthetic drugs, depth of anesthesia and anesthesia methods (6). Therefore, some of the key areas of focus in clinical anesthesia research involve the need for effective reduction of the impact of surgical anesthesia on patients, and the enhancement of the safety of surgery. Based on the above background, the purpose of this study was to compare the effects of propofol and gas anesthesia on postoperative cognitive impairment in elderly patients.

MATERIALS AND METHODS

General data

This is a prospective study, and the sample population was calculated using the following formula: $n = 2*[(\alpha\beta)\sigma / \delta] \wedge 2$ where δ is the required degree of differentiation; α and β can be looked up in the row of freedom degree $\upsilon = \infty$ - in the table of t critical value, and σ is the overall standard deviation or its estimated values.

One hundred and forty elderly patients who underwent orthopedic surgery in our hospital from April 2016 to August 2018 were selected as the study subjects. The inclusive criteria were: (a) meeting the diagnostic criteria of Clinical Guidelines for Diagnosis and Treatment - Orthopaedic Branch (7); (b) undergoing surgeries for fracture of bone shaft, femoral fracture, lumbar, knee, or hip; (c) mini-mental state examination (MMSE) score ≥ 23 points before surgery; and (d) having normal liver and kidney functions. The exclusion criteria included: (a) presence of cardiovascular diseases, or

Key words: propofol; sevoflurane; cognitive function

Corresponding Author:
Dr Liqiong Hong,
Room 2702, NO.16, Guanri West erli, Huli District,
361022, Xiamen, China
Tel./Fax: 0592-6248127
e-mail: hongliqiongh@163.com

0393-974X (2020)
Copyright © by BIOLIFE, s.a.s.
This publication and/or article is for individual use only and may not be further reproduced without written permission from the copyright holder.
Unauthorized reproduction may result in financial and other penalties
DISCLOSURE: ALL AUTHORS REPORT NO CONFLICTS OF INTEREST RELEVANT TO THIS ARTICLE.

respiratory and central nervous system diseases, and (b) presence of a history of severe trauma, surgery or blood pressure > 160/90 mmHg in the previous year. The patients were divided into a propofol group and a sevoflurane group using the random number table method, with 70 patients in each group. The study was approved by the ethics committee of our hospital. All patients signed informed consent forms.

All patients were diagnosed and approved for surgical treatment. Before surgery, patients were required to abstain from food and drink according to the types of disease, and antibiotics were given to treat infections where necessary. All patients were given general anesthesia. A channel was established in the peripheral vein, and fentanyl (2~5 μg/kg), cis-atracurium (0.15~0.25 mg/kg) and midazolam were injected. After tracheal intubation, the ventilation tidal volume was set at 8~10 mL/kg, the respiratory frequency was set at 10-18 times/min, while the partial pressure of carbon dioxide was set as 25~35 mmHg. Patients in the sevoflurane group were given 1%~3% sevoflurane (Jiangsu Shengdi Pharmaceutical Co., Ltd., China; SFDA approval number: H20040771) to maintain anesthesia. Patients in the propofol group were infused with 1~3 μg/kg propofol using target-controlled infusion pump (Sichuan Guorui Pharmaceutical Co., Ltd., China; SFDA approval number: H20040079) to maintain anesthesia. During the operation, the arterial blood pressure levels of patients in the two groups were closely monitored. The anesthesia was stopped during skin suture.

Observation indicators

The MMSE score was used to evaluate the cognitive function in the two groups 24 h before the operation, and at 3, 6 and 24 h post-operation. The evaluation indices were alertness, language ability, orientation, computing ability and immediate memory. The scores ranged from 0 to 30 points. If the score of a patient after operation was 2 points lower than that before operation, it indicated decreased cognitive function. Moreover, if the score of a patient after operation was lower than 23 points, it indicated cognitive impairment.

Postoperative recovery indices such as breathing recovery time, awakening time and orientation recovery time were recorded. The levels of S100β protein in the two groups before and after operation were determined using enzyme-linked immunosorbent assay (ELISA).

Statistical analysis

Measurement data are expressed as mean±SD. The two groups were compared using *t*-test. Categorical data are expressed as numbers [n (%)], and were statistically analyzed using *chi*-squared test. All statistical analyses were carried out with SPSS version 20.0. Differences were considered statistically significant at $P<0.05$.

RESULTS

Comparisons between groups

There were no statistically significant differences in gender, age and weight between the two groups ($P>0.05$), i.e., the two groups were comparable (Table I). There was no significant difference in MMSE score between the propofol group and sevoflurane group 24 hours before surgery ($P>0.05$). However, at the3rd, 6th and 24th hour after the operation, the MMSE scores of the propofol group were significantly higher than those of the sevoflurane group ($P<0.05$, Table II). Recovery indicators in the propofol group were significantly improved, when compared with those in the sevoflurane group ($P<0.05$, Table III).

There was no significant difference in the level of S100β protein between the propofol group and sevoflurane group before induction of anesthesia ($P>0.05$). However, on the first day after surgery, the level of S100β protein in the propofol group was significantly lower than that in the sevoflurane group ($P<0.05$, Table IV).

DISCUSSION

Anesthesia is an important component of surgical treatment. Generally, anesthesia is needed before surgery to reduce pain in patients. In previous surgical treatments for elderly patients, the available narcotic drugs were diverse, and their negative effects also differed. Gas anesthesia is a popular route of anesthesia as it inhibits the central nervous system,

Table I. *Comparison of general data between the two groups*

Group	Gender (male/female)	Age (year)	Weight (kg)
Propofol group	40/30	69.82±2.23	63.23±9.66
Sevoflurane group	37/33	69.62±2.31	62.76±9.87
t/X^2	0.579	0.321	0.268
P	0.9474	0.7912	0.8045

Table II. *Mini-mental state examination score before and after treatment between two groups (*Mean±SD*, point)*

Group	Preoperative 24th h	Postoperative 3rd hour	Postoperative 6th hour	Postoperative 24th hour
Propofol group	29.4±0.7	28.5±0.6	29.6±0.7	29.8±0.7
Sevoflurane group	29.5±0.8	27.2±0.5	27.5±1.1	28.2±0.7
t	0.687	14.121	10.907	11.725
P	0.4912	0.0000	0.0000	0.0000

Data are presented as mean ± SD

Table III. *Recovery indicators in the two groups after operation (*Mean±SD*, min)*

Group	Breathing recovery time	Awakening time	Orientation recovery time
Propofol group	12.2±2.2	13.3±2.6	15.3±3.2
Sevoflurane group	14.6±3.5	15.4±4.5	17.7±4.6
t	3.973	2.784	2.856
P	0.0001	0.0062	0.0047

Data are presented as mean ± SD

Table III. *Recovery indicators in the two groups after operation (*Mean±SD*, min)*

Group	Before induction of anesthesia	Postoperative 1st day
Propofol group	0.046±0.024	0.052±0.027
Sevoflurane group	0.047±0.023	0.073±0.025
t	0.221	4.194
P	0.8217	0.0001

Data are presented as mean ± SD

reduces transmission of pain, and is highly safe. However, since the drugs are slowly metabolized through the respiratory system, their effects on the cognitive function of elderly patients are prolonged.

Propofol is a highly fat-soluble anesthetic drug which has advantages of quick onset and recovery. Unlike gas anesthetics, the metabolites of propofol are eliminated through the urine, which is more efficient than the elimination through the respiratory system. Propofol not only inhibits the synaptic expression of hippocampal cells and promotes the enhancement of GABAA receptor function, but also alleviates the nerve damage in patients, thereby reducing the incidence of postoperative cognitive impairment. A study by Yan et al. (8) found that propofol and sevoflurane reduced early cognitive function of elderly patients after non-cardiac surgery, but the effect of propofol was weaker than that of sevoflurane. The results of the present study demonstrated that cognitive dysfunction occurred in both groups, but the cognitive function score of the sevoflurane group decreased more significantly at the 1st h, 4th h and 6th h after operation. These results indicate that propofol had less effect on the cognitive dysfunction of the elderly patients, and it also had shorter elimination time. These findings are consistent with the results of a previous study (9).

It has been reported by Huseyin et al. (10) that the time taken for eye movement, extubation and speech response were shorter after intravenous anesthesia than after inhalation anesthesia. In an in-depth study on the anesthetic effect of the two drugs, Wu (11) found that self-recovery, eye-opening time, extubation time and orientation recovery time in the sevoflurane group were 15.27±3.20 min, 17.83±3.91 min, 20.24±4.09 min, and 22.63±4.24 min, respectively, which were significantly longer than those in the propofol group. In the present study, the recovery indices in the two groups were similar to those reported in previous studies, indicating that the anesthesia time of propofol was shorter, and that propofol was helpful in the postoperative recovery of patients.

In judging whether there is cognitive impairment after operation, S100β protein is one of the commonly used clinical determination indicators. It exists mainly in glial cells, and its level directly reflects the degree of brain injury. One clinical study (12) confirmed that there is a close relationship between the level of S100β protein and the neurological function of patients; the higher the level of S100β protein, the greater the adverse effects on the neurological function of patients. In this study, at the 24th hour after surgery, the level of S100β protein in the propofol group was significantly lower than that in the sevoflurane group, which confirmed the validity of the clinical research-based conclusion.

In conclusion, the risk of cognitive impairment is low and the serum S100β level has high stability when propofol regimen is used in the intraoperative maintenance anesthesia for elderly patients. This finding is considered worthy of clinical application.

REFERENCES

1. Villablanca PA, Mohananey D, Ramakrishna H. Comparison of local versus general anesthesia in patients undergoing transcatheter aortic valve replacement: A meta analysis. Catheter Cardiovasc Interv 2018; 92(5):1018-19.
2. Jia ZM, Hao HN, Huang ML, Ma DF, Jia XL, Ma B. Influence of dexmedetomidine to cognitive function during recovery period for children with general anesthesia. Eur Rev Med Pharmacol Sci 2017; 21(5):1106-11.
3. Umholtz M, Nader ND. Anesthetic immunomodulation of the neuroinflammation in postoperative cognitive dysfunction. Immunol Invest 2017; 46(8):805-815.
4. Evered L, Scott DA, Silbert B. Cognitive decline associated with anesthesia and surgery in the elderly: does this contribute to dementia prevalence? Curr Opin Psychiatry 2017; 30(3):220-26.
5. Feinkohl I, Winterer G, Spies CD, Pischon T. Cognitive reserve and the risk of postoperative cognitive dysfunction. Dtsch Arztebl Int 2017; 114(7):110-17.
6. Gavrilovska-Brzanov A, Shosholcheva M, Kuzmanovska B, et al. The influence of smoking on the variations in carboxyhemoglobin and methemoglobin during urologic surgery. Med Arch 2017; 71(3):178-82.

7. Fang X, Han Q, Li SY, Zhao YL, Luo AL. Chikusetsu saponin a attenuates isoflurane-induced neurotoxicity and cognitive deficits via SIRT1/ ERK1/2 in developmental rats. Am J Transl Res 2017; 9(9):4288-99.
8. Yan Y, Yu QJ, Tao H. The relationship between propofol, sevoflurane and postoperative cognitive dysfunction in elderly patients undergoing non-cardiac surgery: A meta-analysis. Medical Recapitulate 2016; 22(14):2839-45.
9. Samad N, Ishaq S, Bano S, Manzoor N. Calcium regulation in Alzheimer's disease: mechanistic understanding. J Coll Physicians Surg Pak 2017; 27(9):566-571.
10. Huseyin Toman, Uğur Özdemir, Hasan Ali Kiraz, Nurettin Lüleci. Severe headache following ozone therapy: Pneumocephalus. Agri 2017; 29(3):132-36.
11. Wu D. The effects of sevoflurane and propofol under general anesthesia on the recovery time and postoperative cognitive function of elderly patients. China Pharm 2013;22(5):95-96.
12. Baptista TSA, Petersen LE, Molina JK, et al. Autoantibodies against myelin sheath and S100β are associated with cognitive dysfunction in patients with rheumatoid arthritis. Clin Rheumatol 2017;36(9):1959-68.

LETTER TO THE EDITOR

ANTIMICROBIAL EFFICACY OF A NEW *MIMUSOPS ELENGI (LINN)* INCORPORATED HERBAL PRODUCT ON SELECTED ORAL AND PERIODONTAL PATHOGENS: AN *IN-VITRO* MICROBIOLOGICAL STUDY

S.K. BHAVIKATTI and N.A. ALQAHTANI

Division of Periodontics and Community Dental Sciences,
College of Dentistry, King Khalid University, Abha, Saudi Arabia

Received February 8, 2020 – March 31, 2020

To the Editor,

Dental biofilm eventually leads to the development of caries, gingivitis, and periodontal diseases. Bacterial dental plaque is crucial in the initiation and progression of gingival and periodontal diseases (1). Plaque control can be achieved by mechanical and/or chemical methods. Dentifrices and mouthwashes incorporate compounds, either synthetic and/or natural and are effective mainly by the action on microorganisms by inhibiting their growth and blocking some of their enzymatic reactions (2). Among the mouthwashes, chlorhexidine (CHX) is considered to be the gold standard. However it is known to have side effects such as alteration in patient taste sensation, staining of teeth and less commonly, mucosal erosion or parotid swelling (3). Phytomedicine involving use of traditional medicines has proven safe by the national health care systems. World Health Organization (WHO) guidelines define herbal medicines as finished labeled medicinal products containing an active ingredient, i.e., obtained from the aerial or underground parts of botanicals or other plant materials or their combination (4). Hence, a polyherbal product incorporating *Mimusops elengi (Linn)* (5), known to possess various medicinal properties was used in our study.

A panel of standard strains of microorganisms used in the present study are implicated in oral and periodontal diseases. These include gram-positive organisms including *Streptococcus mutans*, *Lactobacillus acidophilus, Staphylococcus aureus, Enterococcus fecalis*, gram negative bacteria including *Escherchia coli,Pseudomonas aeruginosa, Porphyromonas gingivalis,Fusobacterium nucleatum,* and *Aggregatibacter actinomycetemcomitans* and the pathogenic yeast *Candida albicans* (6,7). To the best of our knowledge, this study is the first of its kind assessing antimicrobial potential with the essential herbal combination. Each component in the formulation was selected after meticulous understanding of their pharmacological actions so that the combination is a product of paramount benefit. This study aimed to assess the antimicrobial efficacy of a polyherbal product (Bakul dant powder^{TM}) (PH) in comparison with CHX against standard oral and periodontal microbial strains.

MATERIALS AND METHODS

The study was conducted in full accordance with the declared ethical principles (World Medical Association Declaration of Helsinki, version VII, 2013. Ethical

Key words: antimicrobial; chlorhexidine; mouthwash; oral bacteria; polyherbal

Corresponding Author:
Dr Shaeesta Khaleelahmed Bhavikatti,
Division of Periodontics and Community Dental Sciences,
College of Dentistry, King Khalid University,
Abha, Saudi Arabia
Tel.: +966550654934
e-mail: sbhavhkatti@kku.edu.sa

0393-974X (2020)
Copyright © by BIOLIFE, s.a.s.
This publication and/or article is for individual use only and may not be further reproduced without written permission from the copyright holder.
Unauthorized reproduction may result in financial and other penalties
DISCLOSURE: ALL AUTHORS REPORT NO CONFLICTS OF INTEREST RELEVANT TO THIS ARTICLE.

clearance was obtained from the institution's independent ethics committee (Approval No. SRC/ETH/2018-19/116).

Preparation of the polyherbal plant product

The freshly prepared polyherbal product was acquired from the senior doctor of Ayurveda, India who is the proprietor of the product. The parts used and proportions of each plant material are listed in Table I. As reported in previous studies, there can be limited antibacterial potency due to the extraction methods employing various chemicals and crude extracts to get the plant extracts (8). It is therefore suggested that pure plant compounds isolated from plants might exhibit better antibacterial activity. Owing to this concept, we used the native pure form of the plants as a mixture to retain their vital properties in natural form.

Microbial strains used

The antimicrobial effects were determined against standard strains of bacteria that are involved in different stages of oral and periodontal diseases. The strains of microorganisms used were gram positive organisms facultative anaerobic bacteria including *Streptococcus mutans (ATCC 25175)* and *Lactobacillus acidophilus (ATCC 4356), Staphylococcus aureus (ATCC 12598)*, gram-negative bacteria including *E. coli (ATCC 25922), Pseudomonas aeruginosa (ATCC 25619), Porphyromonas gingivalis (ATCC 33277), Fusobacterium nucleatum (ATCC 25586), Aggregatibacter actinomycetemcomitans (ATCC 29523), Enterococcus fecalis (ATCC 35550)* and *Candida albicans (ATCC 2091)*. The strains were procured from Himedia laboratories Pvt. Ltd., Mumbai, India.

Preparation of the stock solution

The stock solution was prepared by dissolving 100 mg of PH in 1 ml of 0.25% Dimethyl sulfoxide (DMSO). 0.25% DMSO is not known to exhibit antibacterial activity and it is further diluted as different concentrations of the compound are prepared, ruling out any possible antibacterial activity of its own (9). 50 µl of CHX (0.2% Rexidin™ mouthwash) was used for the assay. A total of 8 concentrations of the PH were prepared as follows: i) 100% - Neat, ii) 75% - 75 µl compound in 25 µl of DMSO, iii) 50% -50 µl compound in 50 µl of DMSO, iv) 25% - 25 µl compound in 75 µl of DMSO, v) 10% - 10 µl compound in 90 µl of DMSO, vi) 5% - 5 µl compound in 95 µl of DMSO, vii) 2.5% - 2.5 µl compound in 97.5 µl of DMSO and viii) 1.25% - 1.25 µl compound in 98.75 µl of DMSO.

Antimicrobial susceptibility assay

Agar disc diffusion method was used for assessing the antimicrobial activity of the PH in comparison with standard CHX. The media used was Brain Heart Infusion agar. The agar plates were brought to room temperature before use. In anti-fungal disc diffusion method, Sabouraud agar medium was used. Using a swab, the colonies were then transferred to the plates. The turbidity was then adjusted with broth to equal that of 0.5 McFarland turbidity standard. Within 15 min of adjusting the inoculum to a McFarland 0.5 turbidity standard, a sterile cotton swab was dipped into the inoculum and rotated against the wall of the tube above the liquid to remove excess inoculum. The entire surface of agar plate was swabbed three times, rotating the plates approximately 60° between streaking to ensure even distribution. The inoculated plate was allowed to stand for at least 3 min but no longer than 15 min before making wells.

Followed by the inoculation of the agar plate, a hollow tube of 5 mm diameter was taken and heated. It was pressed on above the inoculated agar plate and removed immediately by making a well in the plate. Likewise, five wells were made on each plate. 50 µl of dilutions of the compound were added to each of these into the respective wells on each plate. Following this, the plates were incubated for 18-24 h at 37ºC. Bacterial strains were maintained on blood agar media, mitis salivarius agar, and brain-heart infusion agar as appropriate for that species. These media were obtained and prepared in accordance with the manufacturer's instructions (HiMedia Laboratories Pvt Ltd., Mumbai, India). Once the lawn of growth was confluent or nearly confluent, the diameter of inhibition zone was measured in millimeters using a vernier caliper (Fig. 1).

Determination of MIC (Minimum Inhibitory Concentration)

For the broth dilution assays, 9 serial dilutions of PH and CHX ((i.e., 100, 50, 25, 12.5, 6.25, 3.12, 1.6, 0.8, 0.4, and 0.2 mg/ml) were done with Brain–Heart Infusion broth (BHI). The concentration as prepared for disc diffusion for 100% neat was taken and was serially diluted. In the initial tube 20 µl of PH and CHX was added

into the 380 µl of BHI broth. For dilutions 200 µl of BHI broth was added into the next 9 tubes separately. Then from the initial tube 200 µl was transferred to the first tube containing 200 µl of BHI broth. This was considered as 10^{-1} dilution. From 10^{-1} diluted tube 200 µl was transferred to second tube to make 10^{-2} dilution. The serial dilution was repeated up to 10^{-9} dilution for each drug. In each serially diluted tube, 200 µl of bacterial suspension was added. The tubes were then incubated at 35°C for 48-72 h and observed for turbidity. The MIC was read, which was defined as the highest dilution of the agent that inhibited bacterial growth, as determined by lack of turbidity. The experiments were repeated in triplicates for each strain.

RESULTS

In the present study, an initial screening was carried out to assess the antimicrobial efficacy of a new herbal product against standard strains of oral and periodontal pathogens. A zone of inhibition of more than 8 mm signifies that the micro-organisms are susceptible to the tested products. Table II summarizes the result of susceptibility of experimented organisms against different concentrations of the PH and CHX. Zones of inhibition assessed by disc diffusion were 25.00±1.00 mm for *C. albicans*, 23.33±0.57 mm for *S. mutans*, 20.66±0.57 mm for *P. gingivalis* for the PH . In comparison, zones of inhibition for CHX were 28.00±2.00 mm for *C. albicans,* 30.00±1.00 mm for *S. mutans* and 28.00±1.73 mm for *P. gingivalis.* Though CHX had better results, PH also exhibited inhibition against the pathogens (Fig. 2)

Sensitivity of specific organisms to different dilutions of PH and CHX was analysed by treating the selected strains of micro-organisms. Table III presents the MIC exhibited by the PH and CHX against tested micro-organisms. It is noteworthy that, all of the selected bacterial strains were sensitive to both PH and CHX at 100 mg/ml and 50mg/ml. Similar inhibitory effects against *P. aeruginosa* (0.76±0.15), *E. Coli* were observed with both PH and CHX (1.6±0.25), *C. albicans* (0.8±0.16) and *P. gingivalis* (3.10±0.018). However, for the other strains of microorganisms, PH was found to be

Table I. *Plant materials used and their proportions*

Botanical name	Local name	Parts used	Proportions used (%)
Mimusops elengi(Linn)	Bakul saal	Bark	22
Azadirachta indica A	Neem saal	Bark	11
Acacia nilotica	Babul saal	Stem	11
Acacia catechu	Khair saal	Bark	11
Terminalia chebula	Hirda	Fruit	11
Terminalia bellirica	Bahera	Fruit	11
Emblica officinalis	Amalaki	Fruit pulp	11
Alum	Turti	Hydrated double sulfate salt of aluminium	2
Syzygium aromaticum	Lavang	Dried flower buds	5
Rock salt	Saindhav	Mineral	5

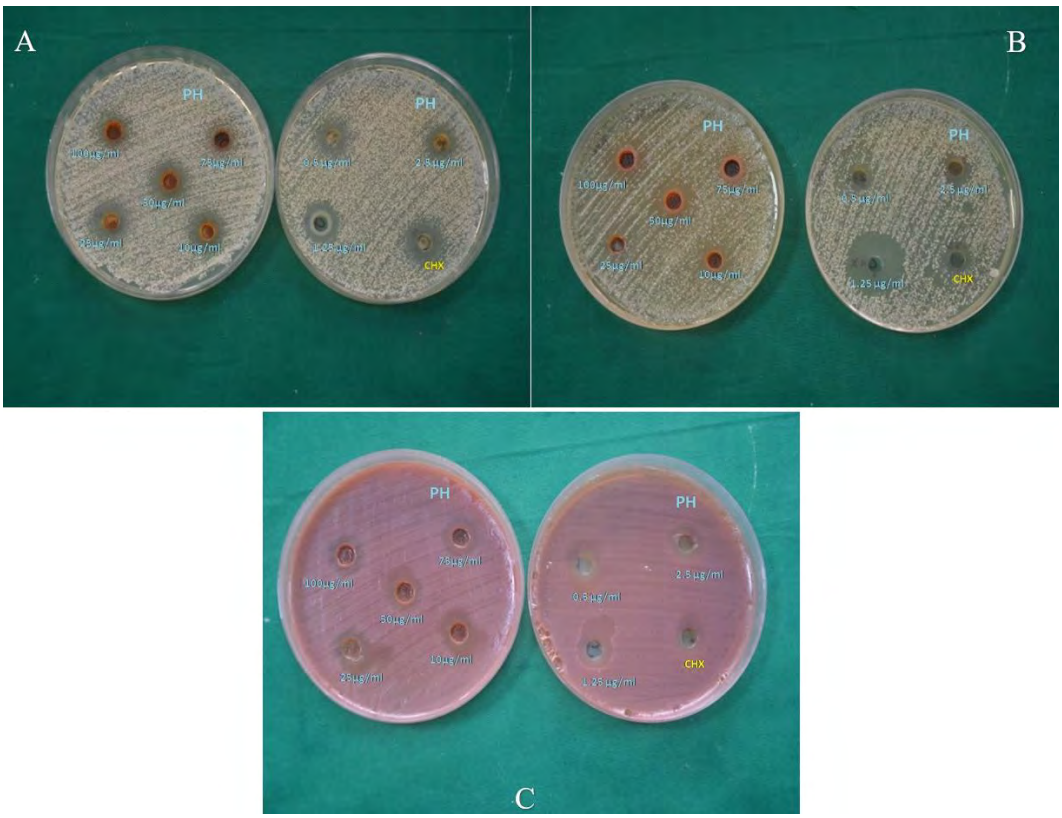


Fig. 1. *Antimicrobial activity of the polyherbal product (PH) and chlorhexidine. (CHX) against* C.albicans ***(A)***, S. mutans ***(B)***, P. gingivalis ***(C)***.

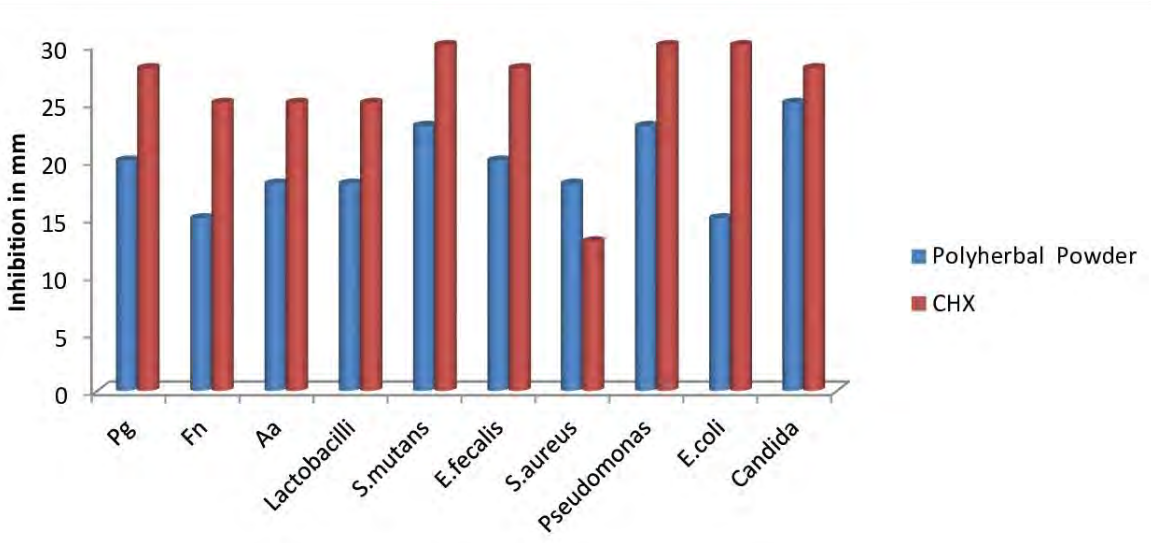


Fig. 2. *Effects of the polyherbal product and chlorhexidine against standard oral and periodontal microorganisms at 100µl/ml.*

Table II. *Comparison of the effects of PH and CHX on standard oral and periodontal microbial strains using Disc Diffusion method at 100 µl/ml*

Microorganisms	Polyherbal product (PH) (100 µl/ml)	CHX (100 µl/ml)
	ZONE OF INHIBITION in mm	
P. gingivalis	20.66 ±0.57	28.00±1.73
F. nucleatum	14.66±1.52	24.66±1.52
A. actinomycetemcomitans	19.33±1.52	26.66±1.52
L. acidophilus	18.66±0.57	25.00±1.00
S. mutans	23.33±0.57	30.00±1.00
E. fecalis	20.00±1.00	27.66±1.52
S. aureus	18.66±2.08	11.66±1.52
P. aeruginosa	22.66±1.52	30.66±1.52
E. coli	15.66±1.15	30.66±1.52
C. albicans	25.00±1.00	28.00±2.00

Table III. *Minimum Inhibitory Concentration (MIC) (mg/ml) of polyherbal product and CHX against the tested micro organisms*

Microbial strains	*P. gingivalis*	*F. nucleatum*	*A. actinomycetm-comitans*	*L. acidophilus*	*S. mutans*	*E. fecalis*	*S. aureus*	*P. aeruginosa*	*E. coli*	*C. albicans*
Poly-herbal Powder	3.10± 0.018	6.17± 0.11	50.66± 3.05	25.66± 2.08	6.2± 0.012	12.26± 0.87	3.12± 0.019	0.76± 0.15	1.6± 0.25	0.8± 0.16
CHX	3.12± 0.019	0.8± 0.016	6.25± 0.012	0. ± 0.16	0.8± 0.016	0.4± 2.00	0.4± 2.00	0.8± 0.016	1.6± 0.25	0.8± 0.16

effective at higher concentrations. Though CHX had better inhibitory effect even at low concentrations against the microorganisms, PH exhibited the inhibitory effects over the micro-organisms at variable concentrations (Fig. 3).

DISCUSSION

Considering the adverse effects of CHX, herbal mouthwashes have gained attention but none has been able to match that of CHX (10). This is the first study of its kind incorporating vital plant products such as *Mimusops elengi (Linn)* and other crucial plant materials in adequate proportions. *Mimusops elengi (Linn)* is well documented in literature to possess antibacterial, antifungal and antiinflammatory potential due to the inherent chemical composition (5). The other herbs incorporated in the product include *Azadirachta indica, Acacia nilotica, Senegalia catechu, Terminalia bellirica, Emblica officinalis, Terminalia chebula, Alum* and *Syzygium aromaticum* are wellknown for their medicinal potential. In our recently published work by Bhavikatt SK and co-workers, we reported good anti-inflammatory potential of the polyherbal product as assessed by gelatin zymography (8).

In the present study, though PH had inhibitory effects at higher concentrations, MIC by broth dilution technique showed highest sensitivity with CHX for all the selected bacterial strains, followed

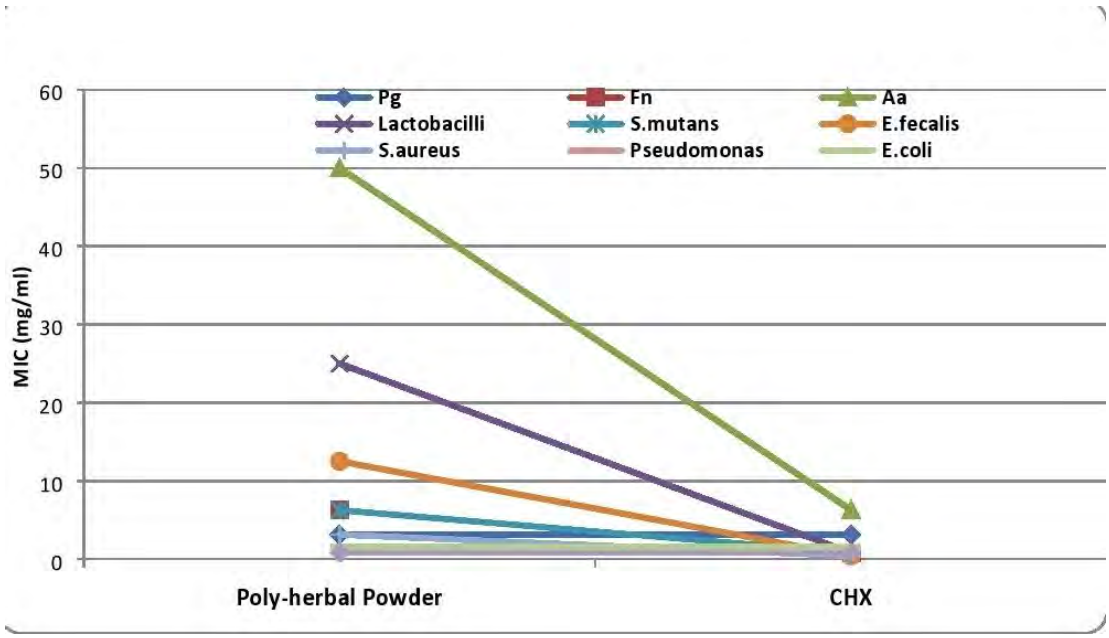


Fig. 3. *Antibacterial sensitivity of the oral and periodontal microorganisms as evaluated by broth dilution.*

by the PH. However, when MIC was assessed, PH had a significantly lesser effect as compared to CHX against *P. gingivalis*, *F. nucleatum*, *A. actinomycetemcomitans*, *L. acidophilus, S. mutans, E. fecalis, S. aureus, P. aeruginosa, E. coli and C. albicans*. CHX was more effective than PH. These findings reinforce the earlier findings that, variation in the media can affect the MIC values of a compound and that MIC values are method dependent. It may be that the constituents of the agar media could have influenced some of the antimicrobial properties of the poly-herbal mouthwash. Similar results were reported by Pathan et al (11) in their study.

PH showed maximum zones of inhibition of against *C. albicans* followed by *S. mutans*, but less as compared to CHX. This inhibition of poly-herbal powder against both Candida and *S. mutans* can be due to both, antifungal and anti-microbial property of the solution. The results are in agreement with Prabhakar et al. (12) in relation to antimicrobial activity. PH showed a comparable inhibitory effects over *S. mutans, S. aureus and C. albicans* to the standard CHX.

In conclusion, although CHX showed superior results, PH proved to have antimicrobial activity against oral and periodontal pathogens. It can therefore be used as a herbal alternative and as an adjunct to the conventional oral hygiene methods. However further studies with clinical efficacy on large samples of population are anticipated to validate the findings of the present study.

ACKNOWLEDGEMENTS

We are grateful to Dr. Prashant Bagewadikar, Proprieter of Bagewadikar Ayurved Rasshala, India for providing us with the formulation for our research. We extend our deep gratitude to Prof. Afaque Ansari Associate Professor, D.S.T.S Mandal's College of Pharmacy, India for all the guidance rendered. We are extremely thankful to Dr. Sandeep B. Patil, Associate Professor and Head, Adarsh College of Pharmacy, Sangli, India for guidance in conducting the lab procedures. This research was funded by Deanship of Research, King Khalid University (G.R.T./158/40).

REFERENCES

1. Colombo APV, do Souto RM, da Silva-Boghossian CM. et al. Microbiology of oral biofilm-dependent diseases: have we made significant progress to understand and treat these diseases? Curr Oral Health Rep 2015; 2:37-47.
2. Teles RP, Teles FRF. Antimicrobial agents used in the control of periodontal biofilms: effective adjuncts to mechanical plaque control? Braz Oral Res 2009; 23(1):39-48.
3. Ernst CP, Canbek K, Dillenburger A, Willershausen B. Clinical study on the effectiveness and side effects of hexetidine and chlorhexidine mouthrinses versus a negative control. Quintess Int 2005; 36(8):641-52.
4. World Health Organization, WHO Traditional Medicine Strategy 2002–2005, World Health Organization, Geneva, Switzerland, 2002.
5. Gami B, Pathak S, Parabia M. Ethnobotanical, phytochemical and pharmacological review of Mimusops elengi Linn. Asian Pac J Trop Biomed 2012; 2(9):743-48.
6. Chenicheri SRU, Ramachandran R, Thomas V, Wood A. Insight into oral biofilm: primary, secondary and residual caries and phyto-challenged solutions. Open Dent J 2017; 11:312-33.b
7. Khatoon Z, McTiernan CD, Suuronen EJ, Mah TF, Alarcon EI. Bacterial biofilm formation on implantable devices and approaches to its treatment and prevention. Heliyon 2018; 4(12):e01067.
8. Bhavikatti SK, Alqahtani NA, Bhat KG, Aggarwal VP, Karobari MI. Evaluation of anti-inflammatory activity of a Mimusops elengi (linn)- incorporated herbal product : a zymographic analysis. J Biol Regul Homeost Agents 2020; 34(1).
9. Valgas C, Souza SM, Smânia Elza FA, Smânia Jr A. Screening methods to determine antibacterial activity of natural products. Braz J Microbiol 2007; 38(2):369-80.
10. Gupta D, Nayan S, Tippanawar HK, et al. Are herbal mouthwash efficacious over chlorhexidine on the dental plaque? Pharmacognosy Res 2015; 7(3):277-81.
11. Pathan MM, Bhat KG, Joshi VM. Comparative evaluation of the efficacy of a herbal mouthwash and chlorhexidine mouthwash on select periodontal pathogens: An in vitro and ex vivo study. J Indian Soc Periodontol 2017; 21(4):270-5.
12. Prabhakar K, Kumar LS, Rajendran S, Chandrasekaran M, Bhaskar K, Sajit Khan AK. Antifungal activity of plant extracts against candida species from oral lesions. Indian J Pharm Sci 2008; 70(6):801-3.

LETTER TO THE EDITOR

SPONTANEOUS RUPTURE OF KIDNEY DURING PREGNANCY

H. MENG[1], Y. MO[2], T. CHENG[1], H. ZHANG[1], L. WU[1], N.K. SHAH[1], C. SHU[1] and J. HE[1]

[1]Department of Obstetrics and Gynecology, The First Hospital of Jilin University, Jilin University, Changchun, Jilin China; [2]Department of Obstetrics and Gynecology, The Norman Bethune Medical Institute of Jilin University, Changchun, Jilin China

Received February 2, 2020 – Accepted April 2, 2020

To the Editor

Angiomyolipoma (AML) is a rare benign tumor of the kidney, with an incidence rate of about 0.30% (1, 2). The incidence in women is four times higher than in men (3). The incidence of renal angiomyolipoma during pregnancy is even rarer. The risk of renal AML rupture increases with its size, although the specific statistics on the frequency of such events is not fully assessed (4, 5). Spontaneous ruptures of AML in pregnancy are usually reported individually (6-10), as the chances of such event are extremely low. Tumor rupture can be severe and life threatening. Acute bleeding of AML is associated with acute flank pain, abdominal tenderness, and signs of internal bleeding such as hematuria (5).

When renal vascular smooth muscle lipoma ruptures and hemorrhage occurs, surgical treatment is usually carried out. When uterine vascular smooth muscle lipoma ruptures during pregnancy, the problem involves both mother and child, and the treatment becomes complicated. A comprehensive evaluation should be conducted to choose the best treatment strategy. In August 2017, a patient with spontaneous rupture of renal angiomyolipoma during pregnancy was treated in our Department of Obstetrics. The diagnosis and treatment of the disease are described in this report.

Clinical data of the case

The patient, a 36-year-old female, was in 36th (±2) week of pregnancy when she started to experience low back pain with irregular periods of lower abdominal pain lasting for 1 hour. The patient was admitted to our Emergency Department. Patient's medical history included: G1P0; left and right fallopian tube resections performed 9 and 5 years ago, respectively, due to ectopic pregnancies in the fallopian tubes. The patient had irregular menstruations, and the date of the last menstrual period was unknown. Due to secondary infertility, the patient received an embryo transfer in our Hospital's reproductive center. Color Doppler ultrasound investigation performed after 50 days of pregnancy showed intrauterine twin pregnancy. The patient was also previously diagnosed with thrombosis in the Department of Rheumatology and Immunology at our Hospital. She was prescribed oral aspirin and subcutaneous injections of heparin sodium for 7 months. One hour before the admission, the patient experienced left low back pain with no obvious cause, characterized by persistent, paroxysmal aggravation and accompanied by dyspnea and irregular lower abdominal pain. The patient had no symptoms of nausea but experienced vomiting, fever, frequent urination with no urgency, urinary pain and gross hematuria. Admission

Key words: renal angiomyolipoma; angiomyolipoma rupture; pregnancy; renal artery embolization; spontaneous rupture

Corresponding Author:
Dr Chang Shu
Department of Obstetrics and Gynecology,
The First Hospital of Jilin University, Jilin University,
No.71 Ximin Road, Changchun, Jilin,
130021, China;
Tel./Fax: +86 431 88782222
e-mail: dr.changshu@aliyun.com

0393-974X (2020)
Copyright © by BIOLIFE, s.a.s.
This publication and/or article is for individual use only and may not be further reproduced without written permission from the copyright holder.
Unauthorized reproduction may result in financial and other penalties
DISCLOSURE: ALL AUTHORS REPORT NO CONFLICTS OF INTEREST RELEVANT TO THIS ARTICLE.

examination revealed poor general state, with body temperature of 36.9°C, pulse 102 times/min, and blood pressure 85/50 mmHg. She was unable to take supine and left lateral positions, was irritable and occasionally unresponsive. There was no uplift in the kidney area, and the left kidney area was tender and painful. Abdominal bulging typical for the third trimester and irregular contractions were present. Obstetrical examination revealed uterus height of 30 cm and abdominal circumference of 110 cm. Extra-pelvic measurements were in the normal range. About 80% of the cervical canal was regressed, and the cervix was 1 cm larger. Auxiliary examination by color ultrasound showed fetus 1 in head position, with double top diameter of 8.6 cm, femur length of 6.7 cm, placenta in the back wall, grade I, thickness 3.6 cm.. Fetus 2 was in breech position, with double top diameter of 9.2 cm, femur length of 6.4 cm, placenta in the anterior wall, grade I, thickness 3.6 cm. Both fetuses had the baseline heart rate at 80 beats/min. Hemoglobin level was at 93 g/L. Admission diagnosis: 1 child 0, pregnancy 36±2 weeks, head position/breech, threatened premature delivery, placental abruption, fetal intrauterine distress, twin pregnancy, test tube baby.

Treatment

After admission, the patient was given oxygen and symptomatic supportive treatments. Appropriate obstetrical tests were performed. Considering the obstetric condition, placental abruption was not excluded. Under these circumstances, there was a risk of fetal death in the uterus, which would threaten the lives of both mother and child. The pregnancy needed to be terminated immediately. The family members were informed, and a cesarean section was performed in the Emergency department under general anesthesia. LST (Left sacrotransverse) was used to deliver a female infant (Apgar score 1 minute 1 minute, 5 minutes tracheal intubation, weight 2500 g, length 48 cm). Another female infant was also delivered using the LOA(left occipitoanterior) (Apgar score 1 minute, 1 minute, 5 minutes tracheal intubation, body weight 2180 g, length 46 cm). After the umbilical cord was broken, the premature infants were transferred to the Neonatology department. Intraoperative exploration found left uterine paraventricular vascular tortuosity and left retroperitoneal perirenal hematoma. After consulting with the Urology department and the Interventional department, we concluded that the rupture of left kidney was a possibility and recommended the CT examination of abdomen. The CT examination (Fig. 1 A,B) showed mixed density of the left dorsal kidney with internal bleeding. This pointed to the renal vascular smooth muscle lipoma rupture, accompanied by peripheral exudation. Left dorsal kidney showed irregularities, and cortical dysplasia was observed. Considering the patient's condition, the left nephrectomy could have caused hemorrhagic aggravation, hemorrhagic shock, and risk to patient's life. Thus, a left renal artery embolization was performed. After the operation, the patient was transferred to the ICU department

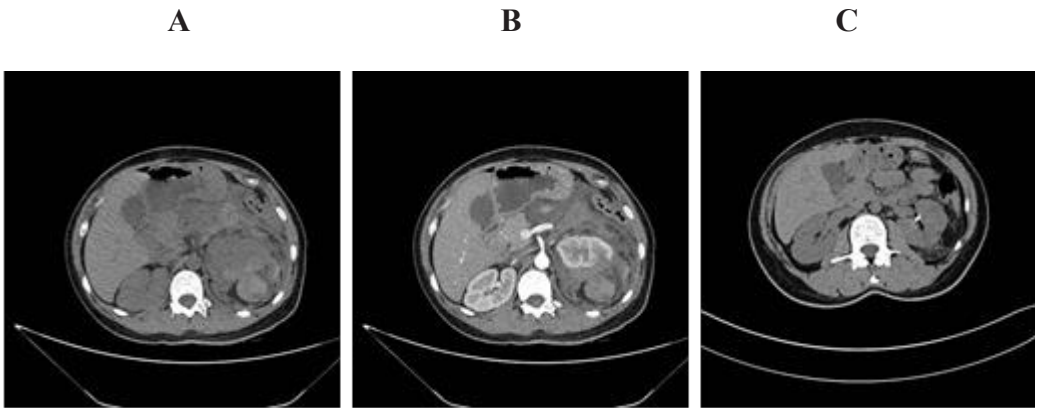


Fig. 1. ***A)*** *CT scan on the day of surgery;* ***B)*** *Enhanced CT scan on the day of surgery;* ***C)*** *CT scan on the 20th day after surgery.*

for intensive care, where blood transfusion and shock correction were administered. The patient was examined on the 7th day after surgery. The general condition was good, and vital signs were stable. The hemoglobin was stable at 85 g/L, and there was no downward trend. On the 7th day after embolization, the abdominal CT examination showed that the left kidney had a mixed density shadow, which was accompanied by hemorrhage and peripheral oozing. Compared with the results obtained on the day of surgery, the front part was partially reduced, and the density was slightly reduced. The left kidney and left peritoneum showed hematoma. The volume of retroperitoneal hematoma was not significantly reduced, but the density was lower. The peritoneal effusion and hemorrhage were reduced compared with the anterior effusion and blood volume, and the density was lower. The kidney function was normal. Considering that the patient's condition was stable, she was discharged. On the 20th day after embolization of the left renal artery, the abdominal CT (Fig. 1C) showed that the left kidney had mixed density, and the left kidney and left peritoneal hematoma were improved compared with the results of previous examination performed one week after surgery. The renal function was normal. After being actively treated in the Obstetrics and Neonatology departments, the premature infants were discharged from hospital on the 8th and 14th days after birth.

The subject provided informed, signed consent for publishing the results of this study.

DISCUSSION

Renal angiomyolipoma (AML) is the most common benign tumor of the mesenchymal epithelium in the kidney (11). AMLs can be divided into two types. The first one is tuberous sclerosis complex (TSC) type. About 20% of TSCs are caused by an autosomal dominant genetic disease involving multiple organs and systems, and the incidence rate is about 1/5800. When the kidney is involved, renal angiomyolipoma is often seen. In 80% of patients with TSC the condition is manifested as center and bilateral AML. Tumor growth is relatively fast, and the tumors are prone to rupture and bleeding. The second type of AML is sporadic. This type is more common and accounts for about 80% of cases (6, 7). The majority of AMLs have a good prognosis. After complete resection, there is generally no recurrence or metastasis. However, once AML has ruptured, a large amount of peritoneal hemorrhage can occur, which is often life-threatening.

Spontaneous rupture of AML is associated with tumor size and composition. The possibility of rupture is usually higher when the tumor diameter is >4 cm, and there are abundant abnormal blood vessels in the tumor tissue. AML easily bleeds. In severe cases, shock may develop very fast due to excessive blood loss. With a diameter of less than or equal to 4 cm, the chances of rupture of a tumor with adipose tissue are relatively small (8). Previous study found that AML expresses estrogen and progesterone receptors (7). During pregnancy, with the increase of estrogen and progesterone levels in the body, AML blood vessels proliferate, the blood flow and speed in the kidney increase, and the AML volume also tends to increase. In addition, due to the increase of intra-abdominal pressure and the increased pressure on uterus and kidney, pregnancy greatly elevates the risk of spontaneous rupture of renal angiomyolipoma (9). The causes of spontaneous rupture of AML also include the use of anticoagulant drugs and other factors (12). Our patient had a late pregnancy, which was a twin pregnancy, and a history of heparin use during the pregnancy. All these factors increase the risk of spontaneous rupture of AML. The treatment approaches should carefully assess the risk to the patient. In our case, we used renal artery embolization, which resulting in successful outcome of treatment.

ACKNOWLEDGEMENTS

This study was supported by funding from Natural Science Foundation of China (grant 81501279), Natural Science Funds in Science and Technology Department of Jilin Province, China (grant 20160101058JC).

REFERENCES

1. Cetin C, Buyukkurt S, Demir C, Evruke C. Renal

angiomyolipoma during pregnancy: Case report and literature review. Turk J Obstet Gynecol 2015; 2:118-21.
2. Zapardiel I, Delafuente-Valero J, Bajo-Arenas JM. Renal angiomyolipoma during pregnancy: review of the literature. Gynecol Obstet Invest 2011; 72:217-19.
3. Mauermann J, de Martino M, Waldert M, Haitel A, Klingler HC, Remzi M, Klatte T: Gender differences in benign renal masses. World J Urol 2013; 31:1051-57.
4. Champagnac J, Melodelima C, Martinelli T, et al. Microaneurysms in renal angiomyolipomas: Can clinical and computed tomography features predict their presence and size? Diagn Interv Imaging. 2016; 97:321-26.
5. Wang C, Li X, Peng L, Gou X, Fan J. An update on recent developments in rupture of renal angiomyolipoma. Medicine (Baltimore) 2018; 97:e0497.
6. Ao L, Ogasahara E, Okuda Y, Hirata S. Spontaneous rupture of renal angiomyolipoma during pregnancy. BMJ Case Rep 2017, 2017:pii:bcr2016217284.
7. dos Santos MM, Proenca SM, Reis MI, et al. Spontaneous rupture of renal angiomyolipoma during pregnancy. Rev Bras Ginecol Obstet 2014; 36:377-80.
8. Myoen S, Mitsuzuka K, Saito H, Ota H, Takase K, Arai Y. Spontaneous rupture of a renal angiomyolipoma at 25 weeks of pregnancy treated with transarterial embolization: A case report and review of the literature. Int J Urol 2015; 22:710-12.
9. Lo KL, Ng CF, Wong WS. Spontaneous rupture of the left renal collecting system during pregnancy. Hong Kong Med J 2007; 13:396-98.
10. 1Nath S, Sadhu S, Dhar D, Nadar D, Wadhawan M, Varshney P. Rupture of renal angiomyolipoma during pregnancy: A case report. J Anaesthesiol Clin Pharmacol. 2018; 34:280-81.
11. 1Urciuoli P, D'Orazi V, Livadoti G, et al. Treatment of renal angiomyolipoma: surgery versus angioembolization. G Chir 2013; 34:326-31.
12. Arslan B, Gürkan O, Çetin B, et al. Evaluation of ABO blood groups and blood-based biomarkers as a predictor of growth kinetics of renal angiomyolipoma. Int Urol Nephrol 2018; 50:2131-37.

LETTER TO THE EDITOR

THE ROLE OF p38MAPK SIGNALING PATHWAY IN HEPATOCELLULAR CARCINOMA RECURRENCE

T. FEI[1*], CX. GUO[1*], J. ZHANG[2], LN. WANG[3] and WW. FAN[4]

[1]Department of Laboratory Diagnosis, Heilongjiang Provincial Hospital, Harbin, China; [2]Department of Cardiovascular, Heilongjiang Provincial Hospital, Harbin, China; [3]Department of Dispensation, Ministry of Pharmacy, The Fourth Affiliated Hospital of Harbin Medical University, Harbin, China; [4]Department of Infectious Medicine, Heilongjiang Provincial Hospital, Harbin, China

Received February 24, 2020 – Accepted April 3, 2020

[*]These authors contributed equally to this work

To the Editor,

Hepatocellular carcinoma (HCC) is the fourth most common cause of cancer-related death worldwide and one of the most common malignant tumors in China (1). Hepatectomy and liver transplantations are the first-line and most effective treatments for primary liver cancer (2). Ischemia-reperfusion injury (IRI) has been shown to represent one of the main risk factors for cancer recurrence by promoting the invasion, metastasis, and formation of small lesions of tumor cells (3, 4). Glantzounis et al. (5) showed that IRI induced by intraoperative blockade of hepatic hilum may promote the recurrence and metastasis of hepatocellular carcinoma. p38 MAPK (mitogen-activated protein kinase) signalling pathways have been shown to be involved in inflammation, IRI and regulation of tumor proliferation and apoptosis (6, 7). After hepatic blood flow occlusion during hepatic surgery, oxygen-free radicals and cytokines are released in large quantities during reperfusion, leading to the activation of the p38MAPK signalling pathway. p38MAPK transmits extracellular information to the nucleus, enhances the expression activity of many transcription factors, and plays a significant role by aggravating inflammation, metabolic disorders and promoting cell apoptosis (6,7). Bundzikova et al. (8) showed that the process of ischemia-reperfusion activated the expression of p38MAPK in the liver, leading to necrosis and apoptosis of hepatocytes. The aim of this study was to investigate the role of p38 MAPK signalling pathway in the IRI induced hepatocellular carcinoma recurrence in order to provide a theoretical basis for further clinical exploration of the pharmacological intervention in the treatment of hepatocellular carcinoma. SB203580 is a pharmacological inhibitor of the p38 MAPK signalling pathway (9) and was used in this study for investigating the biological changes of hepatocellular carcinoma cell line HepG2 after in IRI conditions after blocking the p38 MAPK signalling pathway.

MATERIALS AND METHODS

Cell model of hypoxia-reperfusion

Hepatocellular carcinoma cell line HepG2 and normal hepatocyte HL-7702 cell lines, purchased from Shanghai Honsun Biological Technology Co., Ltd., China, were

Key words: p38MAPK signalling pathway; hepatocellular carcinoma cells; apoptosis; migration; invasion

Corresponding Author:
Dr Weiwei Fan,
Department of Infectious Medicine,
Heilongjiang Provincial Hospital,
82 Zhongshan Road, Xiangfang District,
Harbin, 150036, China
e-mail: fanww7069@163.com

0393-974X (2020)
Copyright © by BIOLIFE, s.a.s.
This publication and/or article is for individual use only and may not be further reproduced without written permission from the copyright holder.
Unauthorized reproduction may result in financial and other penalties
DISCLOSURE: ALL AUTHORS REPORT NO CONFLICTS OF INTEREST RELEVANT TO THIS ARTICLE.

cultured in serum-free medium (Shanghai Aopumei Biotechnology Co., Ltd., China) and their morphology was observed under an inverted microscope (Guilin Microtech Optical Instrument Co., Ltd., China). Logarithmic growth phase cells were collected and after replacing the glucose-free serum-free medium (Shanghai OPM Biosciences Co., Ltd., China), the cell culture dish was placed in a hypoxic incubator with one hole at each end of the incubator (outlet and inlet holes). The samples were put in a box with an atmosphere of 5% CO_2 and 95% N_2. The humidity and the oxygen content in the box were monitored by a display and if the concentration of oxygen was less than 1%, the two holes were sealed. Cells were cultured at 37°C for 4 h, 8 h, 12 h and 24 h, respectively. After culture in hypoxic conditions, the cells were taken out and cultured in high-glucose serum-containing medium (Shanghai OPM Biosciences Co., Ltd., China) for 1 hour.

MTT (3-(4,5-dimethyl-2-thiazolyl)-2,5-diphenyl-2-H-tetrazolium bromide, thiazolyl blue tetrazolium bromide)

The effect of p38MAPK signalling pathway inhibition on HepG2 cells and HL-7702 cells proliferation rates were evaluated by MTT assay. Different concentrations of SB203580 were used to inhibit p38MAPK signalling pathway on HepG2 cells and HL-7702 cells under normal and hypoxic cultures.

In the experiment, 10 groups were used of HepG2 cells: 5 cultured in normal conditions and 5 cultured in hypoxic conditions treated with 0 (control), 0.1μmol/L, 0.5μmol/L, 1μmol/L and 5μmol/L SB203580, respectively and 10 groups of HL-7702 cells - 5 cultured in normal conditions and 5 cultured in hypoxic conditions treated with 0 (control), 0.1μmol/L, 0.5μmol/L, 1μmol/L and 5μmol/L SB203580, respectively.

HepG2 cells and HL-7702 cells in the logarithmic growth phase were inoculated into the 96-well culture plate at a density of 5 x103/well. The cells were cultured in 200 μl 1640 DMEM medium (Dulbecco's modified eagle medium, Beijing Biopeony Co., Ltd., China) containing 10% fetal bovine serum (Beijing Biopeony Co., Ltd., China). After 24 h of culture, different concentrations of SB203580 (0.1μmol/L, 0.5μmol/L, 1.0μmol/L, 2.0μmol/L) were added to the experimental group. Each experimental group was divided into subgroups based on time of culture of 4 h, 8 h, 12 h, and 24 h before changing the medium and then cultured for 1 h in high glucose serum medium. After culture, 20 μL of 5mg/mL MTT (Sigma, USA) was added to each well and incubated for 4 h. After incubation, the liquid in each well was sucked out, and 100 μL DMSO (Sigma, USA) was added into each well and oscillated at 38°C for 10 min. The control group was adjusted to zero. The absorbance of each well was measured at a wavelength of 570nm using a spectrophotometer. The experiment was repeated five times for each group in order to calculate the inhibition rate of cell proliferation.

Western blot for determination of p38 MAPK and p-p38MAPK protein expressions

The effect of p38MAPK signalling pathway inhibition on the expression levels of p38 MAPK and p-p38 MAPK (phosphorylated p38 MAPK) in HepG2 cells cultured in normal and hypoxic conditions was evaluated by Western blot. Radio Immunoprecipitation Assay (RIPA) lysate was used to lyse cells and extract total protein. The protein concentration was measured by the bicinchoninic acid (BCA) method using a BCA test kit (Beijing TransGen Biotech Co., Ltd., China). The protein sample buffer was added and boiled in a water bath at 100°C for 5 min. SDS-PAGE was separated by electrophoresis and then transferred to PVDF membrane by wet rotation. The 5% skimmed milk powder solution, was used for sealing at room temperature for 2 h and then the samples were incubated overnight at 4°C with the first antibody - rabbit anti-human p38MAPK monoclonal antibody, rabbit anti-human p-p38MAPK monoclonal antibody (Santa Cruz, USA) and mouse anti-rat β-actin polyclonal antibody (Beyotime Biotechnology Co., Ltd., China). After washing with TBST (TBS+Tween), the secondary antibody - horseradish peroxidase-labelled goat anti-rabbit IgG (Beijing ZSGB Biotech Co., Ltd., China) was added and incubated for 1 h. After washing with TBST, the luminescent solution, ECL Chemiluminescence Detection Kit (Santa Cruz, USA) was added and analyzed using a gel electrophoresis imaging system (Shanghai Clinx Science Instruments Co., Ltd., China). The experiment was repeated 3 times.

Scratch test

The scratch test was used to evaluate the effect of p38MAPK signalling pathway inhibition on HepG2 cells after hypoxia and reoxygenation. For this experiment, 2

groups of HepG2 cells were used treated with 0 (control) and 1μmol/L SB203580, cultured for 24 h in hypoxic conditions as previously described, and then reoxygenated by cultured in normal conditions for 1 h.

Cell-free scratch zones with a width of about 200 μm were formed by scratching the growth surface of the cells on the bottom of the culture plate with a 100 μL gun head (Shanghai Zeye Biotechnology Co., Ltd., China). PBS was used to wash three times. Photographs were taken under an inverted microscope at intervals of 0 h, 12 h, 24 h, and 48 h. The experiment was repeated three times for each group.

Transwell cell invasion experiment

The Transwell test was used to evaluate the effect of p38MAPK signalling pathway inhibition on the invasion of HepG2 cells after hypoxia and reoxygenation. Two groups were used of HepG2 cells treated with 0 (control) and 1μmol/L SB203580, cultured for 24 h in hypoxic conditions as previously described, and then reoxygenated by cultured in normal conditions for 1h.

The Transwell (Corning, USA) basement membrane was coated with Matrigel matrix glue (BD, USA) and dried overnight at 37°C before being placed in a 24-well plate. 1.0 x 10^5 HepG2 cells in the logarithmic growth phase treated according to the group specification, were inoculated into the upper Transwell chamber. A serum-free medium containing 0.1% BSA was added to 200 μl. The culture medium containing 750 μL DMEM was added into the lower chamber. After incubation at 37°C for 24 h, the Transwell chamber was removed from the 24-well plate and washed three times with PBS, fixed with methanol for 10 min, removed from the chamber and stained with crystal violet for 20 min. The cells passing through Matrigel and micropore to the reverse side of the filter membrane were observed and counted under an inverted microscope. The experiment was carried out in triplicate.

Annexin V-FITC/PI double staining experiment

To test the effect of p38MAPK signalling pathway inhibition on the apoptosis of HepG2 cells and HL-7702 cells after hypoxia and reoxygenation, annexin V-FITC/PI double staining test was used. There were 4 groups: 2 groups of HepG2 cells and 2 groups of HL-7702 cells treated with 0 (control) and 1μmol/L SB203580, cultured for 24 h in hypoxic conditions as previously described, and then reoxygenated by culture in normal conditions for 1 h.

After the model was established, the cells were cultured for 1 h. After 0.25% trypsin digestion, the cells were washed twice with PBS and 1-5x10^5 HepG2 cells and HL-7702 cells were collected, and 500 μL of buffer suspension was added. 1 mL of single-cell suspension was collected and centrifuged at 4°C for 10 min. Cell precipitation was collected before sterile PBS was added and gently sucked several times with a pipette gun. The supernatant was discarded after centrifugation at 1000 rpm at 4°C for 10 min. This step was repeated 2-3 times to remove the residual medium and trypsin. The cells were then suspended in 500 μL conjugated solution, before 10 μL of Annexin V-FITC and 5 μL of PI (Propidine iodide) were added and blended gently. FACS flow cytometry was used for detection after 15 min of reaction at room temperature. The green fluorescence of Annexin V-FITC was detected by FITC channel (FL1) at a wavelength of 488-530nm. The red fluorescence of PI was detected at a wavelength of 488-630nm through PI channel (FL2). At least 10,000 cells were extracted from each batch of samples. The experiment was carried out in triplicate.

Statistical methods

SPSS 19.0 statistical software (IBM, USA) was used to process the data. The data were expressed as mean ± standard deviation. Student's t-test and ANOVA was performed. A value of $P < 0.05$ was considered statistically significant.

RESULTS

The effect of p38MAPK signalling pathway inhibition on HepG2 cells and HL-7702 cells proliferation rates

For HepG2 cells cultured in hypoxic conditions (group A) (Table I), SB203580 inhibited the proliferation of cells in a dose- and time-dependent manner. The effect of SB203580 on cell proliferation of HepG2 cells cultured in normal conditions was different compared to the ones cultured in hypoxic conditions. In the case of HepG2 cells cultured in hypoxic conditions (group A) SB203580 showed the highest effect on inhibition of the proliferation

of cells at 4 h of culture, followed by a decrease in effect after 8 h, 12 h and 24 h. In the case of HepG2 cells cultured in normal conditions, (group B), the concentration of 2.0 μmol/L SB203580, determined a significant increase in the inhibition rate of proliferation. Cell morphology was destroyed, the cell gap was enlarged, and cells detached and attached easily, which might be related to drug toxicity. Therefore, for further studies, the concentration of 1.0μmol/L SB203580 was selected as being suitable for the inhibition of p38MAPK signalling pathway without a toxic effect on the cells.

For HL-7702 cells cultured in hypoxic conditions (group C), the cell activity decreased and the inhibition rate of cell proliferation increased with the treatment time. However, when the concentration of SB203580 reached 0.5μmol/L, the inhibition rate of cell proliferation decreased, which demonstrated the protective effects of cells. When the concentration of SB203580 reached above 1.0μmol/L, the inhibition rate of cell proliferation increased, cell morphology became irregular, and cell spacing enlarged when compared with the control. For HL-7702 cells cultured in normal conditions (group D), the proliferation inhibition rate increased with the increase of SB203580 concentration and with

Table I. *Cell proliferation inhibition rates (%)*

Classification		0.1μmol/L	0.5μmol/L	1.0μmol/L	2.0μmol/L
A	4h	8.37±2.23	12.92±1.38*	16.25±3.56**#	22.10±1.34**#&
	8h	9.88±2.65	19.19±2.04**a	23.28±3.16**#a	30.18±1.34**##&a
	12h	12.29±1.36ab	23.78±1.94**aab	33.13±1.65**#aab	37.92±3.64**##&aab
	24h	15.47±2.39abc	26.82±1.56**aabc	36.03±2.66**#aabbc	41.29±3.08**##&aabbc
B	4h	1.03±0.25	1.12±0.14	1.15±0.21	3.01±0.37*
	8h	0.95±0.15	1.03±0.26	1.07±0.24	2.82±0.21*
	12h	0.44±0.16	0.68±0.27	0.61±0.16	2.01±0.82*
	24h	0.36±0.17a	0.32±0.13a	0.47±0.12a	1.10±0.25*a
C	4h	5.18±3.04	2.19±0.17*	8.15±1.32*#	14.43±4.23*##&
	8h	6.13±2.42	3.02±1.12*	7.12±1.14*#	21.28±6.27**##&a
	12h	9.25±1.94ab	4.1 9±1.35*a	17.32±2.08*##ab	33.92±10.38**##&&aabb
	24h	16.87±3.25aabbc	8.64±2.76*abc	22.32±4.34*##aabbc	52.23±11.39**##&&aabbcc
D	4h	3.23±1.14	4.23±1.29	15.34±3.29*##	34.27±6.23**##&&
	8h	3.54±1.03	4.43±0.89	17.45±4.28**##	43.08±7.84**##&&a
	12h	3.63±1.24	4.65±1.54	24.24±5.63**##ab	56.23±6.26**##&&aabb
	24h	4.34±1.84	6.65±1.48*abc	29.02±7.04**##aabbc	58.65±6.56*##&&aabbc

A)*The inhibition rate of SB203580 on the proliferation of HepG2 cells cultured in hypoxic conditions.* ***B)*** *The inhibition rate of SB203580 on the proliferation of HepG2 cells cultured in normal conditions.* ***C)*** *The inhibition rate of SB203580 on proliferation of HL-7702 cells cultured in hypoxic conditions.* ***D)*** *The inhibition rate of SB203580 on the proliferation of HL-7702 cells cultured in normal conditions. (*P <0.05, **P <0.01 compared with 0.1μmol/L group, #P <0.05, ##P <0.01 compared with 0.5μmol/L group, &P <0.05, &&P < 0.01 compared with 1.0μmol/L group, aP <0.05, aaP<0.01 compared with 4h group, bP <0.05, bbP <0.01 compared with 8h group, cP <0.05, ccP <0.01 compared with 12h group).*

the time of treatment, which may be related to drug toxicity. However, the reactivity of cells from group D to SB203580 was similar to that of the cells from group C and group A. It is suggested that HL-7702 cells in normal conditions are negatively affected by SB203580 (Table I). Therefore, in this study, 0.5μmol/L SB203580 was selected as the intervention concentration for subsequent HL-7702 cell test.

p38MAPK and p-p38MAPK protein expression levels

As shown in Fig.1, the expression of p38MAPK and p-p38MAPK protein expression in HepG2 cells in the hypoxic conditions group was significantly higher than that in HepG2 cells in the normal conditions group ($P < 0.05$). The expression of p38MAPK and p-p38MAPK in HepG2 cells + SB203580 in the hypoxic conditions group was significantly lower than that in HepG2 cells in hypoxic conditions group ($P < 0.05$). SB203580 had no significant effects on the expression of p38MAPK in normal cultured cells ($P > 0.05$).

Effects of p38MAPK signalling pathway inhibition on the migration of HepG2 cells after hypoxia and reoxygenation

After continuous observation for 48 h, the cells in the control group and the drug treatment group migrated to the scratch center. However, the cells in the control group migrated faster than those in the drug treatment group, as shown in Fig. 2, A and B.

Effects of p38MAPK signalling pathway inhibition on the invasion of HepG2 cells

Transwell invasion test (Fig. 2, C and D) showed that after 24 h of culture, in both groups, the HepG2 cells invaded under the Matrigel membrane. Compared with the control group, the number of penetrating cells in the drug treatment group was significantly reduced ($P < 0.01$).

Effects of p38MAPK signalling pathway inhibition on apoptosis of HepG2 cells and HL-7702 cells

The apoptotic rate of HepG2 cells from the HepG2 drug treatment group after hypoxia/reoxygenation was significantly different from that of the HepG2 control group ($P < 0.01$) (Fig. 3). In the case of HL-7702 cells, the trend was different and the inhibition of the p38MAPK signalling pathway determined a decrease in the apoptotic rate compared to the HL-7702 control group ($P < 0.01$).

DISCUSSION

The p38MAPK inhibitor, SB203580, is an imidazole-derived drug (9) that competes with ATP for its binding sites and acts by inhibiting the p38MAPK signalling pathway (10). In this study, the expression level of p38MAPK and p-p38MAPK proteins in HepG2 cells in the hypoxic conditions group was significantly higher than that in the normal condition group ($P < 0.05$). These results showed that hypoxia-reperfusion activates the p38 MAPK

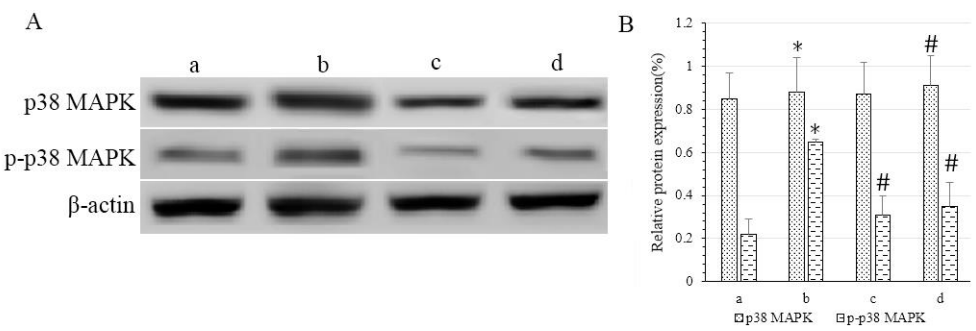


Fig. 1. *Effects of SB203580 on the expression of p38MAPK and p-p38MAPK in HepG2 cells. **A)** Immunoblotting Protein Map. **B)** Relative Gray Level Statistics Map) (a: HepG2 cells in normal conditions group; b: HepG2 cells in hypoxic conditions group; c: HepG2 cells + SB203580 in normal conditions group; d: HepG2 cells + SB203580 in hypoxic conditions group)(*P <0.05 compared with group a; #P <0.05 Compared with group b).*

signaling pathway and determines an increase in protein expression. The expression level of p38MAPK in HepG2 cells + SB203580 in the hypoxic conditions group was significantly lower than that in the HepG2 cells in hypoxic conditions group ($P < 0.05$), showing that the p38MAPK signaling pathway inhibitor, SB203580, inhibits the activation of MAPK.

The MTT results showed that SB203580 inhibited the proliferation of HepG2 cells cultured under hypoxia and protected the HL-7702 cells cultured under hypoxia. It was shown that the inhibition of proliferation of HepG2 cells by SB203580 was not related to the cytotoxicity of SB203580. It was achieved by changing cell cycle and promoting

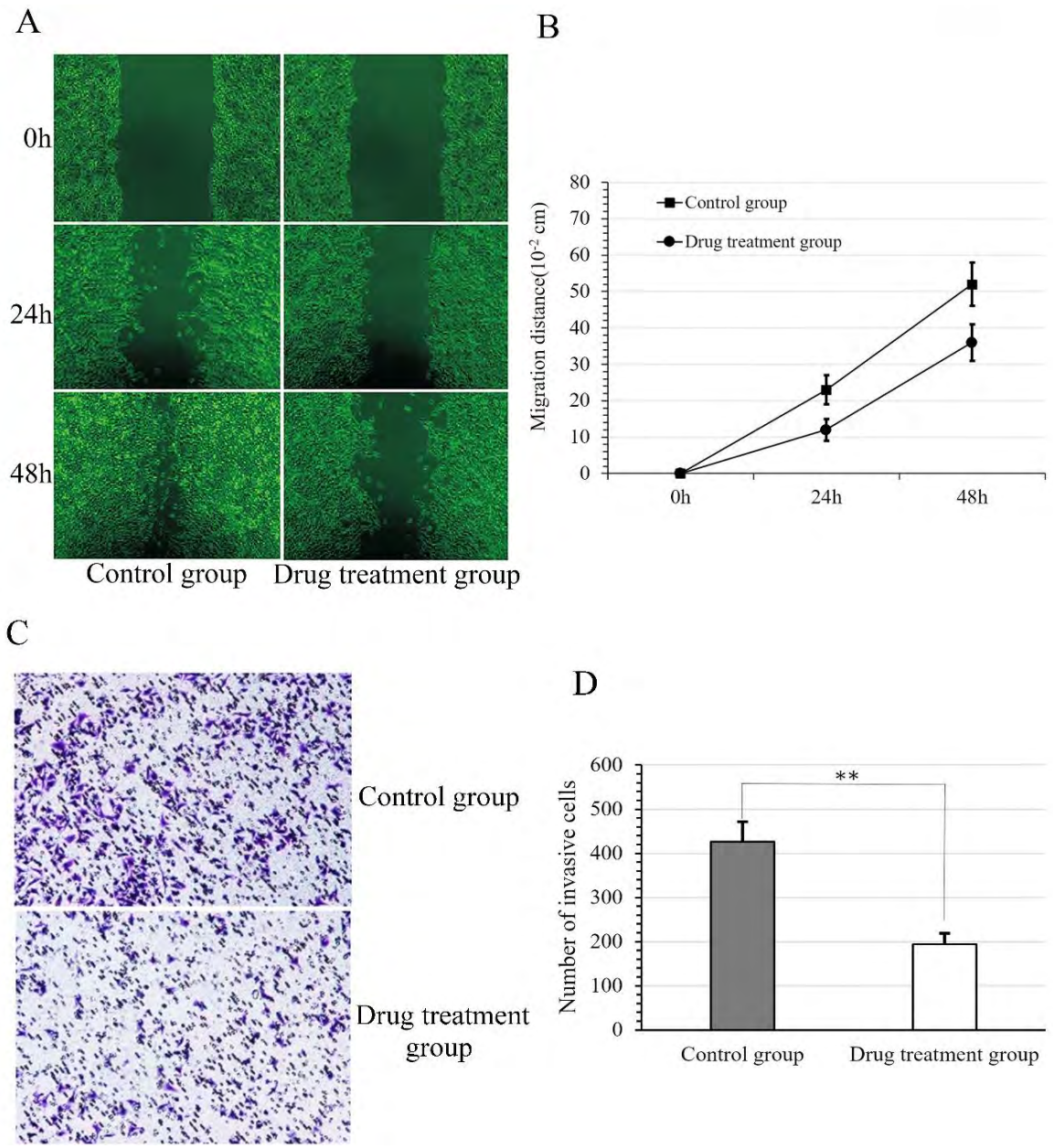


Fig. 2. *Effects of SB203580 on HepG2 cell migration.* ***A)*** *HepG2 cell migration map, ×100.* ***B)*** *migration distance map.* ***C)*** *Transwell analysis of the invasion level of HepG2 cells, ×200.* ***D)*** *Statistical analysis of the number of invaded cells. **P <0.01.*

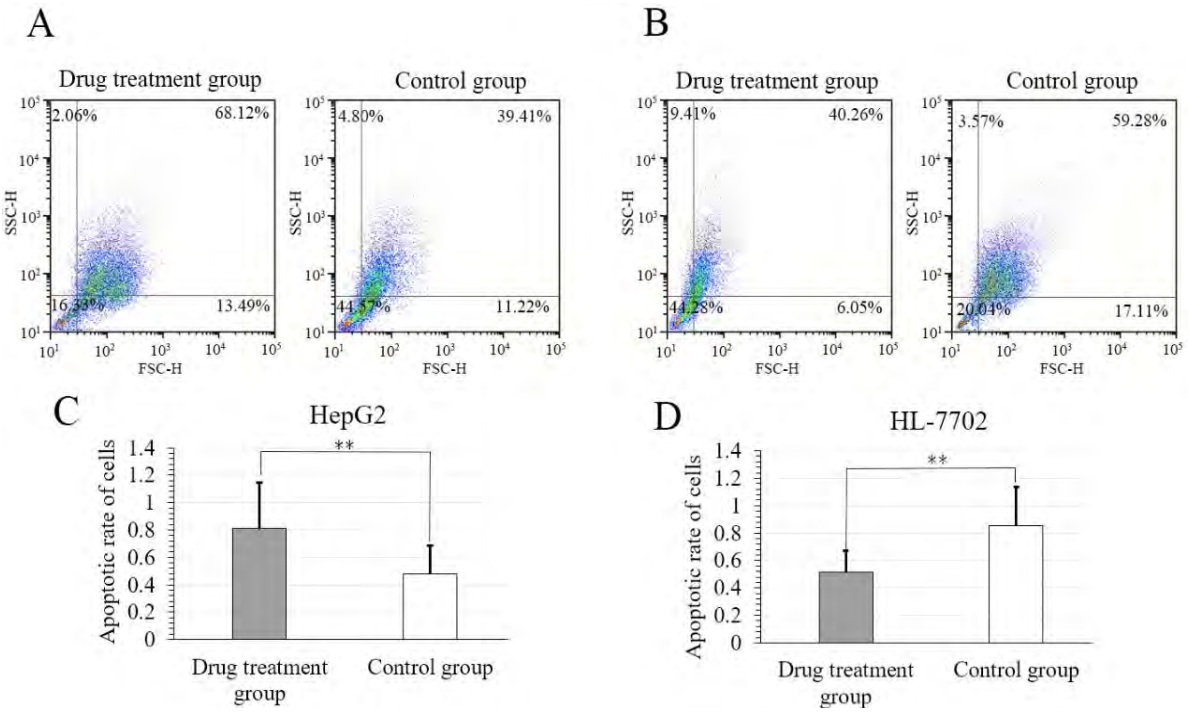


Fig. 3. *Effects of SB203580 on apoptosis of HepG2 cells and HL-7702 cells.* ***A)*** *Apoptosis of HepG2 cells by Annexin V-FITC/PI.* ***B)*** *Apoptosis of HL-7702 cells by Annexin V-FITC/PI.* C*) Apoptotic rates of HepG2* ***D)*** *Apoptotic rates of HL-7702. ** P<0.01 compared to control group.*

apoptosis, while also inhibiting apoptosis of HL-7702 cells cultured under hypoxia.

Hsieh et al. (11) studied the role of activated MAPK pathway in the metastasis and invasion of human hepatocellular carcinoma cell lines mediated by protein kinase Cα (PKCα) and showed that p38 MAPK plays an important role in the invasive formation of hepatocellular carcinoma cells mediated by PKCα. In our experiment, the migration ability and invasiveness of HepG2 cells cultured under hypoxia was significantly inhibited by SB203580. The mechanism may be related to the inhibition of tumor cell motility and migration activity by drugs after inhibiting the p38MAPK signalling pathway. Further research on this topic may be needed.

REFERENCES

1. Yang JD, Hainaut P, Gores GJ, Amadou A, Plymoth A, Roberts LR. A global view of hepatocellular carcinoma: trends, risk, prevention and management. Nat Rev Gastroenterol Hepatol 2019; 16(10):589-604.
2. Zhu XD, Sun HC. The treatment of early-stage liver cancer. Zhonghua Gan Zang Bing Za Zhi 2017; 25(5):333-35.
3. Grąt M, Krawczyk M, Wronka KM, et al. Ischemia-reperfusion injury and the risk of hepatocellular carcinoma recurrence after deceased donor liver transplantation. Sci Rep 2018 2018; 8(1):8935.
4. Ma R, Li X, Kong F, et al. Effect of ischemia reperfusion on rabbit VX2 cells in a hepatocellular carcinoma model. Int J Clin Exp Pathol 2015; 8(1):497-503.
5. Glantzounis GK, Davidson BR. Response to antioxidant therapy in liver ischemia reperfusion injury. Liver Transpl 2010; 12(5):892-93.
6. Urosevic J, Garcia-Albéniz X, Planet E, et al. Colon cancer cells colonize the lung from established

liver metastases through p38 MAPK signalling and PTHLH. Nat Cell Biol 2014; 16 (7):685-94.
7. Zhang A, Lakshmanan J, Motameni A, Harbrecht BG. MicroRNA-203 suppresses proliferation in liver cancer associated with PIK3CA, p38 MAPK, c-Jun, and GSK3 signaling. Mol Cell Biochem 2018; 441(1-2):89-98.
8. Bundzikova J, Pirnik Z, Lackovicova L, Mravec B, Kiss A. Activation of different neuronal phenotypes in the rat brain induced by liver ischemia–reperfusion injury: dual Fos/neuropeptide immunohistochemistry. Cell Mol Neurobiol 2011; 31(2):293-301.
9. Sreekanth GP, Chuncharunee A, Sirimontaporn A, et al. SB203580 modulates p38 MAPK signaling and Dengue virus-induced liver injury by reducing MAPKAPK2, HSP27, and ATF2 phosphorylation. Plos One 2016; 11(2):e0149486.
10. Düzgün ŞA, Yerlikaya A, Zeren S, Bayhan Z, Okur E, Boyacı İ. Differential effects of p38 MAP kinase inhibitors SB203580 and SB202190 on growth and migration of human MDA-MB-231 cancer cell line. Cytotechnology 2017; 69(4):711-24.
11. Hsieh YH, Wu TT, Huang CY, Hsieh YS, Hwang JM, Liu JY. p38 mitogen-activated protein kinase pathway is involved in protein kinase Calpha-regulated invasion in human hepatocellular carcinoma cells. Cancer Res 2007; 67(9):4320-27.

APPLICATION OF ENDOSCOPIC SINUS SURGERY IN HEMOSTASIS FOR EPISTAXIS

S-Z. WANG*, L-R. GUO*, X. DUAN, Y. YAO, D. WANG, X-J. ZHANG and Y-S. TIAN

Department of Otolaryngology Head and Neck Surgery, Aerospace Center Hospital, Beijing, China

Received August 6, 2019 – Accepted April 7, 2020

*These authors contributed equally to this study

To the Editor,

Epistaxis is a common clinical disease and is also an emergency in the ENT Department. The main causes of epistaxis are: i) local cause - abnormal anatomy of the nasal cavity or vascular variations, local trauma, inflammation of the nasal cavity and sinuses; ii) general cause - the most common reason is the long-term oral intake of anticoagulant drugs, such as warfarin and aspirin, due to cardiovascular diseases, followed by coagulation dysfunction caused by systematic diseases, including abnormal liver and renal function, malignant tumors or hemopathy (1) During the entire life of a human being, there is a 60% chance of having epistaxis, and approximately 80-90% of cases involves spontaneous nosebleed without a definite cause. In most cases, the bleeding can be stopped by the patients themselves without going to hospital (2). Approximately 6% of epistaxis are severe, and these patients must immediately go to hospital and seek help from specialist physicians. Adjusting anticoagulants, packing the nasal cavity of the anterior or posterior naris, burning with silver nitrate, and other conventional treatment measures can help to stop the bleeding (1, 3). However, among patients with severe epistaxis, 1% may have a poor outcome of conventional treatment (4), especially the elderly and those who are weak. Hence, they often need to be hospitalized, and receive further specialized examination and treatment (5). For patients with severe nosebleed, it is very important to determine the bleeding sites and stop the bleeding in a timely manner. Endoscopic sinus surgery (ESS) has the advantages of broad field of vision and clear imaging, which provides a good vision for detecting the bleeding site and helps in performing hemostasis more easily and accurately. Furthermore, it causes less injury to the nasal mucosa of patients. In the present study, the application of ESS in hemostasis for nosebleed was analyzed.

MATERIALS AND METHODS

A total of 132 nosebleed patients with a poor outcome of conservative treatment were admitted to the Department of Otolaryngology Head and Neck Surgery, of the Aerospace Center Hospital, Beijing, China between January 2016 and December 2018. Anterior rhinoscopy was performed on all patients at initial presentation. Sixty-three patients had bleeding sites at the Kiesselbach's plexus but conservative treatment did not sufficiently stop the bleeding. Patients (n=69) who did not have clear bleeding sites underwent endoscopic examination. Endoscopic sinus surgery (ESS) was then performed on all patients. Of the 132 patients, 71 were male and 61 were female, and ages ranged from 9-87 years (average 61±17 years). Among these cases, 61 cases were on the left side, 67 cases were on the right side, and

Key words: nasal endoscope; epistaxis; temperature-controlled radiofrequency

Corresponding Author:
Dr Shu-Zhen Wang,
Department of Otolaryngology Head and Neck Surgery,
Aerospace Center Hospital, 15 Yuquan Road, Haidian District,
Beijing 100049, China
Tel.: +86 1059972240
e-mail: wangsz2530147@163.com

0393-974X (2020)
Copyright © by BIOLIFE, s.a.s.
This publication and/or article is for individual use only and may not be further reproduced without written permission from the copyright holder.
Unauthorized reproduction may result in financial and other penalties
DISCLOSURE: ALL AUTHORS REPORT NO CONFLICTS OF INTEREST RELEVANT TO THIS ARTICLE.

4 cases were on both sides. Furthermore, 60 cases were complicated with hypertension, 21 had diabetes, 23 had nasal septum deviation, 13 received anticoagulant drugs after stenting to treat the coronary heart disease, and 4 had a medical history of nasal neoplasm. All patients gave informed written consent to participate in the study.

Surgical approach

After local anesthesia, patients were positioned in a sitting or lying posture. The coagulated blood in the nasal cavity was cleared, and the nasal mucosa was fully narcotized with a cotton pad containing 1% tetracaine adrenaline (10 mL of 1% tetracaine and 1 mL of 0.1% epinephrine). A nasal endoscope in 0 degree (also in 30 degrees, when necessary) was used to check the nasal septum, inferior nasal concha, olfactory cleft of the middle nasal meatus, posterior end of the middle turbinate, posterior end of inferior nasal concha, postnaris, superior nasal turbinate and nasopharynx, from top to bottom, and from medial wall to lateral wall. After the bleeding sites were located, temperature-controlled radiofrequency electrotome (7 W) was adopted to stop the bleeding. All patients were observed for 2-3 days after surgery, and given aseptic and symptomatic and supportive treatment. Among these patients, two who requested general anesthesia received venous inhalation combined anesthesia (VICA), and took a lying position after oral intubation. The surgical operations were the same as the surface anesthesia of the local mucosa.

RESULTS

Among the 132 patients, 63 had bleeding sites in the Kiesselbach's plexus of the anterosuperior and anteroinferior of the nasal septum, which was identified by anterior rhinoscopy. In the remaining 69 patients, the bleeding sites of 55 cases (55/69, 79.7%) were identified under a nasal endoscope: 13 cases were in the middle and posterior of the middle turbinate, 11 cases were in the echinating or ridge processus, 9 cases were in the middle turbinate and unciform process, 17 cases were in the inferior nasal concha and posterior fornix, 5 cases were in the olfactory cleft area. Fourteen cases were not found with definite bleeding sites (or simply manifested as mucosal erosion and bleeding), and were treated with nasal packing under a nasal endoscope (14/69, 20.3%). All patients were followed-up for over one month after treatment. Among these patients, three suffered from rebleeding one week after surgery, while nosebleed did not occur for the remaining 129 patients at the same site.

DISCUSSION

Intractable epistaxis, also called concealed epistaxis, is refractory due to the difficulty in identifying the bleeding sites. Packing of the anterior naris is the most common approach to treat epistaxis. However, this often causes nasal obstruction, dizziness, headache, mucosa injury, and secretory otitis media (6). The key point in diagnosing and treating epistaxis is to quickly and accurately determine the bleeding site, and rapidly stop the bleeding. The bleeding sites of intractable epistaxis often locate in the posterior of the nasal cavity, which cannot be accurately located through a simple anterior rhinoscopic examination (7). With the progress of ESS, all-round detection can be performed on the nasal cavity and sinuses. Also, endoscope makes the anatomy of the nasal cavity and sinuses clearer, and the concealed bleeding can be operated in direct vision. Hence, hemostasis under a nasal endoscope has been considered as the best treatment option for epistaxis (8-11).

In the present study, the intractable bleeding sites were detected without performing fracture displacement in the middle and inferior nasal concha, and electrocautery was performed in direct vision. Nosebleed occurred in three patients at one week after surgery. The last nasal packing was found to cause mucosal erosion and bleeding in the nasal cavity without a definite bleeding site identified. Therefore, it suggests that patients with epistaxis should avoid blind nasal packing, which may cause mucosal injury. The nasal cavity should be detected in direct vision under a nasal endoscope.

In conclusion, using a nasal endoscope to locate the bleeding sites and stop the bleeding with a temperature-controlled radiofrequency electrotome is time-efficient and has a definite curative effect. Patients recovered sooner after surgery with a low

recurrence rate and less pain. Therefore, this is an effective treatment method for epistaxis in clinical practice, especially for intractable epistaxis.

REFERENCES

1. Viehweg TL, Roberson JB, Hudson JW. Epistaxis: diagnosis and treatment. J Oral Maxillofac Surg 2006; 64:511-18.
2. Ha JF, Hodge JC, Lewis R. Comparison of nasendoscopic-assisted cautery versus packing for the treatment of epistaxis. ANZ J Surg 2011; 81:336-39.
3. Dedhia RC, Desai SS, Smith KJ, Lee S, Schaitkin BM, Snyderman CH, Wang EW. Cost-effectiveness of endoscopic sphenopalatine artery ligation versus nasal packing as first-linetreatment for posterior epistaxis. Int Forum Allergy Rhinol 2013; 3:563-66.
4. Saraceni Neto P, Nunes LM, Gregório LC, Santos Rde P, Kosugi EM. Surgical treatment of severe epistaxis: an 11-year experience. Braz J Otorhinolaryngol 2013; 79:59-64.
5. Page C, Biet A, Liabeuf S, Strunski V, Fournier A. Serious spontaneous epistaxis and hypertension in hospitalized patients. Eur Arch Otorhinolaryngol 2011; 268:1749-53.
6. Paul J, Kanotra SP, Kanotra S. Endoscopic management of posterior epistaxis. Indian J Otolaryngol Head Neck Surg. 2011;63:141-44.
7. Zhan J, Fu Z, Wei X. Clinical analysis on the treatment of 132 cases of intractable epistaxis under nasal endoscope. Lin Chung Er Bi Yan Hou Tou Jing Wai Ke Za Zhi 2014; 28:1611-12.
8. Gupta AS, Majumder L, Pal SS. A study of role of nasal endoscopy in the diagnosis and management of epistaxis. JEMDS 2017; 6:1253-55.
9. Lam K, Amber Luong A, Yao WC. Endoscopic management of anterior and posterior epistaxis. Oper Tech Otolayngol Head Neck Surg 2017; 28:199-203.
10. Kumar MVV, Prasad KUR, Gowda PRB. Rigid nasal endoscopy in the diagnosis and treatment of epistaxis. J Clin Diagn Res 2013; 7:831-33.
11. Zou Y, Deng YQ, Xiao CW, et al. Comparison of outcomes between endoscopic surgery and conventional nasal packing for epistaxis in the posterior fornix of the inferior nasal meatus. Pak J Med Sci 2015; 31:1361-65.

LETTER TO THE EDITOR

MICRONEEDLING IMPROVES MINOXIDIL RESPONSE IN ANDROGENETIC ALOPECIA PATIENTS BY UPREGULATING FOLLICULAR SULFOTRANSFERASE ENZYMES

A. SHARMA[1], R. SURVE[1], R. DHURAT[1], R. SINCLAIR[2], Y. TAN[3], Y. ZOU[3], P. MÜLLER RAMOS[4], C. WAMBIER[5], I. VERNER[6], M. KOVACEVIC[7] and A. GOREN[8]

[1]Department of Dermatology, LTM Medical College & Hospital Sion, Mumbai, India; [2]Department of Medicine, University of Melbourne, Parkville. VIC, Australia; [3]Skin & Cosmetic Research Department, Shanghai Skin Disease Hospital, Shanghai, China; [4]Departamento de Dermatologia e Radioterapia, UNESP, Botucatu, SP, Brazil; [5]Department of Dermatology, Brown University, Rhode Island, USA; [6]Verner Clinic for Dermatology and Aesthetics, Tel Aviv, Israel; [7]Department of Dermatovenereology, Sestre Milosrdnice University Hospital Centre, Zagreb, Croatia; [8]Department of Dermatology, Hairmore Hospital Beijing, Beijing, China

Received September 12, 2019 – Accepted February 4, 2020

To the Editor,

Microneedling is a minimally invasive procedure of puncturing the skin with small needles. The technique was developed from the attempts of Orentreich and Orentreich in 1995 to treat scars (1). It was further refined by Fernandes in 2006 with the invention of the dermaroller used for collagen induction (1). Since its introduction, microneedling has been used to treat a wide range of dermatological conditions from skin laxity, striae, acne scarring to vitiligo. The proposed mechanism of action in collagen induction is the initiation of the wound repair mechanism following puncturing of the skin. Schmitt et al. (2) characterized the cascade of molecular signaling following microneedling in a human skin model. In their study, five days post-micro needling, tissue remodeling, wound healing, epithelial proliferation and differentiation genes were up-regulated compared to controls. Moreover, microneedling induces the release of growth factors such as vascular endothelial growth factor, fibroblast growth factor, transforming growth factor alpha and beta, platelet-derived growth factor, Wnt3a, β-catenin and Wnt10b (3, 4). Several weeks post-microneedling, additional Type I collagen is deposited in the dermis leading to skin tightening (4).

Previously, our group demonstrated that microneedling in combination with topical minoxidil in the treatment of androgenetic alopecia (AGA) was superior to minoxidil monotherapy. While it is a common belief that the increased efficacy is due to enhanced penetration of topical minoxidil, the rapid absorption of minoxidil into the blood stream is unlikely to account for the sustained benefit seen in patients who combine microneedling and topical minoxidil.

In the study conducted by Dhurat et al. (5), where subjects who underwent microneedling combined with topical minoxidil had superior regrowth compared to minoxidil monotherapy; topical minoxidil was only applied 24 hours after the microneedling procedure.

Minoxidil is a pro-drug converted to its active

Key words: microneedling, minoxidil, alopecia

Corresponding Author:
Dr Maja Kovacevic,
Department of Dermatovenerology,
Sestre Milosrdnice University Hospital Centre,
Zagreb, Croatia
Tel.: +385 98 171 5059
e-mail: kovacevic.maja01@gmail.com

0393-974X (2020)
Copyright © by BIOLIFE, s.a.s.
This publication and/or article is for individual use only and may not be further reproduced without written permission from the copyright holder.
Unauthorized reproduction may result in financial and other penalties
DISCLOSURE: ALL AUTHORS REPORT NO CONFLICTS OF INTEREST RELEVANT TO THIS ARTICLE.

metabolite, minoxidil sulfate, by the sulfotransferase enzymes (SULT1A1) in the outer root sheath of hair follicles (6). Goren et al. (7) demonstrated that a colorimetric assay using plucked human hairs predicts clinical efficacy to minoxidil therapy in androgenetic alopecia; therefore, we hypothesized that the wound repair mechanism induced by microneedling is likely to up-regulate the sulfotransferase enzyme in hair follicles. In fact, Johnson et al. (8) demonstrated that increased sulfotransferase is a marker for keratinocyte differentiation. In the current study, we investigated the effect of microneedling on the follicular sulfotransferase enzyme.

MATERIALS AND METHODS

Six male subjects were recruited from a dermatology department of LTM Hospital Sion, Mumbai. The average age of the subjects was 28 years. All subjects were diagnosed with androgenetic alopecia and had not undergone minoxidil or microneedling treatment during the twelve months prior to the study. A target area (thinning region) on the top of the scalp was used for microneedling which was performed with a roller (ZGTS 192 needles) once a week at the hospital for a total of 3 sessions. The depth of the needle was 1.5 mm. The microneedling drum device was rolled over the affected areas of the scalp in longitudinal, vertical, and diagonal directions until mild erythema was noted, which was considered as the end point of the procedure. All patients were instructed not to apply minoxidil or change their medical regimes for the duration of the study. No other treatments were applied to the scalp. At baseline, 10 hairs were plucked from the target area and analyzed by the Minoxidil Response Test (Applied Biology, Inc. Irvine, CA, USA) which averages the sulfotransferase activity of the 10 collected hair samples. At the end of the study (day 21), 10 additional hairs were plucked from the target area and analyzed by the Minoxidil Response Test.

Table I. *Sulfotransferase enzyme activity following microneedling treatment.*

Subject Nr.	Day 0 (OD)	Day 21 (OD)	% Change
001	0.021	0.128	525.610%
002	0.298	0.261	-12.269%
003	0.368	0.386	4.752%
004	0.205	0.349	70.244%
005	0.379	0.229	-39.670%
006	0.259	0.596	130.242%

RESULTS

All six subjects completed the study. At baseline the average sulfotransferase enzyme activity for the group was 0.2550±0.1321 (OD units). Following three weekly sessions (21 days) of microneedling, the average sulfotransferase enzyme activity for the group increased to 0.3248±0.1612 (OD units). The median increase in sulfotransferase enzyme activity was 37.5% (range: 525.61% to -39.67%), 66% (4/6) subjects had an increase in sulfotransferase enzyme activity compared to baseline, and 16% (1/6) of the subjects predicted at baseline to be non-responders to topical minoxidil became responders following 21 days of microneedling. The raw data is presented in Table I.

DISCUSSION

The use of microneedling in combination with topical minoxidil in the treatment of AGA demonstrated superior regrowth compared to minoxidil monotherapy. In this pilot study, following 3 weekly sessions of microneedling, 66% of subjects presented an increased follicular sulfotransferase enzymatic activity. Despite the small sample size, the large increase in sulfotransferase enzymatic activity post-microneedling strongly suggests the enhanced efficacy associated with microneedling is due to upregulation of sulfotransferase. To our knowledge, this is the first study to elucidate the synergistic mechanism of action of microneedling in combination with topical minoxidil in the treatment of AGA. Future studies with a larger number of volunteers, and comparing levels of microneedling injury, and a group without microneedling would be necessary to verify the data presented in this pilot study.

REFERENCES

1. Singh A, Yadav S. Microneedling: Advances and widening horizons. Indian Dermatol Online J 2016; 7:244-54.
2. Schmitt L, Marquardt Y, Amann P, et al. Comprehensive molecular characterization of microneedling therapy in a human three-dimensional skin model. PLoS One 2018; 13:e0204318.
3. Kim YS, Jeong KH, Kim JE, Woo YJ, Kim BJ, Kang H. Repeated microneedle stimulation induces enhanced hair growth in a murine model. Ann Dermatol 2016; 28:586-92.
4. Aust MC, Reimers K, Gohritz A, Jahn S, et al. Percutaneous collagen induction. Scarless skin rejuvenation: fact or fiction? Clin Exp Dermatol 2010; 35:437-39.
5. Dhurat R, Sukesh MS, Ganesh A, et al. A randomized evaluator blinded study of effect of microneedling in androgenetic alopecia: a pilot study. Int J Trichology 2013; 5:6-11.
6. Buhl AE, Waldon DJ, Baker CA, Johnson GA. Minoxidil sulfate is the active metabolite that stimulates hair follicles. J Invest Dermatol 1990; 95(5):553-37.
7. Goren A, Castano JA, McCoy J, Bermudez F, Lotti T. Novel enzymatic assay predicts minoxidil response in the treatment of androgenetic alopecia. Dermatol Ther 2014; 27(3):171-73.
8. Johnson GA, Baker CA, Knight KA. Minoxidil sulfotransferase, a marker of human keratinocyte differentiation. J Invest Dermatol 1992; 98(5):730-33.

LETTER TO THE EDITOR

SIGNIFICANCE OF TISSUE TRANSGLUTAMINASE IN MYOCARDIAL FIBROSIS AFTER MYOCARDIAL INFARCTION IN RATS

YH. GAO, GN. LI, J. JIA, WC. WANG, Y. DUAN, H. WEI, T. LI, MY. LI, X. ZHONG and XQ. LI

Department of Cardiology, Fourth Affiliated Hospital of Harbin Medical University, Harbin, China

Received January 13, 2020 - Accepted April 9, 2020

To the Editor,

Myocardial fibrosis is a frequent pathological alteration of myocardial tissue caused by myocardial infarction (MI), hypertension, ischemic cardiomyopathy, and other cardiovascular diseases. It is a critical process of ventricular remodeling (1, 2). Extracellular matrix accumulation is the main manifestation of myocardial fibrosis (3). Tissue transglutaminase (tTG) modifies the extracellular matrix to resist protease degradation, leading to tissue fibrosis. This has attracted extensive attention in recent years. The tTG is one of the most important proteins involved in modifying the extracellular matrix (4). Fibrillin-1 is highly expressed in fibrotic tissue. It participates in the process of fibrosis and the *in vitro* culture of fibroblasts can deposit the fibrillin-1 in the extracellular matrix (5). Myocardial fibroblast proliferation, transformation, and extracellular matrix deposition in myocardial interstitium are the main pathological events in myocardial fibrosis. However, tTG is considered to be an essential factor involved in the fibrosis of tissues and organs. It can be cross-linked with extracellular matrix protein and promote the development of tissue fibrosis. It is reported that the high expression of tTG in myocardial fibrosis rats is closely related to the process of myocardial fibrosis. However, the expression of tTG in myocardial fibrosis after myocardial infarction is rarely reported. Also, the expression of tTG in myocardial fibers and. the role of transformation is unclear. This study aimed to investigate the expression and significance of tTG in myocardial fibers after myocardial infarction. This will provide a potential target for myocardial fibrosis therapy.

MATERIALS AND METHODS

Animals

Forty-five healthy male Sprague Dawley (SD) rats aged eight weeks, with weight 200~250g, were used in this study. All rats were obtained from Shanghai Southern model Biology Research Center Co., Ltd. (Shanghai, China). They were randomly assigned into three groups: sham-operated group (n=15), model group (n=15), enalapril group (n=15). The rats in the enalapril group were orally administrated with l0mg/kg/d enalapril on the day before surgery, while the rats in the sham-operated group and model group received normal water. The protocol was approved by the ethics committee of the Fourth Affiliated Hospital of Harbin Medical University, and the experiments were performed following the regulations of the State Science and Technology Commission on the management of laboratory animals.

Preparation of the myocardial infarction model

The rats in the myocardial infarction model group

Key words: tissue transglutaminase; Fibrillin-1; myocardial fibrosis; myocardial infarction

Corresponding Author:
Dr Xueqi Li,
Department of Cardiology,
Fourth Affiliated Hospital of Harbin Medical University,
37 Yiyuan Street, Nangang District,
Harbin, 150001, China
e-mail: lixueqiqi1011@163.com

0393-974X (2020)
Copyright © by BIOLIFE, s.a.s.
This publication and/or article is for individual use only and may not be further reproduced without written permission from the copyright holder.
Unauthorized reproduction may result in financial and other penalties
DISCLOSURE: ALL AUTHORS REPORT NO CONFLICTS OF INTEREST RELEVANT TO THIS ARTICLE.

were anesthetized with 3% pentobarbital sodium, followed with skin preparation, tracheal intubation, and small animal ventilator assisted breathing. After opening the chest and exposing the heart at the most obvious point of apical fluctuation, the anterior descending coronary artery was ligated with a 4-0 suture needle. The success of the model was judged by evaluating the ST segment of electrocardiography (ECG) and whitening of the myocardium below the ligation site. The chest and neck wounds were sutured after evaluation. Penicillin at 100,000 U was injected intramuscularly after the operation to avoid infection. The rats in the sham-operated group only underwent suture without ligation of the coronary arteries. and the rest of the operation was the same as for the myocardial infarction group. Enalapril maleate tablets (Yuelingding Mershadong Pharmaceutical Factory, USA) were crushed, diluted to 1 mg/ml with normal saline, mixed and then gavaged at l0 mg/kg/d. The tablets were dispensed daily.

Echocardiographic detection of cardiac function

The cardiac size and function were detected with echocardiography four weeks post-surgery. The left ventricular end-diastolic diameter (LVEDD), left ventricular end-systolic diameter (LVESD), short axis shortening rate (FS%) and left ventricular ejection fraction (EF%) were measured, respectively.

Histopathology of myocardium

Rats were euthanasized after ultrasonography. The hearts were washed with 10% potassium chloride (KCl) solution and fixed with 4% polyformaldehyde. The degree of myocardial fibrosis was stained with sirius red. In brief, the paraffin section was immersed in xylene solution for 5 min. The slices were dehydrated with 100%, 90% and 70% ethanol. After that, the slices were washed with tap water continuously for 10 min and and then rinsed with distilled water for 10 min. The paraffin section was incubated in the 0.2% phospho molybdate for 1~5 min. The slices were placed in a moist coloring box, then dripped into 0.1% scarlet picric acid and soaked for 90 min. After fully removing Sirius red picric acid solution, the slices were then immersed in pure water for several times. Lastly, the slices were placed in 70% and 95% ethanol for 30 s each, 100% ethanol for 30 s for 3 times, and xylene for 2 min with 3 times repeat. The slides were sealed with sealing fluid. The samples were observed and photographed with an optical microscope. The percentage of collagen volume was quantified with Image J software.

Real time quantitative PCR (RT-PCR) assay

According to the manual of TaqMan® RNA Reverse Transcription kit from ABI company, the extracted total mRNA was reverse transcripted in vitro and the cDNA product was obtained. RNA extraction and PCR reaction kit were from Tiangen Biochemical Technology Co., Ltd., China. The RNA extraction kit was purchased from Somerfly Biology Company, USA. The reaction was performed in the program: incubation at 16°C for 30 min, incubation at 42°C for 30 min, then heat in 85°C for 5 min, and kept at 4°C. With the obtained cDNA as the template, quantitative Real time PCR was used to quantify the level of mRNAs. TaqMan® Universal PCR Master Mix 20 μl was added and run on the Roche LightCycler480 instrument (Roche Biology, USA). The TaqMan® RNA Reverse Transcription kit was from ABI Biological Company, USA. U6 was set as the internal reference for detection. ΔCT represents the relative expression of tTG. $\Delta CT=CT_{\beta\text{-Actin}}-CT_{tTG}$. The reaction were performed as follows: pre-denaturation with 95°C for 10 min; Repeated cycles for 40 times with 95°C 15 s, 60°C 30 s, and 70°C 30 s. The PCR amplification primers were synthesized from Shanghai Shenggong Biotechnology Co., Ltd., China. The tTG Upstream primers is CAATGGATCCTAGTGAC(5'-3'), Downstream primers is GCAATAGCATTAGCTCG(5'-3'). The fibrillin-1 Upstream primers is TACCTATGATGCGTATGC (5'-3'), Downstream primers is CTGGTGTCGTGGAGTCG (5'-3'). The β-actin Upstream primers is GCGTTCGCTATCTGTATC(5'-3'), Downstream primers is GATCTGTGACTCAGCGT(5'-3').

Western blot detection assay

The Western blot assay was carried out according to the routine experimental steps. After imaging, the intensity of each band was quantified by a density scanner. The relative expression of tTG was expressed by the difference of the gray value, with beta-actin as an internal reference. The relative expression of Fibrillin-1 was detected in the same way. The antibodies of tTG and fibrillin-1 were purchased from Abcam Company, USA.

Statistical analysis

The statistical analyses were performed with

SPSS21.0. The data were calculated with *t*-test. P<0.05 indicates that the difference was statistically significant.

RESULTS

ECG detection

In the electrocardiogram test, after the ligation of the anterior descending coronary artery, the ST segment of ECG in the rats of the model group significantly increased in the inferior lead II (Fig.1).

Enalapril treatment improved the cardiac function of rats

In comparison to the sham-operated group, the LVESD and LVEDD of rat hearts were significantly enlarged in the model group (P < 0.01). In comparison to the sham-operated group, the EF and FS significantly decreased and cardiac function was severely damaged in the rats in the model group (P < 0.01). Compared with the model group, the enlargement of LVESD and LVEDD in the enalapril treated rats were significantly improved, and the EF and FS was significantly decreased. These indicate that the cardiac function of enalapril-treated rats was significantly recovered (P < 0.01). Compared with the sham-operated group, there were significant differences in heart LVESD, LVEDD, EF, and FS between the enalapril group and the sham-operated group (all P < 0.01). These results showed that the drug treatment could effectively reduce myocardial fibrosis in rats (Table I).

Histopathological findings

Sirius red staining revealed obvious degrees of myocardial fibrosis in the model group. The volume fraction of myocardial collagen in the model group (11.7+0.32%) was significantly higher than that in the sham-operated group (2.4+0.25%) (P < 0.01). The degree of myocardial fibrosis and the volume fraction of myocardial collagen in the enalapril group were lower than those in the model group (all P < 0.01), but higher than those in the sham-operated group (all P < 0.01) (Fig. 2).

Table I. *Comparison of cardiac function indexes in each group of rats*

Group	n	EF(%)	FS(%)	LVESD (mm)	LVEDD(mm)
Sham-operated group	15	80.75±5.76	42.23±4.13	1.79±0.28	3.25±0.32
Model group	15	28.64±3.14[a]	21.51±2.32[a]	4.88±0.36[a]	6.36±0.42[a]
Enalapril group	15	57.32±4.15[ab]	38.79±3.43[ab]	2.45±0.31[ab]	4.15±0.37[ab]

[a]*P<0.01 vs sham-operated group* ; [b]*P<0.01 vs model group.*

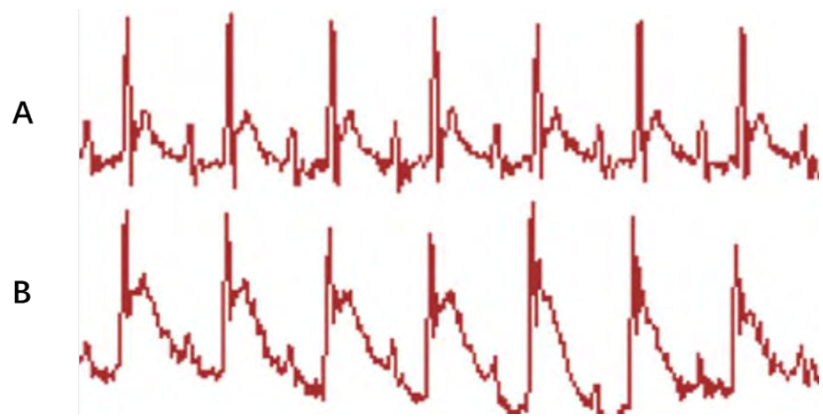


Fig. 1. *Establishment of model. The rats were detected with ECG before (**A**) and after (**B**) the ligation of the anterior descending branch of the coronary artery in rats.*

Expression of tTG and Fibrillin-1 in rat cardiac muscle fiber tissue at RNA level

The expression of tTG and Fibrillin-1 in myocardial fibrosis tissue was detected by RT PCR. Compared with the sham-operated group, the expression of tTG in myocardial fibrosis tissue of the model group was significantly increased. After enalapril treatment, the expression of tTG was still higher than that of the sham-operated group, but the effect was not significant ($P < 0.01$). The rats expressed higher level of fibrillin-1 in the myocardial fibrous tissue in the model group than that in the sham-operated group. The enalapril group showed decreased level of fibrillin-1 in comparison to the model group. The expression of Fibrillin-1 in the enalapril group was also higher than that in the sham-operated group ($P < 0.01$) (Table II).

Expression of tTG and Fibrillin-1 in rat cardiac muscle fiber tissue at protein level

Western blot assay was used to detect the expression of tTG and Fibrillin-1 in myocardial fibrosis tissues. The expression of tTG protein in myocardial fibrosis tissues of the model group were significantly higher in comparison to the sham-operated group ($P < 0.05$). The enalapril treatment decreased tTG of the modeled rats. The expression of Fibrillin-1 protein in the myocardial fibrous tissue of the model group and enalapril group was significantly higher than that of the sham-operated group, while the expression of Fibrillin-1 protein in the model group was higher than that in enalapril group ($P < 0.05$). The results were consistent with those of quantitative RT PCR (Fig. 3).

DISCUSSION

Studies have shown that the synthesis of fibroblast protein and collagen protein in rat myocardium is related to the expression of angiotensin II and angiotensin II receptor type 1. This study used the angiotensin inhibitor enalapril to restore the cardiac function in the rat myocardial infarction model. Rats with myocardial infarction

Table II. *Expression of tTG and Fibrillin-1 in myocardial tissue of rats in the mRNA level*

Group	n	tTG Relative expression (ΔCT)	Fibrillin-1 Relative expression (ΔCT)
Sham-operated group	15	1.12±0.31	1.05±0.27
Model group	15	3.73±0.52 a	3.46±0.67 a
Enalapril group	15	1.57±0.42ab	1.25±0.29ab

[a]P<0.01 vs sham-operated group; [b]P<0.01 vs model group.

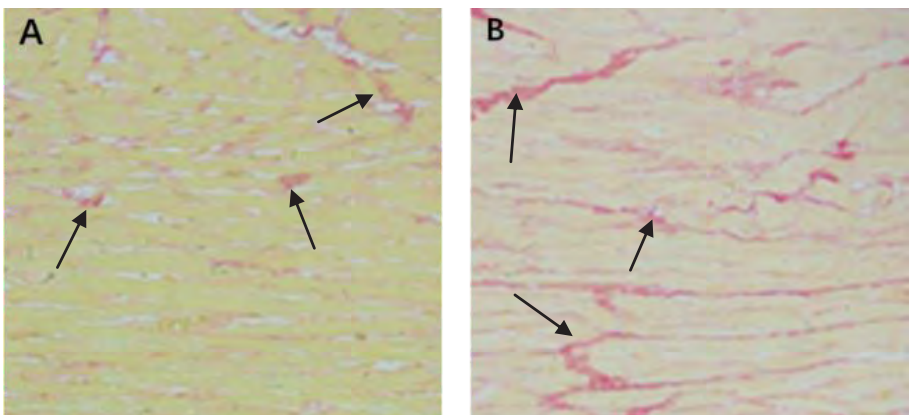


Fig. 2. *Staining results of rats in each group. **A**) Sham-operated group staining; **B**) myocardial infarction group staining (×200).*

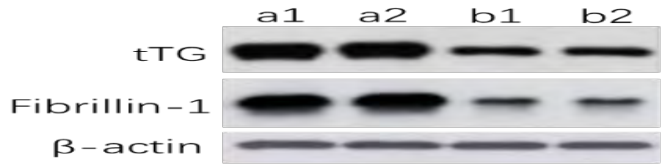


Fig. 3. *Expression of tTG and Fibrillin-1 protein. a1, a2: myocardial infarction model group, enalapril treatment group. b1, b2: sham-operated group.*

were used for control and treatment. Four weeks after myocardial infarction, LVESD and LVEDD increased significantly, while EF and FS decreased significantly in comparison with normal rats (sham group). The enalapril group dramatically abolished this change. Pathological results showed that the hearts of myocardial infarction rats were enlarged. The ventricular wall became thinner, white scar tissue could be seen in the infarcted area, and some ventricular aneurysm and ventricular septal bulge could be seen. A large number of collagen fibers were deposited. These results indicated that the rat model of myocardial infarction was successfully established. The expression level of tTG mRNA and protein in myocardium were determined by RT-PCR and Western blot, respectively. The results showed that the expression of tTG in the heart of model group was higher than that of the sham group. The overexpressed tTG gene suggested that tTG is involved in the process of myocardial fibrosis after myocardial infarction. At the same time, RT-PCR results showed that fibrillin-1 expression increased in myocardial tissue of rats with myocardial infarction, but decreased under drug intervention, which is with the similar trend as tTG, suggesting that tTG may participate in the process of myocardial fibrosis through the interaction of fibrillin-1.

In conclusion, tTG may be involved in the regulation of myocardial fibrosis with fibrillin-1, therefore may be a potential target for myocardial infarction therapy.

REFERENCES

1. Li L, Zhao Q, Kong W. Extracellular matrix remodeling and cardiac fibrosis. Matrix Biol 2018; 68-69:490-506.
2. Verma A, Wang H, Manavathi B, Fok JY, Mann AP, Kumar R, Mehta K. Increased expression of tissue transglutaminase in pancreatic ductal adenocarcinoma and its implications in drug resistance and metastasis. Cancer Res 2006; 66(21):10525-33.
3. Bouzeghrane F, Reinhardt DP, Reudelhuber TL, Thibault G. Enhanced expression of fibrillin-1, a constituent of the myocardial extracellular matrix in fibrosis. Am J Physiol Heart Circ Physiol 2005; 289(3):H982-91.
4. Thackeray JT, Hupe HC, Wang Y, et al. Myocardial inflammation predicts remodeling and neuroinflammation after myocardial infarction. J Am Coll Cardiol 2018; 71(3):263-75.
5. Kuncio GS, Tsyganskaya M, Zhu J, et al. TNF-α modulates expression of the, tissue transglutaminase gene in liver cells. Am J Physiol 1998; 274(2):G240-45.
6. Mouton AJ, Rivera OJ, Lindsey ML. Myocardial infarction remodeling that progresses to heart failure: a signaling misunderstanding. Am J Physiol Heart Circ Physiol 2018; 315(1):H71-H79.
7. Abe I, Teshima Y, Kondo H, et al. Association of fibrotic remodeling and cytokines/chemokines content in epicardial adipose tissue with atrial myocardial fibrosis in patients with atrial fibrillation. Heart Rhythm 2018; 15(11):1717-27.
8. López B, González A, Ravassa S, et al. Circulating biomarkers of Myocardial Fibrosis: The Need for a Reappraisal. J Am Coll Cardiol 2015; 65(22):2449-56.
9. Pellman J, Zhang J, Sheikh F. Myocyte-fibroblast communication in cardiac fibrosis and arrhythmias: Mechanisms and model systems. J Mol Cell Cardiol 2016; 94:22-31.

10. Sandmann S, Li J, Fritzenkötter C, Spormann J, Tiede K, Fischer JW, Unger T. Differential effects of olmesartan and ramipril on inflammatory response after myocardial infarction in rats. Blood Press 2006;15(2):116-28.
11. Rodríguez-Pascual F, Díez J. Myocardial fibrosis in response to pressure overload: elucidating the contribution of tissue transglutaminase. Cardiovasc Res 2017; 113(8):841-43.
12. Shinde AV, Su Y, Palanski BA, Fujikura K, Garcia MJ, Frangogiannis NG. Pharmacologic inhibition of the enzymatic effects of tissue transglutaminase reduces cardiac fibrosis and attenuates cardiomyocyte hypertrophy following pressure overload. J Mol Cell Cardiol 2018; 117:36-48.

LETTER TO THE EDITOR

MECHANISM OF GENISTEIN COMBINED WITH CHANGES IN CaSR ACTIVITY ON GASTRIC CANCER CELLS

DQ. DENG[1], ZF. LANG[2], CX. XING[3] and S. LI[2]

[1]Department of Biology, Mudanjiang Medical University, Mudanjiang, China; [2]Department of Medical Function, Mudanjiang Medical University, Mudanjiang, China; [3]Traditional Chinese Medicine Clinic, The Second Affiliated Hospital of Mudanjiang Medical University, Mudanjiang, China

Received January 13, 2020 – Accepted March 11, 2020

To the Editor,

Gastric cancer is a common malignancy of the digestive tract (1). Traditional chemoradiotherapy and emerging molecular targeted therapy or immunotherapy cannot prolong survival of patients with advanced gastric cancer (2). Meanwhile, many studies have proved that traditional Chinese medicine (TCM) is advantageous in inhibiting growth, recurrence and metastasis of tumors, in prolonging survival of patients with gastric cancer, and in regulating immunity. Genistein (GEN), an isoflavone isolated from the soybeans (3), has been found to exert an anti-tumor effect by influencing a series of cellular processes or enzymes, including cell cycle, apoptosis and angiogenesis (4). Alterations of calcium-sensing receptor (CaSR) signaling are associated with certain pathophysiological status (5). Li T et al. (6) confirmed for the first time that CaSR activation could increase the secretion of tumor necrosis factor beta (TNF-β) and interleukin-6 (IL-6) via the NF-κB pathway, thereby exerting an anti-tumor effect. However, it remains unclear whether the CaSR expression plays a role in the occurrence and development of gastric cancer. Therefore, this study explored the effect of GEN on the growth of gastric cancer cells SGC-7901 and its relevant mechanisms, as a guide for clinical treatment of patients with gastric cancer.

MATERIALS AND METHODS

Cell lines and cell culture

Gastric cancer SGC-7901 cell line was purchased from Shanghai Fuxiang Biotechnology Co., Ltd., China. Human gastric cancer SGC-7901 cell line was placed into modified RPMI 1640 medium containing 10% fetal bovine serum (containing 1% penicillin-streptomycin) and cultured in a 5% CO_2 incubator at 37°C. Cells in the log phase of growth were harvested for the subsequent experiment.

3-(4,5)-dimethylthiahiazo (-z-y1)-3,5-di-phenytetrazoliumromide (MTT) assay for determination of SGC-7901 cell proliferation

SGC-7901 cells in the log phase of growth were inoculated to a 96-well plate (100 μL per well) at a concentration of 1×10^5/mL, and then cultured in a 5% CO_2 incubator at 37°C for 24 h. After that, different concentrations of GEN (0μmol/L, 25μmol/L, 50μmol/L, 100μmol/L, 200μmol/L and 400μmol/L) were applied to

Key words: Genistein; calcium-sensing receptor; gastric cancer; anti-tumor mechanism

Corresponding Author:
Dr Shu Li,
Department of Medical Function,
Mudanjiang Medical University,
No.3 Tongxiang Road,
Mudanjiang, 157011, China
e-mail: lishu_mdjmu@163.com

0393-974X (2020)
Copyright © by BIOLIFE, s.a.s.
This publication and/or article is for individual use only and may not be further reproduced without written permission from the copyright holder.
Unauthorized reproduction may result in financial and other penalties
DISCLOSURE: ALL AUTHORS REPORT NO CONFLICTS OF INTEREST RELEVANT TO THIS ARTICLE.

the SGC-7901 cells. For the combined treatment, calindol was added later. The culture medium was removed from the plate. Negative control group (SGC-7901 cells were cultured without any drug treatment, GEN group (100μmol/L), calindol group (10μmol/L) and GEN (100μmol/L) plus calindol (10μmol/L) group (GEN+Cal group) were set up. There were 3 replicates for each of the groups above, and each experiment was repeated five times, with the marginal wells filled with phosphate buffer saline (PBS). Then the cells were further incubated at 37°C in a 5% CO_2 incubator for 24 h, 48 h and 72 h, respectively. Into each well 20 μL of 5mg/mL MTT reagent was added and the cells were further incubated for 24 h under the same conditions. After that, the culture was terminated. The supernatant was discarded. Into each well 150 μL of dimethylsulfoxide (DMSO) solution was added. After the crystals were completely dissolved by oscillation on the horizontal shaker for 10 min, the optic density (OD) value was detected in each well using a microplate reader at a wavelength of 490nm. The growth inhibition rate was calculated for the cells by taking the means of the 3 wells. Growth inhibition rate of the cells= (1-mean OD of the experimental group/mean OD of the control group) ×100%.

Hoechst staining for cell apoptosis detection

An ordinary coverslip was sterilized under high pressure and then soaked in 75% ethanol for 5 min. It was blown dry on the sterile ultra-clean bench or cleaned with PBS for 3 times. Then it was washed with Roswell Park Memorial Institute (RPMI) 1640 culture medium once. The coverslip was placed into a 6-well plate. SGC-7901 cells in the log phase of growth were inoculated to a 6-well plate (2 ml per well) at a concentration of 1×10^5/mL, and then cultured at 37° in a 5% CO_2 incubator for 24 h. The cells were then grouped and given different treatments. The culture medium was removed from the plate. Negative control group (SGC-7901 cells were cultured without any drug treatment), GEN group (100μmol/L), calindol group (10μmol/L) and GEN (100μmol/L) plus calindol (10μmol/L) group (GEN+Cal group) were set up. The cells of each treatment were cultured at 37°C in a 5% CO_2 incubator for 48 h. The culture medium was removed, and the cells were fixed with 0.5 ml of fixing solution (4% paraformaldehyde) for 10-20 min. The cells were further washed with PBS twice, 3 min each time, and the excess fluid was removed. When washing, the cells were oscillated several times either on a shaker or by hand. Next, 1 ml of Hoechst 33258 stain solution was added and the cells were stained on a shaker for 15-30 min. Excess Hoechst 33258 stain solution was removed, and the cells were washed with PBS for 2-3 times, 3-5 min each time. The cell morphology was observed under an inverted fluorescence microscope, either directly or after sealing, and photos were taken. For each well, 5 fields of view were randomly selected, the apoptotic cells were counted using the Image J software, and the apoptosis rate was calculated as follows: apoptosis rate= (number of apoptotic cells/total cell number) ×100%.

Protein expressions of CaSR, survivin and Runx3 genes in the cells determined by Western blot

SGC-7901 cells were harvested from each treatment. The cells were added with protein lysis buffer and PMSF, and lysed on ice for 30 min. After centrifugation at 4°C (12000r/min) for 15 min, the total proteins were extracted from the cells. Protein concentrations were quantified by using the bicinchoninic acid (BCA) protein assay. Then 40 ug of the protein was loaded, separated by 10% SDS-PAGE and transferred to membranes, which were sealed with sealing solution for 1 h. The cells were incubated with anti-CaSR (1:1000), anti-Survivin (1:500) and anti-Runx3 (1:500) primary antibodies at 4°C overnight. The membrane was washed and further incubated with alkaline phosphatase-labeled anti-IgG secondary antibodies (1:1000) at room temperature for 1 h. Enhanced chemiluminescence (ECL) substrate was added, followed by exposure, color development, fixation and scan.

The images exposed to the X-ray were scanned, and the grayscale analysis of the bands was performed using Gel-Pro Analyzer software. Optical densities were calculated for each target band. The grayscale values of each band were determined using the software after 5 independent experiments. The grayscale ratio of the target gene to β-actin was used to represent the relative expression of the target gene.

mRNA expressions of CaSR, survivin and Runx3 genes in the cells determined by RT-PCR

Total RNA was extracted using high-purity total RNA rapid extraction kit (Bio Teke, China), followed by reverse transcription. CT values of each sample in

PCR were analyzed by using the MX-3000P software (Stratagene, USA).

Statistical analysis

SPSS 19.0 software was used for statistical analysis, and the experimental results were expressed as mean±standard deviation. The means of the two groups were compared by independent samples *t*-test. The means of multiple groups were compared by One-Way ANOVA. First, the homogeneity of variance test was performed. If the variance was homogeneous, LSD was used for pairwise intergroup comparison; otherwise, Dunnett's T3 was used for pairwise intergroup comparison. $P<0.05$ indicated significant difference.

RESULTS

Morphological changes of SGC-7901 cells under inverted microscope following the GEN plus calindol treatment

Control group (Fig. 1A): The SGC-7901 cells showed massive or spherical growth pattern; the intercellular connections were tight, and the cells grew adherent to the bottom of the culture flask; some cells displayed overlapping growth, with enlarged nuclei and clear nucleoli, and the nuclei were darkly stained; nuclear atypia was apparent, with mitotic count.

GEN group (Fig. 1B): After GEN treatment for 48 h, the intercellular connections became loose, and some cells floated and no longer adhered to the culture flask. The nuclei shrank in size, and the degree of nuclear atypia decreased. The nuclei were less darkly stained, and the nucleolus count decreased. The cell morphology changed, and some cells were fragmented.

Calindol group (Fig. 1C): After calindol treatment for 48 h, the number of SGC-7901 cells decreased significantly compared with the control group or the result in Fig. 1B. The intercellular connections were looser, and most of the cells were no longer adherent to the walls. The nuclei shrank in size, and some nuclear fragments were observed.

GEN+Cal group: After GEN+Cal treatment for 48 h (Fig. 1D), the number of SGC-7901 cells decreased significantly, with widened intercellular space. Most cells were no longer adherent to the walls. The nuclei were more significantly pyknotic, with an increasing number of fragments, and most cells were observed without nucleoli.

Table I. *Inhibition rate of GEN plus calindol treatment on the SGC-7901 cells*

Group	24h	48h	72h
Control group	-	-	-
GEN(100μmol/L)	22.174±4.434	36.175±3.430	46.953±4.427
Calindol(10μmol/L)	36.432±6.345	49.123±3.110	66.432±3.224*
GEN(100μmol/L)+ Calindol(10μmol/L)	54.242±3.493*#	61.342±3.155*#	77.312±2.044*#

*Note: *P<0.05, compared with the GEN group; #P<0.05, compared with the calindol group.*

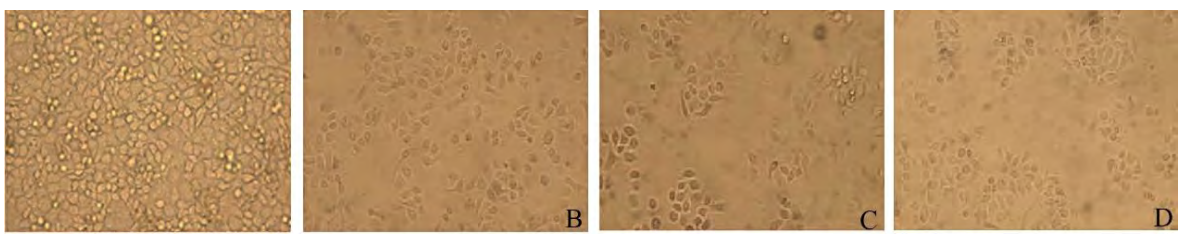


Fig. 1. *The influence of GEN plus calindol on the proliferation of SGC-7901 cells under an inverted microscope (×100) **A**) Negative control group; **B**) GEN group; **C**) Calindol group; **D**) GEN+Cal group.*

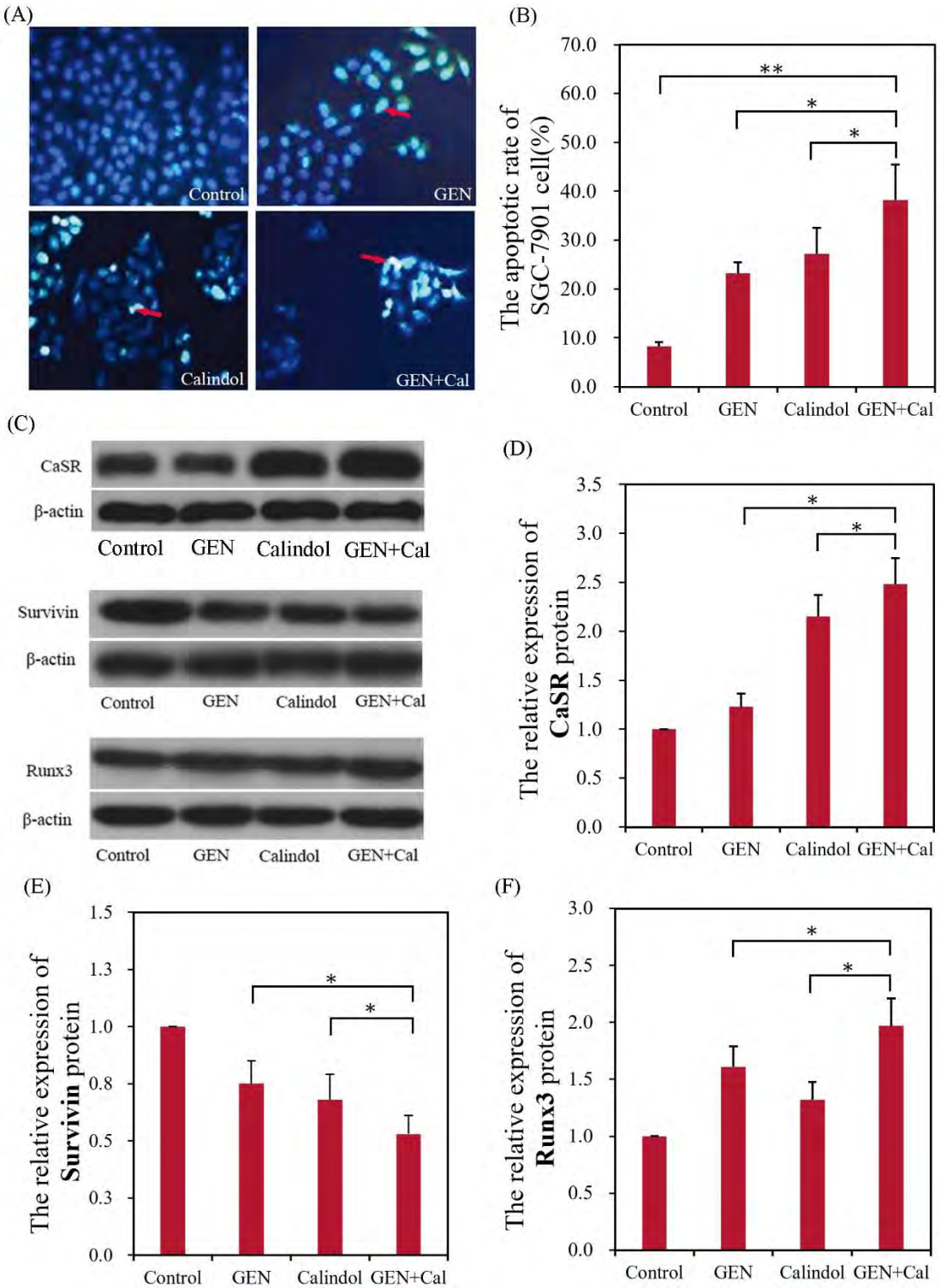


Fig. 2. ***A)*** *Apoptosis of SGC-7901 cells treated by GEN plus calindol, which was observed by an optical microscope, ×200, and the arrow pointed to apoptotic cells;* ***B)****: Statistical results of the apoptosis rate, *P<0.05;* ***C)****: Expressions of CaSR, survivin, and Runx3 proteins in SGC-7901 cells determined by Western Blot;* ***D-F)****: Relative gray-scale statistical charts of CaSR, survivin, and Runx3 proteins, *P<0.05.*

Influence of GEN plus calindol treatment on the proliferation of SGC-7901 cells

The results showed that after SGC-7901 cells were treated by different concentrations of GEN (0μmol/L, 25μmol/L, 50μmol/L, 100μmol/L, 200μmol/L, and 400μmol/L), the cell growth rate also increased in a dose- and time-dependent manner. Therefore, the GEN concentration of 100μmol/L was selected for the subsequent experiments.

As shown in Table I, after the GEN (100μmol/L) plus calindol (10μmol/L) treatment in the SGC-7901 cells, the growth inhibition rate was significantly higher compared to the use of either GEN or calindol alone. The inhibition rate increased with the prolongation of time, in a time-dependent manner.

Influence of GEN plus calindol treatment on the apoptosis of SGC-7901 cells

Observation under the optical microscope indicated that compared with the control group, there were typical apoptotic changes in the three treatment groups, including shrinkage of cells in size, chromatin condensation with dense and dark staining and whitish color. In contrast, the normal cells were of a pale blue color (Fig. 2A). Moreover, compared with the control group, all three treatment groups showed a significant increase in the apoptosis rate ($P<0.05$); the apoptosis rate of the combined treatment group was significantly higher than that of either GEN or calindol treatment alone ($P<0.05$) (Fig. 2B).

Protein expressions of CaSR, survivin and Runx3 determined by Western blot

As shown in Fig. 2 C, D, GEN promoted the upregulation of CaSR protein expressions in SGC-7901 cells; after the combined treatment for 48 h, the CaSR protein content in the cells was significantly higher than that of the use of either agent alone ($P<0.05$). GEN induced the downregulation of survivin protein expressions in SGC-7901 cells (Fig. 2(C, E); after the combined treatment for 48 h, the survivin protein content in the cells was significantly lower than that of the use of either agent alone ($P<0.05$). GEN promoted the upregulation of Runx3 protein expressions in SGC-7901 cells (Fig. 2 C, F); after the combined treatment for 48 h, the Runx3 protein content in the cells was significantly higher than that of the use of either agent alone ($P<0.05$).

mRNA expressions of CaSR, survivin and Runx3 determined by RT-PCR

GEN promoted the upregulation of CaSR protein expressions in SGC-7901 cells; after the combined treatment for 48 h, the CaSR protein content in the cells was significantly higher than that of the use of either agent alone (Table II) ($P<0.05$). GEN induced the downregulation of survivin mRNA expressions in SGC-7901 cells; after the combined treatment for 48 h, the survivin mRNA content in the cells was significantly lower than that of the use of either agent alone ($P<0.05$). GEN promoted the upregulation of Runx3 mRNA expressions in SGC-7901 cells; after the combined treatment for 48h, the Runx3 mRNA content in the cells was significantly higher than that of the use of either agent alone ($P<0.05$).

DISCUSSION

TCM has made enormous progress in cancer treatment, and in particular, many studies have

Table II. *Influence of GEN and changed CaSR activity on mRNA expressions of CaSR, survivin and Runx3 in the SGC-7901 cells.*

	Control group	GEN group	Calindol group	GEN+Cal group
CaSR mRNA	1.00	1.35	1.77	2.40
Survivin mRNA	1.00	0.75	0.60	0.46
Runx3 mRNA	1.00	1.68	1.24	1.96

been devoted to gastric cancer. Experiments (7, 8) have shown that GEN is one of the important active ingredients with anti-tumor effects from the soybeans. *In vitro*, GEN can inhibit the proliferation of cancer cells, promote their differentiation and reduce malignant transformation and migration of cancer cells, thereby inhibiting tumor metastases (9). Our experiments demonstrated that the growth inhibition rate after GEN plus calindol treatment exceeded that after the use of either agent alone ($P<0.05$). In addition, Hoechst staining showed that the apoptosis-inducing effect of GEN plus calindol treatment on SGC-7901 cells surpassed that of GEN treatment alone.

Dysregulation of the cell apoptosis pathway may cause certain diseases such as malignancies (10). Therefore, survivin protein, which directly regulates cell apoptosis, plays a vital role in the occurrence and development of tumors (11). Tumor suppressor gene Runx2 is closely associated with the regulation of cell apoptosis, vascular angiogenesis, epithelial-mesenchymal transition, cell migration and invasion (12). Our study showed that after the GEN plus calindol treatment, the expressions of CaSR and Runx3 genes were upregulated, while the expression of the survivin gene was downregulated. This effect far surpassed the result with the use of either agent alone ($P<0.05$). Moreover, the results of protein and mRNA expressions for each gene were consistent, indicating that the effect of GEN in inhibiting the proliferation and promoting the apoptosis of the SGC-7901 cells was related to the induced upregulation of the Runx3 gene and downregulation of the survivin gene.

ACKNOWLEDGEMENT

This work was supported by The Scientific research projects of basic scientific research in colleges and universities operating expenses of Heilongjiang Province in 2018, China (Grant No. 2018-KYYWFMY-0037).

REFERENCES

1. Díaz-Serrano A, Angulo B, Dominguez C, et al. Genomic profiling of HER2-positive gastric cancer: PI3K/Akt/mTOR pathway as predictor of outcomes in HER2-positive advanced gastric cancer treated with trastuzumab. Oncologist 2018; 23(9):1092-02.
2. Singh P, Toom S, Huang Y. Anti-claudin 18.2 antibody as new targeted therapy for advanced gastric cancer. Journal of Hematology & Oncology 2017; 10(1):105.
3. Yang Y, Liu J, Li X, Li JC. PCDH17 gene promoter demethylation and cell cycle arrest by genistein in gastric cancer. Histol Histopathol 2012; 27(2):217-24.
4. Huang W, Wan C, Luo Q, Huang Z, Luo Q. Genistein-inhibited cancer stem cell-like properties and reduced chemoresistance of gastric cancer.. Int J Mol Sci 2014; 15(3):3432-43.
5. Brennan S C, Thiem U, Roth S, et al. Calcium sensing receptor signalling in physiology and cancer. Biochim Biophys Acta 2013; 1833(7):1732-44.
6. Li T, Sun M, Yin X, et al. Expression of the calcium sensing receptor in human peripheral blood T lymphocyte and its contribution to cytokine secretion through MAPKs or NF-κB pathways. Mol Immunol 2013; 53(4):414-20.
7. Han H, Zhong C, Zhang X, et al. Genistein induces growth inhibition and G2/M arrest in nasopharyngeal carcinoma cells. Nutr Cancer 2010; 62(5):641-47.
8. Vivatvakin S, Werawatganon D, Somanawat K, Klaikeaw N, Siriviriyakul P. Genistein attenuated gastric injury on indomethacin-induced gastropathy in rats. Pharmacogn Mag 2017; 13(S2):S306-S310.
9. Liu YL, Zhang GQ, Yang Y, et al. Genistein induces G2/M arrest in gastric cancer cells by increasing the tumor suppressor PTEN expression. Nutr Cancer 2013; 65(7):1034-41.
10. Deng H, Zhen H, Fu Z, Huang X, Zhou H, Liu L. The antagonistic effect between STAT1 and Survivin and its clinical significance in gastric cancer. Oncol Lett 2012; 3(1):193-99.
11. Liu M L, Zhang SJ. Effects of resveratrol on the protein expression of survivin and cell apoptosis in human gastric cancer cells. J BUON 2014; 19(3):713-17.
12. Guo ZJ, Yang L, Qian F, et al. Transcription factor RUNX2 up-regulates chemokine receptor CXCR4 to promote invasive and metastatic potentials of human gastric cancer. Oncotarget 2016; 7(15):20999-1012.

JOURNAL OF BIOLOGICAL REGULATORS & HOMEOSTATIC AGENTS Vol. 34, no. 2, 675-678 (2020)

LETTER TO THE EDITOR

OXIDATIVE STRESS INVOLVEMENT IN URTICARIA

S.P. CANNAVÒ[1], G. RISO[1], E. DI SALVO[2], M. CASCIARO[3], R. GIUFFRIDA[1], P.L. MINCIULLO[3], F. GUARNERI[1], E. NETTIS[4] and S. GANGEMI[3]

[1]School and Unit of Dermatology, Department of Clinical and Experimental Medicine, University of Messina, Messina, Italy; [2]Department of Veterinary Sciences, University of Messina, Messina, Italy; [3]School and Unit of Allergy and Clinical Immunology, Department of Clinical and Experimental Medicine, University of Messina, Messina, Italy; [4]Department of Emergency and Organ Transplantation, School of Allergology and Clinical Immunology, University of Bari Aldo Moro, Bari, Italy

Received November 13, 2019 – Accepted February 20, 2020

To the Editor,

Urticaria is a disease characterized by the sudden appearance of wheals associated or not to angioedema. It is a mast-cell driven disease, in which there is a release of some mediators, such as histamine, platelet-activating factor (PAF) and cytokines, responsible for sensory nerve activation, vasodilatation and plasma extravasation as well as cell recruitment. The causes that have been described are autoreactivity, pseudo-allergy to foods and drugs, and acute or chronic infections (1).

Oxidative stress is a result of an imbalance between endogenous production of free reactive oxygen species (ROS) and reduced effectiveness of protective enzymatic and non-enzymatic antioxidant defence mechanisms. Oxidative imbalance can modify a great variety of cellular processes, including signal transduction, gene expression, inflammation and apoptosis and is implicated in the pathogenesis of several allergic and cutaneous inflammatory disorders (2).

There are some scavenger enzymes such as superoxide dismutase (SOD), catalase (CAT), or glutathione peroxidase (GSH-Px) with antioxidant activity. Some trace elements take part as cofactors in the structure of these enzymes. Plasma thiols are powerful antioxidants that eliminate free radicals. There are also some non-enzymatic antioxidants such as ceruloplasmin, vitamin C and vitamin E.

The altered balance between ROS production and antioxidants can damage cell components like proteins, lipids, and nucleic acids. The valuation of biomarkers of ROS reactions can reflect the proportion of oxidative damage underlying pathological conditions. ROS cause peroxidation of lipids which leads to the destruction of the lipid structure, an increase of membrane permeability and cellular death. Malondialdehyde (MDA), the end product of lipid peroxidation, is considered a good marker of free radical-mediated damage.

Oxidative attack on proteins results in the formation of protein carbonyls (CO), often with the loss of functionality of the parent protein. Protein carbonyls are the most frequently studied biomarkers of oxidative stress, because of the relatively early formation and stability of carbonylated proteins. Nitric oxide (NO), a product of the normal endothelium, considerably increases in inflammation and contributes to oxidative stress. Advanced glycation end products (AGEs) and advanced oxidation protein products (AOPPs) are compounds

Key words: urticaria, oxidative stress, ROS, inflammation, skin, interleukins

Corresponding Author:
Dr Eleonora Di Salvo,
Department of Veterinary Sciences, University of Messina,
Polo Universitario della Annunziata, 98168 Messina, Italy
Tel.: +39 0902212013
e-mail: edisalvo@unime.it

0393-974X (2020)
Copyright © by BIOLIFE, s.a.s.
This publication and/or article is for individual use only and may not be further reproduced without written permission from the copyright holder.
Unauthorized reproduction may result in financial and other penalties
DISCLOSURE: ALL AUTHORS REPORT NO CONFLICTS OF INTEREST RELEVANT TO THIS ARTICLE.

formed by the transformation of proteins which can serve as densitometric markers of oxidative stress and inflammation in several diseases. We summarized the studies regarding oxidative balance in urticaria reported in the recent literature.

Antioxidant enzymes

In the articles selected, a relatively common decrease was found in the level of the antioxidant enzymes. Kalkan and his collaborators first analyzed the oxidative status in patients with acute urticaria, finding higher levels of CuSOD activity while GSH-Px was lower when compared to controls (3). In the study of Rajappa M. et al., who evaluated platelet oxidative stress in CSU, the activity of antioxidant enzymes SOD and GSH-Px were found decreased, showing a significant correlation with disease severity (4). In children affected by chronic spontaneous urticaria (CSU), Dilek et al. found a decreased plasma level of total antioxidant status (TAS) when compared to controls. Furthermore, TAS showed a negative correlation with disease duration (5). Maouia et al. studied 30 patients affected by CSU before and after treatment with desloratadine 5 mg/day, showing increased levels of SOD and CRP and decreased levels of TAS, CAT, GSH-Px, GST and albumin when compared to controls. After treatment, they found decreased levels of SOD (being still higher than controls), CRP and albumin and increased levels of TAS, GSH-Px, GST compared to levels of patients at baseline. CAT activity did not change. Furthermore, the authors showed a significant correlation between CRP and urticaria activity score, emphasizing CRP relevance for CSU clinical assessment (6).

Oxidative stress products

Kalkan et al., in 2013, showed higher plasma levels of MDA in patients with acute urticaria, as well as NO, compared to controls, whereas the levels of protein carbonyls were surprisingly decreased. They concluded that there was no statistically significant difference between the urticaria triggering factors and the oxidative parameters and antioxidant enzyme levels associated. Moreover, the levels of antioxidant enzymes and the levels of MDA, NO and protein carbonyls did not change according to gender (3).

In the study of Rajappa et al. platelet oxidative stress was investigated in 45 patients suffering from CSU. They found an increase in MDA levels when compared to controls. Furthermore, they showed that IL-6 and hs-CRP, as systemic inflammatory markers, were significantly elevated in patients with CSU and correlated with platelet oxidative stress parameters. Lastly, a significant correlation between markers levels and disease severity was established (4).

In children affected by CSU enrolled by Dilek et al. in 2016, total oxidant status and oxidative stress index were higher than those of healthy controls. TOS and OSI levels also showed a statistically significant positive correlation with the urticaria activity score (5). In a following study of 2017, the same authors reported high levels of nitric oxide metabolites (NOx), nitrite and nitrate stress in 32 children with CSU compared to controls. Moreover, a positive correlation between NOx and nitrite levels with urticaria activity score was found (7). In 2017 Nettis et al. investigated the involvement of new oxidative stress markers in 85 patients with CSU. The levels of AOPP were statistically higher in patients than in controls. However, no statistically significant differences were found between AGE levels in patients and controls (8). In the study of Akbas et al. they compared the disulphide/total thiol ratio in patients with acute and chronic urticaria. The disulphide/thiol balance was increased in CSU patients but not in acute urticaria ones. Moreover, a correlation between disulphide levels and daily urticaria activity score was established. There was also a decrease of native and total thiol levels with the advanced age both in acute and chronic urticaria patients, supporting a relationship between advanced age and oxidative stress (9). Metz et al. investigated gene expression related with oxidative stress in lesional and nonlesional skin of patients with CSU before and after treatment with omalizumab, showing that omalizumab makes the gene expression profile of lesional CSU skin look like that of nonlesional and healthy volunteers' skin (10).

Oxidative stress and urticaria

Urticaria is a skin disease affecting 1% of the

population, difficult to manage and with a negative effect on the quality of life of patients. Different etiological factors and mechanisms have been implicated in the development of urticaria, but a specific cause is unidentifiable in most cases. An exact pathogenic mechanism cannot be currently stated, because CSU results from a complex interplay of several individuals and environmental factors (1). The importance of oxidative damage has been highlighted in a variety of acute and chronic diseases including those immune-related and carcinogenesis (11). Urticaria could have a long and hard-to-follow trend. Finding a reliable disease marker is one of the goals of the researchers. Monitoring the activity of some enzymes (i.e. SOD, GSH-Px) or the concentration of altered biomolecules such as MDA and AOPP could help, in selected cases, to verify therapy efficacy and patient metabolic control. Although the literature demonstrated that ROS and oxidative stress are somehow involved in urticaria, as emerged from the dosage of the oxidation products, few authors focused on how these chemical substances could influence the disease.

In conclusion, it seems there is an oxidative burden in patients with CSU, as shown by the occurrence of a high level of oxidative damage products and low levels of antioxidant enzymes. However, the discordance present in some studies could be ascribed to various procedural limitations, first of all, the heterogeneity of the markers studied. Several biomarkers evaluating the oxidative status have been suggested, such as antioxidant enzymes and products of oxidative damage. The distinct behaviour observed for the different markers is probably due to the activation of specific biochemical pathways related to the disease. Furthermore, most of the studies reported were performed on only a small number of patients. Another limitation is represented by the differences in the analytical procedures or the source (plasma, serum, skin) of markers. Finally, a wide number of physio/pathological conditions related to the increase in circulating levels of oxidative markers may influence the results. Among these, pre-analytical factors, such as fasting, physiological factors (e.g., age), environmental conditions, lifestyle habits, the presence of other morbidity or the intake of drugs can interfere with the levels of some biomarkers. Further studies in larger cohorts with better-specified variables and standardization of the methods could give more homogeneous data. This could be useful to improve our knowledge about the mechanisms involved in urticaria development and progression and to predict the responsiveness to the treatment.

REFERENCES

1. Zuberbier T, Aberer W, Asero R, et al. The EAACI/GA²LEN/EDF/WAO guideline for the definition, classification, diagnosis and management of urticaria. Allergy 2018; 73(7):1393-414.
2. Vaccaro M, Bagnato G, Cristani M, et al. Oxidation products are increased in patients affected by non-segmental generalized vitiligo. Arch Dermatol Res 2017; 309(6):485-90.
3. Kalkan G, Seçkin HY, Duygu F, Akbaş A, Özyurt H, Şahin M. Oxidative stress status in patients with acute urticaria. Cutan Ocul Toxicol 2014; 33(2):109-14.
4. Rajappa M, Chandrashekar L, Sundar I, et al. Platelet oxidative stress and systemic inflammation in chronic spontaneous urticaria. Clin Chem Lab Med 2013; 51(9):1789-94.
5. Dilek F, Ozceker D, Ozkaya E, et al. Oxidative stress in children with chronic spontaneous urticaria. Oxid Med Cell Longev 2016; 2016.
6. Maouia A, Youssef M, Leban N, Ben Chibani J, Helal A, Kassab A. CRP relevance in clinical assessment of chronic spontaneous urticaria Tunisian patients. Cutan Ocul Toxicol 2017; 36(4):387-92.
7. Dilek F, Ozceker D, Ozkaya E, et al. Elevated nitrosative stress in children with chronic spontaneous urticaria. Int Arch Allergy Immunol 2017; 172(1):33-9.
8. Nettis E, Distaso M, Saitta S, et al. Involvement of new oxidative stress markers in chronic spontaneous urticaria. Postępy Dermatol Alergol 2017; 34(5):448.
9. Akbas A, Kilinc F, Sener S, Aktaş A, Baran P, Ergin M. Investigation of thiol-disulphide balance in patients with acute urticaria and chronic spontaneous urticaria. Cutan Ocul Toxicol 2017; 36(3):205-10.

10. Metz M, Torene R, Kaiser S, et al. Omalizumab normalizes the gene expression signature of lesional skin in patients with chronic spontaneous urticaria: A randomized, double blind, placebo controlled study. Allergy 2019; 74(1):141-51.
11. Imbesi S, Musolino C, Allegra A, et al. Oxidative stress in oncohematologic diseases: an update. Expert Rev Hematol 2013; 6(3):317-25.

LETTER TO THE EDITOR

PROPHYLAXIS WITH rFVIIa BEFORE THIRD MOLAR EXTRACTION IN A PATIENT WITH FACTOR VII DEFICIENCY

P.C. PASSARELLI[1], V. DESANTIS[1], P. DE ANGELIS[1], G.B. PICCIRILLO[1], V. GIOVANNINI[1], P. PAPI[2], G. POMPA[2] and A. D'ADDONA[3]

[1]Department of Head and Neck, Oral Surgery and Implantology Unit, Institute of Clinical Dentistry, Catholic University of the Sacred Heart, Gemelli University Polyclinic Foundation, Rome, Italy;
[2]Department of Oral and Maxillo-facial Sciences, "Sapienza" University of Rome, Rome, Italy;
[3]Department of Head and Neck, Oral Surgery and Implantology Unit, Institute of Clinical Dentistry, Catholic University of the Sacred Heart, Gemelli University Polyclinic Foundation, Rome, Italy

Received February 5, 2020 – Accepted February 19, 2020

To the Editor,

Factor VII (FVII) is a vitamin K-dependent glycoprotein, that is produced in the liver and it participates in the extrinsic pathway of blood coagulation. Upon vascular injury, factor VII interacts with factor III which leads to the cleavage to its active form: this is the first step of the blood coagulation process. The complex formed by factor III and activated factor VII activates factors IX, X, and autocatalytically factor VII (1). Alexander et al. in 1951 (2) described for the first time the congenital deficit of factor VII. It is also known as serum prothrombin conversion accelerator (SPCA) deficiency, hypoproconvertinaemia, stable factor or proconvertin deficiency and Alexander's disease. It is a rare autosomal recessive bleeding disorder and its pathogenesis is due to mutations in the gene F7 (13q34), which produces a severe deficiency in the homozygote and moderate deficiency, sometimes even without clinical manifestations, in the heterozygote. This bleeding disorder has a prevalence rate of approximately 1/500,000 in the general population (3). Factor VII deficiency refers to both men and women in the 1:1 ratio. It is more readily recognizable in women because of the characteristic prodromal symptoms of prolonged menstruations (4). The clinical situation may be very severe, with bleeding to the gastrointestinal tract and central nervous system or early recurrent hemarthrosis, or moderate, with bleeding from the oral cavity, epistaxis, menorrhagia. Prophylaxis with recombinant activated factor VII (rFVIIa) [coagulation factor VIIa (recombinant); NovoSeven RT; Novo Nordisk, Bagsvaerd, Denmark] is indicated for the treatment of spontaneous and surgical bleeding in congenital FVII deficiency and also in patients with acquired haemophilia, Glanzmann's thrombasthenia, and congenital haemophilia A and B with inhibitors to factors VIII (FVIII) and IX (FIX) > 5 Bethesda units (BU) (5). The dose is generally in the range of 15-30 μg/kg for any injection for factor VII deficit (3).

Case report

This report describes the case of a 26-year-old woman diagnosed with factor VII deficiency who attended the Oral Surgery Unit, Policlinico

Key words: oral surgery; third molar; extraction; bleeding disorder

Corresponding Author:
Dr Pier Carmine Passarelli,
Department of Head and Neck, Oral Surgery and Implantology Unit,
Institute of Clinical Dentistry, Catholic University of the Sacred Heart,
Gemelli University Polyclinic Foundation, Rome, Italy
Tel.: +39 0630155278 - Fax: +39 0630154751
e-mail: piercarmine.passarelli@unicatt.it

0393-974X (2020)
Copyright © by BIOLIFE, s.a.s.
This publication and/or article is for individual use only and may not be further reproduced without written permission from the copyright holder.
Unauthorized reproduction may result in financial and other penalties
DISCLOSURE: ALL AUTHORS REPORT NO CONFLICTS OF INTEREST RELEVANT TO THIS ARTICLE.

Universitario Agostino Gemelli, Rome, in April 2018 for surgical extraction of the lower left third molar. The patient was sent from the Department of Medical Sciences, Haematology Unit of Policlinico Universitario Agostino Gemelli, where she was in care. She was in good general health and reported occasional epistaxis and heavy menstruation, but no spontaneous oral mucosa bleeding. The results of coagulation studies are shown in Table I.

The prothrombin time (PT) and the International Normalized Ratio (INR) were prolonged, while the activated partial thromboplastin time (APTT) was normal. Factor VII showed a deficit of 33%, compared with the normal range of 70-140%. Factors II, V and X levels were within the range. A digital panoramic radiograph was carried out (Fig. 1), which showed a greater diagnostic precision (6). The mandibular left third molar showed radiographic evidence of a deep carious lesion. After informing the patient, we agreed on the extraction of the tooth. Systemic disease that can cause dental abnormalities (7) were evaluated in order to achieve a better management of the relative contraindications to the extractions and also to avoid absolute contraindications. The study was conducted in accordance with the requirements of the Helsinki Declaration of 1975 and the patient provided the written informed consent.

Recombinant activated factor VII (rFVIIa) (NovoSeven) was transfused intravenously in a single dose of 25μg/kg body weight 30 min before surgical extraction. After oral rinsing with chlorhexidine 0.2% for 1 min, local anesthesia was administered in a standard block and infiltrative manner using 2 cartridges (3.6 mL) of 2% carbocaine with 1:100,000 epinephrine. A triangular flap was made and, after a mild osteotomy, the mandibular third molar was extracted with lever and clamp, without complication or damage of gingival soft tissue, and the alveolar socket was cleaned with a bone curette and physiological saline. Primary closure was obtained using a 3-0 silk suture. The patient had no drug allergies; betamethasone (4 mg intramuscularly) and analgesic (Ketorolac 20mg/ml; 15 drops sublingual) were administered after the extraction. Ice packs were applied locally for the first day, and antibiotic therapy with Amoxicillin + Clavulanic Acid 1g BID for five days was started the day before surgery.

Table I. *Results of coagulations studies.*

Test	***Value***	***Normal range***
Prothorombin time (PT)	15.3s	9.5-12.5 s
International Normalized Ratio (INR)	1.9	0.80-1.20
Activated partial thomboplastin time (APTT)	40.2s	20.0-39.0 s
Coagulation Factors		
Factor II	105.2%	70-140%
Factor V	137.4%	70-140%
Factor VII	33.0%	70-140%
Factor X	97.5%	70-140%

Table II. *Post-operative information*

Day	***Bleeding***	***Pain***	***Swelling***
1	Very mild	No pain	No
2	No	No pain	Mild
3	No	No pain	Mild
4	No	No pain	No
5	No	No pain	No
6	No	No pain	No
7	No	No pain	No

Oral hygiene instructions were given to the patient to enhance the healing process during the following 6 months and to obtain better results in terms of osseous defect filling and to re-establish the supracrestal tissue attachment (8).

No intensive intraoperative bleeding or hemorrhagic complications and no postoperative bleeding were observed (Figs. 2 and 3), and the patient was discharged. All the postoperative clinical outcomes, such as pain, swelling, and bleeding were recorded (9). The patient was asked to annotate from the day of surgery for one week if she had had bleeding, swelling or pain (Table II). For bleeding and swelling, we gave four options: very mild, mild,



Fig. 1. *Panoramic radiograph of the mandibular left third molar shows evidence of a deep carious lesions.*

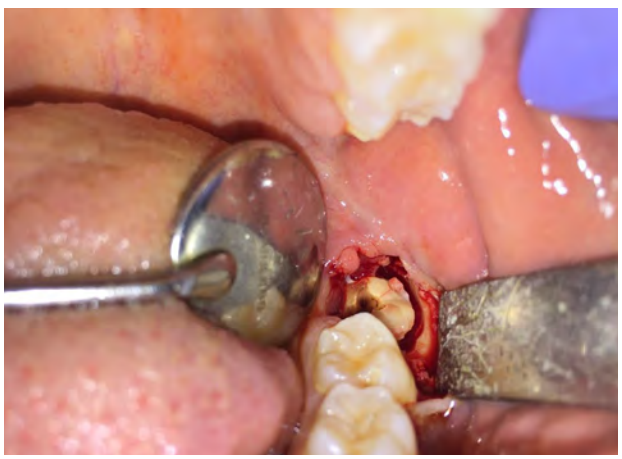


Fig. 2. *Intraoperative photo shows a good hemostasis.*



Fig. 3. *Postoperative photo shows no postoperative bleeding and the good health of the site*

moderate and severe. The pain was registered with VAS scale. She reported very mild bleeding only on the day of surgery, a mild swelling during the second and the third days and no pain in the days after wisdom tooth extraction. She did not take analgesics and antihemorrhagic during the week. The extraction site showed excellent healing at the time of suture removal, 7 days after the surgery. No thromboembolic complications following this single administration of rFVIIa were observed.

DISCUSSION

Management of patients with factor VII deficiency requiring tooth extraction involves close cooperation between the oral surgeon and the hematologist (10). The hematologist characterizes the patient's bleeding risk and determines an appropriate prophylactic regimen to prevent excessive local bleeding during and after oral interventions. Incorrect treatment of patients with factor VII deficiency who must undergo surgery may result in uncontrolled intraoperative and postoperative bleeding and hemorrhagic complications (11).

It is very important to consider the risk of bleeding and serious infections associated with invasive oral cavity procedures, and some protocols underline the importance of evaluating hematologic indices (12). In the present study, the laboratory tests included Prothrombin Time (PT), International Normalized Ratio (INR) and the Partial Thromboplastin Time (aPTT).

Recombinant factor VIIa can be used successfully to prevent copious bleeding in a patient with factor VII deficiency requiring oral surgery (11). The dose and administration frequency should be adjusted to the patient's need and the assessment of each patient before surgery should include such factors as: the risk of hemorrhage, hemorrhagic complications and infections, duration of surgery, scope and range/ extent of surgery, level of inherited FVII deficiency, as well as preoperative clinical symptoms related to FVII deficiency. Percentage of FVII plasma levels is used to estimate the risk of bleeding and hemorrhagic complications in surgical patients: very high risk for FVII plasma levels below 1%; high risk for FVII plasma levels 1-10%, medium risk for 10-25% and

low risk for >25% (3).

In the present case, a single intravenous dose of 25µg/kg body weight 30 minutes before surgical extraction was administered to the patient which prevented excessive intraoperative and postoperative bleeding, reassuring the patient who had given great concern due to her recent diagnosis of deficit of FVII. She had no need of analgesics or antihemorrhagics in the postoperative period, and reported only very mild bleeding on the day of surgery, and a light swelling on the second and third days.

In conclusion, surgical extractions appear to be safe procedures in patients with factor VII deficiency when appropriate prophylaxis with rFVIIa, prescribed by the hematologist, is used and an appropriate protocol for surgical extraction is followed, minimizing postoperative bleeding, swelling and pain.

REFERENCES

1. Wei DC, Wong RW, Robertson EP. Congenital factor VII deficiency presenting as delayed bleeding following dental extraction. A review of the role of factor VII in coagulation. Pathology 1997; 29:234-37.
2. Alexander B, Goldstein R, Landwehr G, et al. Congenital SPCA deficiency. A hitherto unrecognized coagulation defect with haemorrhage rectified by serum and serum fractions. J Clin Invest 1951; 30:596.
3. Wiszniewski A, Szczepanik A, Misiak A, Bykowska K, Szopiński P. Prevention of bleeding and hemorrhagic complications in surgical patients with inherited factor VII deficiency. Blood coagul fibrinolysis 2015; 26:324-30.
4. Perry DJ. Factor VII deficiency. Blood Coagul Fibrinolysis 2003; 14:547-54.
5. Kubisz P, Stasko J. Recombinant activated factor VII in patients at high risk of bleeding. Hematology 2004; 9:317-32.
6. Saccomanno S, Passarelli PC, Oliva B, Grippaudo C. Comparison between two radiological methods for assessment of tooth root resorption: an in vitro study. Biomed Res Int 2018; 2018:5152172.
7. Passarelli PC, Pasquantonio G, Manicone PF, Cerroni L, Condo' R, Mancini M, D'Addona A. Orofacial signs and dental abnormalities in patients with Mulvihill-Smith syndrome: A literature review on this rare progeroid pathology. Medicine (Baltimore) 2018; 97: e0656.
8. Passarelli PC, Lajolo C, Pasquantonio G, D'Amato G, Docimo R, Verdugo F, D'Addona A. Influence of mandibular third molar surgical extraction on the periodontal status of adjacent second molars. J Periodontol 2019; 90:847-55.
9. Passarelli PC, De Angelis P, Pasquantonio G, Manicone PF, Verdugo F, D'Addona A. Management of single uncomplicated dental extractions and postoperative bleeding evaluation in patients with Factor V deficiency: a local antihemorrhagic approach. J Oral Maxillofac Surg 2018; 76:2280-83.
10. Weinstock RJ, Onyejiuwa A, Shnayder G, Clarkson EI. Use of recombinant factor VII for tooth extractions in a patient with severe congenital factor VII deficiency: a case report. J Am Dent Assoc 2015; 146(4):271-75.
11. Passarelli PC, Pasquantonio G, D'Addona A. Management of surgical third lower molar extraction and postoperative progress in patients with Factor VII Deficiency: a clinical protocol and focus on this rare pathologic entity. J Oral Maxillofac Surg 2017; 75:2070.e1-2070.e4.
12. Bollero P, Passarelli PC, D'Addona A, Pasquantonio G, Mancini M, Condò R, Cerroni L. Oral management of adult patients undergoing hematopoietic stem cell transplantation. Eur Rev Med Pharmacol Sci 2018; 22:876-87.

LETTER TO THE EDITOR

PERCEPTIVE AND SUBJECTIVE EVALUATION OF SPEECH DISORDERS IN PARKINSON'S DISEASE

D. MELCHIONDA[1], G. VARVARA[2], D. PERFETTO[3], B. MASCOLO[1] and C. AVOLIO[1]

[1]Neurology Department, University Hospital of Foggia, Foggia, Italy; [2]Department of Medical, Oral and Biotechnological Sciences, University of Chieti–Pescara, Chieti, Italy; [3]Regional Health District of Molise (ASReM), Campobasso, Italy

Received January 7, 2020 – Accepted February 21, 2020

To the Editor,

Parkinson's disease (PD), which is not only a motor disease, is one of the most frequent neurodegenerative diseases and affects 1.5-2% of people worldwide (1). The role of its non motor-symptoms is of first importance on quality of life (2). Speech impairment is considered a part of motor impairment and is widespread in PD (3) where most frequent speech impairment is Hypokinetic dysarthria, a disorder characterized by reduced articulation movements and phonetic monotony (4). Many PD patients show difficulty in accessing the lexicon related to cognitive impairment (5). Clinical evaluation of speech disorders in PD includes the clinical history, verbal and non-verbal assessment of the voice, evaluation of the calibre of the language (6). It is also important to self-assess speech disturbances because PD patients often do not realize their own deficits (7). Self-assessment tests comprise subjective assessment of communicative disorder in different social situations, description of adopted strategies, perception of the reactions of interlocutors (8).

The comparison between perceptive and subjective examination of speech disorders in PD patients are described in order to evaluate the presence of these deficits and their impact on quality of life in order to initiate early treatment with specific speech therapy.

MATERIALS AND METHODS

Forty-two patients affected by idiopathic PD, 21 men and 21 women, aged 56-82 years, with duration of illness between 4 and 11 years, at different stages of the disease were included in the study. All patients gave their informed written consent and the study was approved by an appropriate ethics committee. All clinical data including age, duration of disease, medication usage, score on the Unified Parkinson's Disease Rating Scale (UPDRS) part III, and the Hoehn and Yahr scales are reported in Table I.

For the clinical evaluation the UPDRS III scale was used, which is internationally the most used evaluation scale for motor symptoms in PD. The UPDRS scale comprises Hoehn & Yahr (H&Y) Scale for the definition of motor impairment of the disease and Schwab & England (S&E) scale for the evaluation of disabilities related to the disease (9).

For a perceptive evaluation of speech disturbances, the Robertson's test was used, which comprises 8 items, each with some sub-items for a quantitative and qualitative evaluation of speech abilities of the patients (10). For subjective evaluation of speech disturbances, a self-assessment survey was used which was composed of 7 different items of multiple choice questions regarding subjective judgment of the quality of voice, feelings during conversation with acquaintances and with strangers, ways

Key words: non-motor symptoms; self-assessment; logopedic treatment; language

Corresponding Author:
Dr. Donato Melchionda,
Neurology Department,
University Hospital of Foggia,
Viale Pinto 1, 71100 Foggia, Italy
Tel.: +39 03383308485 - Fax: +39 0881733876
e-mail: donatomelchionda@gmail.com

0393-974X (2020)
Copyright © by BIOLIFE, s.a.s.
This publication and/or article is for individual use only and may not be further reproduced without written permission from the copyright holder.
Unauthorized reproduction may result in financial and other penalties
DISCLOSURE: ALL AUTHORS REPORT NO CONFLICTS OF INTEREST RELEVANT TO THIS ARTICLE.

of expressing thoughts at the beginning of the speech, speaking ability in conversation and discomfort resulting from this activity. For each Item of these two tests, there are 4 responses. All responses are evaluated with a score ranging 1 to 4, according to Therapy Outcomes Measures Scale (11). The score obtained expresses the speech difficulty perceived by patient and the degree of expressive difficulty and the level of communicative effectiveness. Data obtained were matched for three parameters: i) language; ii) verbal fluency; iii) quality of voice.

RESULTS

Perceptive and subjective tests were given to each patient. The self-assessment test was filled in by patients themselves. UPDRS, H&Y, S&E were given to a Parkinson neurologist with 10 years of experience. Speech tests were carried out by a logopedist with 10 years of experience. The score obtained from the perceptive evaluation test was compared with that of the self-assessment test for the three parameters of language, verbal fluency and quality of voice.

The data set obtained for the 42 patients makes it clear that the degree of disease assessed by those affected (subjective assessment) was always lower than evaluations based on perceptive test. No patient assessed the degree of their disease more serious than the objective assessment. Only in the variable "Language" 8 patients expressed a judgment that was equal to the objective evaluation. In order to validate the differences that emerged from the evaluations (subjective *vs* perceptive), the results obtained were submitted to statistical tests. In our case, the "difference" variables derived from the Language, Verbal Fluency and Voice Quality (subjective and perceptive) scores in a single sample with paired data. A non-parametric "Sign test" was used, the results of which, conducted on the three variables, showed statistically significant differences between the pairs of data recorded through subjective and objective tests in all the three variables ($p<0.001$) (Fig. 1A).

In order to evaluate the influence of the age of patients on the subjective *vs* perceptive study the data set was further analyzed, with a stratification of data based on the variable "age of patient". Patients were divided into three groups of 16, 15 and 11 units, respectively (Fig. 1 B,C). No statistically significant differences were found in the three group of patients ($p<0,001$).

In all patients, a statistically significant correlation between language impairment and quality of life was detected. A greater alteration of linguistic abilities was correlated with a worse quality of life measured with the S&E test ($p<0.001$).

DISCUSSION

Language processing in patients with PD shows an array of problems. Some of the observed problems represent a peripheral deficit due to motor impairments, such as articulatory imprecision and poor voice control in speech production (3, 7). It is not easy to distinguish between objective and subjective speech deficits in these patients (4). In the present study we focused on speech alterations in patients with Parkinson's disease, particularly matching results of perceptive and self-assessment evaluation. We preferred to use the term "perceptive" instead of "objective" because we used the perceptive method of the Robertson's test assessed by a "human" operator. The term "objective" would be used for computerized acoustic analysis because it always rates the same speech signal with the same score. We found a statistically significant discrepancy between the severity of the symptoms measured by the perceptive evaluation test and the severity of the same disturbances perceived by the self-evaluation test, indicative of an alteration in the perception of linguistic deficit in PD patients. PD patients are not able to adequately estimate the degree of their deficit, particularly showing reduced self-control to regulate their voice intensity and perform verbal motility, especially in a noisy environment and in conversation. It means that a more detailed logopedic evaluation at any stage of the disease is mandatory, in order to recognize the disorder from the beginning and treat it appropriately. Moreover, the deficits are shown independently of the age of patients and manifests themselves with the same changes in sensory feedback, in production and in

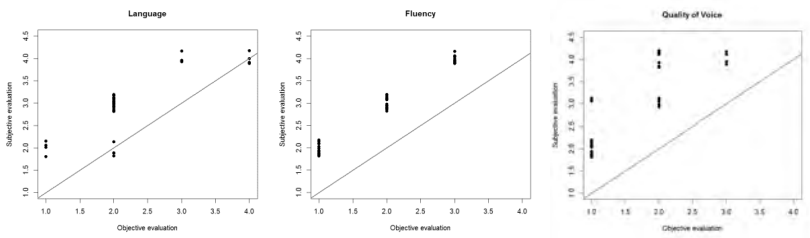
acoustic, proprioceptive and motor perception.

In addition, self-assessment tests gave information about the quality of life of PD patients with speech disorders. By estimating the incidence level of this deficiency in their everyday life, a high degree of psycho-social discomfort emerges. In different

Table I. *Mean (SD) age, Duration of Parkinson, Medications, score on UPDRS III and the Hoehn & Yahr scale.*

	Age	Duration Parkinson (years)	Medication calculated as L-dopa equivalent	UPDRS (scale III)	Hoehn Yahr Scale
Mean	71.6 (8.3)	7.1 (2.4)	550 (255.5)	36.8 (12.1)	2.75 (1.1)
Range	56–82	4–11	200–1300	12-62	1–4

A



B

X	Cluster 1		Cluster 2		Cluster 3	
	Female	*Male*	*Female*	*Male*	*Female*	*Male*
Mean	64.5	66.9	68.9	73	76.3	74.8
Median	63	68	70	71	80	76.5
S.d.	8.0	9.7	8.5	6.4	7.2	7.0
Min	55	54	57	65	68	62
Max	76	78	80	81	81	82
#Patients	8	8	10	5	3	8

C

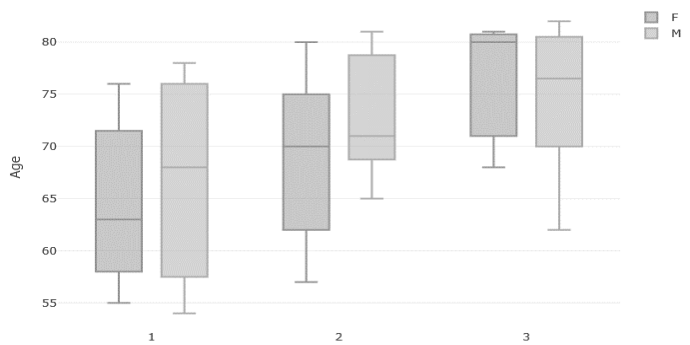


Fig. 1. ***A)*** *Results of the "Sign-test" on the three variables (language, fluency and quality of voice) show statistically significant differences between subjective and objective tests in all three variables (p<0.001).* ***B***, ***C)*** *Stratification of data based on the variable "age". Patients are divided into three groups of 16, 15 and 11 units, in order to evaluate the influence of age on the subjective* vs *perceptive study. F: female; M: male.*

communicative contexts, patients are subject to general misunderstanding by their interlocutors. This sense of inadequacy limits the patients in carrying out various routine activities and dialogues, often inducing them to exclude themselves from conversations.

The limitations of the study are the small number of patients in the series, the "perceptive" evaluation of the patients by a logopedist, reporting a "subjective" evaluation that would be different to a computer analysis, and the lack of a normal control group. Finally, in order to preserve the quality of life of PD patients, an early logopedic assessment is recommended to start an intensive and appropriate logopedic treatment.

REFERENCES

1. Hirsch L, Jette N, Frolkis A, Steeves T, Pringsheim T. The incidence of Parkinson's disease: a systematic review and meta-analysis. Neuroepidemiology 2016; 46:292-300.
2. Gopalakrishna A, Alexander SA. Understanding Parkinson disease: a complex and multifaceted illness. J Neurosci Nurs 2015; 47:320-26.
3. Ho AK, Iansek R, Marigliani CBradshaw JL, Gates S. Speech impairment in a large sample of patients with Parkinson's disease. Behav Neurol 1999; 11:131-37.
4. Pentland B, Gray JM, Riddle WJ, Pitcairn TK. The effects of reduced non verbal communication in Parkinson's disease. Br J Disord Commun 1988; 23:31-34.
5. Worth PF. How to treat Parkinson's disease in 2013. Clin Med 2013; 13:93-96.
6. Huang P, Fang R, Li BY, Chen SD. Exercise-related changes of networks in aging and mild cognitive impairment brain. Front Aging Neurosc 2016; 8:47.
7. Gauvin HS, Mertens J, Mariën P, Santens P, Pickut BA, Hartsuiker RJ. Verbal monitoring in Parkinson's disease: A comparison between internal and external monitoring. PLoS One 2017; 12(8): e0182159. Published online 2017 Aug 23. doi: 10.1371/journal.pone.0182159.
8. Möbes J, Joppich G, Stiebritz F, Schröder C. Emotional speech in Parkinson's disease. Mov Disord 2008; 23:824-29.
9. Movement Disorder Society Task Force on Rating Scales for Parkinson's Disease. The Unified Parkinson's Disease Rating Scale (UPDRS): status and recommendations. Mov Disord 2003; 18:738-50.
10. Fussi F, Cantagallo A. Profilo di valutazione della disartria. Adattamento italiano del test di Robertson, raccolta di dati normativi e linee di trattamento. First ed., Torino, Ed. Omega, 1982.
11. Enderby P, John A, Petheram B. Therapy Outcome Measures for Rehabilitation Professionals: Speech and Language Therapy, Physiotherapy, Occupational Therapy, 2nd Edition. Wiley ed. 2013.

JOURNAL OF BIOLOGICAL REGULATORS & HOMEOSTATIC AGENTS Vol. 34, no. 2, 687-690 (2020)

LETTER TO THE EDITOR

DEXMEDETOMIDINE SEDATION ASSOCIATED WITH SUPRAINGUINAL FASCIA ILIACA BLOCK FOR HIP FRACTURE SURGERY IN HIGH RISK ELDERLY PATIENTS

G. FERRONE[1], E. TAMBURELLO[1], R. NESTORINI[1], G. CONCINA[1], A. CHIERICHINI[1,2], M. ROSSI[1,2] and A. VERGARI[1,2]

[1]Department of Anesthesiology, Intensive Care Medicine and Toxicology, A. Gemelli University Hospital Foundation IRCCS, Rome, Italy; [2]Catholic University of the Sacred Heart, Rome, Italy

Received November 22, 2019 – Accepted February 28, 2020

To the Editor,

Hip fracture is one of the main causes of hospitalization and major surgery in elderly patients (1). It is estimated that the number of elderly people in Europe will double in the next three decades, thus leading to a dramatic increase in hip fracture surgery. Furthermore, elderly patients with hip fracture often present at least one major comorbidity such as cardiac and respiratory disease, for which they receive anticoagulant therapy and are at greater risk of death.

At A. Gemelli University Hospital Foundation, Rome, Italy, the treatment of intertrochanteric fracture in elderly patients consists of intramedullary femoral fixation and it is performed within 48 hours in order to avoid the increase of postoperative mortality and morbidity (2). Thus, selecting an appropriate anesthetic method for high risk patients requires considerable deliberation. In daily clinical practice, the patients scheduled for internal fixation of intertrochanteric fractures are treated with a spinal anesthesia; however, should this technique be contraindicated, a general anesthesia is performed.

In this case series the anesthetic management of three patients treated with dexmedetomidine sedation and suprainguinal fascia iliaca compartment block as an alternative to general anesthesia is presented. The aim of this report is to highlight how this treatment could give benefits in terms of efficacy and faster functional recovery.

Written informed consent was provided by all patients for the use of images and for data publication.

Case series

According to the institutional orthopedic surgery protocol, each patient received preoperative antibiotic prophylaxis and gastric protection. In the preanesthesia room, the patients received dexmedetomidine (Orion Pharma, Espoo, Finland) i.v. at rates of 0.2–1.2 μg/kg/h with a target sedation level of -1 to -3 on the Richmond Agitation-Sedation Scale (RASS) (Table I). Then an ultrasound-guided Fascia Iliaca Block (FIB), with a suprainguinal approach, using ropivacaine 0.375% 40 ml was performed. As the standard procedure prescribes for non-intubated sedated patients, we applied a multiparametric monitoring including exhaled CO_2 and Bispectral Index. Thirty minutes after FIB the patients were positioned on the traction table.

Before the skin incision, a short acting local anesthetic (mepivacaine 1% 20 mL) was infiltrated by the surgeon on the operative site in order to

Key words: regional anesthesia, hip fracture, elderly patient, dexmedetomidine, fascia iliaca block

Corresponding Author:
Dr Alessandro Vergari,
Department of Anesthesiology,
Intensive Care Medicine and Toxicology,
A. Gemelli University Hospital Foundation IRCCS,
Catholic University of the Sacred Heart, Rome, Italy
Tel.: +39 0630154507 - Fax: +39 063013450
e-mail: alessandro.vergari@policlinicogemelli.it

0393-974X (2020)
Copyright © by BIOLIFE, s.a.s.
This publication and/or article is for individual use only and may not be further reproduced without written permission from the copyright holder.
Unauthorized reproduction may result in financial and other penalties
DISCLOSURE: ALL AUTHORS REPORT NO CONFLICTS OF INTEREST RELEVANT TO THIS ARTICLE.

block the sensitive subcostal nervous terminations not covered by the FIB. Intraoperatively the pain level was assessed with the Behavioral Pain Scale for non-intubated patients (BPS-NI, ranging from 3 -no pain- to 12 -most pain-) since this scale exhibited good psychometric properties (3). If BPS-NI was > 6, sufentanil boluses of 0.05 μg/kg were administered intravenously. In the postoperative period all patients were given acetaminophen and ketoprofen by mouth in an around-the-clock dosing regimen. In case of nausea or vomiting ondansetron was prescribed. As a rescue drug for pain control oral tramadol was prescribed. The postoperative pain intensity was measured using Numeric Rating Scale for Pain (NRS Pain), ranging from 0 (no pain) to 10 (the worst imaginable pain).

Case 1

A 95-year-old female, weighing 55 Kg, was an ASA III patient with medical history as follows: atrial fibrillation in therapy with rivaroxaban, kidney failure (CKD Stage 3 KDIGO 2012) and a pharmacologically-treated hypertension. The patient had a normal myocardial contraction as shown by her echocardiogram. She refused spinal anesthesia and, after starting dexmedetomidine sedation, an FIB was performed. A transverse suprainguinal US image was obtained and the needle was introduced using a lateral-to-medial in-plane approach. Adequate local anesthetic spread, (ropivacaine 0.375% 40 ml) both medially and laterally, is essential to obtain a successful block. Target RASS score was obtained with rates of 0.6-0.7 μg/kg/h (BIS was always >75). The patient received sufentanil 7.5 μg in divided doses. A normal respiratory pattern was observed, and she remained hemodynamically stable, presenting a ventricular response around 85-95 beats/min. Postoperative pain evaluated by NRS was 1; the patient had a good functional recovery, and she started rehabilitation on the first post-operative day.

Case 2

A 94-year-old male, weighing 100 Kg, was an ASA III patient with medical history as follows: severe aortic stenosis (mean gradient 45mmHg), implanted pacemaker for sick sinus syndrome (the patient had a spontaneous rhythm), chronic obstructive pulmonary disease, presence of abdominal aortic endoprothesis due to a previous aortic rupture. After evaluating all these comorbidities, FIB and dexmedetomidine sedation was performed. Target RASS score was obtained with rates of 0.7-0.8 μg/kg/h (BIS was always > 70). The patient received sufentanil 17.5 μg in divided doses. A normal respiratory pattern was observed; the patient presented a slight hypotension (Mean arterial pressure was 20% lower than the basal values for about 15 min), correlated to hypovolemia and anemia (starting hemoglobin 8.9 g/dL), which was promptly corrected with blood transfusion. Postoperative pain evaluated by NRS was 2; the patient had a good functional recovery, and he started rehabilitation on the first post-operative day.

Case 3

A 90-year-old male weighing 50 Kg was an ASA III patient with medical history as follow: diabetes, pancreatic cancer, hypertension, moderate mitral insufficiency, taking clopidogrel (last dose: 24 h before surgery). His antiplatelet therapy precluded spinal anesthesia. FIB after starting dexmedetomidine sedation was performed. Target RASS score was obtained with rates of 0.5-0.6 μg/kg/h (BIS was always > 65). The patient received sufentanil 7.5 μg in divided doses. A normal respiratory and hemodynamic pattern was observed throughout the surgery. Postoperative pain evaluated by NRS was 1; the patient had a good functional recovery, and he started rehabilitation on the first post-operative day.

DISCUSSION

The majority of people with hip fracture are elderly and they should be surgically treated within 48 hours (2) because an intervention delay longer than 48 hours is associated with increased mortality and morbidity in 1 year. These patients are often affected by many other diseases associated with ageing, which place them at high risk of mortality after the anesthesia. For hip fracture surgery, the choice of anesthesia (general or neuroaxial) is made by the anesthesiologist and is based on the patient's preference, comorbidities, potential general postoperative complications and the

anesthesiologist's clinical experience. Subarachnoid anesthesia is commonly used for hip fracture surgery at A. Gemelli University Hospital Foundation. However, subarachnoid anesthesia is contraindicated in patients already taking oral anticoagulant drugs (dicumarolic, dabigatran, rivaroxaban) or antiplatelet agents (ticlopidine, clopidogrel). Other contraindications to spinal anesthesia include patient refusal, infection at the injection site, severe and uncorrected hypovolemia, true allergy to any of the drugs, and increased intracranial pressure. Spinal anesthesia is relatively contraindicated in cardiac diseases with fixed cardiac output (CO) states and in aortic stenosis. In all the above mentioned cases, general anesthesia is performed. Adverse reactions to the drugs, possible difficult airway management, perioperative hemodynamic instability, inhalation of gastric content, postoperative nausea and vomiting, and respiratory depression are potential complications during general anesthesia. Unfortunately, in elderly patients undergoing general anesthesia, age is not an independent risk factor for morbidity and mortality, and this affects functional recovery and length of hospital stay.

Ultrasound FIB was chosen as the peripheral nerve block for its role in preoperative and postoperative analgesia (4, 5). FIB is considered an anterior lumbar plexus approach since it targets the femoral nerve, the lateral cutaneous of the femur nerve and (less frequently) the obturator nerve. FIB has three main advantages: first of all, it produces fewer hemodynamic changes than spinal anesthesia; second, FIB may be performed while the patient is supine, unlike the paravertebral lumbar plexus block which requires the lateral position (6); finally, the risk of nerve injury or intravascular injection is very small and nerve stimulation is not needed. A suprainguinal approach to the fascia iliaca allows a better local anesthetic to spread to the lumbar plexus and a better obturator nerve block compared to an infrainguinal approach, as recently demonstrated in healthy volunteers (7).

Dexmedetomidine is an α2-adrenoceptor agonist that provides sedation and anxiolysis via receptors in the locus coeruleus, as well as analgesia via receptors at the spinal cord level. It is able to attenuate stress responses without significant respiratory depression (8). Dexmedetomidine is an effective sedative agent compared with propofol and midazolam and its use is associated with easier communication with patients, better assessment of pain and reduced delirium. This drug is useful in not depressing the

Table I. *The Richmond Agitation–Sedation Scale*

Score	Term	Description
+4	Combative	Overtly combative or violent; immediate danger to staff
+3	Very agitated	Pulls on or removes tube(s) or catheter(s) or has aggressive behavior toward staff
+2	Agitated	Frequent non-purposeful movement or patient–ventilator dyssynchrony
+1	Restless	Anxious or apprehensive but movements not aggressive or vigorous
0	Alert and calm	Spontaneously pays attention to caregiver
-1	Drowsy	Not fully alert, but has sustained (more than 10 seconds) awakening, with eye contact, to voice
-2	Light sedation	Briefly (less than 10 seconds) awakens with eye contact to voice
-3	Moderate sedation	Any movement (but no eye contact) to voice
-4	Deep sedation	No response to voice, but any movement to physical stimulation
-5	Unarousable	No response to voice or physical stimulation

patient's respiratory drive. Several studies showed a beneficial effect on the shivering related to the anesthesia and hypothermia. Side effects described in the literature include hypotension and bradycardia (9). In order to limit the undesired hemodynamic side effects related to dexmedetomidine, the initial bolus prior to the start of the continuous infusion should be avoided since the sympatholytic action occurs more frequently after the initial bolus, especially in patients who take drugs with negative chronotropic action or in a hypovolemic status. The early findings associated with this anesthetic management are encouraging and may contribute to improve pain control, obtaining a more efficient and complete anesthetic plan. We expect to continue to gather data in an effort to further define the scenarios in which this procedure can be mostly beneficial.

REFERENCES

1. Coburn M, Röhl AB, Knobe M, Stevanovic A, Stoppe C, Rossaint R Anesthesiological management of elderly trauma patients. Anaesthesist 2016; 65:98-106.
2. Simunovic N, Devereaux PJ, Sprague S, et al. Effect of early surgery after hip fracture on mortality and complications: systematic review and meta-analysis CMAJ 2010; 182:1609-16.
3. Chanques G, Payen JF, Mercier G, et al. Assessing pain in non-intubated critically ill patients unable to self report: an adaptation of the Behavioral Pain Scale. Intensive Care Med 2009; 35:2060-67.
4. Morau D, Lopez S, Biboulet P, Bernard N, Amar J, Capdevila X. Comparison of continuous 3-in-1 and fascia iliaca compartment blocks for postoperative analgesia: feasibility, catheter migration, distribution of sensory block, and analgesic efficacy. Reg Anesth Pain Med 2003; 28:309-14.
5. Candal-Couto JJ, McVie JL, Haslam N, Innes AR, Rushmer J. Preoperative analgesia for patients with femoral neck fractures using a modified fascia iliaca block technique. Injury 2005; 36:505-10.
6. de Visme V, Picart F, Le Jouan R, Legrand A, Savry C, Morin V. Combined lumbar and sacral plexus block compared with plain bupivacaine spinal anesthesia for hip fractures in the elderly. Reg Anesth Pain Med 2000; 25:158-62.
7. Vermeylen K, Desmet M, Leunen, Soetens F, et al. Supra-inguinal injection for fascia iliaca compartment block results in more consistent spread towards the lumbar plexus than an infra-inguinal injection: a volunteer study. Reg Anesth Pain Med 2019; 44:483-491.
8. Venn RM, Grounds RM. Comparison between dexmedetomidine and propofol for sedation in the intensive care unit: patient and clinician perceptions. Br J Anaesth 2001; 87:684–90.
9. Tan JA, Ho KM. Use of dexmedetomidine as a sedative and analgesic agent in critically ill adult patients: a meta-analysis. Intensive Care Med 2010; 36:926-39.

LETTER TO THE EDITOR

PRIMARY HEMANGIOPERICYTOMA OF THE INFRATEMPORAL FOSSA

G.A. PACINO[1], L.M. REDONDO[2], S. COCUZZA[3], A. MANIACI[3], M.C. DA MOSTO[4], P. BOSCOLO-RIZZO[5], G. TONOLI[6], G. MANNELLI[7] and G. SPINATO[4,5]

[1]Oral and Maxillo-Facial Department, Provincial Rovigo Hospital, Italy; [2]Oral and Maxillofacial Surgery Department. Río Hortega Hospital, Valladolid, Spain; [3]Department of Medical and Surgical Sciences and Advanced Technologies "GF Ingrassia", ENT Section; University of Catania- Italy; [4]Department of Neurosciences, Section of Otolaryngology and Regional Centre for Head and Neck Cancer, University of Padova, Treviso, Italy; [5]Department of Surgery, Oncology and Gastroenterology, Section of Oncology and Immunology, University of Padova, Padova, Italy. [6]Ear, Nose and Throat Department, Rovigo Provincial Hospital, Rovigo, Italy; [7]Academic Clinic of Otolaryngology-Head and Neck Surgery, University of Florence

Received October 10, 2019 – Accepted March 13, 2020

To the Editor,

Hemangiopericytoma (HPC) is a rare perivascular tumour classified as a soft-tissue vascular tumour featuring the uncontrolled proliferation of pericytic cells (1). Showing trend for ubiquitous location, soft tissue of lower extremities, pelvic fossa and retroperitoneum are the predominant sites of origin. Its incidence in the head and neck region has been considered approximately less than 20% (2). In this area, the majority of the reported cases are in the nasal cavity and paranasal sinuses, nasopharynx, jawbones, orbit and scalp; other areas involved have included parotid and submandibular gland, larynx, parapharyngeal space, sinus tract and meninges, trachea, middle ear, oral cavity and thyroid gland (1).

A review of the medical literature on tumours occupying the infratemporal fossa reveals that primary HPCs of this anatomical space are exceedingly rare, secondary involvement due to direct extension from adjacent sites being more commonly found (3). To the best of our knowledge, only nine previous cases of primary HPCs involving the infratemporal fossa have been reported up until the end of 2018 (Table I) (2). We report herein an additional case of HPC arising in the infratemporal fossa, describing the gross and microscopic features of this lesion, as well as clinical presentation, management and outcomes.

In September 2001, a 23-year-old woman was referred to the Oral and Maxillofacial Surgery Department for evaluation and treatment of a left-sided facial swelling. The mass had been growing slowly over a 1-year period with no history of trauma, fever, pain, paraesthesia or dysphagia. The patient gave informed consent to report her case. On examination, a large well-demarcated, smooth-lobular, elastic-hard, compressible, immobile mass was found on the left facial region. The bulging was not adherent to the skin and there was no discoloration, bruit, thrill or pulsation. The examination of the neck did not reveal lymphadenopathies. The patient showed a full range of mandibular motion and normal salivary flow from the major duct of the

Key words: vascular neoplasm; hemangiopericytoma; infratemporal fossa; surgery

Corresponding Author:
Dr. Antonino Maniaci,
ENT Department of University of Catania,
95100, Via Santa Sofia,
Catania, Italy
Tel.: +39.0953781103
e-mail: tnmaniaci29@gmail.com

0393-974X (2020)
Copyright © by BIOLIFE, s.a.s.
This publication and/or article is for individual use only and may not be further reproduced without written permission from the copyright holder.
Unauthorized reproduction may result in financial and other penalties
DISCLOSURE: ALL AUTHORS REPORT NO CONFLICTS OF INTEREST RELEVANT TO THIS ARTICLE.

parotid gland. The intraoral hard and soft tissues were completely normal, and the caudal aspect of the mass was palpated in the posterior maxillary region where a partial obliteration of the left gingiva-buccal sulcus was observed. Fine needle aspiration obtained only blood. A careful intraoral punch biopsy attempt was hampered by copious bleeding, which required haemostatic package and suture. The subsequent histology was inconclusive. A post-contrast computed tomographic scan confirmed an enhanced soft-tissue mass extending from the left infratemporal fossa to the homolateral mandibular ramus with no evidence of bony destruction or of intracranial extension. Magnetic resonance imaging (MRI) with gadolinium enhancement showed a large lobular-shaped mass that was embedding exteriorly the inner surface of the zygomatic arch and of the masseter muscle and posteriorly the temporal muscle and the lateral surface of the external pterygoid muscle (Fig. 1). In all its extension the mass showed clear contouring without signs of surrounding anatomical invasion. The tumour was highly perfused. This was confirmed by angiography (Fig. 2).

The supplying vessel originating from the left maxillary artery was selectively embolized. Thereafter, the tumour was surgically resected via a transfacial route by means of Weber-Ferguson approach. Macroscopically, the specimen consisted of a regularly pseudo capsuled lobular-mass measuring 6.5 x 5 x 2.5 cm in its greatest dimensions (Fig. 3). On cross surface, a solid portion was observed of the lesion intermingled with cystic features with gray-brown haemorrhagic areas and a jelly-like consistency. Sections from formalin-fixed tissue stained with haematoxylin and eosin exhibited round and spindle-shaped tumour cells arranged in nest patterns with ill-defined borders and round-to-oval nuclei surrounding the endothelial-lined vascular channels (Fig. 4). The anastomosing vessel ranged from capillary to large sinusoidal spaces, revealing a multiple staghorn pattern. Cellular pleomorphism was minimal and more than two mitotic figures per 10 high-powered fields were present. The definitive histopathological diagnosis was consistent with HPC.

The postoperative course was entirely uneventful, and the patient was discharged from the hospital on the fifth postoperative day. After 18 years of clinic-instrumental recall examinations there is no evidence of local recurrence or distant metastases.

DISCUSSION

Since its descriptions in 1942 by Stout and Murray, hemangiopericytoma has evoked controversy mainly because of its uncertain pathological entity. Several articles have questioned whether it is a histopathologic pattern or a clinicopathologic entity, a diagnosis of exclusion, a wastebasket diagnosis or a dying breed (4-6). Basically, HPC is characterized as benign or malignant, round to spindle-shaped cell tumour with numerous "staghorn" branching vascular channels. First of all, the histologic, immunohistochemical, and ultrastructural features of HPC seem to be rather unspecific. The HPC-like vascular pattern can be present in many neoplasms such as synovial sarcoma, mesenchymal chondrosarcomas, benign and malignant fibrous histiocytoma, malignant peripheral nerve sheath tumours, solitary fibrous tumours, malignant mesotheliomas, leiomyosarcomas, thymomas, sarcomatous carcinomas, endometrial stromal sarcomas (7). Secondly, there is a clearly noticeable variation in the clinical course, and histologic grading does not necessarily correlate with biological behaviour. According to the World Health Organization, HCP is graded as grade II and III, depending on the mitotic rate (› 5 mitoses per 10 high-power fields), high cellularity, nuclear pleomorphism, haemorrhage and necrosis. Thirdly, there is a lack of understanding regarding the nature and function of the pericytes. Originally identified by Rouget in 1873 and subsequently described by Zimmermann in 1923, these are cells with modified, smooth muscle characteristic that are highly arborized and arranged alongside capillary vessels where they have a contractile capability and are responsible for vessel calibre regulation, and modulating both flux and permeability. However, other authors have postulated that pericytes represent versatile precursors of other mesenchymal cells, such as fibroblasts (8). There is no general agreement as to the aetiology of this neoplasm, although HPC has been linked to infection by an oncogenic virus,

traumatic factors, prolonged steroid therapy and hormonal imbalance. Recent biomolecular research suggests that endothelial and non-endothelial sources of angiogenetic factors seem to regulate pericyte recruitment and influence vascular pattern formation during the pathogenetic development of HPC (9, 10).

Enzinger and Smith have allocated this uncommon tumour to two groups: an adult type and a congenital or infantile type. In elderly patients, the tumour seems to be deeply sited, located in muscle tissue and showing more frequently a malignant course, whereas the congenital or infantile forms are almost invariably superficial in site, and appear to behave in a benign fashion. In the head and neck area, this neoplasm presents in a rather unspecific way; often, symptoms are directly related to the anatomic location of the neoplasm.

Computed tomography scan is superior to most studies, but it often fails to define planes, may not always clearly indicate the vascularity of the lesion,

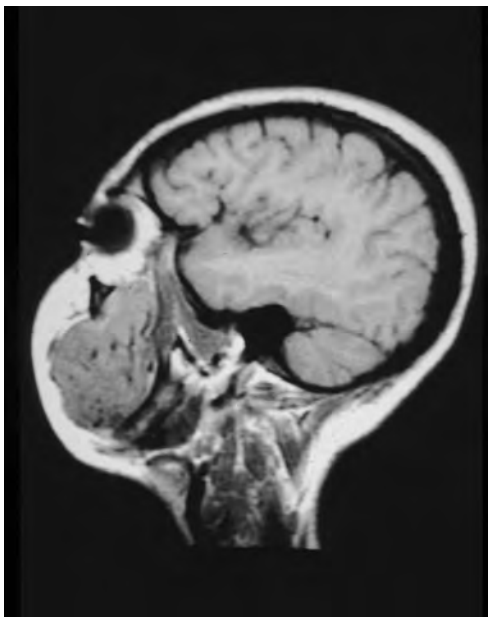


Fig. 1. *Sagittal T1-weighted MR image depicts a large, well demarcated lobular soft-tissue mass extending from the left infratemporal fossa to the mandibular ramus. On this sequence the lesion shows an inhomogeneous matrix with prominent internal flow void.*



Fig. 2. *Common carotid angiography demonstrating a highly vascular lesion with dense staining and displacement of major vessel.*

and can underestimate the full extent of the mass. MR imaging findings, albeit not specific, may reveal a well to fairly circumscribed lobular soft tissue mass with intermediate signal intensity on T1-weighted sequences, mild hyper-intensity on T2-weighted sequences and a marked gadolinium enhancement. A feeder vascular pedicle with radial branching wrapping a well-demarcated tumour stain, such as observed in our case, is reported as a characteristic angiographic finding in HPC, therefore it is not of unequivocal value in all cases.

The large number of possible diagnoses of swelling of the infratemporal fossa and aspecificity of the clinic-instrumental presentation make a suspect diagnosis extremely difficult and only a detailed histopathological assessment can lead to the correct definitive diagnosis (11).

A review of the ten reported cases of infratemporal fossa primary HPC (Table I), including our case described herein, revealed a slight sex predominance (6 females, 4 males) with a mean age of 39 years. The most common clinical complaint was a palpable painless mass (9/10). Radical surgery was the treatment of choice (9/10). Complete surgical resection is considered the mainstay of treatment for localized and resectable tumours, giving an approximately overall cure rate of 50% at all sites. Preoperative embolization has been suggested as



Fig. 3. *Surgical specimen measuring 6.5 x 5 x 2.5 cm in its greatest dimensions.*

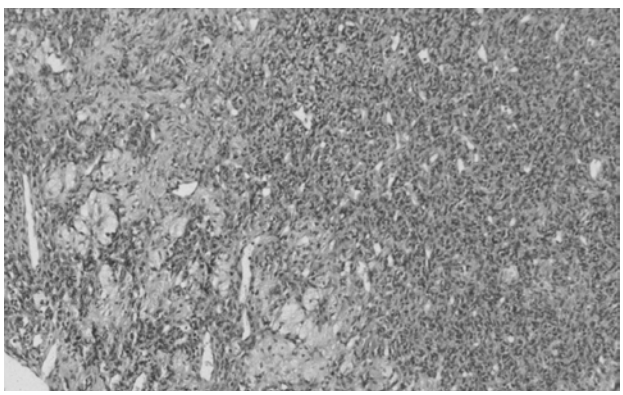


Fig. 4. *Haematoxylin and Eosin section showing marked proliferation of round to spindle-shaped cells with atypical cellularity around branching vessels (Original magnification X 150)*

an adjunct for decreasing tumour vascularity and size in order to obtain a successful resection. Of the ten reported cases, only six patients received perioperative embolization, and virtually no bleeding was encountered during tumour resection, while the remaining HPCs were amenable to surgical resection without embolization.

The usefulness of adjuvant radiant therapy has not been fully supported in the literature, although several studies suggest that radiotherapy can be used in case of incomplete resection, unresectable or recurrent disease. Chemotherapy can be useful for preoperative tumour reduction as a postoperative adjunct for tumour metastases and for palliative purposes. Positive responses have been reported for Adriamycin alone or in combination with cyclophosphamide, vincristine, methotrexate or actinomycin D, although several authors still consider HPC chemotherapy-resistant. In our review, one patient with metastatic disease died within a short period of receiving chemotherapy.

In spite of light, scanning and transmission electron microscopy as well as immunohistochemical and electron microscopical studies, no definite histological criteria indicative of benign or malignant HPCs could be established. The relapses and/or occurrence of metastases even after many years, as observed in our review series, makes the existence of benign variant once again questionable. It appears appropriate to

Table I. *Previous cases of primary HPCs involving the infratemporal fossa reported in the literature.*

Case N°	Source	Sex/Age	Clinical Complaints	Treatment	Tumour size	Mitotic Features	Follow-up	Status
1	Philippou et al. (1992)	M/27	Painless facial swelling	Embolization-Surgery-Radiotherapy	4 cm	8 mitosis x 10 HPF	N.D.	NED
2	Philippou et al. (1992)	F/53	Slow growing mass	Surgery	8 cm	Sparse	16 years	Recurrent multiple relapses treated with radio-chemotherapy; death for liver metastatic disease
3	Piral et al. (1995)	F/24	Painless facial swelling	Embolization-Surgery	5 cm	Sparse	3 years	NED
4	Hemar et al. (1996)	M/61	Otitis, Epistaxis*	Embolization-Surgery	N.D.	N.D.	15 months	NED
5	Kanazawa et al. (2001)	M/42	Painless facial swelling, facial palsy	Embolization-Surgery	2.7 x 2.5 cm	Absent	5 years	NED
6	Bianchi et al. (2002)	F/72	Painless facial mass	Embolization-Surgery	3.2 x 4.2 cm	Sparse	3 years	NED
7	Boulaich et al. (2003)	M/16	Oropharingeal mass, dysphagia	Surgery	N.D.	Sparse	10 years	NED
8	Boulaich et al. (2003)	F/60	Painless facial swelling	Surgery	N.D.	Absent	3 years	Death for untreatable local relaps and bone metastatic disease
9	Shetty et al. (2007)	F/12	Painless facial mass, visual disturbance	N.D.**	10 x 10 cm	Sparse	N.D.	N.D.
10	Pacino et al. 2019	F/23	Painless facial mass, intraoral bulging	Embolization-Surgery	6.5 x 5 cm	2 mitosis x 10 HPF	11 years	NED

*N.D: not defined; NED: no evidence of disease; HPF: High-power fields. * This patient had a history of three prior resection of HPC of the infratemporal fossa. ** In this patient only, a biopsy was performed*

consider all HPCs as potentially malignant. The clinical course alone determines whether or not the tumour is clustered benign or malignant.

HPC of the head and neck are believed to behave more favourably compared with their counterparts in other anatomic sites. No apparent explanation for this less malignant behaviour is evident, and the reported recurrence rate in literature ranges from 40-50%. Data from our review series seem to support the aforementioned contention with a recurrence rate of 22%. Overall, metastases occur in 18-50% of patients, mostly to the lung, liver and bone. Given the rarity and lack of unequivocal opinions on the management of the pathology, it is very important to establish specific guidelines for the correct treatment of the same (12).

REFERENCES

1. Batsakis JG, Rice DH. The pathology of head and neck tumors: vasoformative tumors, part 9B. Head Neck Surg 1981; 3(4):326-39
2. Stout AP, Murray MR. Hemangiopericytoma: a vascular tumor featuring Zimmermann's pericytes. Ann Surg 1942; 116 (1):26-33. doi:10.1097/00000658-194207000-00004
3. McMasterMJ,SouleEH,IvinsJC.Hemangiopericytoma. A clinicopathologic study and long-term followup of 60 patients. Cancer 1975; 36(6):2232-44. doi:10.1002/cncr.2820360942
4. Enzinger FM, Smith BH. Hemangiopericytoma. An analysis of 106 cases. Human Pathol 1976; 7(1):61-82. doi:10.1016/s0046-8177(76)80006-8
5. Spinato G, Cazzato G, Ferlito S, et al. Therapeutical innovations and medical responsibility: What's new in otolaryngology. Acta Medica Mediterranea 2018; 34:307-12. doi:10.19193/0393-6384_2018_2_49
6. Sutbeyaz Y, Selimoglu E, Karasen R, Ciftcioglu A, Ozturk A. Haemangiopericytoma of the middle ear: case report and literature review. J Laryngol Otol 1995; 109:977-79. doi:10.1017/S0022215100131809
7. Cocuzza S, Di Luca M, Maniaci A, et al. Precision treatment of post pneumonectomy unilateral laryngeal paralysis due to cancer. Future Oncol 2020 (London, England). doi:10.2217/fon-2019-0053
8. Galletti B, Gazia F, Freni F, Sireci F, Galletti F. Endoscopic sinus surgery with and without computer assisted navigation: A retrospective study. Auris Nasus Larynx 2019; 46(4):520-25. doi:10.1016/j.anl.2018.11.004
9. Abdel-Fattah HM, Adams GL, Wick MR. Hemangiopericytoma of the maxillary sinus and skull base. Head Neck1990; 12(1):77-83
10. Cocuzza S, Marino S, Gulino A, et al. ENT involvement and orobuccal movements' disorders in Pandas patients: assessment and rehabilitations tools. Eur Rev Med Pharmacol Sci 2019; 2 (10):4110117. doi:10.26355/eurrev_201905_17912
11. Shetty SR, Chatra L, Shenai KP. Orofacial haemangiopericytoma--a rare case. Dentomaxillofac Radiol 2007; 36(7):437-40. doi:10.1259/dmfr/57664386
12. Ciofalo A, Gulotta G, Iannella G et al. Giant Cell Arteritis (GCA): Pathogenesis, Clinical Aspects and Treatment Approaches. Currt Rheumatol Rev 2019; 15(4):259-68. doi:10.2174/1573397115666190227194014

LETTER TO THE EDITOR

CONSERVATIVE TREATMENT OF SACROILIAC JOINT PAIN WITH EXTRACORPOREAL SHOCKWAVE THERAPY

A. NOTARNICOLA[1,2], G. MACCAGNANO[1,2], L. MORETTI[1], M. SALVEMINI[1], F.P. BIANCHI[3], I. COVELLI[1,2], S. TAFURI[2,3] and B. MORETTI[1,2]

[1]Orthopedic Unit, Aldo Moro University of Bari, Department of Basic Medical Science, Neuroscience and Sense Organs, General Hospital, Bari, Italy; [2]Course of Motor and Sports Sciences, Aldo Moro University of Bari, Department of Basic Medical Science, Neuroscience and Sense Organs, Bari, Italy; [3]Hygiene Unit, Aldo Moro University of Bari, Department of Biomedical Science and Human Oncology, General Hospital, Bari, Italy

Received September 8, 2019 – Accepted March 12, 2020

To the Editor,

The largest axial joint in the body is the sacroiliac joint (SIJ) (1). The anatomy and C-shape of sacroiliac (SI) allow to ensure the stability and to cope with the shearing forces, vertical load and movement. On the other hand, several muscles (including the piriformis, biceps femoris, gluteus maximus and minimus, erector spinae, latissimus dorsi, and iliacus muscles), as well as the thoracolumbar fascia, guarantee the mobility of the SIJ.

The SIJ may be affected by pathologic disorders, presenting as low back, sacral, pelvic, gluteal, or general hip pain. There are conservative treatment options which include medication optimization, physical therapy, therapeutic injection and radiofrequency ablation (2). With regard to medical and physical therapy interventions, different options are available: prolotherapy, radiofrequency ablation, repetitive exercises, manual joint mobilization, manipulation, bracing, massage, patient education, aerobic conditioning, general therapeutic exercise and electrotherapeutic modalities such as heat, ultrasound, electrical stimulation, intraarticular SIJ steroid injections, and ablation of the dorsal ramus of L5 as well as the S1-S3 dorsal rami innervating the SIJ. Currently, there are no guidelines nor management plans for this dysfunction; physicians usually refer to it as low back pain (LBP) and physiotherapists treat the pain as LBP. Extracorporeal shockwave therapy (ESWT) is a physical stimulation used in different areas such as urology, plastic and muscular-skeletal pathologies (3-5). ESWT has proved to be effective in treating musculoskeletal disorders due to its angiogenic, analgesic and anti-inflammatory effects. Starting from this assumption and considering the biological effects of the therapy, the aim of this study is to verify the effect of ESWT on low back pain induced by sacroiliac joint dysfunction.

MATERIALS AND METHODS

A prospective randomized study was designed in order to assess the clinical efficiency of ESWT for sacroiliac joint pain. The study was conducted according to the Declaration of Helsinki and the guidelines for Good Clinical Practice. The study was approved by the local Ethics Committee. Prior informed consent to participate in the study was given by all subjects. All subjects' medical

Key words: low back pain; sacroiliac joint dysfunction; pelvic girdle pain; randomized controlled trial; quality of life

Corresponding Author:
Dr Angela Notarnicola,
Orthopedics Unit, Aldo Moro University of Bari, Medical School,
Department of Basic Medical Science, Neuroscience and Sense Organs,
General Hospital, Piazza Giulio Cesare 11, 70124 Bari, Italy
Tel.: +39 0805592938
e-mail: angelanotarnicola@yahoo.it

0393-974X (2020)
Copyright © by BIOLIFE, s.a.s.
This publication and/or article is for individual use only and may not be further reproduced without written permission from the copyright holder.
Unauthorized reproduction may result in financial and other penalties
DISCLOSURE: ALL AUTHORS REPORT NO CONFLICTS OF INTEREST RELEVANT TO THIS ARTICLE.

history was examined for exclusion and inclusion criteria.

Study subjects

Thirty patients were enrolled from our Orthopedic Unit and randomized into two groups. Fifteen subjects (ESWT group) received ESWT, while the other fifteen (exercise group) were treated with an exercise protocol. All the patients enrolled in the study were taking nonsteroidal anti-inflammatory drugs (NSAIDs) or pain killing drugs, and these therapies were interrupted at the beginning of the study, 2 weeks before the start of therapy. Inclusion criteria were: age >18 years, SI pain diagnosis of at least 2 months based on clinic and provocative tests, and diagnosed SIJ dysfunction due to degenerative sacro-ileitis or SIJ disruption, Oswestry Disability Questionnaire (ODQ) ≥ 18%, and Visual Analogic Scale (VAS) ≥ 5. The SIJ was identified as the main pain generator using the following criteria: i) pain close to the posterior superior iliac spine and the patient could point with a single finger to the location of pain (Fortin Finger Test); ii) at least 3 positive findings out of 5 provocative physical examination maneuvers for SIJ pain [including pelvic compression, thigh thrust, flexion abduction external rotation (FABER), distraction, and Gaenslen's test]; and iii) at least 50% pain reduction on fluoroscopically guided injection of local anesthetic into the joint (SIJ block). Patients were excluded from the study if they reported contraindications to ESWT (cancer or current or previous infections of the affected area, a cardiac pacemaker, or pregnancy, epilepsy, coagulation disorders due to pathologies or drugs). Furthermore, patients were excluded for the following reasons: severe back pain due to other causes (e.g., known hip or spine conditions), diagnosed sacral pathology of other origin, recent (<1 year) major trauma to the pelvis, metabolic bone disease (osteoporosis or other bone conditions), any chronic rheumatologic, neurologic or psychiatric condition that could interfere with physical therapy, infection, or suspected drug abuse. The protocol did not allow interventional procedures (e.g., SIJ steroid injections, radiofrequency ablation of the lateral branches of sacral nerve roots) during the previous and the following 6 months. Each patient was evaluated on recruitment (T0), 1 month (T1), 3 months (T2), 6 months (T3) and 1 year (T4).

Sample size

The present study aimed to verify the equality of VAS score means in the two treatment groups: ESWT *vs* exercise therapy. To test this hypothesis, significance level (alpha) was set at 0.050 and a 2-tailed test was used. We proposed a sample size of at least 11 patients for each group of treatment. With this sample size and assuming between two groups a mean difference of 1.5 points and a common within-group standard deviation of 1.3, the study had to have power of 82% to yield a statistically significant result.

Baseline assessments included a detailed medical history and physical examination. Clinical results were evaluated using visual analogic scale (VAS) and Oswestry Disability Questionnaire (QDQ) at the time of recruitment (T0) and at the follow-up (FU) visits at 1 and 3, 6 and 12 months (T1, T2, T3, T4, respectively). At baseline, patients were randomized 1:1 to receive ESWT or exercise therapy. Treatments were allocated according to a sequential randomization list generated using Stata MP12 statistical software. Patients were randomized into an ESWT group (3 sessions, 1 per week) or an Exercise group (2 sessions per week for 8 weeks).

ESWT group

ESWT was applied using an electromagnetic generator (Minilith SL1, Storz Medical, Tägerwilen, Swiss) equipped with in-line ultrasound-guidance (Aloka SSD 900, Aloka Co., Ltd. Tokyo, Japan), and was administered once per week for three sessions, in accordance with guidelines (6). The patient was placed in a prone position (Fig. 1). Under ultrasound guidance, the depth of the probe was adjusted so as to treat structures, which represented the main affected sides in SIJ. The sacrum was flat and wide, leaving space to position the probe along SIJ (between SIJs and the foramina). At the same time, its length and orientation potentially could make all the joint components, such as nerve roots, ligaments, and muscles, well exposed. The probe was oriented perpendicular to the posterior SIJ line, and moved up and down along the joint line (Fig. 2). Coupling gel was used between the shockwave head and low back region. No local anesthesia was needed. We used a low-medium energy level (0.03 mJ/mm2), which was consistent with patient pain tolerance levels, during the treatment. At each treatment session, 2000 impulses were applied. Repetition frequency of shockwave pulses was 4 Hz.

Exercise group

All participants in the Exercise group received

individual treatment sessions of 50 min, generally 2 times per week, for a total of 8 weeks that focused on mobilization and stabilization exercises for control and stability (7). Each patient was followed by a physical therapist and instructed to conduct 8 exercises. In each session all exercises were included. The treatment progression followed a pragmatic approach and was determined by the clinical improvement revealed by a physiotherapist. The first four exercises were unilateral and were reproduced for each side. These exercises were developed to restore good triplanar pelvic and hip position and maintain it during movement: #1 exercise "bridging", #2 exercise "adductor ball squeeze", #3 exercise "abdominal marching" and #4 exercise "reverse curl-ups". The following two exercises were prescribed to facilitate elongation of posterior ligaments and carried out in side-lying position: #5 exercise "a scissor slide" and #6 exercise "a knee-to-knee". The last two exercises were performed in a supine hook lying position and were prescribed for muscle activation: #7 exercise "basic bridge exercise" and #8 exercise "bilateral adductor ball squeezes". The plan of treatment included an average of one to three sets of exercises, consisting of 8-10 repetitions.

Statistical analysis

The compiled forms were put into a database using Excel software and analyzed with STATA MP15 software. Continuous variables were expressed as mean ± standard deviation and range otherwise as median, interquartile range and range, instead categorical variables were expressed as proportions. The Skweness and Kurtosis test was used to evaluate the normality of continuous variables. For the not normally distributed variables a normalization model was built up, using the logarithmic function. The Student's *t*-test for independent data (parametric) was used to compare normal or normalized continuous variables between the two groups. The ANOVA test for repeated measurements was used to compare normal or normalized continuous variables between groups and times.

The Wilcoxon Rank-Sum (non-parametric) test was used to compare the non-normalizable continuous variables between groups, the Friedman test (non-parametric) was used to compare them between several times, and the Wilcoxon signed-rank test (not parametric) was used to compare them between individual times. The chi-squared test and the Fisher exact test were used to compare the categorical variables between groups.

Univariate linear regression was used for each individual outcome to evaluate the association between VAS at T2, Oswestry Disability Questionnaire at T2 (both continuous variables normally distributed or normalizable) and the corresponding variable at T0, age, gender, BMI, tobacco habit (yes/no), the articulation side concerned, previous physiokinesitherapy (yes/no); Student's *t*-test and the correlation coefficient, with a 95% confidence interval (95% CI), were calculated. A multivariate linear regression model was constructed for each outcome, using as determinant the group variable adjusted for those variables associated with the single outcome in the univariate regression; the correlation coefficients were calculated, with 95% confidence interval (95% CI) and the *t*-student test.

To evaluate the association between the number of positive tests at the T2 objective examination (non-normalizable continuous variable) and the respective variable at T0, age, gender, BMI, tobacco habit (yes/no), the affected joint side, previous conservative treatment (yes/no), the univariate non-parametric regression was used; the observed estimate was calculated, with 95% confidence interval (95% CI) and the z-score test.

A non-parametric multivariate regression model was constructed for each outcome, using as determinant the group variable adjusted for those variables associated with the single outcome in univariate regression; Observed Estimates (Obs. Est.) were calculated, indicating 95% confidence interval (coef.) (95% CI) and the z-score test. A p-value <0.05 was considered significant for all the tests.

RESULTS

The average age was 62.6±11.8 (43.0 – 82.0) years old and the BMI was 163.4±7.5 (150.0–179.0) kg/m^2. In 53.3% of patients the SI pain was localized on the right side, in the remaining 46.7% on the left. No adverse effects were noted during the performed procedures. By comparison of the two groups, there were no statistically significant differences in relation to the epidemiological, anthropometric and clinical evaluations at recruitment (Tables I).

We found a statistically significant difference in the comparison of the number of positive tests at the physical examination between times in the total

Table I. *Average, standard deviation and range of number of positive tests at physical examination, of VAS scale and of the Oswestry Disability Questionnaire score, for follow-up and groups.*

Time	ESWT group	Exercise group	Total	z	p
n. positive test at physical examination					
T0	3.9±0.9 (3.0 – 5.0)	4.0±0.8 (3.0 – 5.0)	3.9±0.9 (3.0 – 5.0)	0.4	0.657
T1	3.0±1.3 (0.0 – 5.0)	2.9±0.7 (2.0 – 4.0)	2.9±1.0 (0.0 – 5.0)	0.4	0.720
T2	2.5±1.2 (0.0 – 5.0)	2.7±0.5 (2.0 – 3.0)	2.6±0.9 (0.0 – 5.0)	0.5	0.645
T3	2.2±1.0 (0.0 – 4.0)	2.3±0.6 (2.0 – 4.0)	2.3±0.8 (0.0 – 4.0)	0.1	0.908
T4	2.1±1.7 (0.0 – 7.0)	2.3±0.6 (1.0 – 3.0)	2.2±1.3 (0.0 – 7.0)	1.2	0.216
VAS					
T0	7.5±1.3 (6.0 – 10.0)	7.0±1.3 (5.0 – 9.0)	7.3±1.3 (5.0 – 10.0)	0.9	0.382
T1	5.6±1.4 (4.0 – 8.0)	6.1±1.4 (3.0 – 8.0)	5.9±1.4 (3.0 – 8.0)	1.1	0.251
T2	3.9±2.0 (0.0 – 8.0)	5.6±1.9 (3.0 – 8.0)	4.8±2.1 (0.0 – 8.0)	2.0	0.045
T3	3.8±2.3 (0.0 – 8.0)	5.1±2.0 (2.0 – 8.0)	4.5±2.2 (0.0 – 8.0)	1.4	0.153
T4	3.8±2.0 (0.0 – 7.0)	4.4±2.0 (2.0 – 8.0)	4.1±2.0 (0.0 – 8.0)	0.6	0.528
Oswestry Disability Questionnaire (0-100)					
T0	38.9±9.3 (18.0 – 50.0)	41.3±13.6 (18.0 – 74.0)	40.1±11.5 (18.0 – 74.0)	0.0	0.967
T1	28.7±14.4 (0.0 – 48.0)	35.5±16.2 (10.0 – 74.0)	32.1±15.5 (0.0 – 74.0)	0.8	0.442
T2	22.9±14.4 (0.0 – 48.0)	33.9±17.8 (10.0 – 74.0)	28.4±16.8 (0.0 – 74.0)	1.6	0.100
T3	19.7±14.4 (0.0 – 40.0)	28.3±14.5 (8.0 – 58.0)	24.1±14.9 (0.0 – 58.0)	1.5	0.142
T4	18.1±11.5 (0.0 – 38.0)	26.3±15.4 (8.0 – 58.0)	22.2±14.0 (0.0 – 58.0)	1.4	0.157

The evaluation times are at recruitment (T0) and 1, 3, 6 and 12 months later (T1, T2, T3, T4). Statistical analysis is reported.

sample (Fr = 54.8; p = 0.000) and in the ESWT group (Fr = 17.6; p = 0.000); there was also a statistically significant difference of VAS between FUs (F = 36.5; p = 0.000) and in the interaction between FUs and group (F = 4.0; p = 0.005); there was a statistically significant difference of ODQ score between the FUs (F = 33.6; p = 0.000; Table II).

There were no statistically significant differences in the comparison of outcomes between groups and different FUs (p> 0.05). The comparison between different FUs for each outcome is described in Table II. By the univariate analysis we observed a statistically significant association between the number of positive tests at T2 and at T0 (Obs. Est. = 0.5; 95% CI = 0.2-0.9; z = 2, 6; p = 0.010); between VAS at T2 and group (coef. = - 1.7; 95% CI = -3.1 - -0.2; t = 2.4; p = 0.025); between ODQ at T2 and at T0 (coef. = 1.2; 95% CI = 0.8-1.5; t = 7.2; p = 0.000); between ODQ at T2 and age (coef. = 42.2; 95% CI = 12.8 - 71.6; t = 2.9; p = 0.006). There were no statistical associations between the outcomes and the determinants in the analysis (p> 0.05).

By multivariate analysis a statistically significant association was found between ODQ at T2 and ODQ at T0 (coef. = 0.99; 95% CI = 0.70-1.29; t = 6.9; p = 0.000), the age (coef. = 2.2; 95% CI = 7.7-42.7; t = 3.0; p = 0.007) and group (coef. = - 9.5; 95% CI = - 15.8 - -3.2; t = 3.1; p = 0.005); there was a statistically significant difference between the number of positive tests at T2 and at T0 (Obs. Est. = 0.5; 95% CI = 0.1-0.9; z = 2.4; p = 0.017), whilst there was no statistical association between the number of positive tests at T2 and group (ESWT/exercise) (Obs. Est. = -0.1; 95% CI = -0.7-0.5; z = 0.2; p = 0.829). The population did not undergo other therapeutic interventions during FU nor they did adopt changes in occupational behavior.

DISCUSSION

The results of our experience supported that SW could be useful in management of SIJ pain. We found an improvement in clinical tests, pain and disability

Table II. *Comparison of individual outcomes at different follow-up times*

Comparison	Positive test		VAS		ODQ	
	test	p	test	p	test	p
T0 *vs* T1	z=4.3	0.000	t=5.8	0.000	t=5.8	0.000
T0 *vs* T2	z=4.6	0.000	t=6.2	0.000	t=6.3	0.000
T0 *vs* T3	z=4.7	0.000	t=6.9	0.000	t=6.9	0.000
T0 *vs* T4	z=4.4	0.000	t=7.5	0.000	t=9.1	0.000
T1 *vs* T2	z=2.5	0.012	t=3.8	0.001	t=2.8	0.008
T1 *vs* T3	z=3.4	0.001	t=4.2	0.000	t=3.5	0.002
T1 *vs* T4	z=3.0	0.003	t=5.5	0.000	t=5.3	0.000
T2 *vs* T3	z=2.5	0.012	t=1.7	0.107	t=2.5	0.017
T2 *vs* T4	z=2.5	0.011	t=3.0	0.005	t=3.7	0.001
T3 *vs* T4	z=1.1	0.290	t=1.7	0.094	t=2.1	0.048

Statistical analysis is reported for results of clinical evaluation, pain score (VAS) and disability (Oswestry Disability Questionnaire, QDS) of all the population of the study.

in the population enrolled at the different FUs. At T2 we found a statistically significant difference in the SW group for VAS and Oswestry Disability.

The rationale of this application in SI joint pain is modulating the joint inflammation, reducing the activation of nociceptors, resetting the osteo-articular imbalance and relaxing the muscles involved locally. On the basis of these biological hypotheses, shockwave therapy has been used in the treatment of low back pain and sacro-ileitis (8-10). In low back pain, the ESWT is responsible for the reduction of pain, functional recovery and sensory and motor conduction deficit recovery of peripheral nerves (8-10). To date, in the only work published on the application of shock waves in SIJ pain, the treated group showed a significant reduction of pain at 4 week post-treatment, whilst a trend to improvement in disability was recorded, but it was not significant (11). In our case study, the control group presented an improvement trend at the different FUs. It showed a clinical and functional improvement, even though it was not statistically significant. This result is consistent with the literature, suggesting that exercises only in SI joint pain treatment may have limited benefit, if not integrated in multidisciplinary treatment, for example with pharmacological or instrumental therapy (12).

In conclusion, our work suggests that ESWT is efficient for the treatment of sacro-iliac pain, but the treatment represents a challenge for the clinician. Subsequent studies can verify the effectiveness of a combined treatment of shockwave therapy and therapeutic exercise, allowing to combine the bio-stimulatory effects of physical therapy to the action of stabilization exercises for SIJ.



Fig. 1. *The patient's position and placement of the probe during ESWT.*

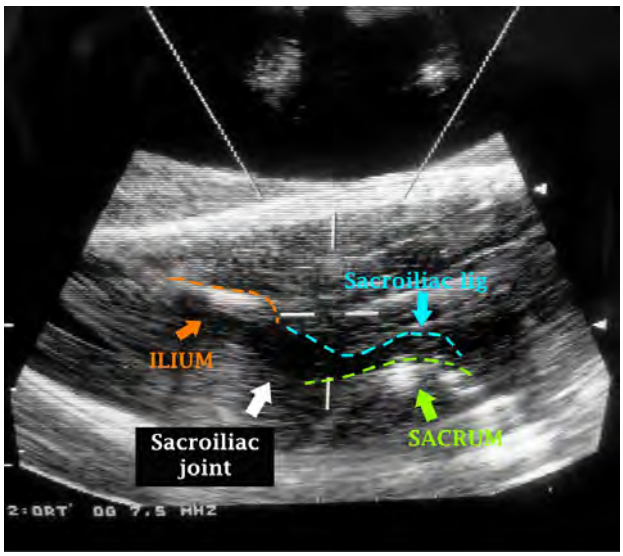


Fig. 2. *Identification of the sacroiliac joint under ultrasound guidance: in transverse projection it is an interruption of the hyperechoic profile of the bone cortex, corresponding to the joint space between the sacrum and the ileum.*

ACKNOWLEDGEMENTS

The authors thank Brian John Molloy B.A. for language revision. Furthermore, the authors thank the photographer Donata Paolini for the adjustments of the two images.

REFERENCES

1. McKenzie-Brown AM, Shah RV, Sehgal N, Everett CR. A systematic review of sacroiliac joint interventions. Pain Physician 2005; 8:115-25.
2. Cohen SP. Sacroiliac joint pain: a comprehensive review of anatomy, diagnosis, and treatment. Anesth Analg 2005; 101(5):1440-53.
3. D'Agostino MC, Frairia R, Romeo P, et al. Extracorporeal shockwaves as regenerative therapy

in orthopedic traumatology: a narrative review from basic research to clinical practice. J Biol Regul Homeost Agents 2016; 30(2):323-32. Review.
4. Moretti B, Iannone F, Notarnicola A, Lapadula G, Moretti L, Patella V, Garofalo R. BMC Musculoskelet Disord 2008; 9:16.
5. Notarnicola A, Moretti L, Tafuri S, et al. Shockwave therapy in the management of complex regional pain syndrome in medial femoral condyle of the knee. Ultrasound Med Biol 2010; 36(6):874-9.
6. Tiele R. New guidelines for ESWT. Newsletter ISMST 2009; 5:20.
7. Vleeming A, Albert HB, Östgaard HC, Sturesson B, Stuge B. European guidelines for the diagnosis and treatment of pelvic girdle pain. Eur Spine J 2008; 17:794-819.
8. Notarnicola A, Maccagnano G, Gallone MF, et al. Extracorporeal shockwave therapy versus exercise program in patients with low back pain: short-term results of a randomised controlled trial. J Biol Regul Homeost Agents 2018; 32(2):385-89.
9. Lee S, Lee D, Park J. Effects of extracorporeal shockwave therapy on patients with chronic low back pain and their dynamic balance ability. J Phys Ther Sci 2014; 26(1):7-10.
10. Han H, Lee D, Lee S, Jeon C, Kim T. The effects of extracorporeal shock wave therapy on pain, disability, and depression of chronic low back pain patients. J Phys Ther Sci 2015; 27(2):397-99.
11. Moon YE, Seok H, Kim SH, Lee SY, Yeo JH. Extracorporeal shock wave therapy for sacroiliac joint pain: A prospective, randomized, sham-controlled short-term trial. J Back Musculoskelet Rehabil 2017; 30(4):779-84.
12. Al-Subahi M, Alayat M, Alshehri MA, et al. The effectiveness of physiotherapy interventions for sacroiliac joint dysfunction: a systematic review. J Phys Ther Sci 2017; 29(9):1689-94.

LETTER TO THE EDITOR

ADVERSE EVENTS IN DRY NEEDLING AND MESOTHERAPY TREATMENT FOR LOCALIZED MYOFASCIAL AND MUSCOLOSKELETAL PAIN

G. RONCONI[1], S. SALINI[1], G. MACCAURO[2], M. MAMMUCARI[3] and P.E. FERRARA[1]

[1]University Policlinic Foundation A. Gemelli IRCCS, Rome, Italy; [2]Orthopedic and Traumatology Institute, Catholic University of the Sacred Heart, Rome, Italy; [3]Primary Care Unit ASL RM 1, Rome, Italy

Received October 28, 2019 – Accepted March 17, 2020

To the Editor,

Myofascial pain is commonly seen in clinical settings and negatively influences patient's daily life. It is a frequent cause of musculoskeletal pain characterized by trigger points and limited range of motion in joints. It affects more than three-quarters of the world's population. Mesotherapy and dry needling are reported as effective treatments for this myofascial and musculoskeletal localized pain.

Mesotherapy consists in intradermal microinjections of drugs (nonsteroidal anti-inflammatory drugs, muscle relaxants, anesthetics, and other analgesics) in the area of localized pain. The advantages of this treatment include higher time of local drug activity, lower risk of adverse events and of interactions with other drugs. The technique of dry needling involves the insertion of needles superficially or deeply into the pain area or trigger point. The needles used, in this case, are usually 0.16–0.3mm thick and 1.5-6 cm long. The needle remains in place for a short time (from 30 s to 3 min), and is then removed. We carried out a narrative review, reporting adverse events of mesotherapy and dry needling in localized myofascial and musculoskeletal pain, because of the increased interest in these arguments, as well as for the higher risk of adverse events if the techniques are practiced by non-expert and non-authorized health subjects. The MEDLINE search was done in February 2020, using PubMed, with the MeSH terms: 'adverse events, mesotherapy, intradermal therapy, dry needling and pain in humans', without limits of time and languages. The results are shown in Table I: two papers describing mesoterapy (1, 2) and six articles regarding dry needling (3-8) adverse events. Serious adverse events were described in 4 patients affected by pneumothorax treated with dry needling, and one patient with acute spinal epidural hematoma after needle application. Mild adverse events were reported in patients treated with mesotherapy for musculoskeletal or myofascial pain.

DISCUSSION

Clinical studies have shown interesting and encouraging results in the treatment of localized pain with mesotherapy (2, 10) and dry needling. The incidence of serious adverse events reported in the literature is rather rare. Pneumotorax and acute spinal epidural hematoma are associated with dry needling insertions (4, 5, 7, 8). During dry needling, bleeding was the most frequently reported adverse event, bruising was the second, followed by pain during treatment and pain after treatment. Aggravation of symptoms was followed by drowsiness, feeling faint, headache and nausea. Only mild adverse events are

Key words: mesotherapy; dry needling; pain; adverse event

Corresponding Author:
Gianpaolo Ronconi MD,
Fondazione Policlinico Universitario "A. Gemelli",
Largo Agostino Gemelli 1,
00168 Rome, Italy
Tel:. +39 3477123940
e-mail: gianpaolo.ronconi@policlinicogemelli.it

0393-974X (2020)
Copyright © by BIOLIFE, s.a.s.
This publication and/or article is for individual use only and may not be further reproduced without written permission from the copyright holder.
Unauthorized reproduction may result in financial and other penalties
DISCLOSURE: ALL AUTHORS REPORT NO CONFLICTS OF INTEREST RELEVANT TO THIS ARTICLE.

described in patients treated with mesotherapy for musculoskeletal pain. In particular, there is a great deal of data showing that this technique is well tolerated, but adverse reactions (allergic reactions, ecchymosis, and urtica) have been described. Mesotherapy can cause mild discomfort when the needle is introduced, and this is more common in sensitive patients (1, 2).

The different pH of some medications may cause pain during injection, and adjustments of pH with NaHCO3 have been suggested to reduce discomfort. Other local transitory effects (itching, hypersensitivity, discomfort, and irritation), probably due to the type of drug or combination of drugs, have been reported (2). The use of a single drug appears to reduce the risk of local side effects, and the risk of infection is avoided if correct aseptic procedures are followed (2). Literature reports that subcutaneous infections (2) are generally caused by external contamination and malpractice rather than to the technique itself. More severe infections are reported when mesotherapy is used in cosmetic fields.

The Italian Mesotherapy Society (12) has issued recommendations to clarify how and when to apply this technique. In fact, thanks to a rigorous medical-scientific approach launched in Italy and now

Table I. *Mild and serious adverse events after mesoterapy and dry needling treatments in myofascial and musculoskeletal pain reported in literature.*

Author	Type of paper	Treatment	Mild adverse event*	Serious adverse event *
D. A. Narvarte et al (1) 2011	Retrospective study	Mesotherapy	25% (n. 67 /n. total patients 267): muscular weakness 1.5%, rash 1.5%, drowsiness 1.1% itching 1.1%	
Mammucari et al (2) 2012	Review	Mesotherapy	**Allergic reactions, ecchymosis, urtica, pain, itching, hypersensitivity discomfort, irritation, subcutaneous infection	
Brady et al (3) 2014	Review	Dry needling	19,18% (n.146 /n.total patients 7629 treated) bruising 7.55% bleeding (4.65%) pain during treatment (3.01%) pain after treatment (2.19%) aggravation of symptoms (0.88%) drowsiness (0.26%), headache (0.14%) nausea (0.13%) fatigue (0.04%) altered emotions (0.04%), shaking, itching, claustrophobia, and numbness 0.01%.	
Grusche et al (4) 2016	Case series	Dry needling		n. 2 Pneumothorax
Ronconi et al (5) 2016	Case report	Dry needling		n.1 Pneumothorax
Uygur E et al (6) 2017	Prospective controlled study	Dry needling	5,8%patiens of n. total 51: n.2 local pain n.1 local hemorrhage	
Uzar T. et al (7) 2018	Case report	Dry needling		n. 1 Pneumothorax
Berrigan et al (8) 2019	Case report	Dry needling		n.1 Acute Spinal Epidural Hematoma

**Number or percentage of patients are reported*

***Number or percentage of patients affected by mild adverse events are not reported in this review*

implemented internationally, the use of compounds not previously studied for safety and efficacy and the practice of mesotherapy by inadequately prepared personnel are strongly discouraged.

In dry needling, the needle used is regulated by the FDA as a class II medical device. In Italy the legislation provides that the practice of this method is an exclusive medical prerogative. Internationally, the practice of this technique is also carried out by physiotherapists. The correct use and application of these techniques require clinical and pharmacological skills by medical doctors and they should be undertaken following a complete clinical workup and subsequent diagnosis.

REFERENCES

1. Narvarte DA, J. Rosset-Llobet, Safety of subcutaneous microinjections (mesotherapy) in musicians Med Probl Perform Art 2011; 26:79-83.
2. Mammucari M, Gatti A, Maggiori S, Sabato AF. Role of mesotherapy in musculoskeletal pain: opinions from the Italian society of mesotherapy. Evid Based Complement Alternat Med 2012; 2012:436959. doi: 10.1155/2012/436959.
3. Brady S, McEvoy J, Dommerholt J, Doody C. Adverse events following trigger point dry needling: a prospective survey of chartered physiotherapists. J Man Manip Ther 2014; 22(3):134-40.
4. Grusche F, Egerton-Warburton D. Traumatic pneumothorax following acupuncture: a case series. Clin Pract Cases Emerg Med 2017; 1:31-32.
5. Ronconi G, De Giorgio F, Ricci E, Maggi L, Spagnolo AG, Ferrara PE. Pneumothorax following dry needling treatment: legal and ethical aspects. Ig Sanita Pubbl 2016; 72(5):505-12.
6. Uygur E1, Aktaş B2, Özkut A3, Erinç S3, Yilmazoglu EG3. Dry needling in lateral epicondylitis: a prospective controlled study. Int Orthop 2017; 41(11):2321-2325. doi: 10.1007/s00264-017-3604-1.
7. Uzar T1, Turkmen I1, Menekse EB2, Dirican A3, Ekaterina P4, Ozkaya S5. A case with iatrogenic pneumothorax due to deep dry needling. Radiol Case Rep 2018; 13(6):1246-48.
8. Berrigan W, Whitehair C, Zorowitz R. Acute spinal epidural hematoma as a complication of dry needling: a case report. PM R 2019; 11(3):313-16.
9. Paolucci T, Bellomo RG, Centra MA, Giannandrea N, Pezzi L, Saggini R. Mesotherapy in the treatment of musculoskeletal pain in rehabilitation: the state of the art. J Pain Res 2019; 12:2391-2401. doi: 10.2147/JPR.S209610.
10. Dommerholt J, Chou LW, Finnegan M, Hooks T. J Bodyw A critical overview of the current myofascial pain literature - February 2019. Mov Ther 2019; 23(2):295-305.
11. Plachouri KM1, Georgiou S1. Mesotherapy: Safety profile and management of complications. J Cosmet Dermatol 2019; 18(6):1601-5.
12. Mammucari M, Gatti A, Maggiori S, Bartoletti CA, Sabato AF Mesotherapy, definition, rationale and clinical role: a consensus report from the Italian Society of Mesotherapy. Eur Rev Med Pharmacol Sci 2011; 15(6):682-94. Review.

LETTER TO THE EDITOR

IS EXTRACORPOREAL SHOCKWAVE THERAPY EFFECTIVE EVEN IN THE TREATMENT OF PARTIAL ROTATOR CUFF TEAR?

A. NOTARNICOLA[1], G. MACCAGNANO[1], L. MARESCA[1], M.C. OLIVA[1,2], G. FARÌ[1,2], G. PAPAGNI[1,2], G. PIGNATELLI[1,2], I. COVELLI[1], G. GIOIA[1], F.P. BIANCHI[3], S. TAFURI[3] and B. MORETTI[1]

[1]Orthopaedics Unit, Department of Basic Medical Science, Neuroscience and Sensory Organs, Faculty of Medicine and Surgery, Aldo Moro University of Bari, General Hospital, Bari, Italy; [2]Rehabilitation Unit, Department of Basic Medical Science, Neuroscience and Sensory Organs, Faculty of Medicine and Surgery, Aldo Moro University of Bari, General Hospital, Bari, Italy; [3]Hygiene Unit, Department of Biomedical Science and Human Oncology, Aldo Moro University of Bari, General Hospital, Bari, Italy

Received October 5, 2019 – Accepted March 18, 2020

To the Editor,

Rotator cuff tear is a major cause of pain and shoulder dysfunction, with a prevalence of 21% in the general population (1). The lesion may be partial (with an estimated prevalence of around 13%) or total (7%). A theory of degeneration and micro-traumas has been postulated, proposing that repeated stresses could be responsible for small lesions of the tendon without the ability to heal, which should follow a more important traumatic event, responsible for the onset of a symptomatic lesion. Forty percent of rotator tears increase in size if left untreated, while none of these cases show a decrease in the tear size or spontaneous healing.

Contrasting results are reported regarding the choice of treatment. Some studies support surgical treatment, especially in the early stages of the disease, in order to prevent the progression of rotator cuff tendon degeneration and the involvement of the gleno-humeral joint (2). Other works suggest a conservative treatment such as physiotherapy to reduce pain and to prevent the progressive loss of function (3). The success rate of conservative treatment ranges from 33% to 82%.

Currently, very few data are available regarding the evidence of clinical outcome of partial rotator cuff tear treated with Extracorporeal Shockwave Therapy (ESWT). Shock waves (SW) are energy sound waves produced under water with a high voltage explosion and evaporation. In musculoskeletal diseases ESWT is able to improve blood supply and to increase cell proliferation, inducing tissue regeneration of tendons and bones (4).

The end point of the study is to verify the effects of shockwave therapy in the presence of injured tendon, also monitoring the clinical and functional aspects and the size of the lesion. The starting hypothesis is null; in fact, to date, there has been no study describing shockwave treatment of tendons with partial lesions.

MATERIALS AND METHODS

We conducted a prospective randomized clinical trial. The study was approved by the local Ethics Committee. Patients who came to our clinic with a diagnosis of a partial lesion of the rotator cuff were included in our study and gave written informed consent to participate.

Corresponding Author:
Dr Angela Notarnicola,
Orthopaedics Unit, Department of Basic Medical Science,
Neuroscience and Sensory Organs, Faculty of Medicine and Surgery,
University of Bari, General Hospital,
Piazza Giulio Cesare 11, 70124 Bari, Italy
Tel.: +39 0805592938
e-mail: angelanotarnicola@yahoo.it

0393-974X (2020)
Copyright © by BIOLIFE, s.a.s.
This publication and/or article is for individual use only and may not be further reproduced without written permission from the copyright holder.
Unauthorized reproduction may result in financial and other penalties
DISCLOSURE: ALL AUTHORS REPORT NO CONFLICTS OF INTEREST RELEVANT TO THIS ARTICLE.

The following were used as inclusion criteria: age > 18 years, capable of understanding; partial tear of supraspinatus, with lesion size in each of the three axes ≤ 11 mm, diagnosed by using ultrasound; symptoms for at least 1 month; indication of conservative treatment (3); no neurological condition that could compromise muscle strength or activity; no history of shoulder surgery during the previous 6 months; no abnormal findings on simple radiography. Exclusion criteria were: contra-indications of SW therapy (tumors, clotting diseases, anticoagulant therapy, history of epilepsy, the presence of pacemaker or defibrillator, pregnancy); massive tendon lesion of supraspinatus (> 11 mm); infiltrative and/or rehabilitative treatment in the three months prior to recruitment; rotator cuff tears which had undergone prior surgical repair or arthroscopy; pre-existing conditions associated with upper extremity pain; difficulties in follow-up; patients in a different on-going trial that would interfere with the assessment; any other reason in the judgment of the researchers. Patients were randomized 1:1 to receive shockwave treatment (ESWT) or therapeutic exercise. Treatments were divided according to a sequential randomization list using Stata MP12 statistical software. Possible adverse effects were monitored for both treatments: increased pain, joint lock, petechiae and hematoma formation, vagal crisis.

ESWT group

ESWT was applied with a Minilith SL1 (Storz Medical, Tägerwilen, Swiss) electromagnetic generator equipped with in-line ultrasound-guidance Aloka SSD 900 (Aloka Co., Ltd. Tokyo, Japan), during three sessions, at 7-day intervals, emitting 2000 impulses with an energy flux density (EFD) of 0.05 mJ/mm^2. No local anesthesia was required.

Exercise group

Patients underwent 12 weeks of therapeutic exercise for strengthening the rotator cuff and shoulder mobility. They were instructed to perform 2 different exercises 5 times a week. The program included an exercise for the anterior deltoid and an exercise for the teres minor muscle, with 2-3 min of warm up before starting the exercise program. Every week the physiotherapist graduated the exercises in relation to each patient's ability according to the pain during and after the exercise.

Sample size

The present study aimed to test the equality of VAS score in the two treatment groups: ESWT group *vs* exercise group. To test this hypothesis a significance level (alpha) was set at 0.050 and a 2-tailed test was used. We proposed a sample size of 11 patients for each group of treatment. With this sample size and assuming both a mean difference of 1.5 point (corresponding to the smallest effect that would be important to detect) between the shockwave and exercise groups and a common within-group standard deviation of 1.3, the study had to have power of 82% to yield a statistically significant result.

Outcome

The assessment times were at the time of recruitment (T0) and 3 months after recruitment (T1). The outcomes were the visual analogic scale (VAS), the American Shoulder and Elbow Surgeons Standardized Shoulder Assessment Form (ASES) and the manual muscle strength testing scale (MMT). Moreover, the size of the lesion on the three axes (longitudinal, transverse and antero-posterior) was measured by ultrasound.

Epidemiological and clinical outcomes data were put in a database built with Office Excel Software (Microsoft Corporation, Redmond, USA) and analyzed with Office Excel and STATA SE14 Software (Microsoft Corporation, Redmond, USA). Continuous variables were expressed as mean ± standard deviation and range, while categorical variables as proportions. The normality of the continuous variables was evaluated and, for those not distributed normally, a normalization model was constructed using a logarithmic function. The *t*-student test was used for independent (parametric) samples to compare the normal or normalized continuous variables between groups; the ANOVA test was performed to compare groups and timing; Fisher's exact test was used to compare the categorical variables between groups.

A simple linear regression was used for every single outcome, in order to evaluate the relationship between pain referred to T1, MMT value at T1, ASES value at T1 and the respective variable at T0, age, gender, group (ESWT/exercise), BMI, affected shoulder (right/left), time between the onset of symptoms and the recruitment (months) between lesion size on the three axes at T1. For each of the previous outcomes, a multivariate linear regression model was constructed, using as determinants

those variables that have been shown to be associated to the respective outcome in simple linear regression. The correlation coefficient was indicated calculating 95% CI and the Student's *t*-test. For all tests a value of $p < 0.05$ was considered significant.

RESULTS

The sample of the study was made up of thirty subjects, of whom 15 (50%) belonged to the ESWT group and the remaining 15 (50%) to the exercise group. Twenty (66.7%) patients were female and there were no statistically significant differences in the distribution of females per group (X2=0.0; p=1.000); the mean age of the group was 65.2±8.7 years (range = 45-81) and no statistically significant differences were observed in the comparison of the mean age between groups (t = 0.2; p=0.807). No drop-out occurred. All patients reported that they did not use drugs to manage the pain during the study period. No patient reported adverse effects. No statistically significant differences were observed between groups for anthropometric variables of weight (mean value: 71.6±10.5 kg; t=0.4; p=0.697), height (mean value: 162.2±8.6 cm; t =0.2; p =0.82) and BMI (mean value: 27.3±4.0 kg/cm^2; t=0.3; p=0.773). Three patients (10%) were tobacco smokers and there were no statistically significant differences in the distribution of smokers per group (X^2=0.4; p=1.000). On average, patients had experienced symptoms for 12.6±8.2 months (range=2.0-24.0) prior to enrollment, and no statistically significant differences were observed between groups (t=1.4; p=0.186). No statistically significant differences were observed in the distribution of right limb patients affected by right shoulder injury(p> 0.05). ANOVA analysis for repeated measurements showed that there was a statistically significant difference in the comparison between variable times (T0-T1) of the

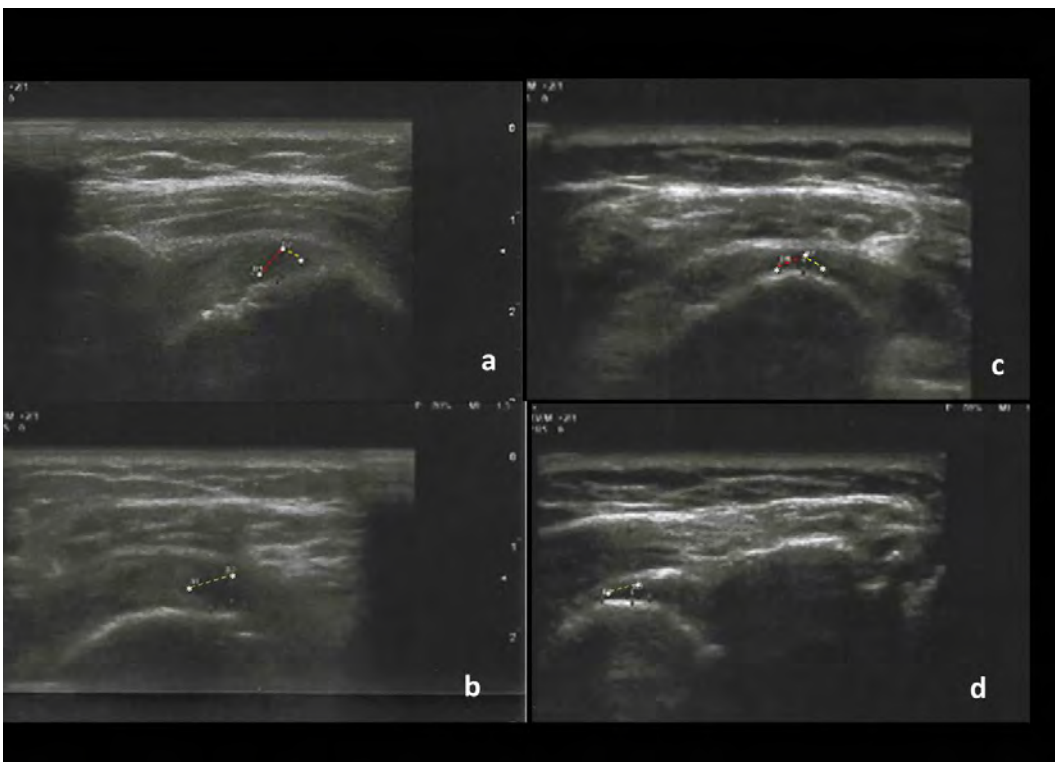


Fig. 1. *The sonographic images of a 71 year-old female showing the tear of the rotator cuff tendon at T0. The tear size is 5.5 mm on the longitudinal axis, 3 mm on the transversal axis (**a**) and 6.4 mm on the antero-posterior axis (**b**). Three months after ESWT the tear size in the same patient is 5.4 on the longitudinal axis, 0.74 mm on the transversal axis (**c**) and and 4.7 mm on the antero-posterior axis (**d**).*

Table I. *Clinical-functional results of the study groups at two follow-ups*

Variable	ESWT group	Exercise group	Total population
T 0			
Pain (VAS)	7.4±1.4 (5.0 – 10.0)	7.5±0.8 (5.0 – 8.0)	7.4±1.1 (5.0 – 10.0)
MMT	2.7±0.7 (1.0 – 4.0)	3.3±0.7 (2.0 – 5.0)	3.0±0.8 (1.0 – 5.0)
ASES	32.2±14.2 (8.4 – 51.6)	31.6±11.3 (18.3 – 54.9)	31.9±12.6 (8.4 – 54.9)
Lenght of lesion (longitudinal axis) (mm)	6.3±1.5 (3.2 – 8.9)	6.4±1.9 (3.2 – 10.7)	6.4±1.7 (3.2 – 10.7)
Length of lesion (transversal axis) (mm)	5.2±1.5 (3.5 – 7.8)	5.5±1.8 (2.6 – 9.1)	5.4±1.6 (2.6 – 9.1)
Lenght of lesion (antero-posterior axis) (mm)	2.9±0.8 (1.5 – 4.3)	2.9±0.8 (1.5 – 4.5)	2.9±0.8 (1.5 – 4.5)
T 1			
Pain (VAS)	3.9±2.2 (1.0 – 8.0)	6.9±1.2 (4.0 – 8.0)	5.4±2.3 (1.0 – 8.0)
MMT	3.3±1.1 (1.0 – 5.0)	3.1±0.6 (2.0 – 5.0)	3.2±0.9 (1.0 – 5.0)
ASES	54.9±21.8 (28.3 – 93.3)	35.3±12.4 (18.3 – 54.9)	45.1±20.1 (18.3 – 93.3)
Lenght of lesion (longitudinal axis) (mm)	5.3±2.4 (2.0 – 10.0)	6.2±1.8 (3.5 – 10.6)	5.8±2.1 (2.0 – 10.6)
Length of lesion (transversal axis) (mm)	4.1±2.1 (1.5 – 8.9)	5.4±3.4 (1.2 – 16.7)	4.7±2.9 (1.2 – 16.7)
Lenght of lesion (antero-posterior axis) (mm)	1.9±0.9 (0.5 – 3.1)	2.5±1.0 (0.7 – 4.5)	2.2±1.0 (0.5 – 4.5)

(T0: at enrollment; T1: after 3 months) (data are expressed as mean +/- standard deviation and range).

VAS value (F=17.4; p=0.000), of the ASES value (F=19.7; p=0.000) and of the size of the lesion (on longitudinal axis: F=5.5, p=0.027; on a transverse axis: F=9.5, p=0.005; on an antero-posterior axis: F=22.9; p =0.000) (Table I). There was a significant difference between groups for the VAS value (F=6.7, p=0.016).

A significant difference was observed in the interaction between time and group for VAS value (F=7.0; p=0.013), for MMT value (F=6.5, p=0.016), for ASES value (F=9.6, p=0.005, Table I) and for the size of the lesion on the antero-posterior axis (F=4.2; p=0.049). Simple linear regression analysis showed a statistically significant link between VAS value at T1 and group (coefficient = -0.7; 95% CI = -1.0 - -0,4; t=4.7; p=0.000). The MMT value at T1 had a

statistically significant association with the MMT value at T0 (coef.=0.5; 95% CI=0.1-0.9; t =2.8; p = 0.009). The ASES value at T1 was associated both with the ASES value to T0 (coef. = 0.8; 95% CI=0.2 -1.3; t = 2.9; p = 0.008) and with group (coefficient = 6.5; 95% CI = 6.4-32.9; t =3.0; p = 0.005). The size of lesion at T1 was associated with the size at T0 on the same axis (on longitudinal axis: coef. = 0.9; 95% CI=0.6 - 1.3; t=5.9; p=0.000) (on axis transverse: coef.=0.2; 95% CI=0.1-0.3; t=4.8; p=0.000) (on antero-posterior axis: coef.=0.7; 95% CI=0.3 - 1.0; t=3.7; p=0.001) (Fig. 1).

There were no further associations between the outcomes and the remaining determinants in analysis (p>0.05). From the multivariate linear analysis we observed an association at the limits of the statistical significance between the MMT value at T1 and the MMT value at T0 (coef. = 0.4, t = 2.0, p=0.055). Multivariate linear analysis showed an association at the limits of statistical significance between ASES value at T1 and ASES value at T0 (coef. = 0.7; t = 3.3; p = 0.003) and group (coefficient = 19.2; t = 3.5; p = 0.002).

DISCUSSION

Our data show that in the treatment of RCT, shockwave therapy allowed to obtain both improvement and reduction in the size of the tendon lesion (on the antero-posterior axis). Our results support the interest of comparing the effects of shock waves with surgery, using either mini-open or arthroscopic methods, which are increasingly popular for the management of tendon lesions (2). Until now, shockwave treatment for rotator cuff tendinopathy has been reserved almost exclusively for cases of calcific tendinosis, in the presence of calcific deposits in phase I and II according to Gartner (5, 6), achieving excellent/good results in 90.9% of the patients. Only recently the indication of shockwave therapy has been extended to different pathologies of the shoulder, such as the sub-acromial conflict syndrome (7) and (non-calcific) tendinosis (8). Unlike calcific tendinopathy, in which a medium-high EDF is used, a lower EDF would be more appropriate for the tendon lesion, in relation to the greater susceptibility of the tissue.

We hypothesize that an important role of shock waves in the treatment of tendon lesions is the anti-oedema and anti-inflammatory effect, which could slow the progression of degeneration and tendon injury (9). Simultaneously, the shock waves determine a trophic and reparative effect on the tendon tissue, improving the differentiation of precursor cells towards tenoblast-like cells, modulating cell morphology and increasing collagen synthesis of type I (10).

The weak points of this study are the short follow-up period, the absence of MRI monitoring, the absence of a placebo or untreated control group. The strength is verification of the effect of shock waves in a new clinical picture, such as tendon tear. It might be interesting to check whether shockwave therapy can also be effective for a preventive action in different clinical conditions in which co-morbidities (for example of a metabolic type, such as thyroid pathologies) (11) or drug administration (e.g. corticosteroids) (12) are responsible for ischemic suffering and degenerative overload of musculoskeletal tissues.

In conclusion, ESWT could be indicated for the treatment of cuff tendon injury. We have excluded that the mechanical stimulation of the shock waves speeds up the opening of the tendon lesion, and we found a stabilization with size reduction on one of the axes. Further studies will allow to verify the effects on longer times and in association with exercise.

ACKNOWLEDGEMENTS

The authors thank Maria Assunta Pinto B.A. for language revision.

REFERENCES

1. Yamamoto A, Takagishi K, Osawa T, et al. Prevalence and risk factors of a rotator cuff tear in the general population. J Shoulder Elb Surg 2010; 19:116-20.
2. Vicenti G, Moretti L, Carrozzo M, Pesce V, Solarino G, Moretti B. Evaluation of long-term postoperative outcomes between mini-open and arthroscopic repair for isolated supraspinatus tears: a retrospective analysis.

Musculoskelet Surg 2018; 102(Suppl 1):21-27.
3. Edwards P, Ebert J, Joss B, Bhabra G, Ackland T, Wang A. Exercise rehabilitation in the non-operative management of rotator cuff tears: a review of the literature. Int J Sports Phys Ther 2016; 11(2):279-301.
4. D Agostino MC, Frairia R, Romeo P, et al. Extracorporeal shockwaves as regenerative therapy in orthopedic traumatology: a narrative review from basic research to clinical practice. J Biol Regul Homeost Agents 2016; 30(2):323-32.
5. Davidson J, Burkhart SS. The geometric classification of rotator cuff tears: a system linking tear pattern to treatment and prognosis. Arthroscopy 2010; 26:417-24.
6. Notarnicola A, Moretti L, Maccagnano G, Tafuri S, Moretti B. Tendonitis of the rotator cuff treated with extracorporeal shock wave therapy: radiographic monitoring to identify prognostic factors for disintegration. J Biol Regul Homeost Agents 2016; 30(4):1195-202.
7. Santamato A, Panza F, Notarnicola A, et al. Is extracorporeal shockwave therapy combined with isokinetic exercise more effective than extracorporeal shockwave therapy alone for subacromial impingement syndrome? A randomized clinical trial. J Orthop Sports Phys Ther 2016; 46(9):714-25.
8. Frizziero A, Vittadini F, Barazzuol M, et al. Extracorporeal shockwaves therapy versus hyaluronic acid injection for the treatment of painful non-calcific rotator cuff tendinopathies: preliminary results. J Sports Med Phys Fitness 2017; 57(9):1162-68.
9. Notarnicola A, Moretti B. The biological effects of extracorporeal shock wave therapy (ESWT) on tendon tissue. Muscles Ligaments Tendons J 2012; 2(1):33-37.
10. Rinella L, Marano F, Paletto L, et al. Extracorporeal shock waves trigger tenogenic differentiation of human adipose-derived stem cells. Connect Tissue Res 2018; 9:1-13.
11. Vicenti G, Moretti L, De Giorgi S, et al. Thyroid and shoulder diseases: the bases of a linked channel. J Biol Regul Homeost Agents 2016; 30(3):867-70.
12. Solarino G, Scialpi L, Bruno M, De Cillis B.On a case of multifocal osteonecrosis in a patient suffering from acute lymphoblastic leukemia. Chir Organi Mov 2008; 92(2):119-22.

LETTER TO THE EDITOR

LARYNGOPHARYNGEAL REFLUX DISEASE IN ADULT PATIENTS: TEARS AND PEPSIN

G. MAGLIULO[1], A. PACE[1], R. PLATEROTI[1], A.M. PLATEROTI[1], R. CASCELLA[2,3], C. SOLITO[1], V. ROSSETTI[1] and G. IANNELLA[1]

[1]Sense Organs Department, Sapienza University of Rome; [2]Laboratory of Genomic Medicine UILDM, IRCCS Santa Lucia Foundation, Rome, Italy; [3]Department of Chemical Pharmaceutical and Biomolecular Technologies, Catholic University "Our Lady of Good Counsel" Laprakë, RrugaDritanHoxha, Tirana, Albania

Received October 17, 2019 – Accepted March 18, 2020

To the Editor,

Laryngopharyngeal reflux disease (LPRD) is defined as the retrograde flow of stomach content to the upper aero-digestive structures, with an estimate incidence about 4-10% of the general population. (1). LPRD is used to describe the pathological condition caused by the reflux of gastric and/or duodenal juices to the larynx, oropharynx and/or nasopharynx, through the upper oesophagus sphincter (UES). The most frequent symptoms are dysphonia, chronic cough, sore throat, excess throat mucus and pharyngeus globous. Endoscopy evidence related to this pathology could be laryngeal oedema, laryngeal hyperaemiagranulomatosis and polypoid lesions of the larynx (2).

Pepsin is a protein produced by the gastric mucosa. In recent years, several studies have shown the existence of a relationship between salivary pepsin and LPRD signs and symptoms (3). Salivary pepsin has therefore been proposed as a biomarker for the diagnosis of LPRD. Some authors reported the positive pepsin expression in middle ear effusion of patients with effusive otitis media and in the nasal cavity of patients with chronic rhinosinusitis. In 2014, Luo et al. investigated the relationship between pepsin and pepsinogen in children affected by otitis media with effusion (OME). The results showed high levels of pepsinogen protein expressed in cytoplasm of epithelial cells in adenoid specimens of the children with OME (4). Magliulo et al., in 2013, hypothesized that, in patients with LPRD, pepsin might reach the tear film through the lacrimal ways eliciting irritation and edema phenomena on the tear ducts (5). Iannella et al., in 2015, were the first to confirm this hypothesis by demonstrating the presence of pepsin in the tears of 20% of children with LPRD enrolled in a prospective study (6).

The aim of this study is to confirm this evidence, evaluating the presence/absence of pepsin in tears of adult patients affected by LPRD. Pepsin was evaluated in tears of healthy patients without LPRD in order to compare the two groups in terms of pepsin expression in tears.

MATERIALS AND METHODS

All patients who came to our Department with signs and symptoms of LPRD between February 2018 and June 2019 were evaluated for possible enrolment in this prospective study. Exclusion criteria was: age <18 years old, pregnancy,

Key words: LPRD; pepsin; tears; larynx

Corresponding Author:
Giuseppe Magliulo, M.D.,
Sapienza University of Rome, Policlinico Umberto I,
Viale dell'Università 33, Rome 00185, Italy
Tel.: +393388622344 - Fax: +390649976817
e-mail: giuseppe.magliulo@uniroma1.it

0393-974X (2020)
Copyright © by BIOLIFE, s.a.s.
This publication and/or article is for individual use only and may not be further reproduced without written permission from the copyright holder.
Unauthorized reproduction may result in financial and other penalties
DISCLOSURE: ALL AUTHORS REPORT NO CONFLICTS OF INTEREST RELEVANT TO THIS ARTICLE.

the presence of ocular diseases and treatment with proton pump inhibitors (PPIs) or other drugs used for the treatment of LPRD at the time of the study. All patients gave their written consent for all the tests and for their enrolment in the study. This research was performed in accordance with the principle of the Declaration of Helsinki and approved by the local ethics committee of the University "Sapienza", Rome (RIF.CE.4841).

Initially, all patients underwent anamnestic evaluation, Reflux Symptom Index (RSI) evaluation and a fiber optic laryngoscopic evaluation with Reflux Finding Score (RFS). RSI is a self-conducted questionnaire, developed by Belafskyet al 2002, based on nine questions, with a maximum of 5 points for each question, giving a total of 45 points. The score was considered pathological when the score was ≥13 (Table I) (7). The RFS evaluates the presence of 8 laryngoscopic findings with a scale that goes from 0 (normal) to 26 (strongly pathological). RFS ≥ 7 is considered pathological and indicative of LPRD (Table I) (8). Using both these scores it is possible to use them as a guide for the clinical diagnosis of LPRD.

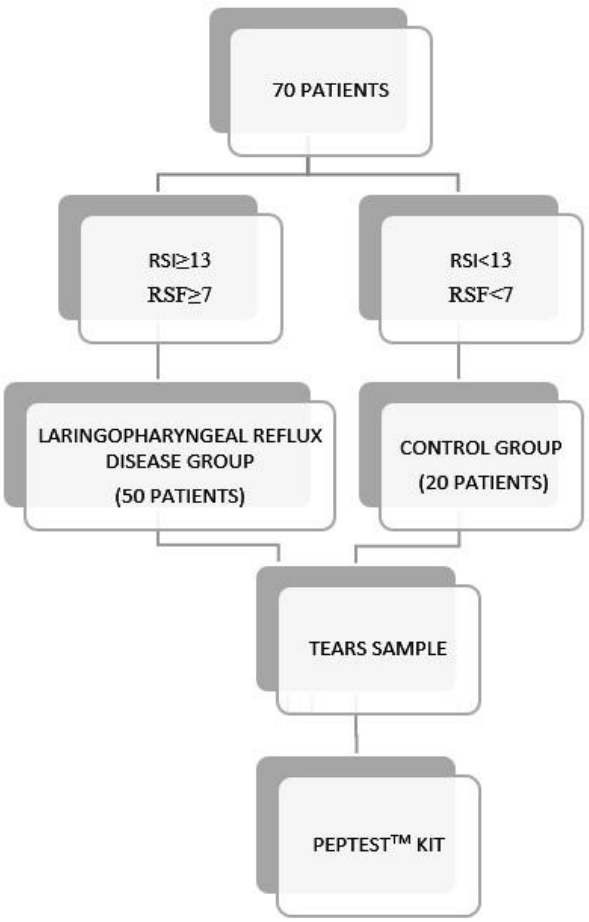


Fig. 1. *Flow chart of the study.*

Fifty adult patients (21 males, 29 females; 19-75 years of age, average 44.1 years) in our study showed pathological values in both questionnaires and they were enrolled in the study group as considered suffering from the symptoms of LPRD. The control group consisted of 20 patients (9 males, 11 females; 26-64 years of age, average 41.8) considered negative for LPRD, because negative to both RSF and RSI questionnaires. A flow-chart of the study is shown in Fig. 1.

A tear sample was taken from all patients in the study in order to estimate the presence of pepsin and its concentration. The tear samples were collected in the early hours of the morning with a micropipette, a silicone tube with a diameter of 0.3 cm, 2 cm long, cut obliquely at 45°, siliconized to a small tank (diameter of 0,5 cm, 2 cm long), provided with a suction tube. The micropipette works by pipetting the tear fluid from the tear lake, located on the bulbar conjunctiva, at the level of the inner chant of the eyelid and depositing the liquid on a glove slide. The collection takes place through the micropipette with a rapid movement, in order to avoid any subsequent tearing. The tears of both eyes were harvested and carried in a single test tube.

The collected tears were analysed by Peptest™ kit (BIOHIT HealthCare) that is a qualitative and quantitative test to determine the pepsin concentration in body fluids. The test required 100 µl of tears with the addition of 100 µl of 0.01M citric acid. Each sample was centrifuged at 4000 rpm for 5 min. Subsequently, 80 µl of supernatant was collected and was added to 240 µl of migration buffer and the mixture was vortexed for 10 s: 80 µl of this mixture was pipetted into the well of the Peptest™ Lateral Flow Device (LFD) and the results were ready after 15 min. The test is based on a chemical reaction antigen-antibody utilizing a monoclonal anti-pepsin antibody (T band reveals the pepsin presence). In addition, the system involves an inner reaction control useful for estimating the system's integrity (C band). The test is valid when it obtains a reaction related to the Internal Control (IC, C band). The existence of T band indicates that pepsin is present in the tested sample and, furthermore, the intensity of the T band is directly proportional to the pepsin quantity. The concentration of pepsin level was accurately measured by Peptest Cube that displays the result directly in ng/ml in just three seconds. The reader is able to detect a minimum amount of pepsin equal to 16ng/ml. The device

Table I. *Reflux Symptoms Index (Belafsky PC et al 2002); Reflux Finding Score (Belafsky PC et al 2001).*

REFLUX SYMPTOMS INDEX	
Hoarsness or a problem with voice	0 1 2 3 4 5
Cleaning your throat	0 1 2 3 4 5
Excess throat mucus or postnasal drip	0 1 2 3 4 5
Difficulty swallowing food, liquids, or pills	0 1 2 3 4 5
Coughing after you ate or after lying down	0 1 2 3 4 5
Breathing difficulties or choking episodes	0 1 2 3 4 5
Troublesome or annoying cough	0 1 2 3 4 5
Sensations of something sticking in your throat or lump in your throat	0 1 2 3 4 5
Heartburn, chest pain, indigestion, or stomach acid coming up	0 1 2 3 4 5
REFLUX FINDING SCORE	
Subglottic edema	2=present 0= absent
Ventricular obliteration	2= partial 4= complete
Erythema/ hyperemia	2= arytenoids only 4=diffuse
Vocal fold edema	1= mild 2= moderate 3= severe 4= polypoid
Diffuse laryngeal edema	1= mild 2= moderate 3= severe 4= obstruction
Posterior commissure hypertrophy	1= mild 2= moderate 3= severe 4= obstruction
Granuloma/ granulation	2=present 0= absent
Thick endolaryngeal mucus	2=present 0= absent

is able to conduct a colorimetric tests based on reflectance measurements that capture the optical density. The test can provide three possible results: negative (only the IC is present), positive (the T and C bands are present), null (absence of IC signal). (9-10)

Statistical analysis was performed using Statview statistical software version 8.0. Student's *t*-test was employed to compare the data (age, RSI, RSF, pepsin) of the study. A value of $p<0.05$ was considered statistically significant.

RESULTS

No statistical significative difference emerged between the LPRD and control groups regarding age ($p=0.6$). In the study group, the average RSI value

Table II. *AGE. Reflux index symptoms and Reflux finding score of study and control groups.*

	AVERAGE VALUE		p-value
	LARYNGOPHARYNGEAL REFLUX DISEASE GROUP	CONTROL GROUP	
AGE	44.1 (range 19-75)	41.8 (range 26- 64)	p=0.6
Reflux index symptoms	21 (range13-36)	10 (range 9-12)	p=0.0001
Reflux finding score	11.4 (range 8-17)	5.6 (range 4-6)	p=0.0001

Table III. *Values of AGE. RSI. RSF and Pepsin concentration level in 32 patients of LPRD group positive to Pep-test.*

PATIENTS	AGE	RSI	RFS	PEPSIN ng/ml
1	35	25	11	179.9
2	33	32	8	43.9
3	39	26	12	65.7
4	19	24	10	58.6
5	34	16	14	200.9
6	63	29	16	58
7	44	28	14	32.2
8	75	28	16	59
9	65	24	10	91.1
10	33	13	11	107.3
11	52	13	11	39.9
12	60	13	11	247.6
13	24	28	8	177.9
14	33	25	10	20.5
15	33	19	17	20.5
16	43	13	8	26.3
17	32	17	12	56.4
18	53	33	12	120.1
19	27	13	8	20.5
20	25	18	8	148.3
21	32	25	12	20.5
22	57	21	8	90.7
23	24	26	14	20.5
24	67	19	9	20.5
25	60	22	12	128
26	26	28	12	20.5
27	39	13	8	189.9
28	41	15	8	96.8
29	34	13	8	129
30	40	15	10	65
31	25	13	9	20.5
32	27	24	12	193.1

was 21 (range 13-36) and the average RFS value was 11.4 (range 8-17). In the control group, the average RSI value was 10 (range 9-12). Statistical difference emerged between the two groups regarding RSI value (p=0.0001). The average RFS value was 5.6 (range 4-6) with a statistically significant difference with respect the LPRD group (p=0,0001) (Table II).

The results of pepsin evaluation in tears showed that 32 of the 50 patients, affected by LPRD, presented a concentration of pepsin in the tear samples obtained. Therefore, the percentage of patients with LPRD positive to pepsin was estimated at 64%. The average level of pepsin concentration in the positive patients of the study group was 86.6 μg/ml (range20.5- 247.6 μg/ml) (Table III).

Regression analysis showed no correlation between the values of RSI and pepsin dosage (p=0.4); the same no correlation emerged between RFS values and pepsin concentration (p=0.3). None of the patients in the control group presented pepsin in the tear samples obtained.

DISCUSSION

Laryngopharyngeal reflux disease is defined as the reflux of gastric contents in the larynx, oropharynx and/or nasopharynx through the upper esophageal sphincter (UES) (1). The present investigation showed that most of the LPRD selected patients presented high levels of pepsin concentration in their eyes, while no patients in the control group presented pepsin in the tear samples obtained.

It has been hypothesized that pepsin arrives in the pre-corneal tear film through the nasolacrimal duct after reaching the nasopharynx during reflux attacks (5-6). However, other mechanisms should be taken into consideration such as arrival of pepsin from blood and pepsin production of lacrimal glands cells. The present study presents some limitations. The first one is the limited number of enrolled patients; other studies on larger series of patients are underway. Another criticism regards the diagnosis of LPRD based on RSI and RSF. These tests are the most used in LPRD diagnosis in clinical practice (11). These tests are also economical and easy to administer. However, the gold standard for LPRD diagnosing remains the multichannel intraluminal impedance (MII) and 24-hour dual probe Phmetry, but they are invasive and more expensive methods with a poor reproducibility due to the position of the proximal sensor (in case of suspected LPRD), and without a clear pH cutoff level (12). In our study no correlation was observed between the values of pepsin concentration in tear samples with those of RSI and RFS using regression analysis. Further studies withMII and 24-hour dual probe Phmetry would be useful to confirm the relationship between pepsin level concentration in tears and the number or type of reflux episodes.

Some patients affected by LPRD in this study also complained of ocular symptoms. They described sensations of burning or the presence of foreign bodies in their eyes (like sand granules). Probably these irritating symptoms may be related to the involvement of the tear film from the LPRD pathology due to the presence of gastric substances in the lacrimal film. How and how much the presence of these gastric substances can cause irritation of the conjunctiva and ocular pathologies will be the subject of further experimental studies.

REFERENCES

1. Hayat JO, Yazaki E, Moore AT, Hickiln L, Dettmar P, Kang JY, Sifrim D. Objective detenction of esophagolaryngeal reflux in patients with hoarsness and endoscopic signs of laryngeal inflammation. J Clin Gastroenterol 2014; 48:318-27.
2. Saritas Yuksel E, Vaezi MF. Extraesophageal manifestations of gastroesophageal reflux disease: cough, asthma, laryngitis, chest pain. Swiss Med Wkly 2012; 142:w13544
3. Iannella G, Vicini C, Polimeni A et al. Laryngopharyngeal reflux diagnosis in obstructive sleep apnoea patients using the pepsin salivary test. Int J Environ Res Public Health 2019; 16(11).
4. Luo HN, Yang QM, Sheng Y, et al. Role of pepsin and pepsinogen: linking laryngopharyngeal reflux with otitis media with effusion in children. Laryngoscope 2014; 124(7):E294-300.
5. Magliulo G, Plateroti R, Plateroti AM. Gastroesophageal reflux disease and the presence of pepsin in the tears.

Med Hypotheses 2013; 80(2):129-30.
6. Iannella G, Di Nardo G, Plateroti R, et al. Investigation of pepsin in tears of children with laryngoesophageal reflux disease. Int J Pediatr Otorhinolaryngol 2015; 79(12):2312-15.
7. Belafsky PC, Postma GN, Koufman JA. Validity and Reliability of the Reflux Symptom Index (RSI). J Voice 2002; 16(2):274-77.
8. Belafsky PC, Postma GN, Koufman JA. Laryngopharingeal reflux symptoms improve before changes in physical findings. Laringoscope 2001; 11:979-81.
9. Wang L, Liu X, Liu YL, et al. Correlation of pepsin-measured laryngopharyngeal reflux disease with symptoms and sign. Otolaryngol Head Neck Surg 2010; 143(6):765-71.
10. Barona Lleo L, Barona- De Guzman R, Krstulovic C, The diagnostic usefulness of salivary pepsin test in symptomatic laryngopharyngeal reflux. J Voice 2018.
11. Park KH, Choi SM, Kwon SU, Yoon SW, Kim SU. Diagnosis of laryngopharigeal reflux among globus patients. Otorinolaryngol Head Neck Surg 2006; 134:81-85.
12. Reichel O, Issing WJ. Impact of different Ph thresholds for 24-Hour dual probe Ph monitoring in patients with suspected laryngopharingeal reflux. J Laryngol Otol 2008 122:485-89.

LETTER TO THE EDITOR

EFFECTS OF ESSENTIAL AMINO ACID SUPPLEMENTATION ON PAIN IN THE ELDERLY WITH HIP FRACTURES: A PILOT, DOUBLE-BLIND, PLACEBO-CONTROLLED, RANDOMISED CLINICAL TRIAL

M. RONDANELLI[1,2], D. GUIDO[3], M.A. FALIVA[4], C. GASPARRI[4], G. PERONI[4], G. IANNELLO[5], M. NICHETTI[4], M. NASO[4], V. INFANTINO[6], D. SPADACCINI[4], S. PERNA[7] and R. AQUILANI[8]

[1]IRCCS Mondino Foundation, Pavia, Italy; [2]Department of Public Health, Experimental and Forensic Medicine, University of Pavia, Pavia, Italy; [3]Epidemiology Unit, Agency for Health Protection of Milan, Milan, Italy; [4]Endocrinology and Nutrition Unit, Azienda di Servizi alla Persona "Istituto Santa Margherita", University of Pavia, Pavia, Italy; [5]General Management, Azienda di Servizi alla Persona "Istituto Santa Margherita", Pavia, Italy; [6]University of Bari, Department of Biomedical Science and Human Oncology, Bari, Italy; [7]University of Bahrain, Department of Biology, College of Science, Sakhir Campus, Kingdom of Bahrain; [8]Department of Biology and Biotechnology University of Pavia

Received October 24, 2019 – Accepted March 24, 2020

To the Editor,

The main three pain-neuromodulators are gamma-amino-butyric acid, serotonin, and endorphin; even a diet that is low in protein can reduce these pain fighters, because they are produced from amino acid (AA) (1). In fact, effective pain control is not consistently achievable without adequate physiological body levels of essential AA (EAA), and of the hormones and neurochemicals they produce (2). Recently, the effectiveness of 8 g/day EAA supplementation versus placebo during rehabilitation in 60 patients following elective hip arthroplasty were investigated. After treatment, there was a similar decrease in inflammation rate for both groups; only EAA patients showed significant improvement in levels of alanine, glycine, tyrosine, and total AA and in their rate of hip function recovery, measured by Harris hip score, that included domains relative to pain (3). A previous study has demonstrated the efficacy of 8g/day EAA on quality of life determinants in institutionalized elderly patients. EAA patients showed improvement of nutritional status and mental and physical components of SF-36, which included 2 items related to bodily pain (4). Furthermore, it has been demonstrated that EAA can improve walking recovery rate of subjects after hip fracture surgery (5). The benefits derived from EAA can be explained by multiple mechanisms. Primarily, the anabolic activity promoted by EEA enhances wound repair, a process which requires the availability of EAA for *de novo* synthesis of proteins and peptides (6). Given the above, this study aims to assess the efficacy on pain (assessed by VAS) of a supplement with a specific formulation of EAA *versus* placebo in elderly patients admitted for rehabilitation management after surgical treatment of hip fracture. The EAA formulation was built on the basis of AA deficits found in a population of subjects similar to that of

Key words: amino acids; pain; hip fracture; dietary supplement

Corresponding Author:
Dr. Gabriella Peroni,
Endocrinology and Nutrition Unit,
Azienda di Servizi alla Persona
''Istituto Santa Margherita'',
University of Pavia, Pavia, 27100, Italy
e-mail: gabriella.peroni01@universitadipavia.it.

0393-974X (2020)
Copyright © by BIOLIFE, s.a.s.
This publication and/or article is for individual use only and may not be further reproduced without written permission from the copyright holder.
Unauthorized reproduction may result in financial and other penalties
DISCLOSURE: ALL AUTHORS REPORT NO CONFLICTS OF INTEREST RELEVANT TO THIS ARTICLE.

the present study: the elderly post-femur fracture (5). The secondary endpoints are the evaluation of body composition, nutritional status, quality of life, muscle function, and hip functionality.

MATERIALS AND METHODS

This pilot study was parallel, randomized, double-blind and placebo-controlled, and sample size had not been determined a priori because the subjects were more than 12 per arm, as previously suggested. Subjects who met the admission criteria, and who had signed and given informed consent for the study were randomized to one of the two treatments (experimental treatment or placebo).

The study was approved by the Ethics Committee of the Department of Internal Medicine of the University of Pavia and written consent was given by participants to take part in this study (NCT02402608). All procedures performed were in accordance with the 1964 Helsinki declaration and its later amendments or comparable ethical standards.

Elderly people were evaluated after admission to the geriatric physical medicine and rehabilitation division at Santa Margherita Hospital, Azienda di Servizi alla Persona of Pavia, Italy. Every subject underwent complete medical screening before participation, which included vital signs, urine tests, blood tests, and a 12-lead electrocardiogram. Any evidence of kidney, liver or heart disease, or of any other disease that could influence the study results resulted in the subject being excluded. Data gathering took place from the end of January 2019 to the end of June 2019. Eligible subjects were 65 years or older and their appendicular skeletal FFM divided by height squared was 2 SD below the mean for young adults. Thus, the relative skeletal muscle mass (RSMM) for men was 7.26 kg/m2 and for women 5.5 kg/m2 (7). None suffered from severe heart, liver, or kidney dysfunction or acute illness, and their body weight was required to have been stable for at least 6 months. Exclusion criteria were: thyroid disorders, altered glycometabolic control, other endocrinopathies, cancer, people treated with steroids and heparin or who had total walking incapacity. The physical ability of the participants selected had to be similar, as assessed by the activities of daily living (ADL) score. Their cognitive function needed to be normal or only mildly disturbed, as defined by a Mini-Mental State Examination.

Body composition, nutritional status, and food intake

Body composition (fat free mass, fat mass, together with gynoid and android fat distribution) was determined by dual-energy X-ray absorptiometry (DXA), using a Lunar Prodigy DXA (GE Medical Systems). *In vivo* coefficients of variation (CVs) were 0.89% for whole body fat (fat mass) and 0.48% for FFM. RSMM was calculated as the sum of the fat-free soft tissue mass present in arms and legs, normalized for height^2 (Kg/m^2). Body weight was measured to the nearest 0.1 kg, using a precision scale; participants wore light clothing, no shoes, and a standardized method was used. The waist was measured at the midpoint between the top of the hip bone (iliac crest) and lowest rib, using a standardized method.

Hydration was assessed with bioelectrical impedance, as fluid status changes would affect the soft tissue composition estimated by DXA. With the patient in supine position on a nonconductive surface, whole-body reactance and resistance were measured using a single-frequency phase-sensitive impedance plethysmograph [400-mA, 50-kHz alternating current (BIA-101; RJL/Akern Systems)]. Adhesive surface electrodes were attached to the right foot and hand, with measurements taken based on NIH Technology Assessment Conference Statement guidelines. Reactance and resistance were standardized using each individual's standing height (i.e., reactance divided by height and resistance divided by height), given in ohms/m and plotted on the resistance-reactance graph. Bioelectrical impedance vector analysis (BIVA) provides a measure of tissue hydration status and body cell mass that only considers the impedance vector in relation to a population of healthy individuals; this method is valid for detecting hydration changes (divided in under-, normal or over-hydration) and changes in body fluid volume. Sex-specific bivariate reference intervals for the Italian healthy population were available as 50%, 75%, and 95% tolerance ellipses on the resistance-reactance graph.

All participants underwent a mini nutritional assessment (MNA). MNA is a test for classifying malnutrition, based on simple measurements and a brief questionnaire divided into 4 sections: anthropometric assessment (height, weight, and weight loss), general assessment (medication, lifestyle, and mobility), dietary assessment (food and fluid intake, number of meals, appetite, autonomy of eating) and perception of health

and nutrition. Patients had 3 meals daily.

A balanced diet was provided by the hospital kitchen (with standard caloric and macro- and micronutrient content). This consisted of a 4-week rotating menu, therefore diet remained similar throughout the study. A trained dietitian was involved for 3 consecutive days at the beginning and end of the study, using a calibrated dietetic spring scale to weigh all foods served. Any foods served to participants between meals by nurses were recorded together with the amount eaten, using household measurements. The energy and macronutrient content of the food consumed was calculated by a computer software (DR3 v3.1.0; Sintesi Informatica).

Muscle function was assessed using the JAMAR Hand Dynamometer (Jamar 5030J1; Sammons Preston Rolyan; accuracy 0.6 N), by means of a standardized procedure.

Biochemical analyses

Venous blood samples were taken during fasting and collected in vacuum tubes, maintained for 1 h at room temperature, and then centrifuged at 1500 3 g at 20°C for 15 min. Thereafter, serum was transferred to plastic tubes, frozen rapidly, and stored at -80°C while awaiting analysis (1 month later). Whole blood (using EDTA as an anticoagulant) was used to assess hematologic variables. Clinical chemistry markers were measured using the Roche Cobas Integra 400 plus analyzer (Roche Diagnostics), together with custom commercial kits supplied by the manufacturer. Cobas Integra 400 is a continuous-access, random, sample-selective analyzer which provides absorbance photometry to measure substrates and enzymes, ion-selective electrode potentiometry for serum electrolytes, and turbidimetry for specific proteins. Total serum and LDL cholesterol, HDL cholesterol, triglycerides, total bilirubin, total proteins, creatinine, iron, uric acid, glucose, and liver enzymes such as aspartate transaminase, alanine transaminase, and g-glutamyltransferase were measured employing enzymatic-colorimetric methods. A nephelometric high-sensitivity CRP was used to determine C-reactive protein (CRP) (Dade Behring). Erythrocyte, platelet counts and white blood cell; mean cell volumes; hemoglobin concentrations; and mean cell hemoglobin concentrations were determined with a Coulter automated cell counter (MAX-M; Beckman Coulter). Serum albumin was determined by a nephelometric method (Behring Nephelometric Analyzer II, Behring Diagnostics), with a 2% CV. Serum samples required to assay for insulin-like growth factor I (IGF-I) were collected upon admission and after 12 weeks of treatment; samples were pretreated so that IGF-I would be released from binding proteins and then assayed with quality controls. A solid-phase quantitative ELISA kit (R&D Systems) was used to measure serum IGF-I concentrations; the IGF-I minimum detectable dose was 0.026 ng/ml. Intra-assay CV was 4% and the inter-assay CV 7.9%.

Health-related quality of life

In order to assess their quality of life, participants completed the Short-Form 36-Item Health Survey (SF-36) before and after the treatment period. This questionnaire is used for rating health-related quality of life in several fields of research due to its validity, and high test–retest reliability and high internal consistency. Two dimensions were used to summarize the SF-36 scales: “physical health”, comprising the first five scales, and “mental health”, comprising the last five scales. General health scales and vitality are part of both, i.e. each dimension includes 3 specific and 2 overlapping scales. Standardised summary scores for mental and physical components were determined and used separately as measures of outcome.

The ability of participants to care for themselves was measured using the Katz Index of Independence in Activities of Daily Living. To assess cognitive function, the participants were tested with the “Mini Mental State Examination”. This test comprises two parts: the first part only requires vocal responses, covering memory, orientation, and attention; the maximum score being 21; the second tests the ability to name, follow written and verbal commands, write a spontaneous sentence, and copy a complex polygon like a Bender-Gestalt Figure; with a maximum score of nine. Given that Part II involves reading and writing, patients with severely impaired vision may experience additional difficulties; usually these can be alleviated by use of large writing and are allowed for in the scoring. A total score of 30 is the maximum value achievable. There is no timing of the test.

We also evaluated the presence of a geriatric depression with the “Geriatric Depression Scale”: a 30-question test with yes/no answers. The scale was designed to avoid most of the symptoms associated with the measurement of geriatric depression.

We also tested the participants’ balance with the

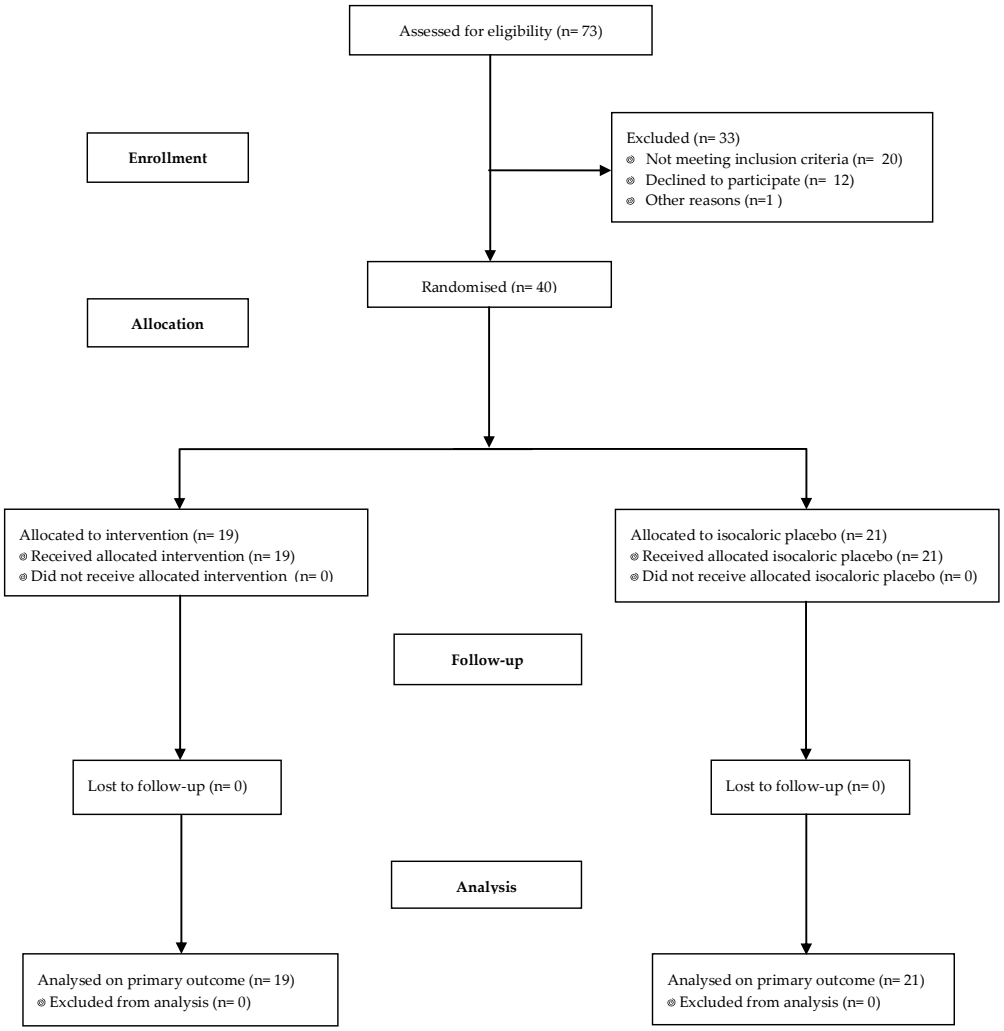


Fig. 1. *Flow diagram of the study.*

Tinetti balance scale (scale from 1 to 40): a simple clinical balance measures characteristics relating to falls. The test uses 14 items to assess balance (with a score out of 24) and 10 items to assess gait (score out of 16). The maximum total score is 40, and the higher the score is, the better the participant's performance.

Hip pathology and hip surgery outcome in participants were assessed using a reliable and valid Italian version of the Harris hip score. The maximum score is 100 points (best possible outcome) and the assessment comprises 10 items, spanning function (7 items, 0–47 points), pain (1 item, 0–44 points), range of motion (2 items, 5 points), absence of deformity (1 item, 4 points). Data analysis uses computer-based algorithms and is performed automatically as part of data processing, taking 5 minutes to complete.

Pain

We evaluated the presence or absence of pain in all participants with the NRS (Numerical Rating Scale) (8), a unidimensional measure of pain intensity in adults. Pain NRS is a single 11-point numeric scale: 0 represents one pain extreme (e.g., "no pain") and 10 represents the other pain extreme (e.g., "pain as bad as you can imagine" and "worst possible pain"). Pain NRS was administered by the

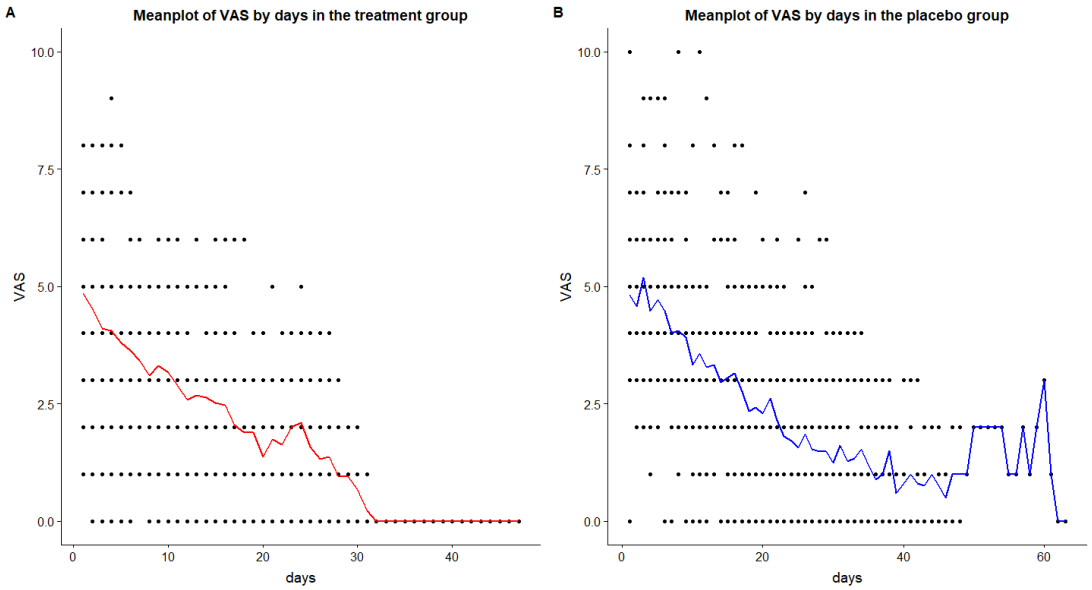


Fig. 2. *Trend of the means of the VAS by day and treatment*

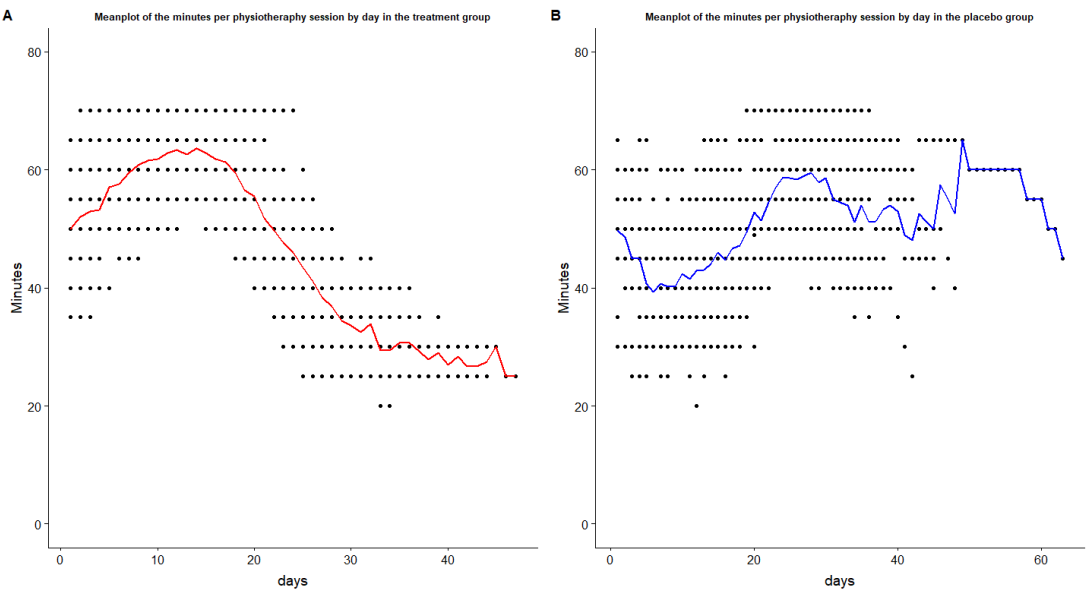


Fig. 3. *Trend of the means of the minutes per daily physiotherapy session by treatment*

physiotherapist every day at the same time, at the end of the morning physiotherapy session, at 11 a.m.

Supplementation

Essential amino acids were administered to participants every day twice a day. Powdered amino acid supplement sachets were provided, and these were taken with water or milk, and the participants were instructed to take the 6.6-gram supplement (1500 mg leucine, 1000 mg lysine, 750 mg glutamine, 550 mg valine, 450 mg isoleucine, 450 mg glycine, 350 mg serine, 250 mg threonine, 250 mg phenylalanine, 350 mg tyrosine, 350 mg histidine, 200 mg

cysteine, 125 mg methionine, 75 mg tryptophan) twice a day, every day, for four weeks. A dietitian checked every day to make sure that every patient complied with the supplementation therapy and took the supplement.

In our clinical practice, we adopt the recommendations for essential amino acids by WHO. On this basis, after considering combined requirements for male and female (mg/Kg BW/d) , the supplemented mixture in the study, relative to the recommended daily amounts, provided leucine + 75.7%; valine -18%; isoleucine + 35.7%; lysine - 27%; threonine + 25.7%; phenylalanine +241.5%.

The control group was administered a placebo consisting in an isocaloric amount of maltodextrin, with the same appearance and flavour as the intervention product, as used in previous studies. As with the case group, a dietitian checked every day to make sure that that every patient took the supplement and complied with the supplementation therapy.

Statistical analysis

Descriptive statistics were expressed as mean (± standard deviation) for numerical variables and the frequencies were computed for the categorical variables. Attrition was addressed through complete cases. Baseline associations between treatment (1= experimental treatment, 0=placebo) and numerical variables were analyzed by two-sample *t*-test, while the associations with gender were analyzed by χ^2 (*chi*-squared) test.

Generalized estimating equation (GEE) models for repeated measures were employed to ascertain the differences in outcomes among individuals across time and treatments. For the outcomes of VAS and minutes per daily physiotherapy session, measured for each hospitalization day, we fitted a GEE model where the time was hospitalization days, and the treatment (i.e. experimental treatment or placebo, with placebo as reference) and their interaction terms were ‘‘focus’’ predictors. In addition, the model on the VAS was adjusted for the whole hospitalization period (in terms of total of the days) and the minutes per daily physiotherapy session, whereas the model on the minutes per daily physiotherapy session was adjusted for the hospitalization period and the VAS measured the day before (i.e., in the afternoon or evening of the day before, after the physiotherapy sessions). For the other outcomes, we used a GEE model where the time – considered as a categorical two-level, three-level or four-level factor, based on the number of time points such as baseline (t0) (as reference), at 15 days (t1), at one month (t2), at 45 days or at discharge (t3) – the treatment (i.e. experimental treatment or placebo, with

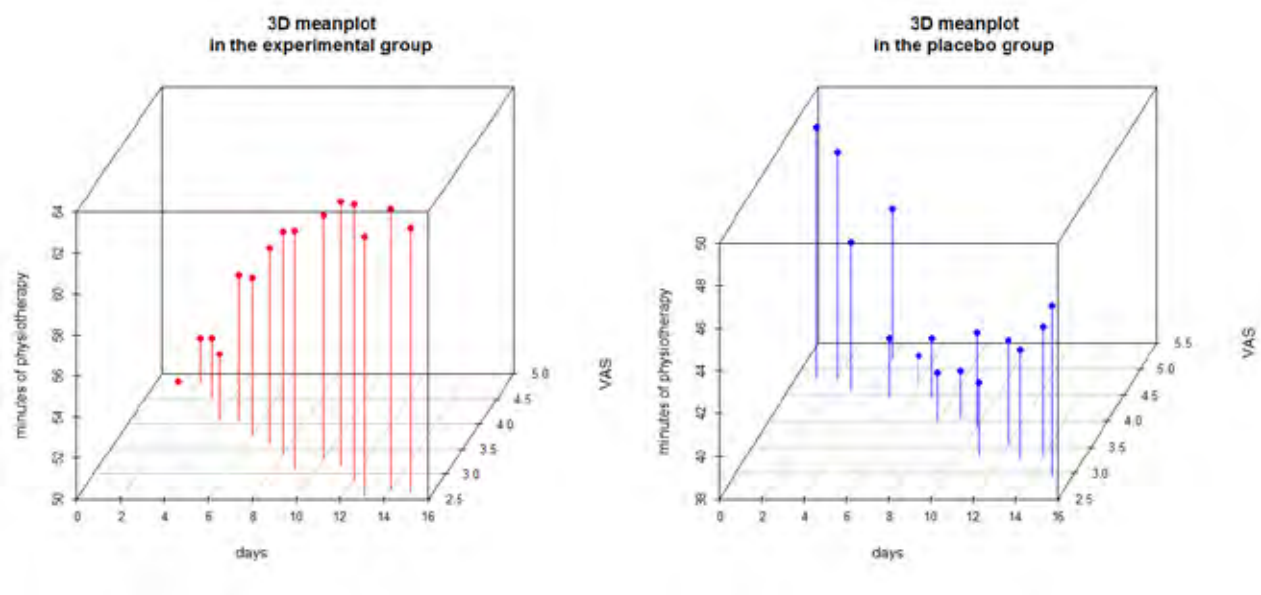


Fig. 4. *Trends of the minutes per daily physiotherapy related to VAS within the first 15 days of treatment*

placebo as reference), and their interaction terms were ''focus'' predictors. An ''identity'' link, an exchangeable correlation structure, and a robust sandwich estimator to consider model misspecifications were used to fit the Gaussian GEE models.

Concerning the GEE models on the VAS and the minutes per daily physiotherapy session, the time parameters (ΔT) were interpreted as adjusted average variation of the outcome for daily increase in the placebo group; the interaction parameters (ΔTxTR) were interpreted as adjusted mean differences of the outcome between treatments for daily increase. Finally, the parameters associated to the treatment (ΔTR) were interpreted as adjusted baseline mean differences between treatments.

For the GEE models on the other outcomes, time parameters (ΔT) were interpreted as adjusted mean differences of the outcome at the time point (t1 or t2 or t3 or t4) from baseline in the placebo group; the interaction parameters (ΔTxTR) were interpreted as adjusted mean differences of the outcome between treatments at a given time point (from baseline). Finally, treatment-associated parameters (ΔTR) were interpreted as baseline mean differences between treatments. GEE models were selected due to their robustness to missing values, and because they allow to manage the intra-subject variability resulting by the three separate measurements performed on each patient.

Wald tests were performed and 95% confidence intervals computed in order to assess statistical significance on model parameters. Two-tailed p-values below 0.05 were considered to be significant.

RESULTS

During the study period, 40 patients met the inclusion criteria: 19 (5 males/14 females, mean age 81.9±8.3) in the experimental group, 21 (5/16, 84.8±8.6) in the placebo group. Fig. 1 shows the patient flow in the two groups. Baseline demographic and clinical data are shown in Table I: the mean of VAS was 4.84±2.09 in the experimental group and 4.81±2.18 in the placebo group. The means of the minutes per daily physiotherapy session were 50±8.82 and 49.8±8.29. Finally, the means of the Tinetti scale were 4.82±6.1 and 2.5±5.3, and 355±153 and 286±130 for the total scores of the SF questionnaire. When examining the baseline associations between treatment and variables, no significant result was found. The mean of the number of hospitalization days was 34.7±5.91 in the experimental group and 37.1±7.91 in the placebo group, but they did not differ statistically.

Table I provides longitudinal outcome details, in terms of mean and standard deviation stratified by treatment. The means of the VAS decreased from baseline until discharge through all considered time points (i.e., 15 days, 3 weeks and 1 month) in both groups, but the decrease in the experimental group was more significant: -47.5% *vs* -37.1% at 15 days, -63.9% *vs* -45.9% at three weeks, and -86.1% *vs* -74.4% at 1 month. Regarding the minutes of physiotherapy session per day, the mean in the experimental group increased at 15 days (from 50 to 62.9) and then decreased until discharge (27.6). Differently, in the placebo group, the mean values were more irregular: they decreased slightly at 15 days (from 49.8 to 46) and then increased at both 3 weeks (51.4) and at 1 month (58.6); finally, at discharge, the daily average minutes were 42.4. In detail, (Figs. 1, 2) the mean plots for the VAS and the minutes per daily physiotherapy session across day and treatment groups (A: experimental treatment, B: placebo). The average trend of the VAS in the experimental group decreased almost constantly compared with the placebo group, where it wavered in the final days (Fig. 2). On the contrary, the trends of the minutes of physiotherapy were fluctuating (Fig. 3): in the experimental group it increased until the 14th day of hospitalization and then steadily decreased, whereas in the placebo group it was very oscillating. Notably, the 11th day of hospitalization reported the biggest difference in average minutes per session (within the first three weeks) between treatments, 21.5 ($P<0.001$), 62.9±6.1 in the experimental group and 41.4±8.8 in the placebo one.

Concerning GEE modelling, in the placebo group the VAS significantly decreased on average per day ($\Delta T = -0.099$, $P<0.001$), but in the experimental treatment the decrease was significantly stronger ($\Delta TxTR = -0.058$, $P<0.001$) (Table II). On the other hand, the result of the model on the minutes of physiotherapy per day was different: in the placebo group, a significant increase was detectable, on average

Table I. *Primary and secondary outcomes across time of treatment* (n.b. values are expressed as means ± standard deviations)

Dietary supplementation (experimental) Group							Placebo Group					
Variable		Baseline	15 days (n=19)	3 weeks (n=19)	1 month (n=15)	At discharge		Baseline (n=21)	15 days (n=21)	3 weeks (n=21)	1 month (n=21)	At discharge
(n=19)	15 days		2.53±1.98	1.74±1.37	0.67±0.72	0.11±0.32		4.81±2.18	3.05±1.91	2.62±1.88	1.24±1.09	1±1.18
(n=19)	3 weeks		62.9±6.52	51.8±8.85	33.7±5.16	27.6±4.82		49.8±8.29	46±9.17	51.4±9.24	58.6±8.68	42.4±6.64
(n=19)	1 month					34.7±5.91						37.1±7.91
(n=15)	At discharge											
(n=21)	15 days		15 days	1 month		45 days or at discharge	n	Baseline	15 days	1 month		45 days or at discharge
(n=21)	3 weeks		NA	63.1±18.9		63.1±18.4	20	63.3±11.5	NA	62.4±11.1		61.3±11
(n=21)	1 month		NA	23.7±5.59		23.7±5.54	20	25.8±5.02	NA	25.4±4.68		24.9±4.62
(n=21)	At discharge		NA	26.1±4.26		25.7±3.87	19	27.8 ±3.17	NA	27.1±3.72		26.4±3.96
VAS (units)			NA	31±5.18		31.1±4.58	19	32.3±3.97	NA	31.4±3.71		30.6±3.99
(primary outcome)		4.84±2.09	NA	NA		17.2±3.86	16	2.5±5.3	NA	NA		15.3±4.8
Daily physioterapy session (minutes)		50±8.82	383±155	NA		NA	21	286±130	284±120	NA		NA
Days of hospitalization			50.4±14.6	NA		NA	21	40.6±17.8	41.3±18.2	NA		NA
			58.1±21.2	NA		NA	21	56.9±19.1	57.7±17.7	NA		NA
Variable	n	Baseline	30.4±32.3	NA		NA	21	12.9±23.7	10.8±17.4	NA		NA
at discharge	n	Baseline	NA	8.94±8.07		9±8.15	19	9.95±6.55	NA	10.6±6.76		11.2±7.07
at discharge			NA	18.2±3.69		18.2±3.67	19	15.9±3.37	NA	15.7±4.31		15.7±4.38
Weight (kg)	18	64±19.1	4.17±0.96	NA		4.193±1.06	12	4.28±1.13	4.31±1.2	NA		4.733±1.45
BMI (kg/m2)	18	24±5.39	6.68±1.97	NA		6.68±1.92	12	7.56±2.15	7.42±2.07	NA		7.85±2.1
Mid-Arm Circumference (cm)	18	26.8 ±3.96	NA	NA		6.10 ± 1.25	11	7.46 ± 1.2	NA	NA		6.85 ± 0.946
Calf Circumference (cm)	18	31.4±4.3	NA	NA		18.99 ± 6.33	10	22.29 ± 7.40	NA	NA		22.16 ± 7.69
Tinetti (units)	17	4.82±6.1	NA	NA		37.28 ± 8.74	11	39.51 ± 7.06	NA	NA		38.19 ± 5.98
SF 36 (units)	18	355±153	NA	NA		2.144±0.752	10	1.964±0.861	NA	NA		1.946±0.885
SF PHS (units)	18	46.2±15.4	NA	NA		3.57 ± 0.91	11	4.14 ± 1.06	NA	NA		4.01 ± 0.85
SF MHS (units)	18	56.4±21.6	NA	NA		12.45 ± 3.23	11	14.56 ± 3.16	NA	NA		14.08 ± 3.04
SF Physical activity (units)	18	22.6±31.1	NA	90.2 ± 13.1		NA	20	87 ± 9.09	NA	87.8 ± 9.23		NA
GDS (units)	16	7.44±7.16	NA	8.40 ± 4.15		NA	20	10.1 ± 7.48	NA	9.62 ± 7.07		NA
MNA (units)	16	17.9±4.33	NA	1.89 ±		NA	20	2.20 ± 1.59	NA	2.09 ±		NA
				0.98						1.48		
Phase Angle (degree)	15	3.91±0.8	NA	6.96 ± 0.36		NA	15	7.06 ± 0.49	NA	6.94 ± 0.52		NA
BCMI (kg/m2)	15	6.49±1.97	NA	4.42 ± 0.32		NA	15	4.34 ± 0.371	NA	4.20 ± 0.25		NA
RSMM (kg/m2)	13	6.31 ± 2.11	NA	0.187 ± 0.147		NA	15	0.229 ± 0.379	NA	0.313 ±0.432		NA
Fat mass (kg)	13	20.57 ± 7.04	NA	28.4 ± 15		NA	15	28.8 ± 11.2	NA	31.0 ± 14		NA
Free fat mass (kg)	13	37.74 ± 9.27	NA	75.9 ± 18.6		NA	21	84.7 ± 37.9	NA	85.6 ± 40		NA

(n.b. values are expressed as means ± standard deviations). ET group: experimental treatment group; n: sample size; VAS: Visual Analogue Scale; BMI: Body Mass Index; SF: Short form; PHS: Physical health status; MHS: Mental health status. GDS: Geriatric Depression Scale; MNA: Mini Nutritional Assessment; BCMI: Body Cell Mass Index; RSMM: Relative Skeletal Muscle Mass; HOMA: homeostasis model assessment; CRP: C-reactive protein. Values are expressed as means ± standard deviations; NA: Not Available.

Table II. *Results of the Generalized Estimating Equation models on VAS and minutes per daily physiotherapy session*

Outcome	MD between treatments at baseline (ref. placebo) (Δ_{TR})	Δ/ day in placebo group (Δ_T)	MD between treatments per day (ref. placebo group) (Δ_{TxTR})
VAS *(primary outcome)*	**Δ_{TR} = 0.586 P=0.005 95%CI= 0.180; 0.993**	**Δ_T = -0.099 P<0.001 95%CI= -0.109; -0.088**	**Δ_{TxTR} = -0.058 P<0.001 95%CI= -0.076; -0.040**
Minutes per daily physiotherapy session	**Δ_{TR} = 24.18 P<0.001 95%CI= 21.922; 26.452**	**Δ_T = 0.263 P<0.001 95%CI= 0.188; 0.339**	**Δ_{TxTR} = -1.285 P<0.001 95%CI= -1.382; -1.189**
Minutes per daily physiotherapy session (only for the first fifteen days)	**Δ_{TR} = 5.463 P<0.001 95%CI= 2.424; 8.502**	**Δ_T = -0.384 P=0.002 95%CI= -0.626; -0.143**	**Δ_{TxTR} = 1.193 P<0.001 95%CI= 0.876; 1.509**
Minutes per daily physiotherapy session (quadratic model with centered time predictor)	**Δ_{TR} = 3.060 P<0.001 95%CI= 1.751; 3.667**	**Δ_T = 0.311 P<0.001 95%CI= 0.237; 0.384**	**Δ_{TxTR} = -1.285 P<0.001 95%CI= -1.379; -1.189**
		Δ_T^2 = -0.011 P<0.001 95%CI= -0.015; -0.007	**$\Delta_T^2{}_{xTR}$ = -0.028 P<0.001 95%CI= -0.036; -0.020**

*MD: Mean difference; Δ: average variation of the outcome. In **bold** the statistically significant evidences (P<0.05). P=P-value. 95%CI: 95% confidence interval. VAS: Visual Analogue Scale. T^2: quadratic centered time predictor.*

by ΔT=0.263 (P<0.001), whereas in the experimental group the mean outcome decreased (ΔTxTR =-1.285, P<0.001) (Table II). However, as pointed out above, the mean of the minutes of physiotherapy did not have a linear trend (not even approximately), but the curves in both groups were a bit fluctuating. Regarding that, firstly, we fitted a further GEE model on the subset of data referring to the first fifteen hospitalization days, whose trends were approximately linear: in this time lag, the results were inverted, and we got a significant decrease in the placebo group (ΔT =-0.394, P=0.002) and a stronger increase in the experimental group (ΔTxTR =1.193, P<0.001) (Table II). Secondly, we fitted a further model where we also included a quadratic term for the predictor time (both as main effect and interaction with treatment) due to the curved trend on the whole hospitalization period. Briefly, if the means were monotonically increasing or decreasing over time, but in a curvilinear way, a model with quadratic terms could be appropriate. In this model, the rate of change in the mean response is not constant, but depends on time, and is expressed by two parameters of main effects (ΔT andΔT2) and two others of interaction (ΔTxTR and ΔT2xTR). At the interpretative level, if there is a positive effect of time and a negative effect of time squared, that means that in patients with a greater number of hospitalization days from the acute event, the effect of time is lessened. On the contrary, a positive effect of the time and a positive effect of the time at squared means that in patients with a greater number of hospitalization days, the effect is stronger. Finally, in order to avoid problems of collinearity we have centered the time predictor, considering it as deviation from the mean. Given that, the last row of Table II shows that in the placebo group the minutes of physiotherapy increased (ΔT= 0.311, P<0.001), but when the number of hospitalization days was increased, the effect tended to lessen (ΔT2= -0.011, P<0.001). On the other hand, in the experimental group, the mean outcome decreased in both linear (ΔTxTR= -1.285, P<0.001) and quadratic form (ΔT2xTR= -0.028, P<0.001), i.e. during long hospitalizations. The significance of the last quadratic term was likely due to the increase in minutes in the first ten days that consequently softened the overall linear decrease.

In addition, in order to detect the direct effects of the VAS on the minutes of physiotherapy within 15 days across treatments, we fitted two further GEE models. This considered, the effect was more

negative in the experimental group (-1.254, P<0.001) than in the placebo group (-0.898, P<0.001), but taking time into account, the trends were opposite: in the experimental group the time effect was positive (0.779, P<0.001), whereas in the placebo group it was negative (-0.358, P=0.004) (Fig. 4).

Regarding the modelling on the other outcomes, only the Tinetti scale reported a significant value, as expected, increasing by 12.81 units (P<0.001) at discharge or after 45 days of hospitalization in the placebo group. Analogously, the expected increase in the experimental treatment was comparable and was represented by the lack of significance of the interaction term (ΔT3xTR= -0.46, P=0.850).

Finally, it is worth emphasizing that the all markers of quality of life, such as SF MHS, SF PHS and SF PA, showed a slight (non-significant) improvement of the means at 15 days in the experimental group, that were more noticeable than the changes seen in the placebo group (Table I). Moreover, in a supplemental analysis carried out by using two-way ANOVA for repeated measures, the interaction of the SF-36 outcome was significant (P=0.036).

DISCUSSION

The study demonstrates the effectiveness of supplemented amino acids in reducing pain levels and the time of its resolution in the experimental patient subgroup after surgical treatment for hip fracture. Pain reduction may be very important for the continuation of physiotherapy and the retrieval of function (3). Pain decrease was associated with a significant increase in the duration of daily physical therapy session. The time needed for physiotherapy was 35% lower in the experimental group than in the placebo one. Of note, at discharge, patients on amino acids did not complain of pain. It is probable that essential amino acid acted both centrally (brain) and peripherically by wound repairing in the operated limb. Centrally, the essential BCAAs i) reduce the excitotoxic extracellular glutamate (9), ii) increase brain contents in GABA, histamine and serotonine (10). Peripherally, essential amino acids favor wound repairing in the operated limb (3) and accelerate post-injury muscle regeneration (11). Amino acid-associated effectiveness and efficiency of physical therapy not observed in the placebo group, were supported by three factors. Firstly, during the first 15 days of treatment, the quicker decline of pain was linked to a more prolonged time dedicated to each session of physical therapy. Secondly, from 15th day to discharge, each session of physical therapy required progressively less time. Thirdly, at discharge, patients on amino acids virtually did not complain of pain. These benefits were associated with enhanced improvement, although not statistically significant, in physical health and mental health dimensions of the SF-36 test. Likely, improved test performance was due to reduced pain levels. Considering the interaction between treatment and 1-month CRP levels, it can be accounted for by the reduction of proinflammatory markers by essential amino acids, in particular branched-chain ones (12). In conclusion, the results of this study indicated that, during the first 15 days of hospitalization, the decrease of average VAS was associated with the increased average duration of the physio-session, therefore indicating the effectiveness of EAA supplementation on pain in the elderly with a hip fracture.

REFERENCES

1. Ross J, Tennant F. Amino acids and diet in chronic pain management. Prat Pain Manag 2009; 9(3):34-40.
2. Ross J, Adema D. Nutritional supplements in pain practice. Prat Pain Manag 2011; 9(9).
3. Baldissarro E, Aquilani R, Boschi F, et al. The hip functional retrieval after elective surgery may be enhanced by supplemented essential amino acids. Biomed Res Int 2016; 2016:9318329.
4. Rondanelli M, Opizzi A, Antoniello N, et al. Effect of essential amino acid supplementation on quality of life, Amino acid profile and strength in institutionalized elderly patients. Clin Nutr 2011; 30(5):571-67.
5. Aquilani R, Zuccarelli Ginetto C, Rutili C, et al. Supplemented amino acids may enhance the walking recovery of elderly subjects after hip fracture surgery. Aging Clin Exp Res 2019; 31(1):157-60.
6. Stechmiller JK. Understanding the role of nutrition and wound healing [Internet]. Vol. 25, Nutrition in Clinical

Practice. John Wiley & Sons, Ltd; 2010. p. 61-68.
7. Janssen I, Baumgartner RN, Ross R, Rosenberg IH, Roubenoff R. Skeletal muscle cutpoints associated with elevated physical disability risk in older men and women. Am J Epidemiol 2004; 159(4):413-21.
8. Farrar JT, Young JP, LaMoreaux L, Werth JL, Poole RM. Clinical importance of changes in chronic pain intensity measured on an 11-point numerical pain rating scale. Pain 2001; 94(2):149-58.
9. Bastone A, Micheli A, Beghi E, Salmona M. The imbalance of brain large-chain aminoacid availability in amyotrophic lateral sclerosis patients treated with high doses of branched-chain aminoacids. Neurochem Int 1995; 27(6):467-72.
10. García-Espinosa MA, Wallin R, Hutson SM, Sweatt AJ. Widespread neuronal expression of branched-chain aminotransferase in the CNS: implications for leucine/glutamate metabolism and for signaling by amino acids. J Neurochem 2007; 100(6):1458-68.
11. Stamler JS, Meissner G. Physiology of nitric oxide in skeletal muscle. Physiol Rev 2001; 81(1):209-37.
12. Solerte SB, Gazzaruso C, Bonacasa R, et al. Nutritional Supplements with oral amino acid mixtures increases whole-body lean mass and insulin sensitivity in elderly subjects with sarcopenia. Am J Cardiol 2008; 101(11 suppl):69E-77E.

JOURNAL OF BIOLOGICAL REGULATORS & HOMEOSTATIC AGENTS Vol. 34, no. 2, 733-737 (2020)

LETTER TO THE EDITOR

THE PIVOTAL ROLE OF ORAL MICROBIOTA IN HEALTH AND DISEASE

L. SANTACROCE[1,2*], N. SARDARO[3*], S. TOPI[4], F. PETTINI[5*], L. BOTTALICO[6], S. CANTORE[5,6,7,8], G. CASCELLA[5], R. DEL PRETE[5], G. DIPALMA[5§] and F. INCHINGOLO[5§]

[1]Ionian Department, University of Bari "Aldo Moro", Bari, Italy; [2]Microbiology and Virology, University Hospital of Bari, Bari, Italy; [3]Department of Basic Medical Sciences, Neurosciences and Sense Organs, University of Bari "Aldo Moro", Bari, Italy; [4]School of Technical Medical Sciences, University of Elbasan "A. Xhuvani", Elbasan, Albania; [5]Department of Interdisciplinary Medicine, University of Bari "Aldo Moro", Bari, Italy; [6]PolyPheno Srl. Academic Spin Off, University of Bari "Aldo Moro", Taranto, Italy; [7]BPP School of Health, University Faculty of Dentistry, Birmingham, United Kingdom; [8]Sorriso & Benessere Ricerca e Clinica S.r.l., Bari, Italy

Received February 27, 2020 – Acceptted April, 2020

[*]These authors contributed equally to this work as co-first Authors

To the Editor,

Human microbiota, especially of the gut and the oral ones, represent one of the most interesting current topics in biomedicine. The term microbiota is considered a neologism originated in the early 21st century thanks to Joshua Lederberg, a US microbiologist awarded with Nobel Prize in 1958 "for his discoveries concerning genetic recombination and the organization of the genetic material of bacteria", but he was actually the first to popularize such term when it was overlapped with the term "microbiome" (1). In fact, the two words "microbiota" and "microbiome" are commonly used as synonyms, also within the medical community. Consulting the main scientific database to find the first reports of these terms in scientific literature, we found that the use of the word microbiota is from 1956, and the first report of the word microbiome appears in 2002. However, the second paper appearing in such search was related to the oral microbiota, starting a long series of documents about this argument (1).

Interest in the biology of microbes hosted in our mouth from the appearance of the theory of focal sepsis, has led to the discovery of a close relationship between dental diseases, e.g. dental decay, and heart diseases (2). Such theory was promptly and universally accepted by dentists, although no clear evidence was available at that time. Most recently, at the beginning of the 3rd millennium, the attention of the scientific community has turned to the idea of possible interactions between the oral microbiota and the health status (2), and in 2007 the Human Microbiome project was started.

Oral microbiota and dental diseases

Dental diseases are the effect of a dangerous change in the balance of the normally stable resident oral microbiota (3). Bacteria are the principal residents of the oral cavity. In healthy individuals, the most abundant bacterial phyla are represented by *Firmicutes, Proteobacteria, Actinobacteria, Bacteroidetes* and *Fusobacteria* (4). In the tissues

Key words: oral microbiota; oral diseases; systemic conditions; cancer; diabetes; immune regulation; probiotics

Corresponding Author:
Prof. Francesco Pettini, DMD
Department of Interdisciplinary Medicine,
University of Bari "Aldo Moro",
Piazza G. Cesare, 11, 70124 Bari, Italy
Tel./Fax: +39 0805478732
e-mail: francesco.pettini@uniba.it

0393-974X (2020)
Copyright © by BIOLIFE, s.a.s.
This publication and/or article is for individual use only and may not be further reproduced without written permission from the copyright holder.
Unauthorized reproduction may result in financial and other penalties
DISCLOSURE: ALL AUTHORS REPORT NO CONFLICTS OF INTEREST RELEVANT TO THIS ARTICLE.

of the oral cavity a certain balance is established between the myriad of physiologically present bacterial species and the elements of the host's immune system. In this scenario it is necessary to consider not only bacterial-host species interactions, but also bacterium-bacterium interactions (5). These indigenous microbes must engage and co-evolve with their neighbors and hosts, as well as adapt to diverse, rapidly fluctuating conditions. Bacteria colonize these areas within a few minutes of birth and co-evolve with shifts in the host through two dentition states, concomitant changes in food habits, oral hygiene practices and lifestyle shifts (6).

Inter-individual variation in microbiota organization results from differences in the environment, genetics, age and lifestyle of the host. Alterations in the microbiome caused by certain stress factors, such as carbohydrate uptake or plaque accumulation, can lead to the evolution of oral diseases, e.g. caries, periodontal diseases (7), endodontic lesions, dry socket, halitosis, and odontogenic infections. Furthermore, oral bacteria can be related or used as markers (8) for some systemic diseases, such as pancreatic cancer, low weight, preterm birth, heart disease, Crohn's pediatric disease, and type II diabetes (2).

In the oral cavity, autochthonal species can reach all surfaces carried by the flow of saliva, but the local corresponding conditions determine which species are able to successfully adhere and colonize. As a result, biofilms that form in different habitats of the oral cavity (e.g. teeth, tongue, gingival fissure, and oral mucosa) have a distinct microbial composition. The composition changes as the biofilm grows (e.g., the hours after oral hygiene), which is most relevant for the non-shedding surfaces. Biofilms on the teeth, or dental plaque, are associated with the most common oral diseases (caries and periodontal diseases). Oral epithelia are lost several times a day, which restricts biofilm accumulation.

When the micro-environment changes, as a function of systemic antibiotics that negate the protective influence of commensals, reduced oxygen tension caused by increase in biofilm thickness, altered host defenses, or nutritional, metabolic and structural stresses within the ecosystem, a dysbiosis occurs in the indigenous microbiome, by reducing the abundance of the commensal population and increasing a pathogen-rich ecosystem (10).

We can divide the oral microbiota into 3 main areas: the first and least colonized is the mucosa, which includes the cheeks, gums, and tongue, and its inhabitants are affected by constant epithelial removing. A healthy oral mucosa is composed of *Streptococcus*, *Rothia*, and *Eubacterium* species, but invasions by *Prevotella*, *Porphyrmonas*, and *Tannerella* can lead to the simple oral condition halitosis (2,3). The second and most different area of the oral microbiome is the saliva, which, although being constantly secreted and swallowed, houses a relatively stable composition of bacteria, fungi, and other microorganisms. The salivary hollow is composed by phyla similar to those of the bowel, including *Bacteroidetes*, *Firmicutes*, *Proteobacteria* and *Actinobacteria*. Saliva is a recognized pool of biological markers that range from changes in biochemical molecules such as DNA, RNA and proteins, to those in the structural composition of the microbiota. Furthermore, saliva plays an important role in the development of oral biofilm and maintenance. The last microhabitat of the oral microbiome is the teeth, whose hard and solid nature differentiate them from all other environments within the human microbiome. The oral microbiome is directly responsible for a variety of common oral disorders, such as dental caries, gingivitis, and periodontitis (Fig. 1).

Oral microbiota and dental caries

Dental caries (or tooth decay) is a common oral disorder mainly caused by the bacterial species *Streptococcus mutans*, although *Veillonella*, *Bifidobacterium*, and *Prevotella* species were also observed in greater abundance in children with multiple dental caries compared to those with none. The bacteria correlated with dental caries prosper in the acid environment that can result from a high-sugar diet. These bacteria can then maintain that environment by producing weak acids that demineralize the teeth and make them susceptible to infection and the development of dental caries. In one study it was observed that the presence of

various species of lactobacillus can drastically reduce the formation of dental caries, suggesting a possible use of probiotics in the prevention and treatment of caries (1).

Oral microbiota and periodontitis

Inside the oral cavity, the dense environment of autochthonous microbes keeps the gingiva in a low activated state so that it is able to respond directly to pathogenic challenges to maintain homeostasis. This homeostatic balance is controlled by the continuous triggering of the hosts via key receptors, known as toll like receptors (TLRs) (11). A dysbiotic oral microbiome and the following inflammatory

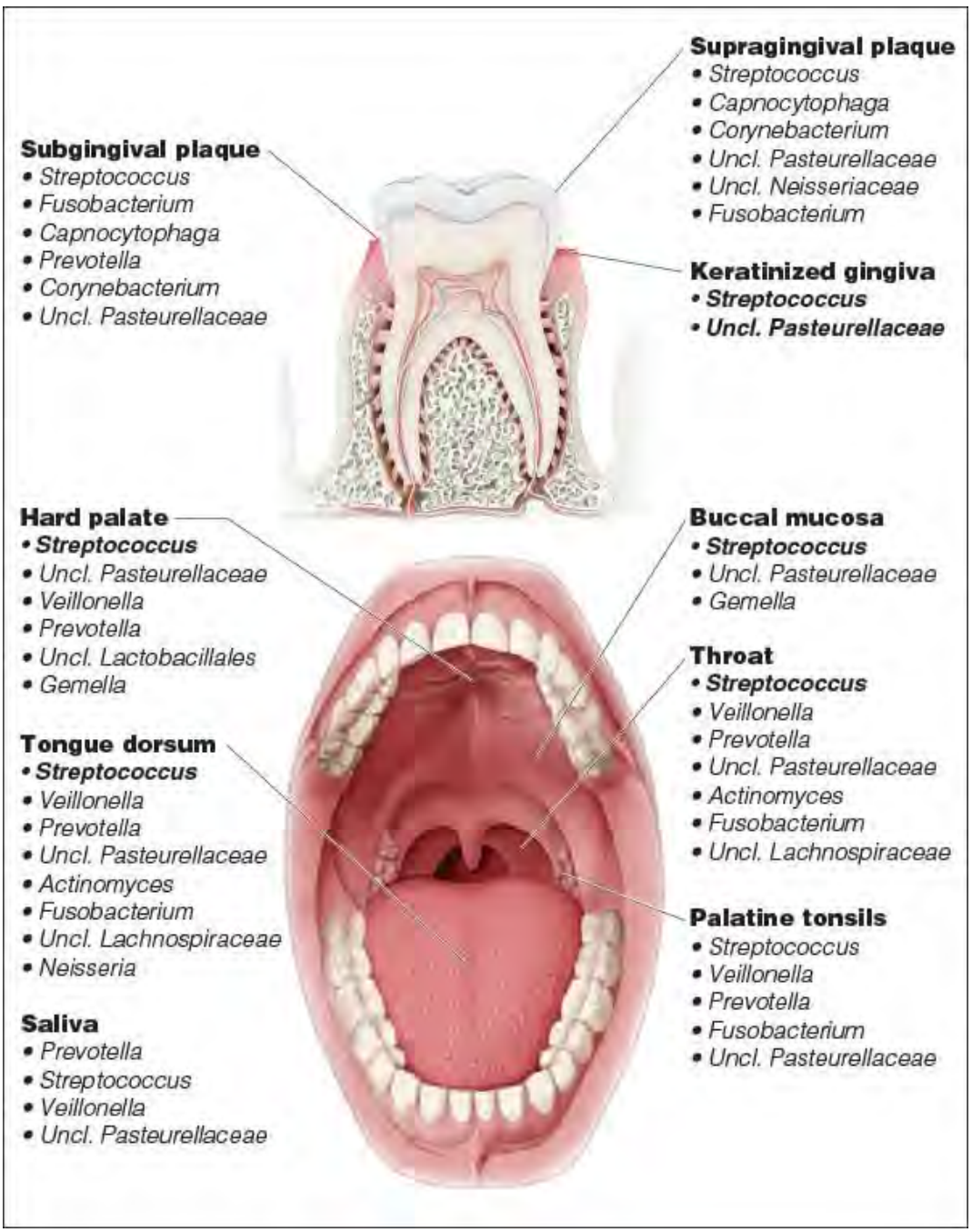


Fig. 1. *Microbial diversity in the oral cavity.*

Table I. *Microbiota present in oral diseases.*

Caries	*Streptococcus mutans, Lactobacillus spp.*
Oral Cancer	*Peptostreptococcus stomatis, Streptococcus salivarius, Streptococcus gordonii, Gemella haemolysans, Gemella morbillorum, Johnsonella ignava, Streptococcus parasanguinis.*
Gingivitis	*Leptotrichia, Selenomonas, Streptococcus, Veillonella, Prevotella, Lautropia, Haemophilus.*
Periodontal Disease	*A. actinomycetemcomitans, P. gingivalis, F. alocis, P. intermedia, F. nucleatum, T. forsythia, E. corrodens, T. denticola.*

events of the host are the origin of the main dental problems, such as periodontitis and caries. TLRs have important roles in host-microbe interactions by recognizing pathogens and activating innate immunity (2). The immune-inflammatory reaction to this pathogenic colonization produces the destruction of the attachment between the tooth and the gingiva, and loss of structures that anchor the tooth to the mandibula. These two events in partnership result in an excavation of the gingival sulcus, which is the space between the tooth and the gingiva (10-12). This inflamed sulcus, known as a periodontal pocket, provides the ideal environmental conditions for the colonization of anaerobic species that are extremely harmful to humans.

Oral status and systemic conditions

Oral bacterial diseases, such as caries and periodontitis, are not caused by a single species, but by a consortium of species that are likely living harmlessly in very low numbers (often below the limit of detection) in the oral cavity. In essence, oral bacterial diseases are opportunistic infections, and thus disease occurs under certain circumstances and conditions, e.g., diet, host immune response, complicating systemic or genetic disorders, pH, poor oral hygiene, lifestyle.

These oral conditions have not only local effects on the dentition and on tooth-supporting tissues, but may also have an impact on many systemic conditions. Emerging evidence suggests that poor oral health influences the initiation and/or progression of diseases such as atherosclerosis, with sequelae including myocardial infarction and stroke, diabetes mellitus, neurodegenerative diseases, such as Alzheimer's disease, rheumatoid arthritis, pulmonary diseases among others (2, 3). Aspiration of oropharyngeal (including periodontal) bacteria causes pneumonia, especially in hospitalized patients and the elderly, and may influence the course of chronic obstructive pulmonary disease (Table I).

Conversely, many systemic conditions may have a negative influence on oral health, e.g. tumors, cardiac diseases, immune disorders (2), and sepsis.

Sepsis is a relatively common life-threatening condition that can arise from dental foci as well as from distant infectious sites, able to determine a cascade of molecular events that determine its clinical expression in the whole body (4, 5).

DISCUSSION

Based on current reported data regardig the relationships between oral and general health status, it is evident that the composition of human oral microbiota is closely linked to wellbeing. Oral microbiota includes up to 400 bacterial species and many yeasts, and its composition is continuously modified and influenced by personal and socio-economic factors, lifestyle (diet, oral hygiene), diseases and therapies, etc. (3).

It is well established that the normal composition of the oral microbiota is warranted by the maintenance of the physiological salivation and the correct lifestyle including routine and professional oral hygiene (11). A balanced diet is very important in such regulation, because of the supply of useful micronutrients for the bacteria and regulatory molecules (i.e., prebiotics, essential oils, etc.) that may help "good" bacteria in controlling "bad" microorganisms. Most recently, the use of probiotics and symbiotics has been proposed as a possible biological modulator of the oral microbiota, based on the known ability of these products to control and regulate the overgrowth of bacterial pathogens.

Probiotics are commonly considered for integrative therapy and prevention of many clinical conditions, but increasing evidence of their utility in oral pathology exists (7). In conclusion, the role of oral microbiota in determining oral and systemic health is currently confirmed by substantial evidence, as well as its possible modulation by probiotics.

REFERENCES

1. Inchingolo F, Dipalma G, Cirulli N, et al. Microbiological results of improvement in periodontal condition by administration of oral probiotics. J Biol Regul Homeost Agents 2018; 32:1323-28.
2. Ballini A, Cantore S, Farronato D, et al. Periodontal disease and bone pathogenesis: the crosstalk between cytokines and porphyromonas gingivalis. J Biol Regul Homeost Agents 2015; 29:273-81.
3. Giudice G, Cutrignelli DA, Sportelli P, et al. Rhinocerebral Mucormycosis with Orosinusal Involvement: Diagnostic and Surgical Treatment Guidelines. Endocr Metab Immune Disord Drug Targets 2016; 16:264-69.
4. Di Serio, F, Lovero, R, D'Agostino, et al. Evaluation of procalcitonin, Vitamin D and C-reactive protein levels in septic patients with positive emocoltures. Our preliminary experience. Acta Medica Mediterr 2016; 32:1911-14.
5. Grassi FR, Ciccolella F, D'Apolito G, et al. Effect of low-level laser irradiation on osteoblast proliferation and bone formation. J Biol Regul Homeost Agents 2011; 25:603-14.
6. Ballini A, Tetè S, Scattarella A, et al. The role of anti-cyclic citrullinated peptide antibody in periodontal disease. Int J Immunopathol Pharmacol 2010; 23:677-81.
7. Ballini A, Santacroce L, Cantore S, et al. Probiotics efficacy on oxidative stress values in inflammatory bowel disease: A randomized double-blinded placebo-controlled pilot study. Endocr Metab Immune Disord Drug Targets 2019; 19:373-81.
8. Cantore S, Ballini A, Farronato D, et al. Evaluation of an oral appliance in patients with mild to moderate obstructive sleep apnea syndrome intolerant to continuous positive airway pressure use: Preliminary results. Int J Immunopathol Pharmacol 2016; 29:267-73.
9. Cicinelli E, Ballini A, Marinaccio M, et al. Microbiological findings in endometrial specimen: our experience. Arch Gynecol Obstet 2012; 285:1325-29.
10. Grassi FR, Pappalettere C, Di Comite M, et al. Effect of different irrigating solutions and endodontic sealers on bond strength of the dentin-post interface with and without defects. Int J Med Sci 2012; 9:642-54.
11. Foti C, Romita P, Rigano L, et al. Isobornyl acrylate: an impurity in alkyl glucosides. Cutan Ocul Toxicol 2016; 35:115-19
12. Scattarella A, Ballini A, Grassi FR, et al. Treatment of oroantral fistula with autologous bone graft and application of a non-reabsorbable membrane. Int J Med Sci 2010; 7:267-71.

LETTER TO THE EDITOR

INFLUENCE OF CLINICIAN'S SKILL ON PRIMARY IMPLANT STABILITY WITH CONVENTIONAL AND PIEZOELECTRIC PREPARATION TECHNIQUES: AN *EX-VIVO* STUDY

A. GIUDICE[1], F. BENNARDO[1], A. ANTONELLI[1], S. BARONE[1], F. WAGNER[2], L. FORTUNATO[1] and H. TRAXLER[3]

[1]School of Dentistry, Department of Health Sciences, Magna Graecia University of Catanzaro, Italy;
[2]Department of Cranio-Maxillofacial and Oral Surgery, Medical University of Vienna, Austria;
[3]Institute of Anatomy, Center for Anatomy and Cell Biology, Medical University of Vienna, Austria

Received February 17, 2020 – Accepted April 3, 2020

To the Editor,

Osseointegration was defined as a direct and functional connection between bone and an artificial implant. This discovery paved the way for the development of modern dental implantology over the last 50 years (1). Success of dental implants is strictly related to their primary stability (PS). The implant body design and the thread geometry significantly influence PS, as well as the surgical technique. PS is influenced also by bone quality, particularly by cortical thickness, and even by implant surface treatment (2). However, the quality of surgical osteotomy, potentially affecting PS, could be influenced by the clinician's surgical experience (3). The main rules for dental implant success include a careful and little traumatic technique for implant bed preparation to avoid bone overheating and obtain sufficient PS without excessive cortical compression (4). Several surgical protocols have been proposed for implant site preparation. The traditional technique involves the use of calibrated rotating drills. The advantages of this protocol are efficiency, reliability and ease of use. Recently, piezoelectric technology has proved to be a valid alternative to traditional methods. Piezoelectric surgery uses ultrasounds to perform selective osteotomies, with the aim to preserve nerves, vessels and soft tissues. The precision of cutting, the cavitation effect which improves intra-operative visibility and a faster bone healing response are the main features of ultrasonic surgery (5). Vercellotti et al. in 2014 analyzed 3579 implants placed after piezoelectric preparation with a 1-to-3-year follow-up (6). In this multicenter case series study, a piezoelectric device was identified as a valuable tool for implant site preparation showing only 2.26% failure rate after up to 3 years of follow-up. Several studies analyzed potential differences between traditional and piezoelectric techniques, evaluating insertion torque (IT) and implant stability quotient (ISQ). A clinical study by Stacchi et al. suggested that ultrasonic implant site preparation showed a limited decrease of ISQ values and an earlier shifting from a decreasing to an increasing stability pattern, when compared with traditional drilling technique (7). However, in this study, PS resulted similar between piezoelectric surgery and traditional technique at baseline. Analysis of the factors affecting implant success have been extensively reported in the literature; however, research conducted on the effects of clinical experience has been very limited.

Key words: cadaver study; dental implantology; experience; implant stability; piezoelectric surgery

Corresponding Author:
Francesco Bennardo DDS, PhDs
School of Dentistry,
Department of Health Sciences,
Magna Graecia University of Catanzaro, Viale Europa,
88100 Catanzaro, Italy
Tel.: +39 346 180 2826 - Fax: +39 0961 712 402
e-mail: francesco.bennardo@unicz.it

0393-974X (2020)
Copyright © by BIOLIFE, s.a.s.
This publication and/or article is for individual use only and may not be further reproduced without written permission from the copyright holder.
Unauthorized reproduction may result in financial and other penalties
DISCLOSURE: ALL AUTHORS REPORT NO CONFLICTS OF INTEREST RELEVANT TO THIS ARTICLE.

The aim of this study was to evaluate PS of implants (in terms of IT and ISQ values) placed into fresh human mandibles by clinicians with different levels of experience using two different site preparation protocols (twist drill *vs* piezoelectric surgery).

MATERIALS AND METHODS

The study was conducted during a hands-on implantology course on fresh non-frozen human cadavers. The study protocol was approved by the Institutional Review Board of reference for the Center of Anatomy and Cell Biology - Medical University of Vienna, authorizing to use the bodies for teaching and medical research (protocol number 161008 – approved on October 31, 2016). All experiments were conducted in full accordance with ethical principles, including the World Medical Association Declaration of Helsinki.

One month before the course all the participants received a survey about their clinical abilities. Considering the survey results, trainees were divided into 3 groups: a basic experienced group (they had never used these surgical techniques or had placed less than 50 implants – Group 1), a medium experienced group (placed from 150 to 300 implants – Group 2) and a highly experienced group (more than 500 implants – Group 3). Two clinicians were randomly selected with basic experience, two with medium experience and two with high experience.

A total of 60 implants (Neoss ProActive Tapered, Neoss, Harrogate, United Kingdom) were inserted in 12 human fresh non-frozen cadaver mandibles: 30 implants placed in sites prepared with traditional technique and 30 implants in sites prepared by piezoelectric technique (Fig. 1). Each surgeon placed 10 implants, 5 for surgical technique in similar mandible sites.

Each mandible, fully or partial edentulous, was analyzed clinically and radiologically (MRI images available for consultation at the Institute of Anatomy of Medical University of Vienna) in order to determine the presence of sufficient bone height and width to receive 4.0 Ø x 9 mm length tapered implants. Neoss ProActive Tapered implants are conical (4.0 Ø x 9 mm in this case), in pure titanium, with a treated surface (blasting, etching).

Surgical procedures

The two surgical techniques were performed on similar sites of the same edentulous area for a better standardization. Twelve human fresh non-frozen cadaver mandibles were used to assure the same experimental conditions for all operators. Traditional technique was performed using a surgical motor drill (ChiroproL, Bien-Air Dental SA, Biel/Bienne, Switzerland), using the drilling protocol recommended by the manufacturer. Instructions were provided to clinicians regarding implant bed preparation in order to ensure a standardized approach. Drilling was performed with an in-and-out movement without stopping the handpiece motor until the drill reached the desired depth (9 mm). Motor setting was the same for all groups: drilling speed of 800 rpm with irrigation. Drills were replaced after ten uses as recommended by the manufacturer.

Drilling for Neoss ProActive Tapered implant (4.0 Ø x 9 mm length) in type II bone started with the first 1.5 mm diameter drill, then 2.2 mm diameter pilot drill, 3.0 mm diameter tapered drill, 3.4 mm tapered drill and finished with the countersink Ø4.0T (Fig. 1 A). Piezoelectric technique was performed using Piezosurgery Touch with an Implant preparation kit pro (Mectron, Carasco, Italy) for each skull. Site preparation protocol started with IM1S insert, followed by IM2P (2.0mm diameter). P2-3 tip was then used to optimize preparation concentricity and, finally, IM3P (3.0 mm diameter) and P3-4 were used (Fig. 1 B).

In order to make sure that the osteotomies had the same final diameter, the clinician fitted a 3.4 mm tapered drill into the site after completing piezoelectric preparation. Execution of the two techniques was monitored by an expert tutor for Group 1, who followed the surgical operation sequence and checked the instructions of the manufacturer's protocols.

At the end of site preparations, implants were inserted (Fig. 2 A) with the same surgery motor drill (ChiroproL, Bien-Air Dental SA, Biel/Bienne, Switzerland). Whenever implant placement stopped, the insertion was completed manually.

PS evaluation

Evaluation of PS was performed by measuring IT and RFA. Final IT value was measured using a manual torque gauge (Dial Torque Screwdriver FTD100CN, Tohnichi Mfg, Tokyo, Japan) and was recorded in Newton x centimeter (Ncm) (min. 20, max. 100 – grad.

2). Each placed implant resulted in a single value at the end of the insertion, and mean values were collected by groups and compared. Resonance frequency analysis (RFA) was determined in ISQ values with the PenguinRFA device (Integration Diagnostics Sweden AB, Gothenburg, Sweden). This instrument measures the resonance frequency of a customized autoclavable titanium MultiPegTM with a non-contacting technique. The MultiPeg was screwed inside the implant, and magnetic waves produced by PenguinRFA simulated the stress of the prosthetic load. Measurements were taken as follows: the probe was laterally oriented in relation to the transducer and ISQ values were recorded for each fixture in two directions (mesio-distal, bucco-lingual). Every single measurement was repeated at least twice and the highest value was taken as reference for the statistical analysis (Fig. 2 B). The time required to perform surgical site preparation was recorded with a digital chronometer by an independent operator.

Statistical analysis

Statistical analysis was performed with the software STATA version 14 (STATA Corp., Texas, USA). A two-way ANOVA test was used to evaluate differences within groups and the impact of the operator on the stability parameters. Multiple comparisons were performed using Student's *t*- test. Significance level was set at p=0.05. Data were expressed as mean value ± S.D. and ranges were calculated for each group.

RESULTS

In this study 60 implants were placed in edentulous mandible using two different surgical techniques: 30 were placed following traditional drill protocol and 30 after ultrasonic site preparation. Clinicians were divided into three groups according to their experience (group 1 basic, group 2 medium, group 3 expert). Each group placed 10 implants preparing the sites with traditional twist drills, and 10 implants using piezoelectric surgery. Mean values of IT, ISQ and time are reported in Table I.

IT analysis

Mean IT of implants placed after traditional site preparation was 42±10.5 Ncm in group 1, 49.8±7.3 Ncm in group 2 and 50.8±8.0 Ncm in group 3. IT exhibited statistically significant differences between group 1 and group 2 ($p = 0.02$) and between group 1 and group 3 ($p = 0.01$). No differences were detected between group 2 and group 3 ($p = 0.33$) (Fig. 3 A).

Implants placed after piezoelectric preparation protocol showed the following mean IT values: 48.0±8.7 Ncm in group 1, 49.4±8.1 Ncm in group 2 and 51.6±7.9 Ncm in group 3. Analysis of IT values did not demonstrate statistically significant differences between group 1 and group 2 ($p = 0.31$), between group 1 and group 3 ($p = 0.11$) and between group 2 and group 3 ($p = 0.20$). Comparison between piezoelectric technique and traditional technique showed a statistically significant difference for IT values only in group 1 ($p = 0.029$). No differences were detected in groups 2 and 3 ($p > 0.05$) (Fig. 3 B).

ISQ value analysis

After traditional preparation, mean ISQ was 60.7±8.4 in group 1, 75.3±3.1 in group 2 and 81.3±3.4 in group 3. ISQ values were statistically different between the 3 groups. Specifically, group 1 showed ISQ values lower than those of group 2 ($p <0.01$) and group 3 ($p <0.01$) and group 2 showed ISQ values lower than those of the group 3 ($p <0.01$) (Fig. 4 A). Similar results were obtained for implants inserted after piezoelectric site preparation: mean ISQ was 65.0±4.7 in group 1, 75.1±4.3 in group 2 and 81.7±1.5 in group 3. ISQ value was significantly lower both in group 1 compared to groups 2 ($p < 0.01$) and 3 ($p <0.01$), and in the group 2 compared to the group 3 ($p <0.01$) (Fig. 4 B). Comparing the two surgical techniques, only group 1 showed a statistically significant difference in favor of piezoelectric surgery ($p <0.01$).

Time analysis

Mean time required for surgery using traditional technique was 492.1±13.9 s in group 1, 297.9±14.0 s in group 2 and 187.7±5.7 s in group 3. Mean time required for ultrasonic implant site preparation was 650.7±14.5 s in group 1, 518.6±16.2 s in group 2 and 427.3±9.0 s in group 3. Both for piezo and traditional techniques, the time was longer in group 1 compared to group 2 ($p < 0.01$) and to group 3 (p

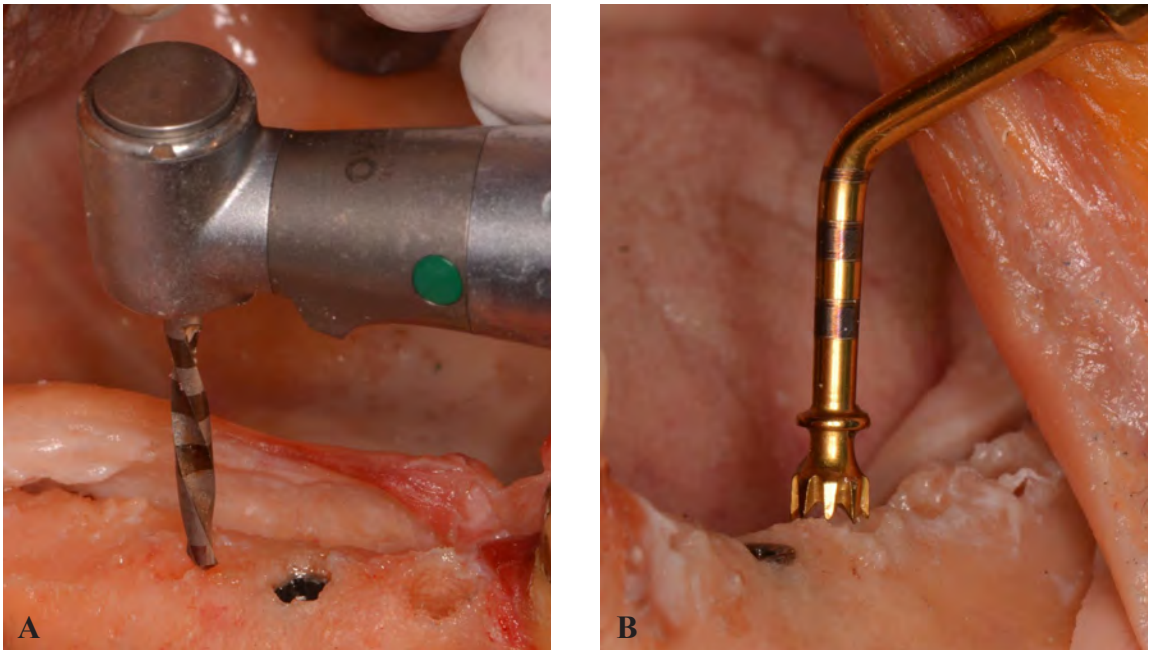


Fig. 1. ***A)*** *Traditional implant site preparation with 3.0 Ø tapered drill.* ***B)*** *Implant site preparation with piezoelectric surgery.*



Fig. 2. ***A)*** *Implant insertion.* ***B)*** *Recording of ISQ with PenguinRFA.*

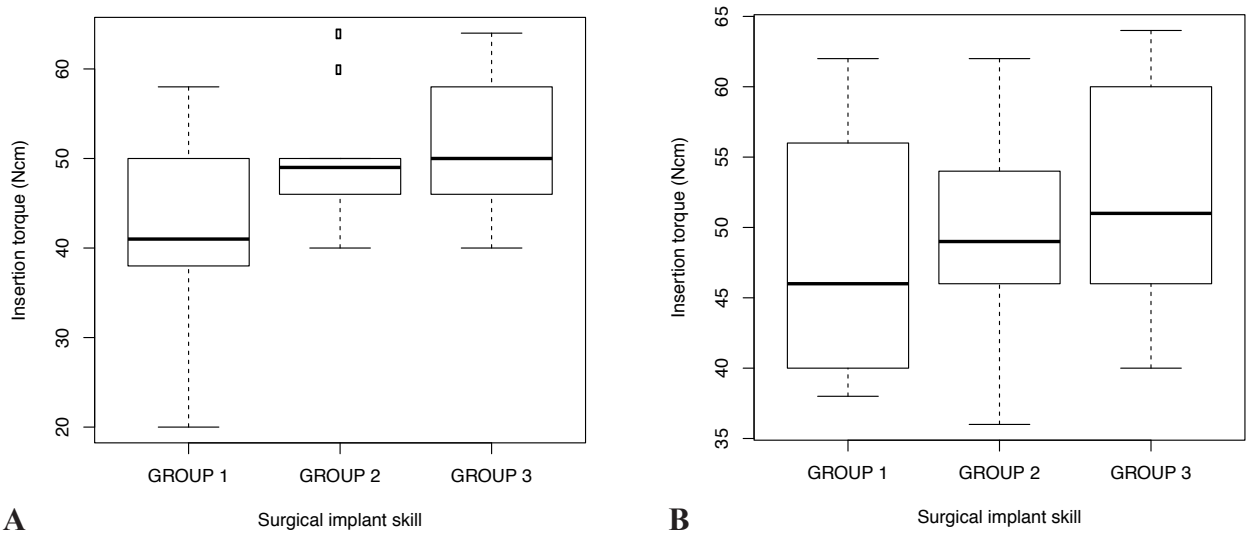


Fig. 3. ***A)*** *Boxplot of the distribution of IT according to the different clinician's experience groups related to traditional implant site preparation.* ***B)*** *Boxplot of the distribution of IT according to the different clinician's experience groups related to piezoelectric implant site preparation.*

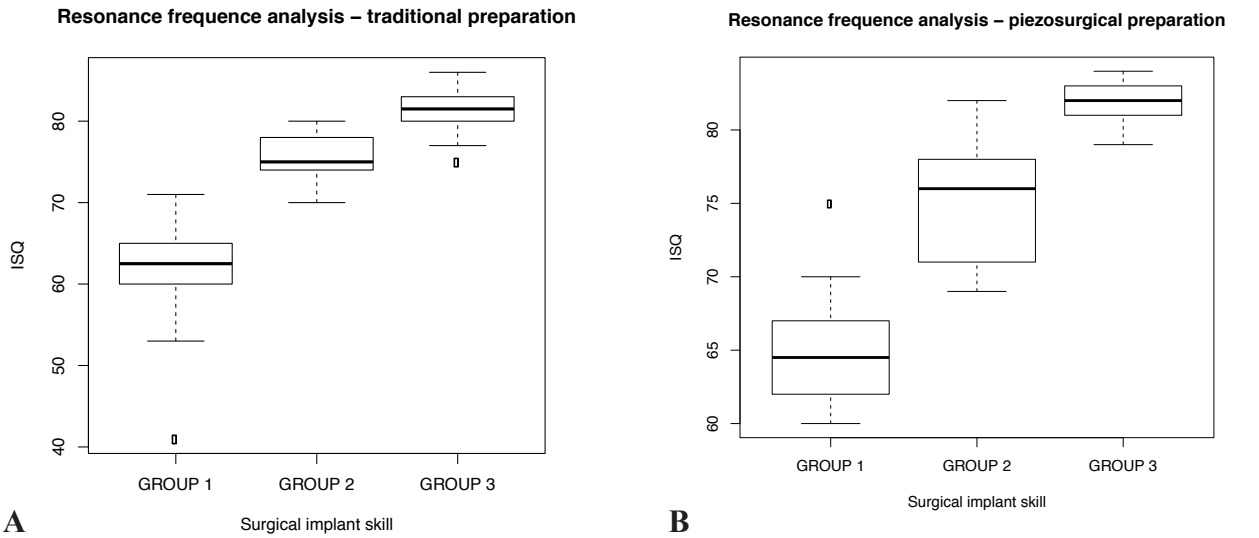


Fig. 4. ***A)*** *Boxplot of the distribution of ISQ values according to the different clinician's experience groups related to traditional implant site preparation.* ***B)*** *Boxplot of the distribution of ISQ values according to the different clinician's experience groups related to piezoelectric implant site preparation.*

< 0.01), and it was longer in group 2 compared to group 3 ($p < 0.01$). In all three groups, piezoelectric site preparation required a longer surgical time than traditional approach ($p < 0.01$).

DISCUSSION

As PS is one of the prerequisites for achieving successful osseointegration, without doubt the clinician's experience in implant placement is important to prevent failures (8). The insertion of an implant without an adequate PS or poor bone integration commonly leads to implant failure and rarely to its accidental migration (9). There is a lack of research in the literature regarding the effect of the level of experience on PS (3). To the best of the

Table I. *Mean values of IT, ISQ and time.*

Surgical Preparation Technique	Clinicians' experience	IT (Ncm)	ISQ	Time (s)
Traditional	Basic	42.0±10.5	60.7±8.4	492.1±13.9
	Medium	49.8±7.3	75.3±3.1	297.9±14.0
	Expert	50.8±8.0	81.3±3.4	187.7±5.7
Piezoelectric surgery	Basic	48.0±8.7	65.0±4.7	650.7±14.5
	Medium	49.4±8.1	75.1±4.3	518.6±16.2
	Expert	51.6±7.9	81.7±1.5	427.3±9.0

IT: insertion torque; ISQ: implant stability quotient

Authors' knowledge, the present study is the only one to compare the influence of the experience of the clinician on implant IT and RFA in fresh non-frozen cadaver mandibles with conventional and piezoelectric preparation techniques. IT alone is not a predictable value to assess implant PS. IT and RFA were demonstrated to be different and not comparable systems to assess implant stability (10, 11). We found significant relationship between the clinician's experience and IT among the three groups performing implant site preparation with twist drills. There were statistically significant differences between values of group 1 compared with groups 2 and 3 but no difference between groups 2 and 3. Conversely, no significant differences were found analyzing the three groups preparing implant sites using the piezoelectric technique. This result can be explained because of piezosurgical tips being slower and not customized for the implant system. ISQ values resulted significantly related to clinician's experience both in piezoelectric and traditional preparation groups: ISQ was significantly lower in group 1 compared to groups 2 and 3, also in group 2 compared to the group 3. Considering that RFA is more related to the amount of crestal bone surrounding the coronal part of the implant and high ISQ values are related to stiffness of the implant-bone interface, especially in the coronal region (12), the Authors hypothesised that high ISQ values in group 3 could be related to a proper implant vertical position and a better bone/implant contact, especially in the crestal area. The preparation technique had an influence on PS only considering the group of basic experience. Piezoelectric site preparation in group 1 resulted in higher IT and ISQ values than the traditional technique in the same group. This result is probably related to a better control compared with twist drills. Implant osteotomy with piezoelectric surgery needed more time for implant site preparation in all the three groups compared with traditional drilling osteotomy. In conclusion, our results showed that the clinician's experience seems to affect osteotomy preparation and implant placement, resulting in higher IT and ISQ values, especially when the traditional preparation technique was considered. Both experienced and inexperienced clinicians consistently achieved satisfactory PS in terms of IT and ISQ, especially after piezoelectric osteotomy.

ACKNOWLEDGEMENTS

The authors thank the companies Neoss, Mectron, Bien-Air for providing the materials for this study.

The authors also respect and are grateful to all the people who donated their bodies to the Institute of Anatomy of the Medical University of Vienna for teaching and medical research.

REFERENCES

1. Buser D, Sennerby L, Bruyn HD. Modern implant dentistry based on osseointegration: 50 years of progress, current trends and open questions. Periodontol 2000 2016; 73(1):7-21.
2. Attanasio F, Antonelli A, Brancaccio Y, et al. Primary stability of three different osteotomy techniques in medullary bone: an in vitro study. Dent J (Basel) 2020; 8(1) pii: E21. doi: 10.3390/dj8010021.

3. Romanos GE, Basha-Hijazi A, Gupta B, Ren Y-F, Malmstrom H. Role of clinicians experience and implant design on implant stability. an ex vivo study in artificial soft bones. Clin Implant Dent Relat Res 2012; 16(2):166-71.
4. Barone A, Alfonsi F, Derchi G, Tonelli P, Toti P, Marchionni S, Covani U. The effect of insertion torque on the clinical outcome of single implants: a randomized clinical trial. Clin Implant Dent Relat Res 2016; 18(3):588-600.
5. Stacchi C, Vercellotti T, Toschetti A, Speroni S, Salgarello S, Di Lenarda R. Intraoperative complications during sinus floor elevation using two different ultrasonic approaches: a two-center, randomized, controlled clinical trial. Clin Implant Dent Relat Res 2015; 17:e117-e125.
6. Vercellotti T, Stacchi C, Russo C, et al. Ultrasonic implant site preparation using piezosurgery: a multicenter case series study analyzing 3,579 implants with a 1- to 3-year follow-up. Int J Periodontics Restorative Dent 2014; 34(1):11-18.
7. Stacchi C, Vercellotti T, Torelli L, Furlan F, Lenarda RD. Changes in implant stability using different site preparation techniques: twist drills versus piezosurgery. a single-blinded, randomized, controlled clinical trial. Clin Implant Dent Relat Res 2011; 15(2):188-97.
8. Zupnik J, Kim S-W, Ravens D, Karimbux N, Guze K. Factors associated with dental implant survival: a 4-year retrospective analysis. J Periodontol 2011; 82(10):1390-95.
9. Giudice A, Colangeli W, Barca I, Riccelli U, Novembre D, Cristofaro MG. Accidental Displacement and Migration of an Endosseous Implant Into Submandibular Fossa. J Oral Implantol 2015; 41(3):323-25.
10. Lages FS, Douglas-de Oliveira DW, Costa FO. Relationship between implant stability measurements obtained by insertion torque and resonance frequency analysis: A systematic review. Clin Implant Dent Relat Res 2018; 20(1):26-33.
11. Baldi D, Lombardi T, Colombo J, Cervino G, Perinetti G, Di Lenarda R, Stacchi C. Correlation between insertion torque and implant stability quotient in tapered implants with knife-edge thread design. Biomed Res Int 2018; Article ID 7201093.
12. Sennerby L, Meredith N. Implant stability measurements using resonance frequency analysis: biological and biomechanical aspects and clinical implications. Periodontol 2000 2008; 47(1):51-66.

WITHDRAWAL STATEMENT

The Authors have requested to withdraw the following article from JBRHA Vol. 33 No. 6:

miR-1290 promotes proliferation and suppresses apoptosis in acute myeloid leukemia by targeting FOXG1/SOCS3